OVERLAPPING GRID SPECTRAL COLLOCATION METHODS FOR NONLINEAR DIFFERENTIAL EQUATIONS MODELLING FLUID FLOW PROBLEMS

A THESIS SUBMITTED TO THE UNIVERSITY OF KWAZULU-NATAL

FOR THE DEGREE OF DOCTOR OF PHILOSOPHY

IN THE COLLEGE OF AGRICULTURE, ENGINEERING & SCIENCE

By

Musawenkhosi Patson Mkhatshwa

School of Mathematics, Statistics & Computer Science

December 2020

Contents

i

Part A : Application of the overlapping grid spectral method in one space variable

Abstract

The focus of this thesis is on computational grid-manipulation to enhance the accuracy, convergence and computational efficiency of spectral collocation methods for the solution of differential equations in fluid mechanics. The need to develop highly accurate, convergent and computationally efficient numerical techniques for solving nonlinear problems is an ever-recurring theme in numerical mathematics. Spectral methods have been shown in the literature to be more accurate and efficient than some common numerical methods, such as finite difference methods. However, their accuracy deteriorates as the computational domain increases and when the number of grid points reaches a certain critical value. The spectral collocation algorithm produces dense matrix equations, for which there is no known efficient solution method. These deficiencies necessitate the development of spectral techniques that produce less dense matrix equations using fewer grid points. This thesis presents a new improvement in spectral collocation methods with particular application to nonlinear differential equations that model problems arising in fluid mechanics. The improvement described in this thesis requires the use of overlapping grids when descritizing the solution domain for Chebyshev spectral collocation method. The thesis is presented in two related subdivisions. In Part A, the overlapping grid approach is used only in space variable when solving nonlinear ordinary and partial differential equations. Subsequently, the overlapping grid approach is used in both the space and time variables in the solution of partial differential equations.

This thesis is also devoted to analysing solutions of fluid flow models through various practical geometries with particular interest in non-Newtonian fluid flows. The physics of these fluid flows is studied through parametric studies on the effects of diverse thermophysical parameters on the fluid properties, changes in shear stresses, and heat and mass transport. Key findings, are *inter alia*, that the overlapping multi-domain spectral techniques are computationally efficient, produce

stable and accurate results using a small number of grid points in each subinterval and in the entire computational domain. Using the overlapping grids yields less dense coefficient matrices that invert easily. Changes in thermophysical parameters has significant consequences for the fluid properties, and heat and mass transfer processes.

Preface

The work described in this thesis was carried out under the supervision of Prof S. S. Motsa and Prof P. Sibanda in the School of Mathematics, Statistics, & Computer Science, College of Agriculture, Engineering and Science, University of KwaZulu-Natal, Pietermaritzburg campus, from July 2018 to December 2020.

I hereby declare that except where due credit and reference is given, no portion of this work has been submitted wholly or in part for the award of any degree or qualification at this or any other university or institution of learning.

Signature:..................................

Musawenkhosi P. Mkhatshwa

17/12/2020

....

Date

Signature:..................................

Prof. S. S. Motsa

17 Dec 2020

....

Date

Signature:..................................

Prof. P. Sibanda

17-Dec-2020

....

Date

Declaration 1 - Plagiarism

I, **Musawenkhosi Patson Mkhatshwa** declare that:

1. the work reported in this thesis, except where otherwise indicated or acknowledged, represents my original research work;

2. this thesis has not been submitted in full or in part for any degree or examination at any other university;

3. this thesis does not contain other person's data, pictures, graphs or other information, unless specifically acknowledged as being sourced from other persons;

4. this thesis does not contain other person's writing, unless specifically acknowledged as being sourced from other researchers. Where other written sources have been quoted, then:

(a) their words have been rewritten but the general information attributed to them has been referenced;

(b) where their exact words have been used, their writing has been placed in italics and inside quotation marks, and fully referenced;

5. this thesis does not contain text, graphics or tables copied and pasted from internet, unless specifically acknowledged, and the source being detailed in the thesis and the References section.

17/12/2020

Signature: ....

Musawenkhosi P. Mkhatshwa   Date

Declaration 2 - Publications

This thesis is comprised of 7 published papers and 1 paper under review. All these papers were written by the student under the supervision of Prof S. S. Motsa and Prof P. Sibanda.

1. **M. P. Mkhatshwa**, S. S. Motsa, M. S. Ayano and P. Sibanda, Overlapping grid spectral collocation method for unsteady 3D hydromagnetic radiative flow of Casson nanofluid over a stretching surface with variable fluid properties, (Under Review: *Applied Mathematics and Computation*).

2. **M. P. Mkhatshwa**, S. S. Motsa and P. Sibanda, Overlapping Multi-domain Bivariate Spectral Method for Systems of Nonlinear PDEs with Fluid Mechanics Applications. In: Rushi Kumar B., Sivaraj R., Prakash J. (Eds). Advances in Fluid Dynamics. *Lecture Notes in Mechanical Engineering*, Springer, Singapore, 2021, 685-699. https://doi.org/10.1007/978-981-15-4308-1_54.

3. **M. P. Mkhatshwa**, S. S. Motsa, M. S. Ayano and P. Sibanda, MHD mixed convective nanofluid flow about a vertical slender cylinder using overlapping multi-domain spectral collocation approach, *Case Studies in Thermal Engineering*, 18 (2020) 100598. https://doi.org/10.1016/j.csite.2020.100598.

4. **M. P. Mkhatshwa**, S. S. Motsa and P. Sibanda, Overlapping multi-domain spectral method for conjugate problems of conduction and MHD free convection flow of nanofluids over flat plates, *Mathematical and Computational Applications*, 24 (3), 75, 2019. https://doi.org/10.3390/mca24030075.

5. **M. P. Mkhatshwa**, S. S. Motsa and P. Sibanda, Overlapping multi-domain spectral method for MHD mixed convection slip flow over an exponentially decreasing mainstream with

non-uniform heat source/sink and convective boundary conditions, *International Journal of Computational Methods*, 2020. https://doi.org/10.1142/S0219876221500043.

6. **M. P. Mkhatshwa**, S. S. Motsa and P. Sibanda, MHD bioconvective radiative flow of chemically reactive Casson nanofluid from a vertical surface with variable transport properties, *International Journal of Ambient Energy*, 2020.
   https://doi.org/10.1080/01430750.2020.1818126.

7. **M. P. Mkhatshwa**, S. S. Motsa and P. Sibanda, Numerical solution of time-dependent Emden-Fowler equations using bivariate spectral collocation method on overlapping grids, *Nonlinear Engineering-Modelling and Application*, 2020; 9: 299–318.
   https://doi.org/10.1515/nleng-2020-0017.

8. **M. P. Mkhatshwa**, S. S. Motsa and P. Sibanda, MHD mixed convective radiative flow of Eyring-Powell fluid over an oscillatory stretching sheet using bivariate spectral method on overlapping grids, *Heat Transfer*, 2020; 1–33. https://doi.org/10.1002/htj.21898.

In all these articles, my contribution was to formulate the research problems, to solve the mathematical equations, conduct simulations and prepare a draft of each paper.

Signature: ....

Musawenkhosi P. Mkhatshwa

17/12/2020

....

Date

Acknowledgments

Dedication

This thesis is dedicated to my lovely wife Fezile and my son Nkosiyenzile who have been my source of inspiration and gave me strength during difficult times in my studies. I will forever be grateful for the moral, spiritual, emotional and financial support my wife gave me.

Chapter 1

Introduction

1.1   Background and motivation

Most real life problems occurring in diverse disciplines in science, economics and engineering are modelled using ordinary and partial differential equations [1]. In engineering for instance, differential equations are encountered in fluid dynamics. These differential equations are used in the design of containers and funnels, in heat conduction analysis for the design of heat spreaders in micro-electronics, and in combined heat conduction and convection on which the design of heating and cooling chambers is dependent [2]. According to Hale and Moore [3], solutions of differential equations are important in modelling and predicting the future state of the phenomena being studied. However, most differential equations are highly nonlinear, and thus challenging to solve using analytic approaches. For this reason, we make use of numerical methods to tackle complex differential equations with strong nonlinearities The challenge remains to find sufficiently accurate, convergent and computationally efficient numerical methods for solving highly nonlinear differential equations. As a result, many researchers devote time to developing numerical techniques that are not computationally expensive, are accurate and converge quickly, so that deficiencies in existing methods may be alleviated. The objective of this study is to propose numerical techniques that are computationally efficient and make use of the least number of possible grid points to obtain suitably accurate solutions. The complexity in obtaining solutions to differential equations increases from ordinary to partial differential equations. For this reason, the central theme of this thesis is the testing of the new methods on some problems modelled using partial differential

equations, to establish the applicability and efficiency of the methods.

Flow problems, with heat and mass transport, arise in both natural and man-made practical situations. In the recent past years, a growing number of researchers have used various fluid flow models to study such problems. Among these models, are Newtonian and non-Newtonian fluid flow models. Much research attention has been given to non-Newtonian fluids because heat and mass transport are complicated to understand through Newtonian fluid models. Also, non-Newtonian fluids contribute significantly in engineering, biomedical, petroleum and industrial applications. The flow properties of non-Newtonian fluids vary from those of Newtonian fluids in many ways. For example, a constant coefficient of viscosity is inappropriate for non-Newtonian fluids due to the relationship between the strain rate and the shear stress being nonlinear, and time-dependent [4]. The fluid viscosity depends on the applied shear force and, on the rate at which the resultant shear takes place. There is, however, no single constitutive equation to describe the flow and features of non-Newtonian fluids, due to the complexity and wide differences in the physical structure of these fluids. Consequently, non-Newtonian fluid models take into account different constitutive relations that model their behaviour and rheological characteristics. The equations characterizing such relations are highly nonlinear and complex in comparison to those of a Newtonian fluid. Also, the viscosity of non-Newtonian fluids is generally higher than that of Newtonian fluids. Accordingly, in flow and heat transfer processes, the pressure drop is high and heat transfer coefficient is particularly low [5].

To enhance heat transfer in fluids, solid nanoparticles are suspended in base fluids such as oil and water. Nanoparticles are exceptionally small, with a diameter of the order of a nanometre. The fluid formed is called a nanofluid [6]. When traditional fluids have these tiny solid particles suspended in them, their thermal conductivity improves leading to their heat transfer characteristics being enhanced [7]. According to Bhanvase et al. [8], the higher thermal conductivity of the suspended nanoparticles accounts for the improved thermophysical properties and thermal performance of the nanofluid compared to the base fluids. Traditional fluids with nanoparticles incorporated into them form non-Newtonian nanofluids. Several researchers focused attention on

2

flow characteristics and behaviour of non-Newtonian nanofluids due to their applications in industry and transportation [9]. Since the motion of non-Newtonian nanofluids is complex and difficult to model owing to the nonlinear relationship between the stress and the rate of strain, they are modelled using nonlinear equations. Solving these complex nonlinear equations necessitates applying computationally efficient, fast converging and sufficiently accurate numerical methods. The current work investigates flow, heat and mass transport and the movement of motile microorganisms in various non-Newtonian fluids. We also focus on numerical solution of flow models for nanofluids in various flow geometries and subject to different boundary conditions. The chemical and physical behaviours of nanofluids are investigated for the the impact of various physical and chemical parameters. In this study, efficient overlapping grid spectral collocation methods are presented and used to obtain numerical solutions. In the rest of this chapter, we give a brief discussion of heat, mass and motile microorganisms movement, non-Newtonian fluids, nanofluids, thermal radiation, variable fluid properties and relevant numerical approaches in the literature. We end with a statement of the research objectives and a statement on the structure of the thesis.

1.2   Heat, mass and motile microorganisms transports

In this study, we investigate heat and mass transport, and the movement of motile microorganisms in various fluid flow models. The importance of heat transfer in modern engineering designs cannot be overemphasized. When designing and operating devices like air-conditioners and refrigeration systems it is crucial to take into consideration efficiency in heat exchangers [10]. Thus, an efficient design makes allowances for maintaining reasonable temperatures through sufficient transfer of heat. Heat transfer involves thermal energy transfer because of temperature differences [11, 12]. There are three forms of heat transfer, namely, conduction, convection and radiation [13]. Conduction is a mechanism in which heat energy is transmitted from a region of higher temperature to a region of lower temperature by kinetic molecular motion and molecular collisions, whether the bulk medium is stationary or in motion. Heat transportation by conduction is a result of temperature differences, the material comprising the medium and its thickness [14]. In the overall layer, the rate of heat conduction is proportionally correlated to the heat transfer region and the temper-

ature differences, and is inversely related to the thickness of the layer. Convection takes place in fluids by either diffusion or advection, or a combination of both [15]. Diffusion is characterized by random molecular motion of the fluid, while advection occurs when the fluid motion itself transports energy from one region to another in the medium. Lastly, radiation occurs when heat energy is transported by electromagnetic waves in the absence or presence of an intervening medium [16]. Pure conduction occurs in solids whereas heat transfer by convection takes into account fluid motion and heat conduction. Convective heat transfer involves heat transfer by both conduction and convection. Forced, natural and mixed convection are classes of convective heat transfer which depend on how the fluid motion is started. Forced convection is due to the external forces acting on a heated body [17]. Natural convection takes place as result of buoyancy forces which emerge from density differences in a fluid. These differences are due to temperature and concentration gradients in the fluid. Researchers who have considered natural convection flows include Jaluria and Himasekhar [18], and Kraus et al. [19] to name a few. Mixed convection is a blending of forced and free convection through an external forcing mechanism and internal volumetric forces.

Mass transfer involves the transportation of one constituent from a region of high concentration to a region of low concentration due to difference in concentration [20]. Mass transfer is important in countless industrial processes, such as the removal of pollutants from plant discharge streams by absorption, the stripping of gases from waste water, or neutron diffusion within nuclear reactors. Molecular diffusion and convection are two forms of mass transfer. Diffusion is on account of the movement of molecules in a fluid by random motion, from a region of high concentration to one of low concentration. Mass convection is due to a mechanical force or action to maximize the rate of molecular diffusion. Motile microorganism transfer involves the transportation of microorganisms through physical mechanisms. Convection, self-propelled motion and random movement are the basic modes of motile microorganism transfer. In convective transport, microorgansisms are transported by the fluid. Self-propelled motion is due to the swimming of the microorganisms, while the random microorgansisms motion may be due to diffusion processes.

1.3 Non-Newtonian fluids

Many industrial and biological fluids including synthetic lubricants display nonlinear behavioural characteristics. The constitutive relations for non-Newtonian fluids are complex and of a higher order to those of Newtonian equations. There is a variety of non-Newtonian fluid models [21–23] that have been proposed to describe fluids of practical interest. Fluids demonstrating non-Newtonian rheology have captured the attention of a lot of researchers owing to their variety of practical use in metallurgical processes, crystal growth, fiber technology, wire drawing and food products. To demonstrate the complete properties of these fluids, any single fluid model is not enough since it may address only some properties and fail to predict others. The non-Newtonian fluid models of particular interest in this study include Casson and Eyring-Powell fluid models.

1.3.1 Casson fluid

The Casson fluid model has been extensively used in several flow scenarios, after the first proposal in Casson [24]. This model involves a plastic fluid model which exhibits shear thinning characteristics, yield stress and higher shear viscosity. The Casson fluid model becomes a Newtonian fluid model when the wall shear stress is considerable higher than yield stress [25]. Casson fluid model is also suitable in approximating the rheological behaviour of other fluids involving physiological suspensions, foams, cosmetics, and syrups. The Casson fluid model is still the most significant non-Newtonian fluid possessing a yield value. Studies involving Casson fluids plays a significant role in heat transfer processes, food processing, bioengineering operations, mechanical, chemical and engineering processes. Because of these applications, several researchers have considered characteristics of Casson fluid in various geometries. For instance, Oyelakin et al. [26] solved the problem of MHD flow of Casson nanofluid over an unsteady stretching sheet using the spectral quasilinearisation method. They found that increasing the Casson fluid parameter leads to the fluid reducing to Newtonian behaviour. Prashu and Nandkeolyar [27] applied the spectral quasilinearisation method in solving the equations that describe the MHD flow of a Casson fluid over a stretching surface. Their results showed that as the yield stress increases, the momentum boundary

layer in the *x*- direction becomes thinner and the change in shear stress along the *x*- direction diminished. Also, the velocity of the fluid in the *z*- direction increased near the surface and reduced away from the surface with increment in the yield stress. However, the skin friction coefficient in the *z*- direction enhanced with increasing the yield stress.

1.3.2   Eyring-Powell fluid

Many researchers have examined the behaviour of the Eyring-Powell fluid model [28] in various flow geometries, owing to its particular advantages when compared with other non-Newtonian fluids. Eyring-Powell fluid model is beneficial in the sense that it is deduced from kinetic theory of liquids rather than the empirical relation. Also, it correctly reduces to Newtonian (viscous) behaviour for low and high shear rates. Such model signifies the behaviour of viscoelastic suspension and polymeric solutions against extensive ranges of shear rates. The Eyring-Powell liquid can be used to express the flows of modern industrialised equipments like powdered graphite and ethylene glycol. Agbaje et al. [29] used the multi-domain bivariate spectral quasilinearisation method to solve the equations that model the flow of Powell-Eyring nanofluid over a shrinking surface. Their results showed that the flow velocity together with momentum boundary layer thickness accelerated with Eyring-Powell fluid parameters. Ogunseye et al. [30] used the Eyring-Powell fluid to scrutinize thermal properties and flow structure of a nanofluid over a cylinder using spectral quasilinearisation method. They reported that the changes in shear stress decreased with increasing the Eyring-Powell fluid parameter. The bivariate spectral quasilinearisation method was used by Ogunseye et al. [31] in analyzing the flow of Eyring-Powell nanofluid through a permeable stretching surface. Among their findings, they found that increment in the Eyring-Powell fluid parameter caused decrement in the fluid viscosity.

1.4   Nanofluids

The relevance of nanofluids in the current study lies in their performance being significantly better in heat and mass transfer processes when compared to traditional fluids. In the past few years,

flow, heat and mass transmission in nanofluids have been an area of interest to a lot of scholars owing to their valuable applications in industry, technology and medicine. These applications are found in transportation, micro-electronics, fuel cells, hybrid-powdered engines, cancer therapy and drug delivery [32, 33]. The notion of nanofluids was introduced by Choi and Eastman [6] and entails the suspension of solid nanoparticles in traditional fluids like water, ethylene glycol, kerosene and engine oil. These base fluids possess low thermal conductivity and the addition of nano-sized metallic or non-metallic particles into the base fluids enhances their thermal conductivity. Choi and Eastman [6] found that adding as little as 1% of nanoparticles to the base fluid doubles the thermal conductivity of the normal fluid. The heat transfer improvement technology has been mostly utilized in heat exchangers, refrigerators, automobiles and the chemical industry. The most significant parameters for improving the heat transfer of nanofluids are the nanoparticle concentration and size of the particles [34]. In the Buongiorno model [34], the concentration of nanoparticles are assumed to fluctuate, through mechanisms such as Brownian motion and particle thermophoresis. Many researchers [35–37] have considered flow, heat and mass transfer problems in nanofluids over various geometries.

1.5   Impact of variable fluid properties

Most existing surveys on flow, heat and mass transfer in fluids have considered constant physical properties of the ambient fluid. Nevertheless, it is common cause that these features may vary significantly with temperature [38]. For accurate modelling of the flow, heat and mass transport, it is essential to regard changes in the fluid viscosity, thermal conductivity and mass diffusivity. Flows of a viscous and incompressible fluid have been studied under various physical assumptions such as variable fluid properties [39, 40]. By considering variable transport properties the impact on the velocity and temperature profiles can frequently be established, thus giving better insights into friction and heat transfer rates than could be understood if the properties were constant. Several researchers have considered flows of non-Newtonian fluids in different geometries taking into account fluid properties of a variable nature. Elgazery and Abd Elazem [41] studied the influence of variable thermal conductivity on an unsteady MHD free convection in a micropolar fluid flow

over a semi-infinite vertical porous plate using the Chebyshev collocation method. They found that the fluid temperature increased as the thermal conductivity and radiation parameters increase. Oyelakin and Sibanda [42] considered the importance of variable fluid properties on a tangent hyperbolic fluid flow past a flat impermeable surface. Their major findings included that altering the viscosity minimizes fluid flow resistance and causes an increase in the fluid velocity whereas the temperature and species concentration increase with the variable fluid viscosity. The Chebyshev-spectral collocation method was used by Idowu et al. [43] in analyzing MHD free convective flow, heat and mass transfer in dissipative Casson fluid with variable transport properties. They reported that the introduction of variable viscosity diminishes the velocity field near the wall while improving the velocity and temperature of the fluid in the free stream region. Also, the variable thermal conductivity enhances the temperature field throughout the entire boundary region. Flow and heat transport in a non-Newtonian Eyring-Powell nanofluid over a stretching sheet with variable viscosity and thermal conductivity was studied by Ogunseye et al. [44] via the spectral local linearization method. Idowu and Falodun [45] applied the spectral homotopy analysis method in the numerical study of a Waters-B viscoelastic and a Casson fluid flow taking into account variable thermal conductivity and viscosity. Their outcomes indicated that the inclusion of thermal conductivity and viscosity of a variable nature improves the velocity and temperature distributions because of augmentation in the Casson and Walters-B viscoelastic parameters.

1.6 Thermal radiation

Thermal radiation is radiation emitted by all bodies when the body's internal energy is transformed to electromagnetic radiation by the movement of electrons and protons in the material [46]. Examples of sources of thermal radiation include the sun, an open fire, heating elements on a stove or a radiator, etc. The influence of thermal radiation on boundary layer flow problems is significant owing to its extensive applications in physics, engineering, industry and space technology. Such applications are found in glass production, furnace design, polymer processing, gas-cooled nuclear reactors, rockets propulsion systems, power plants and spacecraft which operate at high temperature. In such applications, the effects of thermal radiation may not be neglected. The sig-

nificance of thermal radiation in modelling the flow and heat transportation in a viscous fluid past an unsteady stretched sheet was emphasized by Pal [47]. Thermal radiation is often approximated using the Rosseland approximation [48] to describe the radiation heat flux in the energy equation. Most previous studies have considered a Rosseland approximation with a linear form, instead of the nonlinear form, which has been recently used by several scholars. The linearized Rosseland approximation is appropriate only for smaller temperature variances. However, the nonlinear Rosseland diffusion is authentic for both smaller and greater temperature variances. The current work presents fluid flow problems that use both linear and nonlinear Rosseland approximation. Oyelakin et al. [49] considered the importance of nonlinear radiative heat flux and variable transport properties on heat and mass transport in the flow along a wedge of a bioconvective Casson nanofluid comprising gyrotactic microorganisms. Gangadhar et al. [50] employed the spectral quasilinearisation approach to analyze the flow of micropolar ferrofluid with thermal radiation. They showed that the temperature field of a micropolar magnetic ferrofluid is higher than that in a classical micropolar fluid when radiation effects are taken into account.

1.7   Numerical solution techniques

This section gives a brief review of recently developed spectral collocation methods of interest in this study. The strengths and weaknesses of these methods are described. The deficiencies in existing methods that will be mitigated by the current work are highlighted. Many fluid flow problems arising in science and engineering are modelled using highly nonlinear differential equations with strong coupling. The complexity of such systems of differential equations makes it difficult to find closed form analytic solutions. For this reason, we often resort to obtaining approximate solutions using numerical methods. Over the years, various numerical techniques have been introduced and used successfully for finding numerical solutions of systems of nonlinear differential equations. These traditional methods include the Runge-Kutta method [51], finite difference method [52], finite element method [53], element free Galerkin method [54] and Keller-Box method [55]. These methods have good properties but also have limitations such as being computationally expensive, having low convergence rates and requiring many grid points to achieve sufficiently accurate re-

sults. These numerical approaches have also been reported as being ineffective in problems with discontinues, singularities or multiple solutions [56]. Consequently, the development of numerical approaches that are computationally fast, converge quickly, and utilize fewer grid points to give accurate solutions of nonlinear problems remains an active area of research. Spectral methods have been established to have such desirable features. When compared to many common methods, they are computationally less expensive, converge rapidly and utilize a low number of grid points to yield sufficiently accurate solutions, particularly when the solution is smooth. The algorithm for the spectral collocation method is easy to apply to practical problems. Among the recently developed spectral collocation-based methods, is the spectral perturbation method (SPM), spectral homotopy analysis method (SHAM), spectral quasilinearisation method (SQLM), bivariate spectral local linearisation method (BSLLM) and bivariate spectral quasilinearisation method (BSQLM). These spectral methods converge quickly and give accurate results when the time domains are small. Nevertheless, the accuracy deteriorates when the computational domain becomes large. To overcome this limitation, utility of techniques such as the SQLM and BSQLM has been improved by using the multi-domain technique in the time variable. In these procedure, the computational time domain is partitioned into non-overlapping subintervals. A continuity condition is utilized to advance the solution throughout the non-overlapping subintervals.

The above-mentioned spectral methods have many advantages, but there remain limitations that need to be addressed. The spectral collocation methods lead to dense matrix equations, for which there is no known efficient solution method. Also, the accuracy should increase with increment in the number of grid points, however, when the number of grid points exceed a particular number, the accuracy has been noted to deteriorate rapidly. This is explained by the large number of grid points in the spectral method yielding bigger and fuller matrices, which require large memory for storage. In this study, we develop spectral collocation methods with improved accuracy achieved using the least number of grid points and through making the coefficient matrices in the matrix equation to be less dense. The novelty of the modified algorithm involves computational grid-manipulation by using the overlapping grids in the Chebyshev spectral collocation method. Numerous researchers have used overlapping multi-domain approaches together with pseudo-spectral methods. Olmos

10

and Shizgal [57] used the overlapping multi-domain pseudo-spectral approach in finding numerical solutions of the Fisher's equation. On the other hand, Taleei and Dehghan [58] applied the overlapping multi-domain pseudo-spectral method to obtain the numerical solution of one and two dimensional sine Gordon equations. Their findings showed that round-off error in the Chebyshev spectral collocation can be reduced by decomposing the main domain into smaller subintervals. The multi-domain technique establishes sparsity in the differential matrices, utilizes low memory and less computational time. As a result, the overlapping multi-domain scheme yields stable and accurate solutions. In this study, we propose using overlapping grid spectral collocation methods for the numerical simulation of highly nonlinear differential equations modelling problems in fluid mechanics. The overlapping grid spectral collocation scheme is used together with the SQLM and BSQLM techniques. The solution procedure multi-faceted involves linearisation, domain decomposition, grid manipulation and numerical discretization of the linearised equations. The applicability, accuracy and reliability of these methods are verified through a determination of convergence and residual errors. In cases where exact solutions are available, approximate solutions are collated with analytic solutions to authenticate the accuracy of the numerical approximations. Unlike other versions of multi-domain spectral collocation methods, solutions in the overlapping grid spectral methods are computed simultaneously across all the overlapping subintervals.

1.7.1   Spectral quasilinearisation method

The Chebyshev spectral quasilinearisation method (SQLM) is a generalisation of the Newton-Raphson quasilinearisation method (QLM) developed by Bellman and Kalaba [59] for numerical solution of nonlinear differential equations. The SQLM approach [56] entails linearisation of the nonlinear differential equations using the Taylor series by assuming that the difference between the current and previous iteration is small. The Chebyshev spectral method is then used to solve the resultant system of linear equations. Several studies [60–62] have successfully used the SQLM to solve nonlinear ordinary differential equations arising in boundary layer fluid flows. Motsa et. al [63] was the first to apply the SQLM approach in solving systems of nonlinear partial differential equations that modelled unsteady boundary layer flows. They used the spectral collocation method

for the numerical discretization of the space variable while the implicit finite difference method was used to discretize the time variable. In this study, the SQLM is modified and used in Chapter 2 to solve a system of ordinary differential equations.

1.7.2 Bivariate spectral quasilinearisation method

It is known that using implicit finite difference methods to discretize in the time variable compromises the accuracy of the method because finite differences need much computational time and a lot of grid points to achieve accurate solutions. To overcome this weakness, Motsa et al. [64] established the bivariate spectral quasilinearisation method (BSQLM), which applies the spectral collocation method independently in space and time. The BSQLM uses the QLM technique, Chebyshev spectral collocation method and bivariate Lagrange interpolation polynomial with Chebyshev-Gauss-Lobatto grid points. It was found that the accuracy improved, particularly for small sized computational time domains. Nevertheless, the level of accuracy was found to deteriorate with larger time domain. Subsequently, the multi-domain bivariate spectral quasilinearisation method (MD-BSQLM) [65, 66] was introduced as an alternative to improve accuracy for larger time domains. The method has been used to solve nonlinear evolution PDEs and a system of nonlinear PDEs of boundary layer flow. It was concluded that, when compared to the single-domain spectral method, the multi-domain spectral method is more accurate and uses less computational time. Also, the accuracy of the multi-domain spectral method did not deteriorate rapidly with an increase in the time domain. In this study, the BSQLM is improved and used to obtain solutions of partial differential equations in Chapters 3 - 9.

1.8 Thesis objectives

The intention of this thesis is to present a new improvement to spectral collocation methods by using a multi-domain technique together with an overlapping grid approach. The development of the overlapping grid spectral collocation methods is described for highly nonlinear and coupled differential equations with fluid mechanics applications. We also demonstrate the applicability,

reliability and general performance in terms of efficiency, accuracy and convergence of the overlapping grid spectral collocation schemes in systems of nonlinear differential equations. The convergence of the methods is assessed through the evaluation of error norms between two successive iterations. The accuracy of the numerical schemes is measured through a determination of residual errors. The results obtained are validated by comparison with those in previously published works to evaluate the accuracy and efficiency of the new method. The study further considers the construction and analysis of fluid flow models in various geometries, and subject to different source terms and boundary conditions. The geometries include an oscillatory stretched surface, vertical cylinder, vertical and horizontal flat plates, that pose several challenges in terms of complexities of the flow equations. Several models of non-Newtonian fluid flows are analyzed and the equations are solved using the overlapping grid spectral collocation methods. To gain an understanding of the physical importance of the variables that affect the flow, a limited parametric studies are presented focusing on the influence of key fluid and physical parameters, including variable fluid properties, nanoparticle volume fraction, thermal radiation, cross-diffusion effects, chemical reaction, Brownian motion, thermophoresis, Hall and ion-slip currents on the fluid properties including the heat and mass transport.

1.9 Thesis structure

The main body of the thesis is divided into two related parts comprising eight chapters. Part A comprises Chapters 2 - 7, which are concerned with the use of overlapping grid approach only in space variable when extending the SQLM and BSQLM. Part B consists of Chapters 8 - 9, whose purpose is to demonstrate the development and application of the overlapping grid approach in space and time variables when extending the BSQLM. In chapter 2, the overlapping grid spectral quasilinearisation method is developed and used to solve nonlinear ordinary differential equations describing an unsteady three-dimensional MHD flow of Casson nanofluid over a stretching surface. The domain is partitioned into overlapping subintervals and the solutions are computed simultaneously across all subintervals. Chapters 3 -7 are concerned with the application of the multi-domain technique and the extension of the use of the overlapping grid approach for strongly coupled non-

linear parabolic differential equations of boundary layer flow. The time domain is partitioned into non-overlapping subintervals while the space domain is divided into overlapping subintervals of equal length. The linearized partial differential equations are solved independently through each time subinterval, while the solutions in the space interval are obtained simultaneously throughout all the overlapping subintervals. Because naturally arising phenomena and their respective dynamics are captured using partial differential equations with strong nonlinearity, the numerical methods have been tested in systems of partial differential equations modelling some fluid flow problems in various geometries. Chapter 3 gives a detailed presentation on the development of the overlapping multi-domain bivariate spectral quasilinearisation method (OMD-BSQLM) and its application in finding solutions of higher order partial differential equations. The numerical technique has been tested on two-and three- equation coupled systems from literature. In Chapter 4, the OMD-BSQLM is used to solve the equations that describe an MHD-conjugate heat transfer problem in nanofluids over both a vertical and horizontal flat plate. The study considers the significance of heat generation and radiative heat flux on the MHD-conjugate flow of nanofluids. Chapter 5 focuses on the use of the OMD-BSQLM in solving equations that model MHD convective flow, heat and mass transport of nanofluids through a vertical cylinder. The study take into account the impact of chemical reaction, Hall current and cross-diffusion effects on the fluid properties in the case of nanofluid and pure fluid, and vertical cylinder and flat plate. In Chapter 6, an exploration of the performance of the OMD-BSQLM on MHD mixed convective flow for an exponentially decreasing free stream velocity with a chemical reaction and non-uniform heat source/sink effects is presented. The study considers the scrutiny of the flow problem subject to suction/injection, velocity slip and convective boundary conditions. Chapter 7 demonstrates the use of the OMD-BSQLM in finding solutions of partial differential equations that model the MHD flow of Casson nanofluid over a vertical surface with gyrotactic microorganisms and temperature dependent fluid properties. The zero nanoparticle flux is assumed and nonlinear thermal radiation, chemical reaction, Brownian motion and thermophoresis effects are discussed.

In Chapters 8 - 9, the BSQLM is extended by splitting both the time and space intervals into overlapping subintervals of equal length. The solutions are computed simultaneously across all

overlapping subintervals. Chapter 8 focuses on testing the numerical technique on linear and non-linear Emden-Fowler partial differential equations with applications in fluid mechanics. Chapter 9 is concerned with the use of the overlapping grid BSQLM to find solutions of coupled nonlinear partial differential equations modelling the flow of Powell-Eyring fluid through an oscillatory stretched surface. Nonlinear thermal radiation, chemical reaction, heat generation/absorption and variable fluid properties are assumed in this study. Finally, in Chapter 10, we conclude the study with a summary of the main findings. We highlight the main contributions of the study, with possible future extensions.

Part A:
Application of the overlapping grid spectral method in one space variable

Chapter 2

Overlapping grid spectral collocation method for unsteady three-dimensional hydromagnetic radiative flow of Casson nanofluid over a stretching surface with variable fluid properties

In this chapter, the overlapping grid approach is introduced and used in the spectral quasilineari-sation method to solve ordinary differential equations that model the three-dimensional hydro-magnetic Casson nanofluid flow along a stretching sheet. In the analysis, we take into account the effects of nonlinear thermal radiation, thermophoresis, Brownian motion, suction/injection and Hall current. The fluid viscosity and thermal conductivity are assumed to vary with the temper-ature. The convergence and accuracy of the numerical approximations are assessed through the evaluation and analysis of error norms and residual errors. The influence of various dimensionless parameters on the flow profiles, skin friction coefficient, heat and mass transfer characteristics are studied.

Overlapping grid spectral collocation method for unsteady 3D hydromagnetic radiative flow of Casson nanofluid over a stretching surface with variable fluid properties

M. P. Mkhatshwa [1a], S. S. Motsa[a,b], Mekkonen S. Ayano[b], P. Sibanda[a]

[a]*School of Mathematics, Statistics & Computer Science University of Kwazulu Natal, Private Bag X01, Scottsville, 3209, Pietermaritzburg, South Africa*
[b]*Department of Mathematics, University of Eswatini, Eswatini*

Abstract

In this work, modified spectral quasilinearisation method (SQLM) is presented and applied in the analysis of unsteady three-dimensional hydromagnetic flow of Casson nanofluid along a stretching sheet with nonlinear thermal radiation, thermophoresis, Brownian motion, suction/injection and Hall effects. The viscosity and thermal conductivity of the Casson nanofluid are assumed to be temperature-dependent. The time dependent flow equations are first non-dimensionalized and then solved numerically using the SQLM on overlapping grids. The convergence and accuracy of the method are demonstrated using convergence and residual error analysis. The SQLM on overlapping grids is computationally fast and yields accurate results after few iterations and using less grid points in each sub-domain and the whole domain. The overlapping grid improves accuracy through making the coefficient matrix in the equations resulting from the collocation process to be less dense. The influence of important physical parameters on the flow profiles, skin friction coefficient, heat and mass transfer characteristics are scrutinized. We found that escalating variable fluid parameters diminishes the velocity profiles while enhancing thermal and concentration fields. The heat and mass transfer rates intensify when nonlinear radiation heat fluxes and temperature dependent thermal conductivity are introduced into the system, whereas decrease with the inclusion of variable viscosity. The impact of

---

[1]Corresponding author. Email:patsonmkhatshwa@gmail.com

physical parameters is more sensitive with variable thermal conductivity and unsteadiness when compared with constant thermal conductivity and steadiness case. Applications of the current study arise in magnetic field control of materials processing systems, printing industry and polymer engineering.

Keywords: Casson nanofluid, variable fluid properties, radiation, Hall current, Spectral quasilinearisation method, multidomain overlapping grid

1. Introduction

The flow, heat and mass transfer problem due to a stretching surface has many applications in industrial and manufacturing processes, aerodynamic extrusion of plastic or rubber sheets, wire drawing, hot rolling, cooling of an infinite metallic plate in a cooling bath, crude oil extrusion. Considering that a quick stretching can damages the characteristics of the final product because of sudden solidification, it is very important to manage the stretching rate. Crane [1] was the first to consider the problem of boundary layer theory for linearly stretching surface. The flow along stretching surface has been subsequently extended by many authors [2, 3, 4, 5, 6, 7, 8] in Newtonian and non-Newtonian flow models.

Nanofluid describes the suspension of a nanometer-size solid particles and fibres in convectional base fluids like water, ethylene glycol, engine oil, etc. The word "nanofluid" along with a mixture of nanoparticles and base fluids such as oil, water and ethylene glycol came into existance through the work of Choi [9]. Nanoparticles are suspended much longer than mille and micrometer-sized particle with low gravitational properties and increase the heat transfer rate at any physical aspects. In the era of energy saving and the widespread use of battery operated devices, such as cellphones and laptops, a smart technological handling of energetic resources is necessary. Nanofluids have been demonstrated to be able to play this role in some instances. A comprehensive survey of convective transport in nanofluids was made by Buongiorno [10] who considered seven slip mechanisms that can produce a relative velocity between nanoparticles and the base fluid. Amongst these mechanisms, only Brownian diffusion and thermophoresis were found to be important. Haroun et al. [11] investigated magnetohydrodynamic (MHD) nanofluid flow past an impulsively stretching surface with chemical reaction, applied magnetic field, Brownian motion and thermophoresis. Makinde et al. [12] studied the combined effects of buoyancy force, convective heating,

Brownian motion, thermophoresis and a magnetic field on stagnation point flow and heat transfer due to a nanofluid flow from a stretching/shrinking sheet under the assumption that the magnetic Reynolds number was small. Makinde and Aziz [14] obtained the similarity solution for the thermal boundary layer of a nanofluid past a stretching sheet with Brownian motion and thermophoresis effects. The importance of thermophoresis as well as Brownian diffusion for the deposition of micro and nanoparticles were examined by Zahmatkesh [15].

The study of magnetic field effects has important applications in engineering and science fields. The interaction of magnetic field with nanofluids can be utlized in overcoming problems consisting of cooling nuclear reactors by liquid sodium and inducting the flow meter which relies on the potential difference in the fluid along the direction perpendicular to the motion and to the magnetic field. Sheikholeslami et al. [16] employed Lattice Boltzmann method to analyze MHD flow of copper-water nanofluid in a concentric annulus. Hayat [17] considered MHD three-dimensional flow of couple stress nanofluid in the presence of thermophoresis and Brownian motion effects.

The importance of non-Newtonian nanofluids has attracted attention of many researchers due to their various applications in mechanical, chemical and engineering processes. Casson fluid model [18] is one of the non-Newtonian fluid models which gives yield stress. If shear stress is less than yield stress, then the fluid behaves like a solid, and if shear stress is greater than yield stress, the fluid start moving. Examples of Casson fluids include honey, soup, jelly, tomato sauce, blood and concentrated fruit juice. Casson fluid model has possible applications in polymer industries and biomechanics [19]. Owing to these applications, many authors have studied the characteristics of Casson fluid along stretched surface. Mukhopadhyay [20] analyzed MHD flow and heat transfer of Casson fluid over a stretching surface. Mukhopadhyay and Vajravelu [21] considered MHD flow, heat and mass transfer of Casson fluid over an unsteady stretching surface. Butt et al. [22] explored unsteady three-dimensional flow of Casson fluid over a stretching surface.

Radiative heat transfer on viscous flow occurs when there exist temperature differences between the surrounding and the ambient fluid. Radiation effects play an important role in controlling heat transfer processes in polymer industry. In most studies, radiation is taken as constants in the flow region. However, it is difficult to maintain the constant temperature in the entire flow region, thus incorporating nonlinear radiation become necessary.

Nonlinear thermal radiation plays a significant role in many industrial, scientific and technological applications. Hall effects emerge in ionized fluid when the conductivity normal to the magnetic field diminishes because of the spiralling of electrons and ions about the magnetic lines of the force before the collisions and a current is induced in a direction normal to both the electric and magnetic fields. Studies on MHD flow, heat and mass transfer where Hall current is considered can be utilized in various industrial and engineering applications. Pal [23] scrutinized the effects of Hall current and thermal radiation on MHD flow and heat transfer of a viscous fluid over an unsteady stretched surface. Ashraf et al. [24] studied MHD mixed convection flow of a Casson fluid along a stretching surface with Hall effect. El-Aziz et al. [26] examined Hall effects on MHD slip flow of Casson nanofluid along a stretching sheet. Prashu and Nandkeolyar [25] used spectral quasilinearisation method to analyze three-dimensional flow of Casson fluid induced by a stretched surface with radiation and Hall effects.

The efficiency of heat transfer in fluids is mostly dependent on their physical features. Among these features, viscosity and thermal conductivity are significant factors in the heat transfer process. Viscosity and thermal conductivity have been taken as constants in most studies conducted. However, fluid properties may vary significantly with temperature. To accurately analyze flow and heat transfer processes it is necessary to consider variable viscosity and thermal conductivity. Animasaun [27] investigated Casson fluid flow past an exponentially stretching sheet with variable viscosity and thermal conductivity. Animasaun [28] also studied the effects of thermophoresis, variable viscosity and thermal conductivity on MHD Casson fluid flow along a vertical porous plate with suction. Bisht and Sharma [29] investigated flow of Casson nanofluid past a vertical nonlinear stretching surface with variable viscosity and thermal conductivity. Prasad et al. [30] explored the impact of variable viscosity and thermal conductivity on Casson nanofluid flow over a Riga plate. Gbadeyan et al. [31] analyzed the effects of variable thermal conductivity and viscosity on MHD Casson nanofluid flow over a vertical flat plate.

Motivated by the aforementioned studies and the importance of obtaining accurate results, the intention of this work is to investigate unsteady MHD three-dimensional flow of Casson nanofluid past a stretching surface under the influence of exponentially variable fluid viscosity, linearly variable thermal conductivity, thermal radiation, suction/injection, thermophoresis, Brownian motion and Hall current. To the authors' best knowledge, such

study has not been reported in literature. The governing equations are first reduced into dimensionless ordinary differential equations (ODEs) and then solved numerically using efficient spectral quasilinearisation method (SQLM) on overlapping grids. The previous SQLM [32] has been applied to solve problems over a single domain and it has been found that its accuracy deteriorates when the computational domain becomes large. However, this limitation can be overcome by splitting the single domain into sub-domains. In the present work, we extend the solution algorithm by using overlapping grid strategy when splitting the main domain into sub-domains. It worth noting that in the proposed method, the solution is computed simultaneously across all subdomains. The pseudospectral method that uses the multi-domain overlapping technique has been considered by some researchers including Yang et al. [33], Olmos and Shizgal [34], and Teleei and Dehghan [35]. The overlapping grid approach can improve accuracy and minimise computational time since it produces less dense matrices that can be inverted in a computationally efficient manner.

2. Formulation of problem

We consider the unsteady three-dimensional hydromagnetic flow of a viscous, incompressible and electrically conducting Casson nanofluid over a stretching sheet with suction/injection and radiative heat transfer. The nanofluid flow is analyzed by considering thermophoresis and Brownian effects. All the fluid properties are assumed to be constant except for the viscosity, which varies as an exponential function of temperature and the thermal conductivity altering as a linear function of temperature. A set of coordinates (x, y, z) is measured normal to the sheet. The x-direction located at the surface of the sheet is stretched with a time dependent velocity $u = u_w(x, t)$. We assume the surface to be along the plane $y = 0$ and the liquid to be confined in the region $y \geq 0$. The ambient fluid temperature and nanoparticle concentration are considered to be T_∞ and C_∞. The externally applied time-dependent magnetic field $B(t)$ is acting along $y-$direction, which is normal to the surface of the sheet. The Hall effect is retained in the present study. It is assumed that the induced magnetic field is negligible in comparison to the applied magnetic field. The rheological equation of an

isotropic and incompressible flow of Casson fluid [28, 31] is given by

$$
\tau_{ij} = \begin{cases} 2\left(\mu_B + \dfrac{P_y}{\sqrt{2\pi}}\right)e_{ij}, & \text{if } \pi > \pi_c, \\[2mm] 2\left(\mu_B + \dfrac{P_y}{\sqrt{2\pi_c}}\right)e_{ij}, & \text{if } \pi < \pi_c, \end{cases} \tag{1}
$$

Here, P_y is the yield stress of the Casson fluid, which can be expressed in the form

$$
P_y = \frac{\mu_B \sqrt{2\pi}}{\beta}, \tag{2}
$$

$\pi = e_{ij}e_{ij}$ is the product of the component of deformation rate, with e_{ij} being the (i,j)-th component of the deformation rate, π_c is critical value of π based on the non-Newtonian model, μ_B is the plastic dynamic viscosity of the non-Newtonian fluid. For the case of Casson fluid flow, where $\pi > \pi_c$, the dynamic viscosity is given by

$$
\mu_f = \mu_B + \frac{P_y}{\sqrt{2\pi}}. \tag{3}
$$

Substituting equation (3) into equation (2), the kinematic viscosity becomes

$$
\nu_f = \frac{\mu_f}{\rho_f} = \frac{\mu_B}{\rho_f}\left(1 + \frac{1}{\beta}\right), \tag{4}
$$

By employing the boundary layer and Boussinesq's approximations, and making use of the above assumptions, governing equations of the unsteady incompressible viscous Casson nanofluid flow are [36, 25]

$$
\frac{\partial u}{\partial x} + \frac{\partial v}{\partial y} + \frac{\partial w}{\partial z} = 0, \tag{5}
$$

$$
\frac{\partial u}{\partial t} + u\frac{\partial u}{\partial x} + v\frac{\partial u}{\partial y} + w\frac{\partial u}{\partial z} = \frac{1}{\rho_f}\left(1 + \frac{1}{\beta}\right)\frac{\partial}{\partial y}\left(\mu_B(T)\frac{\partial u}{\partial y}\right) - \frac{\sigma B^2(t)}{\rho_f(1+m^2)}\{u + mw\}, \tag{6}
$$

$$
\frac{\partial w}{\partial t} + u\frac{\partial w}{\partial x} + v\frac{\partial w}{\partial y} + w\frac{\partial w}{\partial z} = \frac{1}{\rho_f}\left(1 + \frac{1}{\beta}\right)\frac{\partial}{\partial y}\left(\mu_B(T)\frac{\partial w}{\partial y}\right) + \frac{\sigma B^2(t)}{\rho_f(1+m^2)}\{mu - w\}, \tag{7}
$$

$$
\frac{\partial T}{\partial t} + u\frac{\partial T}{\partial x} + v\frac{\partial T}{\partial y} + w\frac{\partial T}{\partial z} = \frac{1}{\rho_f c_p}\frac{\partial}{\partial y}\left(k_f(T)\frac{\partial T}{\partial y}\right) + \frac{16\sigma^*}{3k^*\rho_f c_p}\frac{\partial}{\partial y}\left(T^3\frac{\partial T}{\partial y}\right)
$$
$$
+ \tau\left[D_B\left(\frac{\partial T}{\partial y}\frac{\partial C}{\partial y}\right) + \frac{D_T}{T_\infty}\left(\frac{\partial T}{\partial y}\right)^2\right], \tag{8}
$$

$$
\frac{\partial C}{\partial t} + u\frac{\partial C}{\partial x} + v\frac{\partial C}{\partial y} + w\frac{\partial C}{\partial z} = D_B\frac{\partial^2 C}{\partial y^2} + \frac{D_T}{T_\infty}\left(\frac{\partial^2 T}{\partial y^2}\right), \tag{9}
$$

where u, v, w are fluid velocities in the x, y, z directions, T is temperature, C is the nanoparticles volume fraction, m is Hall current parameter, c_p is the specific heat, σ fluid electrical conductivity, ρ_f is the density of the fluid, D_B the Brownian diffusion coefficient, D_T is the thermophoretic diffusion coefficient, σ^* is the Stefan-Boltzmann constant, k^* is the coefficient of Rosseland mean absorption, $\tau = \frac{(\rho c)_p}{(\rho c)_f}$ is the ratio of nanoparticle heat capacity to the base fluid, T_w and T_∞ are the respective temperature of the surface and temperature far away from the surface, β is the Casson fluid parameter, C_w and C_∞ are the nanoparticle concentration of the fluid at the wall and ambient, respectively, $B(t) = \frac{B_0}{\sqrt{1-\gamma t}}$ is the time dependent magnetic field with γ being a constant. The temperature dependent fluid viscosity $\mu_B(T)$ and thermal conductivity $k_f(T)$ are given by [31, 37, 38, 39, 40]

$$\mu_B(T) = \mu_\infty e^{-\xi \frac{T - T_\infty}{T_w - T_\infty}}, \quad k_f(T) = k_\infty \left[1 + \varepsilon \frac{T - T_\infty}{T_w - T_\infty} \right], \quad (10)$$

where u_∞ is the value of the coefficient of viscosity away from the sheet, k_∞ is the value of thermal diffusivity at the ambient, ξ is the variable viscosity parameter which is greater than zero ($\xi > 0$) for liquids and less than zero ($\xi < 0$) for gases, and $\varepsilon (= \frac{k_w - k_\infty}{k_\infty})$ is thermal conductivity parameter.

The boundary conditions are:

$$u = u_w = \frac{ax}{1 - \gamma t}, \quad v = v_w, \quad w = 0, \quad T = T_w, \quad C = C_w \quad at \quad y = 0$$

$$u \to 0, \quad w \to 0, \quad T \to \infty, \quad C \to \infty, \text{as} \quad y \to \infty \quad (11)$$

We introduce the following non-dimensional variables [25]:

$$u = \frac{ax}{1 - \gamma t} f'(\eta), \quad v = -\sqrt{\frac{ax}{1 - \gamma t}} f(\eta)), \quad w = \frac{ax}{1 - \gamma t} g(\eta),$$

$$\eta = y \sqrt{\frac{a}{\nu_f(1 - \gamma t)}}, \quad \theta(\eta) = \frac{T - T_\infty}{T_w - T_\infty}, \quad \phi(\eta) = \frac{C - C_\infty}{C_w - C_\infty} \quad (12)$$

Substituting Eq. (12) into Eqs. (5)-(9), we get the dimensionless equations

$$\left(1 + \frac{1}{\beta} \right) e^{-\xi\theta} \left[f''' - \xi\theta' f'' \right] + f f'' - A(f' + \frac{\eta}{2} f'') - f'^2 - \frac{M}{1 + m^2}(f' + mg) = 0, \quad (13)$$

$$\left(1 + \frac{1}{\beta} \right) e^{-\xi\theta} \left[g'' - \xi\theta' g' \right] + f g' - f' g - A(g + \frac{\eta}{2} g') + \frac{M}{1 + m^2}(mf' - g) = 0, \quad (14)$$

7

$$\left[1 + \varepsilon\theta + \frac{4}{3}Rd\left(1 + (\theta_w - 1)\theta\right)^3\right]\theta'' + 4Rd\left(1 + (\theta_w - 1)\theta\right)^2(\theta_w - 1)\theta'^2 + \varepsilon\theta'^2$$

$$+Pr\left[f\theta' + Nb\theta'\phi' + Nt(\theta')^2 - A\frac{\eta}{2}\theta'\right] = 0 \quad (15)$$

$$\phi'' + Le\left[f\phi' - \frac{A}{2}\eta\phi'\right] + \frac{Nt}{Nb}\theta'' = 0 \tag{16}$$

subject to the boundary conditions

$$f(0) = S, \quad f'(0) = 1, \quad g(0) = 0, \quad \theta(0) = 1, \quad \phi(0) = 1,$$

$$\eta \to \infty: \quad f' \to 0, \quad g \to 0, \quad \theta \to 0, \quad \phi \to 0, \tag{17}$$

where prime denote differentiation with respect to η, $A = \frac{\gamma}{a}$ is the unsteadiness parameter, $Nb = \frac{\tau D_B(C_w - C_\infty)}{\nu_f}$ is the Brownian motion parameter, $Nt = \frac{\tau D_T(T_w - T_\infty)}{T_\infty \nu_f}$, $Pr = \frac{\mu_f c_p}{k_f}$ is the Prandtl number, $Rd = \frac{4\sigma^* T_\infty^3}{k_f k^*}$ is the nonlinear radiation parameter, $Le = \frac{\nu_f}{D_B}$ is the Lewis number, $M = \dfrac{\sigma B_0^2}{\rho_f a}$ magnetic strength parameter, $S = -\frac{v_w}{\sqrt{u_w}}$ is the suction $(S > 0)$ or injection $(S < 0)$ parameter.

The skin friction coefficients, heat and mass transfer are respectively defined as follows

$$C_{fx} = \frac{\tau_{wx}}{\rho_f u_w^2}, \ C_{fz} = \frac{\tau_{wz}}{\rho_f u_w^2}, \ Nu_x = \frac{xq_w}{k_\infty(T_w - T_\infty)}, \ Sh_x = \frac{xq_m}{D_B(T_w - T_\infty)} (18)$$

where the shearing stress component τ_{wx}, τ_{wz} at the plate, the rate of heat transfer q_w and the rate of mass transfer q_m at the surface are given by

$$\tau_{wx} = \mu_B(T)\left(1 + \frac{1}{\beta}\right)\left(\frac{\partial u}{\partial y}\right)_{y=0}, \ \tau_{wz} = \mu_B(T)\left(1 + \frac{1}{\beta}\right)\left(\frac{\partial w}{\partial y}\right)_{y=0},$$

$$q_w = -k_f(T)\left(\frac{\partial T}{\partial y}\right)_{y=0}, \ q_m = -D_B\left(\frac{\partial C}{\partial y}\right)_{y=0}, \tag{19}$$

Substituting the dimensionless variables (12) into Eq. (19) and using Eq. (18), the dimensionless skin friction coefficients, local Nusselt number and Sherwood number are obtained as

$$C_{fx}Re_x^{1/2} = \left(1 + \frac{1}{\beta}\right)e^{-\xi\theta(0)}f''(0), \ C_{fz}Re_x^{1/2} = \left(1 + \frac{1}{\beta}\right)e^{-\xi\theta(0)}g'(0),$$

$$Nu_x Re_x^{-1/2} = -\left[1 + \varepsilon\theta(0) + \frac{4}{3}Rd\left(1 + (\theta_w - 1)\theta(0)\right)^3\right]\theta'(0),$$

$$Sh_x Re_x^{-1/2} = -\phi'(0) \tag{20}$$

8

where $Re_x = \frac{xu_w}{\nu_f}$ is the Reynolds number.

3. Solution procedure

In this section, we present the overlapping grid SQLM and its application in solving the nonlinear ODEs (13)-(16). The solution algorithm uses the notion of multi-domain overlapping grid, quasilinearisation method (QLM) [42], spectral collocation method and Lagrange interpolation polynomials with Gauss-Lobatto grid points [43]. Since, the problem is defined on the semi-infinite domain $[0, \infty)$, for implementing the numerical method, we use the truncated interval of integration $[0, \eta_\infty]$. To apply the overlapping grid SQLM, we let $\eta \in I$, then the interval $I = [0, \eta_\infty]$ is split into p overlapping sub-domains denoted by

$$I_\iota = [\eta_0^\iota, \eta_{N_\eta}^\iota], \quad \iota = 1, 2, 3, ..., p, \tag{21}$$

where each sub-interval will be further discretized into $N_\eta + 1$ collocation points. The grid describing how the truncated interval is decomposed into p overlapping sub-domains is shown in Figure 1. For the overlap to be possible, the sub-domains must have same length defined as

$$L = \frac{\eta_\infty}{p + (1 - p)(1 - \cos \frac{\pi}{N_\eta})/2}, \tag{22}$$

To derive Eq. (22), we note that the total length of the domain is

$$\eta_\infty = 2L - \kappa + (2L - 2\kappa)\left(\frac{p}{2} - 1\right)$$
$$= 2L - \kappa + (L - \kappa)(p - 1) = \kappa(1 - p) + pL, \tag{23}$$

where κ is the overlapping distance between two intervals. Also, we note that $\kappa = \eta_0 - \eta_1$. Considering the first interval I_1 in which $\eta \in [0, L]$, the linear transformation $\eta = \frac{L}{2}(z + 1)$, can be used to transform the interval $[0, L]$ to $[-1, 1]$. Thus, using the Gauss-Lobatto collocation points $z_i = \cos\left(\frac{\pi i}{N_\eta}\right)$, $i = 0, 1, 2, 3, ..., N_\eta$, we obtain $\eta_0 - \eta_1 = \frac{L}{2}(z_0 - z_1) = \frac{L}{2}\left(1 - \cos\left(\frac{\pi}{N_\eta}\right)\right)$. Finally,

$$\eta_\infty = \kappa(1 - p) + pL = \frac{L}{2}\left(1 - \cos\left(\frac{\pi}{N_\eta}\right)\right)(1 - p) + pL, \tag{24}$$

9

which upon rearranging gives Eq. (22).
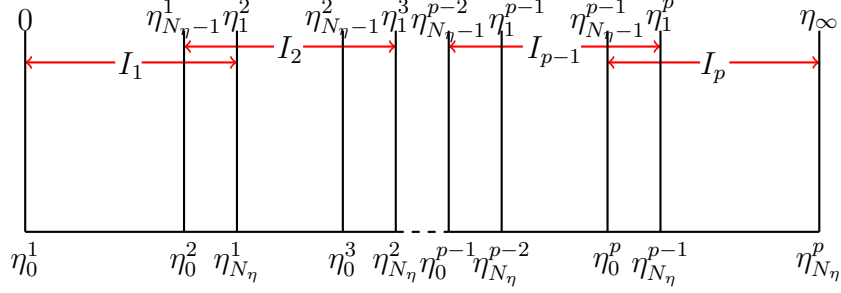
Figure 1: Overlapping grid.

In each sub-interval I_ι, we must solve

$$\left(1 + \frac{1}{\beta}\right)e^{-\xi\theta^\iota}\frac{d^3 f^\iota}{d\eta^3} - \xi\left(1 + \frac{1}{\beta}\right)e^{-\xi\theta^\iota}\frac{d\theta^\iota}{d\eta}\frac{d^2 f^\iota}{d\eta^2} + f^\iota\frac{d^2 f^\iota}{d\eta^2} - A\left(\frac{df^\iota}{d\eta} + \frac{\eta^\iota}{2}\frac{d^2 f^\iota}{d\eta^2}\right)$$

$$-\left(\frac{df^\iota}{d\eta}\right)^2 - \frac{M}{1 + m^2}\left(\frac{df^\iota}{d\eta} + mg^\iota\right) = 0, \qquad (25)$$

$$\left(1 + \frac{1}{\beta}\right)e^{-\xi\theta^\iota}\frac{d^2 g^\iota}{d\eta^2} - \xi\left(1 + \frac{1}{\beta}\right)e^{-\xi\theta^\iota}\frac{d\theta^\iota}{d\eta}\frac{dg^\iota}{d\eta} + f^\iota\frac{dg^\iota}{d\eta} - A\left(g^\iota + \frac{\eta^\iota}{2}\frac{dg^\iota}{d\eta}\right)$$

$$-\frac{df^\iota}{d\eta}g^\iota + \frac{M}{1 + m^2}\left(m\frac{df^\iota}{d\eta} - g^\iota\right) = 0, \qquad (26)$$

$$\left[1 + \varepsilon\theta^\iota + \frac{4}{3}Rd\left(1 + (\theta_w - 1)\theta^\iota\right)^3\right]\frac{d^2\theta^\iota}{d\eta^2} + Pr\left[Nb\frac{d\theta^\iota}{d\eta}\frac{d\phi^\iota}{d\eta} + Nt\left(\frac{d\theta^\iota}{d\eta}\right)^2\right] \quad (27)$$

$$+Prf^\iota\frac{d\theta^\iota}{d\eta} + \left[\varepsilon + 4Rd\left(1 + (\theta_w - 1)\theta^\iota\right)^2(\theta_w - 1)\right]\left(\frac{d\theta^\iota}{d\eta}\right)^2 - PrA\frac{\eta^\iota}{2}\frac{d\theta^\iota}{d\eta} = 0,$$

$$\frac{d^2\phi^\iota}{d\eta^2} + LePr\left[f^\iota\frac{d\phi^\iota}{d\eta} - \frac{A}{2}\eta^\iota\frac{d\phi^\iota}{d\eta}\right] + \frac{Nt}{Nb}\frac{d^2\theta^\iota}{d\eta^2} = 0. \qquad (28)$$

To solve Eqs. (25)-(28), we first linearize the nonlinear boundary value problem using the QLM. The QLM assumes that the difference between approximate solutions at two successive iterations is very small. Applying QLM

10

on Eqs. (25)-(28) yields the following iterative sequence of linear ODEs:

$$\alpha_{1,3,r}^{(1,\iota)}\frac{d^3 f_{r+1}^\iota}{d\eta^3} + \alpha_{1,2,r}^{(1,\iota)}\frac{d^2 f_{r+1}^\iota}{d\eta^2} + \alpha_{1,1,r}^{(1,\iota)}\frac{df_{r+1}^\iota}{d\eta} + \alpha_{1,0,r}^{(1,\iota)}f_{r+1}^\iota + \alpha_{3,1,r}^{(1,\iota)}\frac{d\theta_{r+1}^\iota}{d\eta}$$

$$+\alpha_{2,0,r}^{(1,\iota)}g_{r+1}^\iota + \alpha_{3,0,r}^{(1,\iota)}\theta_{r+1}^\iota = R_{1,r}^\iota, \qquad (29)$$

$$\alpha_{2,2,r}^{(2,\iota)}\frac{d^2 g_{r+1}^\iota}{d\eta^2} + \alpha_{2,1,r}^{(2,\iota)}\frac{dg_{r+1}^\iota}{d\eta} + \alpha_{2,0,r}^{(2,\iota)}g_{r+1}^\iota + \alpha_{3,1,r}^{(2,\iota)}\frac{d\theta_{r+1}^\iota}{d\eta} + \alpha_{3,0,r}^{(2,\iota)}\theta_{r+1}^\iota$$

$$+\alpha_{1,1,r}^{(2,\iota)}\frac{df_{r+1}^\iota}{d\eta} + \alpha_{1,0,r}^{(2,\iota)}f_{r+1}^\iota = R_{2,r}^\iota, \qquad (30)$$

$$\alpha_{3,2,r}^{(3,\iota)}\frac{d^2\theta_{r+1}^\iota}{d\eta^2} + \alpha_{3,1,r}^{(3,\iota)}\frac{d\theta_{r+1}^\iota}{d\eta} + \alpha_{3,0,r}^{(3,\iota)}\theta_{r+1}^\iota + \alpha_{4,1,r}^{(3,\iota)}\frac{d\phi_{r+1}^\iota}{d\eta} + \alpha_{1,0,r}^{(3,\iota)}f_{r+1}^\iota = R_{3,r}^\iota, (31)$$

$$\alpha_{4,2,r}^{(4,\iota)}\frac{d^2\phi_{r+1}^\iota}{d\eta^2} + \alpha_{4,1,r}^{(4,\iota)}\frac{d\phi_{r+1}^\iota}{d\eta} + \alpha_{3,2,r}^{(4,\iota)}\frac{d^2\theta_{r+1}^\iota}{d\eta^2} + \alpha_{1,0,r}^{(4,\iota)}f_{r+1}^\iota = R_{4,r}^\iota, \qquad (32)$$

where $f^\iota, g^\iota, \theta^\iota$ and ϕ^ι are the solutions at ιth interval, r and $r+1$ symbolize previous and current iterations, and the variable coefficients are given by

$$\alpha_{1,3,r}^{(1,\iota)} = \left(1+\frac{1}{\beta}\right)e^{-\xi\theta_r^\iota}, \ \alpha_{1,2,r}^{(1,\iota)} = f_r^\iota - \frac{\eta^\iota}{2}A - \left(1+\frac{1}{\beta}\right)\xi e^{-\xi\theta_r^\iota}\frac{d\theta_r^\iota}{d\eta}, \ \alpha_{1,1,r}^{(1,\iota)} = A$$

$$-2\frac{df_r^\iota}{d\eta} - \frac{M}{1+m^2}, \ \alpha_{1,0,r}^{(1,\iota)} = \frac{d^2 f_r^\iota}{d\eta^2}, \ \alpha_{2,0,r}^{(1,\iota)} = -\frac{mM}{1+m^2},$$

$$\alpha_{3,1,r}^{(1,\iota)} = -\left(1+\frac{1}{\beta}\right)\xi e^{-\xi\theta_r^\iota}\frac{d^2 f_r^\iota}{d\eta^2}, \ \alpha_{3,0,r}^{(1,\iota)} = -\left(1+\frac{1}{\beta}\right)\xi e^{-\xi\theta_r^\iota}\frac{d^3 f_r^\iota}{d\eta^3}$$

$$+\xi^2 e^{-\xi\theta_r^\iota}\frac{d\theta_r^\iota}{d\eta}\frac{d^2 f_r^\iota}{d\eta^2}, \ \alpha_{2,2,r}^{(2,\iota)} = \left(1+\frac{1}{\beta}\right)e^{-\xi\theta_r^\iota}, \ \alpha_{2,1,r}^{(2,\iota)} = f_r^\iota - \frac{\eta^\iota}{2}A$$

$$-\left(1+\frac{1}{\beta}\right)\xi e^{-\xi\theta_r^\iota}\frac{d\theta_r^\iota}{d\eta}, \ \alpha_{2,0,r}^{(2,\iota)} = -A - \frac{df_r^\iota}{d\eta} - \frac{M}{1+m^2}, \ \alpha_{1,1,r}^{(2,\iota)} = -g_r^\iota + \frac{mM}{1+m^2},$$

$$\alpha_{1,1,r}^{(2,\iota)} = \frac{dg_r^\iota}{d\eta}, \ \alpha_{3,1,r}^{(2,\iota)} = -\left(1+\frac{1}{\beta}\right)\xi e^{-\xi\theta_r^\iota}\frac{dg_r^\iota}{d\eta}, \ \alpha_{3,0,r}^{(2,\iota)} = -\left(1+\frac{1}{\beta}\right)\xi e^{-\xi\theta_r^\iota}\frac{d^2 g_r^\iota}{d\eta^2}$$

$$+\xi^2 e^{-\xi\theta_r^\iota}\frac{d\theta_r^\iota}{d\eta}\frac{dg_r^\iota}{d\eta}, \ \alpha_{3,2,r}^{(3,\iota)} = 1 + \varepsilon\theta_r^\iota + \frac{4}{3}Rd + 4Rd(\theta_w - 1)\theta_r^\iota$$

$$+4Rd(\theta_w - 1)^2\left(\theta_r^\iota\right)^2 + \frac{4}{3}Rd(\theta_w - 1)^3\left(\theta_r^\iota\right)^3, \ \alpha_{3,1,r}^{(3,\iota)} = 2\varepsilon\frac{d\theta_r^\iota}{d\eta}$$

$$+Prf_r^\iota + PrNb\frac{d\phi_r^\iota}{d\eta} + 2PrNt\frac{d\theta_r^\iota}{d\eta} - \frac{1}{2}APr\eta^\iota + 8Rd(\theta_w - 1)\frac{d\theta_r^\iota}{d\eta}$$

$$+16Rd(\theta_w - 1)^2\theta_r^\iota\frac{d\theta_r^\iota}{d\eta} + 8Rd(\theta_w - 1)^3\left(\theta_r^\iota\right)^2\frac{d\theta_r^\iota}{d\eta}, \ \alpha_{3,0,r}^{(3,\iota)} = \varepsilon\frac{d^2\theta_r^\iota}{d\eta^2}$$

$$+4Rd(\theta_w - 1)\frac{d^2\theta_r^\iota}{d\eta^2} + 8Rd(\theta_w - 1)^2\theta_r^\iota\frac{d^2\theta_r^\iota}{d\eta^2} + 4Rd(\theta_w - 1)^3\left(\theta_r^\iota\right)^2\frac{d^2\theta_r^\iota}{d\eta^2}$$

11

$$+8Rd(\theta_w - 1)^2 \left(\frac{d\theta_r^\iota}{d\eta}\right)^2 + 8Rd(\theta_w - 1)^3 \theta_r^\iota \left(\frac{d\theta_r^\iota}{d\eta}\right)^2, \ \alpha_{1,0,r}^{(3,\iota)} = Pr\frac{d\theta_r^\iota}{d\eta},$$

$$\alpha_{4,1,r}^{(3,\iota)} = PrNb\frac{d\theta_r^\iota}{d\eta}, \ \alpha_{4,2,r}^{(4,\iota)} = 1, \ \alpha_{4,1,r}^{(4,\iota)} = Lef_r^\iota - \frac{1}{2}LeA\eta^\iota, \ \alpha_{1,0,r}^{(4,\iota)} = Le\frac{d\phi_r^\iota}{d\eta},$$

$$\alpha_{3,2,r}^{(4,\iota)} = \frac{Nt}{Nb}, R_{1,r}^\iota = \xi^2 e^{-\xi\theta_r^\iota} \theta_r^\iota \frac{d\theta_r^\iota}{d\eta}\frac{d^2 f_r^\iota}{d\eta^2} - \left(1 + \frac{1}{\beta}\right)\xi e^{-\xi\theta_r^\iota}\left[\theta_r^\iota \frac{d^3 f_r^\iota}{d\eta^3} + \frac{d\theta_r^\iota}{d\eta}\frac{d^2 f_r^\iota}{d\eta^2}\right]$$

$$+f_r^\iota \frac{d^2 f_r^\iota}{d\eta^2} - \left(\frac{df_r^\iota}{d\eta}\right)^2, \ R_{2,r}^\iota = \xi^2 e^{-\xi\theta_r^\iota} \theta_r^\iota \frac{d\theta_r^\iota}{d\eta}\frac{dg_r^\iota}{d\eta} + f_r^\iota \frac{dg_r^\iota}{d\eta} - \frac{df_r^\iota}{d\eta}g_r^\iota$$

$$-\left(1 + \frac{1}{\beta}\right)\xi e^{-\xi\theta_r^\iota}\left[\theta_r^\iota \frac{d^2 g_r^\iota}{d\eta} + \frac{d\theta_r^\iota}{d\eta}\frac{dg_r^\iota}{d\eta}\right], \ R_{3,r}^\iota = \varepsilon\theta_r^\iota \frac{d^2\theta_r^\iota}{d\eta^2} + \varepsilon\left(\frac{d\theta_r^\iota}{d\eta}\right)^2$$

$$+Prf_r^\iota \frac{d\theta_r^\iota}{d\eta} + PrNb\frac{d\theta_r^\iota}{d\eta}\frac{d\phi_r^\iota}{d\eta} + PrNt\left(\frac{d\theta_r^\iota}{d\eta}\right)^2 + 4Rd(\theta_w - 1)\theta_r^\iota \frac{d^2\theta_r^\iota}{d\eta^2}$$

$$+8Rd(\theta_w - 1)^2 (\theta_r^\iota)^2 \frac{d^2\theta_r^\iota}{d\eta^2} + 4Rd(\theta_w - 1)^3 (\theta_r^\iota)^3 \frac{d^2\theta_r^\iota}{d\eta^2} + 4Rd(\theta_w - 1)\left(\frac{d\theta_r^\iota}{d\eta}\right)^2$$

$$+16Rd(\theta_w - 1)^2\theta_r^\iota \left(\frac{d\theta_r^\iota}{d\eta}\right)^2 + 12Rd(\theta_w - 1)^3 (\theta_r^\iota)^2 \left(\frac{d\theta_r^\iota}{d\eta}\right)^2, \ R_{4,r}^\iota = Lef_r^\iota \frac{d\phi_r^\iota}{d\eta},$$

Before the spectral collocation method is applied at each sub-interval, the interval $I_\iota = [\eta_0^\iota, \eta_{N_\eta}^\iota]$ is converted into $z \in [-1, 1]$ utilizing the linear transformation

$$\eta_i^\iota = \frac{L}{2}(z_i + 1), \quad z_i = \cos\left(\frac{\pi i}{N_\eta}\right). \tag{33}$$

Applying the pseudospectral method on Eqs. (29)-(32) gives

$$\alpha_{1,3,r}^{(1,\iota)}\Lambda^3 \sum_{j=0}^{N_\eta} \left[D_{i,j}^{(\iota)}\right]^3 f_{j,r+1}^\iota + \alpha_{1,2,r}^{(1,\iota)}\Lambda^2 \sum_{j=0}^{N_\eta} \left[D_{i,j}^{(\iota)}\right]^2 f_{j,r+1}^\iota + \alpha_{1,1,r}^{(1,\iota)}\Lambda \sum_{j=0}^{N_\eta} D_{i,j}^{(\iota)} f_{j,r+1}^\iota$$

$$+\alpha_{1,0,r}^{(1,\iota)} f_{i,r+1}^\iota + \alpha_{2,0,r}^{(1,\iota)} g_{i,r+1}^\iota + \alpha_{3,1,r}^{(1,\iota)}\Lambda \sum_{j=0}^{N_\eta} D_{i,j}^{(\iota)} \theta_{j,r+1}^\iota + \alpha_{3,0,r}^{(1,\iota)} \theta_{i,r+1}^\iota = R_{1,r}^\iota, \quad (34)$$

$$\alpha_{2,2,r}^{(2,\iota)}\Lambda^2 \sum_{j=0}^{N_\eta} \left[D_{i,j}^{(\iota)}\right]^2 g_{j,r+1}^\iota + \alpha_{2,1,r}^{(2,\iota)}\Lambda \sum_{j=0}^{N_\eta} D_{i,j}^{(\iota)} g_{j,r+1}^\iota + \alpha_{2,0,r}^{(2,\iota)} g_{i,r+1}^\iota + \alpha_{1,0,r}^{(2,\iota)} f_{i,r+1}^\iota$$

$$+\alpha_{1,1,r}^{(2,\iota)}\Lambda \sum_{j=0}^{N_\eta} D_{i,j}^{(\iota)} f_{j,r+1}^\iota + \alpha_{3,1,r}^{(2,\iota)} \sum_{j=0}^{N_\eta} D_{i,j}^{(\iota)} \theta_{j,r+1}^\iota + \alpha_{3,0,r}^{(2,\iota)} \theta_{i,r+1}^\iota = R_{2,r}^\iota, \quad (35)$$

12

$$\alpha_{3,2,r}^{(3,\iota)} \Lambda^2 \sum_{j=0}^{N_\eta} \left[D_{i,j}^{(\iota)} \right]^2 \theta_{j,r+1}^\iota + \alpha_{3,1,r}^{(3,\iota)} \Lambda \sum_{j=0}^{N_\eta} D_{i,j}^{(\iota)} \theta_{j,r+1}^\iota + \alpha_{3,0,r}^{(3,\iota)} \theta_{i,r+1}^\iota$$

$$+ \alpha_{4,1,r}^{(3,\iota)} \Lambda \sum_{j=0}^{N_\eta} D_{i,j}^{(\iota)} \phi_{j,r+1}^\iota + \alpha_{1,0,r}^{(3,\iota)} f_{i,r+1}^\iota = R_{3,r}^\iota, \qquad (36)$$

$$\alpha_{4,2,r}^{(4,\iota)} \Lambda^2 \sum_{j=0}^{N_\eta} \left[D_{i,j}^{(\iota)} \right]^2 \phi_{j,r+1}^\iota + \alpha_{4,1,r}^{(4,\iota)} \Lambda \sum_{j=0}^{N_\eta} D_{i,j}^{(\iota)} \phi_{j,r+1}^\iota$$

$$+ \alpha_{3,2,r}^{(4,\iota)} \Lambda \sum_{j=0}^{N_\eta} \left[D_{i,j}^{(\iota)} \right]^2 \theta_{j,r+1}^\iota + \alpha_{1,0,r}^{(4,\iota)} f_{i,r+1}^\iota = R_{4,r}^\iota, \quad (37)$$

where $\Lambda = \frac{2}{L}$.

The boundary conditions become

$$f_{r+1}^1(z_{N_\eta}) = S, \ \sum_{j=0}^{N_\eta} D_{N_\eta,j}^{(1)} \phi_{j,r+1}^1 = 0, \ g_{r+1}^1(z_{N_\eta}) = 0,$$

$$\theta_{r+1}^1(z_{N_\eta}) = 1, \ \phi_{r+1}^1(z_{N_\eta}) = 1,$$

$$\sum_{j=0}^{N_\eta} D_{0,j}^{(p)} \phi_{j,r+1}^p = 0, \ g_{r+1}^p(z_0) = 0, \ \theta_{r+1}^p(z_0) = 0, \ \phi_{r+1}^p(z_0) = 0, \quad (38)$$

In terms of original variable η, the collocation points are arranged as

$$\{\eta_k\}_{k=0}^N$$
$$= \left\{ \eta_0^1, ..., \eta_{N_\eta-1}^1 = \eta_0^2, \eta_{N_\eta}^1 = \eta_1^2, ..., \eta_0^\iota, ..., \eta_{N_\eta-1}^\iota = \eta_0^{\iota+1}, \eta_{N_\eta}^\iota = \eta_1^{\iota+1}, ..., \eta_{N_\eta}^p \right\}$$
$$= \left\{ \eta_0^1, ..., \eta_{N_\eta-1}^1, \eta_1^2, ..., \eta_{N_\eta-1}^2, ..., \eta_1^\iota, ..., \eta_{N_\eta-1}^\iota, ..., \eta_1^p, ..., \eta_{N_\eta}^p \right\}, \qquad (39)$$

where $N = N_\eta + (N_\eta - 1)(p - 1)$ represent the total number of collocation points in $[0, \eta_\infty]$. It is easy to show that the grid points can be obtained as

$$\eta_i^1 = \frac{L}{2} \left[1 - \cos\left(\frac{\pi i}{N_\eta} \right) \right], \quad i = 0, 1, ..., N_\eta - 1,$$

$$\eta_i^\iota = \eta_{N_\eta-1}^{\iota-1} + \frac{L}{2} \left[1 - \cos\left(\frac{\pi i}{N_\eta} \right) \right], \quad i = 0, 1, ..., N_\eta - 1, \quad \iota = 2, 3, ..., p - 1,$$

$$\eta_i^p = \eta_{N_\eta-1}^{p-1} + \frac{L}{2} \left[1 - \cos\left(\frac{\pi i}{N_\eta} \right) \right], \quad i = 1, ..., N_\eta, \qquad (40)$$

In terms of transformed variable z, the collocation points are arranged as

$$\{z_k\}_{k=0}^{N} = \left\{z_{N_\eta}^1, ..., z_1^1 = z_{N_\eta}^2, z_0^1 = z_{N_\eta-1}^2, ..., z_{N_\eta}^\iota, ..., z_1^\iota = z_{N_\eta}^{\iota+1}, z_0^\iota = z_{N_\eta-1}^{\iota+1}, ..., z_0^p\right\}$$

$$= \left\{z_{N_\eta}^1, ..., z_1^1, z_{N_\eta-1}^2, ..., z_1^2, ..., z_{N_\eta-1}^\iota, ..., z_1^\iota, ..., z_{N_\eta-1}^p, ..., z_0^p\right\}, \tag{41}$$

The unknown functions can be expressed in terms of the global indexing as

$$\{f_k\} = \left\{f_{N_\eta}^1, ..., f_1^1, f_{N_\eta-1}^2, ..., f_1^2, ..., f_{N_\eta-1}^\iota, ..., f_1^\iota, ..., f_{N_\eta-1}^p, ..., f_0^p\right\} \tag{42}$$

$$= \left\{f_0^p, ..., f_{N_\eta-1}^p, f_1^{p-1}, ..., f_{N_\eta-1}^{p-1}, ..., f_1^\iota, ..., f_{N_\eta-1}^\iota, ..., f_1^2, ..., f_{N_\eta-1}^2, f_1^1, ..., f_{N_\eta}^1\right\},$$

$$\{g_k\} = \left\{g_0^p, ..., g_{N_\eta-1}^p, g_1^{p-1}, ..., g_{N_\eta-1}^{p-1}, ..., g_1^\iota, ..., g_{N_\eta-1}^\iota, ..., g_1^2, ..., g_{N_\eta-1}^2, g_1^1, ..., g_{N_\eta}^1\right\},$$

$$\{\theta_k\} = \left\{\theta_0^p, ..., \theta_{N_\eta-1}^p, \theta_1^{p-1}, ..., \theta_{N_\eta-1}^{p-1}, ..., \theta_1^\iota, ..., \theta_{N_\eta-1}^\iota, ..., \theta_1^2, ..., \theta_{N_\eta-1}^2, \theta_1^1, ..., \theta_{N_\eta}^1\right\},$$

$$\{\phi_k\} = \left\{\phi_0^p, ..., \phi_{N_\eta-1}^p, \phi_1^{p-1}, ..., \phi_{N_\eta-1}^{p-1}, ..., \phi_1^\iota, ..., \phi_{N_\eta-1}^\iota, ..., \phi_1^2, ..., \phi_{N_\eta-1}^2, \phi_1^1, ..., \phi_{N_\eta}^1\right\},$$

where the size of each vector is $N+1$. The first derivative at the sub-interval I_ι, for $f(\eta)$ is evaluated as

$$\frac{df^\iota}{dz} = \sum_{j=0}^{N_\eta} D_{i,j}^{(\iota)} f^\iota(z_j), \text{ where } D_{i,j}^{(\iota)} = \frac{2}{\eta_{N_\eta}^\iota - \eta_0^\iota}\hat{D}_{i,j}, \; i = 0, 1, 2, ..., N \tag{43}$$

Here, $\hat{D}_{i,j}$ is the first order differential operator in a single domain $[-1, 1]$. The global structure of the first derivative $\frac{df^\iota}{dz}$ can be expressed in the form

$$\tag{44}$$

where the derivative coefficient matrix is of order $(N+1)\times(N+1)$. It is worth noting that the empty entries in the coefficient matrix are zeros, which makes

the matrix less dense or sparse. We remark that the derivative operator become a full matrix if only a single domain is utilized in the computation. The nth order derivative at the sub-interval I_ι is evaluated as

$$\frac{d^n f^\iota}{dz^n} = \sum_{j=0}^{N_\eta} \left[D_{i,j}^{(\iota)} \right]^n f^\iota(z_j), \quad i = 0, 1, 2, ..., N, \tag{45}$$

The derivatives of the other functions at the sub-interval I_ι are evaluated in the similar manner. Expanding, the discretized form of the ODEs (34)-(37) gives matrix equations with unknown vectors

$$\begin{aligned}
\mathbf{F} &= \left\{ f^\iota(z_0), f^\iota(z_1), ..., f^\iota(z_{N_\eta-1}), f^\iota(z_{N_\eta}) \right\}, \\
\mathbf{G} &= \left\{ g^\iota(z_0), g^\iota(z_1), ..., g^\iota(z_{N_\eta-1}), g^\iota(z_{N_\eta}) \right\}, \\
\mathbf{\Theta} &= \left\{ \theta^\iota(z_0), \theta^\iota(z_1), ..., \theta^\iota(z_{N_\eta-1}), \theta^\iota(z_{N_\eta}) \right\}, \\
\mathbf{\Phi} &= \left\{ \phi^\iota(z_0), \phi^\iota(z_1), ..., \phi^\iota(z_{N_\eta-1}), \phi^\iota(z_{N_\eta}) \right\},
\end{aligned} \tag{46}$$

Taking into account that the last two points in the ιth sub-interval and the first two points in the $(\iota+1)$th sub-interval overlap and remain common, there will be a duplicate of equations which can be removed from the set of equations to be solved. After removing the duplicate equations, the left hand side of the equations becomes

$$\begin{bmatrix} \mathbf{A}^{11} & \mathbf{A}^{12} & \mathbf{A}^{13} & \mathbf{A}^{14} \\ \mathbf{A}^{21} & \mathbf{A}^{22} & \mathbf{A}^{23} & \mathbf{A}^{24} \\ \mathbf{A}^{31} & \mathbf{A}^{32} & \mathbf{A}^{33} & \mathbf{A}^{34} \\ \mathbf{A}^{41} & \mathbf{A}^{42} & \mathbf{A}^{43} & \mathbf{A}^{44} \end{bmatrix} \begin{bmatrix} \mathbf{F}^\iota_{k,r+1} \\ \mathbf{G}^\iota_{k,r+1} \\ \mathbf{\Theta}^\iota_{k,r+1} \\ \mathbf{\Phi}^\iota_{k,r+1} \end{bmatrix}, \tag{47}$$

where each matrix $\mathbf{A}^{\varrho,\varsigma}(\varrho = 1, 2, 3, 4; \varsigma = 1, 2, 3, 4)$ is of order $(N+1) \times (N+1)$, vectors $\mathbf{F}^\iota_{k,r+1}, \mathbf{G}^\iota_{k,r+1}, \mathbf{\Theta}^\iota_{k,r+1}, \mathbf{\Phi}^\iota_{k,r+1}$ are each of order $(N+1) \times 1$, and $\mathbf{A}^{11}$, for example, is given by

15

$$\mathbf{A}^{11} = \begin{bmatrix}
A_{0,0}^{(11,p)} & A_{0,1}^{(11,p)} & \cdots & A_{0,N_\eta-1}^{(11,p)} & A_{0,N_\eta}^{(11,p)} & & & & & & & & \\
A_{1,0}^{(11,p)} & A_{1,1}^{(11,p)} & \cdots & A_{1,N_\eta-1}^{(11,p)} & A_{1,N_\eta}^{(11,p)} & & & & & & & & \\
\ddots & \ddots & \ddots & \ddots & \ddots & & & & & & & & \\
A_{N_\eta-1,0}^{(11,p)} & A_{N_\eta-1,1}^{(11,p)} & \cdots & A_{N_\eta-1,N_\eta-1}^{(11,p)} & A_{v-1,v}^{(11,p)} & & & & & & & & \\
& & & & A_{1,0}^{(11,p-1)} & A_{1,1}^{(11,p-1)} & \cdots & A_{1,N_\eta-1}^{(11,p-1)} & A_{1,N_\eta}^{(11,p-1)} & & & & \\
& & & & A_{2,0}^{(11,p-1)} & A_{2,1}^{(11,p-1)} & \cdots & A_{2,N_\eta-1}^{(11,p-1)} & A_{2,N_\eta}^{(11,p-1)} & & & & \\
& & & & \ddots & \ddots & \ddots & \ddots & \ddots & & & & \\
& & & & A_{N_\eta-1,0}^{(11,p-1)} & A_{N_\eta-1,1}^{(11,p-1)} & \cdots & A_{N_\eta-1,N_\eta-1}^{(11,p-1)} & A_{N_\eta-1,N_\eta}^{(11,p-1)} & & & & \\
& & & & & & & \ddots & \ddots & & & & \\
& & & & & & & & & A_{1,0}^{(11,1)} & A_{1,1}^{(11,1)} & \cdots & A_{1,N_\eta-1}^{(11,1)} & A_{1,N_\eta}^{(11,1)} \\
& & & & & & & & & A_{2,0}^{(11,1)} & A_{2,1}^{(11,1)} & \cdots & A_{2,N_\eta-1}^{(11,1)} & A_{2,N_\eta}^{(11,1)} \\
& & & & & & & & & \ddots & \ddots & \ddots & \ddots & \ddots \\
& & & & & & & & & A_{N_\eta,0}^{(11,1)} & A_{N_\eta,1}^{(11,1)} & \cdots & A_{N_\eta,N_\eta-1}^{(11,1)} & A_{N_\eta,N_\eta}^{(11,1)}
\end{bmatrix} \tag{48}$$

with $\mathbf{A}_{q,\omega}^{11,\iota} = \alpha_{1,3,r}^{(1,\iota)} \Lambda^3 \left[D_{q,\omega}^{(\iota)} \right]^3 + \alpha_{1,2,r}^{(1,\iota)} \Lambda^2 \left[D_{q,\omega}^{(\iota)} \right]^2 + \alpha_{1,1,r}^{(1,\iota)} \Lambda D_{q,\omega}^{(\iota)} + \alpha_{1,0,r}^{(1,\iota)} \mathbf{I}$, and $\mathbf{I}$ is an $(N+1) \times (N+1)$ identity matrix. The rest of the coefficient matrices ($\mathbf{A}^{\varrho,\varsigma}$) are defined in the similar manner. Imposing the boundary conditions on the equations gives the following less dense matrix system:

$$\left[\begin{array}{cccc|cccc|cccc|cccc}
D_{0,0}^{(p)} & D_{0,1}^{(p)} & \cdots & D_{0,N_\eta}^{(p)} & 0 & 0 & \cdots & 0 & 0 & 0 & \cdots & 0 & 0 & 0 & \cdots & 0 \\
 & \mathbf{A}^{11} & & & & \mathbf{A}^{12} & & & & \mathbf{A}^{13} & & & & \mathbf{A}^{14} & & \\
D_{N_\eta-1,0}^{(1)} & D_{N_\eta-1,1}^{(1)} & \cdots & D_{N_\eta-1,N_\eta}^{(1)} & 0 & 0 & \cdots & 0 & 0 & 0 & \cdots & 0 & 0 & 0 & \cdots & 0 \\
0 & 0 & \cdots & 1 & 0 & 0 & \cdots & 0 & 0 & 0 & \cdots & 0 & 0 & 0 & \cdots & 0 \\
\hline
0 & 0 & \cdots & 0 & 1 & 0 & \cdots & 0 & 0 & 0 & \cdots & 0 & 0 & 0 & \cdots & 0 \\
 & \mathbf{A}^{21} & & & & \mathbf{A}^{22} & & & & \mathbf{A}^{23} & & & & \mathbf{A}^{24} & & \\
0 & 0 & \cdots & 0 & 0 & 0 & \cdots & 1 & 0 & 0 & \cdots & 0 & 0 & 0 & \cdots & 0 \\
\hline
0 & 0 & \cdots & 0 & 0 & 0 & \cdots & 0 & 1 & 0 & \cdots & 0 & 0 & 0 & \cdots & 0 \\
 & \mathbf{A}^{31} & & & & \mathbf{A}^{32} & & & & \mathbf{A}^{33} & & & & \mathbf{A}^{34} & & \\
0 & 0 & \cdots & 0 & 0 & 0 & \cdots & 0 & 0 & 0 & \cdots & 1 & 0 & 0 & \cdots & 0 \\
\hline
0 & 0 & \cdots & 0 & 0 & 0 & \cdots & 0 & 0 & 0 & \cdots & 0 & 1 & 0 & \cdots & 0 \\
 & \mathbf{A}^{41} & & & & \mathbf{A}^{42} & & & & \mathbf{A}^{43} & & & & \mathbf{A}^{44} & & \\
0 & 0 & \cdots & 0 & 0 & 0 & \cdots & 0 & 0 & 0 & \cdots & 0 & 0 & 0 & \cdots & 1
\end{array} \right]$$

$$\begin{bmatrix}
f_{0,r+1}^p \\
\vdots \\
f_{N_\eta-1,r+1}^1 \\
f_{N_\eta,r+1}^1 \\
\hline
g_{0,r+1}^p \\
\vdots \\
g_{N_\eta,r+1}^1 \\
\hline
\theta_{0,r+1}^p \\
\vdots \\
\theta_{N_\eta,r+1}^1 \\
\hline
\phi_{0,r+1}^p \\
\vdots \\
\phi_{N_\eta,r+1}^p
\end{bmatrix} = \begin{bmatrix}
0 \\
\vdots \\
0 \\
S \\
\hline
0 \\
\vdots \\
0 \\
\hline
0 \\
\vdots \\
1 \\
\hline
0 \\
\vdots \\
1
\end{bmatrix} \tag{49}$$

Starting from suitable initial approximations, expressed in the form

$$f_0(\eta) = 1 - e^{-\eta} + S, \ g_0(\eta) = e^{-\eta} - e^{-2\eta}, \ \theta_0(\eta) = e^{-\eta}, \ \phi_0(\eta) = e^{-\eta}, \quad (50)$$

the approximate solutions can be obtained iteratively by solving the matrix system (49).

4. Results and discussion

The nonlinear ODEs (13)-(16) were solved numerically using the overlapping grid SQLM. In the entire numerical computational process, the base amount of the parameters were chosen as $\beta = 1, \xi = 0.5, \varepsilon = 0.3, Nt = 0.5, Nb = 0.5, S = 0.5, Pr = 1, A = 0.01, M = 6, m = 0.1, Rd = 0.2, \theta_w = 1.2, Le = 0.6$, unless otherwise stated. It the present study, $p = 4$ overlapping sub-domains and $N_\eta = 20$ collocation points in each sub-domain were sufficient to give accurate and consistent results, since a further increase in the number of collocation points did not change the numerical results. The domain was truncated to $\eta_\infty = 20$. To benchmark the proposed method, our numerical results for the particular case were compared with previously published results obtained by Prashu and Nandkeolyar [25] using the single domain SQLM. The results are presented in Table 1, which indicates that the two set of results are in satisfactory accordance. It is also noted that the overlapping grid SQLM give comparable results using few grid points when compared to the single domain SQLM. It is clear that the overlapping grid SQLM is much faster compared to the single domain SQLM in computing the comparable numerical results. These observations suggests that the overlapping grid SQLM is computational efficiency and highly accurate than the single domain SQLM. This is due to the fact that the overlapping grid produces less dense or sparse coefficient matrices (in the matrix equations that results from collocation process) with a lot of zero entries. The sparsity of matrices minimizes the storage of large matrices and make it easy to perform matrix-vector multiplications. This is because there will be a lot of multiplication by zero, thus the matrices take less time to invert.

4.1. Residual error and convergence error analysis

To understand the convergence of the proposed method, we have considered solution errors, which are defined as the difference between approximate

values of the functions at two successive iterations. The following infinity norms are used to illustrate the convergence of the method:

$$E_f = \max_{0 \leq j \leq N} ||\mathbf{F}_{j,r+1}^{(\iota)} - \mathbf{F}_{j,r}^{(\iota)}||_\infty, \quad E_g = \max_{0 \leq j \leq N} ||\mathbf{G}_{j,r+1}^{(\iota)} - \mathbf{G}_{j,r}^{(\iota)}||_\infty,$$

$$E_\theta = \max_{0 \leq j \leq N} ||\mathbf{\Theta}_{j,r+1}^{(\iota)} - \mathbf{\Theta}_{j,r}^{(\iota)}||_\infty, \quad E_\phi = \max_{0 \leq j \leq N} ||\mathbf{\Phi}_{j,r+1}^{(\iota)} - \mathbf{\Phi}_{j,r}^{(\iota)}||_\infty. \quad (51)$$

It is noted in Fig. 2 that the error norms decrease rapidly with an increase in the number of iterations. This is an indication that the single domain SQLM and overlapping grid SQLM converge after about 5 iterations with the size of the error close to 10^{-11} and 10^{-14}, respectively. The smaller values of error norms for the overlapping grid SQLM is due to the few number of grid points used.
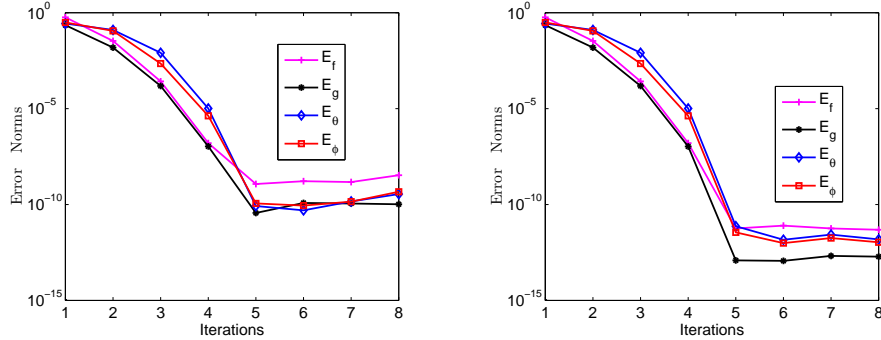
(a) Single domain SQLM when $N_\eta = 150$ and $p = 1$ (b) Overlapping grid SQLM when $N_\eta = 20$ and $p = 4$

Figure 2: Error norm graphs

To gain insights as to the accuracy of the proposed method, we have calculated residual errors, which measure the extent to which the numerical solution approximates the genuine solution. Consequently, the residual errors are defined as

$$||Res(\varsigma)||_\infty = ||\Delta_\varsigma \left[\mathbf{F}_{j,r+1}^{(\iota)}, \mathbf{G}_{j,r+1}^{(\iota)}, \mathbf{\Theta}_{j,r+1}^{(\iota)}, \mathbf{\Phi}_{j,r+1}^{(\iota)} \right] ||_\infty, \quad \varsigma = \{f, g, \theta, \phi\} \, (52)$$

where Δ_ς represents the nonlinear ODEs (13)-(16), $\mathbf{F}_j^{(\iota)}, \mathbf{G}_j^{(\iota)}, \mathbf{\Theta}_j^{(\iota)}$ and $\mathbf{\Phi}_j^{(\iota)}$ are the overlapping grid SQLM solutions. The change in residual errors against the number of iterations has been studied for various flow parameters such as Casson fluid parameter, variable viscosity parameter, variable

thermal conductivity parameter and Brownian motion parameter as seen in Fig. 3. The residual errors are observed to decrease significantly with the increase in the number of iterations and converge with errors of close to 10^{-15} after about 4 iterations. The smaller values of the residual errors imply the accuracy of the method. The above results sufficiently confirm the accuracy and convergence of the overlapping grid SQLM, thus the method can be trusted.
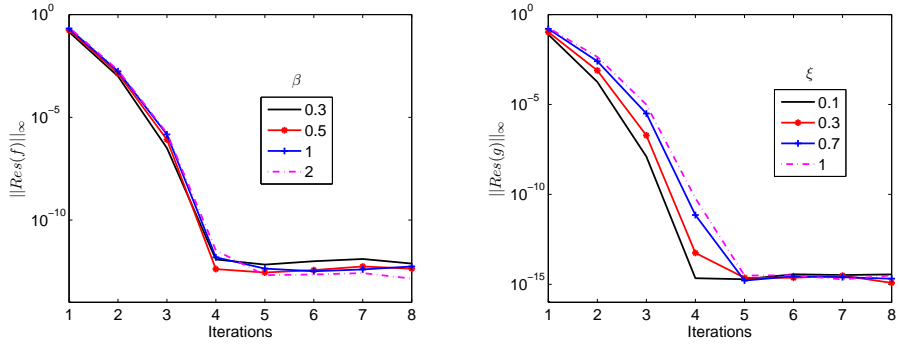
(a) $||Res(f)||_\infty$ for β on primary velocity

(b) $||Res(g)||_\infty$ for ξ on secondary velocity
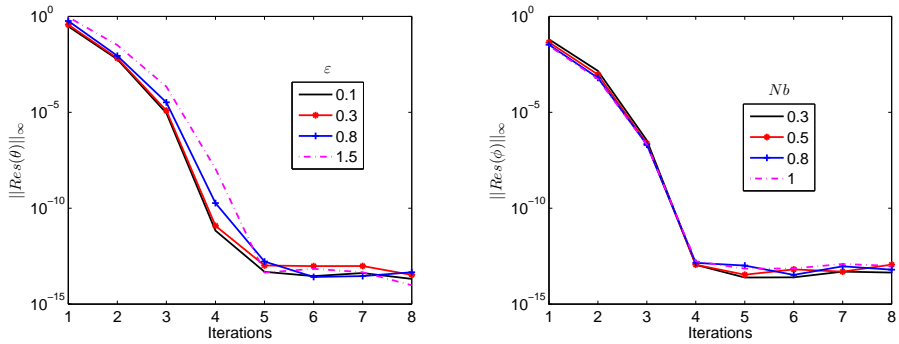
(c) $||Res(\theta)||_\infty$ for ε on temperature

(d) $||Res(\phi)||_\infty$ for Nb on concentration

Figure 3: Residual error graphs

In this study, we have also examined the effect of varying the number of sub-domains and the number of collocation points. Table 2 shows that the residual errors for the overlapping grid SQLM is always smaller than those errors from single domain SQLM. Indeed, the use of overlapping grid in the proposed method significantly improves the performance and accuracy of the

method. Table 2 and Table 3 indicate that increasing the number of overlapping sub-domains improves the accuracy and computational efficiency of the method. This is evident from diminishing residual errors as the number of sub-domains increases. Interestingly, as the number of subintervals increases, the total number of collocation points in the entire interval decreases. This suggests that the accurate results are obtained using few grid points in each sub-domain and the entire domain of integration. Table 3 also depicts that the single domain SQLM on single domain produce instability for $N = 600$. However, the overlapping grid SQLM generate good results with increasing number of sub-domains and using fewer grid points.

Table 1: Comparison of single domain SQLM (p =1) with overlapping grid SQLM (p =4) for the values of skin friction coefficients when $Rd = 0.5, \theta_w = 1, Pr = 10, \xi = \varepsilon = Nt = Nb = S = 0 = Le = 0$

M	m	A	β	Prashu and Nandkeolyar [25]			Present results		
				$-C_{fx}Re_x^{1/2}$	$C_{fz}Re_x^{1/2}$	N_η	$-C_{fx}Re_x^{1/2}$	$C_{fx}Re_x^{1/2}$	N_η
6	0.1	0.1	0.3	5.51874456	0.23905696	150	5.51874456	0.23905696	20
2	0.1	0.1	0.3	3.63997437	0.12517671	150	3.63997437	0.12517671	20
8	0.1	0.1	0.3	6.24973648	0.27988605	150	6.24973648	0.27988605	20
CPU Time(s)				0.537642	0.537642		0.112738	0.112738	
6	0.1	0.1	0.3	5.51874456	0.23905696	150	5.51874456	0.23905696	20
6	0.5	0.1	0.3	5.15310039	1.03810463	150	5.15310038	1.03810463	20
6	1	0.1	0.3	4.47154368	1.50968576	150	4.47154369	1.50968576	20
CPU Time(s)				0.505501	0.505501		0.119190	0.119190	
6	0.1	0.1	0.3	5.51874456	0.23905696	150	5.51874456	0.23905696	20
6	0.1	0.13	0.3	5.52749427	0.23866458	150	5.52749426	0.23866458	20
6	0.1	0.15	0.3	5.53332180	0.23840377	150	5.53332180	0.23840377	20
CPU Time(s)				0.504099	0.504099		0.125541	0.125541	
6	0.1	0.1	0.3	5.51874456	0.23905696	150	5.51874456	0.23905696	20
6	0.1	0.1	1	3.74924863	0.16240722	150	3.74924863	0.16240722	20
6	0.1	0.1	2.3	3.17557443	0.13755722	150	3.17557443	0.13755722	20
CPU Time(s)				0.578798	0.578798		0.111359	0.111359	

Table 2: Residual errors for different number of sub-domains and collocation points

p	N_η	N	$||Res(f)||_\infty$	$||Res(g)||_\infty$	$||Res(\theta)||_\infty$	$||Res(\phi)||_\infty$	CPU Time(s)
1	150	150	2.48579e-08	1.08189e-09	8.28448e-09	5.45453e-09	0.539001
2	75	149	1.49750e-010	1.62830e-012	1.01762e-011	2.75853e-012	0.463883
3	50	146	1.00797e-010	2.50352e-013	6.03160e-012	8.86478e-013	0.438762
5	30	148	2.47139e-011	6.03505e-014	3.92769e-013	1.74071e-012	0.424025
6	25	145	1.34972e-011	3.48253e-014	3.04333e-013	2.37144e-013	0.414315
10	15	141	3.46177e-012	3.04114e-014	5.84290e-014	4.70131e-013	0.362145
15	10	136	9.37221e-013	2.11527e-014	2.33390e-014	4.35138e-014	0.347288
25	6	126	2.03657e-013	5.12967e-015	3.49061e-014	3.29667e-014	0.301444

Table 3: Residual errors for different number of sub-domains and collocation points

p	N_η	N	$\|\|Res(f)\|\|_\infty$	$\|\|Res(g)\|\|_\infty$	$\|\|Res(\theta)\|\|_\infty$	$\|\|Res(\phi)\|\|_\infty$	CPU Time(s)
1	600	600	NAN	NAN	NAN	NAN	-
10	60	591	1.23787e-008	1.93328e-011	1.56635e-010	3.15281e-011	17.966692
12	50	589	7.05924e-009	3.04149e-011	6.31122e-011	1.61040e-011	17.591444
15	40	586	4.37061e-009	1.54583e-010	3.93456e-011	2.46298e-011	17.313163
20	30	581	2.69678e-009	4.40096e-011	2.30873e-011	6.11119e-012	16.916099
25	24	576	1.10545e-009	4.51961e-012	1.32917e-011	4.15594e-012	16.514835
30	20	571	6.12933e-010	3.20320e-011	2.61675e-012	1.22301e-011	15.904365
40	15	561	2.93832e-010	9.62040e-012	5.87679e-012	4.73957e-012	15.719455
50	12	551	1.63476e-010	1.83267e-012	9.51635e-013	1.23945e-012	15.484445
60	10	541	8.91546e-011	5.37796e-012	8.47239e-013	1.04693e-012	13.922720
100	6	501	2.02419e-011	1.29579e-012	4.43978e-013	3.95448e-013	11.292669
150	4	451	4.50318e-012	5.93313e-013	1.71280e-013	1.34281e-013	8.504460

4.2. Velocity profiles

Fig. 4-6 depicts the impact of notable flow parameters on the velocity distribution for constant$(\xi = 0)$ and variable $(\xi = 1)$ viscosity. It is noted that the velocity profiles and momentum boundary layer thickness reduce when the variable viscosity parameter increases. This is due to the fact that higher values of variable viscosity parameter suggests higher temperature difference between the surface and the ambient fluid. The figures suggest that the consequence of introducing the variable viscosity into the system has a remarkable effect on the velocity fields. Fig. 4a and Fig. 4b shows the effect of the Hall parameter on the velocity distribution. From Fig. 4a, it is noted that the fluid flow velocity displays an increasing trend with escalating values of the Hall parameter. This is because the effective thermal conductivity diminishes with the increase in Hall parameter which decreases the magnetic damping force. The fall in the magnetic damping force is coupled with the fact that magnetic field has a propelling effect on fluid velocity. An increase in the magnetic strength leads to a thinner boundary layer that is caused by the magnetic force, thereby augmenting the velocity in both primary and secondary velocity.

Fig. 5a and Fig. 5b present the repercussion of the Casson fluid parameter on the velocity profiles. Physically, the inverse relation of Casson fluid number with yield stress causes the large values of the Casson fluid parameter to diminish the yield stress, thus reducing the momentum boundary layer thickness. Both figures show that as the Casson fluid parameter intensifies, the primary and secondary velocity decline. An augmentation in the Casson fluid number strengthen viscosity and causes resistance to the fluid motion,

which in turn reduces the fluid velocity. The velocity fields are noted to be elevated in the case of Casson fluid than in Newtonian fluid case ($\beta \to \infty$). It is evident in Fig. 6a and Fig. 6b that velocity profiles are more suppressed in the case of suction than in the case of injection. When the suction parameter escalate, the amount of fluid particles are drawn into the surface, thus diminishing the velocity field.
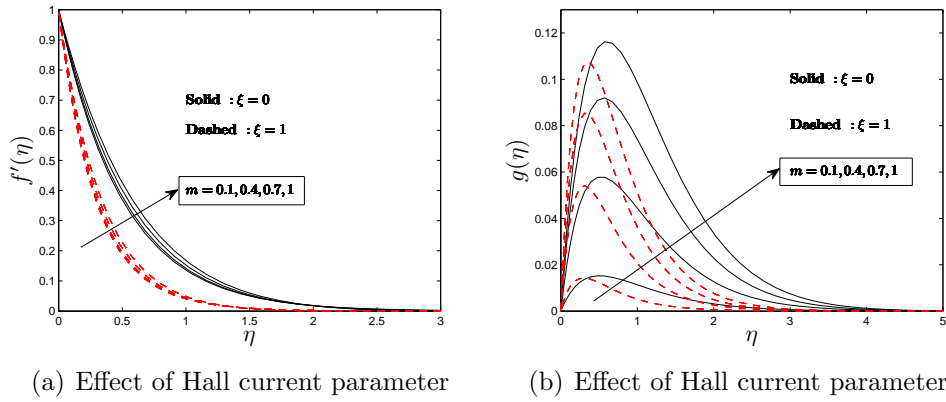

(a) Effect of Hall current parameter (b) Effect of Hall current parameter

Figure 4: Velocity profiles

(a) Effect of Casson fluid parameter (b) Effect of Casson fluid parameter
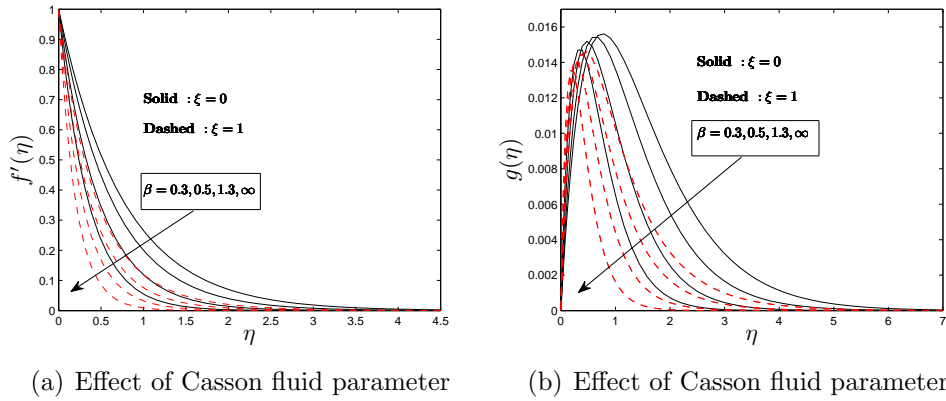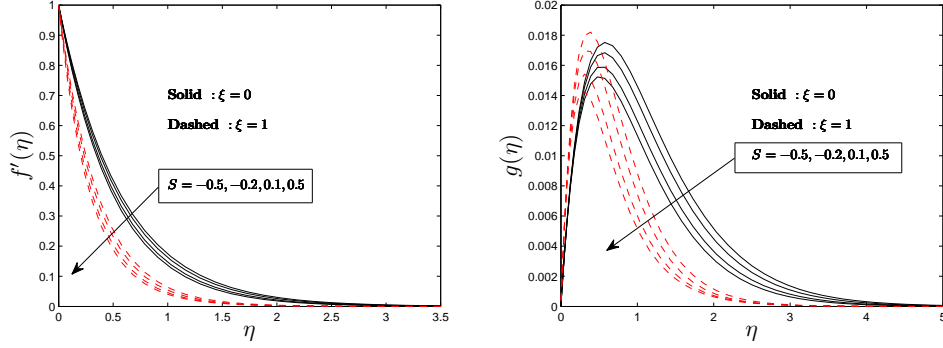
Figure 5: Velocity profiles

22

(a) Effect of suction/injection parameter   (b) Effect of suction/injection parameter

Figure 6: Velocity profiles

4.3. Temperature profiles

Fig. 7-9 elucidate the impact of important parameters on the temperature profiles for constant ($\varepsilon = 0$) and variable ($\varepsilon = 2$) thermal conductivity. It is seen that the temperature fields augment with increasing values of the variable thermal conductivity parameter. In accordance with Eq. (10), large values of the variable thermal conductivity parameter results to more thermal conductivity coefficient, which causes additional thermal diffusion through the fluid. Thus, the values of dimensionless temperature in the thermal boundary layer escalate and temperature gradient on the wall and heat transfer rate from the sheet decrease. The influence of flow parameters on the temperature is very sensitive with variable thermal conductivity when compared with constant thermal conductivity. It can be concluded that the inclusion of temperature-dependent thermal conductivity in the energy equation has a potential of rising the fluid temperature significantly, thus it cannot be neglected. Fig. 7a shows that the temperature profiles increase as thermal radiation parameter increases. This is because increase in radiation parameter releases heat energy into the flow. The heat transfer from the heated wall to the fluid thermal boundary layer thickness increases, fluid absorbs its own radiations. Fig. 7b shows that the temperature profiles augment with increasing values of the temperature ratio parameter. This is because increasing temperature ratio parameter indicate larger wall temperature compared to ambient temperature. It is noted in Fig. 8a that increasing the Casson fluid parameter enhances the thermal field and associated boundary layer thickness. This is because rising values of Casson fluid parameter

23

increases the viscous forces, and these forces generate some heat energy in the flow, thus increasing the fluid temperature. The thermal boundary layer thickness is seen to be thicker in the case of Newtonian fluid than in the case of Casson fluid. Fig. 8b shows that the thermal boundary layer thickness enhances as the unsteady parameter increases. This is due to an upsurge in convection currents with unsteadiness, which assist in intensifying thermal diffusion through the boundary layer. Fig. 9a and Fig. 9a shows that thermal fields and boundary layer thickness enhance as the variable viscosity and Brownian motion parameters increase. As the Brownian motion parameter shoot up, nanoparticles collide with the base fluid molecules, which enhance the kinetic energy and elevate the fluid temperature.
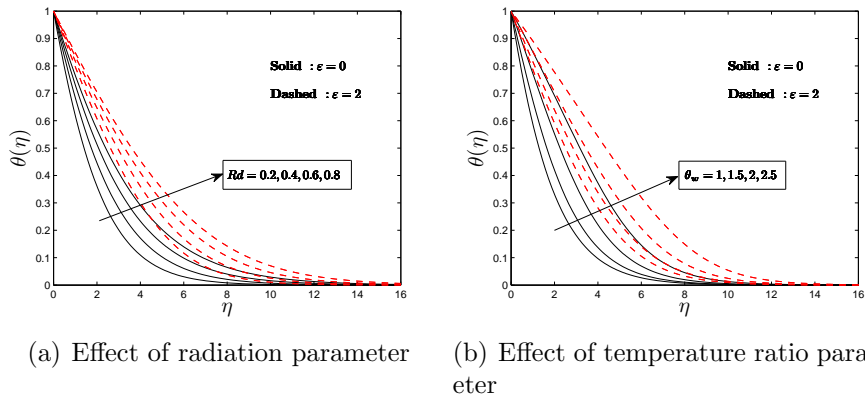

(a) Effect of radiation parameter

(b) Effect of temperature ratio parameter

Figure 7: Temperature profiles

(a) Effect of Casson fluid parameter
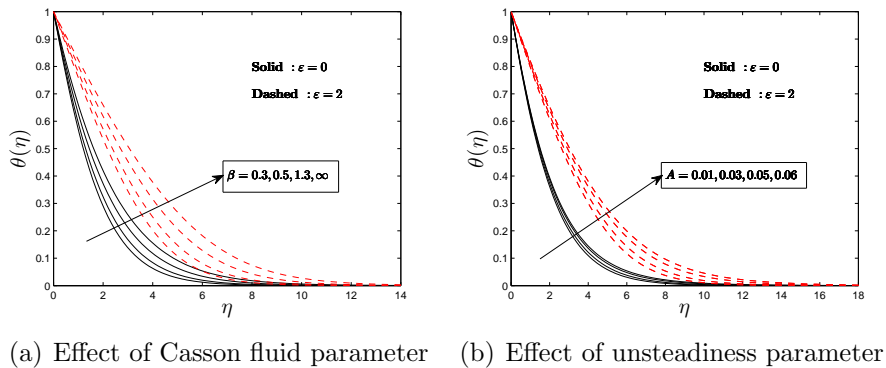
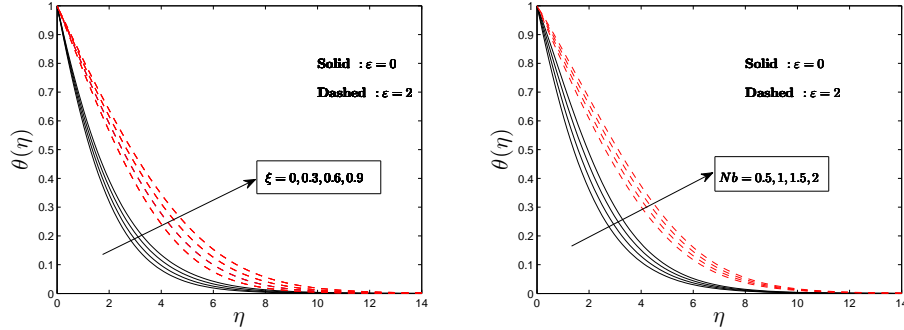(b) Effect of unsteadiness parameter

Figure 8: Temperature profiles

24

(a) Effect of variable viscosity parameter (b) Effect of Brownian motion parameter

Figure 9: Temperature profiles

4.4. Nanoparticle concentration profiles

Fig. 10-11 present the effect of pertinent parameters on the nanoparticle concentration profiles for the steadiness ($A = 0$) and unsteadiness ($A = 0.06$) case. It is observed noted that considering the unsteadiness case enhances the concentration profiles significantly. This is because a growth in the unsteadiness parameter causes the concentration boundary layer to be thick. The impact of flow parameters on nanoparticle concentration is noted to be very sensitive in the case of unsteadiness than in the case of steadiness. Fig. 10a and Fig. 10b display an elevation in the nanoparticle concentration profiles with the enhancement in variable viscosity parameter and Casson fluid parameter. Moreover, the nanoparticle concentration boundary layer thickness is seen to be thicker in Newtonian fluid than in Casson fluid.

The Brownian motion and thermophoresis parameters appear due to presence of nanoparticles. As the Brownian motion parameter increases, the species diffusion is suppressed, thus nanoparticle concentration boundary layer thickness shrink as seen in Fig. 11a . This is due to the fact that when Brownian motion parameter increases, nanoparticles collisions and random motion accelerate, which generate more heat and lessen the concentration of fluid. For thermophoresis parameter, the opposite trend is true for nanoparticle concentration as noted in Fig. 11b. This is because elevation of the thermophoresis force cause nanoparticles to move away from the hot surface resulting in increment of the concentration field.
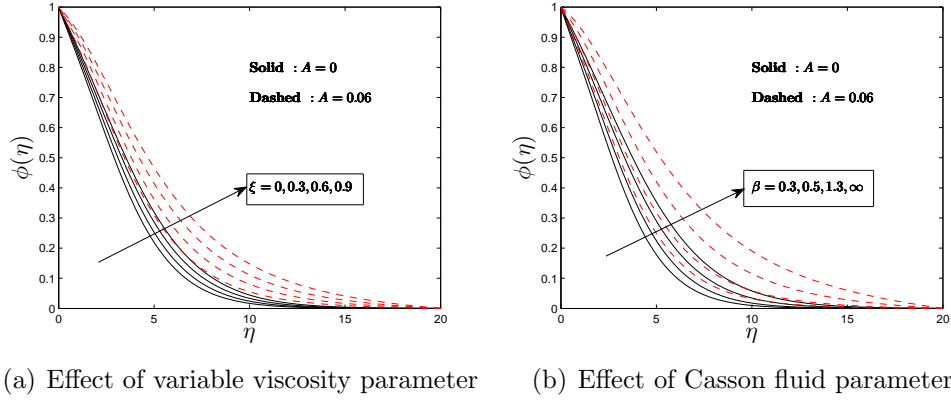
25

(a) Effect of variable viscosity parameter   (b) Effect of Casson fluid parameter

Figure 10: Concentration profiles

(a) Effect of Brownian motion parameter   (b) Effect of thermophoresis parameter
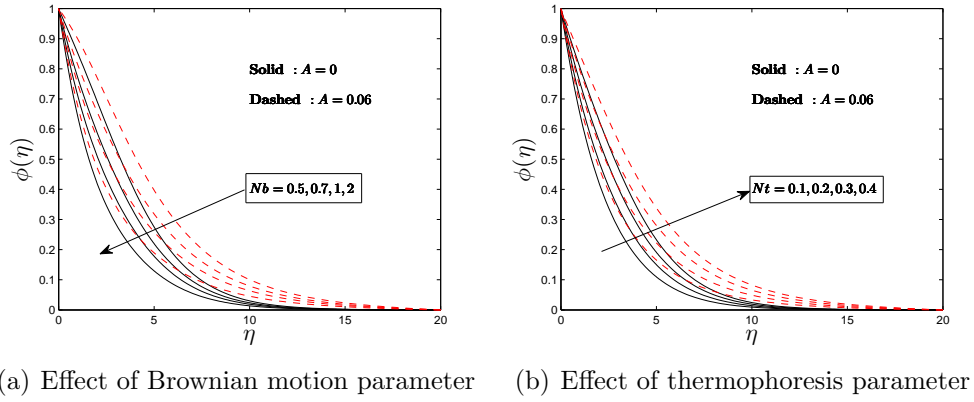
Figure 11: Concentration profiles

Table 4 shows that the skin friction coefficients on both primary and secondary flow at the wall decrease with increasing values of Casson fluid parameter, temperature ratio parameter, variable viscosity parameter, thermophoresis parameter and Brownian motion parameter. The Nusselt number and Sherwood number increase with radiation parameter, temperature ratio parameter and variable thermal conductivity, while decrease with Casson fluid parameter, thermophoresis parameter and variable viscosity parameter. It is also found that increasing the Brownian motion parameter reduce the Nusselt number while augmenting the Sherwood number.

Table 4: Overlapping grid SQLM results for skin friction coefficients, Nusselt Number and Sherwood number for various values of $Rd, \theta_w, \beta, \xi, \varepsilon, Nt$ and Nb when $Pr = 1, A = 0.01, M = 6, m = 0.1, S = 0.5$ and $Le = 0.6$

Rd	θ_w	β	ξ	ε	Nt	Nb	$-C_{fx}Re_x^{1/2}$	$C_{fz}Re_x^{1/2}$	$Nu_xRe_x^{-1/2}$	$Sh_xRe_x^{-1/2}$
0.2	1.2	1	0.5	0.3	0.5	0.5	3.22031297	0.12670781	0.64335216	0.14437506
0.4	1.2	1	0.5	0.3	0.5	0.5	3.21098042	0.12666449	0.66837321	0.20419754
0.6	1.2	1	0.5	0.3	0.5	0.5	3.20446812	0.12663928	0.68758160	0.24559418
0.2	1	1	0.5	0.3	0.5	0.5	3.22548296	0.12675186	0.63335388	0.10800497
0.2	1.5	1	0.5	0.3	0.5	0.5	3.21149289	0.12664298	0.66141459	0.20473605
0.2	2	1	0.5	0.3	0.5	0.5	3.19736709	0.12657761	0.69570873	0.29550147
0.2	1.2	0.3	0.5	0.3	0.5	0.5	4.66799135	0.18714475	0.72997195	0.19434966
0.2	1.2	1.5	0.5	0.3	0.5	0.5	2.95770772	0.11555730	0.62382297	0.13545775
0.2	1.2	∞	0.5	0.3	0.5	0.5	2.34352830	0.08919796	0.57315115	0.11548926
0.2	1.2	1	0	0.3	0.5	0.5	3.98967102	0.16273988	0.69561684	0.17035645
0.2	1.2	1	0.4	0.3	0.5	0.5	3.36310952	0.13324077	0.65367941	0.14917204
0.2	1.2	1	1	0.3	0.5	0.5	2.58773056	0.09844238	0.59376503	0.12355675
0.2	1.2	1	0.5	0	0.5	0.5	3.22883353	0.12677895	0.62673610	0.08488114
0.2	1.2	1	0.5	0.6	0.5	0.5	3.21385230	0.12666628	0.65747129	0.18747213
0.2	1.2	1	0.5	1.5	0.5	0.5	3.20137995	0.12661154	0.68967083	0.26716760
0.2	1.2	1	0.5	0.3	0.1	0.5	3.22400779	0.12672123	0.68686265	0.41578510
0.2	1.2	1	0.5	0.3	0.5	0.5	3.22031297	0.12670781	0.64335216	0.14437506
0.2	1.2	1	0.5	0.3	0.7	0.5	3.21857072	0.12670177	0.62283873	0.02152817
0.2	1.2	1	0.5	0.3	0.5	0.5	3.22031297	0.12670781	0.64335216	0.14437506
0.2	1.2	1	0.5	0.3	0.5	0.8	3.21585229	0.12666734	0.58275111	0.29375215
0.2	1.2	1	0.5	0.3	0.5	1.5	3.20653109	0.12659056	0.45856407	0.40654170

5. Conclusion

In this work, a numerical analysis on unsteady MHD radiative flow of Casson nanofluid with variable fluid properties over an inclined stretching sheet in the presence of suction/injection, thermophoresis, Brownian motion and Hall current is presented. The dimensionless conservation equations have been solved using the overlapping grid SQLM. The influence of significant non-dimensional flow parameters on the fluid properties has been established both qualitatively and quantitatively. We have carried out convergence and residual error analysis to assess the accuracy and convergence of the method. The method converges to the desired accurate solution after few iterations and using minimal number of grid points in each sub-domain as well as in the whole domain. The accuracy improves as the number of overlapping sub-domains increases. An increase in the number of overlapping sub-domains significantly minimizes the number of grid points required in the whole domain. The accuracy improvement is attributed to the overlapping grid which makes the coefficient matrices to be less dense. The rest of interesting findings are summarised as follows:

- Increasing Casson parameter and variable viscosity parameter decelerates the velocity flow and the flow characteristics, whereas the opposite is true for the temperature and concentration fields.

- The fluid velocity amplify significantly with Hall parameter while diminish with suction/injection parameter.

- The inclusion of temperature dependent thermal conductivity and non-linear thermal radiation into the system enhances the fluid temperature along with heat and mass transfer rate.

- Thermophoresis parameter tends to appreciate the nanoparticle concentration distribution but suppressing the mass transfer rate. The opposite trend occurs for the Brownian motion parameter.

- Improving the unsteadiness parameter enhances temperature and concentration profiles together with associated thermal and nanoparticle concentration boundary layer thickness.

- The influence of flow parameters is more sensitive with variable thermal conductivity and unsteadiness compared to constant thermal conductivity and steadiness.

- The thermal and concentration boundary layer is thicker for Newtonian fluid while the velocity boundary layer is thicker for Casson fluid.

References

[1] L. J. Crane, Flow past a stretching plate, Z. Angrew. Math. Phys. 21 (1970) 645-647.

[2] F. K. Tsou, E. M. Sparrow, R. J. Goldstein, Flow and heat transfer in the boundary layer on a continuous moving surface, Int. J. Heat Mass Transfer. 10 (1967) 219-235.

[3] H. Xu, S. J. Liao, Laminar flow and heat transfer in the boundary-layer of non-Newtonian fluids over a stretching flat sheet, Comput. Math. Appl. 57 (2009) 1425-1431.

[4] R. Cortell, A note on flow and heat transfer of a viscoelastic fluid over a stretching sheet, Int. J. Nonlin. Mech. 41 (2006) 78-85.

[5] A. Ishak, R. Nazar, I. Pop, Heat transfer over an unsteady stretching permeable surface with prescribed wall temperature, Nonlinear Analy. Real World Appl. 10 (2009) 2909-2913.

[6] M. S. Ayano, O. Otegbeye, S. S. Motsa, MHD mixed convection chemically reactive Casson fluid flow over an inclined stretching/shrinking sheet: Paired quasilinearization approach, Mathematical Mod. Eng. problems. 6 (2019) 188-196.

[7] L. G. Grubka, K. M. Bobba, Heat transfer characteristics of a continuous stretching surface with variable temperature, ASME J. Heat Transfer. 107 (1985) 248-250.

[8] P. D. Ariel, On computation of the three-dimensional flow past a stretching sheet, Appl. Math. Comput. 188 (2007) 1244-1250.

[9] S.U. Choi, Enhancing thermal conductivity of fluids with nanoparticles in developments and applications of Non-Newtonian flows, FED-vol. 231/MD-vol. 66 (1995) 99-105.

[10] J. Buongiorno, Convective transport in nanofluids, ASME J. Heat Trans. 128 (2006) 240-250.

[11] N. A. Haroun, P. Sibanda, S. Mondal, S. S. Motsa, M.M Rashidi, Heat and mass transfer of nanofluid through an impulsively vertical stretching surface using the spectral relaxation method, Bound. Value Probl. 2015, 161 (2015). https://doi.org/10.1186/s13661-015-0424-3

[12] O. D. Makinde, W. A. Khan, Z. H. Khan, Buoyancy effects on MHD stagnation point flow and heat transfer of nano fluid past a convectively heated stretching/shrinking sheet, Int. J. of Heat Mass Transf. 62 (2013) 526-533.

[13] N. Freidoonimehr, M. M. Rashidi, S. Mahmud, Unsteady MHD free convective flow past a permeable stretching vertical surface in a nanofluid, Int. J. Therm. Sci. 87 (2015) 136-145.

[14] O. D. Makinde, A. Aziz, Boundary layer flow of a nanofluid past a stretching sheet with a convective boundary condition, Int. J. Therm. Sci. 50 (2011) 1326-1332.

[15] I. Zahmatkesh, On the importance of thermophoresis and Brownian diffusion for the deposition of micro and nanoparticles, Int. Commun. Heat Mass Transf. 35 (2008) 369-375.

[16] M. Sheikholeslami, M. Gorji-Bandpy, D. D. Ganji, Lattice Boltzmann method for MHD natural convection heat transfer using nanofluid, Powder Technol. 254 (2014) 82-93.

[17] T. Hayat, T. Muhammad, A. Alsaedi, M. S. Alhuthali, Magnetohydrodynamics three dimensional flow of viscoelastic nano-fluid in the presence of nonlinear thermal radiation, J. Magn. Magn. Mater. 385 (2015) 222-229.

[18] N. A. Casson, A Flow Equation for Pigment-Oil Suspensions of the Printing Ink Type; Mill, C.C., Ed.; Rheol. Disperse Syst. Pergamon Press: Oxford, UK, (1959) 84-104.

[19] S. K. Nandy, Analytical Solution of MHD Stagnation-Point Flow and Heat Transfer of Casson Fluid over a Stretching Sheet with Partial slip, Thermodynamics, (2013). https://doi.org/10.1155/2013/108264.

[20] S. Mukhopadhyay, Casson fluid flow and heat transfer over a nonlinearly stretching surface, Chin Phys. B 22 (2013) 074701.

[21] S. Mukhophadhyay, K. Vajravelu, Diffusion of chemically reactive species in Casson fluid flow over an unsteady permeable stretching surface, J. Hydrodyn. 25 (2013) 591-598.

[22] A. S. Butt, M. N. Tufail, A. Alia, Three-dimensional flow of a magnetohydrodynamic Casson fluid over an unsteady stretching sheet embedded into a porous medium, J. Appl. Mech. Tech. Phys. 57 (2016) 283-292.

[23] D. Pal, Hall current and MHD effects on heat transfer over an unsteady stretching permeable surface with thermal radiation, Comput. Math. Appl. 66 (2013) 1161-80.

[24] M. B. Ashraf, T. Hayat, A. Alsaedi, Mixed convection flow of Casson fluid over a stretching sheet with convective boundary conditions and Hall effect, Bound. Value Probl. 2017, 137 (2017). https://doi.org/10.1186/s13661-017-0869-7

[25] Prashu, R. Nandkeolyar, A numerical treatment of unsteady three-dimensional hydromagnetic flow of a Casson fluid with Hall and radiation effects, Results in Phys. 11 (2018) 966-974.

[26] M. A. El-Aziz, A. A. Afify, Effect of Hall current on MHD slip flow of Casson nanofluid over a stretching sheet with zero nanoparticle mass flux, Thermophys Aeromech. 26 (20019) 429-443.

[27] I. L. Animasaun, Casson Fluid Flow with Variable Viscosity and Thermal Conductivity along Exponentially Stretching Sheet Embedded in a Thermally Stratified Medium with Exponentially Heat Generation, J. Heat and Mass Transf. Res. 2 (2015) 63-78.

[28] I. L. Animasaun, Effect of thermophoresis, variable viscosity and thermal conductivity on free convective heat and mass transfer of non-Darcian MHD dissipative Casson fluid flow with suction and nth order chemical reaction, J. Niger. Math. Soc. 34 (2015) 11-31.

[29] A. Bisht, R. Sharma, Non-similar solution of Casson nanofluid with variable viscosity and variable thermal conductivity. Int. J. Numer. Methods Heat Fluid Flow, (2019). https:// doi.org/10.1108/HFF-08-2019-0629

[30] K. V. Prasad, H. Vaidya, G. Mnjunatha, K. Vajravelu, C. Rajashekhar, V. Ramanjini, Influence of Variable Transport Properties on Casson Nanofluid Flow over a Slender Riga Plate: Keller Box Scheme, J. Adv. Res. Fluid Mech. Therm. Sci. 64 (2019) 19-42.

[31] J. A. Gbadeyan, E. O. Titiloye, A. T. Adeosun, Effect of variable thermal conductivity and viscosity on Casson nanofluid flow with convective heating and velocity slip. Heliyon. 6 (2020), e03076. https://doi.org/10.1016/j.heliyon.2019.e03076

[32] S. S. Motsa, A New Spectral Local Linearization Method for Nonlinear Boundary Layer Flow Problems, J. Appl. Math. 2013 (2013), Article ID 423628. https://doi.org/10.1155/2013/423628

[33] H. H. Yang, B. R. Seymour, B. D. Shizgal, A chebyshev pseudospectral multidomain method for steady flow past a cylinder up to Re = 150, Comput. Fluids, 23 (1994) 829-851.

[34] D. Olmos, B. D. Shizgal, A pseudospectral method of solution of Fisher's equation, J. Comput. Appl. Math. 193 (2006) 219-242.

[35] A. Teleei, M. Dehghan, A pseudo-spectral method that uses an overlapping multidomain technique for the numerical solution of sine-Gordon equation in one and two spatial dimensions, Math. Meth. Appl. Sci. 37 (2013) 1909-1923.

[36] M. Abd-Elziz, Flow and heat transfer over an unsteady stretching surface with Hall effect, Meccanica, 45 (2010) 97-109.

[37] C. U. Jawali, A. J. Chamkha, Combined effect of variable viscosity and thermal conductivity on free convection flow of a viscous fluid in a vertical channel. Int. J. Numer. Methods Heat Fluid Flow, 26 (2015) 18–39.

[38] M. A. Mahmoud, A. M. Megahed, MHD flow and heat transfer in a non-Newtonian liquid film over an unsteady stretching sheet with variable fluid properties, Can. J. Phys. 87 (2009) 1065-1071.

[39] A. M. Megahed, Williamson fluid flow due to a nonlinearly stretching sheet with viscous dissipation and thermal radiation, J. Egypt. Math. Soc. 27 (2019) 12.

[40] I. S. Oyelakin, P. Sibanda, Analysis of exponentially varying viscosity and thermal conductivity on a tangent hyperbolic fluid. SeMA (2020). https://doi.org/10.1007/s40324-020-00215-0.

[41] S. Jangilis, S. O. Adesanya, H. A. Ogunseye, R. S. Lebelo, Couple stress fluid flow with variable properties: a second law analysis, Math. Methods Appl. Sci. 42 (2019) 85-98.

[42] R. E. Bellman, R. E. Kalaba, Quasilinearization and Nonlinear Boundary Value Problems, RAND Corporation: Santa Monica, CA, USA, 1965.

[43] L. N. Trefethen, Spectral Methods in MATLAB, 10, SIAM, 2000.

Chapter 3

Overlapping multi-domain bivariate spectral method for systems of nonlinear PDEs with fluid mechanics applications

In Chapter 2, we discussed the development and application of the overlapping grid spectral collocation method for the purpose of solving ordinary differential equations. In this chapter, we introduce the overlapping multi-domain bivariate spectral quasilinearisation method and use the method to solve coupled nonlinear partial differential equations of non-similar boundary layer flow. The solution procedure involves the decomposition of the domains into overlapping and non-overlapping subintervals, discretization, linearisation using the quasilinearisation method (QLM), domain transformation into $[-1, 1]$ where the spectral method is valid. Also, the bivariate Lagrange interpolating polynomial is used to approximate the functions, and the Chebyshev spectral collocation method is applied through evaluating the linearised equations at the collocation points. Error norms and residual errors are used to analyze the convergence and accuracy of the numerical approximations. Lastly, series solutions are used to validate the accuracy of the numerical method.

Overlapping Multi-domain Bivariate Spectral Method for Systems of Nonlinear PDEs with Fluid Mechanics Applications

Musawenkhosi Mkhatshwa, Sandile Motsa, and Precious Sibanda

Abstract An efficient overlapping multi-domain bivariate spectral quasilineariza-tion method (OMD-BSQLM) is introduced for non-similar boundary layer equations arising in fluid mechanics. Previously, the multi-domain approach has been applied to either space or time interval but not both. The new method applies the multi-domain technique in both space and time interval. The time interval is decomposed into non-overlapping sub-intervals, and the space interval is split into overlapping sub-domains. Numerical experiments are carried out to highlight the accuracy and efficiency of the method. An analysis of the convergence and accuracy of the OMD-BSQLM is given using error norms and residual errors. The series solutions are used to validate the accuracy of the OMD-BSQLM results. The new method converges rapidly and gives accurate results after a few iterations and using a few grid points. Moreover, the accuracy does not worsen when a large time domain is considered.

Keywords Multi-domain overlapping technique · Bivariate interpolation · Spectral quasilinearisation method

1 Introduction

Most heat and mass transfer problems arising in fluid dynamics are modelled by non-similar boundary layer partial differential equations (PDEs). These differential equations are often difficult to solve analytically or their exact solutions may not exist. In such instances, we have to solve the differential equations using numerical methods. Analytical solutions can give an insight into the influence of various parameters that have a bearing on the solution, which is not generally the case with numerical

M. Mkhatshwa ( ) · S. Motsa · P. Sibanda
School of Mathematics, Statistics and Computer Science, University of Kwazulu Natal,
Private Bag X01, Scottsville, Pietermaritzburg 3209, South Africa
e-mail: patsonmkhatshwa@gmail.com

S. Motsa
Department of Mathematics, University of Eswatini, Kwaluseni, Kingdom of Eswatini

methods. However, numerical methods are efficient tools that can be used in solving highly nonlinear differential equations that are complex and even impossible to solve analytically. The challenge of finding more accurate, robust and computationally efficient numerical methods for solving strongly nonlinear problems still exists. The development of numerical methods that converge quickly and most accurate is currently attracting the attention of a growing number of researchers. Traditional methods such as the finite difference method require a large number of grid points to produce accurate results. Their accuracy also deteriorates fast as the time domain increases for parabolic nonlinear PDEs.

Spectral collocation-based methods have been used to solve many non-similar boundary layer differential equations. They have shown to be reliable and efficient in solving nonlinear systems of ordinary differential equations (ODEs) and PDEs. Spectral methods have many advantages over traditional methods such as high accuracy and efficiency [1]. When applied to problems with smooth solutions, they use few grid points and require minimal computational time to generate accurate solutions, thus better than traditional methods. Motsa et. al [2] applied the spectral method in space and finite differences in time when solving non-similar boundary layer differential equations. To improve the accuracy and computational speed of spectral methods several researchers [3–5] applied spectral collocation method independently in both space and time. The method gives accurate results for smaller time domains. The accuracy of the method decreases with an increase in the time domain. One of the effective techniques to overcome this problem is using a multi-domain grid. Motsa et al. [6] introduced a non-overlapping multi-domain bivariate spectral quasilinearization method (MD-BSQLM) to increase the accuracy of spectral collocation-based methods for large time variable. The non-overlapping MD-BSQLM applies the multi-domain technique only in the time interval. Following the discretization process, the multi-domain technique can help to make the matrices to be less dense. This means that most of the elements will be zeros. The sparsity of matrices can help to minimize storage for large matrices and make it easy to perform matrix-vector multiplications. This is because there will be a lot of multiplication by zero which reduces the computational time and enable the matrices to be stored efficiently. Yang [7] introduced an overlapping multi-domain technique and used it to solve PDEs exhibiting discontinuous solutions. The technique was found to give accurate results compared to existing numerical methods. The concept of overlapping sub-domains has been discussed by several researchers [8–10].

The need to continually improve on existing spectral collocation-based methods for solving nonlinear differential equations that cannot be solved analytically cannot be overstated. Most studies in the literature used the multi-domain technique in either space or time but not both. However, applying the multi-domain technique in both space and time interval and further utilizing the strategy of overlapping sub-domains can increase the accuracy of spectral collocation-based methods for small and large time variable. The objective of the study is to introduce a method that uses the multi-domain technique, spectral collocation method, bivariate Lagrange interpolation polynomials based on Chebyshev–Gauss Lobatto grid points [11, 12] and quasilinearization method (QLM) [13] in finding solutions of coupled non-similar

boundary layer PDEs over a large time interval. The multi-domain technique employs the strategy of non-overlapping and overlapping sub-domains. Thus, the time interval is partitioned into non-overlapping sub-domains, and the space interval is decomposed into overlapping sub-intervals. The applicability, accuracy and reliability of the proposed method have been tested by solving systems of n coupled non-similar boundary layer partial differential equations arising in fluid mechanics.

2 The Overlapping Multi-domain Bivariate Spectral Quasilinearization Method (OMD-BSQLM)

In this section, we introduce the OMD-BSQLM for a system of n nonlinear PDEs expressed in the form

$$\Gamma_1[F_1, F_2, \ldots, F_n] = 0, \tag{1}$$

$$\Gamma_2[F_1, F_2, \ldots, F_n] = 0, \tag{2}$$

$$\vdots$$

$$\Gamma_n[F_1, F_2, \ldots, F_n] = 0, \tag{3}$$

where the operators $F_i\,(i = 1, 2, 3, \ldots, n)$ are given by

$$F_1 = \left\{ g_1, \frac{\partial g_1}{\partial \eta}, \frac{\partial^2 g_1}{\partial \eta^2}, \ldots, \frac{\partial^s g_1}{\partial \eta^s}, \frac{\partial g_1}{\partial \xi}, \frac{\partial}{\partial \xi}\left(\frac{\partial g_1}{\partial \eta}\right) \right\}$$

$$\vdots$$

$$F_n = \left\{ g_n, \frac{\partial g_n}{\partial \eta}, \frac{\partial^2 g_n}{\partial \eta^2}, \ldots, \frac{\partial^s g_n}{\partial \eta^s}, \frac{\partial g_n}{\partial \xi}, \frac{\partial}{\partial \xi}\left(\frac{\partial g_n}{\partial \eta}\right) \right\}. \tag{4}$$

We denote the order of differentiation by s, *and* the required solution by $g_k(\eta, \xi)$ and Γ_k denotes the nonlinear operators containing all the spatial and time derivatives of $g_k(\eta, \xi)$. The Chebyshev–Gauss–Lobatto grid points and their corresponding differentiation are defined in the interval $[-1, 1]$. In order to apply the OMD-BSQLM, the time interval $\xi \in [0, T]$ is decomposed into q non-overlapping sub-intervals defined as

$$J_\upsilon = (\xi_{\upsilon-1}, \xi_\upsilon), \quad \upsilon = 1, 2, 3, \ldots, q. \tag{5}$$

The space interval $[a, b]$ is decomposed into p overlapping sub-intervals of length L, denoted by

$$I_\mu = [\eta_0^\mu, \eta_{N_\eta}^\mu], \quad \mu = 1, 2, 3, \ldots, p, \tag{6}$$
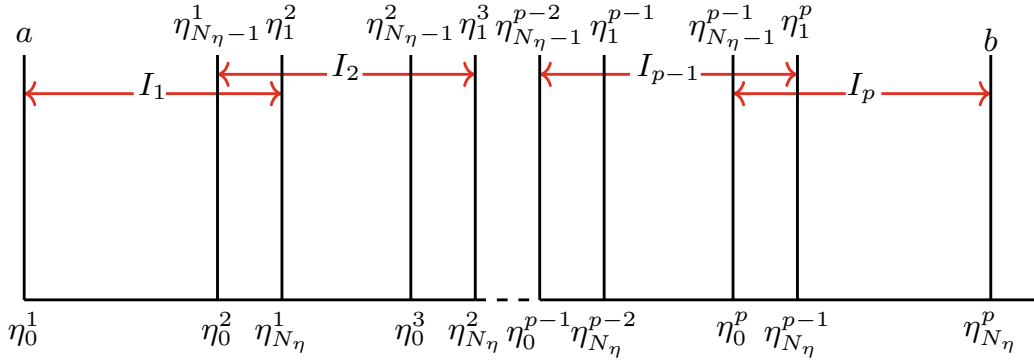
Fig. 1 Overlapping grid

where each I_μ interval is further discretized into $N_\eta + 1$ collocation points. For the overlap to be possible, the sub-intervals must be of equal length given by

$$L = \frac{b - a}{p + \frac{1}{2}(1 - p)(1 - \cos \frac{\pi}{N_\eta})}. \tag{7}$$

In the overlapping multi-domain grid, the first two points of the interval $I_{\mu+1}$ coincide with the last two points of the interval I_μ as shown in Fig. 1. To derive the result in Eq. (7), we note that the total length of the domain is

$$\begin{aligned} b - a &= 2L - \varepsilon + (2L - 2\varepsilon)\left(\frac{p}{2} - 1\right) \\ &= 2L - \varepsilon + (L - \varepsilon)(p - 2) = \varepsilon(1 - p) + pL, \end{aligned} \tag{8}$$

where ε is the overlapping distance between two intervals. We remark that $\varepsilon = \eta_0 - \eta_1$. Considering the first interval I_1 in which $\eta \in [a, \eta_{N_\eta}^1]$, we can define the length $L = \eta_{N_\eta}^1 - a$. The linear transformation $\eta = \frac{L}{2}z + \frac{a + \eta_{N_\eta}^1}{2}$ can be used to transform the interval $[a, \eta_{N_\eta}^1]$ to $[-1, 1]$. Thus, using the Gauss–Lobatto collocation points $z_i = \cos\left(\frac{\pi i}{N_\eta}\right)$, where $i = 0, 1, 2, 3, \ldots, N_\eta$, we obtain $\eta_0 - \eta_1 = \frac{L}{2}(z_0 - z_1) = \frac{L}{2}\left(1 - \cos \frac{\pi}{N_\eta}\right)$. Therefore, Eq. (8) becomes

$$b - a = \frac{L}{2}\left(1 - \cos \frac{\pi}{N_\eta}\right)(1 - p) + pL, \tag{9}$$

and making L the subject in Eq. (9) yields Eq. (7).

Generally, before the spectral collocation method is applied at each sub-interval, the time interval $\xi \in J_\upsilon$ and space interval $\eta \in I_\mu$ are transformed into $\tau \in [-1, 1]$ and $z \in [-1, 1]$ using the linear transformations

$$\xi_j = \frac{1}{2}(\xi_\upsilon - \xi_{\upsilon-1})\tau_j + \frac{1}{2}(\xi_\upsilon + \xi_{\upsilon-1}), \quad \tau_j = \cos\left(\frac{\pi j}{N_\xi}\right), \tag{10}$$

$$\eta_i^\mu = \frac{L}{2}(z_i + 1), \quad z_i = \cos\left(\frac{\pi i}{N_\eta}\right). \tag{11}$$

In terms of the original variable η, the collocation points are arranged as

$$\{\eta_r\}_{r=0}^M = \left\{\eta_0^1, \ldots, \eta_{N_\eta-1}^1 = \eta_0^2, \eta_{N_\eta}^1 = \eta_1^2, \ldots, \eta_k^\mu, \ldots, \eta_{N_\eta-1}^\mu = \eta_0^{\mu+1}, \eta_{N_\eta}^\mu = \eta_1^{\mu+1}, \ldots, \eta_{N_\eta}^p\right\},$$

$$= \left\{\eta_0^1, \ldots, \eta_{N_\eta-1}^1, \eta_1^2, \ldots, \eta_k^\mu, \ldots, \eta_{N_\eta-1}^\mu, \eta_1^{\mu+1}, \ldots, \eta_{N_\eta}^p\right\}, \tag{12}$$

where $M = N_\eta + (N_\eta - 1)(p - 1)$ is the total number of collocation points over the entire space interval. It can be shown that the grid points can be obtained as follows

$$\eta_i^1 = a + \frac{L}{2}(z_i + 1), \quad i = 1, 2, 3, \ldots, N_\eta,$$

$$\eta_i^{p-\mu} = \frac{L}{2}(z_i - 1) + b - \frac{L\mu}{2}\left[1 + \cos\left(\frac{\pi}{N_\eta}\right)\right], \quad i = 1, 2, \ldots, N_\eta - 1, \mu = 2, 3, \ldots, p - 1,$$

$$\eta_i^p = a + \frac{L}{2}(1 + z_i), \quad i = 0, 1, 2, \ldots, N_\eta - 1. \tag{13}$$

In terms of the transformed variables z and τ, the collocation points are arranged as

$$\{z_r\}_{r=0}^M = \left\{z_{N_\eta}^1, \ldots, z_1^1 = z_{N_\eta}^2, z_0^1 = z_{N_\eta-1}^2, \ldots, z_k^\mu, \ldots, z_1^\mu = z_{N_\eta}^{\mu+1}, z_0^\mu = \eta_{N_\eta-1}^{\mu+1}, \ldots, \eta_0^p\right\},$$

$$= \left\{z_{N_\eta}^1, \ldots, z_1^1, z_{N_\eta-1}^2, \ldots, z_k^\mu, \ldots, z_1^\mu, z_{N_\eta-1}^{\mu+1}, \ldots, z_0^p\right\},$$

$$\{\tau_r\}_{r=0}^{N_\xi} = \left\{\tau_{N_\xi}^1, \ldots, \tau_1^1, \tau_{N_\xi}^2, \ldots, \tau_k^\upsilon, \ldots, \tau_1^\upsilon, \tau_{N_\xi}^{\upsilon+1}, \ldots, \tau_0^q\right\}. \tag{14}$$

We assume that at each sub-interval, the solution can be approximated by a bivariate Lagrange interpolation polynomial of the form

$$g_k^{(\mu,\upsilon)}(\eta, \xi) \approx \sum_{i=0}^{N_\eta} \sum_{j=0}^{N_\xi} g_k^{(\mu,\upsilon)}(\eta_i, \xi_j)\mathcal{L}_i(\eta)\mathcal{L}_j(\xi), \tag{15}$$

where the bivariate interpolation polynomial interpolates $g_k^{(\mu,\upsilon)}(\eta, \xi)$ at selected points (η_i, ξ_j) in both η and ξ directions. Applying the QLM on Γ_k gives

$$\Gamma_k[F_1, F_2, \ldots, F_n] \approx (F_{1,r+1} - F_{1,r}, F_{2,r+1} - F_{2,r}, \ldots, F_{n,r+1} - F_{n,r}).\nabla\Gamma_k[F_{1,r}, F_{2,r}, \ldots, F_{n,r}]$$

$$+\Gamma_k[F_{1,r}, F_{2,r}, \ldots, F_{n,r}], \tag{16}$$

where r and $r + 1$ denote previous and current iteration, respectively. The vector of the partial derivatives denoted by ∇ is defined as

$$\nabla = \left\{\nabla_{g_1}, \nabla_{g_2}, \ldots, \nabla_{g_n}\right\}, \tag{17}$$

and

$$\nabla_{g_1} = \left\{ \frac{\partial}{\partial g_1}, \frac{\partial}{\partial g_1'}, \frac{\partial}{\partial g_1''}, \ldots, \frac{\partial}{\partial g_1^{(s)}}, \frac{\partial}{\partial\left(\frac{\partial g_1}{\partial\xi}\right)}, \frac{\partial}{\partial\left(\frac{\partial g_1'}{\partial\xi}\right)} \right\}, \tag{18}$$

$$\vdots$$

$$\nabla_{g_n} = \left\{ \frac{\partial}{\partial g_n}, \frac{\partial}{\partial g_n'}, \frac{\partial}{\partial g_n''}, \ldots, \frac{\partial}{\partial g_n^{(s)}}, \frac{\partial}{\partial\left(\frac{\partial g_n}{\partial\xi}\right)}, \frac{\partial}{\partial\left(\frac{\partial g_n'}{\partial\xi}\right)} \right\}, \tag{19}$$

where the prime denotes differentiation with respect to η. The linearized Eq. (16) can be expressed in a compact form as

$$\sum_{l=1}^{n} F_{l,r+1} \cdot \nabla_{f_l} \Gamma_k \left[F_{1,r}, F_{2,r}, \ldots, F_{n,r} \right] = \sum_{l=1}^{n} F_{l,r} \cdot \nabla_{f_l} \Gamma_k \left[F_{1,r}, F_{2,r}, \ldots, F_{n,r} \right]$$
$$- \Gamma_k \left[F_{1,r}, F_{2,r}, \ldots, F_{n,r} \right], \tag{20}$$

for $k = 1, 2, \ldots, n$. Equation (20) forms a system of n coupled linear PDEs which are solved iteratively for $g_{1,r+1}^{(\mu,\upsilon)}(\eta, \xi), g_{2,r+1}^{(\mu,\upsilon)}(\eta, \xi), \ldots, g_{n,r+1}^{(\mu,\upsilon)}(\eta, \xi)$. Equation (20) can further be expressed as

$$\sum_{v=1}^{n} \left[\sum_{l=0}^{s} \alpha_{v,l,r}^{(1,\mu,\upsilon)} g_{v,r+1}^{(l,\mu,\upsilon)} + \beta_{v,r}^{(1,\mu,\upsilon)} \frac{\partial g_{v,r+1}^{(\mu,\upsilon)}}{\partial\xi} + \gamma_{v,r}^{(1,\mu,\upsilon)} \frac{\partial}{\partial\xi}\left(\frac{\partial g_{v,r+1}^{(\mu,\upsilon)}}{\partial\eta} \right) \right] = R_1^{(\mu,\upsilon)}$$

$$\sum_{v=1}^{n} \left[\sum_{l=0}^{s} \alpha_{v,l,r}^{(2,\mu,\upsilon)} g_{v,r+1}^{(l,\mu,\upsilon)} + \beta_{v,r}^{(2,\mu,\upsilon)} \frac{\partial g_{v,r+1}^{(\mu,\upsilon)}}{\partial\xi} + \gamma_{v,r}^{(2,\mu,\upsilon)} \frac{\partial}{\partial\xi}\left(\frac{\partial g_{v,r+1}^{(\mu,\upsilon)}}{\partial\eta} \right) \right] = R_2^{(\mu,\upsilon)} \tag{21}$$

$$\vdots$$

$$\sum_{v=1}^{n} \left[\sum_{l=0}^{s} \alpha_{v,l,r}^{(n,\mu,\upsilon)} g_{v,r+1}^{(l,\mu,\upsilon)} + \beta_{v,r}^{(n,\mu,\upsilon)} \frac{\partial g_{v,r+1}^{(\mu,\upsilon)}}{\partial\xi} + \gamma_{v,r}^{(n,\mu,\upsilon)} \frac{\partial}{\partial\xi}\left(\frac{\partial g_{v,r+1}^{(\mu,\upsilon)}}{\partial\eta} \right) \right] = R_n^{(\mu,\upsilon)},$$

where $\alpha_{n,s,r}^{(k,\mu,\upsilon)}(\eta, \xi)$, $\beta_{v,r}^{(k,\mu,\upsilon)}(\eta, \xi)$ and $\gamma_{v,r}^{(k,\mu,\upsilon)}(\eta, \xi)$ are variable coefficients of $g_{n,r+1}^{(s,\mu,\upsilon)}$, $\frac{\partial g_{v,r+1}^{(\mu,\upsilon)}}{\partial\xi}$ and $\frac{\partial}{\partial\xi}\left(\frac{\partial g_{v,r+1}}{\partial\xi} \right)$, respectively. These variable coefficients correspond to the kth equation, for $k = 1, 2, \ldots, n$. The variable coefficients are obtained as

$$\alpha_{n,s,r}^{(k,\mu,\upsilon)} = \frac{\partial\Gamma_k}{\partial g_{n,r}^{(s,\mu,\upsilon)}}, \; \beta_{v,r}^{(k,\mu,\upsilon)} = \frac{\partial\Gamma_k}{\partial\left(\frac{\partial g_{v,r}^{(\mu,\upsilon)}}{\partial\xi} \right)}, \; \gamma_{v,r}^{(k,\mu,\upsilon)} = \frac{\partial\Gamma_k}{\partial\left(\frac{\partial}{\partial\xi}\left(\frac{\partial g_{v,r}^{(\mu,\upsilon)}}{\partial\eta} \right) \right)}.$$

Equation (21) is evaluated at the Chebyshev–Gauss–Lobatto grid points $\xi_j (j = 0, 1, 2, \ldots, N_\xi)$ and $\eta_i (i = 0, 1, 2, \ldots, N_\eta)$. The time derivatives at the Chebyshev–Gauss–Lobatto points (η_i, ξ_j) is computed as

$$\left. \frac{\partial g_n^{(\mu,\upsilon)}}{\partial \xi} \right|_{(\eta_i,\xi_j)} = \left(\frac{2}{\xi_\upsilon - \xi_{\upsilon-1}} \right) \sum_{\tau=0}^{N_\xi} d_{j,\tau} g_n^{(\mu,\upsilon)}(\eta_i, \xi_\tau), \tag{22}$$

The sth order space derivative is computed as

$$\left. \frac{\partial^s g_n^{(\mu,\upsilon)}}{\partial \eta^s} \right|_{(\eta_i,\xi_j)} = \left(\frac{2}{\eta_{N_\eta}^\mu - \eta_0^\mu} \right)^s \sum_{v=0}^{N_\eta} \left[D_{i,v}^{(\mu)} \right]^s g_n^{(\mu,\upsilon)}(\eta_v, \xi_j) = \left[\mathbf{D}^{(\mu)} \right]^s \mathbf{G}_{n,j}^{(\mu,\upsilon)}, \tag{23}$$

where the vector $\mathbf{G}_{n,j}^{(\mu,\upsilon)}$ is defined as

$$\mathbf{G}_{n,j}^{(\mu,\upsilon)} = \left[g_n^{(\mu,\upsilon)}(\eta_0^{(\mu)}, \xi_j^{(\upsilon)}), g_n^{(\mu,\upsilon)}(\eta_1^{(\mu)}, \xi_j^{(\upsilon)}), \ldots, g_n^{(\mu,\upsilon)}(\eta_{N_\eta}^{(\mu)}, \xi_j^{(\upsilon)}) \right]^T \tag{24}$$

and T denotes matrix transpose. Substituting Eqs. (22) and (23) into Eq. (21) yields

$$\sum_{v=1}^{n} \left[A_{1,v}^{(i,\mu,\upsilon)} \mathbf{G}_{v,i}^{(\mu,\upsilon)} + \boldsymbol{\beta}_{v,r}^{(1,\mu,\upsilon)} \sum_{j=0}^{N_\xi} d_{i,j} \mathbf{G}_{v,j}^{(\mu,\upsilon)} + \boldsymbol{\gamma}_{v,r}^{(1,\mu,\upsilon)} \sum_{j=0}^{N_\xi} d_{i,j} \mathbf{D}^{(\mu)} \mathbf{G}_{v,j}^{(\mu,\upsilon)} \right] = \mathbf{R}_{1,i}^{(\mu,\upsilon)},$$

$$\sum_{v=1}^{n} \left[A_{2,v}^{(i,\mu,\upsilon)} \mathbf{G}_{v,i}^{(\mu,\upsilon)} + \boldsymbol{\beta}_{v,r}^{(2,\mu,\upsilon)} \sum_{j=0}^{N_\xi} d_{i,j} \mathbf{G}_{v,j}^{(\mu,\upsilon)} + \boldsymbol{\gamma}_{v,r}^{(2,\mu,\upsilon)} \sum_{j=0}^{N_\xi} d_{i,j} \mathbf{D}^{(\mu)} \mathbf{G}_{v,j}^{(\mu,\upsilon)} \right] = \mathbf{R}_{2,i}^{(\mu,\upsilon)},$$

$$\vdots$$

$$\sum_{v=1}^{n} \left[A_{n,v}^{(i,\mu,\upsilon)} \mathbf{G}_{v,i}^{(\mu,\upsilon)} + \boldsymbol{\beta}_{v,r}^{(n,\mu,\upsilon)} \sum_{j=0}^{N_\xi} d_{i,j} \mathbf{G}_{v,j}^{(\mu,\upsilon)} + \boldsymbol{\gamma}_{v,r}^{(n,\mu,\upsilon)} \sum_{j=0}^{N_\xi} d_{i,j} \mathbf{D}^{(\mu)} \mathbf{G}_{v,j}^{(\mu,\upsilon)} \right] = \mathbf{R}_{n,i}^{(\mu,\upsilon)}, \tag{25}$$

where $A_{k,v}^{(i,\mu,\upsilon)} = \sum_{l=0}^{s} \boldsymbol{\alpha}_{v,l,r}^{(k,\mu,\upsilon)} \left[\mathbf{D}^{(\mu)} \right]^l$.

3 Numerical Experiments

We first consider the problem of steady two-dimensional laminar free convection flow past a non-isothermal vertical porous cone with variable temperature [14].

$$f''' + \frac{n+7}{4} f f'' - \frac{n+1}{2} f'^2 + \theta + \xi f'' = \frac{1-n}{4} \xi \left(f' \frac{\partial f'}{\partial \xi} - f'' \frac{\partial f}{\partial \xi} \right) \tag{26}$$

$$\frac{1}{Pr} \theta'' + \frac{n+7}{4} f \theta' - n f' \theta + \xi \theta' = \frac{1-n}{4} \xi \left(f' \frac{\partial \theta}{\partial \xi} - \theta' \frac{\partial f}{\partial \xi}, \right) \tag{27}$$

$$f(0, \xi) = 0, \quad f'(0, \xi) = 0, \quad \theta(0, \xi) = 1, \quad f'(\infty, \xi) = 0, \quad \theta(\infty, \xi) = 0. \tag{28}$$

In this example, the highest order of differentiation is $s = 3$, and the number of equations is $n = 2$. Applying OMD-BSQLM to Eqs. (26) and (27) yields

$$\sum_{\nu=1}^{2}\left[A_{1,\nu}^{(i,\mu,\upsilon)}\mathbf{G}_{\nu,i}^{(\mu,\upsilon)}+\boldsymbol{\beta}_{\nu,r}^{(1,\mu,\upsilon)}\sum_{j=0}^{N_\xi}d_{i,j}\mathbf{G}_{\nu,j}^{(\mu,\upsilon)}+\boldsymbol{\gamma}_{\nu,r}^{(1,\mu,\upsilon)}\sum_{j=0}^{N_\xi}d_{i,j}\mathbf{D}^{(\mu)}\mathbf{G}_{\nu,j}^{(\mu,\upsilon)}\right]=\mathbf{R}_{1,i}^{(\mu,\upsilon)},\quad(29)$$

$$\sum_{\nu=1}^{2}\left[A_{2,\nu}^{(i,\mu,\upsilon)}\mathbf{G}_{\nu,i}^{(\mu,\upsilon)}+\boldsymbol{\beta}_{\nu,r}^{(2,\mu,\upsilon)}\sum_{j=0}^{N_\xi}d_{i,j}\mathbf{G}_{\nu,j}^{(\mu,\upsilon)}+\boldsymbol{\gamma}_{\nu,r}^{(2,\mu,\upsilon)}\sum_{j=0}^{N_\xi}d_{i,j}\mathbf{D}^{(\mu)}\mathbf{G}_{\nu,j}^{(\mu,\upsilon)}\right]=\mathbf{R}_{2,i}^{(\mu,\upsilon)},\quad(30)$$

In order to apply the OMD-BSQLM, we let $f(\eta,\xi)=g_1(\eta,\xi)$ and $\theta(\eta,\xi)=g_2(\eta,\xi)$. Imposing the boundary conditions for $j=0,1,2,\ldots,N_\xi-1$, Eqs. (29) and (30) can be expressed as the following $N_\xi(M+1)\times N_\xi(M+1)$ matrix system

where

$$A_{i,i}^{(1,1,p,\upsilon)}=\boldsymbol{\alpha}_{1,3,r}^{(1,\mu,\upsilon)}\left[\mathbf{D}^{(\mu)}\right]^3+\boldsymbol{\alpha}_{1,2,r}^{(1,\mu,\upsilon)}\left[\mathbf{D}^{(\mu)}\right]^2+\boldsymbol{\alpha}_{1,1,r}^{(1,\mu,\upsilon)}\left[\mathbf{D}^{(\mu)}\right]^1+\boldsymbol{\alpha}_{1,0,r}^{(1,\mu,\upsilon)}$$
$$+\boldsymbol{\beta}_{1,r}^{(1,\mu,\upsilon)}d_{i,i}\mathbf{I}+\boldsymbol{\gamma}_{1,r}^{(1,\mu,\upsilon)}d_{i,i}\mathbf{D}^{(\mu)},\,i=j$$

$$A_{i,i}^{(1,2,p,\upsilon)}=\boldsymbol{\alpha}_{2,0,r}^{(1,\mu,\upsilon)}\mathbf{I},\,A_{i,i}^{(2,1,p,\upsilon)}=\boldsymbol{\alpha}_{1,1,r}^{(2,\mu,\upsilon)}\left[\mathbf{D}^{(\mu)}\right]^1+\boldsymbol{\alpha}_{1,0,r}^{(2,\mu,\upsilon)}+\boldsymbol{\beta}_{1,r}^{(2,\mu,\upsilon)}d_{i,i}\mathbf{I},\,i=j$$

$$A_{i,i}^{(2,2,p,\upsilon)}=\boldsymbol{\alpha}_{2,2,r}^{(2,\mu,\upsilon)}\left[\mathbf{D}^{(\mu)}\right]^2+\boldsymbol{\alpha}_{2,1,r}^{(2,\mu,\upsilon)}\left[\mathbf{D}^{(\mu)}\right]^1+\boldsymbol{\alpha}_{2,0,r}^{(2,\mu,\upsilon)}+\boldsymbol{\beta}_{2,r}^{(2,\mu,\upsilon)}d_{i,i}\mathbf{I},\quad i=j$$

$$A_{i,j}^{(1,1,p,\upsilon)}=\boldsymbol{\beta}_{1,r}^{(1,\mu,\upsilon)}d_{i,j}\mathbf{I}+\boldsymbol{\gamma}_{1,r}^{(1,\mu,\upsilon)}d_{i,j}\mathbf{D}^{(\mu)},\quad A_{i,j}^{(1,2,p,\upsilon)}=\mathbf{0},\,i\neq j$$

$$A_{i,j}^{(2,1,p,\upsilon)}=\boldsymbol{\beta}_{1,r}^{(2,\mu,\upsilon)}d_{i,j}\mathbf{I},\quad A_{i,j}^{(2,2,p,\upsilon)}=\boldsymbol{\beta}_{2,r}^{(2,\mu,\upsilon)}d_{i,j}\mathbf{I},\quad i\neq j,$$

$$\mathbf{K}_{1,i}^{(\mu,\upsilon)} = \mathbf{R}_{1,i}^{(\mu,\upsilon)} - \boldsymbol{\beta}_{1,r}^{(1,\mu,\upsilon)} d_{i,N_\xi} \mathbf{G}_{1,N_\xi}^{(\mu,\upsilon)} - \boldsymbol{\gamma}_{1,r}^{(1,\mu,\upsilon)} d_{i,N_\xi} \mathbf{D}^{(\mu)} \mathbf{G}_{1,N_\xi}^{(\mu,\upsilon)}$$

$$\mathbf{K}_{2,i}^{(\mu,\upsilon)} = \mathbf{R}_{2,i}^{(\mu,\upsilon)} - \boldsymbol{\beta}_{1,r}^{(2,\mu,\upsilon)} d_{i,N_\xi} \mathbf{G}_{1,N_\xi}^{(\mu,\upsilon)} - \boldsymbol{\beta}_{2,r}^{(2,\mu,\upsilon)} d_{i,N_\xi} \mathbf{G}_{2,N_\xi}^{(\mu,\upsilon)},$$

and $\mathbf{I}$ is an $(M+1) \times (M+1)$ identity matrix. The matrix system (31) can be solved iteratively for $\mathbf{G}_{k,\delta}^{(\mu,\upsilon)}$ for $k = 1, 2$ and $\delta = 0, 1, 2, \ldots N_\xi - 1$.

We also consider a two-dimensional steady free convective flow of a viscous incompressible fluid over a vertical plate in the presence of soluble species [15].

$$f''' + \frac{n+3}{4} ff'' - \frac{n+1}{2} f'^2 + \xi f'' + (1-w)g + wh$$
$$= \frac{1-n}{4} \xi \left(f' \frac{\partial f'}{\partial \xi} - f'' \frac{\partial f}{\partial \xi} \right) \tag{32}$$

$$\frac{1}{Pr} g'' + \frac{n+3}{4} fg' + \xi g' = \frac{1-n}{4} \xi \left(f' \frac{\partial g}{\partial \xi} - g' \frac{\partial f}{\partial \xi} \right) \tag{33}$$

$$\frac{1}{Sc} h'' + \frac{n+3}{4} fh' + \xi h' = \frac{1-n}{4} \xi \left(f' \frac{\partial h}{\partial \xi} - h' \frac{\partial f}{\partial \xi} \right), \tag{34}$$

$$f(0,\xi) = f'(0,\xi) = 0, g(0,\xi) = h(0,\xi) = 1, f'(\infty,\xi) = g(\infty,\xi) = h(\infty,\xi) = 0,$$

For the sake of brevity, details on the application of OMD-BSQLM are omitted for this problem.

4 Results and Discussion

In this section, we present and analyse the numerical results of the system of non-similar boundary layer equations obtained using the OMD-BSQLM. In the entire calculations, we have taken the edge of the boundary to be $\eta_\infty = 4$. Grid independence tests revealed that $N_\xi = 5$ collocation points in time were sufficient to give accurate and consistent results. The time interval was decomposed into $q = 40$ non-overlapping sub-intervals. The series solutions obtained using Mathematica NDSolve were used to validate the accuracy of the OMD-BSQLM results. The convergence and stability of the proposed method were determined by considering the norm of the difference in the values of the approximate solution of the unknown function between two subsequent iterations. For brevity, we define the solution errors for the two equation system as

$$E_f = \max_{0 \le k \le N_\xi} ||\mathbf{F}_{r+1,k}^{(\mu,\upsilon)} - \mathbf{F}_{r,k}^{(\mu,\upsilon)}||_\infty, \quad E_\theta = \max_{0 \le k \le N_\xi} ||\boldsymbol{\Theta}_{r+1,k}^{(\mu,\upsilon)} - \boldsymbol{\Theta}_{r,k}^{(\mu,\upsilon)}||_\infty, \tag{35}$$

The decrease in the solution errors as the number of iteration increases shows that the OMD-BSQLM converges. It can be seen from Fig. 2 that full convergence is reached after approximately three iterations with a solution error near 10^{-12}. The node [100,1] represents 100 collocation points and one interval in space, while the other node [20,5] stands for 20 collocation points and five overlapping sub-intervals in space. There-

(a) Two equation system   (b) Three equation system
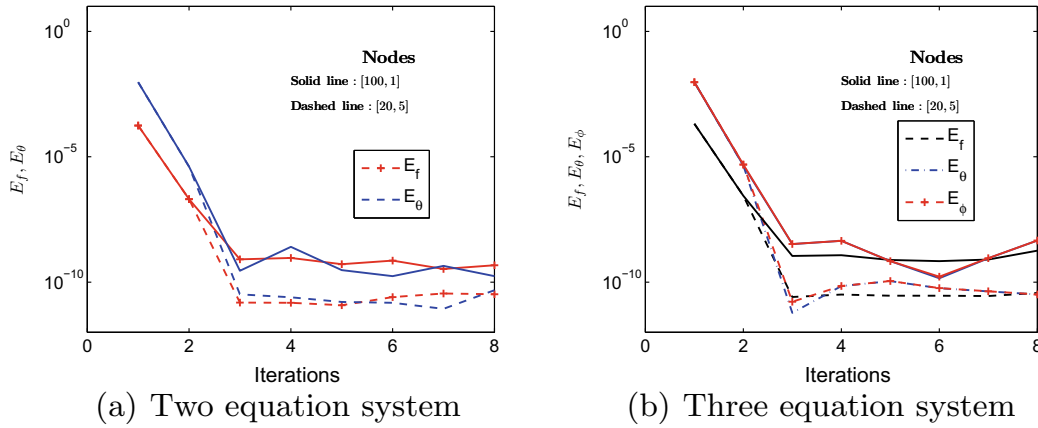
Fig. 2 Solution errors against iterations at different nodes

fore, [100,1] correspond to non-overlapping MD-BSQLM [6], and [20,5] correspond to the OMD-BSQLM. We remark that the total number of collocation points used over the entire space domain was $N_\eta = 100$ and $M = 20 + (20 - 1)(5 - 1) = 96$ in the MD-BSQLM and OMD-BSQLM, respectively. Figure 2 shows that the errors resulting from the OMD-BSQLM were smaller compared to those from the MD-BSQLM. Hence, the OMD-BSQLM provides high accuracy and uses fewer grid points compared to the MD-BSQLM.

The accuracy of the OMD-BSQLM can also be evaluated by considering the residual errors which measure the extent to which the numerical solutions approximate the true solution of the flow PDEs. For the two equation system, we define the residual error functions

$$Res(f) = ||\Gamma_f[\mathbf{F}_i^{(\mu,\upsilon)}, \boldsymbol{\Theta}_i^{(\mu,\upsilon)}]||_\infty, \quad Res(\theta) = ||\Delta_\theta[\mathbf{F}_i^{(\mu,\upsilon)}, \boldsymbol{\Theta}_i^{(\mu,\upsilon)}]||_\infty, \quad (36)$$

where, Γ_f and Γ_θ represent the nonlinear PDEs (26) and (27), respectively, and $\mathbf{F}_i^{(\mu,\upsilon)}$ and $\boldsymbol{\Theta}_i^{(\mu,\upsilon)}$ are the OMD-BSQLM approximate solutions at the time collocation points ξ_i. To calculate the residual errors, we have considered the maximum infinity over all the collocation points. The decrease in the residual errors across the time scale ξ depicts the convergence of the method as observed in Fig. 3. It can also be noted from the figure that the residual error is nearly uniform across ξ. This implies that the accuracy of the OMD-BSQLM does not deteriorate when ξ becomes large. The residual error graphs were plotted using $N_\eta = 120([20, 1])$, $M = 117([30, 40])$ and $M = 115([20, 6])$ collocation points over the whole space domain. Figure 3 exhibits the effect of varying the number of sub-intervals and the number of points. It is seen from the figure that increasing the number of overlapping sub-intervals minimizes the total number of grid points required. However, the accuracy is improved since increasing the number of sub-intervals produces smaller residual errors as observed in Fig. 3. Since the solution and residual errors are always smaller for the OMD-BSQLM, the method can provide accurate, rapidly convergent results with relatively

(a) Two equation system

(b) Two equation system

(c) Three equation system

(d) Three equation system

(e) Three equation system
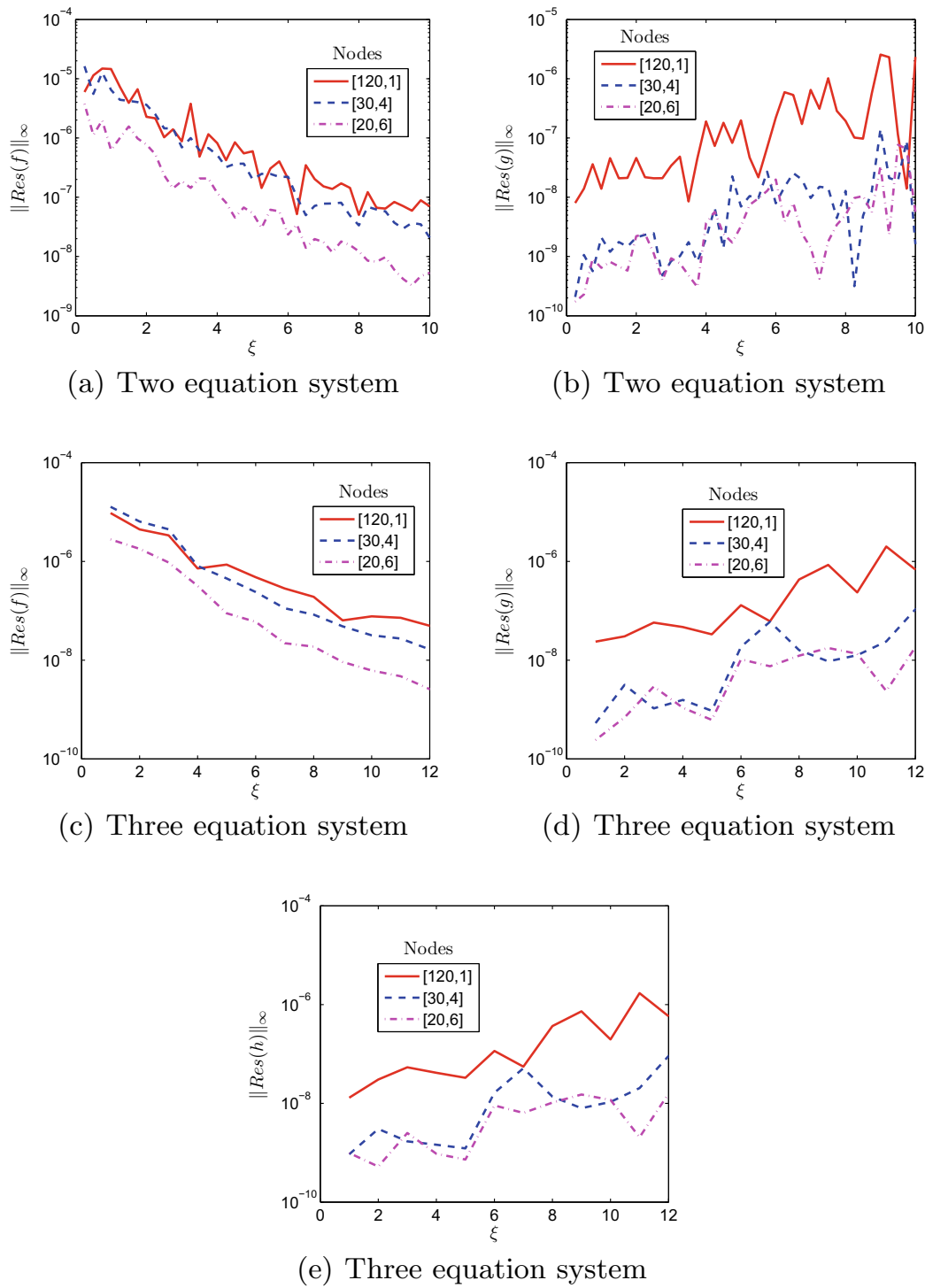
Fig. 3 Residual errors against ξ at different nodes

few grid points compared to existing numerical methods including the MD-BSQLM. The above analysis of the convergence and accuracy of the method shows that we can trust the numerical solutions obtained using the OMD-BSQLM.

Table 1 Skin friction and Nusselt Number for two equation system

| | MD-BSQLM | | OMD-BSQLM | | Series solution | | |
| | [120,1] | | [40,3] | | [20,6] | | |
ξ	$f''(0,\xi)$	$\theta'(0,\xi)$	$f''(0,\xi)$	$\theta'(0,\xi)$	$f''(0,\xi)$	$\theta'(0,\xi)$	k
5	0.2842685	−3.5066704	0.2842719	−3.5066704	0.2842719	−3.5066677	3
10	0.1428115	−7.0008400	0.1428115	−7.0008399	0.1428115	−7.0008399	2
15	0.0952321	−10.5002489	0.0952321	−10.5002490	0.0952321	−10.5002490	1
20	0.0714271	−14.0001051	0.0714171	−14.0001050	0.0714171	−14.0001050	1
25	0.0571424	−17.5000538	0.0571424	−17.5000538	0.0571424	−17.5000538	1
30	0.0476188	−21.0000311	0.0476189	−21.0000311	0.0476189	−21.0000311	1
35	0.0408162	−24.5000196	0.0408162	−24.5000196	0.0408162	−24.5000196	1
40	0.0357142	−28.0000132	0.0357142	−28.0000131	0.0357142	−28.0000131	1
Iter.	3		3				

Table 2 Skin friction, Nusselt and Sherwood Number for three equation system

ξ	MD-BSQLM [120,1]			OMD-BSQLM [20,6]			Series solution		
	$f''(\eta,\xi)$	$\theta'(0,\xi)$	$\phi'(0,\xi)$	$f''(0,\xi)$	$\theta'(0,\xi)$	$\phi'(0,\xi)$	$f''(0,\xi)$	$\theta'(0,\xi)$	$\phi'(0,\xi)$
5	0.3088066	−3.5018993	−3.0018843	0.3088214	−3.5018961	−3.0018658	0.3088214	−3.5018961	−3.0018658
10	0.1547399	−7.0002370	−6.0002332	0.1547399	−7.0002370	−6.0002332	0.1547399	−7.0002370	−6.0002332
15	0.1031717	−10.5000705	−9.0000693	0.1031717	−10.5000702	−9.0000691	0.1031717	−10.5000702	−9.0000691
20	0.0773803	−14.0000293	−12.0000289	0.0773803	−14.0000296	−12.0000292	0.0773803	−14.0000296	−12.0000292
25	0.0619045	−17.5000154	−15.0000151	0.0619045	−17.5000152	−15.0000149	0.0619045	−17.5000152	−15.0000149
30	0.0515872	−21.0000087	−18.0000086	0.0515872	−21.0000088	−18.0000086	0.0515872	−21.0000088	−18.0000086
35	0.0442176	−24.5000055	−21.0000054	0.0442176	−24.5000055	−21.0000054	0.0442176	−24.5000055	−21.0000054
40	0.0386905	−28.0000037	−24.0000036	0.0386905	−28.0000037	−24.0000036	0.0386905	−28.0000037	−24.0000036

To validate the OMD-BSQLM results, values of the skin friction, Nusselt and Sherwood Number were compared with those obtained using the series solution method in Tables 1 and 2. Three iterations were enough for the OMD-BSQLM to give comparable results. It can be seen from the tables that the OMD-BSQLM gives accurate results which are in excellent agreement with those obtained using the series solution method, thus validating the accuracy of the proposed method. Moreover, few grid points were needed to generate comparable results in the OMD-BSQLM than in the non-overlapping MD-BSQLM. We remark that the OMD-BSQLM has a great potential to produce highly accurate numerical solutions for bigger time variables ξ with the minimal number of grid points and few iterations compared to existing numerical methods.

5 Conclusion

In this work, we introduced the OMD-BSQLM and applied it in solving non-similar boundary equations to assess its accuracy, robustness and effectiveness. The method applies the QLM technique to linearize the nonlinear PDEs. The space domain is split into overlapping sub-domains, and the time interval is partitioned into non-overlapping sub-intervals. The discretization process is then implemented on both space and time using the spectral collocation method. The approximate solution is obtained by solving the resultant linear matrix system. We have shown the convergence behaviour and accuracy of the OMD-BSQLM scheme. The method was found to be convergent and uses minimal grid points and iterations to produce accurate results. Moreover, the accuracy did not worsen when a large time domain was considered. The results obtained were validated against series solutions and were found to be in excellent concurrence, thus confirming the accuracy of the method over smaller and larger domains. The overlapping grid can improve the accuracy of spectral collocation-based methods by making the coefficient matrix in the matrix equation resulting from the collocation process to be less dense. This work has added to literature an efficient technique for solving the nonlinear system of PDEs defined in smaller and larger domains.

References

1. Boyd JP (1989) Chebyshev and fourier spectral methods. Springer, Berlin, New York
2. Motsa SS, Dlamini PG, Khumalo M (2014) Spectral relaxation method and spectral quasi-linearisation method for solving unsteady boundary layer flow problems. Adv Math Phys 2014:1–12. https://doi.org/10.1155/2014/341964
3. Motsa SS, Magagula VM, Sibanda P (2014) A bivariate Chebyshev spectral collocation quasi-linearization method for nonlinear evolution parabolic equations. Sci World J 2014:1–13. https://doi.org/10.1155/2014/581987

4. Motsa SS, Ansari MS (2015) Unsteady boundary layer flow and heat transfer of Oldroyd- B nanofluid towards a stretching sheet with variable thermal conductivity. Therm Sci 19:239–248
5. Motsa SS, Animasaum IL (2018) Bivariate spectral quasi-linearisation exploration of heat transfer in the boundary layer flow of micropolar fluid with strongly concentrated particles over a surface at absolute zero due to impulsive. Int J Comput Math 9:455–473
6. Magagula VM, Motsa SS, Sibanda P (2017) A multi-domain bivariate pseudospectral method for evolution equations. Int J Comput Meth 14:17500414 https://doi.org/10.1142/s0219876217500414
7. Yang HH (1993) A one-grid-overlapped spectral multi-domain method for the PDEs. Comput Math Appl 26:27–33. https://doi.org/10.1016/0898-1221(93)90023-o
8. Yang HH, Shizgal B (1994) Chebyshev pseudospectral multi-domain technique for viscous calculation. Comput Meth Appl Mech Eng 118:47–61. https://doi.org/10.1016/0045-7825(94)90106-6
9. Olmos D, Shizgal BD (2006) A spectral method for solution of Fisher's equation. J Comput Appl Math 193:219–242
10. Taleei A, Dehgham M (2014) A pseudo-spectral method that uses overlapping multi-domain technique for the numerical solution of sine-Gordon equation in one and two spatial dimensions. Math Meth Appl Sci 37:1909–1923
11. Canuto C, Hussaini MY, Quarteroni A, Zang TA (1988) Spectral methods in fluid dynamics. Springer, Berlin
12. Trefethen, LN (2000) Spectral methods in matlab. SIAM, Philadelphia
13. Bellman RE, Kalaba RE (1965) Quasilinearization and nonlinear boundary-value problems
14. Hossain MA, Paul SC (2001) Free convection from a vertical permeable circular cone with non-uniform surface temperature. Acta Mech 151:103–114. https://doi.org/10.1007/bf01272528
15. Hussain S, Hossain MA, Wilson M (2000) Natural convection flow from a vertical permeable at plate with variable surface temperature and species concentration. Eng Comput 17:789–812. https://doi.org/10.1108/02644400010352261

Chapter 4

Overlapping multi-domain spectral method for conjugate problems of conduction and MHD free convection flow of nanofluids over flat plates

In Chapter 3, we only focused on the applicability, accuracy and reliability of the overlapping multi-domain spectral method on some common problems from literature through a determination of convergence and residual errors. In this chapter, we construct and analyze a fluid flow models in different geometries. The conjugate heat transfer problems in nanofluids over both a vertical and horizontal flat plate are solved using the overlapping multi-domain spectral method. Numerical computations are carried out to investigate the behaviour of fluid properties for various emerging dimensionless parameters. The variations of the skin friction coefficient and the heat transport are presented for different parameter values. The results are compared with those in the literature as a mechanism to validate the accuracy of the method.

Article

Overlapping Multi-Domain Spectral Method for Conjugate Problems of Conduction and MHD Free Convection Flow of Nanofluids over Flat Plates

Musawenkhosi Mkhatshwa [1,*] , Sandile Motsa [1,2] and Precious Sibanda [1]

[1] School of Mathematics, Statistics and Computer Science, University of Kwazulu Natal, Scottsville, Pietermaritzburg 3209, South Africa

[2] Department of Mathematics, Faculty of Science and Engineering, University of Eswatini, Private Bag 4, Kwaluseni, Eswatini

* Correspondence: patsonmkhatshwa@gmail.com; Tel.: +268-7836-8742

check for updates

Abstract: An efficient overlapping multi-domain spectral method is used in the analysis of conjugate problems of heat conduction in solid walls coupled with laminar magnetohydrodynamic (MHD) free convective boundary layer flow of copper (Cu) water and silver (Ag) water nanofluids over vertical and horizontal flat plates. The combined effects of heat generation and thermal radiation on the flow has been analyzed by imposing a magnetic field along the direction of the flow to control the motion of electrically conducting fluid in nanoscale systems. We have assumed that the nanoparticle volume fraction at the wall may be actively controlled. The dimensionless flow equations are solved numerically using an overlapping multi-domain bivariate spectral quasilinearisation method. The effects of relevant parameters on the fluid properties are shown graphically and discussed in detail. Furthermore, the variations of the skin friction coefficient, surface temperature and the rate of heat transfer are shown in graphs and tables. The findings show that the surface temperature is enhanced due to the presence of nanoparticles in the base fluid and the inclusion of the thermal radiation, heat generation and transverse magnetic field in the system. An increase in the nanoparticle volume fraction, heat generation, thermal radiation, and magnetic field parameter enhances the nanofluid velocity and temperature while reducing the heat transfer rate. The results also indicate that the Ag–water nanofluid has higher skin friction and surface temperature than the Cu–water nanofluid, while the opposite behaviour is observed in the case of the rate of heat transfer. The computed numerical results are compared with previously published results and found to be in good agreement.

Keywords: multi-domain overlapping technique; bivariate spectral quasilinearisation method; conjugate heat transfer; MHD free convection; radiation; heat generation; nanofluid; vertical and horizontal flat plates

1. Introduction

Conjugate heat transfer (CHT) is the interaction between the conduction and the buoyancy forced flow of fluid along a solid surface. In numerous applications, the effect of conduction within the solid wall is significant and thus must be taken into account. Such applications include heat exchangers, heaters, nuclear reactors, and pipe insulation systems. In these applications, the analysis of CHT mechanisms, the coupling of the conduction in the solid body and the convection in the fluid surrounding is important [1]. CHT problems, in which the coupled heat transfer processes between conduction and convection mechanisms are considered simultaneously, have been studied by several researchers in the case of Newtonian fluids. For example, Miyamoto et al. [2] reviewed the early theoretical and experimental work of conjugate free convection including the methods and

the principal results in the previously obtained solutions of conjugate problems. Miyamoto et al. [2] considered CHT problems of free convection from a vertical plate with a uniform temperature or a uniform heat flux on the outside surface of the plate. Sparrow and Chyu [3] studied CHT problems for a vertical fin with forced convection. Merkin and Pop [4] analyzed CHT over a vertical flat plate using an efficient finite-difference scheme. Pop et al. [5] presented a detailed numerical study of the conjugate mixed convection flow along a vertical flat plate. Luna et al. [6] investigated CHT across a thin horizontal wall separating two fluids at different temperatures numerically and asymptotically. Vasquez and Bula [7] studied the CHT process in cooling a horizontal plate in a steady state condition. Hajmohammadi and Nourazar [8] investigated conjugate forced convection heat transfer from a good conducting horizontal plate with temperature-dependent thermal conductivity. The horizontal plate was heated with uniform heat flux at the lower surface and cooled at the upper surface under laminar forced convection flow. Findings showed that, for a good conducting plate with a finite thickness, the distribution of the conjugate heat flux at the upper surface is significantly affected by the plate thickness. Yu and Lin [9] analyzed conjugate free convection over a vertical and horizontal plate using Keller's finite-difference method. They proposed the new conjugate parameters and novel dimensionless coordinates to solve the conjugate free convection problem on vertical and horizontal plates. Hsiao [10] analysed the conjugate problems of conduction in solid and free convection in fluid flow using a novel improved formula. The flow equations were solved numerically using the finite difference, Runge–Kutta and Shooting method.

Many studies have been performed on magnetic field and heat generation effects on magnetohydrodynamic (MHD)-conjugate heat transfer. Azim and Chowdhury [11] investigated MHD-conjugate free convection from an isothermal horizontal circular cylinder with Joule heating and heat generation in the presence of a magnetic field. Azim et al. [12] studied the problem of steady CHT through an electrically-conducting fluid for a vertical flat plate with a transverse uniform magnetic field. Kaya [13] investigated mixed convection heat transfer about a thin vertical plate with magneto and CHT effects in a porous medium. Kaya [14] studied the effect of CHT on MHD mixed convection about a vertical slender hollow cylinder. Mamun et al. [15] studied the effects of conduction and viscous dissipation on natural convection flow of an incompressible, viscous and electrically conducting fluid with a transverse magnetic field. Mamun et al. [16] investigated the magnetic field, viscous dissipation and heat generation effects on natural convection flow of incompressible, viscous and electrically conducting fluid along a vertical flat plate with conduction. Hosain and Azim [17] studied the effects of viscous dissipation and heat generation on MHD conjugate free convection flow from an isothermal horizontal circular cylinder when the magnetic field was applied.

In the studies mentioned above, the fluid was assumed to be regular. However, traditional fluids such as water, oil and ethylene glycol might not have enough thermal conductivity to provide the desired efficiency. A good way to overcome this limitation is to add some solid nanoparticles with high thermal conductivity to the fluid. The resulting fluid is a suspension of the solid nanoparticles in the base fluid, which is called nanofluid. The thermal conductivities of nanofluids are believed to be greater than those of the base fluid due to the high thermal conductivity of the nanoparticles. Numerous investigations have been done on the effect of nanoparticles on thermal performance. For example, Choi et al. [18] experimentally studied the effective thermal conductivity of a nano-solid-liquid mixture. Their results revealed that the dispersion of a small amount ($<$1% by volume) of carbon nanotubes in a liquid increases its thermal conductivity remarkably (nearly 200%). Nanofluids have many applications in heat transfer such as microelectronics, fuel cells, Pharmaceutical processes, Hybrid-powered engines, engine cooling vehicles, domestic refrigerator, heat exchanger, nuclear reactor coolant, space technology, and boiler flue gas temperature reduction. Nanoparticles can exist in a variety of types such as metals, metal oxides, carbides, and carbon. The most common types of nanofluids available commercially include Aluminium oxide (Al_2O_3), Titanium oxide (TiO_2), Copper (Cu), and Silver (Ag)–water nanofluid [19].

The study of CHT in nanofluids has attracted the interest of many researchers. Jafarian et al. [20] studied CHT in MHD mixed convective flows of nanofluid about a vertical slender hollow Cylinder embedded in a porous medium. Nimmagadda and Venkatasubbaiah [21] analyzed CHT in a micro-channel using novel hybrid nanofluids (Al_2O_3 + Ag/Water). Patrulescu and Grosan [22] studied CHT in a vertical channel filled with a nanofluid adjacent to a heat generating solid domain. Zahan and Alim [23] investigated the problem of developing laminar CHT of copper water nanofluid in a rectangular enclosure. Malvandi et al. [24] studied fluid flow and heat transfer of nanofluids over a flat plate with conjugate heat transfer by including the fluid effects of thermal resistance of the plate in the formulation. Zahan et al. [25] also studied the problem of MHD conjugate natural convection flow in a rectangular frame filled with a copper water nanofluid. Alsabery et al. [26] investigated the conjugate natural convection of Al_2O_3-water nanofluid in a square cavity using Buongiorno's two-phase model. Amongst their findings, they reported that, when the heat conduction is dominated, the heat transfer is increased with the increment of the nanoparticles volume fraction.

High temperatures are required to perform many engineering processes. Nuclear power plants, gas turbines, missiles, satellites, different types of equipment for aircraft, to name a few, can be included in such processes. Accordingly, radiation heat transfer knowledge is very important to design relevant devices. Furthermore, radiation has a significant effect on MHD flow and heat transfer characteristics from an industrial point of view. Industrial applications of thermal radiation include polymer technology, food production, engineering and spinning of fibers and advanced energy conversion in heat transfer at high temperatures. The effect of thermal radiation on MHD convection flow has been investigated by many researchers in the case of regular fluids and nanofluids. Takhar et al. [27] studied the effect of radiation on natural convection flow and heat transfer for a semi-infinite vertical plate with the transverse magnetic field. Emad [28] investigated free convection heat transfer characteristics of an electrically conducting fluid along an isothermal sheet with a transverse magnetic field. In this analysis, the simultaneous effects of buoyancy and radiation with internal heat generation or absorption were considered over the linearly stretched sheet taking into account a uniform free stream of constant velocity and temperature. El-Naby et al. [29] investigated natural convection unsteady flow over a semi-finite vertical plate with variable temperature, radiation, and transverse magnetic field. Ali et al. [30] investigated thermal radiation effects on the time-independent hydromagnetic forced convective flow of an electrically conducting and heat generating-absorbing fluid over a non-isothermal wedge. Mbeledogu et al. [31] obtained the perturbation solutions of the problem formed by the simultaneous action of buoyancy and transverse magnetic field on free convection flow of compressible Boussinesq fluid past a moving vertical plate. The viscosity and thermal conductivity of the fluid were a function of temperature and the radiative flux was confirmed using the Rosseland approximation. Ali et al. [32] analyzed the effect of thermal radiation and heat generation on viscous Joule heating MHD-conjugate heat transfer along a vertical flat plate. Their results showed that thermal radiation, viscous Joule heating and internal heat generation in the presence of conduction effects have a significant effect on MHD natural convection flow and thermal fields. In the case of nanofluids, Elazem et al. [33] considered the effect of radiation on the steady MHD flow and heat transfer of *Cu*–water and *Ag*–water nanofluids flow over a stretching sheet. Raju et al. [34] investigated the influence of the magnetic field, radiation, and non-uniform heat source/sink on Cu–Ethyline glycol and Ag–Ethyline glycol nanofluids flow over a moving vertical plate in a porous medium. The results from these studies reveal that, as thermal radiation increases, the rate of energy transported to the fluid increases, consequently an increase in temperature occurs.

The thermal radiation effect on the MHD-conjugate flow of nanofluids over flat plates with internal heat generation can be important in many industrial and theoretical applications. However, the literature review shows that no significant study investigated the combined effects of thermal radiation and heat generation on MHD-conjugate heat transfer flow on natural convection in a nanofluid filled enclosure. The objective of this study is to extend the work of Yu and Lin [9] by analyzing the conjugate heat transfer in MHD free convective flow of Cu–water and Ag–water

nanofluids along the vertical and horizontal plates with internal heat generation and thermal radiation. This study is theoretical and can have practical significance in designing and operation of plate heat exchangers. It is worth mentioning that the problem considered has applications in industries such as flat fins and cooling of electronic boards due to the inclusion of nanoparticles. The flow is subject to a uniform magnetic field imposed along the direction of the flow. We further demonstrate the application of efficient overlapping multi-domain bivariate spectral quasilinearisation method in solving a nonlinear system of partial differential equations (PDEs) modeling CHT problems. This method is more accurate than the non-overlapping multi-domain bivariate spectral quasilinearisation method (MD-BSQLM) [35]. The non-overlapping MD-BSQLM applies the multi-domain technique only in the time interval. However, the method considered in the present work applies the multi-domain technique in both space and time intervals. In addition to that, the method uses the overlapping multi-domain technique in the space interval. The overlapping grid strategy can improve the accuracy of spectral collocation based methods. The accuracy improvement is achieved through making the coefficient matrix in the matrix equation (resulting from the collocation process) less dense. This means that the coefficient matrix will be sparse. The sparsity of matrices caused by overlapping sub-domains can help to minimize the storage of large matrices and make it easy to perform matrix-vector multiplications. This is because there will be a lot of multiplication by zero which reduces the computational time and enables the matrices to be stored efficiently. Since the method combines the bivariate spectral quasilinearisation method [36], non-overlapping and overlapping multi-domain technique, for reference purposes, we shall refer to the method as the overlapping multi-domain bivariate spectral quasilinearisation method (OMD-BSQLM). The use of spectral collocation-based methods such as the OMD-BSQLM for solving systems of PDEs can be a most promising tool in the study of conjugate heat transfer problems. From the literature review, several studies [2,9] concluded that it is very difficult to obtain analytical solutions of conjugate heat transfer problems due to the matching conditions at the solid–fluid interface. These studies proposed the use of numerical methods such as finite difference schemes as the most promising procedures for performing this matching. However, the finite difference methods have a lot of limitations when compared to spectral methods. Spectral methods are highly accurate and more efficient than traditional methods such as the finite difference methods [37]. When applied to problems with smooth solutions, they use few grid points and require minimal computational time to generate accurate solutions, thus they are better than traditional methods. The spectral method algorithm is easy to implement in scientific computing software. To establish the accuracy of the OMD-BSQLM, certain limiting solutions of the flow equations are studied.

2. Mathematical Formulation

Let us consider the viscous, steady, incompressible, electrically conducting and free convection flow of nanofluid over a vertical flat plate and a horizontal flat plate of finite length l and thickness b. The thickness of the plates is assumed to be smaller than the length. The base fluid is water and nanoparticles (Cu and Ag) are in thermal equilibrium with no slip between them. The thermophysical properties of the base fluid and different nanoparticles are shown in Table 1. It is assumed that the left side of the vertical plate and the lower side of the horizontal plate are maintained at the constant temperature T_b, such that $T_b > T_\infty$, where T_∞ is the temperature of the ambient nanofluid. Heat is transferred by conduction from the outside surface of the solid plates coupled with the free convection in the nanofluid, while the axial heat conduction in the plates is neglected. A uniform magnetic field $B(x)$ is imposed along the direction of flow. The applied transverse magnetic field can be chosen in its special form as $B(x) = B_0 \alpha_f^{1/2} x^{-1}$, where B_0 is the steady strength of the magnetic field towards the y-axis. It is assumed that the induced magnetic field and the external electric field are negligible. Thermal radiation and internal heat generation terms are included in the energy equation. The geometry and coordinate system for the vertical and horizontal flat plates are shown in Figure 1.

With the above assumptions, equations of the conservation of mass, momentum, and energy are given by

$$\frac{\partial u}{\partial x} + \frac{\partial v}{\partial y} = 0, \tag{1}$$

$$u\frac{\partial u}{\partial x} + v\frac{\partial u}{\partial y} = -\frac{1}{\rho_{nf}}\frac{\partial p}{\partial x} + \nu_{nf}\frac{\partial^2 u}{\partial y^2} + g\beta_{nf}(T - T_\infty)\sin\varphi - \frac{\sigma_{nf}B^2(x)}{\rho_{nf}}u, \tag{2}$$

$$0 = -\frac{1}{\rho_{nf}}\frac{\partial p}{\partial y} + g\beta_{nf}(T - T_\infty)\cos\varphi, \tag{3}$$

$$u\frac{\partial T}{\partial x} + v\frac{\partial T}{\partial y} = \frac{k_{nf}}{(\rho C_p)_{nf}}\frac{\partial^2 T}{\partial y^2} + \frac{Q_0}{(\rho C_p)_{nf}}(T - T_\infty) - \frac{1}{(\rho C_p)_{nf}}\frac{\partial q_r}{\partial y}, \tag{4}$$

where u and v are the velocity components in the x- and y- directions, p is the pressure, g is the acceleration due to gravity, T is the fluid temperature near the plate, q_r is the radiative heat flux, Q_0 is the rate of heat generation, σ_{nf} is the electrical conductivity, ν_{nf} is the kinematic viscosity, μ_{nf} is the dynamic viscosity, ρ_{nf} is the effective density, α_{nf} is the thermal diffusivity, k_{nf} is the effective thermal conductivity, β_{nf} is the thermal expansion coefficient and $(\rho C_p)_{nf}$ is the heat capacity of the nanofluid. The term $Q_0(T - T_\infty)$ represents the amount of heat generated or absorbed per unit volume, where Q_0 is a constant which may be either positive for a heat sink or negative for a heat source. The radiative heat flux q_r with Rosseland approximation has the form $q_r = -\frac{4\sigma^*}{3k^*}\frac{\partial T^4}{\partial y}$, where σ^* is the Stefan–Boltzmann constant and k^* is the mean absorption coefficient. The temperature differences within the flow are assumed to be sufficiently small such that T^4 may be expressed as a linear function of temperature. Expanding T^4 using Taylor series and neglecting higher order terms yields $T^4 \cong 4T_\infty^3 T - 3T_\infty^4$. The nanofluid constants are defined as [38–40]

$$\nu_{nf} = \frac{\mu_{nf}}{\rho_{nf}}, \ \mu_{nf} = \frac{\mu_f}{(1 - \phi)^{2.5}}, \ \frac{k_{nf}}{k_f} = \left[\frac{(k_s + 2k_f) - 2\phi(k_f - k_s)}{(k_s + 2k_f) + \phi(k_f - k_s)}\right], \ \frac{\sigma_{nf}}{\sigma_f} = \left[1 + \frac{3\left(\frac{\sigma_s}{\sigma_f} - 1\right)\phi}{\left(\frac{\sigma_s}{\sigma_f} + 2\right) - \left(\frac{\sigma_s}{\sigma_f} - 1\right)\phi}\right],$$

$$\rho_{nf} = (1 - \phi)\rho_f + \phi\rho_s, \ (\rho C_p)_{nf} = (1 - \phi)(\rho C_p)_f + \phi(\rho C_p)_s, \ \beta_{nf} = (1 - \phi)\beta_f + \phi\beta_s, \ \alpha_{nf} = \frac{k_{nf}}{(\rho C_p)_{nf}}, \tag{5}$$

where ϕ is the solid volume fraction of nanoparticles, β is the thermal expansion, subscripts $_{f, s}$ and $_{nf}$ denote fluid, solid and nanofluid, respectively. For the vertical plate, the angle φ is $\pi/2$ and $\partial p/\partial x$, and $\partial p/\partial y$ are both equal to zero. For the horizontal plate, the angle φ to the horizontal is equal to zero. In formulating Equations (1)–(4), viscous dissipation and compression work have been neglected. Moreover, the physical properties of the fluid are assumed to be constant except for the density variation that induces a buoyancy force. The boundary conditions for Equations (1)–(4) are

$$u = 0, \ v = 0, \quad \text{at} \quad y = 0, \tag{6}$$

$$u \to 0, \ p \to 0, \quad T \to T_\infty \quad \text{as} \quad y \to \infty. \tag{7}$$

Table 1. Thermophysical properties of the base fluid and the nanoparticles [38].

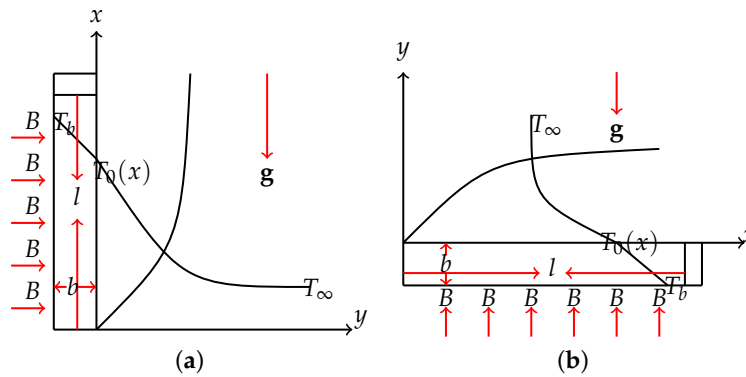| Base Fluid		Nanoparticles	
Physical Properties	**Water**	**Copper (Cu)**	**Silver (Ag)**
C_p (J/kgK)	4179	385	235
ρ (Kg/m^3)	997.1	8933	10,500
k (W/mK)	0.613	401	429
σ (Sm^{-1})	0.05	5.96×10^7	6.3×10^7
$\beta \times 10^5$ (K^{-1})	21	1.67	1.89

Figure 1. Physical model and coordinate system. (**a**) vertical plate; (**b**) horizontal plate.

2.1. Dimensionless Equations for the Vertical Plate

Yu and Lin [9] developed the following non-dimensional variables:

$$\psi(x,y) = \alpha_f \lambda f(\xi, \eta), \quad \eta(x,y) = (y/x)\lambda, \ \xi(x) = \left[1 + \sigma R_{a_t}/(\sigma R_{a_h})^{4/5}\right]^{-1}, \quad \theta(\xi, \eta) = \frac{T - T_\infty}{T_b - T_\infty}\xi^{-1}, \ (8)$$

where $R_{a_t} = g\beta(T_b - T_\infty)x^3/\alpha_f \nu$ is the Rayleigh number, $R_{a_h} = g\beta(q_h x/k_r)x^3/\alpha_f \nu$ is the Reyleigh number for a plate with constant wall flux $q_h = k_s(T_b - T_\infty)/b$, $\lambda = \left[(\sigma R_{a_t})^{-1} + (\sigma R_{a_h})^{-4/5}\right]^{-1/4}$, $\sigma = Pr/(1 + Pr)$, $\psi(x,y)$ is the stream function defined by $u = \partial\psi/\partial y$ and $v = -\partial\psi/\partial x$, $\eta(x,y)$ and $\xi(x)$ are the dimensionless coordinates, $f(\xi, \eta)$ is the dimensionless stream function and $\theta(\xi, \eta)$ is the dimensionless temperature. By using Equation (8), Equations (1)–(4) along with the boundary conditions (6) and (7) are reduced to the following two-point boundary value problem:

$$Prf''' + \phi_1\left[\frac{16 - \xi}{20}ff'' - \frac{6 - \xi}{10}f'^2 - M^2\phi_2 f' + \phi_3(1 + Pr)\theta\right] = \frac{\phi_1}{5}\xi(1 - \xi)\left[f'\frac{\partial f'}{\partial \xi} - f''\frac{\partial f}{\partial \xi}\right], \quad (9)$$

$$\left(1 + \frac{k_f}{k_{nf}}Rd\right)\theta'' + \phi_4\left[\frac{16 - \xi}{20}f\theta' - \frac{1 - \xi}{5}f'\theta\right] + \frac{k_f}{k_{nf}}Q\xi\theta = \frac{\phi_4}{5}\xi(1 - \xi)\left[f'\frac{\partial \theta}{\partial \xi} - \theta'\frac{\partial f}{\partial \xi}\right], \quad (10)$$

where $M^2 = \frac{\sigma_f B_0^2}{\rho_f \lambda^2}$ is the magnetic field parameter, $Pr = \frac{\nu_f}{\alpha_f}$ is the Prandtl number, $Rd = \frac{16\sigma^* T_\infty^3}{3k^* k_f}$ is the radiation parameter and $Q = \frac{Q_0 x^2}{k_f \lambda^2}$ is the heat generation parameter. The nanoparticle volume fractions ϕ_1, ϕ_2, ϕ_3 and ϕ_4 depend on the thermal properties of the nanofluid and are defined as

$$\phi_1 = [1 - \phi]^{2.5}\left(1 - \phi + \phi\frac{\rho_s}{\rho_f}\right), \ \phi_2 = \left(1 + \frac{3(\sigma_s/\sigma_f - 1)\phi}{(\sigma_s/\sigma_f + 2) - (\sigma_s/\sigma_f - 1)\phi}\right)\frac{1}{\left((1 - \phi) + \phi(\frac{\rho_s}{\rho_f})\right)},$$

$$\phi_3 = (1 - \phi) + \phi(\beta_s/\beta_f), \quad \phi_4 = \left[\frac{k_s + 2k_f + \phi(k_f - k_s)}{k_s + 2k_f - 2\phi(k_f - k_s)}\right]\left((1 - \phi) + \phi\frac{(\rho C_p)_s}{(\rho C_p)_f}\right). \quad (11)$$

The corresponding boundary conditions in dimensionless form are

$$f(\xi, 0) = 0, \ f'(\xi, 0) = 0, \ \xi\theta(\xi, 0) - (1 - \xi)^{5/4}\theta'(\xi, 0) = 1,$$
$$f'(\xi, \infty) = 0, \ \theta(\xi, \infty) = 0. \quad (12)$$

2.2. Dimensionless Equations for the Horizontal Plate

Using the following non-dimensional variables in [9], namely

$$\psi(x,y) = \alpha_f \lambda f(\xi,\eta), \quad \eta(x,y) = (y/x)\lambda, \quad \xi(x) = \left[1 + \sigma Ra_t/(\sigma Ra_h)^{5/6}\right]^{-1.5}, \qquad (13)$$

$$\theta(\xi,\eta) = \frac{T - T_\infty}{T_b - T_\infty}\xi^{-1}, \quad \omega(\xi,\eta) = \sigma p x^2/\rho\alpha_f\nu\lambda^4, \qquad (14)$$

where $\lambda = \left[(\sigma Ra_t)^{-1} + (\sigma Ra_h)^{-5/6}\right]^{-1.5}$ and $\omega(\xi,\eta)$ is the dimensionless pressure. Equations (1)–(4) along with their boundary conditions (6) and (7) for the horizontal plate are reduced to

$$Pr f''' + \phi_1\left[\frac{10-\xi}{15}ff'' - \frac{5-2\xi}{15}f'^2 - \phi_2 M^2 f'\right] + \frac{(1-\phi)^{2.5}}{15}(1+Pr)[(5+\xi)\eta\omega' - (10-4\xi)\omega]$$

$$= \frac{\phi_1}{3}\xi(1-\xi)\left[f'\frac{\partial f'}{\partial\xi} - f''\frac{\partial f}{\partial\xi} + (1+Pr)\frac{\partial\omega}{\partial\xi}\right], \qquad (15)$$

$$\omega' = \theta, \qquad (16)$$

$$\left(1 + \frac{k_f}{k_{nf}}Rd\right)\theta'' + \phi_4\left[\frac{10-\xi}{15}f\theta' - \frac{1-\xi}{3}f'\theta\right] + \frac{k_f}{k_{nf}}Q\xi\theta = \frac{\phi_4}{3}\xi(1-\xi)\left[f'\frac{\partial\theta}{\partial\xi} - \theta'\frac{\partial f}{\partial\xi}\right]. \qquad (17)$$

The corresponding boundary conditions in dimensionless form are

$$f(\xi,0) = 0, \quad f'(\xi,0) = 0, \quad \xi\theta(\xi,0) - (1-\xi)^{6/5}\theta'(\xi,0) = 1, \qquad (18)$$

$$f'(\xi,\infty) = 0, \quad \theta(\xi,\infty) = 0, \quad \omega(\xi,\infty) = 0. \qquad (19)$$

3. Solution Procedure

In this section, we describe the application of the OMD-BSQLM to find numerical solutions of the transformed nonlinear PDEs. The method uses the overlapping multi-domain technique, Chebyshev–Gauss–Lobatto grid points [41,42], and the quasilinearisation method [43], together with spectral collocation on approximate functions defined as bivariate Lagrange interpolation polynomials. The multi-domain approach divides the time interval into non-overlapping sub-intervals and the space interval into overlapping sub-intervals. The quasilinearisation technique helps to linearise the nonlinear PDEs. The spectral collocation method is applied independently both in space and time variables in the linearized equations. In order to apply the OMD-BSQLM, the time interval $\xi \in [0, \xi_F]$ is decomposed into q non-overlapping sub-intervals defined as

$$J_v = (\xi_{v-1}, \xi_v), \quad v = 1, 2, 3, \ldots, q, \quad \text{with} \quad 0 = \xi_0 < \xi_1 < \xi_2 < \cdots < \xi_{q-1} < \xi_q = \xi_F, \quad (20)$$

For the semi-finite space domain $[0, \infty)$, a truncated grid $[0, \eta_\infty]$ is used. We choose a finite value of η_∞ that is large enough such that the flow properties at η_∞ resemble those at ∞. The truncated space interval $[0, \eta_\infty]$ is decomposed into p overlapping sub-intervals of length L, denoted by

$$I_\mu = [\eta_0^\mu, \eta_{N_\eta}^\mu], \quad \mu = 1, 2, 3, \ldots, p, \qquad (21)$$

where each I_μ interval is further discretized into $N_\eta + 1$ collocation points. Without loss of generality, we will consider that each subinterval has the same length given by

$$L = \frac{\eta_\infty}{p + \frac{1}{2}(1-p)(1 - \cos\frac{\pi}{N_\eta})} \qquad (22)$$

for the overlap to be possible, and the same number of collocation points $(N_\eta + 1)$ is used in each subinterval. In the domain decomposition scheme, we use overlapping subintervals I_μ, where the

first two points of the interval $I_{\mu+1}$ coincide with the last two points of the interval I_μ, that is, $\eta_0^1 = 0$, $\eta_{N_\eta}^p = \eta_\infty, \eta_{N_\eta-1}^\mu = \eta_0^{\mu+1}$ and $\eta_{N_\eta}^\mu = \eta_1^{\mu+1}$. The non-overlapping and overlapping multi-domain grids are shown in Figures 2 and 3, respectively.
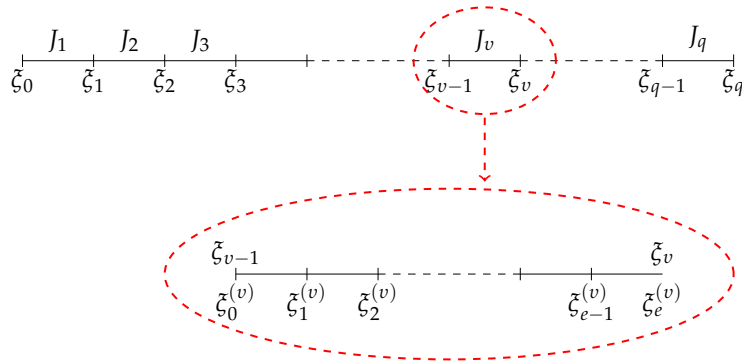
Figure 2. Non-overlapping grid (ξ-domain).
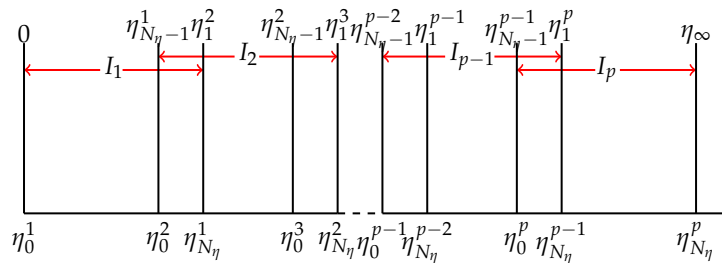
Figure 3. Overlapping grid (η-domain).

3.1. Numerical Solution for the Vertical Plate

Applying the quasilinearisation method in each sub-interval to Equations (9) and (10) gives the following system of linear PDEs:

$$\alpha_{1,3,r}^{(1,\mu,v)} \frac{\partial^3 f_{r+1}^{(\mu,v)}}{\partial \eta^3} + \alpha_{1,2,r}^{(1,\mu,v)} \frac{\partial^2 f_{r+1}^{(\mu,v)}}{\partial \eta^2} + \alpha_{1,1,r}^{(1,\mu,v)} \frac{\partial f_{r+1}^{(\mu,v)}}{\partial \eta} + \alpha_{1,0,r}^{(1,\mu,v)} f_{r+1}^{(\mu,v)} + \alpha_{2,0,r}^{(1,\mu,v)} \theta_{r+1}^{(\mu,v)}$$

$$+\gamma_{1,r}^{(1,\mu,v)} \frac{\partial}{\partial \xi} \left(\frac{\partial f_{r+1}^{(\mu,v)}}{\partial \eta} \right) + \beta_{1,r}^{(1,\mu,v)} \frac{\partial f_{r+1}^{(\mu,v)}}{\partial \xi} = R_{1,r}^{(\mu,v)}, \tag{23}$$

$$\alpha_{2,2,r}^{(2,\mu,v)} \frac{\partial^2 \theta_{r+1}^{(\mu,v)}}{\partial \eta^2} + \alpha_{2,1,r}^{(2,\mu,v)} \frac{\partial \theta_{r+1}^{(\mu,v)}}{\partial \eta} + \alpha_{2,0,r}^{(2,\mu,v)} \theta_{r+1}^{(\mu,v)} + \alpha_{1,1,r}^{(2,\mu,v)} \frac{\partial f_{r+1}^{(\mu,v)}}{\partial \eta} + \alpha_{1,0,r}^{(2,\mu,v)} f_{r+1}^{(\mu,v)}$$

$$+\beta_{2,r}^{(2,\mu,v)} \frac{\partial \theta_{r+1}^{(\mu,v)}}{\partial \xi} + \beta_{1,r}^{(2,\mu,v)} \frac{\partial f_{r+1}^{(\mu,v)}}{\partial \xi} = R_{2,r}^{(\mu,v)}, \tag{24}$$

where the variable coefficients are given by

$$\alpha_{1,3,r}^{(1,\mu,v)} = Pr, \quad \alpha_{1,2,r}^{(1,\mu,v)} = \frac{\phi_1(16-\xi)}{20}f_r^{(\mu,v)} + \frac{\phi_1\xi(1-\xi)}{5}\frac{\partial f_r^{(\mu,v)}}{\partial\xi}, \quad \alpha_{1,0,r}^{(1,\mu,v)} = \frac{\phi_1(16-\xi)}{20}\frac{\partial^2 f_r^{(\mu,v)}}{\partial\eta^2},$$

$$\alpha_{1,1,r}^{(1,\mu,v)} = -\frac{\phi_1(6-\xi)}{5}\frac{\partial f_r^{(\mu,v)}}{\partial\eta} - M\phi_1\phi_2 - \frac{\phi_1\xi(1-\xi)}{5}\frac{\partial}{\partial\xi}\left(\frac{\partial f_r^{(\mu,v)}}{\partial\eta}\right), \quad \alpha_{2,0,r}^{(1,\mu,v)} = \phi_1\phi_3(1+Pr),$$

$$\alpha_{2,2,r}^{(2,\mu,v)} = 1 + \left(1 + \frac{k_f}{k_{nf}}Rd\right), \quad \alpha_{2,0,r}^{(2,\mu,v)} = \frac{k_k}{k_{nf}}Q\xi - \frac{\phi_4(1-\xi)}{5}\frac{\partial f_r^{(\mu,v)}}{\partial\eta}, \quad \alpha_{2,1,r}^{(2,\mu,v)} = \frac{\phi_4(16-\xi)}{20}f_r^{(\mu,v)}$$

$$+\frac{\phi_4\xi(1-\xi)}{5}\frac{\partial f_r^{(\mu,v)}}{\partial\xi}, \quad \alpha_{1,1,r}^{(2,\mu,v)} = -\frac{\phi_4(1-\xi)}{5}\theta_r^{(\mu,v)} - \frac{\phi_4\xi(1-\xi)}{5}\frac{\partial\theta_r^{(\mu,v)}}{\partial\xi}, \quad \alpha_{1,0,r}^{(2,\mu,v)} = \frac{\phi_4(16-\xi)}{20}\frac{\partial\theta_r^{(\mu,v)}}{\partial\eta},$$

$$\gamma_{1,r}^{(1,\mu,v)} = -\frac{\phi_1\xi(1-\xi)}{5}\frac{\partial f_r^{(\mu,v)}}{\partial\eta}, \quad \beta_{1,r}^{(1,\mu,v)} = \frac{\phi_1\xi(1-\xi)}{5}\frac{\partial^2 f_r^{(\mu,v)}}{\partial\eta^2}, \quad \beta_{2,r}^{(2,\mu,v)} = -\frac{\phi_4\xi(1-\xi)}{5}\frac{\partial f_r^{(\mu,v)}}{\partial\eta},$$

$$\beta_{1,r}^{(2,\mu,v)} = \frac{\phi_4\xi(1-\xi)}{5}\frac{\partial\theta_r^{(\mu,v)}}{\partial\eta}, \quad R_{1,r}^{(\mu,v)} = \frac{\phi_1(16-\xi)}{20}f_r^{(\mu,v)}\frac{\partial^2 f_r^{(\mu,v)}}{\partial\eta^2} - \frac{\phi_1(6-\xi)}{10}\left(\frac{\partial f_r^{(\mu,v)}}{\partial\eta}\right)^2$$

$$-\frac{\phi_1\xi(1-\xi)}{5}\frac{\partial f_r^{(\mu,v)}}{\partial\eta}\frac{\partial}{\partial\xi}\left(\frac{\partial f_r^{(\mu,v)}}{\partial\eta}\right) + \frac{\phi_1\xi(1-\xi)}{5}\frac{\partial^2 f_r^{(\mu,v)}}{\partial\eta^2}\frac{\partial f_r^{(\mu,v)}}{\partial\xi}, \quad R_{2,r}^{(\mu,v)} = \frac{\phi_4(16-\xi)}{20}f_r^{(\mu,v)}\frac{\partial\theta_r^{(\mu,v)}}{\partial\eta}$$

$$-\frac{\phi_4(1-\xi)}{5}\theta_r^{(\mu,v)}\frac{\partial f_r^{(\mu,v)}}{\partial\eta} - \frac{\phi_4\xi(1-\xi)}{5}\frac{\partial f_r^{(\mu,v)}}{\partial\eta}\frac{\partial\theta_r^{(\mu,v)}}{\partial\xi} + \frac{\phi_4\xi(1-\xi)}{5}\frac{\partial\theta_r^{(\mu,v)}}{\partial\eta}\frac{\partial f_r^{(\mu,v)}}{\partial\xi},$$

subject to boundary conditions

$$f_{r+1}^{(\mu,v)}(\xi,0) = 0, \quad \frac{\partial f_{r+1}^{(\mu,v)}}{\partial\eta}(\xi,0) = 0, \quad \xi\theta_{r+1}^{(\mu,v)}(\xi,0) - (1-\xi)^{5/4}\frac{\partial\theta_{r+1}^{(\mu,v)}}{\partial\eta}(\xi,0) = 1,$$

$$\frac{\partial f_{r+1}^{(\mu,v)}}{\partial\eta}(\xi,\infty) = 0, \quad \theta_{r+1}^{(\mu,v)}(\xi,\infty) = 0. \tag{25}$$

The constants r and $r+1$ denote previous and current iterations, respectively. The system of linear PDEs (23) and (24) is discretized using the spectral collocation method in both η and ξ directions. Before applying the spectral method on the sub-intervals, the time interval $\xi \in [\xi_{v-1}, \xi_v]$ is transformed to $\tau \in [-1, 1]$ using the linear transformation

$$\xi_j^v = \frac{1}{2}(\xi_v - \xi_{v-1})\tau_j + \frac{1}{2}(\xi_v + \xi_{v-1}), \quad \tau_j = \cos\left(\frac{\pi j}{N_\xi}\right), \tag{26}$$

and the space region $\eta \in [\eta_0^\mu, \eta_{N_\eta}^\mu]$ is transformed to $z \in [-1, 1]$ using the linear transformation

$$\eta_i^\mu = \frac{L}{2}(z_i + 1), \quad z_i = \cos\left(\frac{\pi i}{N_\eta}\right). \tag{27}$$

We assume that, at each sub-interval, the required solution, say $f(\eta, \xi)$, can be approximated by a bivariate Lagrange interpolation polynomial of the form

$$f^{(\mu,v)}(\eta, \xi) \approx \sum_{i=0}^{N_\eta}\sum_{j=0}^{N_\xi} f^{(\mu,v)}(z_i, \tau_j)\mathcal{L}_i(z)\mathcal{L}_j(\tau), \tag{28}$$

for $\mu = 1, 2, 3, \ldots, p$ and $v = 1, 2, 3, \ldots, q$. The bivariate interpolation polynomial interpolates $f^{(\mu,v)}(z, \tau)$ at selected points (z_i, τ_j) in both z and τ directions, for $i = 0, 1, 2, \ldots, N_\eta$ and $j = 0, 1, 2, \ldots, N_\xi$. The function $\mathcal{L}_i(z)$ and $\mathcal{L}_j(\tau)$ are the well known characteristic Lagrange cardinal polynomial based on the Chebyshev–Gauss–Lobatto points. The required solution for $\theta(\eta, \xi)$ can be approximated in a similar manner. The solution procedure requires that the derivatives of $\mathcal{L}_i(z)$ and

$\mathcal{L}_j(\tau)$ with respect to z and τ, respectively be evaluated at the Chebyshev–Gauss–Lobatto grid points. The derivatives of $f^{(\mu,v)}(\eta,\xi)$ with respect to η and ξ at the Chebyshev–Gauss–Lobatto points (z_k,τ_i), are computed as

$$\left.\frac{\partial f^{(\mu,v)}}{\partial \eta}\right|_{(z_k,\tau_i)} = \sum_{\omega}^{N_\eta}\sum_{j=0}^{N_\xi} f^{(\mu,v)}(z_\omega,\tau_j)\frac{d\mathcal{L}_\omega(z_k)}{dz}L_j(\tau_i) \tag{29}$$

$$= \sum_{\omega=0}^{N_\eta} D_{k,\omega}^{(\mu)} f^{(\mu,v)}(z_\omega,\tau_i) = \left[\mathbf{D}^{(\mu)}\right]\mathbf{F}_i^{(\mu,v)}, \tag{30}$$

$$\left.\frac{\partial f^{(\mu,v)}}{\partial \xi}\right|_{(z_k,\tau_i)} = \sum_{\omega}^{N_\eta}\sum_{j=0}^{N_\xi} f^{(\mu,v)}(z_\omega,\tau_j)\mathcal{L}_\omega(z_k)\frac{d\mathcal{L}_j(\tau_i)}{d\tau}$$

$$= \sum_{j=0}^{N_\xi} d_{i,j} f^{(\mu,v)}(z_k,\tau_j) = \sum_{j=0}^{N_\xi} d_{i,j}\mathbf{F}_j^{(\mu,v)}, \tag{31}$$

where $d_{i,j} = \frac{d\mathcal{L}_j(\tau_i)}{d\tau}$ is the ith and jth entry of the standard first derivative Chebyshev–Gauss–Lobatto based differentiation matrix $\mathbf{d} = [d_{i,j}]$, for $i,j = 0,1,2,3,\dots,N_\xi$, of size $(N_\xi + 1) \times (N_\xi + 1)$, $D_{k,\omega}^{(\mu)} = \frac{2}{\eta_{N_\eta}^\mu - \eta_0^\mu} D_{k,\omega}$ with $D_{k,\omega} = \frac{d\mathcal{L}_\omega(z_k)}{dz}$ being the kth and ωth entries of the standard first derivative Chebyshev–Gauss–Lobatto differentiation matrix of size $(M + 1) \times (M + 1)$, where $M = N_\eta + (N_\eta - 1)(p - 1)$ is the total number of collocation points over a single domain $[-1,1]$. In general, to find an sth order derivative with respect to η, we have

$$\left.\frac{\partial^s f^{(\mu,v)}}{\partial \eta^s}\right|_{(z_k,\tau_i)} = \sum_{\omega=0}^{N_\eta} \left[D_{k,\omega}^{(\mu)}\right]^s f^{(\mu,v)}(z_\omega,\tau_i) = \left[\mathbf{D}^{(\mu)}\right]^s \mathbf{F}_i^{(\mu,v)}. \tag{32}$$

The vector $\mathbf{F}_i^{(\mu,v)}$ is defined as

$$\mathbf{F}_i^{(\mu,v)} = \left[f^{(\mu,v)}(z_0^{(\mu)},\tau_i^{(v)}), f^{(\mu,v)}(z_1^{(\mu)},\tau_i^{(v)}), f^{(\mu,v)}(z_2^{(\mu)},\tau_i^{(v)}),\dots,f^{(\mu,v)}(z_{N_\eta}^{(\mu)},\tau_i^{(v)})\right]^T, \tag{33}$$

where T denotes the matrix transpose. The derivatives d and $\left[\mathbf{D}^{(\mu)}\right]^s$ are scaled by multiplying by the factors $\Lambda = \frac{2}{\xi_v - \xi_{v-1}}$ and $\Omega^s = \left(\frac{2}{\eta_{N_\eta}^\mu - \eta_0^\mu}\right)^s = \left(\frac{2}{L}\right)^s$, respectively. The space and time derivatives of θ at each sub-interval can be transformed to discrete matrix form in a similar manner. Applying the spectral collocation method by evaluating Equations (23) and (24) at the collocation points and making use of the derivative matrices as well as incorporating the initial condition which corresponds to $\xi_{N_\xi} = -1$ gives

$$A_{1,1}^{(\mu,v)}\mathbf{F}_{i,r+1}^{(\mu,v)} + A_{1,2}^{(\mu,v)}\mathbf{\Theta}_{i,r+1}^{(\mu,v)} + \gamma_{1,r}^{(1,\mu,v)}\sum_{j=0}^{N_\xi-1} d_{i,j}\mathbf{D}^{(\mu)}\mathbf{F}_j^{(\mu,v)} + \beta_{1,r}^{(1,\mu,v)}\sum_{j=0}^{N_\xi-1} d_{i,j}\mathbf{F}_j^{(\mu,v)} = \mathbf{K}_{1,i}^{(\mu,v)}, \tag{34}$$

$$A_{2,1}^{(\mu,v)}\mathbf{F}_{i,r+1}^{(\mu,v)} + A_{2,2}^{(\mu,v)}\mathbf{\Theta}_{i,r+1}^{(\mu,v)} + \beta_{1,r}^{(2,\mu,v)}\sum_{j=0}^{N_\xi-1} d_{i,j}\mathbf{F}_j^{(\mu,v)} + \beta_{2,r}^{(2,\mu,v)}\sum_{j=0}^{N_\xi-1} d_{i,j}\mathbf{\Theta}_j^{(\mu,v)} = \mathbf{K}_{2,i}^{(\mu,v)}, \tag{35}$$

where

$$\mathbf{K}_{1,i}^{(\mu,v)} = \mathbf{R}_{1,i}^{(\mu,v)} - \gamma_{1,r}^{(1,\mu,v)} d_{i,N_\xi}\mathbf{D}^{(\mu)}\mathbf{F}_{N_\xi}^{(\mu,v)} - \beta_{1,r}^{(1,\mu,v)} d_{i,N_\xi}\mathbf{F}_{N_\xi}^{(\mu,v)},$$

$$\mathbf{K}_{2,i}^{(\mu,v)} = \mathbf{R}_{2,i}^{(\mu,v)} - \beta_{1,r}^{(2,\mu,v)} d_{i,N_\xi}\mathbf{F}_{N_\xi}^{(\mu,v)} - \beta_{2,r}^{(2,\mu,v)} d_{i,N_\xi}\mathbf{\Theta}_{N_\xi}^{(\mu,v)}$$

For $i = 0, 1, 2, \ldots N_\xi$, Equations (34) and (35) form an $N_\xi(M+1) \times N_\xi(M+1)$ matrix system

$$
\left[
\begin{array}{cc|cc}
\begin{matrix}
A^{(1,1,p,v)}_{0,0} & \cdots & A^{(1,1,p,v)}_{0,N_\xi} \\
A^{(1,1,p,v)}_{1,0} & \cdots & A^{(1,1,p,v)}_{1,N_\xi} \\
\ddots & \ddots & \ddots \\
A^{(1,1,p,v)}_{N_\xi-1,0} & \cdots & A^{(1,1,p,v)}_{N_\xi-1,N_\xi} \\
& A^{(1,1,p-1,v)}_{1,0} & \cdots & A^{(1,1,p-1,v)}_{1,N_\xi} \\
& A^{(1,1,p-1,v)}_{2,0} & \cdots & A^{(1,1,p-1,v)}_{2,N_\xi} \\
& \ddots & \ddots \\
& A^{(1,1,p-1,v)}_{N_\xi-1,0} & \cdots & A^{(1,1,p-1,v)}_{N_\xi-1,N_\xi} \\
& \ddots \\
& A^{(1,1,1,v)}_{1,0} & \cdots & A^{(1,1,1,v)}_{1,N_\xi} \\
& A^{(1,1,1,v)}_{2,0} & \cdots & A^{(1,1,1,v)}_{2,N_\xi} \\
& \ddots & \ddots \\
& A^{(1,1,1,v)}_{N_\xi,0} & \cdots & A^{(1,1,1,v)}_{N_\xi,N_\xi}
\end{matrix}
&
\begin{matrix}
A^{(1,2,p,v)}_{0,0} & \cdots & A^{(1,2,p,v)}_{0,N_\xi} \\
A^{(1,2,p,v)}_{1,0} & \cdots & A^{(1,2,p,v)}_{1,N_\xi} \\
\ddots & \ddots & \ddots \\
A^{(1,2,p,v)}_{N_\xi-1,0} & \cdots & A^{(1,2,p,v)}_{N_\xi-1,N_\xi} \\
A^{(1,2,p-1,v)}_{1,0} & \cdots & A^{(1,2,p-1,v)}_{1,N_\xi} \\
A^{(1,2,p-1,v)}_{2,0} & \cdots & A^{(1,2,p-1,v)}_{2,N_\xi} \\
\ddots & \ddots \\
A^{(1,2,p-1,v)}_{N_\xi-1,0} & \cdots & A^{(1,2,p-1,v)}_{N_\xi-1,N_\xi} \\
\ddots \\
A^{(1,2,1,v)}_{1,0} & \cdots & A^{((1,2,1,v)}_{1,N_\xi} \\
A^{((1,2,1,v)}_{2,0} & \cdots & A^{(1,2,1,v)}_{2,N_\xi} \\
\ddots & \ddots \\
A^{(1,2,1,v)}_{N_\xi,0} & \cdots & A^{(1,2,1,v)}_{N_\xi,N_\xi}
\end{matrix} \\[1em]
\hline
\begin{matrix}
A^{(2,1,p,v)}_{0,0} & \cdots & A^{(2,1,p,v)}_{0,N_\xi} \\
A^{(2,1,p,v)}_{1,0} & \cdots & A^{(2,1,p,v)}_{1,N_\xi} \\
\ddots & \ddots & \ddots \\
A^{(2,1,p,v)}_{N_\xi-1,0} & \cdots & A^{(2,1,p,v)}_{N_\xi-1,N_\xi} \\
& A^{(2,1,p-1,v)}_{1,0} & \cdots & A^{(2,1,p-1,v)}_{1,N_\xi} \\
& A^{(2,1,p-1,v)}_{2,0} & \cdots & A^{(2,1,p-1,v)}_{2,N_\xi} \\
& \ddots & \ddots \\
& A^{(2,1,p-1,v)}_{N_\xi-1,0} & \cdots & A^{(2,1,p-1,v)}_{N_\xi-1,N_\xi} \\
& \ddots \\
& A^{(2,1,1,v)}_{1,0} & \cdots & A^{(2,1,1,v)}_{1,N_\xi} \\
& A^{(2,1,1,v)}_{2,0} & \cdots & A^{(2,1,1,v)}_{2,N_\xi} \\
& \ddots & \ddots \\
& A^{(2,1,1,v)}_{N_\xi,0} & \cdots & A^{(2,1,1,v)}_{N_\xi,N_\xi}
\end{matrix}
&
\begin{matrix}
A^{(2,2,p,v)}_{0,0} & \cdots & A^{(2,2,p,v)}_{0,N_\xi} \\
A^{(2,2,p,v)}_{1,0} & \cdots & A^{(2,2,p,v)}_{1,N_\xi} \\
\ddots & \ddots & \ddots \\
A^{(2,2,p,v)}_{N_\xi-1,0} & \cdots & A^{(2,2,p,v)}_{N_\xi-1,N_\xi} \\
A^{(2,2,p-1,v)}_{1,0} & \cdots & A^{(2,2,p-1,v)}_{1,N_\xi} \\
A^{(2,2,p-1,v)}_{2,0} & \cdots & A^{(2,2,p-1,v)}_{2,N_\xi} \\
\ddots & \ddots \\
A^{(2,2,p-1,v)}_{N_\xi-1,0} & \cdots & A^{(2,2,p-1,v)}_{N_\xi-1,N_\xi} \\
\ddots \\
A^{(2,2,1,v)}_{1,0} & \cdots & A^{((2,2,1,v)}_{1,N_\xi} \\
A^{((2,2,1,v)}_{2,0} & \cdots & A^{(2,2,1,v)}_{2,N_\xi} \\
\ddots & \ddots \\
A^{(2,2,1,v)}_{N_\xi,0} & \cdots & A^{(2,2,1,v)}_{N_\xi,N_\xi}
\end{matrix}
\end{array}
\right]
\left[
\begin{matrix}
\mathbf{F}^{(p,v)}_{0,r+1} \\
\mathbf{F}^{(p,v)}_{1,r+1} \\
\vdots \\
\mathbf{F}^{(p,v)}_{N_\xi-1,r+1} \\
\mathbf{F}^{(p-1,v)}_{1,r+1} \\
\mathbf{F}^{(p-1,v)}_{2,r+1} \\
\vdots \\
\mathbf{F}^{(p-1,v)}_{N_\xi-1,r+1} \\
\vdots \\
\mathbf{F}^{(1,v)}_{1,r+1} \\
\mathbf{F}^{(1,v)}_{2,r+1} \\
\vdots \\
\mathbf{F}^{(1,v)}_{N_\xi,r+1} \\
\mathbf{\Theta}^{(p,v)}_{0,r+1} \\
\mathbf{\Theta}^{(p,v)}_{1,r+1} \\
\vdots \\
\mathbf{\Theta}^{(p,v)}_{N_\xi-1,r+1} \\
\mathbf{\Theta}^{(p-1,v)}_{1,r+1} \\
\mathbf{\Theta}^{(p-1,v)}_{2,r+1} \\
\vdots \\
\mathbf{\Theta}^{(p-1,v)}_{N_\xi-1,r+1} \\
\vdots \\
\mathbf{\Theta}^{(1,v)}_{1,r+1} \\
\mathbf{\Theta}^{(1,v)}_{2,r+1} \\
\vdots \\
\mathbf{\Theta}^{(1,v)}_{N_\xi,r+1}
\end{matrix}
\right]
=
\left[
\begin{matrix}
\mathbf{K}^{(p,v)}_{1,0} \\
\mathbf{K}^{(p,v)}_{1,1} \\
\vdots \\
\mathbf{K}^{(p,v)}_{1,N_\xi-1} \\
\mathbf{K}^{(p-1,v)}_{1,1} \\
\mathbf{K}^{(p-1,v)}_{1,2} \\
\vdots \\
\mathbf{K}^{(p-1,v)}_{1,N_\xi-1} \\
\vdots \\
\mathbf{K}^{(1,v)}_{1,1} \\
\mathbf{K}^{(1,v)}_{1,2} \\
\vdots \\
\mathbf{K}^{(1,v)}_{1,N_\xi} \\
\mathbf{K}^{(p,v)}_{2,0} \\
\mathbf{K}^{(p,v)}_{2,1} \\
\vdots \\
\mathbf{K}^{(p,v)}_{2,N_\xi-1} \\
\mathbf{K}^{(p-1,v)}_{2,1} \\
\mathbf{K}^{(p-1,v)}_{2,2} \\
\vdots \\
\mathbf{K}^{(p-1,v)}_{2,N_\xi-1} \\
\vdots \\
\mathbf{K}^{(1,v)}_{2,1} \\
\mathbf{K}^{(1,v)}_{2,2} \\
\vdots \\
\mathbf{K}^{(1,v)}_{2,N_\xi}
\end{matrix}
\right] , \tag{36}
$$

where

$$A_{i,i}^{(1,1,p,v)} = \boldsymbol{\alpha}_{1,3,r}^{(1,\mu,v)} \left[\mathbf{D}^{(\mu)}\right]^3 + \boldsymbol{\alpha}_{1,2,r}^{(1,\mu,v)} \left[\mathbf{D}^{(\mu)}\right]^2 + \boldsymbol{\alpha}_{1,1,r}^{(1,\mu,v)} \mathbf{D}^{(\mu)} + \boldsymbol{\alpha}_{1,0,r}^{(1,\mu,v)} + \boldsymbol{\beta}_{1,r}^{(1,\mu,v)} d_{i,i}\mathbf{I} + \boldsymbol{\gamma}_{1,r}^{(1,\mu,v)} d_{i,i}\mathbf{D}^{(\mu)},$$

$$A_{i,i}^{(1,2,p,v)} = \boldsymbol{\alpha}_{2,0,r}^{(1,\mu,v)}\mathbf{I}, \; A_{i,i}^{(2,1,p,v)} = \boldsymbol{\alpha}_{1,1,r}^{(2,\mu,v)} \mathbf{D}^{(\mu)} + \boldsymbol{\alpha}_{1,0,r}^{(2,\mu,v)} + \boldsymbol{\beta}_{1,r}^{(2,\mu,v)} d_{i,i}\mathbf{I}, \qquad (37)$$

$$A_{i,i}^{(2,2,p,v)} = \boldsymbol{\alpha}_{2,2,r}^{(2,\mu,v)} \left[\mathbf{D}^{(\mu)}\right]^2 + \boldsymbol{\alpha}_{2,1,r}^{(2,\mu,v)} \mathbf{D}^{(\mu)} + \boldsymbol{\alpha}_{2,0,r}^{(2,\mu,v)} + \boldsymbol{\beta}_{2,r}^{(2,\mu,v)} d_{i,i}\mathbf{I}, \quad \text{when } i = j$$

and

$$A_{i,j}^{(1,1,p,v)} = \boldsymbol{\beta}_{1,r}^{(1,\mu,v)} d_{i,j}\mathbf{I} + \boldsymbol{\gamma}_{1,r}^{(1,\mu,v)} d_{i,j}\mathbf{D}^{(\mu)}, \quad A_{i,j}^{(1,2,p,v)} = \mathbf{0}, \; A_{i,j}^{(2,1,p,v)} = \boldsymbol{\beta}_{1,r}^{(2,\mu,v)} d_{i,j}\mathbf{I},$$

$$A_{i,j}^{(2,2,p,v)} = \boldsymbol{\beta}_{2,r}^{(2,\mu,v)} d_{i,j}\mathbf{I}, \quad \text{when } i \neq j. \qquad (38)$$

The vectors $\mathbf{F}_{i,r+1}^{(\mu,v)}$, and $\boldsymbol{\Theta}_{i,r+1}^{(\mu,v)}$ denote the values of f and θ approximated at the collocation points, and $\mathbf{I}$ is the standard $(M+1) \times (M+1)$ identity matrix. Starting from suitable initial guesses, the numerical solution for $f(\eta, \xi)$ and $\theta(\eta, \xi)$ are obtained by solving matrix Equation (36) iteratively for $r = 1, 2, \ldots, \sigma$, where σ is the number of iterations to be used.

3.2. Numerical Solution for the Horizontal Plate

Applying a quasilinearisation method in each subinterval to the system of nonlinear PDEs (15)–(17) gives the following system of linear PDEs:

$$\alpha_{1,3,r}^{(1,\mu,v)} \frac{\partial^3 f_{r+1}^{(\mu,v)}}{\partial \eta^3} + \alpha_{1,2,r}^{(1,\mu,v)} \frac{\partial^2 f_{r+1}^{(\mu,v)}}{\partial \eta^2} + \alpha_{1,1,r}^{(1,\mu,v)} \frac{\partial f_{r+1}^{(\mu,v)}}{\partial \eta} + \alpha_{1,0,r}^{(1,\mu,v)} f_{r+1}^{(\mu,v)} + \alpha_{2,1,r}^{(1,\mu,v)} \frac{\partial \omega_{r+1}^{(\mu,v)}}{\partial \eta},$$

$$+\alpha_{2,0,r}^{(1,\mu,v)} \omega_{r+1}^{(\mu,v)} + \gamma_{1,1,r}^{(1,\mu,v)} \frac{\partial}{\partial \xi}\left(\frac{\partial f_{r+1}^{(\mu,v)}}{\partial \eta}\right) + \beta_{1,1,r}^{(1,\mu,v)} \frac{\partial f_{r+1}^{(\mu,v)}}{\partial \xi} + \beta_{2,1,r}^{(1,\mu,v)} \frac{\partial \omega_{r+1}^{(\mu,v)}}{\partial \xi} = R_{1,r}^{(\mu,v)}, \qquad (39)$$

$$\alpha_{2,1,r}^{(2,\mu,v)} \frac{\partial \omega_{r+1}^{(\mu,v)}}{\partial \eta} + \alpha_{3,0,r}^{(2,\mu,v)} \theta_{r+1}^{(\mu,v)} = 0, \qquad (40)$$

$$\alpha_{3,2,r}^{(3,\mu,v)} \frac{\partial^2 \theta_{r+1}^{(\mu,v)}}{\partial \eta^2} + \alpha_{3,1,r}^{(3,\mu,v)} \frac{\partial \theta_{r+1}^{(\mu,v)}}{\partial \eta} + \alpha_{3,0,r}^{(3,\mu,v)} \theta_{r+1}^{(\mu,v)} + \alpha_{1,1,r}^{(3,\mu,v)} \frac{\partial f_{r+1}^{(\mu,v)}}{\partial \eta} + \alpha_{1,0,r}^{(3,\mu,v)} f_{r+1}^{(\mu,v)}$$

$$+\beta_{3,1,r}^{(3,\mu,v)} \frac{\partial \theta_{r+1}^{(\mu,v)}}{\partial \xi} + \beta_{1,1,r}^{(3,\mu,v)} \frac{\partial f_{r+1}^{(\mu,v)}}{\partial \xi} = R_{3,r}^{(\mu,v)}, \qquad (41)$$

where the variable coefficients are given by

$$\alpha_{1,3,r}^{(1,\mu,v)} = Pr, \quad \alpha_{1,2,r}^{(1,\mu,v)} = \frac{\phi_1(10-\xi)}{15}f_r^{(\mu,v)} + \frac{\phi_1\xi(1-\xi)}{3}\frac{\partial f_r^{(\mu,v)}}{\partial\xi}, \quad \alpha_{1,0,r}^{(1,\mu,v)} = \frac{\phi_1(10-\xi)}{15}\frac{\partial^2 f_r^{(\mu,v)}}{\partial\eta^2},$$

$$\alpha_{1,1,r}^{(1,\mu,v)} = -\frac{\phi_1(10-4\xi)}{15}\frac{\partial f_r^{(\mu,v)}}{\partial\eta} - M^2\phi_1\phi_2 - \frac{\phi_1\xi(1-\xi)}{3}\frac{\partial}{\partial\xi}\left(\frac{\partial f_r^{(\mu,v)}}{\partial\eta}\right),$$

$$\alpha_{2,1,r}^{(1,\mu,v)} = -\frac{(1-\phi)^{2.5}}{15}(1+Pr)(10-4\xi), \quad \frac{(1-\phi)^{2.5}}{15}(1+Pr)(5+\xi)\eta, \quad \alpha_{2,1,r}^{(2,\mu,v)} = 1, \quad \alpha_{3,0,r}^{(2,\mu,v)} = -1,$$

$$\alpha_{3,2,r}^{(3,\mu,v)} = 1 + \left(1 + \frac{k_f}{k_{nf}}Rd\right), \quad \alpha_{3,1,r}^{(3,\mu,v)} = \frac{\phi_4(10-\xi)}{15}f_r^{(\mu,v)} + \frac{\phi_4\xi(1-\xi)}{3}\frac{\partial f_r^{(\mu,v)}}{\partial\xi}, \quad \alpha_{3,0,r}^{(3,\mu,v)} = \frac{k_f}{k_{nf}}Q\xi$$

$$-\frac{\phi_4(1-\xi)}{3}\frac{\partial f_r^{(\mu,v)}}{\partial\eta}, \quad \alpha_{1,1,r}^{(3,\mu,v)} = -\frac{\phi_4(1-\xi)}{3}\theta_r^{(\mu,v)} - \frac{\phi_4\xi(1-\xi)}{3}\frac{\partial\theta_r^{(\mu,v)}}{\partial\xi}, \quad \alpha_{1,0,r}^{(3,\mu,v)} = \frac{\phi_4(10-\xi)}{15}\frac{\partial\theta_r^{(\mu,v)}}{\partial\eta},$$

$$\gamma_{1,1,r}^{(1,\mu,v)} = -\frac{\phi_1\xi(1-\xi)}{3}\frac{\partial f_r^{(\mu,v)}}{\partial\eta}, \quad \beta_{1,1,r}^{(1,\mu,v)} = \frac{\phi_1\xi(1-\xi)}{3}\frac{\partial^2 f_r^{(\mu,v)}}{\partial\eta^2}, \beta_{2,1,r}^{(1,\mu,v)} = -\frac{\phi_1\xi(1-\xi)}{3}(1+Pr),$$

$$\beta_{3,1,r}^{(3,\mu,v)} = -\frac{\phi_4\xi(1-\xi)}{3}\frac{\partial f_r^{(\mu,v)}}{\partial\eta}, \quad \beta_{1,1,r}^{(3,\mu,v)} = \frac{\phi_4\xi(1-\xi)}{5}\frac{\partial\theta_r^{(\mu,v)}}{\partial\eta}, \quad R_{1,r}^{(\mu,v)} = \frac{\phi_1(10-\xi)}{15}f_r^{(\mu,v)}\frac{\partial^2 f_r^{(\mu,v)}}{\partial\eta^2}$$

$$-\frac{\phi_1(5-2\xi)}{15}\left(\frac{\partial f_r^{(\mu,v)}}{\partial\eta}\right)^2 - \frac{\phi_1\xi(1-\xi)}{3}\frac{\partial f_r^{(\mu,v)}}{\partial\eta}\frac{\partial}{\partial\xi}\left(\frac{\partial f_r^{(\mu,v)}}{\partial\eta}\right) + \frac{\phi_1\xi(1-\xi)}{3}\frac{\partial^2 f_r^{(\mu,v)}}{\partial\eta^2}\frac{\partial f_r^{(\mu,v)}}{\partial\xi},$$

$$R_{2,r}^{(\mu,v)} = 0, \quad R_{3,r}^{(\mu,v)} = \frac{\phi_4(10-\xi)}{15}f_r^{(\mu,v)}\frac{\partial\theta_r^{(\mu,v)}}{\partial\eta} - \frac{\phi_4(1-\xi)}{3}\theta_r^{(\mu,v)}\frac{\partial f_r^{(\mu,v)}}{\partial\eta}$$

$$-\frac{\phi_4\xi(1-\xi)}{5}\frac{\partial f_r^{(\mu,v)}}{\partial\eta}\frac{\partial\theta_r^{(\mu,v)}}{\partial\xi} + \frac{\phi_4\xi(1-\xi)}{5}\frac{\partial\theta_r^{(\mu,v)}}{\partial\eta}\frac{\partial f_r^{(\mu,v)}}{\partial\xi},$$

subject to boundary conditions

$$f_{r+1}^{(\mu,v)}(\xi,0) = 0, \quad \frac{\partial f_{r+1}^{(\mu,v)}}{\partial\eta}(\xi,0) = 0, \quad \xi\theta_{r+1}^{(\mu,v)}(\xi,0) - (1-\xi)^{6/5}\frac{\partial\theta_{r+1}^{(\mu,v)}}{\partial\eta}(\xi,0) = 1,$$

$$\frac{\partial f_{r+1}^{(\mu,v)}}{\partial\eta}(\xi,\infty) = 0, \quad \omega_{r+1}^{(\mu,v)}(\xi,\infty) = 0 \quad \theta_{r+1}^{(\mu,v)}(\xi,\infty) = 0. \tag{42}$$

We apply the Chebyshev spectral collocation method that uses bivariate Lagrange interpolation polynomials as basic functions as in the vertical plate. Thus, evaluating Equations (39) and (41) at the collocation points and making use of the derivative matrices as well as incorporating the initial conditions which corresponds to ξ_{N_ξ}, we obtain

$$A_{1,1}^{(\mu,v)}\mathbf{F}_{i,r+1}^{(\mu,v)} + A_{1,2}^{(\mu,v)}\mathbf{\Omega}_{i,r+1}^{(\mu,v)} + A_{1,3}^{(\mu,v)}\mathbf{\Theta}_{i,r+1}^{(\mu,v)} + \gamma_{1,r}^{(1,1,\mu,v)}\sum_{j=0}^{N_\xi}d_{i,j}\mathbf{D}^{(\mu)}\mathbf{F}_j^{(\mu,v)} + \beta_{1,1,r}^{(1,\mu,v)}\sum_{j=0}^{N_\xi}d_{i,j}\mathbf{F}_j^{(\mu,v)},$$

$$+\beta_{2,1,r}^{(1,\mu,v)}\sum_{j=0}^{N_\xi}d_{i,j}\mathbf{\Omega}_j^{(\mu,v)} = \mathbf{R}_{1,i}^{(\mu,v)}, \tag{43}$$

$$A_{2,1}^{(\mu,v)}\mathbf{F}_{i,r+1}^{(\mu,v)} + A_{2,2}^{(\mu,v)}\mathbf{\Omega}_{i,r+1}^{(\mu,v)} + A_{2,3}^{(\mu,v)}\mathbf{\Theta}_{i,r+1}^{(\mu,v)} = \mathbf{R}_{2,i}^{(\mu,v)}, \tag{44}$$

$$A_{3,1}^{(\mu,v)}\mathbf{F}_{i,r+1}^{(\mu,v)} + A_{3,2}^{(\mu,v)}\mathbf{\Omega}_{i,r+1}^{(\mu,v)} + A_{3,3}^{(\mu,v)}\mathbf{\Theta}_{i,r+1}^{(\mu,v)} + \beta_{1,1,r}^{(3,\mu,v)}\sum_{j=0}^{N_\xi}d_{i,j}\mathbf{F}_j^{(\mu,v)} + \beta_{3,1,r}^{(3,\mu,v)}\sum_{j=0}^{N_\xi}d_{i,j}\mathbf{\Theta}_j^{(\mu,v)} = \mathbf{R}_{3,i}^{(\mu,v)}. \tag{45}$$

The vectors $\mathbf{F}_{i,r+1}^{(\mu,v)}, \mathbf{\Omega}_{i,r+1}^{(\mu,v)}$ and $\mathbf{\Theta}_{i,r+1}^{(\mu,v)}$ denote the values of f, ω and θ approximated at the collocation points. Imposing boundary conditions for $i = 0, 1, 2, 3, \ldots, N_\xi - 1$, Equations (43)–(45) can be expressed as a matrix system of size $N_\xi(M+1) \times N_\xi(M+1)$ as in the previous subsection.

4. Results and Discussion

The transformed nonlinear PDEs for the vertical and horizontal plates were solved numerically using the OMD-BSQLM for Cu–water and Ag–water nanofluids. Numerical computations are carried out using $Pr = 0.7$ [9], $M = 0.5$ and $Q = 0.01$ [12,16]. However, the parametric values of the radiation parameter and nanoparticle volume fraction were chosen as $Rd = 0.6$ and $\phi = 0.3$. All of these values are treated the same in the entire study except the varied values in respective figures. The space domain η was truncated to $\eta_\infty = 15$. The numerical results were generated using $N_\xi = 5$, $N_\eta = 20$ collocation points. The number of sub-intervals in both space and time are taken as $p = q = 5$. In order to obtain a clear understanding of the physics of the problem, a parametric study was undertaken to determine the impact of the different physical parameters on the fluid properties and flow characteristics.

To determine the accuracy of our numerical results, the local skin friction coefficient and the surface temperature are compared with the non-overlapping MD-BSQLM and published results by Yi and Lin [9] in Table 2. The table gives a comparison of the OMD-BSQLM results when $\xi = M = \phi = 0$ for different values of the Prandtl number Pr. It is observed that, for increasing values of the Prandtl number, the results are in good agreement with values in the literature and those obtained using the non-overlapping MD-BSQLM. Hence, the use of the present method is justified. It is also noted that the OMD-BSQLM can give accurate results with a minimal number of grid points compared to the non-overlapping MD-BSQLM. Table 3 presents results for the local skin friction $f''(\xi, 0)$, surface temperature $\theta(\xi, 0)$ and heat transfer rate $-\theta'(\xi, 0)$ for varying values of the dimensionless streamwise coordinate ξ and different nanofluids. The table shows clearly that the skin friction, interfacial temperature, and heat transfer rate decrease with increasing values of ξ. This is due to the increase of the momentum boundary layer thickness and thermal boundary layer thickness.

Table 2. Comparison of the OMD-BSQLM results with MD-BSQLM, Yi and Lin [9] for $f''(0,0)$ and $\theta(0,0)$ at different values of Pr when $\xi = M = \phi = 0$.

	η_∞	Pr	Yi and Lin [9] $f''(0,0)$	$\theta(0,0)$	MD-BSQLM $f''(0,0)$	$\theta(0,0)$	N_η	OMD-BSQLM $f''(0,0)$	$\theta(0,0)$	N_η
Vertical plate										
	12	0.001	54.745	1.3345	54.7463521	1.3344356	100	54.7463521	1.3344356	20
	12	0.01	16.929	1.3759	16.9295516	1.3758562	100	16.9295516	1.3758562	20
	12	0.1	5.2502	1.4824	1.2502342	1.4823999	100	1.2502342	1.4823999	20
	15	0.7	2.3123	1.6132	2.3123480	1.6129166	100	2.3123480	1.6129166	20
	15	7	1.5748	1.6520	1.5743519	1.6518940	100	1.5743519	1.6518940	20
Horizontal plate										
	12	0.001	47.166	1.2258	47.2048673	1.2257703	100	47.2048673	1.2257703	20
	12	0.01	14.549	1.2720	14.5501264	1.2720149	100	14.5501264	1.2720149	20
	12	0.1	4.5424	1.3944	4.5423369	1.3943724	100	4.5423369	1.3943724	20
	15	0.7	2.0205	1.5583	2.0757356	1.5530446	100	2.0757356	1.5530446	20
	15	7	1.3622	1.6410	1.3618515	1.6413464	100	1.3618515	1.6413464	20

Table 3. OMD-BSQLM results for the skin friction coefficient, heat transfer rate and surface temperature at different values of ξ when $Pr = 0.7, \phi = 0.3, M = 0.5, Q = 0.01$ and $Rd = 0.6$.

	Vertical Plate					
	Cu-Water Nanofluid			**Ag-Water Nanofluid**		
ξ	$f''(\xi,0)$	$-\theta'(\xi,0)$	$\theta(\xi,0)$	$f''(\xi,0)$	$-\theta'(\xi,0)$	$\theta(\xi,0)$
0.1	3.1502197	0.8886284	2.2102538	3.4901209	0.8859706	2.2335515
0.2	2.9783142	0.7836947	2.0353093	3.2954705	0.7791175	2.0526246
0.3	2.8055275	0.6874567	1.8661087	3.1006493	0.6816661	1.8784674
0.4	2.6354158	0.6013814	1.7060758	2.9096575	0.5949833	1.7145224
0.5	2.4711001	0.5260086	1.5576812	2.7259292	0.5194660	1.5631829
0.6	2.3149074	0.4610286	1.4222383	2.5519493	0.4546541	1.4256179
0.7	2.1681887	0.4055214	1.2999488	2.3890815	0.3994990	1.3018590
0.8	2.0312907	0.3582374	1.1901080	2.2375714	0.3526578	1.1910409
0.9	1.9034739	0.3177938	1.0912546	2.0964877	0.3126913	1.0915734
1	1.7808520	0.2824192	1.0000000	1.9615149	0.2778150	1.0000000
	Horizontal plate					
0.1	2.0929952	0.8768285	2.2730937	2.1709163	0.8703743	2.3299696
0.2	1.9147577	0.7603163	2.0914784	1.9651128	0.7490266	2.1346661
0.3	1.7431456	0.6537272	1.9129913	1.7696198	0.6393135	1.9443078
0.4	1.5857671	0.5595096	1.7422446	1.5936813	0.5435780	1.7638210
0.5	1.4492674	0.4788634	1.5831252	1.4450572	0.4627300	1.5971702
0.6	1.3381426	0.4116324	1.4381961	1.3286458	0.3962184	1.4467514
0.7	1.2542162	0.3565745	1.3084563	1.2459879	0.3424128	1.3132268
0.8	1.1970874	0.3118610	1.1934924	1.1960098	0.2991830	1.1957896
0.9	1.1656347	0.2755951	1.0917901	1.1770321	0.2644615	1.0925707
1	1.1674280	0.2464322	1.0000000	1.2005270	0.2370678	1.0000000

Figures 4–7 depict the effects of nanoparticle volume fraction, thermal radiation, heat generation and magnetic field parameter on the velocity profiles for both Ag and Cu nanofluids. It is observed from the figures that Ag–water nanofluid shows better enhancement in the velocity profiles than Cu–water nanofluid. This is because the viscosity of the Ag–water nanofluid is higher compared to that of Cu–water nanofluid. The effect of using different types of nanofluids is more significant in the vertical plate than on the horizontal plate. Figure 4 shows the influence of the magnetic parameter on the dimensionless velocity. It is noted that the velocity is higher near the wall and lower far from the wall for hydrodynamic flows ($M = 0$). The opposite trend is observed for the hydromagnetic flows ($M \neq 0$). Moreover, increasing the magnetic parameter reduces the velocity distribution near the wall. The magnetic parameter is known to represent the Lorentz force that opposes the flow. The peak velocity decreases with the increasing values of the magnetic parameter due to the retarding effect in the boundary layer region. As a result, the separation of the boundary layer occurs earlier since the momentum boundary layer becomes thick. These findings concur with results reported by Mamun et al. [12] and Azim et al. [16] in regular fluids.

Figure 5 shows the effect of nanoparticle volume fraction on the velocity profiles. It is seen that the flow velocity increases around the vertical and horizontal plates with an increase in the nanoparticle volume fraction. For both the vertical and horizontal plates, it is clear that the flow velocity is significantly low for the conventional fluid ($\phi = 0$) than for nanofluids ($\phi \neq 0$). As expected, for the conventional fluid, there is no change in velocity profiles for both plates. However, as the volume fraction of nanoparticles increases, the velocity distribution also increases. This is due to an increase in the momentum boundary layer thickness which is attributed to adding nanoparticles to the base fluid. The nanoparticles enhance the velocity profiles due to the higher thermal conductivity of nanofluids. For the horizontal plate, we also observe that, near the wall, the momentum boundary layer thickness decreases as the volume fraction of silver particles increases and away from the wall, the boundary layer thickness increases. Figure 6 is presented to show the effect of the heat generation parameter on the dimensionless velocity. It is observed that more heat is generated within the boundary as the heat generation parameter increases and, consequently, the fluid velocity increases as well. The increase in

velocity is consistent with the physical consequence as the internal energy generation resulted from the heat generation increases the buoyancy forces, which in turn enhance more flow along both the vertical and horizontal plates. The effect of the thermal radiation parameter on the velocity distribution is shown in Figure 7 for both Ag–water and Cu–water nanofluids. We observe that the velocity increases within the boundary layer thickness as the thermal radiation parameter increases. Radiation accelerates the fluid motion, thus enhancing the velocity of nanofluids.
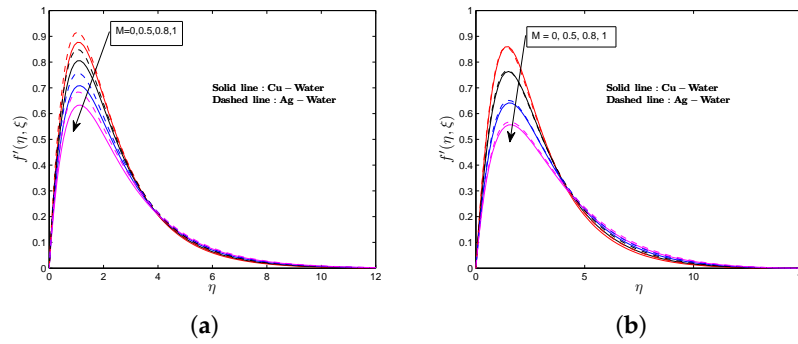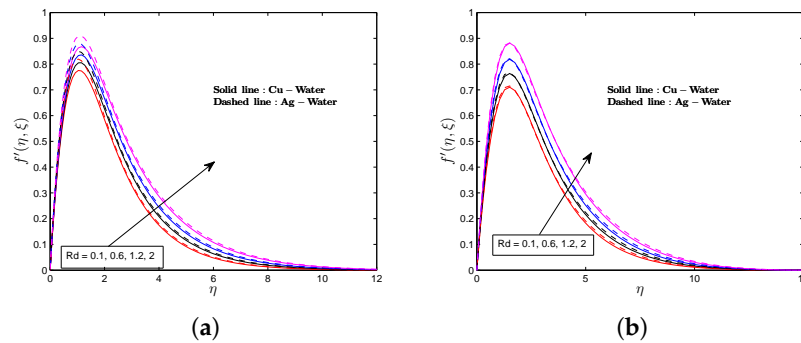

Figure 4. Velocity profiles for various values *M*. (**a**) vertical plate; (**b**) horizontal plate.
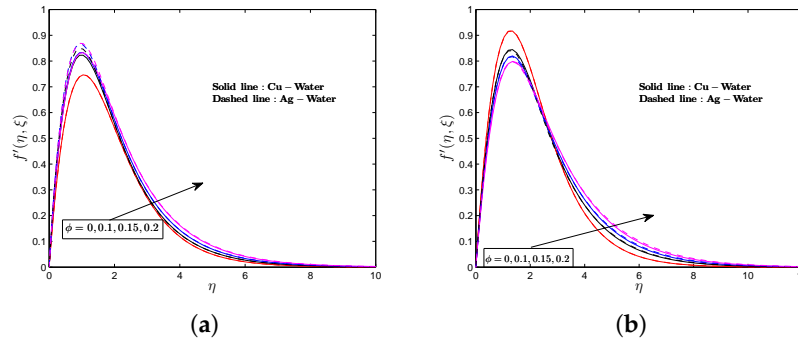
Figure 5. Velocity profiles for various values ϕ. (**a**) vertical plate; (**b**) horizontal plate.
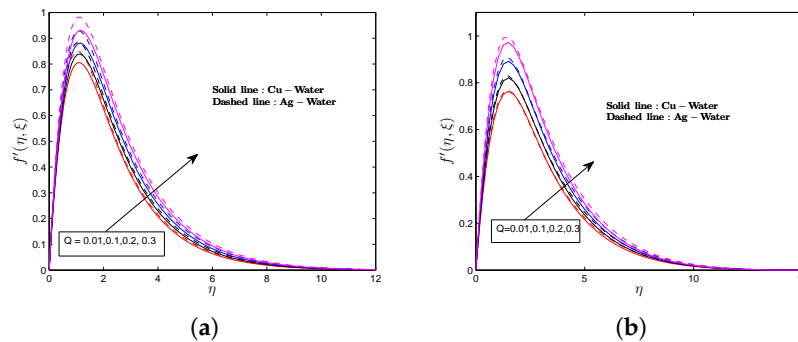
Figure 6. Velocity profiles for various values *Q*. (**a**) vertical plate; (**b**) horizontal plate.

Figure 7. Velocity profiles for various values Rd. (**a**) vertical plate; (**b**) horizontal plate.

Figures 8–11 show the influence of thermal radiation, nanoparticle volume fraction, heat generation and magnetic field parameter on the temperature profiles for both nanofluids. The temperature distribution in the case of Ag–water nanofluid is relatively higher than in the case of Cu–water nanofluid. This is because the thermal conductivity of silver nanoparticles is higher than that of Copper nanoparticles. The effect of using different types of nanofluids is more clear on the horizontal plate than for the vertical plate. Figure 8 depicts the influence of the magnetic field parameter on the temperature profiles. The figure shows that the magnetic field enhances the thickness of the thermal boundary layer, thus increasing the temperature profiles. The effect of nanoparticle volume fraction on the temperature profiles is shown in Figure 9. For the vertical and horizontal plates, the thermal boundary layer thickness is enhanced when the nanoparticle volume fraction increases. Physically, increasing the nanoparticle volume fraction causes an increase in the thermal conductivity of the nanofluid, which in turn enhances the boundary layer thickness and an augmentation in the temperature profiles. Similar results were reported by Shahzad et al. [44]. It is worth mentioning that the temperature is significantly higher in the case of nanofluids than in the regular fluid ($\phi = 0$). This is due to the presence of high conductive silver and copper nanoparticles.

Figure 10 illustrates the effect of the heat generation parameter on the temperature profiles. It is seen that the thermal boundary layer is enhanced when the heat generation parameter increases. The energy resulted from internal heat generation increases the temperature of the fluid within the boundary and increases the motion of the fluid. The influence of thermal radiation on the temperature profiles is shown in Figure 11. The figure depicts that an increase in the thermal radiation parameter improves the temperature profiles. As the temperature increases with increasing radiation parameter, the thickness of the thermal boundary layer is enhanced. The larger values of the amount of $\frac{k^* k_{nf}}{4\sigma^* T_\infty^3}$ in the radiation parameter indicate dominance in the thermal radiation over conduction. Thus, there is a large amount of radiative heat energy being poured into the system. The fluid within the boundary layer absorbs imitated heat from the heated plate because of the radiation effect. The radiated heat ultimately increases the temperature of the fluid. The greater values of thermal radiation parameter generate higher temperature and, consequently, the fluid motion is accelerated. Similar results were obtained by Ali et al. [32] in the case of regular fluid.
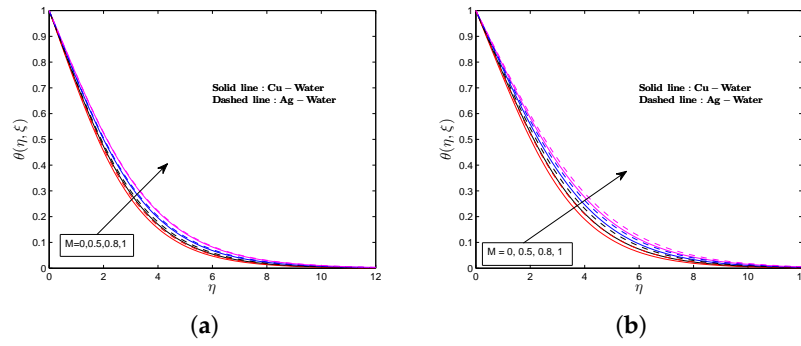
Figure 8. Temperature profiles for various values of *M*. (**a**) vertical plate; (**b**) horizontal plate.
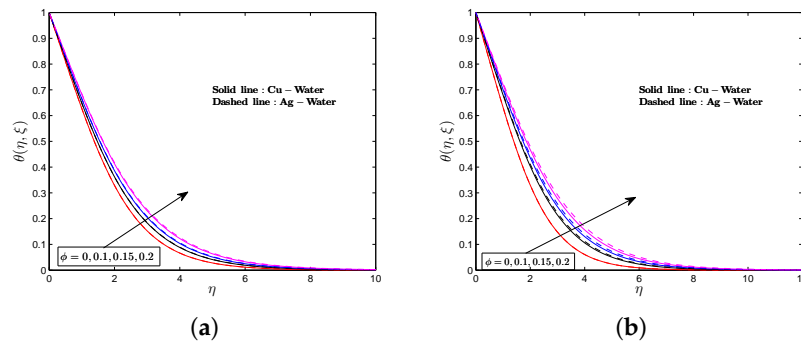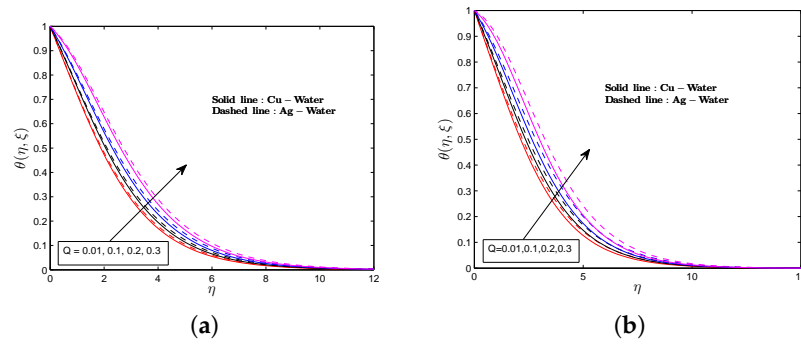

Figure 9. Temperature profiles for various values ϕ. (**a**) vertical plate; (**b**) horizontal plate.

Figure 10. Temperature profiles for various values of *Q*. (**a**) vertical plate; (**b**) horizontal plate.
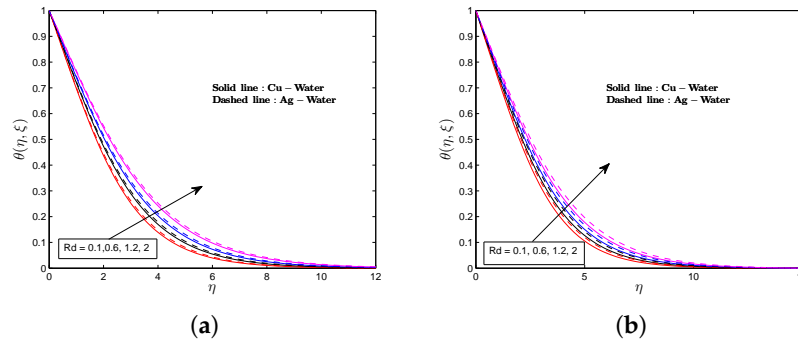
Figure 11. Temperature profiles for various values Rd. (**a**) vertical plate; (**b**) horizontal plate.

Figures 12–15 present the variation of the local skin friction at different values of the thermal radiation, heat generation, nanoparticle volume fraction and magnetic parameter for the Ag–water and Cu–water nanofluids. The skin friction coefficient is higher in the Ag–water nanofluid compared to the Cu–water nanofluid. Hence, the Ag–water nanofluid gives a high drag force in opposition to the flow compared to the Cu–water nanofluid. For the vertical plate, the skin friction is higher for the Ag–water nanofluid throughout the surface. However, for the horizontal plate, the skin friction is higher for a Ag–water nanofluid close to the wall and higher for a Cu–water nanofluid far from the wall. The effect of the magnetic parameter on the skin friction coefficient is shown in Figure 12. The figure shows that, when the magnetic parameter increases, the skin friction coefficient decreases. The magnetic force that opposes the flow decreases the shear stress at the wall, thus reducing the skin friction coefficient.

The behaviour of the skin friction coefficient against the streamwise coordinate ξ for different values of the nanoparticle volume fraction is plotted in Figure 13. The figure shows that an increase in the nanoparticle volume fraction causes a decrease in the skin friction at the plates. In Figure 14, the impact of the heat generation parameter on the local skin friction is exhibited. The figure reflects that the skin friction factor increases with increasing heat generation parameter. As mentioned earlier, increasing the heat generation parameter accelerates the flow and generates greater buoyancy force and thus increases the skin friction coefficient. The influence of the thermal radiation parameter on the skin friction coefficient is shown in Figure 15. The increase in the fluid motion due to thermal radiation enhances the shear stress at the wall which in turn causes an increase in the skin friction coefficient.
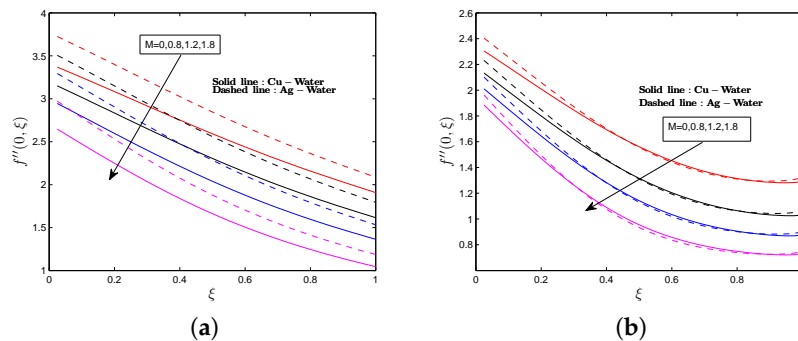

Figure 12. Skin friction coefficient for various values of M. (**a**) vertical plate; (**b**) horizontal plate.
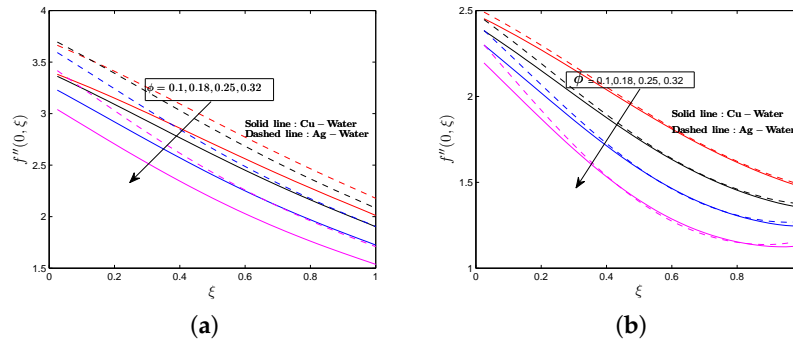
Figure 13. Skin friction coefficient for various values of ϕ. (**a**) vertical plate; (**b**) horizontal plate.
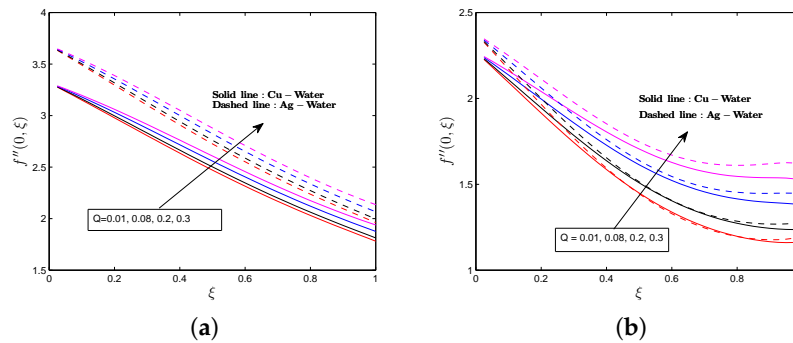

Figure 14. Skin friction for various values of Q. (**a**) vertical plate; (**b**) horizontal plate.
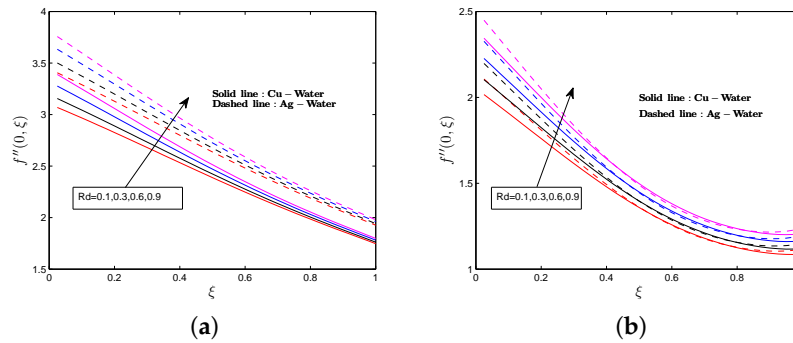

Figure 15. Skin friction coefficient for various values of Rd. (**a**) vertical plate; (**b**) horizontal plate.

Figures 16–19 show the effects of the thermal radiation, heat generation, nanoparticle volume fraction and magnetic field parameter on the rate of heat transfer for both Ag and Cu nanofluids. The rate of heat transfer is observed to be higher in the Cu–water nanofluid than in the Ag–water nanofluid for both vertical and horizontal plates. An increase in the magnetic parameter reduces the rate of heat transfer as seen in Figure 16. The increasing magnetic field parameter enhances the thermal boundary layer thickness and consequently the heat transfer rate decreases due to an increase in the magnetic field strength. In addition, the rate of heat transfer depends on the gradient of temperature and, as the temperature gradient decreases with increasing values of the magnetic parameter, the heat transfer rate also decreases.

Figure 17 depicts the impact of the nanoparticle volume fraction on the skin friction for the different nanofluids. Increasing the nanoparticle volume fraction enhances the thermal conductivity of

the nanofluids, which reduces the thermal boundary layer thickness and the temperature gradient at the wall as observed from the figure. The influence of the heat generation on the heat transfer rate is depicted in Figure 18. The figure shows that the heat transfer rate decreases with increasing heat generation parameter. Since higher values of the heat generation parameter create a hot layer of fluid near the surface which results in the temperature of the fluid to exceed the surface temperature, accordingly, the rate of heat transfer from the surface decreases. Figure 19 depicts that increasing values of the thermal radiation parameter enhances the fluid interfacial temperature, which in turn makes the flow of the heat rate slower.

Figure 16. Heat transfer rate for various values of *M*. (**a**) vertical plate; (**b**) horizontal plate.

Figure 17. Heat transfer rate for various values of ϕ. (**a**) vertical plate; (**b**) horizontal plate.
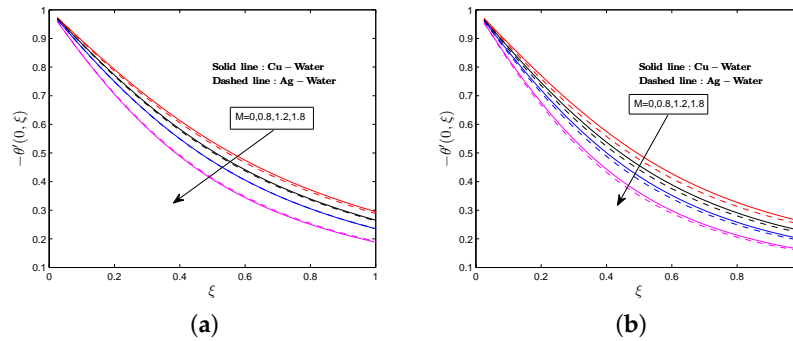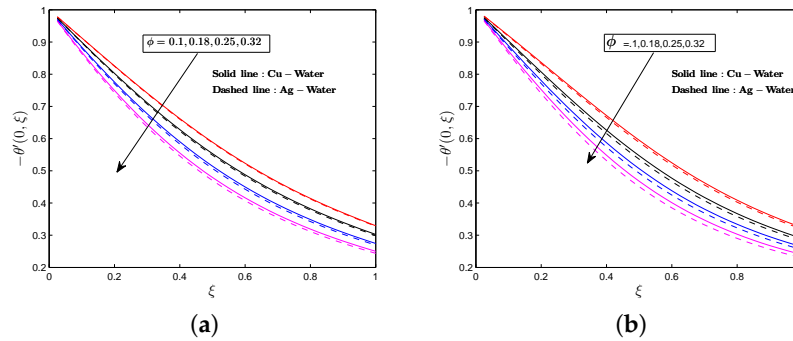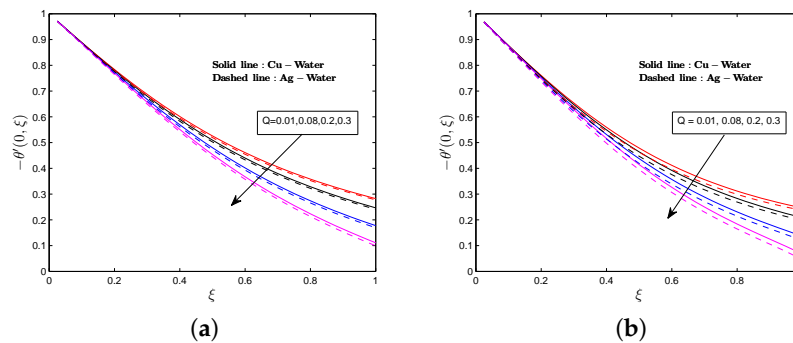

Figure 18. Heat transfer rate for various values of *Q*. (**a**) vertical plate; (**b**) horizontal plate.
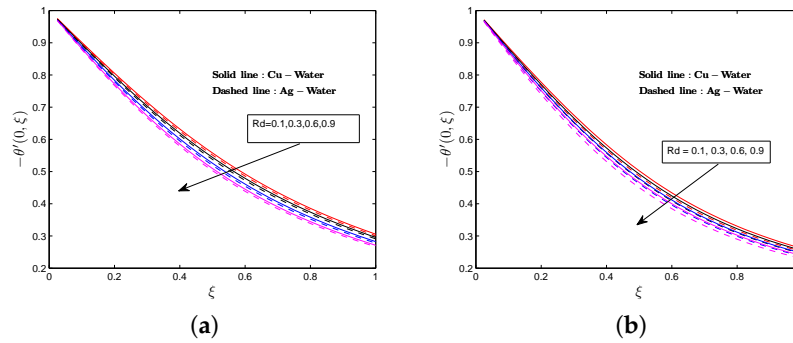
Figure 19. Heat transfer rate for various values of Rd. (**a**) vertical plate; (**b**) horizontal plate.

Figures 20–23 display the influence of the thermal radiation, heat generation, nanoparticle volume fraction and magnetic field parameter on the surface temperature for the Ag–water and Cu–water nanofluids. The surface temperature is noted to be higher in the Ag–water nanofluid than in the Cu–water nanofluid for both the vertical and horizontal plates. In Figure 20, we observe that, when the magnetic field is applied in the system, the surface temperature is enhanced for both the vertical and horizontal plates. As the magnetic field increases, the surface temperature is enhanced. The interaction between the magnetic field and the fluid motion increases the temperature of the fluid within the boundary layer which in turn increases the thermal boundary layer thickness as well as the surface temperature. Figure 21 shows that adding nanoparticles to the fluid enhances the surface temperature since the surface temperature increases with increasing nanoparticle volume fraction. The surface temperature increases with increasing values of the heat generation parameter as observed in Figure 22. This is because the temperature within the boundary layer increases for increasing heat generation parameter and thus enhances the surface temperature. Figure 23 shows that increasing the thermal radiation parameter also enhances the surface temperature.
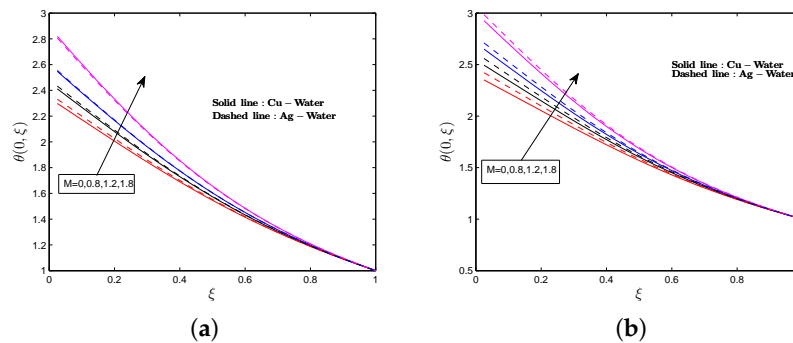
Figure 20. Surface temperature for various values of M. (**a**) vertical plate; (**b**) horizontal plate.
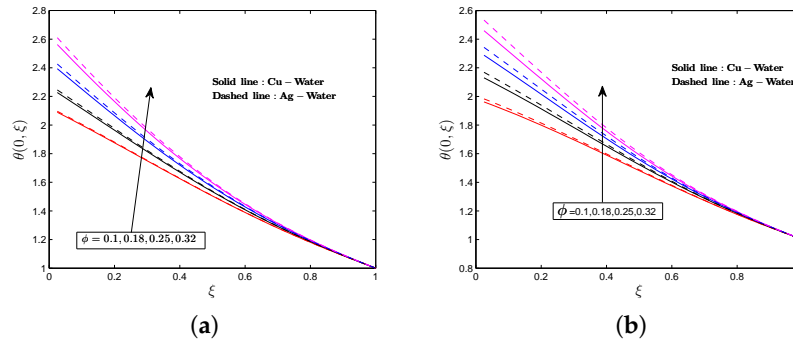
Figure 21. Surface temperature for various values of ϕ. (**a**) vertical plate; (**b**) horizontal plate.
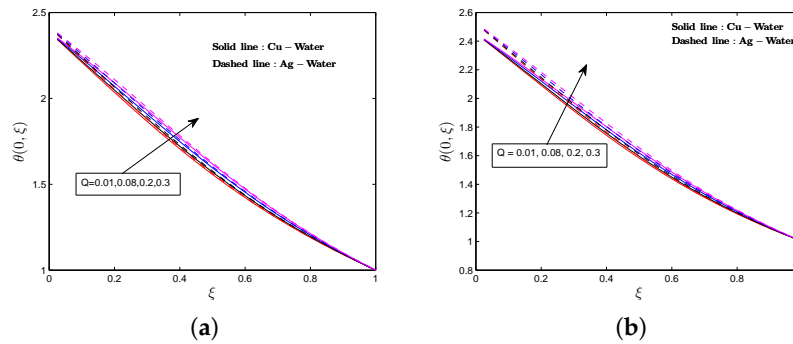
Figure 22. Surface temperature for various values of Q. (**a**) vertical plate; (**b**) horizontal plate.
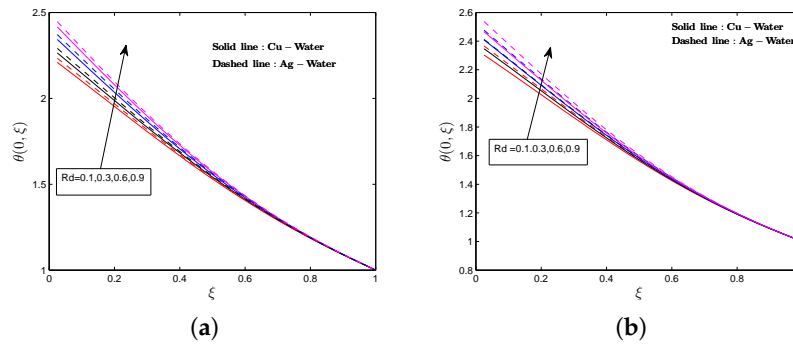
Figure 23. Surface temperature for various values of Rd. (**a**) vertical plate; (**b**) horizontal plate.

5. Conclusions

The multi-domain bivariate spectral quasilinearisation method was used to analyze conjugate heat transfer in MHD free convection flow of copper water and silver water nanofluids over vertical and horizontal plates. The comparison with previously published results was performed and the results were in good agreement. The effects of nanofluids, heat generation, thermal radiation, nanoparticle volume fraction and magnetic field parameter on the fluid properties and flow characteristics were discussed appropriately with numerical computations. The results obtained in the present study can have practical importance in various problems such as ablation or perspiration cooling problems. The results of the paper are of engineering interest where heat transfer processes are controlled in

polymer processing and nuclear reactor cooling systems. and designing and operation of plate heat exchangers. From the obtained results and discussion, the following conclusions can be drawn:

- The Ag–water nanofluid has higher velocity and temperature profiles, skin friction coefficient, and surface temperature than the Cu–water nanofluid. However, the reverse is true for the rate of heat transfer.
- Heat generation, thermal radiation, nanoparticle volume fraction and magnetic field parameter enhance the velocity of the nanofluid far from the wall. However, an increase in the magnetic field parameter significantly decreases the velocity of the nanofluid near the wall.
- Increasing the heat generation, thermal radiation, nanoparticle volume fraction and magnetic field parameter improves the temperature distribution and the surface temperature while reducing the rate of heat transfer.
- The overlapping multi-domain bivariate spectral quasilinearisation method holds great potential for solving highly nonlinear conjugate heat transfer problems since the method gives accurate results using a minimal number of grid points.

Abbreviations

The following abbreviations are used in this manuscript:

$B(x)$	External uniform magnetic field
B_0	Magnetic strength
p	Pressure
R_a	Rayleigh number
g	Gravitational acceleration
k	Thermal conductivity (W/m K)
C_p	Specific heat capacity
T	Fluid temperature (K or °C)
q_h	Heat flux
f	Dimensionless stream function
(u, v)	Velocity component in Cartesian coordinate
T_b	Constant temperature
T_∞	Ambient temperature
Q_0	Rate of heat generation
q_r	Radiative heat flux
M	Magnetic field parameter
Pr	Prandtl number
Rd	Radiation parameter
Q	Heat generation parameter

Greek Symbols

η Scaled boundary layer coordinate

ξ Streamwise coordinate

σ Electrical conductivity (S m^{-1})

α Thermal diffusivity m^{2}s^{-1}

μ Dynamic viscosity kg m^{-1}s^{-1}

θ Dimensionless temperature

ϕ Nanoparticle volume fraction parameter

ψ Stream function m^{2}s^{-1}

ρ Density of the fluid (Kg/m^3)

β Thermal expansion coefficient

ν Kinematic viscosity m^{2}s^{-1}

Subscripts

nf Nanofluid phase

f Fluid phase

s Solid phase

References

1. Chang, C.L. Buoyancy and wall conduction effects on forced convection of micropolar fluid flow along a vertical slender hollow circular cylinder. *Int. J. Heat Mass Transf.* **2006**, *49*, 4932–4942. [CrossRef]
2. Miyamoto, M.; Sumikawa, J.; Akiyoshi, T.; Nakamura, T. Effects of axial heat conduction in a vertical flat plate on free convection heat transfer. *Int. J. Heat Mass Transf.* **1980**, *23*, 1545–1553. [CrossRef]
3. Sparrow, E.M.; Chyu, M.K. Conjugated forced convection-conduction analysis of heat transfer in a plate fin. *ASME J. Heat Transf.* **1982**, *104*, 204–206. [CrossRef]
4. Merkin, J.H.; Pop, I. A note on the free convection boundary layer on a horizontal circular cylinder with constant heat flux. *Wärme Stoffübertrag.* **1988**, *22*, 79–81. [CrossRef]
5. Pop, I.; Lesnic, D.; Ingham D.B. Conjugate mixed convection on a vertical surface in a porous medium. *Int. J. Heat Mass Transf.* **1995**, *38*, 1517–1525. [CrossRef]
6. Luna, E.; Trevino, C.; Higuera, F.J. Conjugate natural convection heat transfer between two fluids seperated by a horizontal wall: Steady-state analysis. *Heat Mass Transf.* **1996**, *31*, 353–358. [CrossRef]
7. Vasquez, R.S.; Bula, A.J. Uncoupling the Conjugate Heat Transfer Problem in a Horizontal Plate Under the Influence of a Laminar Flow, Heat Transfer. In Proceedings of the ASME 2003 International Mechanical Engineering Congress and Exposition, Washington, DC, USA, 15–21 November 2003; Volume 1, pp. 11–18.
8. Hajmohammadi, M.R.; Nourazar, S.S. Conjugate Forced Convection Heat Transfer From a Heated Flat Plate of Finite Thickness and Temperature-Dependent Thermal Conductivity. *Heat Transf. Eng.* **2014**, *35*, 863–874. [CrossRef]
9. Yu, W.S.; Lin, H.T. Conjugate problems of conduction and free convection on vertical and horizontal flat plates. *Int. J. Heat Mass Transf.* **1993**, *36*, 1303–1313. [CrossRef]
10. Hsiao, K.L. Conjugate heat transfer for free convection along vertical plate fin. *J. Therm. Sci.* **2010**, *19*, 337–345. [CrossRef]
11. Azim, N.H.M.; Chowdhury, M.K. MHD-conjugate free convection from an isothermal horizontal circular cylinder with Joule heating and heat generation. *J. Comput. Meth. Phys.* **2013**, *2013*, 1–11. [CrossRef]
12. Azim, M.; Mamun, A.; Rahman, M. Viscous Joule heating MHD-conjugate heat transfer for a vertical flat plate in the presence of heat generation. *Int. J. Commun. Heat. Mass. Transf.* **2010**, *37*, 666–674. [CrossRef]
13. Kaya, A. Effects of Conjugate Heat Transfer on Steady MHD Mixed Convective Heat Transfer Flow over a Thin Vertical Plate Embedded in a Porous Medium with High Porosity. *Math. Prob. Eng.* **2012**, *2012*, 1–19. [CrossRef]
14. Kaya, A. The effect of conjugate heat transfer on MHD mixed convection about a vertical slender hollow cylinder. *Commun. Nonlinear Sci. Numer. Simul.* **2012**, *16*, 1905–1916. [CrossRef]
15. Al-Mamun, A.; Azim, N.H.M.A.; Maleque, M.A. Combined effect of conduction and viscous dissipation on MHD free convection flow along a vertical flat plate. *J. Naval Archit. Mar. Eng.* **1970**, *4*, 87–98. [CrossRef]

16. Mamun, A.A.; Chowdhury, Z.R.; Azim, M.A.; Molla M.M. MHD-conjugate heat transfer analysis for a vertical flat plate in the presence of viscous dissipation and heat generation. *Int. Commun. Heat Mass Transf.* **2008**, *35*, 1275–1280. [CrossRef]

17. Azim, N.H.M.A. Effects of Viscous Dissipation and Heat Generation on MHD Conjugate Free Convection Flow from an Isothermal Horizontal Circular Cylinder. *SOP Trans. Appl. Phys.* **2014**, *2014*, 1–11. [CrossRef]

18. Choi, S.U.S.; Zhang, Z.G.; Yu, W.; Lockwood, F.E.; Grulke, E.A. Anomalous thermal conductivity enhancement in nanotube suspensions. *Appl. Phys. Lett.* **2001**, *79*, 2252–2254. [CrossRef]

19. Malvandi, A.; Hedayati, F.; Nobari, M.R.H. An HAM analysis of stagnation-point flow of nanofluid over a porous stretching sheet with heat generation. *J. Appl. FluidMech.* **2014**, *7*, 135–145.

20. Jafarian, B.; Hajipour, M.; Khademi, R. Conjugate Heat Transfer of MHD non-Darcy Mixed Convection Flow of a Nanofluid over a Vertical Slender Hollow Cylinder Embedded in Porous Media. *Trans. Phenom. Nano Micro Scales* **2016**, *4*, 1–10.

21. Nimmagadda, R.; Venkatasubbaiah, K. Conjugate heat transfer analysis of micro-channel using novel hybrid nanofluids (Al$_2$O$_3$ + Ag/Water). *Eur. J. Mech. B Fluids.* **2015**, *52*, 19–27. [CrossRef]

22. Patrulescu, F.; Grosan, T. Conjugate heat transfer in a vertical channel filled with a nanofluid adjacent to a heat generating solid domain. *Rev. Anal. Numer. Theor. Approx.* **2010**, *36*, 141–149.

23. Zahan, I.; Alim, M.A. Effect of Conjugate heat transfer on flow of nanofluid in a rectangular enclosure. *Int. J. Heat Tech.* **2008**, *36*, 397–405. [CrossRef]

24. Malvandi, A.; Hedayati, F.; Ganji, D.D. Fluid and Heat Transfer of Nanofluids over a flat plate with conjugate heat transfer. *Trans. Phenom. Nano. Micro Scales* **2014**, *2*, 108–117.

25. Zahan, I.; Nasrin, R.; Alim, M.A. MHD effect on conjugate heat transfer in a nanofluid filled rectangular enclosure. *Int. J. Petrochem. Sci. Eng.* **2018**, *3*, 114–123. [CrossRef]

26. Alsabery, A.I.; Sheremet, M.A.; Chamkha, A.J.; Hashim, I. Conjugate natural convection of Al$_2$O$_3$-water nanofluid in a square cavity with a concentric solid insert using Buongiorno's two-phase model. *Int. J. Mech. Sci.* **2018**, *136*, 200–219. [CrossRef]

27. Takher, H.S.; Gorla, R.S.R.; Soundalgekar, V.M. Short communication radiation effects on MHD free convection flow of a gas past a semi-finite vertical plate. *J. Numer. Meth. Heat Fluid Flow.* **1996**, *6*, 77–83. [CrossRef]

28. AboEldahab, E.M. Radiation effects on heat transfer in an electrically conducting fluid at a stretching surface with a uniform free stream. *J. Phys. D Appl. Phys.* **2000**, *33*, 3180. [CrossRef]

29. El-Naby, A.; Elbarbary, E.M.E.; Abdelazem, N.Y. Finite difference solution of radiation effects on MHD unsteady free convection flow over vertical plate with variable surface temperature. *J. Appl. Math.* **2003**, *2*, 65–86. [CrossRef]

30. Chamkha, A.J.; Mujtaba, M.; Quadri, A.; Issa, C. Thermal radiation effects on MHD forced convection flow adjacent to a non-isothermal wedge in the presence of a heat source/sink. *Heat Mass Transf.* **2003**, *39*, 305–312. [CrossRef]

31. Mbeledogu, I.U.; Amakiri, A.R.C.; Ogulu, A. Unsteady MHD free convective flow of a compressible fluid past a moving vertical plate in the presence of radiative heat transfer. *Int. J. Heat Mass Transf.* **2007**, *50*, 1668–1674. [CrossRef]

32. Ali, M.M.; Mamun, A.A.; Maleque, M.A. Radiation and heat generation effects on viscous Joule heating MHD-conjugate heat transfer for a vertical flat plate. *Can. J. Phys.* **2014**, *92*, 509–521. [CrossRef]

33. Elazem, N.Y.A.; Ebaid, A.; Aly, E.H. Radiation effects of MHD on Cu-water and Ag-water nanofluids flow over a stretching sheet: Numerical study. *J. Appl. Comput. Math.* **2015**, *4*, 235. [CrossRef]

34. Raju, C.S.K.; Babu, M.J.; Sandeep, N.; Krishna, P.M. Influence of non-uniform heat source/sink on MHD nanofluid flow over a moving vertical plate in porous medium. *Chem. Process Eng. Res.* **2015**, *6*, 31–42.

35. Magagula, V.M.; Motsa, S.S.; Sibanda, P. A Multi-domain Bivariate Pseudospectral Method for Evolution Equations. *Int. J. Comput. Meth.* **2017**, *14*, 1750041. [CrossRef]

36. Motsa, S.S.; Magagula, V.M.; Sibanda, P. A Bivariate Chebyshev Spectral Collocation Quasilinearization Method for Nonlinear Evolution Parabolic Equations. *Sci. World J.* **2014**, *2014*, 1–13. [CrossRef]

37. Boyd, J.P. *Chebyshev and Fourier Spectral Methods*; Springer: Berlin, Germany; New York, NY, USA, 1989.

38. Hayat, T.; Kiran, A.; Imtiaz, M.; Alsaedi, A. Hydromagnetic mixed convection flow of copper and silver water nanofluids due to a curved stretching sheet. *Results Phys.* **2016**, 6, 904–910. [CrossRef]

39. Raza, J.; Rohni, A.M.; Omar, Z. MHD flow and heat transfer of Cu-water nanofluid in a semi porous channel with stretching walls. *Int. J. Heat Mass Transf.* **2016**, *103*, 336–340. [CrossRef]

40. Prasad, P.D.; Kumar, R.V.M.S.S.; Varma, S.V.K. Heat and mass transfer analysis for the MHD flow of nanofluid with radiation absorption. *Ain Shaims Eng. J.* **2018**, *9*, 801–813. [CrossRef]

41. Canuto, C.; Hussaini M.Y.; Quarteroni, A.; Zang, T.A. *Spectral Methods in Fluid Dynamics*; Springer: Berlin, Germany, 1988.

42. Trefethen, L.N. *Spectral Methods in Matlab*; SIAM: Philadelphia, PA, USA, 2000.

43. Bellman, R.E.; Kalaba, R.E. *Quasilinearization and Nonlinear Boundary Value Problems*; RAND Corporation: Santa Monica, CA, USA, 1965.

44. Shahzad, F.; Sagheer, M.; Hussain, S. Numerical simulation of MHD Jeffrey nanofluid flow and heat transfer over a stretching sheet considering Joule heating and viscous dissipation. *AIP Adv.* **2018**, *8*, 065316. [CrossRef]

Chapter 5

MHD mixed convective nanofluid flow about a vertical slender cylinder using overlapping multi-domain spectral collocation approach

This chapter extends from the work in Chapter 4 by considering a curved surface instead of a flat plate. We present the analysis of MHD flow of a nanofluid through a vertical slender cylinder. The impact of different flow variables on nanofluid velocity, temperature and concentration is presented. From an engineering point of view, values of local skin friction coefficient, Nusselt and Sherwood numbers are important, and are presented and analyzed. The dimensionless conservation equations are solved using the overlapping multi-domain bivariate spectral quasilinearisation method.
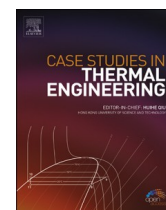
MHD mixed convective nanofluid flow about a vertical slender cylinder using overlapping multi-domain spectral collocation approach

M.P. Mkhatshwa [a,*], S.S. Motsa [a,b], M.S. Ayano [b], P. Sibanda [a]

[a] School of Mathematics, Statistics & Computer Science University of Kwazulu Natal, Private Bag X01 Scottsville, 3209, Pietermarittzburg, South Africa
[b] Department of Mathematics, University of Eswatini, Private Bag 4, M201, Kwaluseni, Kingdom of Eswatini

A B S T R A C T

This paper investigates the magnetohydrodynamic flow, heat and mass transfer characteristics in a silver water nanofluid about a vertical slender cylinder by considering diffusion-thermal, thermo-diffusion, chemical reaction and Hall effects. The nonlinear partial differential equations modelling the flow problem are non-dimensionalized and the overlapping multi-domain bivariate spectral quasilinearisation method is used to solve the dimensionless equations. The impact of flow parameters on the fluid properties and physical quantities of interest are determined. Amongst other findings, we found that increment in the nanoparticle volume fraction, Hall current and curvature parameter augments the skin friction coefficient and diminishes the heat transfer rate, while the introduction of chemical reaction, silver nanoparticles, Hall current and Soret effect into the system enhances the mass transfer rate. Also, the fluid properties amplifies in the curved surface than in the flat plate.

1. Introduction

Base fluids, for instance, water, mineral oils and ethylene glycol have low thermal conductivity and these fluids find applications in heat transfer processes in industries. When used as cooling tools, they maximize manufacturing and operating costs. To enhance thermal conductivity of base fluids, several researchers have suspended micro/nano particles in liquids. However, there is no single fluid model found to be efficient in enhancing thermal conductivity. For that reason, different fluid models have been suggested as alternatives to enrich thermal conductivity of fluids in the recent past years. Amongst these fluids, we have the nanofluid which was introduced by Choi [1]. The inclusion of small amount (less than 1% by volume) of nanoparticles in the conventional heat transfer liquids can boost the thermal conductivity of the fluids about two times [1]. Therefore, nanofluid can be regarded as a special sort of multi-component fluid containing nanometer-sized particles (diameter less than 100 nm) or fibers suspended in an ordinary fluid. Nanoparticles are available in forms of metals including Copper (Cu), Gold (Au) and Silver (Ag), metal oxides such as Aluminium oxide (Al_2O_3), Magnetite (Fe_3O_4) and Titanium oxide (TiO_2), non-metals involving graphite and carbon nanotubes, and Carbides. Nanofluids are more stable, have acceptable viscosity, better wetting, spreading and dispersion properties [2]. Many researchers [3–5] have

Nomenclature

u, v	Velocity components in $x-$ and $r-$ directions
x, r	Axial coordinate and radius of the cylinder
L	Length of the cylinder
g	Gravitational acceleration
T, C	Temperature and concentration of the fluid
u_∞	Free stream velocity
T_∞, C_∞	Ambient temperature and concentration
T_w, C_w	Wall temperature and concentration
K_T	Thermal diffusion ratio
D_m	Coefficient of diffusion
C_s	Concentration susceptibility
T_m	Mean fluid temperature
D_B	Brownian diffusion coefficient
k_1	Chemical reaction rate
B_0	Magnetic field flux density
f	Dimensionless stream function
Ri	Richardson number
Pr	Prandtl number
Re	Reynolds number
N	Buoyancy ratio parameter
G_r, G_r^*	Thermal and mass Grashof numbers
Ec	Eckert number
Df	Dufour number
Sr	Soret number
K	Chemical reaction parameter
Sc	Schmidt number
Mn	Magnetic field parameter
C_f	Skin friction coefficient
Nu_x	Local Nusselt number
Sh_x	Local Sherwood number

Greek Symbols

ν, μ	Kinematic and dynamic viscosities
k	Thermal conductivity
ρ	Density of the fluid
σ	Electrical conductivity
C_p	Specific heat capacity
β_T, β_C	Coefficient of thermal and concentration expansions
β_i, β_h	Ion-slip and Hall current parameters
ϕ	Nanoparticle volume fraction
λ	Curvature parameter
η	Dimensionless coordinate
θ, φ	Dimensionless temperature and concentration

Subscripts

w	Wall condition
∞	Ambient
f	Base fluid
s	Solid nanoparticles
nf	Nanofluid

studied thermal properties of nanofluids by taking into account two definite approaches reported by Das et al. [6] and Buongiorno [7].

The study of hydromagnetic flow, heat and mass transfer over stretched surfaces with applied transverse magnetic field has received much attention from researchers due to their industrial applications involving metallurgical processes (drawing, annealing and tinning of copper wires). Making use of an electrically-conducting fluid with applied magnetic field help to control the cooling rate in these processes, thus affecting the properties of the end product. Several researchers extended the study of hydromagnetic flow, heat and mass transfer over stretching surfaces with uniform magnetic field to the case of nanofluids. Taseer et al. [8] investigated the

magnetohydrodynamic (MHD) flow of Maxwell nanofluid over a stretching surface with uniform applied magnetic field. Hayat et al. [9] studied MHD flow, heat and mass transfer of viscous nanofluid along a stretched surface in the presence of non-uniform applied magnetic field. Hayat et al. [10] analyzed MHD flow of couple stress nanofluid over a stretching sheet by taking into account the effect of constant applied magnetic field. Hayat et al. [11] investigated MHD flow of an Oldroyd-B nanofluid along stretching surface with uniform applied magnetic field.

There has been much interest in studying hydromagnetic flow, heat and mass transfer over a vertical slender cylinder in regular fluids. Aydin and Kaya [12] studied MHD mixed convection heat transfer over a vertical slender cylinder with viscous dissipation and uniform magnetic field. Kaya [13] considered MHD mixed convection heat transfer about a vertical slender hollow cylinder with applied uniform magnetic field. Aydin and Kaya [14] studied MHD mixed convection heat transfer about a heated or cooled vertical slender cylinder by taking into account the effects of transverse curvature, viscous dissipation and uniform magnetic field. The study of hydromagnetic flow, heat and mass transfer characteristics along a vertical slender cylinder in nanofluids has attracted the interest of some researchers in the recent past years. Gholinia et al. [15] investigated MHD mixed convection flow of ethylene glycol-based nanofluid containing Ag and Cu nanoparticles over a vertical permeable circular cylinder with magnetic field effect. Jafarian et al. [16] analyzed MHD mixed convection flow and conjugate heat transfer of Cu-water nanofluid about a vertical slender hollow cylinder in porous media.

When heat and mass transfer take place concurrently in fluid motion, the connections between the fluxes and the driving potentials are very complicated. In addition to temperature gradients, it has been reported that energy flux can also be produced by concentration gradients. The Soret effect (thermal-diffusion) can be noticed in mixtures of mobile particles where the different particles show distinct responses to the cause of a temperature gradient. Regularly, the name Soret effect relates to aerosol mixtures, but sometimes refer to the phenomenon in all phases of matter. The Soret effect, for example, has been used for isotope separation in mixtures between gases with very light molecular weight (H_2, He). For medium molecular weight (N_2, air), the diffusion-thermo effect (Dufour number) was observed to be of significant magnitude and for that reason it cannot be neglected [17]. El-Kabeir and Chamkha [18] investigated mixed convection flow, heat and mass transfer over a vertical slender cylinder with chemical reaction, Soret and Dufour effects. Diffusion rates can be extremely changed by chemical reactions. Chemical reactions can be classified as either heterogeneous or homogeneous processes. This rely on whether they occur at an interface or as a single phase volume reaction. In well-mixed systems, the reaction is heterogeneous if it occurs at an interface and homogeneous if it occurs in the solution. Muhammad et al. [19] studied MHD flow of viscous fluid in the presence of chemical reaction and viscous dissipation. Hayat et al. [20] investigated chemical reaction effects in nanofluid flows over a stretching sheet. Sharma and Konwar [21] studied MHD flow, heat and mass transfer over a moving cylinder with thermal diffusion and chemical reaction. Chamkha [22] explored hydromagnetic flow, heat and mass transfer over a moving cylinder with chemical reaction and uniform magnetic field.

In view of these facts, the present study focuses on the numerical investigation of hydromagnetic flow, heat and mass transfer of Ag-water nanofluid over a vertical slender cylinder with Hall current, chemical reaction and cross-diffusion effects. To the best of the author's knowledge, no attempt has been made so far to analyze this problem. The results obtained in the current study have realistic significance in industrial applications involving heating and cooling (electronic devices) processes due to the inclusion of nanoparticles with high thermal conductivity. The boundary layer equations are first non-dimensionalized and then solved using the overlapping multi-domain bivariate spectral quasilinearisation method (OMD-BSQLM) [23]. This method remains to be generalised and its robustness remains to be tested in the case of highly nonlinear partial differential equations (PDEs) with strong coupling.

2. Mathematical analysis

We consider the steady, two-dimensional, laminar and MHD mixed convective boundary layer flow of an incompressible viscous Ag-water nanofluid along a vertical slender cylinder of length L and outer radius $r_0(L \gg r_o)$. It is assumed that the conventional fluid and silver nanoparticles are in thermal equilibrium with no slippage occurring between them. Table 1 presents the thermophysical properties of the base fluid and silver nanoparticles. The gravitational acceleration, g, acts in the downward direction. The ambient nanofluid velocity, temperature and concentration far away from the cylinder are denoted by u_∞, T_∞ and C_∞, respectively. The cylinder surface has a uniform temperature T_w ($T_w >$ or $< T_\infty$ i.e the cylinder is either heated or cooled) and constant concentration $C_w(C_w > C_\infty)$. A uniform magnetic field is applied in the r-direction causing a flow resistive force in the *x*-direction. It is assumed that the induced magnetic field, the external or imposed electric field are negligible. The relative movement of the particles in the fluid can take place and the electron-atom collision frequency is assumed to be sufficiently high for Hall and ion-slip currents to be important. The chemical reaction and cross-diffusion effects have been incorporated in the mathematical flow model. Under the aforementioned assumptions and considering the Boussinesq approximation and the boundary layer approximation, the continuity, momentum,

Table 1
Thermophysical properties of the base fluid and the nanoparticles [25].

Physical properties	Pure water	Silver (Ag)
C_p (J /kgK)	4179	235
ρ (Kg /m^3)	997.1	10,500
k (W /mK)	0.613	429
σ (Sm^{-1})	0.05	6.3×10^7

energy and concentration equations are [13,14,18].

$$\frac{\partial(ru)}{\partial x} + \frac{\partial(rv)}{\partial r} = 0, \tag{2.1}$$

$$u\frac{\partial u}{\partial x} + v\frac{\partial u}{\partial r} = \left(\frac{\nu_{nf}}{r}\right) \frac{\partial}{\partial r}\left(r\frac{\partial u}{\partial r}\right) \mp g[\beta_T(T - T_\infty) + \beta_C(C - C_\infty)] - \frac{\sigma_{nf}\alpha_e B_0^2}{\rho_{nf}(\alpha_e^2 + \beta_h^2)}(u - u_\infty) \tag{2.2}$$

$$u\frac{\partial T}{\partial x} + v\frac{\partial T}{\partial r} = \frac{k_{nf}}{(\rho C_p)_{nf}} \frac{1}{r}\frac{\partial}{\partial r}\left(r\frac{\partial T}{\partial r}\right) + \frac{D_m K_T}{C_s(\rho C_p)_{nf}} \frac{1}{r}\frac{\partial}{\partial r}\left(r\frac{\partial C}{\partial r}\right)$$

$$+ \frac{\mu_{nf}}{(\rho C_p)_{nf}}\left(\frac{\partial u}{\partial r}\right)^2 + \frac{\sigma_{nf}\alpha_e B_0^2}{(\rho C_p)_{nf}(\alpha_e^2 + \beta_h^2)}(u - u_\infty)^2 \tag{2.3}$$

$$u\frac{\partial C}{\partial x} + v\frac{\partial C}{\partial r} = D_B\frac{1}{r}\frac{\partial}{\partial r}\left(r\frac{\partial C}{\partial r}\right) + \frac{D_m K_T}{T_m}\frac{1}{r}\frac{\partial}{\partial r}\left(r\frac{\partial T}{\partial r}\right) - k_1(C - C_\infty), \tag{2.4}$$

where u and v are the velocity constituents in the x and r directions, respectively, T and C are the respective temperature and species concentration of the fluid, β_T and β_C are the respective coefficients of thermal and concentration expansions, g is the acceleration due to gravity, B_0 is the magnetic flux density, $\alpha_e = 1 + \beta_h\beta_i$, β_h is the Hall current parameter, β_i is the Ion-slip parameter, K_T is the thermal diffusion ratio, D_m is the coefficient of diffusivity, C_s is the concentration susceptibility, T_m is the mean fluid temperature, D_B is the Brownian diffusion coefficient and k_1 is the rate of chemical reaction. Furthermore, ν_{nf} is the kinematic viscosity, k_{nf} is the thermal conductivity, μ_{nf} is the dynamic viscosity, ρ_{nf} is the density, σ_{nf} is the electrical conductivity and $(\rho C_p)_{nf}$ is the specific heat capacity of the nanofluid which are given as [24].

$$\mu_{nf} = \frac{\mu_f}{(1 - \phi)^{2.5}}, \frac{k_{nf}}{k_f} = \left[\frac{(k_s + 2k_f) - 2\phi(k_f - k_s)}{(k_s + 2k_f) + \phi(k_f - k_s)}\right], \rho_{nf} = (1 - \phi)\rho_f + \phi\rho_s,$$

$$\nu_{nf} = \frac{\mu_{nf}}{\rho_{nf}}, (\rho C_p)_{nf} = (1 - \phi)(\rho C_p)_f + \phi(\rho C_p)_s, \frac{\sigma_{nf}}{\sigma_f} = \left[1 + \frac{3\left(\frac{\sigma_s}{\sigma_f} - 1\right)\phi}{\left(\frac{\sigma_s}{\sigma_f} + 2\right) - \left(\frac{\sigma_s}{\sigma_f} - 1\right)\phi}\right], \tag{2.5}$$

where ϕ is the nanoparticle volume fraction and subscripts nf, f and s denote the thermo physical properties of the nanofluid, base fluid and solid nanoparticles, respectively.

The boundary value problem (2.1)–(2.4) is subject to the following boundary conditions

$$r = r_0; \quad u = v = 0, \quad T = T_w, \quad C = C_w, \tag{2.6}$$

$$r \to \infty; \quad u \to u_\infty, \quad T \to T_\infty, \quad C \to C_\infty, \tag{2.7}$$

We introduce the following dimensionless variables to obtain non-dimensional equations

$$\xi = \left(\frac{x}{r_0}\right), \quad \eta = \left[\frac{r^2 - r_0^2}{2r_0}\right]\left(\frac{u_\infty}{\nu_f x}\right)^{1/2}, \quad \theta = \frac{T - T_\infty}{T_w - T_\infty}, \quad \varphi = \frac{C - C_\infty}{C_w - C_\infty}, \tag{2.8}$$

$$\psi(x, r) = r_0\left(\nu_f x u_\infty\right)^{1/2} f(\xi, \eta), \frac{r^2}{r_0^2} = [1 + \lambda\eta], \quad u = \left(\frac{1}{r}\right)\frac{\partial\psi}{\partial r}, \quad v = -\left(\frac{1}{r}\right)\frac{\partial\psi}{\partial x}. \tag{2.9}$$

In view of equations (2.8)-(2.9), we find that the continuity equation (2.1) is trivially satisfied and the non-dimensional form of the momentum, energy and concentration equations are given as

$$\phi_1\left[(1 + \lambda\eta)f''' + \frac{\lambda}{2}f''\right] + \frac{1}{2}ff'' \mp \xi Ri(\theta + N\varphi) - \phi_2\xi Mn\frac{\alpha_e}{\alpha_e^2 + \beta_h^2}[f' - 1] = \xi\left[f'\frac{\partial f'}{\partial\xi} - f''\frac{\partial f}{\partial\xi}\right] \tag{2.10}$$

$$\frac{\phi_3}{Pr}\left[(1 + \lambda\eta)\theta'' + \frac{\lambda}{2}\theta'\right] + \frac{1}{2}f\theta' + \phi_4 Ec(1 + \lambda\eta)f''^2 + \phi_5 EcMn\xi\frac{\alpha_e}{\alpha_e^2 + \beta_h^2}[f' - 1]^2$$

$$+ \frac{1}{(1 - \phi) + \phi(\rho C_p)_s/(\rho C_p)_f}Df\left[(1 + \lambda\eta)\varphi'' + \frac{\lambda}{2}\varphi'\right] = \xi\left[f'\frac{\partial\theta}{\partial\xi} - \theta'\frac{\partial f}{\partial\xi}\right] \tag{2.11}$$

$$\frac{1}{Sc}\left[(1 + \lambda\eta)\varphi'' + \frac{\lambda}{2}\varphi'\right] + \frac{1}{2}f\varphi' + Sr\left[(1 + \lambda\eta)\theta'' + \frac{\lambda}{2}\theta'\right] - K\varphi = \xi\left[f'\frac{\partial\varphi}{\partial\xi} - \varphi'\frac{\partial f}{\partial\xi}\right] \tag{2.12}$$

with the boundary conditions:

$$\eta = 0; \quad f + \xi \frac{\partial f}{\partial \xi} = 0, \quad f' = 0 \quad \theta = 1 \quad \varphi = 1 \tag{2.13}$$

$$\eta \to \infty; \quad f' = 1, \quad \theta = 0, \quad \varphi = 0, \tag{2.14}$$

where

$$Ri = \frac{G_r}{Re^2}, N = \frac{G_r^*}{G_r}, G_r = \frac{g\beta_T(T_w - T_\infty)r_0^3}{\nu_f^2}, G_r^* = \frac{g\beta_C(C_w - C_\infty)r_0^3}{\nu_f^2}, Re = \frac{u_\infty r_0}{\nu_f}, Pr = \frac{\mu_f(C_p)_f}{k_f},$$

$$Ec = \frac{u_\infty^2}{C_p(T_w - T_\infty)}, Df = \frac{D_m K_T(C_w - C_\infty)}{C s C_p \nu_f(T_w - T_\infty)}, Sr = \frac{D_m K_T(T_w - T_\infty)}{T_m \nu_f(C_w - C_\infty)}, K = \frac{k_1 r_0}{u_\infty}, Sc = \frac{\nu_f}{D_B},$$

$$\phi_1 = \frac{1}{(1-\phi)^{2.5}\left[(1-\phi) + \varphi\left(\frac{\rho_s}{\rho_f}\right)\right]}, \quad \phi_2 = \left(1 + \frac{3(\sigma_s/\sigma_f - 1)\phi}{(\sigma_s/\sigma_f + 2) - (\sigma_s/\sigma_f - 1)\phi}\right) \frac{1}{\left((1-\phi) + \phi\left(\frac{\rho_s}{\rho_f}\right)\right)},$$

$$\phi_3 = \frac{(k_s + 2k_f) - 2\phi(k_f - k_s)}{\left[(k_s + 2k_f) + \phi(k_f - k_s)\right]\left((1-\phi) + \phi\frac{(\rho C_p)_s}{(\rho C_p)_f}\right)}, \quad \phi_4 = \frac{1}{(1-\phi)^{2.5}\left[(1-\phi) + \phi\frac{(\rho C_p)_s}{(\rho C_p)_f}\right]},$$

$$\phi_5 = \left(1 + \frac{3(\sigma_s/\sigma_f - 1)\phi}{(\sigma_s/\sigma_f + 2) - (\sigma_s/\sigma_f - 1)\phi}\right) \frac{1}{\left((1-\phi) + \varphi\frac{(\rho C_p)_s}{(\rho C_p)_f}\right)}, \quad Mn = \frac{\sigma_f B_0^2 r_0^2}{\mu_f Re}, \lambda = 2\left(\frac{\xi}{Re}\right)^{1/2}.$$

Here, Ri is the mixed convection parameter (Richardson number), N is the buoyancy ratio parameter, G_r and G_r^* are respective thermal and mass Grashof numbers, Ec is the Eckert number, Df is the Dufour number, Sr is the Soret number, Re is the Reynolds number, K is the chemical reaction parameter, Mn is the magnetic field parameter, Pr is the Prandtl number, Sc is the Schmidt number, $\phi_\varepsilon(\varepsilon = 1, 2, 3, 4, 5)$ are the nanoparticle volume fractions and λ is the transverse curvature parameter.

The quantities of engineering interest are the skin friction coefficient Cf, local Nusselt number Nu_x and Sherwood number Sh_x defined in dimensionless form as

$$CfRe_x^{1/2} = \frac{1}{(1-\phi)^{2.5}}f''(\xi, 0), Nu_x Re_x^{-1/2} = -\frac{k_{nf}}{k_f}\theta'(\xi, 0), Sh_x Re_x^{-1/2} = -\varphi'(\xi, 0), \tag{2.15}$$

where $Re_x = u_\infty x/\nu_f$

3. Numerical solution

In this section we present the application of the OMD-BSQLM in solving the system of nonlinear PDEs (2.10)–(2.12). The basic principle of this numerical technique is decomposing the intervals of integration into non-overlapping and overlapping sub-intervals. Consequently, the time interval $[0, \xi_p]$ and the truncated interval of integration in space $[0, \eta_\infty]$ are respectively split into p non-overlapping and s overlapping sub-intervals denoted by

$$J_\omega = (\xi_{\omega-1}, \xi_\omega), \quad \omega = 1, 2, 3, \ldots, p, \tag{3.1}$$

$$I_\varepsilon = \left[\eta_0^\varepsilon, \eta_{N_\eta}^\varepsilon\right], \quad \varepsilon = 1, 2, 3, \ldots, s. \tag{3.2}$$

For the overlap to be possible, the sub-intervals must be of equal length given by

$$L_x = \frac{\eta_\infty}{s + \frac{1}{2}(1-s)\left(1 - \cos\frac{\pi}{N_\eta}\right)}, \tag{3.3}$$

and each sub-interval make use of $(N_\eta + 1)$ collocation points. To derive equation (3.3), we note that the total length of the domain of integration is

$$\eta_\infty = 2L_x - \varrho + (2L_x - 2\varrho)\left(\frac{s}{2} - 1\right) = 2L_x - \varrho + (L_x - \varrho)(s-2) = \varrho(1-s) + sL_x, \tag{3.4}$$

where ϱ is the overlapping distance between two sub-intervals. Considering the first interval I_1 in which $\eta \in [0, \eta_{N_\eta}^1]$, we can define the

length $L_x = \eta^1_{N_\eta}$. The linear transformation $\eta = \frac{L_x}{2}\widehat{\eta} + \frac{\eta^1_{N_\eta}}{2}$ can be used to transform the interval $[0, \eta^1_{N_\eta}]$ to $[-1, 1]$. Thus, using the Gauss-Lobatto collocation points $\widehat{\eta}_i = \cos\left(\frac{\pi i}{N_\eta}\right)$ [26], where $i = 0, 1, 2, 3, \ldots, N_\eta$, we obtain

$$\eta_0 - \eta_1 = \frac{L_x}{2}\left(\widehat{\eta}_0 - \widehat{\eta}_1\right) = \frac{L_x}{2}\left(1 - \cos\frac{\pi}{N_\eta}\right). \tag{3.5}$$

Therefore, equation (3.4) becomes

$$\eta_\infty = \frac{L_x}{2}\left(1 - \cos\frac{\pi}{N_\eta}\right)(1 - s) + sL_x, \tag{3.6}$$

which upon rearranging gives

$$L_x = \frac{\eta_\infty}{s + \frac{1}{2}(1 - s)\left(1 - \cos\frac{\pi}{N_\eta}\right)}. \tag{3.7}$$

Applying the quasilinearisation method (QLM) [27] at each sub-interval, we obtain the following linear equations:

$$\vartheta^{(1,\varepsilon,\omega)}_{1,3,\iota}\frac{\partial^3 f^{(\varepsilon,\omega)}_{\iota+1}}{\partial\eta^3} + \vartheta^{(1,\varepsilon,\omega)}_{1,2,\iota}\frac{\partial^2 f^{(\varepsilon,\omega)}_{\iota+1}}{\partial\eta^2} + \vartheta^{(1,\varepsilon,\omega)}_{1,1,\iota}\frac{\partial f^{(\varepsilon,\omega)}_{\iota+1}}{\partial\eta} + \vartheta^{(1,\varepsilon,\omega)}_{1,0,\iota}f^{(\varepsilon,\omega)}_{\iota+1} + \vartheta^{(1,\varepsilon,\omega)}_{2,0,\iota}\theta^{(\varepsilon,\omega)}_{\iota+1}$$

$$+ \vartheta^{(1,\varepsilon,\omega)}_{3,0,\iota}\varphi^{(\varepsilon,\omega)}_{\iota+1} + \vartheta^{(1,\varepsilon,\omega)}_{4,0,\iota}\chi^{(\varepsilon,\omega)}_{\iota+1} + \gamma^{(1,\varepsilon,\omega)}_{1,\iota}\frac{\partial}{\partial\xi}\left(\frac{\partial f^{(\varepsilon,\omega)}_{\iota+1}}{\partial\eta}\right) + \beta^{(1,\varepsilon,\omega)}_{1,\iota}\frac{\partial f^{(\varepsilon,\omega)}_{\iota+1}}{\partial\xi} = R^{(\varepsilon,\omega)}_{1,\iota}, \tag{3.8}$$

$$\vartheta^{(2,\varepsilon,\omega)}_{2,2,\iota}\frac{\partial^2 \theta^{(\varepsilon,\omega)}_{\iota+1}}{\partial\eta^2} + \vartheta^{(2,\varepsilon,\omega)}_{2,1,\iota}\frac{\partial \theta^{(\varepsilon,\omega)}_{\iota+1}}{\partial\eta} + \vartheta^{(2,\varepsilon,\omega)}_{3,2,\iota}\frac{\partial^2 \varphi^{(\varepsilon,\omega)}_{\iota+1}}{\partial\eta^2} + \vartheta^{(2,\varepsilon,\omega)}_{3,1,\iota}\frac{\partial \varphi^{(\varepsilon,\omega)}_{\iota+1}}{\partial\eta} + \vartheta^{(2,\varepsilon,\omega)}_{1,2,\iota}\frac{\partial^2 f^{(\varepsilon,\omega)}_{\iota+1}}{\partial\eta^2}$$

$$+ \vartheta^{(2,\varepsilon,\omega)}_{1,1,\iota}\frac{\partial f^{(\varepsilon,\omega)}_{\iota+1}}{\partial\eta} + \vartheta^{(2,\varepsilon,\omega)}_{1,0,\iota}f^{(\varepsilon,\omega)}_{\iota+1} + \beta^{(2,\varepsilon,\omega)}_{2,\iota}\frac{\partial\theta^{(\varepsilon,\omega)}_{\iota+1}}{\partial\xi} + \beta^{(2,\varepsilon,\omega)}_{1,\iota}\frac{\partial f^{(\varepsilon,\omega)}_{\iota+1}}{\partial\xi} = R^{(\varepsilon,\omega)}_{2,\iota}, \tag{3.9}$$

$$\vartheta^{(3,\varepsilon,\omega)}_{3,2,\iota}\frac{\partial^2 \varphi^{(\varepsilon,\omega)}_{\iota+1}}{\partial\eta^2} + \vartheta^{(3,\varepsilon,\omega)}_{3,1,\iota}\frac{\partial \varphi^{(\varepsilon,\omega)}_{\iota+1}}{\partial\eta} + \vartheta^{(3,\varepsilon,\omega)}_{3,0,\iota}\varphi^{(\varepsilon,\omega)}_{\iota+1} + \vartheta^{(3,\varepsilon,\omega)}_{2,2,\iota}\frac{\partial^2 \theta^{(\varepsilon,\omega)}_{\iota+1}}{\partial\eta^2} + \vartheta^{(3,\varepsilon,\omega)}_{2,1,\iota}\frac{\partial \theta^{(\varepsilon,\omega)}_{\iota+1}}{\partial\eta}$$

$$+ \vartheta^{(3,\varepsilon,\omega)}_{1,1,\iota}\frac{\partial f^{(\varepsilon,\omega)}_{\iota+1}}{\partial\eta} + \vartheta^{(3,\varepsilon,\omega)}_{1,0,\iota}f^{(\varepsilon,\omega)}_{\iota+1} + \beta^{(3,\varepsilon,\omega)}_{3,\iota}\frac{\partial\varphi^{(\varepsilon,\omega)}_{\iota+1}}{\partial\xi} + \beta^{(3,\varepsilon,\omega)}_{1,\iota}\frac{\partial f^{(\varepsilon,\omega)}_{\iota+1}}{\partial\xi} = R^{(\varepsilon,\omega)}_{3,\iota}, \tag{3.10}$$

where ι and $\iota + 1$ stand for previous and current iterations, respectively. For details on approximating the functions $f(\eta, \xi), \theta(\eta, \xi), \varphi(\eta, \xi)$ and computing the derivatives, the reader is refereed to the paper by Mkhatshwa et al. [23]. Applying the spectral method by evaluating equations (3.8)-(3.10) at the collocation points, using the derivative matrices and imposing the boundary conditions gives

$$[[\mathbf{D}^{(\varepsilon)}]^3 + \vartheta^{(1,\varepsilon,\omega)}_{1,2,\iota}[\mathbf{D}^{(\varepsilon)}]^2 + \vartheta^{(1,\varepsilon,\omega)}_{1,1,\iota}\mathbf{D}^{(\varepsilon)} + \vartheta^{(1,\varepsilon,\omega)}_{1,0,\iota}]\mathbf{F}^{(\varepsilon,\omega)}_{j,\iota+1} + \left[\vartheta^{(1,\varepsilon,\omega)}_{2,0,\iota}\right]\mathbf{\Theta}^{(\varepsilon,\omega)}_{j,\iota+1} + \left[\vartheta^{(1,\varepsilon,\omega)}_{3,0,\iota}\right]\mathbf{\Phi}^{(\varepsilon,\omega)}_{j,\iota+1}$$

$$+ \boldsymbol{\gamma}^{(1,\varepsilon,\omega)}_{1,r}\sum_{m=0}^{N_\xi-1}d_{j,m}\mathbf{D}^{(\varepsilon)}\mathbf{F}^{(\varepsilon,\omega)}_m + \boldsymbol{\beta}^{(1,\varepsilon,\omega)}_{1,\iota}\sum_{m=0}^{N_\xi-1}d_{j,m}\mathbf{F}^{(\varepsilon,\omega)}_m = \mathbf{K}^{(\varepsilon,\omega)}_{1,j} \tag{3.11}$$

$$\left[\vartheta^{(2,\varepsilon,\omega)}_{1,2,\iota}[\mathbf{D}^{(\varepsilon)}]^2 + \vartheta^{(2,\varepsilon,\omega)}_{1,1,\iota}\mathbf{D}^{(\varepsilon)} + \vartheta^{(2,\varepsilon,\omega)}_{1,0,\iota}\right]\mathbf{F}^{(\varepsilon,\omega)}_{j,\iota+1} + \left[\vartheta^{(2,\varepsilon,\omega)}_{2,2,\iota}[\mathbf{D}^{(\varepsilon)}]^2 + \vartheta^{(2,\varepsilon,\omega)}_{2,1,\iota}\mathbf{D}^{(\varepsilon)}\right]\mathbf{\Theta}^{(\varepsilon,\omega)}_{j,\iota+1}$$

$$+ \left[\vartheta^{(2,\varepsilon,\omega)}_{3,2\iota}[\mathbf{D}^{(\varepsilon)}]^2 + \vartheta^{(2,\varepsilon,\omega)}_{3,1,\iota}\mathbf{D}^{(\varepsilon)}\right]\mathbf{\Phi}^{(\varepsilon,\omega)}_{j,\iota+1} + \boldsymbol{\beta}^{(2,\varepsilon,\omega)}_{1,\iota}\sum_{m=0}^{N_\xi-1}d_{j,m}\mathbf{F}^{(\varepsilon,\omega)}_m + \boldsymbol{\beta}^{(2,\varepsilon,\omega)}_{2,\iota}\sum_{m=0}^{N_\xi-1}d_{j,m}\mathbf{\Theta}^{(\varepsilon,\omega)}_m = \mathbf{K}^{(\varepsilon,\omega)}_{2,j}, \tag{3.12}$$

$$\left[\vartheta^{(3,\varepsilon,\omega)}_{1,1,\iota}\mathbf{D}^{(\varepsilon)} + \vartheta^{(3,\varepsilon,\omega)}_{1,0,\iota}\right]\mathbf{F}^{(\varepsilon,\omega)}_{j,\iota+1} + \left[\vartheta^{(3,\varepsilon,\omega)}_{2,2,\iota}[\mathbf{D}^{(\varepsilon)}]^2 + \vartheta^{(3,\varepsilon,\omega)}_{2,1,\iota}\mathbf{D}^{(\varepsilon)},\right]\mathbf{\Theta}^{(\varepsilon,\omega)}_{j,\iota+1} + \boldsymbol{\beta}^{(3,\varepsilon,\omega)}_{1,\iota}\sum_{m=0}^{N_\xi-1}d_{j,m}\mathbf{F}^{(\varepsilon,\omega)}_m$$

$$+ \left[\vartheta^{(3,\varepsilon,\omega)}_{3,2,\iota}[\mathbf{D}^{(\varepsilon)}]^2 + \vartheta^{(3,\varepsilon,\omega)}_{3,1,\iota}\mathbf{D}^{(\varepsilon)} + \vartheta^{(3,\varepsilon,\omega)}_{3,0,\iota}\right]\mathbf{\Phi}^{(\varepsilon,\omega)}_{j,\iota+1} + \boldsymbol{\beta}^{(3,\varepsilon,\omega)}_{3,\iota}\sum_{m=0}^{N_\xi-1}d_{j,m}\mathbf{\Phi}^{(\varepsilon,\omega)}_m = \mathbf{K}^{(\varepsilon,\omega)}_{3,j}, \tag{3.13}$$

where

$$\mathrm{K}^{(\varepsilon,\omega)}_{1,j} = \mathbf{R}^{(\varepsilon,\omega)}_{1,j} - \boldsymbol{\gamma}^{(1,\varepsilon,\omega)}_{1,\iota}d_{j,N_\xi}\mathbf{D}^{(\varepsilon)}\mathbf{F}^{(\varepsilon,\omega)}_{N_\xi} - \boldsymbol{\beta}^{(1,\varepsilon,\omega)}_{1,\iota}d_{j,N_\xi}\mathbf{F}^{(\varepsilon,\omega)}_{N_\xi},$$

$$\mathrm{K}^{(\varepsilon,\omega)}_{2,j} = \mathbf{R}^{(\varepsilon,\omega)}_{2,j} - \boldsymbol{\beta}^{(2,\varepsilon,\omega)}_{1,\iota}d_{j,N_\xi}\mathbf{F}^{(\varepsilon,\omega)}_{N_\xi} - \boldsymbol{\beta}^{(2,\varepsilon,\omega)}_{2,\iota}d_{j,N_\xi}\mathbf{\Theta}^{(\varepsilon,\omega)}_{N_\xi},$$

$$\mathbf{K}_{3,j}^{(\varepsilon,\omega)} = \mathbf{R}_{3,j}^{(\varepsilon,\omega)} - \boldsymbol{\beta}_{3,l}^{(3,\varepsilon,\omega)} d_{j,N_\xi} \mathbf{F}_{N_\xi}^{(\varepsilon,\omega)} - \boldsymbol{\beta}_{3,l}^{(3,\varepsilon,\omega)} d_{j,N_\xi} \boldsymbol{\Phi}_{N_\xi}^{(\varepsilon,\omega)},$$

Equations (3.11)-(3.13) can be converted into $N_\xi(M+1) \times N_\xi(M+1)$ matrix system of the form

$$\begin{bmatrix} \mathbf{A}_{11} & \mathbf{A}_{12} & \mathbf{A}_{13} \\ \mathbf{A}_{21} & \mathbf{A}_{22} & \mathbf{A}_{23} \\ \mathbf{A}_{31} & \mathbf{A}_{32} & \mathbf{A}_{33} \end{bmatrix} \begin{bmatrix} \mathbf{F}_{j,t+1}^{(\mu,v)} \\ \boldsymbol{\Theta}_{j,t+1}^{(\mu,v)} \\ \boldsymbol{\Phi}_{j,t+1}^{(\mu,v)} \end{bmatrix} = \begin{bmatrix} \mathbf{K}_{1,j}^{(\mu,v)} \\ \mathbf{K}_{2,j}^{(\mu,v)} \\ \mathbf{K}_{3,j}^{(\mu,v)} \end{bmatrix}, \tag{3.14}$$

where $M = N_\eta + (N_\eta - 1)(s - 1)$ is the total number of collocation points over a single domain $[-1, 1]$. The coefficient of matrices $\mathbf{A}_{\delta,\sigma}$ ($\delta, \sigma = 1, 2, 3$) has the following structure

$$\begin{bmatrix} A_{0,0}^{(s)} & A_{0,1}^{(s)} & \cdots & A_{0,N_\eta-1}^{(s)} & A_{0,N_\eta}^{(s)} \\ A_{1,0}^{(s)} & A_{1,1}^{(s)} & \cdots & A_{1,N_\eta-1}^{(s)} & A_{1,N_\eta}^{(s)} \\ \ddots & \ddots & \ddots & \ddots & \ddots \\ A_{N_\eta-1,0}^{(s)} & A_{N_\eta-1,1}^{(s)} & \cdots & A_{N_\eta-1,N_\eta-1}^{(s)} & A_{v-1,v}^{(s)} \\ & & & A_{1,0}^{(s-1)} & A_{1,1}^{(s-1)} & \cdots & A_{1,N_\eta-1}^{(s-1)} & A_{1,N_\eta}^{(s-1)} \\ & & & A_{2,0}^{(s-1)} & A_{2,1}^{(s-1)} & \cdots & A_{2,N_\eta-1}^{(s-1)} & A_{2,N_\eta}^{(s-1)} \\ & & & \ddots & \ddots & \ddots & \ddots & \ddots \\ & & & A_{N_\eta-1,0}^{(s-1)} & A_{N_\eta-1,1}^{(s-1)} & \cdots & A_{N_\eta-1,N_\eta-1}^{(s-1)} & A_{N_\eta-1,N_\eta}^{(s-1)} \\ & & & & & \ddots & \ddots \\ & & & & & A_{1,0}^{(1)} & A_{1,1}^{(1)} & \cdots & A_{1,N_\eta-1}^{(1)} & A_{1,N_\eta}^{(1)} \\ & & & & & A_{2,0}^{(1)} & A_{2,1}^{(1)} & \cdots & A_{2,N_\eta-1}^{(1)} & A_{2,N_\eta}^{(1)} \\ & & & & & \ddots & \ddots & \ddots & \ddots & \ddots \\ & & & & & A_{N_\eta,0}^{(1)} & A_{N_\eta,1}^{(1)} & \cdots & A_{N_\eta,N_\eta-1}^{(1)} & A_{N_\eta,N_\eta}^{(1)} \end{bmatrix} \tag{3.15}$$

4. Results and discussion

The OMD-BSQLM has been used to solve the nonlinear flow equations (2.10)-(2.12). Numerical solutions were obtained using $N_\xi = 5$ and $N_\eta = 20$ collocation points in time and space, respectively. The value of η_∞ was chosen as 15. Throughout the entire calculations, we have fixed the parametric values as $Ri = 5, Pr = 1, Ec = 0.1, Sc = 0.6, \lambda = 0.5, Mn = 0.5, Df = 0.15, Sr = 0.4, K = 0.5, \beta_h = 1.2, \beta_i = 0.5, N = 0.3, \phi = 0.05$ and $\xi = 1$. All plotted graphs and presented tables correspond to these values unless otherwise stated. To validate the accuracy of the applied method, the present results are compared with previously published results. The set of results corresponding to values of skin friction and heat tranfer rate in case of pure fluid is presented in Table 2. The results are in satisfactory accordance, thus give assurance that the obtained numerical results are accurate.

In order to understand the behaviour of the flow fields and quantities of engineering interest under the influence of various physical parameters, numerical computations have been carried out. The nanoparticle volume fraction was considered in the range of $0 \leq \phi \leq 0.2$. When $\phi = 0$, the study reduces the conservation equations to those of a regular Newtonian fluid and $\phi > 0.2$ is not physically realizable due to accumulation. In the present study, we have considered spherical nanoparticles with thermal conductivity and dynamic viscosity given in equation (2.5). The effects of selected physical parameters on flow, thermal and concentration fields for both Ag-water nanofluid and pure fluid ($\phi = 0$) are depicted in Figs. 1–3. It is clear that the velocity and temperature of the Ag-water nanofluid are greater than that of the regular fluid while the concentration of Ag-water nanofluid is exceeded by that for pure

Table 2

Comparison of $f''(\xi, 0)$ and $-\theta'(\xi, 0)$ for $Pr = 0.7$, $\phi = Df = Mn = Sr = Sc = Ec = Ri = N = K = 0$ and different value of $\xi = \dfrac{4}{r_0}\left(\dfrac{\nu_f x}{u_\infty}\right)^{1/2}$ with Chen and Mucoglu [28], Chang [29], Aydin and Kaya [14] and Kabeir and Chamkha [18].

ξ	[28]		[29]		[14]		[18]		Present results	
	$f''(\xi,0)$	$-\theta'(\xi,0)$	$f''(\xi,0)$	$-\theta'(\xi,0)$	$f''(\xi,0)$	$-\theta'(\xi,0)$	$f''(\xi,0)$	$-\theta'(\xi,0)$	$f''(\xi,0)$	$-\theta'(\xi,0)$
0	1.3282	0.5854	1.3280	0.5852	1.3281	0.5856	1.329103	0.5856271	1.3281580	0.5856834
1	1.9172	0.8669	1.933	0.8658	1.9134	0.8659	1.913843	0.8657098	1.9134982	0.8659768
2	2.3981	1.0986	2.3900	1.0940	2.3922	1.0958	2.391991	1.094318	2.3922251	1.0958167
3	2.8270	1.3021	2.8159	1.2982	2.8198	1.2988	2.814610	1.296471	2.8198761	1.2988832
4	3.2235	1.4921	3.2187	1.4925	3.2212	1.4918	3.217243	1.489833	3.2212544	1.4918923
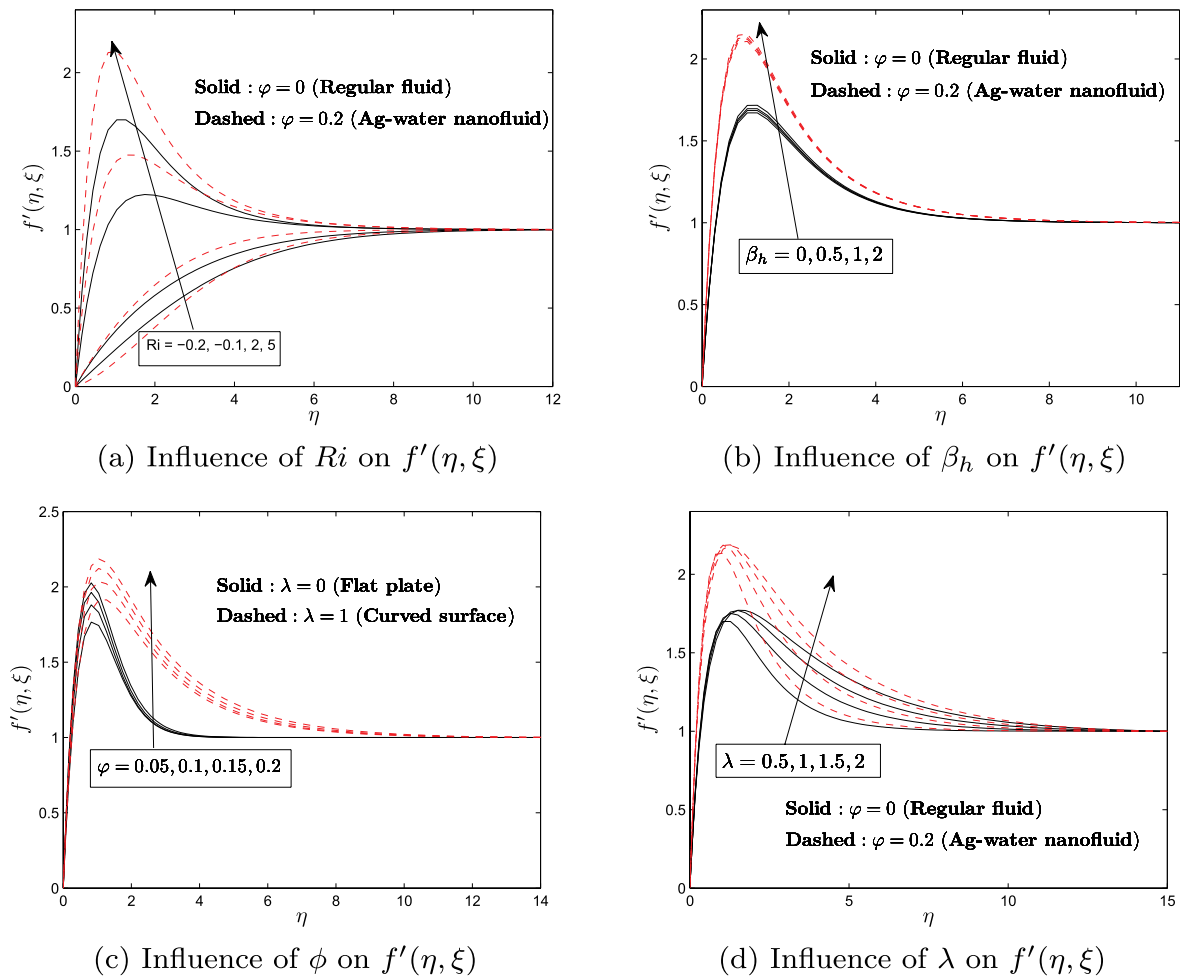
Fig. 1. Velocity profiles.

fluid. This observation suggests that the introduction of silver nanoparticles into the system has an ability to improve the velocity and temperature while diminishing the concentration field. It is also evident that the influence of controlling parameters on the velocity, temperature and concentration profiles are more pronounced in the vertical cylinder ($\lambda = 1$) than in the flat plate ($\lambda = 0$) due the large lateral surface area. The velocity profile is noted to be higher near the surface of the cylinder compared to the edge of the boundary layer. This is because the buoyancy force that enhances the motion acts as pressure gradient and increase the momentum boundary layer which in turn overshoots the velocity near the surface, and thereafter the velocity falls to 1 at the edge of the boundary layer. As expected from the boundary conditions, the temperature and concentration profiles reach their maximum values near the surface of the cylinder and their minimum values at the end of the boundary layer region.

The velocity distribution of Ag-water nanofluid and regular fluid for various values of the Richardson number, Hall current parameter, nanoparticle volume fraction and curvature parameter are shown in Fig. 1. The Richardson number serves as a measure of the buoyancy effect in comparison with that of inertia of the external forced or free stream flow on the heat and fluid flow. It is worth mentioning that when $Ri > 1$, the flow is dominated by natural convection, when $Ri < 1$, the flow is leading forced convection and $Ri = 0$ corresponds to pure forced convection. Fig. 1(a) shows that increasing values of the Richardson number accelerates the velocity gradients at the wall, thus suppressing the momentum boundary layer thickness. For greater values of the Richardson number ($Ri = 5$), the velocity is observed to overshoot near the surface of the cylinder. Similar results were reported by Aydin and Kaya [14] in the absence of the ratio of buoyancy forces. From Fig. 1(b) it is observed that the velocity profile enhances with escalating values of the Hall current parameter. The Hall current produces the cross flow effect in magnetohydrodynamics. This observation suggests that the occurrence of the Hall current parameter through the cross-flow coupling terms, $-\phi_2 \xi Mn \frac{\alpha_e}{\alpha_e^2 + \beta_h^2} [f' - 1]$ and $\phi_5 EcMn \xi \frac{\alpha_e}{\alpha_e^2 + \beta_h^2} [f' - 1]^2$ has an ability to increase the velocity since the inclusion of Hall current parameter in the system lowers the effective conductivity, thus decelerating the magnetic resistive force. It can be observed in Fig. 1(c) that the velocity increases with nanoparticle volume fraction. This is because increasing the nanoparticle volume fraction leads to enhancement in the energy transportation, which in turn accelerates the fluid flow. Fig. 1(d) shows that the velocity also augments with the curvature parameter since a rise in the curvature parameter lessen the radius of the cylinder, hence the contact area of the fluid decreases.

Fig. 2 presents the impact of Dufour number, magnetic field, curvature parameter and nanoparticle volume fraction on the

(a) Influence of Df on $\theta(\eta, \xi)$

(b) Influence of Mn on $\theta(\eta, \xi)$

(c) Influence of λ on $\theta(\eta, \xi)$

(d) Influence of ϕ on $\theta(\eta, \xi)$
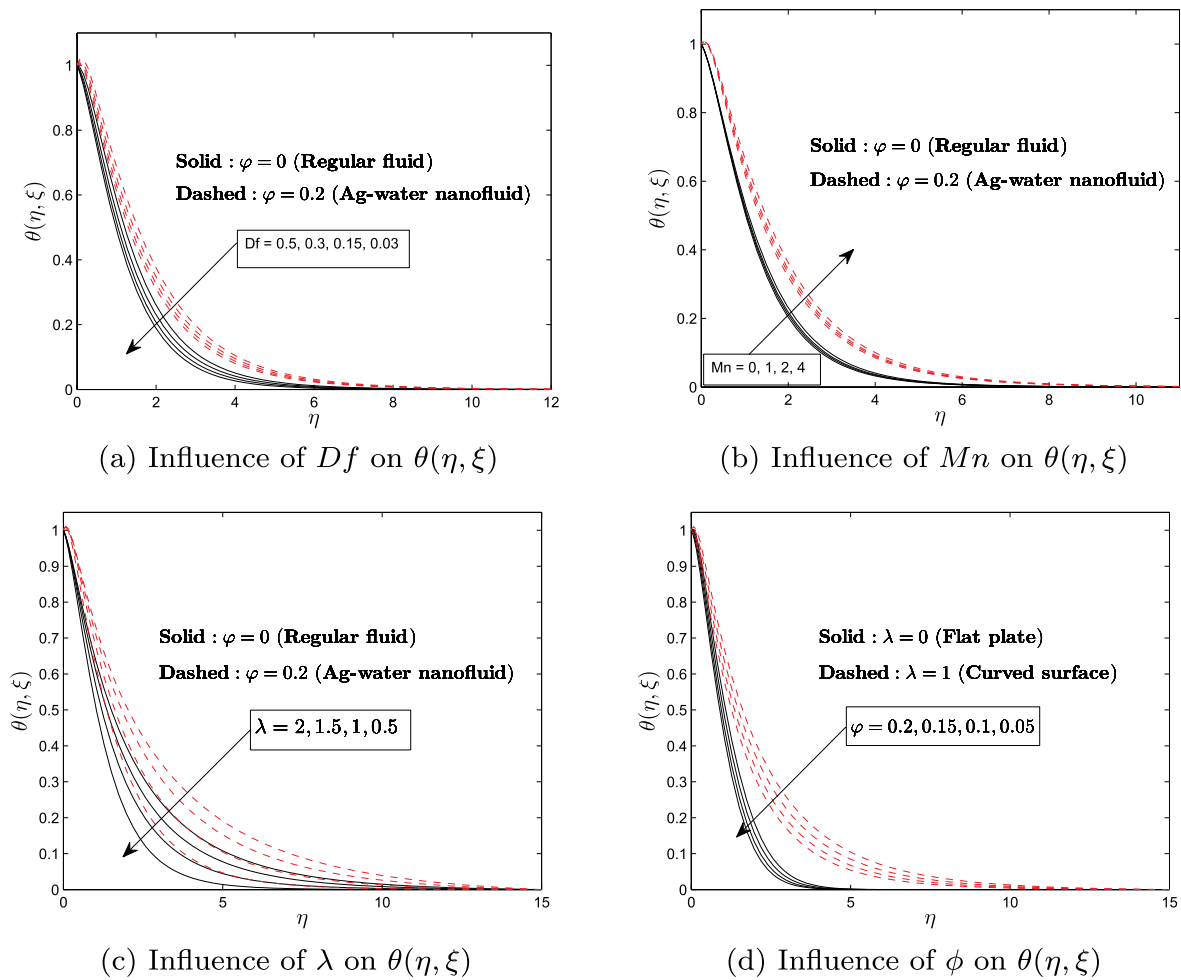
Fig. 2. Temperature profiles.

temperature field for both nanofluid and regular fluid. The Dufour number produces thermal energy flux through the concentration gradients. The Dufour term arise in the energy equation and give rise to the fluid temperature. It is clear in Fig. 2(a) that rising the Dufour number enriches the thermal boundary layer thickness. Fig. 2(b) shows that the temperature augments with strengthening the magnetic field. This is because the strong Lorentz force tends to slow down the fluid flow, thus causing more collision between the molecules of the fluid. As a result, more heat is produced, hence improving the temperature of the fluid. It is evident in Fig. 2(c) that thermal field and thickness of the boundary layer augment due to the surface curvature. Growing values of the transverse curvature increases the heat transport, thus causes a rise in the temperature field. Fig. 2(d) shows that the temperature and thermal boundary layer thickness enrich with accumulating values of the nanoparticle volume fraction. This is because increasing the silver nanoparticles enhances the thermal conductivity.

Fig. 3 exhibits the influence of chemical reaction parameter, Soret number, transverse curvature and buoyancy ratio parameter on the concentration profile for Ag-water nanofluid and regular fluid. Fig. 3(a) demonstrates that the concentration decreases with increasing values of destructive chemical reaction ($K > 0$). This is caused by the slight reduction in the solutal boundary layer thickness and the negative wall slope of the concentration profile. Similar observation was reported by Sharma and Konwar [21]. Fig. 3(b) shows that the concentration field augments with a rise in the Soret number. This is due to the fact that the Soret effect produces a mass flux from lower to higher concentration driven by the concentration gradient. The Soret term occurs in the concentration equation, thus it is expected to enhance the species concentration significantly. It is clear in Fig. 3(c) that as the curvature parameter intensify, solutal concentration enriches because the thickness of concentration boundary layer improves with escalating curvature. Fig. 3(d) shows that the concentration decline as the buoyancy ratio parameter escalates. As the fluid moves faster, the species are removed, thus causing stabilization and reduction in growth of the diffusion boundary layers along the vertical walls of the cylinder.

Table 3 shows the behaviour of flow characteristics when significant parameters are varied. It is noted that the skin friction co-efficient rises with the curvature parameter, nanoparticle volume fraction, Soret number and Hall current but diminish with chemical reaction. The heat transfer coefficient augments with the Hall current while decreasing with Soret number, curvature parameter, nanoparticle volume fraction and chemical reaction. The rate of mass transfer amplifies when nanoparticle volume fraction, Soret number, Hall current and chemical reaction parameter escalates but fall when the curvature intensify.
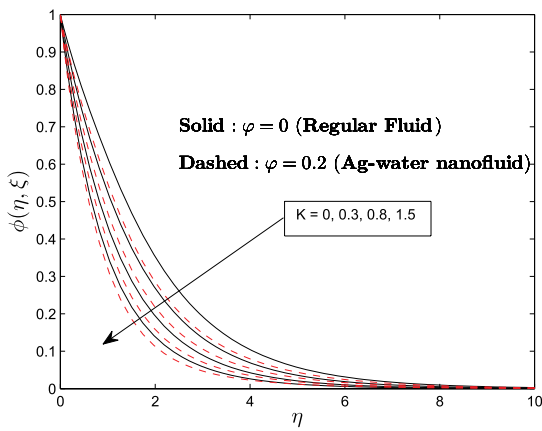
(a) Influence of K on $\phi(\eta, \xi)$
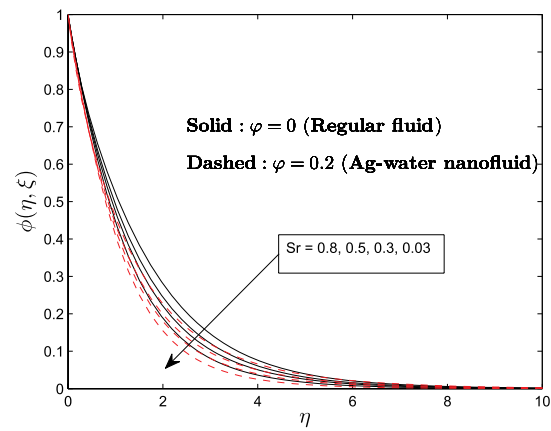
(b) Influence of Sr on $\phi(\eta, \xi)$
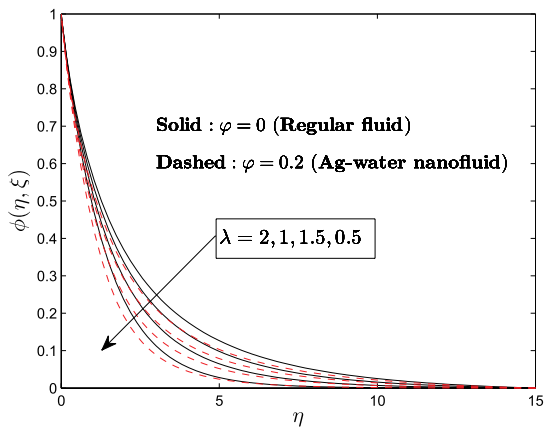
(c) Influence of λ on $\phi(\eta, \xi)$
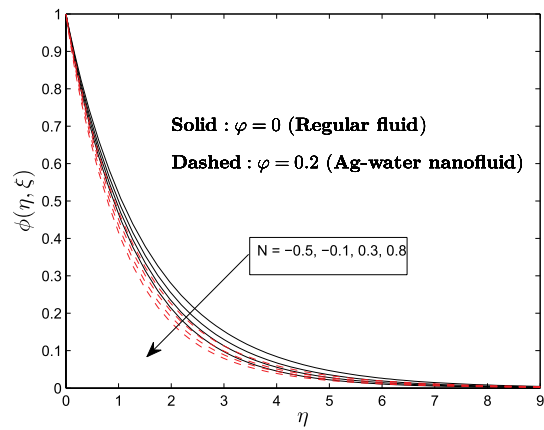
(d) Influence of N on $\phi(\eta, \xi)$

Fig. 3. Concentration profiles.

Table 3
Numerical values of skin friction coefficient, heat and mass transfer rates.

λ	φ	Sr	β_h	K	$\dfrac{1}{(1-\varphi)^{2.5}}f''(\xi,0)$	$-\dfrac{k_{nf}}{k_f}\theta'(\xi,0)$	$-\varphi'(\xi,0)$
0	0.05	0.4	1.2	0.5	5.6753426	0.1819607	0.8410197
0.3	0.05	0.4	1.2	0.5	5.7800846	0.1220118	0.8384166
1	0.05	0.4	1.2	0.5	5.8966682	0.0464319	0.8337267
0.5	0	0.4	1.2	0.5	4.2628704	0.2136086	0.7885252
0.5	0.02	0.4	1.2	0.5	4.8889589	0.1688260	0.8094784
0.5	0.08	0.4	1.2	0.5	6.7822860	0.0068364	0.8610880
0.5	0.05	0.05	0.4	0.5	5.8115596	0.1046210	0.7827361
0.5	0.05	0.3	0.4	0.5	5.8234648	0.0961420	0.8210689
0.5	0.05	0.8	0.4	0.5	5.8474534	0.0778335	0.9057702
0.5	0.05	0.4	0	0.5	5.8137606	0.0906011	0.8326568
0.5	0.05	0.4	0.5	0.5	5.8208506	0.0916620	0.8349326
0.5	0.05	0.4	10	0.5	5.8383907	0.0937826	0.8399162
0.5	0.05	0.4	1.2	0	5.9207613	0.1125123	0.5765439
0.5	0.05	0.4	1.2	0.5	5.8282439	0.0926281	0.8371263
0.5	0.05	0.4	1.2	2	5.7139965	0.0471790	1.3056787

5. Conclusion

In this article, we have investigated Hall current, chemical reaction and cross-diffusion effects on MHD mixed convective flow, heat and mass transfer over a vertical slender cylinder in a water-based silver nanofluid. Amongst other results, we found that the fluid properties were elevated for the vertical slender cylinder than for the flat plate. The incorporation of silver nanoparticles into the base

fluid significantly improved the velocity and temperature fields, while suppressing the concentration field. The outcomes of this work can be useful in industrial and engineering applications such as nuclear reaction cooling, geothermal power extraction, cooling of electronic devices, automobile fuels and smart fluids. The OMD-BSQLM was employed in solving the dimensionless conservation equations. Comparisons of the numerical results with earlier published work disclosed that the numerical method can be effective and accurate in solving nonlinear coupled PDEs. The rest of the findings are outlined as follows:

- The flow accelerates due to increasing values of the Richardson number, Hall current parameter, nanoparticle volume fraction and transverse curvature parameter.
- Temperature distribution amplifies with rising magnetic field parameter, Dufour number, curvature parameter and nanoparticle volume fraction.
- The solute concentration diminishes due to increasing buoyancy effect and destructive chemical reaction, whereas amplifies with curvature and Soret effect.
- The function of the Hall current is to enhance the flow characteristics in the system.
- Increasing the curvature parameter, nanoparticle volume fraction and Soret number augments the coefficient of skin friction while reducing the heat transfer rate.
- The introduction of chemical reactive species, nanoparticle volume fraction and Soret effect into the system leads to enhancement of the mass transfer characteristics.

Declaration of competing interest

The authors declare that they have no known competing financial interests or personal relationships that could have appeared to influence the work reported in this paper.

CRediT authorship contribution statement

M.P. Mkhatshwa: Conceptualization, Data curation, Methodology, Writing - original draft. **S.S. Motsa:** Supervision, Validation, Methodology, Writing - review & editing. **M.S. Ayano:** Formal analysis, Validation, Writing - review & editing. **P. Sibanda:** Supervision, Validation, Writing - review & editing.

Acknowledgements

Appendix A

The coefficients are defined as

$$\vartheta_{1,3,\iota}^{(1,\varepsilon,\omega)} = 1 + \lambda\eta, \, \vartheta_{1,2,\iota}^{(1,\varepsilon,\omega)} = \frac{1}{2}\lambda + \frac{1}{2}f_{\iota}^{(\varepsilon,\omega)} + \xi\frac{\partial f_{\iota}^{(\varepsilon,\omega)}}{\partial\xi}, \, \vartheta_{1,0,\iota}^{(1,\varepsilon,\omega)} = \frac{1}{2}\frac{\partial^2 f_{\iota}^{(\varepsilon,\omega)}}{\partial\eta^2},$$

$$\vartheta_{1,1,\iota}^{(1,\varepsilon,\omega)} = -\frac{\xi Mn\vartheta_e}{\alpha_e^2 + \beta_h^2} - \xi\frac{\partial}{\partial\xi}\left(\frac{\partial f_{\iota}^{(\varepsilon,\omega)}}{\partial\eta}\right), \, \vartheta_{2,0,\iota}^{(1,\varepsilon,\omega)} = \xi Ri, \, \vartheta_{3,0,\iota}^{(1,\varepsilon,\omega)} = \xi RiN,$$

$$\vartheta_{2,2,\iota}^{(2,\varepsilon,\omega)} = \frac{1}{Pr}(1 + \lambda\eta), \, \vartheta_{2,1,\iota}^{(2,\varepsilon,\omega)} = \frac{1}{2Pr}\lambda + \frac{1}{2}f_{\iota}^{(\varepsilon,\omega)} + \xi\frac{\partial f_{\iota}^{(\varepsilon,\omega)}}{\partial\xi}, \, \vartheta_{3,2,\iota}^{(2,\varepsilon,\omega)} = Df(1 + \lambda\eta),$$

$$\vartheta_{3,1,\iota}^{(2,\varepsilon,\omega)} = \frac{1}{2}Df\lambda, \, \vartheta_{1,2,\iota}^{(2,\varepsilon,\omega)} = 2Ec(1 + \lambda\eta)\frac{\partial^2 f_{\iota}^{(\varepsilon,\omega)}}{\partial\eta^2}, \, \vartheta_{1,0,\iota}^{(2,\varepsilon,\omega)} = \frac{1}{2}\frac{\partial\theta_{\iota}^{(\varepsilon,\omega)}}{\partial\eta},$$

$$\vartheta_{1,1,\iota}^{(2,\varepsilon,\omega)} = \frac{2EcMn\xi\alpha_e}{\alpha_e^2 + \beta_h^2}f_{\iota}^{(\varepsilon,\omega)} - \frac{2EcMn\xi\alpha_e}{\alpha_e^2 + \beta_h^2} - \xi\frac{\partial\theta_{\iota}^{(\varepsilon,\omega)}}{\partial\xi}, \, \vartheta_{2,2,\iota}^{(3,\varepsilon,\omega)} = \frac{1}{Sc}(1 + \lambda\eta),$$

$$\vartheta_{3,1,\iota}^{(3,\varepsilon,\omega)} = \frac{1}{2Sc} + \frac{1}{2}f_{\iota}^{(\varepsilon,\omega)} + \xi\frac{\partial f_{\iota}^{(\varepsilon,\omega)}}{\partial\xi}, \, \vartheta_{3,0,\iota}^{(3,\varepsilon,\omega)} = -K, \, \vartheta_{1,1,\iota}^{(3,\varepsilon,\omega)} = -\xi\frac{\partial\varphi_{\iota}^{(\varepsilon,\omega)}}{\partial\xi},$$

$$\vartheta_{1,0,\iota}^{(3,\varepsilon,\omega)} = \frac{1}{2}\frac{\partial\varphi_{\iota}^{(\varepsilon,\omega)}}{\partial\eta}, \, \vartheta_{2,2,\iota}^{(3,\varepsilon,\omega)} = Sr(1 + \lambda\eta), \, \vartheta_{2,1,\iota}^{(3,\varepsilon,\omega)} = \frac{1}{2}Sr\lambda, \, \gamma_{1,\iota}^{(1,\varepsilon,\omega)} = -\xi\frac{\partial f_{\iota}^{(\varepsilon,\omega)}}{\partial\eta},$$

$$\beta_{1,\iota}^{(1,\varepsilon,\omega)} = \xi\frac{\partial^2 f_{\iota}^{(\varepsilon,\omega)}}{\partial\eta^2}, \, \beta_{2,\iota}^{(2,\varepsilon,\omega)} = -\xi\frac{\partial f_{\iota}^{(\varepsilon,\omega)}}{\partial\eta}, \, \beta_{1,\iota}^{(2,\varepsilon,\omega)} = \xi\frac{\partial\theta_{\iota}^{(\varepsilon,\omega)}}{\partial\eta}, \, \beta_{3,\iota}^{(3,\varepsilon,\omega)} = -\xi\frac{\partial f_{\iota}^{(\varepsilon,\omega)}}{\partial\eta},$$

$$\beta_{1,i}^{(3,\varepsilon,\omega)} = \xi\frac{\partial\varphi_i^{(\varepsilon,\omega)}}{\partial\eta}, \quad R_{1,i}^{(\varepsilon,\omega)} = \frac{1}{2}f_i^{(\varepsilon,\omega)}\frac{\partial^2 f_i^{(\varepsilon,\omega)}}{\partial\eta^2} - \frac{\xi Mn\alpha_e}{\alpha_e^2+\beta_h^2} - \xi\frac{\partial f_i^{(\varepsilon,\omega)}}{\partial\eta}\frac{\partial}{\partial\xi}\left(\frac{\partial f_i^{(\varepsilon,\omega)}}{\partial\eta}\right)\beta_{1,i}^{(3,\varepsilon,\omega)} = \xi\frac{\partial\varphi_i^{(\varepsilon,\omega)}}{\partial\eta}, \quad R_{1,i}^{(\varepsilon,\omega)} = \frac{1}{2}f_i^{(\varepsilon,\omega)}\frac{\partial^2 f_i^{(\varepsilon,\omega)}}{\partial\eta^2} - \frac{\xi Mn\alpha_e}{\alpha_e^2+\beta_h^2}$$

$$- \xi\frac{\partial f_i^{(\varepsilon,\omega)}}{\partial\eta}\frac{\partial}{\partial\xi}\left(\frac{\partial f_i^{(\varepsilon,\omega)}}{\partial\eta}\right)$$

$$+ \xi\frac{\partial^2 f_i^{(\varepsilon,\omega)}}{\partial\eta^2}\frac{\partial f_i^{(\varepsilon,\omega)}}{\partial\xi}, \quad R_{2,i}^{(\varepsilon,\omega)} = \frac{1}{2}f_i^{(\varepsilon,\omega)}\frac{\partial\theta_i^{(\varepsilon,\omega)}}{\partial\eta} + Ec(1+\lambda\eta)\left(\frac{\partial^2 f_i^{(\varepsilon,\omega)}}{\partial\eta^2}\right)^2$$

$$+ \frac{EcMn\xi\alpha_e}{\alpha_e^2+\beta_h^2}\left(\frac{\partial f_i^{(\varepsilon,\omega)}}{\partial\eta}\right)^2 - \xi\frac{\partial f_i^{(\varepsilon,\omega)}}{\partial\eta}\frac{\partial\theta_r^{(\varepsilon,\omega)}}{\partial\xi} + \xi\frac{\partial\theta_i^{(\varepsilon,\omega)}}{\partial\eta}\frac{\partial f_i^{(\varepsilon,\omega)}}{\partial\xi},$$

$$R_{3,i}^{(\varepsilon,\omega)} = \frac{1}{2}f_i^{(\varepsilon,\omega)}\frac{\partial\varphi_i^{(\varepsilon,\omega)}}{\partial\eta} - \xi\frac{\partial f_i^{(\varepsilon,\omega)}}{\partial\eta}\frac{\partial\varphi_i^{(\varepsilon,\omega)}}{\partial\xi} + \xi\frac{\partial\varphi_i^{(\varepsilon,\omega)}}{\partial\eta}\frac{\partial f_i^{(\varepsilon,\omega)}}{\partial\xi},$$

References

[1] S.U.S. Choi, Enhancing Thermal Conductivity of Fluids with Nanoparticles, 1995, pp. 99–105. USA, ASME, FED 231/MD 66.

[2] C.T. Nguyen, G. Roy, C. Gauthier, N. Galanis, Heat transfer enhancement using Al_2O_3-water nanofluid for an electronic liquid cooling system, Appl. Therm. Eng. 27 (2007) 1501–1506.

[3] X. Wang, X. Xu, S.U.S. Choi, Thermal conductivity of nanoparticle fluid mixture, J. Thermophys. Heat Tran. 13 (1999) 474–480.

[4] P. Rana, R. Bhargava, Flow and heat transfer of a nanofluid over a nonlinearly stretching sheet: a numerical study, Commun. Nonlinear Sci. Numer. Simulat. 17 (2012) 212–226.

[5] J.A. Eastman, S.U.S. Choi, S. Li, W. Yu, L.J. Thompson, Anomalously increased effective thermal conductivity of ethylene glycol-based nanofluids containing copper nanoparticles, Appl. Phys. Lett. 78 (2001) 718–720.

[6] S.K. Das, S. Choi, W. Yu, T. Pradeep, Nanofluids : Science and Technology, Wiley Interscience, New Jersey, 2007.

[7] J. Buongiorno, Convective transport in nanofluids, ASME J. Heat Transf. 128 (2006) 240–250.

[8] T. Muhammad, A. Alsaedi, S.A. Shehzad, A revised model for Darcy-Forchheimer flow of Maxwell nanofluid subject to convective boundary condition, Chin. J. Phys. 55 (2017) 963–976.

[9] T. Hayat, A. Aziz, T. Muhammad, A. Alsaedi, On magnetohydrodynamic three-dimensional flow of nanofluid over a convectively heated nonlinear stretching surface, Int. J. Heat Mass Tran. 100 (2016) 566–572.

[10] T. Hayat, T. Muhammad, A. Alsaedi, M.S. Alhuthali, Magnetohydrodynamic three-dimensional flow of viscoelastic nanofluid in the presence of nonlinear thermal radiation, J. Magn. Magn Mater. 385 (2015) 222–229.

[11] T. Hayat, T. Muhammad, S.A. Shehzad, A. Alsaedi, An analytical solution for magnetohydrodynamic Oldroyd-B nanofluid flow induced by a stretching sheet with heat generation/absorption, Int. J. Therm. Sci. 111 (2017) 274–288.

[12] O. Aydin, A. Kaya, MHD-mixed convection from a vertical slender cylinder, Commun. Nonlinear Sci. Numer. Simulat. 16 (2011) 1863–1873.

[13] A. Kaya, The effect of conjugate heat transfer on MHD mixed convection about a vertical slender hollow cylinder, Commun. Nonlinear Sci. Numer. Simulat. 16 (2011) 1905–1916.

[14] O. Aydin, A. Kaya, MHD mixed convection of a viscous dissipating fluid about a vertical slender cylinder, Desal. Water Treat. 51 (2013) 3576–3583.

[15] M. Gholinia, S. Gholinia, Kh Hosseinzadeh, D.D. Ganji, Investigation on ethylene glycol Nano fluid flow over a vertical permeable circular cylinder under effect of magnetic field, Results Phys 9 (2018) 1525–1533.

[16] B. Jafarian, M. Hajipour, R. Khademi, Conjugate heat transfer of MHD non-Darcy mixed convection flow of a nanofluid over a vertical slender hollow cylinder embedded in porous media, Trans. Phenom. Nano Micro Scales 4 (2016) 1–10.

[17] E.R.G. Eckert, R.M. Drake, Analysis of Heat and Mass Transfer, McGraw-Hill, New York, 1972.

[18] S.M.M. El-Kabeir, A. Chamkha, Heat and mass transfer by mixed convection from a vertical cylinder with chemical reaction and Soret and Dufour effects, Heat Tran. Asian Res. 42 (2013) 618–629.

[19] T. Muhammad, T. Hayat, S.A. Shehzad, A. Alsaedi, Viscous dissipation and Joule heating effects in MHD 3D flow with heat and mass fluxes, Results Phys 8 (2018) 365–371.

[20] T. Hayat, Z. Hussain, T. Muhammad, A. Alsaedi, Effects of homogeneous and heterogeneous reactions in flow of nanofluids over a nonlinear stretching surface with variable surface thickness, J. Mol. Liq. 221 (2016) 1121–1127.

[21] B.R. Sharma, H. Konwar, MHD flow, heat and mass transfer due to axially moving cylinder in the]presence of thermal diffusion, radiation and chemical reaction in binary fluid mixture, Int. J. Comput. Appl. 110 (2015) 52–59.

[22] A.J. Chamkha, Heat and mass transfer from MHD flow over a moving permeable cylinder with heat generation or absorption and chemical reaction, Commun. Numer. Anal. 2011 (2011) 1–20.

[23] M. Mkhatshwa, S.S. Motsa, P. Sibanda, Overlapping multi-domain spectral method for conjugate problems of conduction and MHD free convection flow of nanofluids over flat plates, Math. Comput. Appl. 24 (2019) 75.

[24] H.F. Oztop, E. Abu-Nada, Numerical study of natural convection in partially heated rectangular enclosures filled with nanofluids, Int. J. Heat Fluid Flow 29 (2008) 1326–1336.

[25] T. Hayat, A. Kiran, M. Imtiaz, A. Alsaedi, Hydromagnetic mixed convection flow of copper and silver water nanofluids due to a curved stretching sheet, Results Phys 6 (2016) 904–910.

[26] L.N. Trefethen, Spectral Methods in MATLAB, vol. 10, SIAM, 2000.

[27] R.E. Bellman, R.E. Kalaba, Quasilinearization and Nonlinear Boundary Value Problems, American Elseiver, New York, 1965.

[28] T.S. Chen, A. Mucoglu, Buoyancy effects on forced convection along a vertical cylinder, ASME J. Heat Transf. 97 (1975) 198–203.

[29] C.L. Chang, Buoyancy and wall conduction effects on forced convection of micropolar fluid flow along a vertical slender hollow circular cylinder, Int. J. Heat Mass Tran. 49 (2006) 4932–4942.

Chapter 6

Overlapping multi-domain spectral method for MHD mixed convection slip flow over an exponentially decreasing mainstream with non-uniform heat source/sink and convective boundary conditions

The work presented in this chapter is an extension of the work in previous chapters and considers an exponentially decreasing free stream velocity, suction/blowing, velocity slip and convective boundary conditions. These pose additional challenges in terms of the complexities of the flow equations. This chapter gives an application of the overlapping multi-domain spectral quasilinearisation method to the MHD mixed convection flow with viscous dissipation, a chemical reaction and a non-uniform heat source/sink. To check that the iterative scheme converges and is accurate, we have analyzed the convergence and residual error results. The fluid properties, skin friction, heat and mass transfer coefficients are given for numerous values of the fluid parameters.

Overlapping multi-domain spectral method for MHD mixed convection slip flow over an exponentially decreasing mainstream with non-uniform heat source/sink and convective boundary conditions

Musawenkhosi P. Mkhatshwa*

School of Mathematics, Statistics & Computer Science University of Kwazulu Natal, Private Bag X01, Scottsville, 3209, Pietermarittzburg, South Africa
*patsonmkhatshwa@gmail.com**

Sandile S. Motsa

Department of Mathematics, University of Eswatini, Eswatini
School of Mathematics, Statistics & Computer Science University of Kwazulu Natal, Private Bag X01, Scottsville, 3209, Pietermarittzburg, South Africa
sandilemotsa@gmail.com

Precious Sibanda

School of Mathematics, Statistics & Computer Science University of Kwazulu Natal, Private Bag X01, Scottsville, 3209, Pietermarittzburg, South Africa
sibandap@ukzn.ac.za

Overlapping multi-domain bivariate spectral quasilinearisation method is applied on magnetohydrodynamic mixed convection slip flow over an exponentially decreasing mainstream with convective boundary conditions and non-uniform heat source/sink effects. The method is employed in solving the transformed flow equations. The convergence properties and accuracy of the method are determined. The method gives highly accurate results after few iterations and using few grid points in each space subinterval and the entire interval. The use of minimal numbers of grid points at each subinterval minimizes the effects of round-off errors that can lead to instabilities. The accuracy increases as the number of overlapping subintervals increases. The accuracy improvement is achieved through making the coefficient matrices less dense. The effects of controlling parameters on the flow fields and physical quantities of interest are studied. Results show that increasing Biot number and non-uniform heat source/sink enhances the flow fields while reducing skin friction and heat transfer rate. The fluid properties improve with injection whereas the flow characteristics augment with suction. The considered exponentially decreasing external flows have particular applications in diverging channel flows. The current study has practical significance in various boundary layer problems such as in controlling and delaying boundary layer separation on control surfaces and in

*patsonmkhatshwa@gmail.com

2   *M. P. Mkhatshwa, S. S. Motsa & P. Sibanda*

suppressing recirculating bubbles.

Keywords: Overlapping multi-domain bivariate spectral quasilinearisation method; Non-uniform heat source/sink; Chemical reaction; Suction/blowing; Slip and convective boundary conditions.

1. Introduction

The combined heat and mass transfer in between flows over exponentially stretching surface has a lot of practical implications in science and engineering. Most often, the end product depend on the heat transfer coefficient at the stretching continuous surface along with exponential differences of the stretching velocity. According to Merkin *et al.* [2017], annealing and thinning of copper wires can exhibit such characteristics and that becomes a possible application of exponentially stretching surface. In such cases, the simultaneous heating and cooling, and the kinematics of the stretching surface can influence the quality of the final product. Curle [1981] considered the steady two-dimensional laminar boundary layer flow with the external flow velocity $u_e = u_0(1 - \varepsilon e^{\xi})$, where u_0 is constant, ε is a decelerating parameter and ξ is the stream-wise coordinate. The smaller values of ε and ξ cause weaker effects of εe^{ξ} and consequently, u_e is approximated as a constant. However, higher values of ξ enhance the influence of εe^{ξ}. As the stream-wise coordinate ξ approaches to $log(\varepsilon^{-1})$, the external flow velocity u_e suddenly decreases exponentially and causes boundary layer separation. This imply that smaller values of u_e establish the adverse pressure gradient. Extensive studies have been carried out on the characteristics of boundary layer separation and control of flow separation. This is due to its various applications in polymer fibre coating, coating of wires and film cooling as mentioned by Patil *et al.* [2017a]. According to Mukhopadhyay and Layek [2008], the occurrence of separation can enhance the pressure drag during the exponentially stretching phenomenon and that may affect the fluid flow. Hence, to overcome the boundary layer separation in the study of mixed convection over an exponentially stretching surface, one may require various techniques.

In the present work, magnetohydrodynamics(MHD), suction/injection and non-uniform heat source/sink are considered as controlling tools to study the separation of the boundary layer over an exponentially decreasing flow velocity. Mukhopadhyay [2013a] reported that applications of MHD flow involve metallurgical processes, nuclear industry, military submarines, geophysics, astrophysics, drug delivery, power generator design and petroleum industries. Since MHD can delay the boundary layer separation, it is used in various engineering and industrial applications as a controlling factor. The technique of suction/blowing is one of the powerful tools in controlling the boundary layer separation. Suction/blowing can be found in applications such as enhancing the inner portion of the boundary in adverse pressure gradient (see Roy and Saikrishman [2004]), thermal protection (see Datta *et al.* [2006]), and skin-friction over control surfaces (see Roy *et al.* [2009]). The process of suction/blowing manages the boundary layer growth and in turn helps in delay-

ing the boundary layer separation. The heat source/sink is another technique that can help accomplish the process of controlling the boundary layer separation.

Several studies have been carried out on the influence of MHD, suction/blowing and heat source/sink on steady mixed convection flow over an exponentially stretching surface. Patil *et al.* [2017b] studied the steady mixed convection flow over an exponentially decreasing free stream velocity with suction/injection and heat source/sink. Patil *et al.* [2018a] investigated the influence of chemically reactive species and a volumetric heat source/sink on steady mixed convection over an exponentially decreasing mainstream with suction/blowing. The present work attempt to study the combined effects of suction/blowing and non-uniform heat source/sink on steady mixed convection over an exponentially decreasing velocity. Little work has been reported on the effect of non-uniform heat source/sink on mixed convection along exponentially stretching surface. Patil and Kumbarwadi [2017], and Patil *et al.* [2018b] studied MHD mixed convection flow over an exponentially stretching vertical sheet with non-uniform heat source/sink. Both studies have ignored the effect of suction/injection in controlling the boundary layer separation.

Most studies found in the literature on steady mixed convection flow over an exponentially stretching surface have been carried out with no-slip boundary conditions. For a viscous fluid, when the wall is impermeable, the overall boundary condition at a wall is such that there will be no relative motion between the wall, and the fluid immediately become in contact with the wall. According to Day [2004], when such motion is perpendicular, then the condition will be impermeable, and if it is a tangential motion, then the condition will be called no-slip condition. The presence of permeable wall causes various regimes in some extents. Bhattacharyya *et al.* [2011] concluded that the no-slip condition becomes inconsistent for all physical situations. That means, in fluid flows, the no-slip condition should be replaced with velocity slip or partial slip boundary conditions. Velocity slip is the non-adherence of the fluid to a solid boundary. In the present paper, the permeability condition is included at the boundary constraints to assist the investigation of partial slip flow. When the fluid is particulate such as polymer solutions, blood, emulsions, foams and suspensions, the partial slip at the exponential stretching surface can be expected. The fluid slip flow has industrial and technological applications such as in the polishing of artificial heart valves and internal cavities. Mukhopadhyay [2013b] replaced no-slip conditions with velocity slip at the boundary when studying MHD boundary layer flow over an exponentially stretching sheet with suction/blowing and thermal radiation. Patil and Shashikant [2018] considered the influence of slip flow and thermal jump on mixed convection over an exponentially stretching surface with suction/injection and volumetric heat source/sink. Another mechanism in the study of viscous fluids is the thermal convective boundary condition at the boundary wall. A lot of literature is devoted to constant wall temperature and constant heat flux at the wall. However, consideration of convective heat transfer at the temperature wall is more practical. The convective heat transfer involves

4   *M. P. Mkhatshwa, S. S. Motsa & P. Sibanda*

engineering procedures, gas turbines, nuclear plants, storage of thermal energy to name a few. These processes obtain high temperature when the flow is subject to the convective boundary condition. Isa *et al.* [2017] studied the effect of convective boundary condition on MHD mixed convection flow over an exponentially stretching vertical sheet. Srinivasacharya and Jagadeeshwar [2017] analyzed the effects of velocity slip on boundary layer flow on an exponentially stretching sheet with suction/injection and convective heat boundary conditions. Hayat *et al.* [2014] investigated MHD three-dimensional flow by an exponentially stretching surface with convective boundary conditions.

The purpose of this study is to analyze partial slip flow, thermal convective boundary conditions and non-uniform heat source/sink effects on steady MHD mixed convection over an exponentially decreasing mainstream with viscous dissipation, suction/injection and chemical reaction. According to the author's best knowledge, this work has not been reported so far in the literature. An effective and powerful overlapping multi-domain bivariate spectral quasilinearisation method (OMD-BSQLM) recently developed by Mkhatshwa *et al.* [2019] is used to obtain numerical solutions of the problem. The need to develop numerical methods that are computationally fast, converge quickly and uses fewer grid points to give accurate solutions for nonlinear partial differential equations (PDEs) cannot be overstated. Spectral methods have been found to have such qualities since they require minimal computational time and uses few grid points to achieve a high degree of numerical accuracy. Motsa *et al.* [2014a] introduced spectral quasilinearisation method (SQLM) for solving nonlinear PDEs describing unsteady boundary layer flow. The SQLM uses the quaslinearisation method (QLM) developed by Bellman and Kalaba [1965] to simplify the nonlinear problems into linear equations. The spectral collocation method is used to descretize in space and the implicit finite difference method is implemented in time. From the literature, it has been noted that the implicit finite difference method in combination with the QLM are the commonly used numerical methods in the analysis of mixed convection flow over an exponentially stretched surface. However, finite differences generally require more computational time and use many grid points for accurate solutions. This implies that applying spectral method in space and finite difference in time leads to slower and less accurate solution. Motsa *et al.* [2014b] introduced the bivariate spectral quasilinearisation method (BSQLM) which uses the spectral collocation method independently in both space and time to improve the accuracy and computational speed. It was found that the BSQLM gives accurate results for smaller time domains and the level of accuracy deteriorates with an increase in the time domain. To overcome this limitation, Magagula *et al.* [2017] extended the work of Motsa *et al.* [2014b] by using the multidomain technique only in the time domain. The resulting method was termed multidomain bivariate spectral quasilinearisation method (MD-BSQLM) and it was found to improve the accuracy of the method for large time domain. In the MD-BSQLM, the time domain is divided into small non-overlapping subintervals. The

continuity condition is used to advance the solution across the subintervals. Recently, Mkhatshwa *et al.* [2019] and Mkhatshwa *et al.* [2020] extended the work of Motsa *et al.* [2014b] by applying the multi-domain technique in both space and time to improve accuracy. In addition to that, they introduced the overlapping grid strategy in the spatial domain. The method was abbreviated using OMD-BSQLM and it was found to use few grid points to achieve highly accurate results. It is known that the accuracy of spectral methods increases with an increase in grid points but beyond a certain number of grid points, the accuracy rapidly deteriorates. However, the findings by Mkhatshwa *et al.* [2019] can help to overcome this limitation. It is worth noting that convergence and residual error analysis of the OMD-BSQLM were not performed in the previous studies. In the present work, applicability, accuracy and reliability of the method are confirmed using convergence and residual error analysis. The use of OMD-BSQLM in the current work is motivated by the benefits of the spectral method, multi-domain technique, overlapping grid and QLM which is known to have a quadratic rate of convergence.

2. Mathematical analysis

We consider the steady mixed convection flow of electrically conducting and chemically reacting incompressible viscous fluid over an exponentially decreasing mainstream when the surface mass transfer $v_w(x)$ occurs along the vertical surface. The influence of suction/injection, velocity slip and convective conditions are explored by considering the respective terms in the boundary conditions. The magnetic field, non-uniform heat source/sink and viscous dissipation effects are introduced in the energy equation to control the system. The surface moves with velocity $u_w(x)$ in an exponentially free stream velocity u_e along the positive $x-$direction. The blowing rate of the fluid is assumed to be small and it does not affect the inviscid flow at the edge of the boundary layer. It is also assumed that the injected fluid preserves the same physical properties as the boundary layer fluid. Figure 1 shows the flow model and coordinate system, where the normal coordinate y is measured from the vertical surface and the coordinate x is measured vertically upwards so that $x = 0$ corresponds to the leading edge. The temperature and concentration far away from the surface are denoted as T_∞ and C_∞, respectively. The surface temperature is maintained by convective heat transfer at a certain value T_w. The differences in the density of the fluid flow results in a body force term in momentum equation and other all thermo-physical properties are assumed to be the constants. To conjoin the temperature field $[g\beta_t(T - T_\infty)]$ and concentration field $[g\beta_c(C - C_\infty)]$ to the flow model, the changes in the density are related by employing the Boussinesq approximation for the energy and species concentration (see Schlichting and Gersten [2000]). A uniform magnetic field B_0 is applied normal to the surface. There is no applied power and this imply that the electrical field is absent. The magnetic Reynolds number of the flow is assumed to be small enough so that the induced magnetic field is negligible. With the above assumptions, the governing equations

6 *M. P. Mkhatshwa, S. S. Motsa & P. Sibanda*

for conservation of mass, momentum, energy and species concentration are given as
(Patil *et al.* [2017b] Patil *et al.* [2018a] Patil *et al.* [2017c])

$$\frac{\partial u}{\partial x} + \frac{\partial v}{\partial y} = 0, \tag{1}$$

$$u\frac{\partial u}{\partial x} + v\frac{\partial u}{\partial y} = u_e\frac{du_e}{dx} + \nu\frac{\partial^2 u}{\partial y^2} + g\beta_t\left(T - T_\infty\right) + g\beta_c\left(C - C_\infty\right), \tag{2}$$

$$u\frac{\partial T}{\partial x} + v\frac{\partial T}{\partial y} = \alpha_m\frac{\partial^2 T}{\partial y^2} + \frac{1}{\rho C_p}q''' + \frac{\mu}{\rho C_p}\left(\frac{\partial u}{\partial y}\right)^2 + \frac{\sigma B_0^2}{\rho C_p}(u_e - u)^2 \tag{3}$$

$$u\frac{\partial C}{\partial x} + v\frac{\partial C}{\partial y} = D_B\frac{\partial^2 C}{\partial y^2} - R(C - C_\infty), \tag{4}$$

where u and v are the velocity components in the x and y directions, T is the fluid temperature, C is the concentration, g is the acceleration due to gravity, ρ is the fluid density, β_t is the coefficient of thermal expansion, β_c is the coefficient of concentration expansion, D_B is the Brownian diffusion coefficient, C_p is the specific heat capacity, α_m is the thermal diffusivity, ν is the kinematic viscosity, μ is the dynamic viscosity, R is the variable chemical reaction rate, q''' is the non-uniform heat source/sink defined as

$$q''' = \frac{ku_w}{x\nu}\left[A^*(T_w - T_\infty)f'(\xi,\eta) + (T - T_\infty)B^*\right], \tag{5}$$

where A^* and B^* are the coefficients of space and temperature dependent heat source/sink, respectively. The case $A^* > 0, B^* > 0$ represents heat source or heat generation and $A^* < 0, B^* < 0$ corresponds to heat sink or heat absorption.

The physical boundary conditions are given by

$$u(x,0) = u_e + k_1\nu\frac{\partial u}{\partial y}, \ v(x,0) = v_w(x), \ -k_w\frac{\partial T}{\partial y} = h_w(T_w - T), \ C = C_w, \ \text{at y} = 0,$$

$$u(x,\infty) = u_e(x), \quad T(x,\infty) \to T_\infty, \quad C(x,\infty) \to C_\infty \quad \text{at} \quad y = \infty, \tag{6}$$

where $v_w(x) > 0$ is the velocity of suction and $v_w(x) < 0$ is the velocity of blowing, k_1 is the velocity slip factor, k_w is the thermal conductivity of the fluid and h_w is the convective heat transfer coefficient. We introduce the following non-similar transformations:

$$u_e(x) = u_\infty(1 - \varepsilon e^\xi), \quad \xi = \frac{x}{L}, \quad \eta = \left(\frac{u_e}{\nu x}\right)^{0.5}y, \ \psi(x,y) = (\nu u_e x)^{0.5}f(\xi,\eta),$$

$$u = u_e f'(\xi,\eta), \ G(\xi,\eta) = \frac{T - T_\infty}{T_w - T_\infty}, \ H(\xi,\eta) = \frac{C - C_\infty}{C_w - C_\infty}, \ f'(\xi,\eta) = F(\xi,\eta),$$

$$v = -\frac{1}{2}\left(\frac{\nu u_e}{x}\right)^{0.5}\left\{2\xi\frac{\partial f}{\partial\xi} + \eta\left(\frac{x}{u_e}\frac{du_e}{dx} - 1\right)f' + \left(\frac{x}{u_e}\frac{du_e}{dx} + 1\right)f\right\}, \tag{7}$$

where u_e is the external flow velocity at the edge of the boundary layer defined by Curle [1981], ξ is a scaled stream-wise coordinate, u_∞ is a constant, L is the characteristic length, ε denotes the decelerating small parameter such that $0 < \varepsilon < 1$, ψ is the physical stream function defined by $u = \frac{\partial\psi}{\partial y}$ and $v = -\frac{\partial\psi}{\partial x}$.

Overlapping multi-domain spectral method for MHD mixed convection slip flow   7

Fig. 1. Schematic diagram and coordinate system

The continuity Eq. (1) satisfies identically and introducing similarity variables (7) into Eqs. (2)-(4), we obtain the following dimensionless system of PDEs:

$$F'' + \frac{1}{2}(m+1)fF' + m(1-F^2) + \frac{\xi Re}{(1-\varepsilon e^\xi)}(1-F) + \frac{\xi Ri}{(1-\varepsilon e^\xi)^2}[G + NH]$$
$$= \xi\left(F\frac{\partial F}{\partial \xi} - F'\frac{\partial f}{\partial \xi}\right), \qquad (8)$$

$$G'' + \frac{Pr}{2}(m+1)fG' + PrEc(1-\varepsilon e^\xi)^2 F'^2 + M^2 EcPrRe\xi(1-\varepsilon e^\xi)(1-F)^2$$
$$+ A^*F + B^*G = Pr\xi\left(F\frac{\partial G}{\partial \xi} - G'\frac{\partial f}{\partial \xi}\right), \quad (9)$$

$$H'' + \frac{Sc}{2}(m+1)fH' - \frac{ScK\xi Re}{(1-\varepsilon e^\xi)}H = Sc\xi\left(F\frac{\partial H}{\partial \xi} - H'\frac{\partial f}{\partial \xi}\right), \qquad (10)$$

where $m = \frac{\xi}{u_e}\frac{du_e}{d\xi} = \frac{-\xi\varepsilon e^\xi}{1-\varepsilon e^\xi}$ is the dimensionless pressure gradient defined by Curle [1981] and Chiam [1998]). Here, $f(\xi,\eta) = \int_0^\eta Fd\eta + f_w$ and f_w can be obtained from the following equation

$$v = -\frac{\partial \psi}{\partial x} = -(\nu u_e x)^{1/2}\left\{\frac{\partial f}{\partial \xi}\frac{d\xi}{dx} + \frac{\partial f}{\partial \eta}\frac{\partial \eta}{\partial x} + \frac{1}{2u_e}\frac{du}{dx}f + \frac{1}{2x}f\right\}, \qquad (11)$$

where $\frac{d\xi}{dx} = \frac{\partial \xi}{\partial x} = \frac{1}{L}$ and $\frac{\partial \eta}{\partial x} = -\frac{\eta}{2x}\left[\frac{1+\varepsilon(\xi-1)e^\xi}{1-\varepsilon e^\xi}\right]$. Thus, at the surface $y = 0$ i.e at

8   *M. P. Mkhatshwa, S. S. Motsa & P. Sibanda*

$\eta = 0, v$ can be expressed as

$$v_w(\xi) = -\left(\frac{u_\infty \nu}{L}\right)^{1/2}\left[\frac{d}{d\xi}\left([\xi(1-\varepsilon e^\xi)]^{1/2}\right)f(\xi,0) + [\xi(1-\varepsilon e^\xi)]^{1/2}\frac{\partial f}{\partial \xi}(\xi,0)\right]\ (12)$$

i.e $v_w(\xi) = -\left(\frac{u_\infty \nu}{L}\right)^{1/2}\frac{d}{d\xi}\left([\xi(1-\varepsilon e^\xi)]^{1/2}f(\xi,0)\right).$ Integrating from 0 to ξ with respect to ξ, we get

$$f(\xi,0) = f_w(\xi) = -\left(\frac{u_\infty \nu}{L}\right)^{-1/2}[\xi(1-\varepsilon e^\xi)]^{-1/2}\int_0^\xi v_w(\xi)d\xi,\qquad (13)$$

i.e $f_w(\xi,0) = A(1-\varepsilon e^\xi)^{-1/2}$, where $v_w(\xi) = v_0\xi^{-1/2}$ and $A = -2v_0\left(\frac{u_\infty \nu}{L}\right)^{-1/2} = $ constant is the wall suction/injection parameter so that $A < 0$ indicates injection (blowing), $A > 0$ represents suction and $A = 0$ implies an impermeable surface. The transformed boundary conditions are expressed as

$$F(\xi,0) = 1 + \delta\xi^{-1/2}(1-\varepsilon e^\xi)^{1/2}F'(\xi,0),\ f(\xi,0) = A\left(1-\varepsilon e^\xi\right)^{-1/2},$$
$$G'(\xi,0) = -B_i\xi^{1/2}(1-\varepsilon e^\xi)^{-1/2}(1-G(\xi,0)),\ H(\xi,0) = 1,\qquad (14)$$
$$F(\xi,\infty) = 1,\quad G(\xi,\infty) = 0,\ H(\xi,\infty) = 0,$$

The parameters are defined as

$$Gr = \frac{g\beta_t(T_w - T_\infty)L^3}{\nu^2},\ Gr^* = \frac{g\beta_c(C_w - C_\infty)L^3}{\nu^2},\ Re = \frac{u_\infty L}{\nu},$$
$$\delta = k_1\sqrt{\frac{\nu u_\infty}{L}},\ B_i = \frac{h_w}{k_w}\sqrt{\frac{\nu L}{u_\infty}},\ Ri = \frac{Gr}{Re^2},\ N = \frac{Gr^*}{Gr},\ Pr = \frac{\nu}{\alpha_m},$$
$$Ec = \frac{u_\infty^2}{C_p(T_w - T_\infty)},\ Sc = \frac{\nu}{D_B},\ K = \frac{R\nu}{u_\infty^2}, M = \frac{B_0}{u_\infty}\sqrt{\frac{\sigma\nu}{\rho}},$$

where Ri (Richardson number) is the dimensionless parameter that characterizes the mixed convection effects arising from the buoyancy force with $Ri > 0(T_w > T_\infty)$ corresponding to the heated source (assisting flow), $Ri < 0(T_w < T_\infty)$ indicating the cooled surface (opposing flow) and $Ri = 0(T_w = T_\infty)$ representing the forced convection flow, Re is the Reynolds number, Gr is the Grashof number indicating the exponentially stretching wall temperature, Gr^* is the solutal Grashof number indicating the exponentially stretching wall concentration, Pr is the Prandtl number, Ec is the Eckert number, Sc is the Schmidt number, K is the chemical reaction parameter with $K < 0$ representing generative reaction and $K > 0$ representing destructive reaction, N is the ratio between the thermal and the solutal buoyancy forces, δ is the velocity slip parameter, B_i is the Biot number and M is the magnetic field parameter.

The physical quantities of interest are the local skin friction C_f, Nusselt number Nu and Sherwood number Sh which are defined as

$$C_f = \mu\frac{2(\partial u/\partial y)_{y=0}}{\rho u_e^2}, Nu = -x\frac{(\partial T/\partial y)_{y=0}}{(T_w - T_\infty)},\ Sh = -x\frac{(\partial C/\partial y)_{y=0}}{(C_w - C_\infty)}.\quad (15)$$

Using the similarity variables (7), the skin friction coefficient, local Nusselt number and local Sherwood number become

$$Re^{1/2}C_f = 2\xi^{-1/2}(1-\varepsilon e^\xi)^{-1/2}F'(\xi,0),$$
$$Re^{-1/2}Nu = -\xi^{1/2}(1-\varepsilon e^\xi)^{1/2}G'(\xi,0),$$
$$Re^{-1/2}Sh = -\xi^{1/2}(1-\varepsilon e^\xi)^{1/2}H'(\xi,0), \tag{16}$$

3. Solution procedure

This section provides a description of the OMD-BSQLM and its application in solving the nonlinear PDEs (8)-(10). It is worth mentioning that the method applies the multi-domain approach in both space and time intervals. Moreover, the overlapping grid strategy is utilized in the spatial domain. To apply the OMD-BSQLM, we let $\xi \in J$, where the time interval $J = [0, \xi_p]$ is split into p equal non-overlapping subintervals (see Figure 2) defined as

$$J_v = (\xi_{v-1}, \xi_v), \ v = 1,2,3,...,p, \ 0 = \xi_0 < \xi_1 < \xi_2 < ... < \xi_{p-1} < \xi_p = 1, \tag{17}$$

where each subinterval is discretized into $N_\xi + 1$ collocation points (Chebyshev-Gauss-Lobatto points). For the semi-finite space domain $[0,\infty)$, a truncated grid $[0,\eta_\infty]$ is used. The truncated spatial domain $[0,\eta_\infty]$ is decomposed into s overlapping subintervals L_η, denoted by

$$I_\mu = [\eta_0^\mu, \eta_{N_\eta}^\mu], \quad \mu = 1,2,3,...,s, \tag{18}$$

where each subinterval I_μ is further discretized into $N_\eta + 1$ collocation points. The subintervals are decomposed by overlapping one grid point. It is worth noting that the first two grid points of the interval $I_{\mu+1}$ coincide with the last two grid points of the interval I_μ as seen in Figure 3. For the overlap to be possible, we consider that each subinterval has the same length given by

$$L_\eta = \frac{\eta_\infty}{s + \frac{1}{2}(1-s)(1-\cos\frac{\pi}{N_\eta})}, \tag{19}$$

and the same number of collocation points $(N_\eta + 1)$ are used in each sub-interval. To derive the formula for the length in Eq. (19), we remark that the total length of the space domain is

$$\eta_\infty = 2L_\eta - \sigma + (2L_\eta - 2\sigma)\left(\frac{s}{2} - 1\right) \tag{20}$$
$$= 2L_\eta - \sigma + (L_\eta - \sigma)(s-2) = \sigma(1-s) + sL_\eta, \tag{21}$$

where σ is the overlapping distance between two subintervals. Considering the first interval I_1 in which $\eta \in [0, \eta_{N_\eta}^1]$, we can define the length $L_\eta = \eta_{N_\eta}^1$. The linear transformation $\eta = \frac{L_\eta}{2}\hat\eta + \frac{\eta_{N_\eta}^1}{2}$ can be used to transform the interval $[0, \eta_{N_\eta}^1]$ to

10   *M. P. Mkhatshwa, S. S. Motsa & P. Sibanda*

$[-1, 1]$. Thus, using the Gauss-Lobatto collocation points $\hat{\eta}_i = \cos\left(\frac{\pi i}{N_\eta}\right)$, where $i = 0, 1, 2, 3, ..., N_\eta$, we obtain

$$\eta_0 - \eta_1 = \frac{L_\eta}{2}(\hat{\eta}_0 - \hat{\eta}_1) = \frac{L_\eta}{2}\left(1 - \cos\frac{\pi}{N_\eta}\right). \tag{22}$$

Therefore, equation (21) becomes

$$\eta_\infty = \frac{L_\eta}{2}\left(1 - \cos\frac{\pi}{N_\eta}\right)(1 - s) + sL_\eta, \tag{23}$$

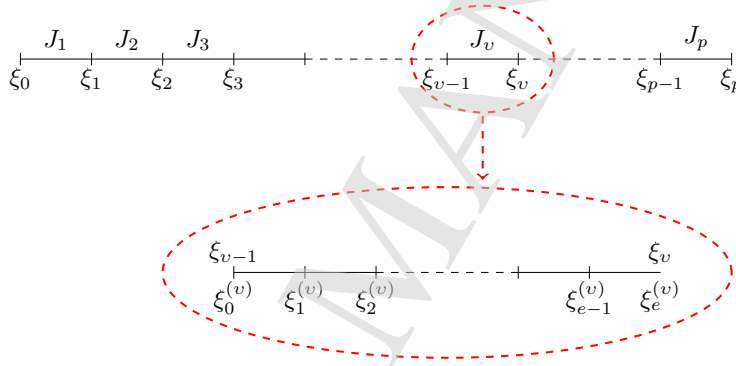and making L_η the subject of the formula in Eq. (23) gives equation (19).
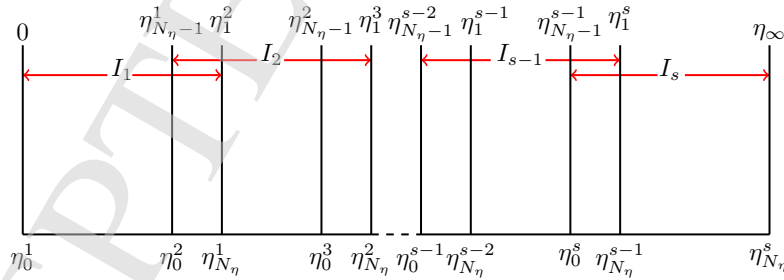

Fig. 2. Non-overlapping grid ($\xi-$ domain)

Fig. 3. Overlapping grid ($\eta-$ domain)

Applying the QLM at each subinterval I_μ, the nonlinear PDEs (8)-(10) are

Overlapping multi-domain spectral method for MHD mixed convection slip flow 11

replaced by the following set of linear PDEs:

$$
\frac{\partial^3 f_{r+1}^{(\mu,v)}}{\partial \eta^3} + \alpha_{1,2,r}^{(1,\mu,v)} \frac{\partial^2 f_{r+1}^{(\mu,v)}}{\partial \eta^2} + \alpha_{1,1,r}^{(1,\mu,v)} \frac{\partial f_{r+1}^{(\mu,v)}}{\partial \eta} + \alpha_{1,0,r}^{(1,\mu,v)} f_{r+1}^{(\mu,v)} + \alpha_{2,0,r}^{(1,\mu,v)} G_{r+1}^{(\mu,v)}
$$
$$
+ \alpha_{3,0,r}^{(1,\mu,v)} H_{r+1}^{(\mu,v)} + \gamma_{1,r}^{(1,\mu,v)} \frac{\partial}{\partial \eta}\left(\frac{\partial f_{r+1}^{(\mu,v)}}{\partial \xi} \right) + \beta_{1,r}^{(1,\mu,v)} \frac{\partial f_{r+1}^{(\mu,v)}}{\partial \xi} = R_{1,r}^{(\mu,v)}, \tag{24}
$$

$$
\frac{\partial^2 G_{r+1}^{(\mu,v)}}{\partial \eta^2} + \alpha_{2,1,r}^{(2,\mu,v)} \frac{\partial G_{r+1}^{(\mu,v)}}{\partial \eta} + \alpha_{2,0,r}^{(2,\mu,v)} G_{r+1}^{(\mu,v)} + \alpha_{1,2,r}^{(2,\mu,v)} \frac{\partial^2 f_{r+1}^{(\mu,v)}}{\partial \eta^2} + \alpha_{1,1,r}^{(2,\mu,v)} \frac{\partial f_{r+1}^{(\mu,v)}}{\partial \eta}
$$
$$
+ \alpha_{1,0,r}^{(2,\mu,v)} f_{r+1}^{(\mu,v)} + \beta_{2,r}^{(2,\mu,v)} \frac{\partial G_{r+1}^{(\mu,v)}}{\partial \xi} + \beta_{1,r}^{(2,\mu,v)} \frac{\partial f_{r+1}^{(\mu,v)}}{\partial \xi} = R_{2,r}^{(\mu,v)}, \tag{25}
$$

$$
\frac{\partial^2 H_{r+1}^{(\mu,v)}}{\partial \eta^2} + \alpha_{3,1,r}^{(3,\mu,v)} \frac{\partial H_{r+1}^{(\mu,v)}}{\partial \eta} + \alpha_{3,0,r}^{(3,\mu,v)} H_{r+1}^{(\mu,v)} + \alpha_{1,1,r}^{(3,\mu,v)} \frac{\partial f_{r+1}^{(\mu,v)}}{\partial \eta} + \alpha_{1,0,r}^{(3,\mu,v)} f_{r+1}^{(\mu,v)}
$$
$$
+ \beta_{3,r}^{(3,\mu,v)} \frac{\partial H_{r+1}^{(\mu,v)}}{\partial \xi} + \beta_{1,r}^{(3,\mu,v)} \frac{\partial f_{r+1}^{(\mu,v)}}{\partial \xi} = R_{3,r}^{(\mu,v)}, \tag{26}
$$

where the linearisation coefficients are given by

$$
\alpha_{1,2,r}^{(1,\mu,v)} = \frac{1}{2}\left(\frac{-\xi \varepsilon e^\xi}{1 - \varepsilon e^\xi} + 1 \right) f_r^{(\mu,v)} + \xi \frac{\partial f_r^{(\mu,v)}}{\partial \xi}, \ \alpha_{1,0,r}^{(1,\mu,v)} = \frac{1}{2}\left(\frac{-\xi \varepsilon e^\xi}{1 - \varepsilon e^\xi} + 1 \right) \frac{\partial^2 f_r^{(\mu,v)}}{\partial \eta^2},
$$

$$
\alpha_{1,1,r}^{(1,\mu,v)} = \frac{2\xi \varepsilon e^\xi}{1 - \varepsilon e^\xi} \frac{\partial f_r^{(\mu,v)}}{\partial \eta} - \frac{\xi Re}{(1 - \varepsilon e^\xi)} - \xi \frac{\partial}{\partial \eta}\left(\frac{\partial f_r^{(\mu,v)}}{\partial \xi} \right), \ \alpha_{2,0,r}^{(1,\mu,v)} = \frac{\xi Ri}{(1 - \varepsilon e^\xi)^2},
$$

$$
\alpha_{3,0,r}^{(1,\mu,v)} = \frac{\xi RiN}{(1 - \varepsilon e^\xi)^2}, \ \alpha_{2,1,r}^{(2,\mu,v)} = \frac{1}{2}Pr\left(\frac{-\xi \varepsilon e^\xi}{1 - \varepsilon e^\xi} + 1 \right) f_r^{(\mu,v)} + Pr\xi \frac{\partial f_r^{(\mu,v)}}{\partial \xi}, \ \alpha_{2,0,r}^{(2,\mu,v)} = B^*,
$$

$$
\alpha_{1,2,r}^{(2,\mu,v)} = 2PrEc(1 - \varepsilon e^\xi)^2 \frac{\partial^2 f_r^{(\mu,v)}}{\partial \eta^2}, \ \alpha_{1,1,r}^{(2,\mu,v)} = A^* - 2M^2 EcPrRe\xi(1 - \varepsilon e^\xi) \frac{\partial f_r^{(\mu,v)}}{\partial \eta}
$$

$$
-\xi Pr \frac{\partial G_r^{(\mu,v)}}{\partial \xi}, \ \alpha_{1,0,r}^{(2,\mu,v)} = \frac{1}{2}Pr\left(\frac{-\xi \varepsilon e^\xi}{1 - \varepsilon e^\xi} + 1 \right) \frac{\partial G_r^{(\mu,v)}}{\partial \eta}, \ \alpha_{3,1,r}^{(3,\mu,v)} = \xi Sc \frac{\partial f_r^{(\mu,v)}}{\partial \xi}
$$

$$
+\frac{1}{2}Sc\left(\frac{-\xi \varepsilon e^\xi}{1 - \varepsilon e^\xi} + 1 \right) f_r^{(\mu,v)}, \ \alpha_{3,0,r}^{(3,\mu,v)} = -\frac{ScK\xi Re}{(1 - \varepsilon e^\xi)}, \ \alpha_{1,1,r}^{(3,\mu,v)} = -\xi Sc \frac{\partial H_r^{(\mu,v)}}{\partial \xi},
$$

$$
\alpha_{1,0,r}^{(3,\mu,v)} = \frac{1}{2}Sc\left(\frac{-\xi \varepsilon e^\xi}{1 - \varepsilon e^\xi} + 1 \right) \frac{\partial H_r^{(\mu,v)}}{\partial \eta}, \ \gamma_{1,r}^{(1,\mu,v)} = -\xi \frac{\partial f_r^{(\mu,v)}}{\partial \eta}, \ \beta_{1,r}^{(1,\mu,v)} = \xi \frac{\partial^2 f_r^{(\mu,v)}}{\partial \eta^2},
$$

$$
\beta_{2,r}^{(2,\mu,v)} = -\xi Pr \frac{\partial f_r^{(\mu,v)}}{\partial \eta}, \ \beta_{1,r}^{(2,\mu,v)} = \xi Pr \frac{\partial G_r^{(\mu,v)}}{\partial \eta}, \ \beta_{3,r}^{(3,\mu,v)} = -\xi Sc \frac{\partial f_r^{(\mu,v)}}{\partial \eta},
$$

$$
\beta_{1,r}^{(3,\mu,v)} = \xi Sc \frac{\partial H_r^{(\mu,v)}}{\partial \eta}, \ R_{1,r}^{(\mu,v)} = \frac{1}{2}\left(\frac{-\xi \varepsilon e^\xi}{1 - \varepsilon e^\xi} + 1 \right) f_r^{(\mu,v)} \frac{\partial^2 f_r^{(\mu,v)}}{\partial \eta^2} - \frac{-\xi \varepsilon e^\xi}{1 - \varepsilon e^\xi}
$$

$$
\frac{\xi \varepsilon e^\xi}{1 - \varepsilon e^\xi}\left(\frac{\partial f_r^{(\mu,v)}}{\partial \eta} \right)^2 - \xi \frac{\partial F_r^{(\mu,v)}}{\partial \eta} \frac{\partial}{\partial \eta}\left(\frac{\partial f_r^{(\mu,v)}}{\partial \xi} \right) + \xi \frac{\partial^2 f_r^{(\mu,v)}}{\partial \eta^2} \frac{\partial f_r^{(\mu,v)}}{\partial \xi},
$$

$$
R_{2,r}^{(\mu,v)} = \frac{1}{2}Pr\left(\frac{-\xi \varepsilon e^\xi}{1 - \varepsilon e^\xi} + 1 \right) f_r^{(\mu,v)} \frac{\partial G_r^{(\mu,v)}}{\partial \eta} - M^2 EcPrRe\xi(1 - \varepsilon e^\xi)\left(\frac{\partial f_r^{(\mu,v)}}{\partial \eta} \right)^2
$$

12   *M. P. Mkhatshwa, S. S. Motsa & P. Sibanda*

$$-M^2 EcPrRe\xi(1-\varepsilon e^\xi) - \xi Pr\frac{\partial f_r^{(\mu,\upsilon)}}{\partial\eta}\frac{\partial G_r^{(\mu,\upsilon)}}{\partial\xi} + \xi Pr\frac{\partial G_r^{(\mu,\upsilon)}}{\partial\eta}\frac{\partial f_r^{(\mu,\upsilon)}}{\partial\xi}$$

$$+PrEc(1-\varepsilon e^\xi)^2\left(\frac{\partial^2 f_r^{(\mu,\upsilon)}}{\partial\eta^2}\right)^2, \ R_{3,r}^{(\mu,\upsilon)} = \frac{1}{2}Sc\left(\frac{-\xi\varepsilon e^\xi}{1-\varepsilon e^\xi}+1\right)f_r^{(\mu,\upsilon)}\frac{\partial H_r^{(\mu,\upsilon)}}{\partial\eta}$$

$$-\xi Sc\frac{\partial f_r^{(\mu,\upsilon)}}{\partial\eta}\frac{\partial H_r^{(\mu,\upsilon)}}{\partial\xi} + \xi Sc\frac{\partial H_r^{(\mu,\upsilon)}}{\partial\eta}\frac{\partial f_r^{(\mu,\upsilon)}}{\partial\xi}.$$

The constants r and $r+1$ denote previous and current iterations, respectively. The system of linear PDEs (24)-(26) is discretized using the spectral collocation method in both η and ξ directions. It is important to mention that the linearized PDEs are solved independently over each time subinterval, while the approximate solutions in space direction are obtained simultaneously across all subintervals. Generally, before the spectral collocation method is applied at each subinterval, the time interval J_υ and space interval I_μ are transformed into $\hat\xi \in [-1,1]$ and $\hat\eta \in [-1,1]$ using the linear transformations

$$\xi_j^\upsilon = \frac{1}{2}(\xi_\upsilon - \xi_{\upsilon-1})\hat\xi_j + \frac{1}{2}(\xi_\upsilon + \xi_{\upsilon-1}), \quad \left\{\hat\xi_j\right\}_{j=0}^{N_\xi} = \cos\left(\frac{\pi j}{N_\xi}\right), \tag{27}$$

$$\eta_i^\mu = \frac{L}{2}(\hat\eta_i + 1), \quad \{\hat\eta_i\}_{i=0}^{N_\eta} = \cos\left(\frac{\pi i}{N_\eta}\right). \tag{28}$$

We assume that at each subinterval, the required solution, say $f(\eta,\xi)$ can be approximated by a bivariate Lagrange interpolation polynomial of the form

$$f^{(\mu,\upsilon)}(\eta,\xi) \approx F^{(\mu,\upsilon)}(\eta,\xi) = \sum_{k=0}^{N_\eta}\sum_{\tau=0}^{N_\xi} F^{(\mu,\upsilon)}(\eta_k,\xi_\tau)\mathcal{L}_k(\eta)\mathcal{L}_\tau(\xi), \tag{29}$$

where the function $\mathcal{L}_k(\eta)$ and $\mathcal{L}_\tau(\xi)$ are the well known characteristic Lagrange cardinal polynomial based on the Chebyshev-Gauss-Lobatto points (see Trefethen [2000]). The required solution for $G(\eta,\xi)$ and $H(\eta,\xi)$ are approximated in a similar manner. The solution procedure requires that the derivatives of $\mathcal{L}_k(\eta)$ and $\mathcal{L}_\tau(\xi)$ with respect to η and ξ, respectively be evaluated at the Chebyshev-Gauss-Lobatto grid points. The derivatives of $f^{(\mu,\upsilon)}(\eta,\xi)$ with respect to η and ξ at the Chebyshev-Gauss-Lobatto points $(\hat\eta_i, \hat\xi_j)$, are computed as

$$\left.\frac{\partial F^{(\mu,\upsilon)}}{\partial\eta}\right|_{(\eta=\eta_i,\xi=\xi_j)} = \sum_{k=0}^{N_\eta}\sum_{\tau=0}^{N_\xi} F^{(\mu,\upsilon)}(\eta_k,\xi_\tau)\mathcal{L}_\tau(\xi_j)\left.\frac{d\mathcal{L}_k(\eta)}{d\eta}\right|_{\eta=\eta_i}$$

$$= \sum_{k=0}^{N_\eta}\hat{D}_{i,k}^{(\mu)}F^{(\mu,\upsilon)}(\eta_k,\xi_j) = \left[\mathbf{D}^{(\mu)}\right]\mathbf{F}_j^{(\mu,\upsilon)}, \quad i=0,1,2,...,M_\eta, \tag{30}$$

$$\left.\frac{\partial F^{(\mu,\upsilon)}}{\partial\xi}\right|_{(\eta=\eta_i,\xi=\xi_j)} = \sum_{k=0}^{N_\eta}\sum_{\tau=0}^{N_\xi} F^{(\mu,\upsilon)}(\eta_k,\xi_\tau)\mathcal{L}_k(\eta_i)\left.\frac{d\mathcal{L}_\tau(\xi)}{d\xi}\right|_{\xi=\xi_j}$$

$$= \sum_{\tau=0}^{N_\xi} d_{j,\tau}F^{(\mu,\upsilon)}(\eta_i,\xi_\tau) = \sum_{\tau=0}^{N_\xi} d_{j,\tau}\mathbf{F}_\tau^{(\mu,\upsilon)}, \quad j=0,1,2,...,N_\xi, \tag{31}$$

Overlapping multi-domain spectral method for MHD mixed convection slip flow 13

where

$$\hat{D}_{i,k}^{(\mu)} = \frac{2}{\eta_{N_\eta}^\mu - \eta_0^\mu} D_{i,k}, \tag{32}$$

and $D_{i,k}$ is the standard first order differential operator of size $(N_\eta+1) \times (N_\eta+1)$ in a single domain $[-1,1]$, $d_{j,\tau}$ is the standard first derivative Chebyshev differentiation matrices of size $(N_\xi+1) \times (N_\xi+1)$, $M_\eta = N_\eta + (N_\eta-1)(s-1)$ is the total number of collocation points in the whole domain, $\mathbf{F}_j^{(\mu,\upsilon)}$ is the vector defined as

$$\mathbf{F}_j^{(\mu,\upsilon)} = \left[f^{(\mu,\upsilon)}(\eta_0^{(\mu)}, \xi_j), f^{(\mu,\upsilon)}(\eta_1^{(\mu)}, \xi_j), \ldots, f^{(\mu,\upsilon)}(\eta_{N_\eta}^{(\mu)}, \xi_j) \right]^T, \tag{33}$$

where T denotes the matrix transpose, $\mathbf{D}^{(\mu)}$ is an $(M_\eta+1) \times (M_\eta+1)$ derivative operator with a global structure given by

$$\mathbf{D}^{(\mu)} = \begin{bmatrix}
\hat{D}_{0,0}^{(s)} & \hat{D}_{0,1}^{(s)} & \cdots & \hat{D}_{0,N_\eta-1}^{(s)} & \hat{D}_{0,N_\eta}^{(s)} \\
\hat{D}_{1,0}^{(s)} & \hat{D}_{1,1}^{(s)} & \cdots & \hat{D}_{1,N_\eta-1}^{(s)} & \hat{D}_{1,N_\eta}^{(s)} \\
\ddots & \ddots & \ddots & \ddots & \ddots \\
\hat{D}_{N_\eta-1,0}^{(s)} & \hat{D}_{N_\eta-1,1}^{(s)} & \cdots & \hat{D}_{N_\eta-1,N_\eta-1}^{(s)} & \hat{D}_{N_\eta-1,N_\eta}^{(s)} \\
& & \hat{D}_{1,0}^{(s-1)} & \hat{D}_{1,1}^{(s-1)} & \cdots & \hat{D}_{1,N_\eta-1}^{(s-12)} & \hat{D}_{1,N_\eta}^{(s-1)} \\
& & \hat{D}_{2,0}^{(s-1)} & \hat{D}_{2,1}^{(s-1)} & \cdots & \hat{D}_{2,N_\eta-1}^{(s-1)} & \hat{D}_{2,N_\eta}^{(s-1)} \\
& & \ddots & \ddots & \ddots & \ddots & \ddots \\
& & \hat{D}_{N_\eta-1,0}^{(s-1)} & \hat{D}_{N_\eta-1,1}^{(s-1)} & \cdots & \hat{D}_{N_\eta-1,N_\eta-1}^{(s-1)} & \hat{D}_{N_\eta-1,N_\eta}^{(s-1)} \\
& & & & \ddots & \ddots \\
& & & & \hat{D}_{1,0}^{(1)} & \hat{D}_{1,1}^{(1)} & \cdots & \hat{D}_{1,N_\eta-1}^{(1)} & \hat{D}_{1,N_\eta}^{(1)} \\
& & & & \hat{D}_{2,0}^{(1)} & \hat{D}_{2,1}^{(1)} & \cdots & \hat{D}_{2,N_\eta-1}^{(1)} & \hat{D}_{2,N_\eta}^{(1)} \\
& & & & \ddots & \ddots & \ddots & \ddots & \ddots \\
& & & & \hat{D}_{N_\eta,0}^{(1)} & \hat{D}_{N_\eta,1}^{(1)} & \cdots & \hat{D}_{N_\eta,N_\eta-1}^{(1)} & \hat{D}_{N_\eta,N_\eta}^{(1)}
\end{bmatrix} \tag{34}$$

and the entries of $\hat{D}_{i,k}^{(\mu)}$ are obtained from equation (10). It is worth noting that the derivative operator becomes a full matrix if only a single domain is used in the computation. Since the last two points in the μth subinterval and the first two points in the $(\mu+1)^{\text{th}}$ subinterval overlap and remains common, the differentiation matrix $\mathbf{D}^{(\mu)}$ for overlapping grid is assembled by carefully discarding the rows corresponding to the recurrent points as shown in equation (34). The empty entries of the coefficient matrix are zeros, which makes the matrix to be less dense or sparse. The nth order derivative with respect to η is obtained as

$$\left. \frac{\partial^n F^{(\mu,\upsilon)}}{\partial \eta^n} \right|_{(\eta=\eta_i, \xi=\xi_j)} = \sum_{k=0}^{N_\eta} \left[\hat{D}_{i,k}^{(\mu)} \right]^n F^{(\mu,\upsilon)}(\eta_k, \xi_j) = \left[\mathbf{D}^{(\mu)} \right]^n \mathbf{F}_j^{(\mu,\upsilon)}, \tag{35}$$

The derivatives $d_{j,\tau}$ and $\left[\mathbf{D}^{(\mu)} \right]^n$ are scaled by multiplying by the factors $\Lambda = \frac{2}{\xi_\upsilon - \xi_{\upsilon-1}}$ and $\Omega^n = \left(\frac{2}{\eta_{N_\eta}^\mu - \eta_0^\mu} \right)^n$, respectively. These factors result from applying the chain rule of differentiation due to the transformation used in equation (27)-(28) to map the computational domains to $[-1,1]$. The space and time derivatives of G and H at each subinterval can be transformed to discrete matrix form in a similar manner. Applying the spectral collocation method by evaluating Eqs. (24)-(26) at

14   *M. P. Mkhatshwa, S. S. Motsa & P. Sibanda*

the collocation points and using the derivative matrices as well as incorporating the initial conditions which correspond to $\xi_{N_\xi} = -1$ gives

$$\left[\left[\mathbf{D}^{(\mu)}\right]^3 + \boldsymbol{\alpha}_{1,2,r}^{(1,\mu,v)}\left[\mathbf{D}^{(\mu)}\right]^2 + \boldsymbol{\alpha}_{1,1,r}^{(1,\mu,v)}\mathbf{D}^{(\mu)} + \boldsymbol{\alpha}_{1,0,r}^{(1,\mu,v)}\right]\mathbf{F}_{j,r+1}^{(\mu,v)} + \left[\boldsymbol{\alpha}_{2,0,r}^{(1,\mu,v)}\right]\mathbf{G}_{j,r+1}^{(\mu,v)}$$

$$+ \left[\boldsymbol{\alpha}_{3,0,r}^{(1,\mu,v)}\right]\mathbf{H}_{j,r+1}^{(\mu,v)} + \boldsymbol{\gamma}_{1,r}^{(1,\mu,v)}\sum_{\tau=0}^{N_\xi-1}d_{j,\tau}\mathbf{D}^{(\mu)}\mathbf{F}_\tau^{(\mu,v)} + \boldsymbol{\beta}_{1,r}^{(1,\mu,v)}\sum_{\tau=0}^{N_\xi-1}d_{j,\tau}\mathbf{F}_\tau^{(\mu,v)} = \mathbf{K}_{1,j}^{(\mu,v)} \quad (36)$$

$$\left[\boldsymbol{\alpha}_{1,2,r}^{(2,\mu,v)}\left[\mathbf{D}^{(\mu)}\right]^2 + \boldsymbol{\alpha}_{1,1,r}^{(2,\mu,v)}\mathbf{D}^{(\mu)} + \boldsymbol{\alpha}_{1,0,r}^{(2,\mu,v)}\right]\mathbf{F}_{j,r+1}^{(\mu,v)} + \boldsymbol{\beta}_{1,r}^{(2,\mu,v)}\sum_{\tau=0}^{N_\xi-1}d_{j,\tau}\mathbf{F}_\tau^{(\mu,v)}$$

$$+ \left[\left[\mathbf{D}^{(\mu)}\right]^2 + \boldsymbol{\alpha}_{2,1,r}^{(2,\mu,v)}\mathbf{D}^{(\mu)} + \boldsymbol{\alpha}_{2,0,r}^{(2,\mu,v)}\right]\mathbf{G}_{j,r+1}^{(\mu,v)} + \boldsymbol{\beta}_{2,r}^{(2,\mu,v)}\sum_{\tau=0}^{N_\xi-1}d_{j,\tau}\mathbf{G}_\tau^{(\mu,v)} = \mathbf{K}_{2,l}^{(\mu,v)} \quad (37)$$

$$\left[\boldsymbol{\alpha}_{1,1,r}^{(3,\mu,v)}\mathbf{D}^{(\mu)} + \boldsymbol{\alpha}_{1,0,r}^{(3,\mu,v)}\right]\mathbf{F}_{j,r+1}^{(\mu,v)} + \left[\left[\mathbf{D}^{(\mu)}\right]^2\boldsymbol{\alpha}_{3,1,r}^{(3,\mu,v)}\mathbf{D}^{(\mu)} + \boldsymbol{\alpha}_{3,0,r}^{(3,\mu,v)}\right]\mathbf{H}_{j,r+1}^{(\mu,v)}$$

$$+ \boldsymbol{\beta}_{1,r}^{(3,\mu,v)}\sum_{\tau=0}^{N_\xi-1}d_{j,\tau}\mathbf{F}_\tau^{(\mu,v,)} + \boldsymbol{\beta}_{3,r}^{(3,\mu,v)}\sum_{\tau=0}^{N_\xi-1}d_{j,\tau}\mathbf{H}_\tau^{(\mu,v)} = \mathbf{K}_{3,j}^{(\mu,v)}, \quad (38)$$

where

$$\mathbf{K}_{1,j}^{(\mu,v)} = \mathbf{R}_{1,j}^{(\mu,v)} - \boldsymbol{\gamma}_{1,r}^{(1,\mu,v)}d_{j,N_\xi}\mathbf{D}^{(\mu)}\mathbf{F}_{N_\xi}^{(\mu,v)} - \boldsymbol{\beta}_{1,r}^{(1,\mu,v)}d_{j,N_\xi}\mathbf{F}_{N_\xi}^{(\mu,v)},$$

$$\mathbf{K}_{2,j}^{(\mu,v)} = \mathbf{R}_{2,j}^{(\mu,v)} - \boldsymbol{\beta}_{1,r}^{(2,\mu,v)}d_{j,N_\xi}\mathbf{F}_{N_\xi}^{(\mu,v)} - \boldsymbol{\beta}_{2,r}^{(2,\mu,v)}d_{j,N_\xi}\mathbf{G}_{N_\xi}^{(\mu,v)},$$

$$\mathbf{K}_{3,j}^{(\mu,v)} = \mathbf{R}_{3,j}^{(\mu,v)} - \boldsymbol{\beta}_{1,r}^{(3,\mu,v)}d_{j,N_\xi}\mathbf{F}_{N_\xi}^{(\mu,v)} - \boldsymbol{\beta}_{3,r}^{(3,\mu,v)}d_{j,N_\xi}\mathbf{H}_{N_\xi}^{(\mu,v)},$$

Equations (36)-(38) can be expressed as a matrix system of size $N_\xi(M_\eta + 1) \times N_\xi(M_\eta + 1)$

$$\begin{bmatrix}\mathbf{A}_{11} & \mathbf{A}_{12} & \mathbf{A}_{13} \\ \mathbf{A}_{21} & \mathbf{A}_{22} & \mathbf{A}_{23} \\ \mathbf{A}_{31} & \mathbf{A}_{32} & \mathbf{A}_{33}\end{bmatrix}\begin{bmatrix}\mathbf{F}_{j,r+1}^{(\mu,v)} \\ \mathbf{G}_{j,r+1}^{(\mu,v)} \\ \mathbf{H}_{j,r+1}^{(\mu,v)}\end{bmatrix} = \begin{bmatrix}\mathbf{K}_{1,j}^{(\mu,v)} \\ \mathbf{K}_{2,j}^{(\mu,v)} \\ \mathbf{K}_{3,j}^{(\mu,v)}\end{bmatrix}, \quad (39)$$

Starting from suitable initial approximations, which are chosen to satisfy the boundary conditions, the approximate solutions are obtained by iteratively solving the matrix system. The initial guesses are given as

$$f_0(\eta) = \eta - \frac{1}{4}A(1-\varepsilon)^{-1/2}e^{-2\eta} + A(1-\varepsilon)^{-1/2}e^{-\eta} + \frac{1}{4}A(1-\varepsilon)^{-1/2},$$

$$G_0(\eta) = \frac{1}{2}e^{-2\eta} - e^{-\eta}, \quad H_0(\eta) = e^{-\eta}. \quad (40)$$

The OMD-BSQLM can be summarised in five main steps:

- *Domain decomposition and descretization*: Time interval is decomposed into equal non-overlapping subintervals and truncated space domain is split into overlapping subdomains of equal length. Each time and each space subinterval is discretized into $N_\xi + 1$ and $N_\eta + 1$ collocation points, respectively.

- *Linearisation*: The QLM is used to simplify the nonlinear PDEs to obtain the linear iterative scheme.
- *Domain transformation*: Both space and time domain are transformed into the interval $[-1, 1]$, where the spectral collocation method is implemented.
- *Bivariate interpolation*: At each subinterval, the functions are approximated by a bivariate Lagrange interpolation polynomial.
- *Spectral collocation*: The spectral differentiation matrices are introduced and used to approximate the derivatives of unknown functions at the collocation points as matrix vector product. Then approximate functions and differentiation matrices are substituted into the linearized iterative scheme to obtain a matrix system. The boundary conditions are then imposed on the matrix system. Starting from suitable initial guesses, approximate solutions are obtained by solving this matrix system.

4. Results and discussion

The numerical results obtained using the OMD-BSQLM are presented and discussed in this section. The spectral quasilinearisation method combined with implicit finite difference method has been used as a benchmarking tool to test the accuracy, and hence the reliability of the OMD-BSQLM results. In the entire computational process, the values of pertinent parameters were chosen as $Re = 10, Ri = 10, Pr = 1, \varepsilon = 0.01, Ec = 0.1, Sc = 0.94, N = 1, K = 0.1, A^* = 0.5, B^* = 0.5, Bi = 1, A = 1, M = 0.01, \delta = 1$, and $\xi = 1$. All these values were treated the same in the entire numerical study except the varied values in respective graphs and tables. The edge of the boundary has been taken as $\eta_\infty = 5$. The number collocation points was assigned as $N_\eta = 20$ and $N_\xi = 5$ in space and time, respectively. These values were sufficient to give accurate and consistent results, since a further increase in the number of collocation points did not change the numerical results. The space and time intervals were decomposed into $s = 5$ and $p = 40$ subintervals, respectively. The proposed numerical scheme is validated by comparing the present results of $F'(\xi, 0)$ with previously published work by Chiam [1998]) for the particular case when $\varepsilon = 0.1, Re = 0, A = 0$, and $Ri = 0$. The results are depicted in Figure 4 and good agreement is observed between the two set of results. Hence, the use of the present method is justified. In addition, Table 1 is presented for the skin friction, heat and mass transfer coefficients obtained using SQLM with finite differences, BSQLM, MD-BSQLM and OMD-BSQLM. It is noted that the methods that use the spectral method is both space and time uses few grid grid points to give comparable results. In all the methods, the OMD-BSQLM uses the minimal number of grid points in space since $N_\eta = 20$ collocation points is enough in each subinterval. The formula $M_\eta = N_\eta + (N_\eta - 1)(s - 1)$ also reduces the number of collocation points used when the number of overlapping subintervals are increased. In the table, a total number of $M_\eta = 20 + (20 - 1)(5 - 1) = 96$ collocation points is eventually used instead of the 100 collocation points from the other methods.

16   *M. P. Mkhatshwa, S. S. Motsa & P. Sibanda*

Thus, it can be concluded that the OMD-BSQLM gives stable and accurate results using few grid points in each space subinterval and the whole domain. The use of less grid points at each subinterval minimizes the effects of round-off errors that are attributed to approximating functions with an interpolating polynomial of higher degrees.

The numerical solutions are also tested for convergence and accuracy using convergence and residula error analysis. The convergence error norm is the difference between successive approximations, while the residual error measures the extent to which the numerical solutions approximate the true solution of the flow equations (8)-(10). To assess the convergence of the iteration scheme, we have considered the L_∞ and L_2 error norms between two successive iterations, define as

$$||E_{\mathbf{\Phi}}||_\infty = \max_{0 \leq j \leq N_\xi} ||\mathbf{\Phi}_{j,r+1} - \mathbf{\Phi}_{j,r}||_\infty, \quad ||E_{\mathbf{\Phi}}||_2 = \left(\sum_{j=0}^{N_\xi} |\mathbf{\Phi}_{j,r+1} - \mathbf{\Phi}_{j,r}|^2 \right)^{\frac{1}{2}}, (41)$$

where $\mathbf{\Phi} = \left\{ \mathbf{F}^{(\mu,v)}, \mathbf{G}^{(\mu,v)}, \mathbf{H}^{(\mu,v)} \right\}$. Figure 5 shows the variation in the error norms against the number of iterations. It can be seen that the error norms decrease monotonically with increasing number of iterations. This is an indication that the method converges as the number of iterations increases. Full convergence is achieved after about four iterations for all solutions with error norms close to 10^{-12}. Figure 6 depicts the effect of the number of time collocation points(at each subinterval in ξ) on the convergence of the solutions. Figure 6a represents a case where the multidomain technique (overlapping) is applied only in space. Figure 6b corresponds to the BSQLM case (no use of multidomain). The case of MD-BSQLM and OMD-BSQLM are represented in Figure 6c and Figure 6d, respectively. Usually, an increase in the number of collocation points results in a reduction of the convergence error. However, after a certain point (a point at which full convergence is reached), an increase in the number of collocation points does not have a significant effect on the convergence error. Similar behaviour is noted in the figure. However, the MD-BSQLM and OMD-BSQLM shows that full convergence can be reached using 2 collocation points in ξ with solution error of up to 10^{-7} and 10^{-11}, respectively. This shows that the multi-domain technique in time indeed plays a significant role in improving convergence. The small solution errors for the OMD-BSQLM can attributed to the few space collocation points used.

On the other hand, the accuracy of the OMD-BSQLM can be estimated by considering the residual errors defined as

$$||Res(w)||_\infty = ||\Delta_w \left[\mathbf{F}_{j,r+1}^{(\mu,v)}, \mathbf{G}_{j,r+1}^{(\mu,v)}, \mathbf{H}_{j,r+1}^{(\mu,v)} \right] ||_\infty, \quad w = \{f, G, H\}, \quad (42)$$

where Δ_w represents the nonlinear PDEs (8)-(10), $\mathbf{F}_j^{(\mu,v)}, \mathbf{G}_j^{(\mu,v)}$ and $\mathbf{H}_j^{(\mu,v)}$ are the OMD-BSQLM solutions at the time collocation points ξ_j. Figure 7(a) depicts the residual errors against the time scale ξ for both OMD-BSQLM and MD-BSQLM. It is seen that the residual errors are nearly uniform across ξ. This observation suggests that the accuracy of the method does not deteriorates when ξ becomes

large. It is also evident that the residual errors resulting from the OMD-BSQLM are always smaller compared to those residual errors from the MD-BSQLM when the same number of iterations are used in both methods. Moreover, the number of collocation points used over the entire spatial domain are $N_\eta = 100$ and $M_\eta = 96$ in the MD-BSQLM and OMD-BSQLM, respectively. Figure 7 shows the effect of varying the number of overlapping subdomains and the number of space collocation points on the accuracy of the solutions obtained. It is clear from the figure that the residual errors for the OMD-BSQLM is always smaller than those errors from the MD-BSQLM. Indeed, the use of multidomain overlapping grid in the proposed method significantly improves the accuracy of the method. This is due to the fact that the overlapping grid produces less dense or sparse matrices with a lot of zero elements. The use of sparse matrices can help to minimize the storage of large matrices and make it easy to perform matrix-vector multiplications since there is a lot of multiplication by zero. From the figure, we also notice that increasing the number of overlapping subdomains improves the accuracy of the method. This is evident from diminishing residual errors as the number of subdomains increases. Based on these observations, it can be deduced that the OMD-BSQLM provides high accuracy and uses minimal number of grid points compared to other methods such as the MD-BSQLM. Increasing the number of overlapping subdomains in space minimizes the number of collocation points used in the collocation process.
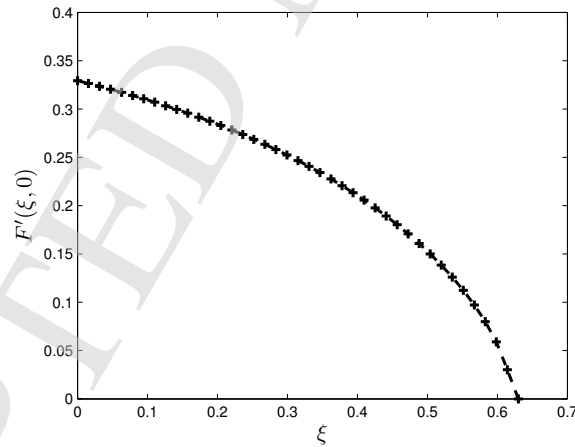

Fig. 4. Comparison of current results $(- - -)$ of $F'(\xi, 0)$ with Chiam [1998] $(+ + +)$ for $\varepsilon = 0.1$, $Re = 0$, $A = 0$, and $Ri = 0$.

In order to gain an insight into the physics of the flow problem, the influence of various parameters on the flow fields are presented in Figures 8-16. Figure 8 shows

18 *M. P. Mkhatshwa, S. S. Motsa & P. Sibanda*

(a) $||E_f||_2, ||E_G||_2$ and $||E_H||_2$ against iterations (b) $||E_f||_\infty, ||E_G||_\infty$ and $||E_H||_\infty$ against iterations
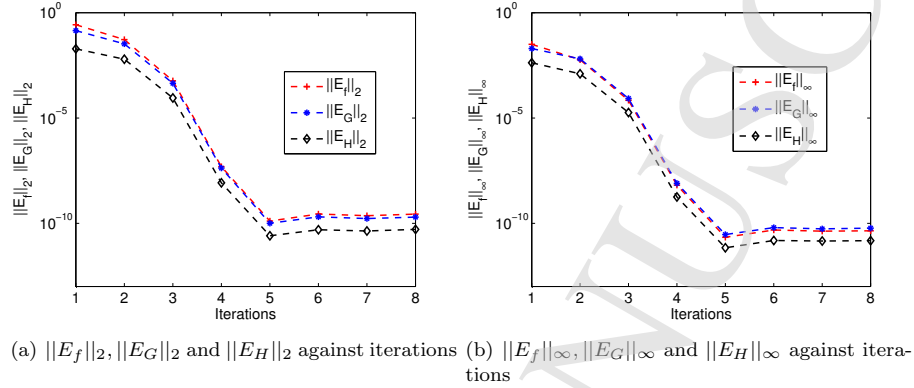
Fig. 5. Convergence error graphs for the OMD-BSQLM

Table 1. Comparison of the SQLM, BSQLM, MD-BSQLM and OMD-BSQLM results for the skin friction coefficient, Nusselt number and Sherwood number when $A = 1, N = 1, Ri = 10, M = 0.1, Re = 10, Pr = 1, \varepsilon = 0.01, Ec = 0.1$ and $Sc = 0.94$.

ξ	$|Re^{1/2}C_f|$	$|Re^{-1/2}Nu|$	$|Re^{-1/2}Sh|$	N_η	N_ξ	$|Re^{1/2}C_f|$	$|Re^{-1/2}Nu|$	$|Re^{-1/2}Sh|$	N_η	N_ξ
		SQLM					**BSQLM**			
0.2	0.0175172	3.9362184	1.5643919	60	200	0.0175171	3.9362184	1.5643919	100	10
0.4	0.0188221	4.0813009	1.6159583	60	200	0.0188222	4.0813009	1.6159584	100	10
0.6	0.0822637	4.1176114	1.6627046	60	200	0.0822637	4.1176114	1.6627045	100	10
0.8	0.1595088	4.1237206	1.7111452	60	200	0.1595089	4.1237206	1.7111452	100	10
1	0.2439225	4.1212948	1.7627782	60	200	0.2439227	4.1212949	1.7627783	100	10
1.2	0.3323398	4.1183033	1.8178491	60	200	0.3323397	4.1183032	1.8178491	100	10
1.4	0.4235000	4.1182703	1.8764234	60	200	0.4235002	4.1182703	1.8764235	100	10
1.6	0.5172776	4.1232973	1.9387512	60	200	0.5172776	4.1232972	1.9387512	100	10
1.8	0.6143349	4.1352420	2.0054139	60	200	0.6143350	4.1352421	2.0054137	100	10
2	0.7160290	4.1563051	2.0774319	60	200	0.7160289	4.1563052	2.0774319	100	10
		MD-BSQLM					**OMD-BSQLM**			
0.2	0.0175171	3.9362184	1.5643919	100	5	0.0175171	3.9362184	1.5643919	20	5
0.4	0.0188222	4.0813009	1.6159584	100	5	0.0188222	4.0813009	1.6159584	20	5
0.6	0.0822637	4.1176114	1.6627046	100	5	0.0822637	4.1176114	1.6627046	20	5
0.8	0.1595089	4.1237206	1.7111452	100	5	0.1595089	4.1237206	1.7111452	20	5
1	0.2439227	4.1212948	1.7627783	100	5	0.2439227	4.1212948	1.7627783	20	5
1.2	0.3323397	4.1183033	1.8178491	100	5	0.3323397	4.1183033	1.8178491	20	5
1.4	0.4235002	4.1182704	1.8764235	100	5	0.4235002	4.1182704	1.8764235	20	5
1.6	0.5172777	4.1232972	1.9387511	100	5	0.5172777	4.1232972	1.9387511	20	5
1.8	0.6143349	4.1352420	2.0054138	100	5	0.6143349	4.1352420	2.0054138	20	5
2	0.7160289	4.1563052	2.0774319	100	5	0.7160289	4.1563052	2.0774319	20	5

the effect of the velocity slip parameter on the velocity and concentration profiles in the presence of suction. From Figure 8(a), the fluid velocity is observed to decrease with increasing values of both positive and negative velocity slip parameters near the wall. This is due to the fact that when slip occurs, the flow velocity near the wall is no longer equal to the exponentially decreasing mainstream velocity. Away from the

Overlapping multi-domain spectral method for MHD mixed convection slip flow 19
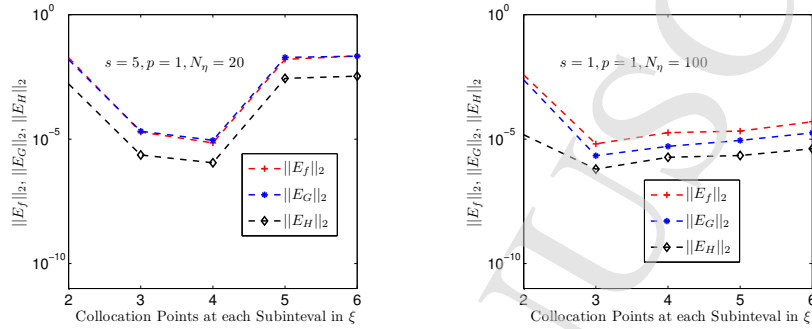
(a) $||E_f||_2, ||E_G||_2$ and $||E_H||_2$ against collocation points in ξ

(b) $||E_f||_2, ||E_G||_2$ and $||E_H||_2$ against collocation points in ξ
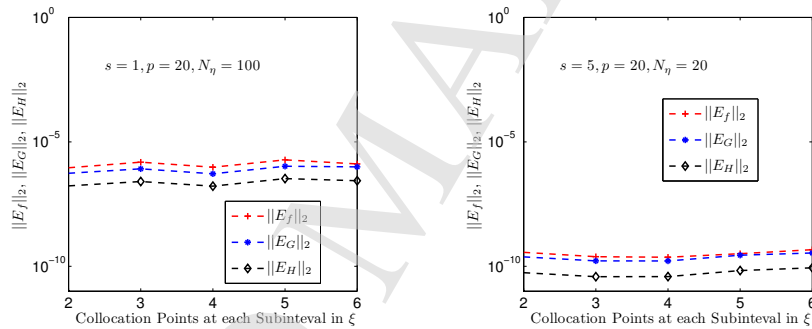
(c) $||E_f||_2, ||E_G||_2$ and $||E_H||_2$ against collocation points in ξ

(d) $||E_f||_2, ||E_G||_2$ and $||E_H||_2$ against collocation points in ξ

Fig. 6. Effect of the number of collocation points at each subinterval in ξ on the convergence errors

wall, the velocity is enhanced with increasing values of the velocity slip parameter. This is because increasing the velocity slip parameter permits more fluids to slip over the surface due to which the flow near the wall reduces and the slip effect away from the wall is less pronounced. It can be inferred from Figure 8(b) that an increase in both positive and negative values of the velocity slip parameter enriches the species concentration and associated boundary layer thickness. Furthermore, it can be concluded that the presence of surface slipperiness in the system can significantly affect the velocity and concentration of the fluid.

Figure 9(a) depicts the influence of the Richardson number on the velocity profiles in the case of suction. The fluid velocity is seen to increase with increasing values of the mixed convection parameter. The Richardson number represents the ratio of the Grashof number and Reynolds number such that increasing values of the

20   *M. P. Mkhatshwa, S. S. Motsa & P. Sibanda*
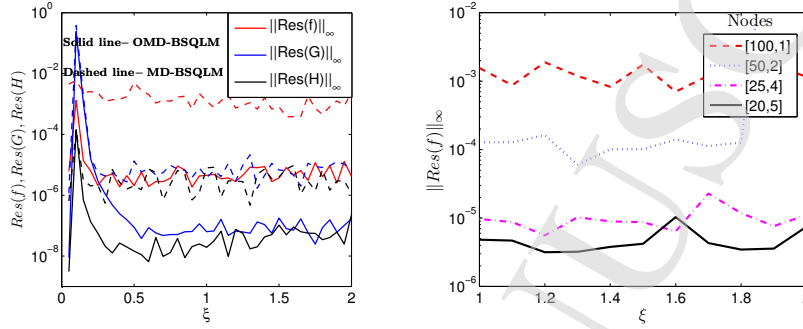
(a) $||Res(f)||_\infty, ||Res(G)||_\infty$ and $||Res(H)||_\infty$ for MD-BSQLM ($N_\eta = 100$) and OMD-BSQLM ($N_\eta = 20$)

(b) $||Res(f)||_\infty$ at different nodes when $p = 20$
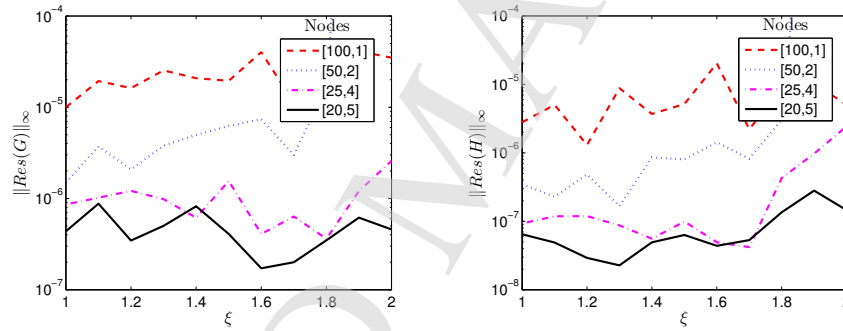
(c) $||Res(G)||_\infty$ at different nodes when $p = 20$ (d) $||Res(H)||_\infty$ at different nodes when $p = 20$

Fig. 7. Graphs of residual errors plotted against ξ

mixed convection parameter can enhance the momentum boundary layer thickness, thus increasing the fluid velocity. The positive values of the Richardson number indicate that the fluid velocity is accelerated in the direction of the mainstream due to pressure gradient. The negative values of the Richardson number depict the back-flow due to buoyancy forces opposing the induced flow, which reduces the magnitude of the fluid velocity within the exponentially decreasing main stream boundary layer flow. Similar results were reported by Patil *et al.* [2018a]. For larger values of the Richardson number ($Ri = 10$), the fluid velocity is noted to overshoot near the wall and this observation concur with those from El-Aziz [2013]. In the absence of the mixed convection parameter ($Ri = 0$) the velocity is observed to remain constant throughout the surface and this corresponds to pure forced convection flow. From Figure 9(b), we observe that the influence of the Biot number

Overlapping multi-domain spectral method for MHD mixed convection slip flow 21

(a) Effect of δ on $F(\xi, \eta)$ (b) Effect of δ on $H(\xi, \eta)$
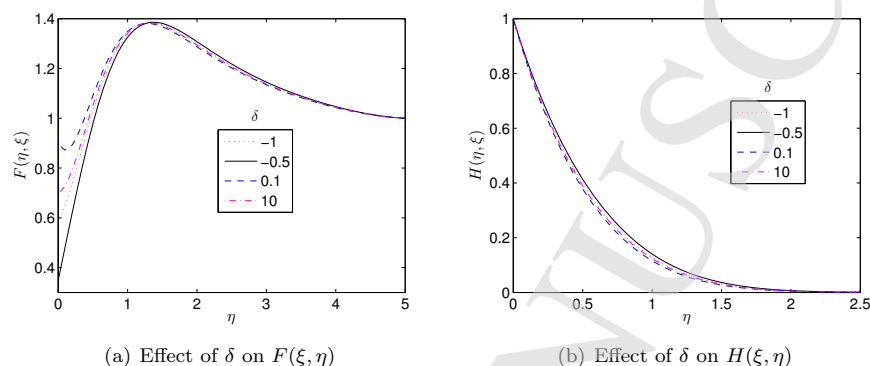
Fig. 8. Velocity and concentration profiles in case of suction

is more pronounced near the wall in the case of suction. Biot numbers are related with convective boundary conditions of the model near the surface. Thus, convective boundary conditions reduce the fluid temperature near the wall. Away from the boundary, both thermal boundary layer thickness and temperature profiles are enhanced by increasing values of the Biot number. Physically, an increase in the strength of the Biot number results to an increase in the convective heat transfer coefficient h_w due to the strong convection. The rise in the heat transfer coefficient is responsible for enhancing the thermal boundary layer thickness, thus increasing the fluid temperature. These results are in good agreement with the results obtained by Hayat *et al.* [2014] in the absence of suction/injection. It is also noted that the temperature remain almost the same at the surface vicinity for high values of the Biot number ($Bi = 10, 30$). This is connected with the convective heat transfer from the surface to its surrounding at high Biot numbers. Since the Biot number is high, the heat transfer from the surface become comparable to that attained from the irradiation field. This, in turn suppresses the temperature increase at the surface.

The influence of the Biot number on the velocity and concentration profiles is plotted in Figure 10 in the presence of suction. From Figure 10(a) it is observed that the influence of the Biot number on the velocity profiles is higher near the boundary, where increasing values of the thermal Biot number decreases the velocity. Away from the boundary, the fluid velocity is enhanced with increasing values of the Biot number. Figure 10(b) shows that concentration increases with increasing values of the Biot number throughout the boundary layer regime. High Biot numbers are expected to promote deeper penetration of the concentration due to the fact that the concentration profiles are driven by the temperature field. Figure 10 implies that the velocity and concentration boundary layer thickness slightly increase with an increase in the Biot number due to convective heat transfer at the surface.
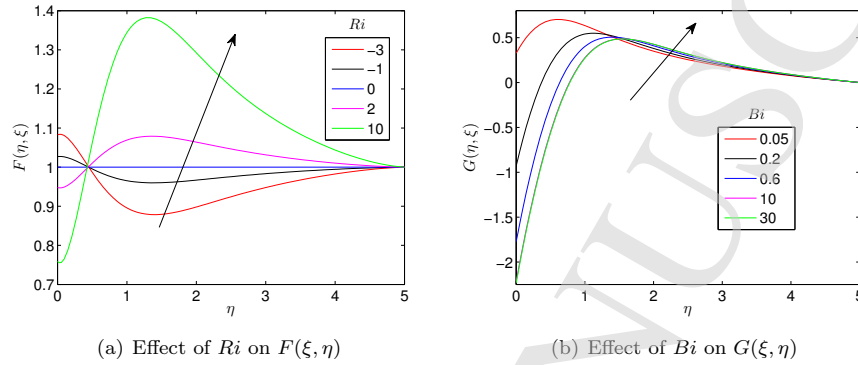
22 *M. P. Mkhatshwa, S. S. Motsa & P. Sibanda*

(a) Effect of Ri on $F(\xi, \eta)$ (b) Effect of Bi on $G(\xi, \eta)$

Fig. 9. Velocity and temperature profiles in case of suction

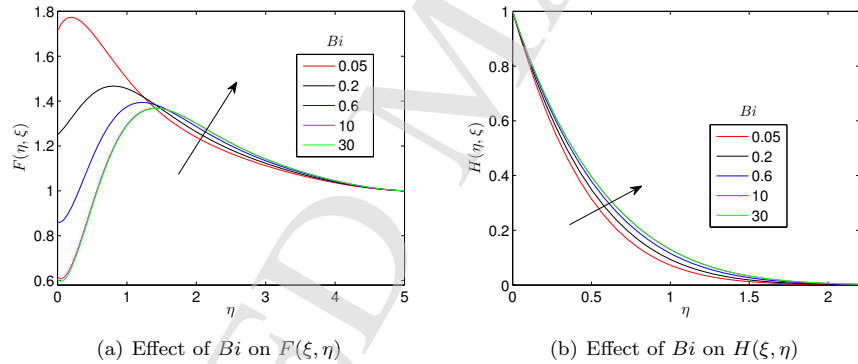(a) Effect of Bi on $F(\xi, \eta)$ (b) Effect of Bi on $H(\xi, \eta)$

Fig. 10. Velocity and concentration profiles in case of suction

Figure 11 provides the analysis for various values of the space and temperature dependent heat source or sink parameters on the velocity distribution in the case of injection and suction. We observe a mixed response in velocity profile, where the profile takes a reverse action at $\eta_\infty \approx 1$. The inclusion of space and temperature heat source or sink has an ability to reduce the velocity of the fluid near the boundary. Away from the wall, the fluid velocity is observed to increase with increasing values of the non-uniform heat source or sink parameters. This is due to the fact that an increase in the heat source ($A^* > 0, B^* > 0$) enhances the velocity boundary layer thickness while the heat sink ($A^* < 0, B^* < 0$) reduces the velocity boundary layer thickness. From Figure 11(a), we observe that the influence of the space-

Overlapping multi-domain spectral method for MHD mixed convection slip flow 23

dependent heat source parameter is more effective in the injection case compared
with the suction case. The opposite trend in seen with the effect of space-dependent
heat absorption. Figure 11(b) depicts that the effect of temperature-dependent heat
source/sink parameter is more sensitive in the case of injection than in suction. The
velocity boundary layer thickness is enhanced with the injection parameter while
reduced with the suction parameter.

(a) Effect of A^* and A on $F(\xi,\eta)$ (b) Effect of B^* and A on $F(\xi,\eta)$
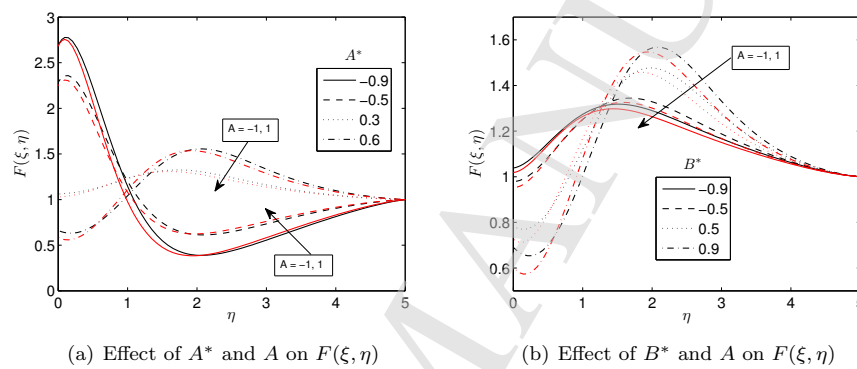
Fig. 11. Velocity profiles

Figure 12 shows the influence of the space and temperature dependent heat
source or sink parameters on the temperature field in the presence of both injection
and suction. The fluid temperature decreases near the boundary when the space
and temperature heat source or sink coefficients increase. Away from the wall, the
temperature is noted to be boosted with increasing values of the non-uniform heat
source or sink parameters. As expected, the temperature is enhanced with heat gen-
eration ($A^* > 0, B^* > 0$) and reduced with heat absorption ($A^* < 0, B^* < 0$). These
observation coincides with the general physical behaviour of the heat source/sink
that positive values of A^* and B^* acts like heat generators and negative values
of A^* and B^* operate like heat absorbers. An increase in the heat generation pa-
rameters significantly enhance the thermal boundary layer thickness. The boundary
layer generates heat energy to the flow which enhances the temperature field as the
heat source parameter increases. The reverse effects is true in the case of heat ab-
sorption. Also, the thickness of the thermal boundary layer thickness increases with
the injection parameter. This is because the injection parameter reduces the fluid
temperature and heat energy, whereas suction reduces the temperature, thus caus-
ing a thin thermal boundary layer. This observation concurs with findings reported
by Patil and Kumbarwadi [2017]. Figure 13 shows the effects of the non-uniform
heat source/sink parameters A^* and B^* on the concentration profile in the case

24   *M. P. Mkhatshwa, S. S. Motsa & P. Sibanda*

of injection and suction. It is clear that increasing values of A^* and B^* enhances
the concentration boundary layer thickness. The solutal boundary layer thickness
is enhanced by the energy released to the flow. Moreover, the injection parameter
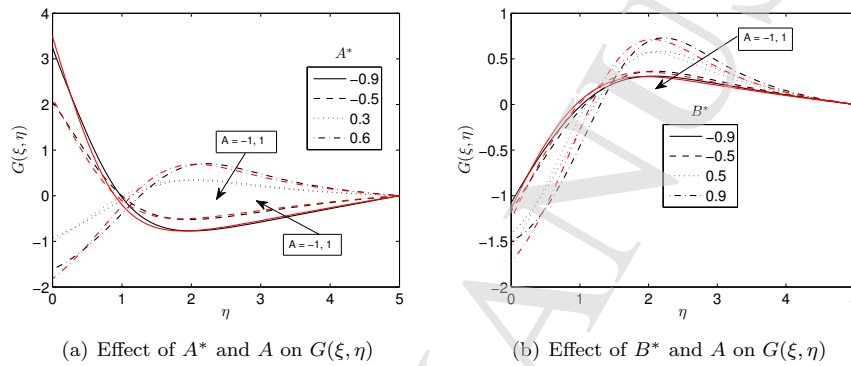improves the concentration profiles while suction reduces the concentration.

(a) Effect of A^* and A on $G(\xi, \eta)$

(b) Effect of B^* and A on $G(\xi, \eta)$

Fig. 12. Temperature profiles

(a) Effect of A^* and A on $H(\xi, \eta)$

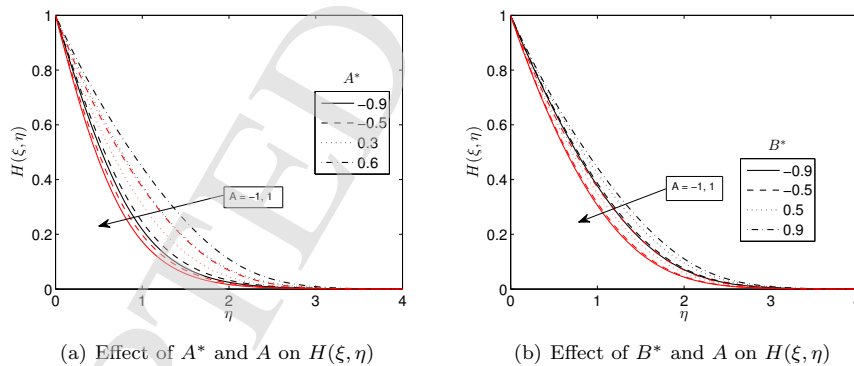(b) Effect of B^* and A on $H(\xi, \eta)$

Fig. 13. Concentration profiles

The effect of the magnetic field parameter and buoyancy ratio parameter on the
temperature field is depicted in Figure 14 in the presence of both for suction and
injection. We observe from Figure 14(a) that near the wall, the fluid temperature
decreases with increasing values of the magnetic field parameter. Away from the

Overlapping multi-domain spectral method for MHD mixed convection slip flow 25

boundary, the thermal boundary layer thickness increases, which in turn enhances the fluid temperature. An increase in the magnetic field parameter implies the increment in the strength of Lorentz force. Due to the stronger Lorentz force, the fluid becomes hot and causes the fluid temperature to rise. As expected, the temperature and thermal boundary layer thickness are noted to be higher for hydromagnetic flow ($M \neq 0$) compared to hydrodynamic ($M = 0$) case. Figure 14(b) shows that the temperature increases with increasing values of the buoyancy ratio parameter (N) near the wall. Away from the wall, the temperature and thermal boundary layer thickness decrease with increase in the ratio of buoyancy forces. Since the buoyancy ratio parameter is the concentration and thermal buoyancy forces ratio, the increment of the buoyancy ratio parameter minimizes the thermal buoyancy force which in turn reduces the fluid temperature. It is worth mentioning that here we used $N > 0$ and that means the thermal and concentration buoyancy forces act in the same direction. It is also noted that the magnetic field strength and buoyancy forces are more influential in the case of injection in contrast with suction.

(a) Effect of M and A on $G(\xi, \eta)$ (b) Effect of N and A on $G(\xi, \eta)$
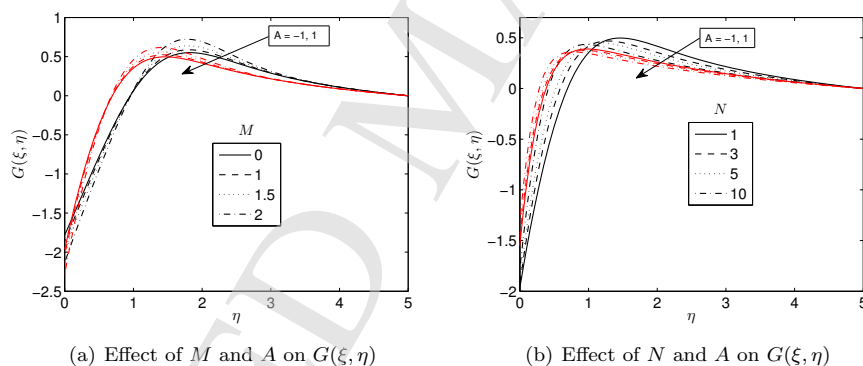
Fig. 14. Temperature profiles

Figure 15 depicts the influence of the chemical reaction and buoyancy ratio parameters on the concentration profiles. From Figure 15(a), it is noted that the concentration increases with destructive chemical reaction ($K < 0$) and decreases with the constructive chemical reaction ($K > 0$). This is due to the fact that introducing chemical reaction in the system produces consumption of the chemical, thus reducing the concentration profiles. It is worth noting that destructive chemical reaction overshoots the concentration profiles in the solutal boundary layer. Figure 15(b) shows that the increase in the buoyancy ratio parameter reduces the concentration buoyancy force, thus reducing concentration profiles. Figure 15 shows that concentration is higher in the injection case compared to the suction case. It

26 *M. P. Mkhatshwa, S. S. Motsa & P. Sibanda*

is important to mention that the influence of chemical reaction is clearly high in the presence of injection and similar findings were reported by Raju *et al.* [2018]. Figure 16 elucidate the repercussions of the Reynolds number on the velocity and concentration profiles. It is noted that the velocity increases for some distance from the wall and then decreases away from the wall as seen in Figure 16a. The velocity profile is also observed to be parabolic and symmetric. On the other hand, the concentration profile and associated boundary layer thickness also diminish with intensifying Reynolds number as shown in Figure 16b.

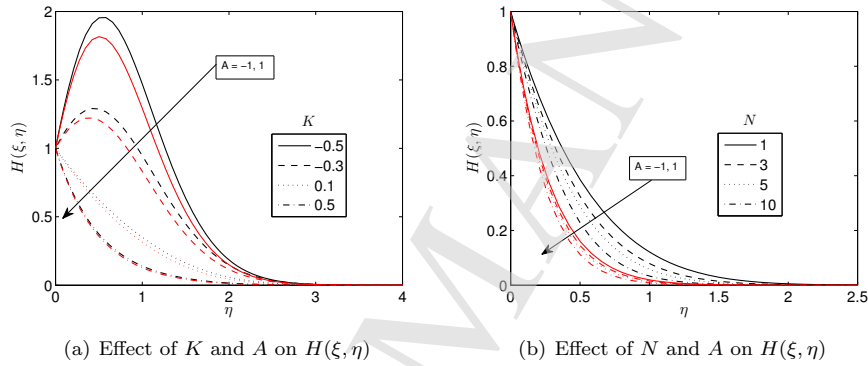(a) Effect of K and A on $H(\xi, \eta)$
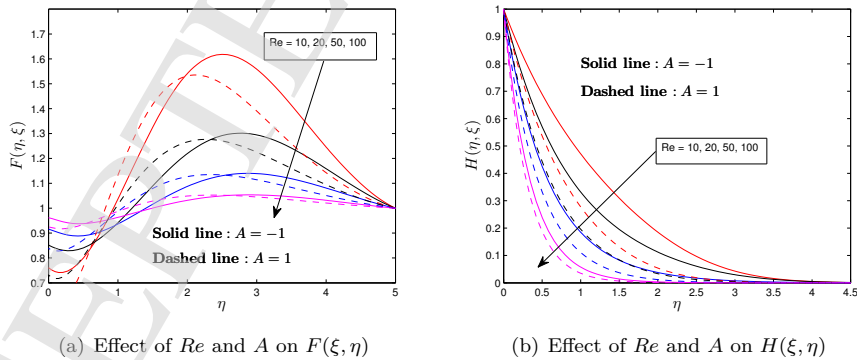
(b) Effect of N and A on $H(\xi, \eta)$

Fig. 15. Concentration profiles

(a) Effect of Re and A on $F(\xi, \eta)$

(b) Effect of Re and A on $H(\xi, \eta)$

Fig. 16. Velocity and concentration profiles

Overlapping multi-domain spectral method for MHD mixed convection slip flow 27

Figures 17 - 23 illustrate the behaviours of some important controlling parameters on the skin friction, heat and mass transfer characteristics in the case of suction. An increase in the values of the non-uniform heat source/sink helps to depreciate the local skin friction as seen in Figure 17. From these observation, it can be deduced that the heat sink parameter has ability to increase the friction between the wall and the fluid layers. Due to the increase in friction, the fluid velocity decreases while the skin friction coefficient enhances. The opposite trend occurs in the case of heat source parameter. Figure 18 displays the influence of the Biot number and velocity slip parameter on the skin friction coefficient. The skin friction coefficient is found to increase significantly with increasing values of the velocity slip parameter and decreases with increasing values of the Biot number.

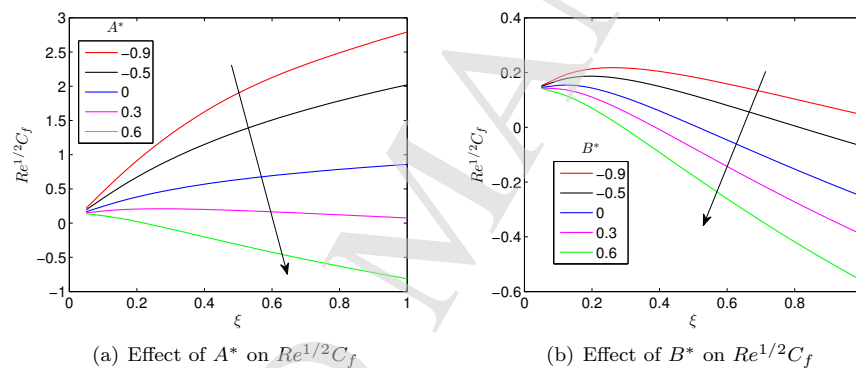(a) Effect of A^* on $Re^{1/2}C_f$ (b) Effect of B^* on $Re^{1/2}C_f$

Fig. 17. Skin friction coefficient in case of suction

Figure 19 shows the effect of the space-dependent and temperature-dependent heat source/sink on the heat transfer rate. The heat transfer rate decreases with increasing values of the non-uniform heat source/sink parameter. As mentioned earlier, for the case of heat source, the thermal boundary layer generates the energy which causes a fall in the rate of heat transfer within the thermal boundary layer. As a result, the thickness of the boundary layer is enhanced with space-dependent and temperature-dependent parameter. For the case of heat sink, the thermal energy is absorbed causing enhancement in the heat transfer rate and similar results were reported by Patil *et al.* [2018b]. Figure 20 exhibits the rate of heat transfer as a function of the Biot number and buoyancy ratio parameter. It is clear from the figure that rate of heat transfer decreases with increasing values of the Biot number and buoyancy ratio parameter.

Figure 21 depicts the nature of the Sherwood number with the space and temperature dependent heat source/sink parameters. It is observed that the Sherwood
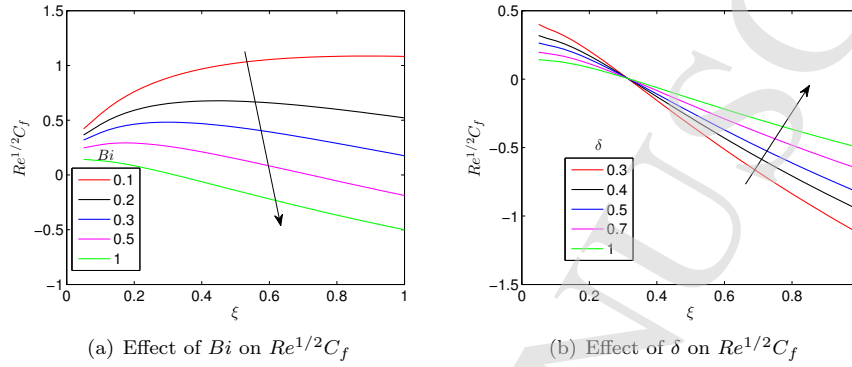
28   *M. P. Mkhatshwa, S. S. Motsa & P. Sibanda*

(a) Effect of Bi on $Re^{1/2}C_f$ (b) Effect of δ on $Re^{1/2}C_f$

Fig. 18. Skin friction coefficient in case of suction

(a) Effect of A^* on $Re^{-1/2}Nu$ (b) Effect of B^* on $Re^{-1/2}Nu$
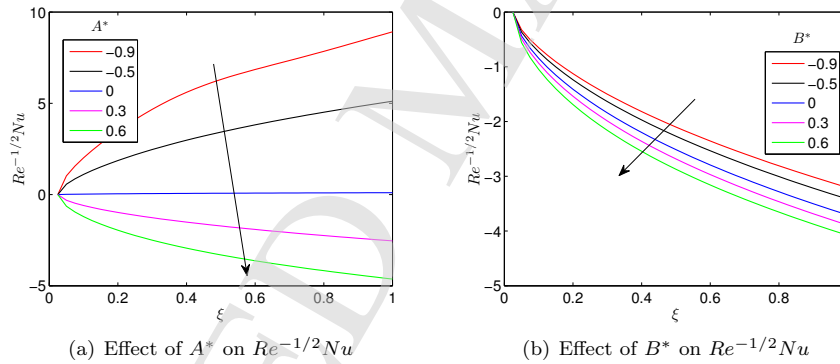
Fig. 19. Heat transfer coefficient in case of suction

number decreases with the heat source and increases with the heat sink. The mass transfer characteristics is weakly influenced by the presence of the temperature dependent heat source/sink coefficient. The impact of chemical reaction and buoyancy ratio parameter on the Sherwood number is shown in Figure 22. The Sherwood number decreases with increasing the constructive chemical reaction and enhances with the destructive chemical reaction. This is because as the chemical reaction parameter increases, the concentration difference between the surface and the fluid decreases, thus enhancing the rate of mass transfer. On the other hand, the mass transfer rate also enhances with increasing the buoyancy ratio parameter. This is because the flow is assisted by the concentration buoyancy effects. Figure 23 indi-

Overlapping multi-domain spectral method for MHD mixed convection slip flow 29

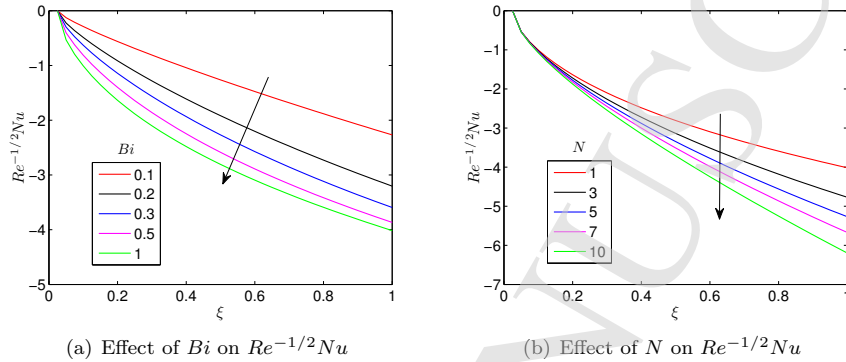(a) Effect of Bi on $Re^{-1/2}Nu$ (b) Effect of N on $Re^{-1/2}Nu$

Fig. 20. Heat transfer coefficient in case of suction

cate that as the Reynolds number increases the local skin friction coefficient decays exponentially. This means that escalating Reynolds number leads to fluctuation in the magnitude of the skin friction coefficient. The opposite trend is true for the local Sherwood number as it is an increasing function of the Reynolds number.

(a) Effect of A^* on $Re^{-1/2}Sh$ (b) Effect of B^* on $Re^{-1/2}Sh$
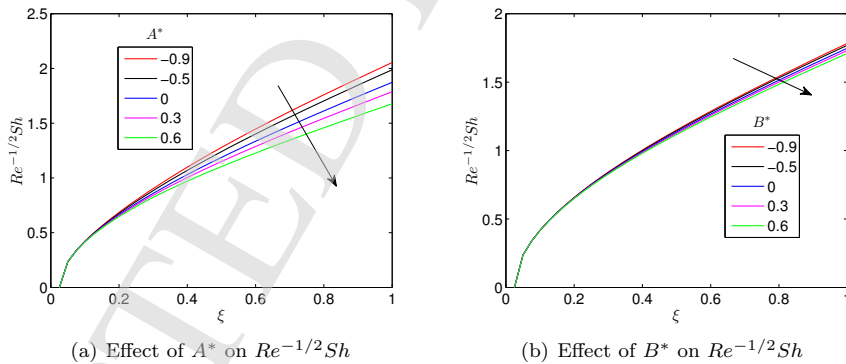
Fig. 21. Mass transfer coefficient in case of suction

Table 2 presents the numerical results for dimensionless skin friction, Nusselt number and Sherwood number for suction and injection cases. The table shows that the suction plays a significant role in improving the skin friction, heat and mass transfer coefficients compared to the injection. This is evident from higher values of the skin friction, heat and mass transfer coefficients in the suction case.
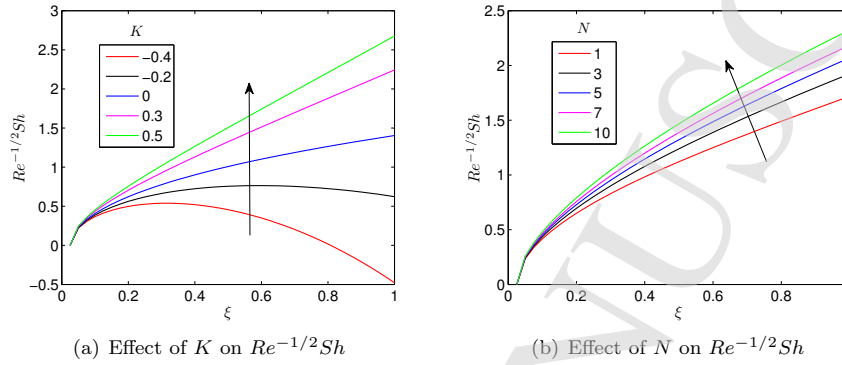
30   *M. P. Mkhatshwa, S. S. Motsa & P. Sibanda*

(a) Effect of K on $Re^{-1/2}Sh$ (b) Effect of N on $Re^{-1/2}Sh$

Fig. 22. Mass transfer coefficient in case of suction

(a) Skin friction coefficient versus Reynolds number   (b) Local Sherwood number versus Reynolds number
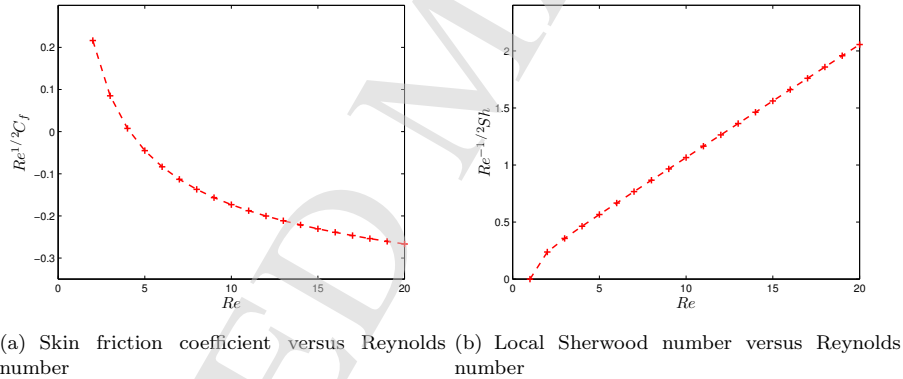
Fig. 23. Skin friction and Sherwood number in the case of suction

5. Conclusion

In this study, steady MHD mixed convection slip flow, heat and mass transfer along an exponentially decreasing mainstream with first order chemical reaction, non-uniform heat source/sink and convective boundary conditions were analyzed using overlapping multi-domain bivariate spectral quasilinearisation method. Numerical simulations were carried out to determine the convergence and accuracy of the numerical method. The main advantage of the proposed method is that it generate accurate results using few iterations and minimal number of grid points in each space subinterval as well as the entire interval. The use of minimal numbers of grid

Overlapping multi-domain spectral method for MHD mixed convection slip flow 31

Table 2. Skin friction coefficient, Nusselt Number and Sherwood number for the case of suction ($A = 1$) and injection ($A = -1$) when $N = 1, Ri = 10, M = 0.1, Re = 10, Pr = 1, \varepsilon = 0.01, Ec = 0.1, Sc = 0.94$ and $\xi = 1$.

δ	Bi	A^*	B^*	$|Re^{1/2}C_f|$	$|Re^{-1/2}Nu|$	$|Re^{-1/2}Sh|$	$|Re^{1/2}C_f|$	$|Re^{-1/2}Nu|$	$|Re^{-1/2}Sh|$
					Suction			Injection	
1	1	0.5	0.5	0.2439227	4.1212948	1.7627783	0.2008870	0.6398087	0.6849361
5	1	0.5	0.5	0.0584304	4.0828993	1.7524138	0.0494957	0.6232413	0.6814297
10	1	0.5	0.5	0.0299579	4.0769098	1.7507928	0.0254877	0.6206566	0.6808708
1	1	0.5	0.5	0.2439227	4.1212948	1.7627783	0.2008870	0.6398087	0.6849361
1	2	0.5	0.5	0.3236331	4.1794524	1.7460563	0.2036866	0.6291255	0.6845098
1	15	0.5	0.5	0.3935490	4.2214230	1.7320557	0.2060662	0.6202246	0.6841433
1	1	-0.5	0.5	0.9844270	5.2483552	2.0398501	1.3074576	1.9166681	0.9289285
1	1	0.4	0.5	0.1002207	3.4003299	1.7999717	0.0697824	0.6175523	0.7062063
1	1	0.8	0.5	0.7282864	5.6581648	1.6240270	0.5283801	0.5009251	0.6347123
1	1	0.5	-0.5	0.0335763	3.5063021	1.8161290	0.0128988	1.1404192	0.7182340
1	1	0.5	0.4	0.2165867	4.0576015	1.7698482	0.1794568	0.7138252	0.6887694
1	1	0.5	0.9	0.3380287	4.3054004	1.7380890	0.2670998	0.3731032	0.6730068

points at each subinterval minimizes the effects of round-off errors that can lead to instabilities. The accuracy improves as the number of overlapping subdomains increases. An increase in the number of overlapping subdomains minimizes the number of grid points required in the whole domain. The accuracy improvement is attributed to the overlapping grid which makes the coefficient matrices (in matrix equations that results from collocation process) to be less dense. The following conclusions are drawn from the obtained results:

- The higher values of the velocity slip parameter enhance the velocity, concentration profiles and the skin friction coefficient.
- The higher values of the thermal Biot number and non-uniform heat source/sink augment the velocity, temperature and concentration distributions while reducing the skin friction and heat transfer coefficients.
- The introduction of chemical reactive species in the system diminishes the concentration field while enhancing the rate of mass transfer.
- The influence of magnetic field strength, buoyancy forces, chemical reactive species and non-uniform heat source/sink coefficients is more sensitive in the case of injection than in suction.
- The presence of suction parameter in the system can significantly improve the skin friction coefficient, heat transfer and mass transfer rate.

The success of the study provokes the need for extending the application of the method to complex problems, which include problems modelling unsteady mixed convection flows with two-time dependent variables. Thus, future investigations will consider unsteady mixed convection from exponentially decreasing mainstream velocity, where we will also examine the computational efficiency and stability of the method.

32 *M. P. Mkhatshwa, S. S. Motsa & P. Sibanda*

References

Merkin, J. H., Najib, N., Bachok, N., Ishak, A. and Pop. I. (2017). Stagnation point flow and heat transfer over an exponentially stretching/shrinking cylinder. *J. Taiwan Institute Chem. Eng.*, **74**: 65–72.

Curle, N. (1981). Development and separation of a laminar boundary layer with an exponentially increasing pressure gradient. *Quarterly J. Mech. Appl. Math.*, **34**: 383–395.

Patil, P. M., Latha, D. N., Roy, S. and Momoniat, E. (2017). Double-diffusive mixed convection flow from a vertical exponentially stretching surface in presence of the viscous dissipation. *Int. J. Heat Mass Transf.*, **112**: 758–766.

Mukhopadhyay, S. and Layek, G. C. (2008). Effects of thermal radiation and variable fluid viscosity on free convection flow and heat transfer past a porous stretching surface. *Int. J. Heat Mass Transf.*, **51**: 2167–2178.

Mukhopadhyay, S. (2013). MHD boundary layer slip flow along a stretching cylinder. *Ain Shams Eng. J.*, **4**: 317–324.

Roy, S. and Saikrishnan, P. (2004). Non-uniform slot injection/suction into water boundary layer flow past yawed cylinder. *Int. J. Eng. Sci.*, **42**: 2147–2157.

Datta, P. Anilkumar, D. Roy, S. and Mahanti, N. C. (2006). Effect of non-uniform slot injection (suction) on a forced flow over a slender cylinder. *Int. J. Heat Mass Transf.*, **49**: 2366–2371.

Roy, S. Saikrishnan, P. and Ravindran, R. (2009). Role of non-uniform slot injection (suction) model on the separation of a laminar boundary layer flow. *Math. Comput. Model.*, **50**: 45–52.

Patil, P. M. Ramane, H. S. Roy, S. Vijaykumar, H. and Momoniat, E. (2017). Influence of mixed convection in an exponentially decreasing external flow velocity. *Int. J. Heat Mass Transf.*, **104**: 392–399.

Patil, P. M. Kumbarwadi, N. and Mamoniat, E. (2018). Influence of chemically reactive species and a volumetric heat source or sink on mixed convection over an exponentially decreasing mainstream. *Heat Transfer - Asian Res.*, **47**: 111–125.

Patil, P. M. and Kumbarwadi, N. (2017). Effects of non-Darcy porous medium on MHD mixed convection with cross diffusion and non-uniform heat source/sink over an exponentially stretching sheet, *Int. J. Petrochem. Sci. Eng.*, **2**; 292 – 300.

Patil, P. M. Kumbarwadi, N. and Shashikant, A. (2018). Effects of MHD mixed convection with non-uniform heat source/sink and cross diffusion over an exponentially stretching sheet. *J. Numer. Meth. Heat Fluid Flow*, **28**: 1238–1255.

Day, M. A. (2004). The no-slip condition of fluid dynamics. *Erkenntnis*. **33**: 285–296.

Bhattacharyya, K. Mukhopadhyay, S. and Layek, G. C. (2011). Slip effects on boundary layer stagnation-point flow and heat transfer towards a shrinking sheet. *Int. J. Heat Mass Transf.*, **54**: 308–313.

Mukhopadhyay, S. (2013). Slip effects on MHD boundary layer flow over an exponentially stretching sheet with suction/blowing and thermal radiation, *Ain Shams Eng. J.*, **4**: 485–491.

Patil, P. M. and Shashikant, A. (2018). Unsteady mixed convection along a permeable exponentially stretching surface: Influence of velocity slip and thermal jump, *Int. J. Numer. Meth. Heat Fluid Flow*, https://doi.org/10.1108/HFF-07-2017-0283

Isa, S. S. P. M. Arifin, Md. N. Bachek, N. Ali, F. Md. (2017). The effect of convective boundary condition on MHD mixed convection boundary layer flow over an exponentially stretching vertical sheet. *J. Phys.: Conference Series*, **949** 012016.

Srinivasacharya, D. and Jagadeeshwar, P. (2017). Slip viscous flow over exponentially stretching porous sheet with thermal convective boundary conditions, *Int. J. Appl. Comput. Math.* **3**:3525–3537.

Chapter 7

MHD bioconvective radiative flow of chemically reactive Casson nanofluid from a vertical surface with variable transport properties

This chapter extends the work in previous chapters to a non-Newtonian fluid flow which is described by partial differential equations. The movement of motile microoganisms in non-Newtonian fluid flow model is also taken into account. This chapter provides an analysis of MHD bioconvective flow of Casson nanofluid past a vertical surface by considering fluid properties of a variable nature. The conservation equations are solved using the overlapping multi-domain bivariate spectral quasilinearisation method. The solution error and residual errors are presented to gain an understanding of the convergence rate and accuracy of the numerical scheme. The solutions of dimensionless velocity, temperature, concentration and density of motile microorganisms are presented for various flow parameters.

MHD bioconvective radiative flow of chemically reactive Casson nanofluid from a vertical surface with variable transport properties

Musawenkhosi Patson Mkhatshwa [ID],[a], Sandile Motsa[a,b] and Precious Sibanda[a]

[a]School of Mathematics, Statistics & Computer Science, University of Kwazulu Natal, Scottsville, South Africa; [b]Department of Mathematics, University of Eswatini, Kwaluseni, Kingdom of Eswatini

ABSTRACT

In this paper, we analyse magnetohydrodynamic bioconvective flow of Casson nanofluid comprising gyro-tactic microorganisms from a vertical surface with variable thermo-physical features, nonlinear radiation, chemical reaction, Hall and ion-slip currents. The Casson fluid model incorporates zero nanoparticle mass flux at the boundary along with aspects of Brownian motion and thermophoresis to improve the motion of nanoparticles. The inclusion of motile microorganisms is considered to be beneficial for the stability of the nanoparticles. The model equations are first reduced into dimensionless form and then solved numerically using overlapping multi-domain bivariate spectral quasilinearisation method. Numerical analysis of the residual error and convergence properties of the method are discussed. For validation, our numerical results were compared with those available in the literature, and an excellent agreement was found. The impact of significant parameters on the flow fields, skin friction coefficients, heat, mass and motile microorganism transfer rates are analysed. We found that the flow fields improve due to enhancement of variable thermal conductivity, whereas retard with increment in variable viscosity and Casson fluid parameter. The inclusion of variable thermal conductivity and nonlinear radiative heat flux augments the fluid temperature, heat and mass transfer rates. An increment in variable fluid viscosity and Casson fluid parameter enhances heat and motile microorganism transfer rates, whereas diminishes the mass transfer rate. The reported observations find applications in enrobing processes for electric-conductive nano-materials, can be used in aerospace, smart coating transport situation, polymer processing and other industries. This type of flow can efficiently be utilised in solar energy system, enhancement of extrusion systems, and improvement of heat transfer devices as well as microbial fuel cells.

1. Introduction

The topic of nanofluids was introduced by Choi (1995) and it involves tiny nanoparticles with various metallic elements, metal oxides, Carbides or carbon nanotubes having particular chemical and physical properties, which are suspended in the base fluid such as water, ethylene glycol and engine oil. Nanofluids have been a subject of interest to many researchers due to their extensive need for efficient heat transfer fluid as it possesses high thermal conductivity properties than the base fluids. According to Eastman et al. (2001), the inclusion of nanoparticles in the base fluid produce a significant improvement in heat transfer capabilities and stability of suspensions. Due to high thermal conductivity, nanofluids have many industrial applications including power generation, wire drawing, metal spinning, extrusion, lubricant, glass fibre production, hot rolling and cooling process. Nanofluids are also utilised in crucial fields in modern science and technology as nuclear reactors, electronics, biomedicine and transportation. A comprehensive survey of convective transport in nanofluids was made by Buongiorno (2006) who considered seven slip mechanisms that can produce a relative velocity between nanoparticles and the base fluid. Amongst these mechanisms, only Brownian diffusion and thermophoresis were found to be the most significant slip mechanisms in nanofluids. For further understanding of nanofluids one can read (Ibrahim and Khan 2020; Gireesha et al. 2020; Khan et al. 2019; Hayat et al. 2018; Rashid et al. 2018).

In recent past years, flow, heat and mass transfer of non-Newtonian nanofluids from a vertical flat surface has attracted attention of several researchers due their valuable applications in mechanical, chemical and engineering processes. These applications include polymer, biological solutions, manufacturing crude soft material, greases, glues, chemicals, paints, petroleum and oil reservoir engineering. Unfortunately, there is no specific constitutive equation available that describes the entire non-Newtonian materials. Thus, researchers have used various constitutive equations according to their rheological properties about non-Newtonian behaviour. Javed et al. (2019) considered the flow of Jeffrey nanofluid over a variable thick surface with Joule heating and nonlinear radiative heat flux. It was noted that the temperature increase for higher values of radiative heat flux and Eckert number. Javed et al. (2019) scrutinised nonlinear radiative nanofluid flow of power law model induced by a stretched surface with heat generation/absorption, Joule heating, viscous dissipation and chemical reaction. Von

Kármán swirling analysis of Oldroyd-B nanofluid flow under the influence of heat generation/absorption, thermophoresis and Brownian motion aspects was discussed by Abbas et al. (2019). Amongst their findings, they found that increment in Brownian motion enhances temperature, while nanoparticle concentration intensifies with escalating thermophoresis parameter. Qayyum et al. (2018) explored flow characteristics of Williamson fluid between two rotating disks with Viscous dissipation, thermal radiation and heat source/sink effects. Two-dimensional flow of second grade fluid between two parallel plates in the presence of temperature-dependent viscosity and heat source/sink was considered by Hayat et al. (2017) and they reported that fluid temperature enhances in the case of variable thermal conductivity. Hayat et al. (2018) also studied flow of third grade nanofluid due to stretching rotating disk by taking into account chemical reaction and internal heat generation. The concentration field was observed to diminish for stronger thermophoretic force and higher chemical reaction. Gaffar, Prasad, and Reddy (2016) analysed mgnetohydrodynamic (MHD) free convection flow of Eyring-Powell fluid from a vertical surface in a non-Darcy porous medium. Gaffar, Prasad, and Reddy (2016) also studied MHD free convection flow of tangent hyperbolic fluid over a vertical surface. Both studies used the Darcy-Forchheimer model to describe the inertia effects in porous media, and take into account the effects of Joule heating, viscous dissipation, Hall and ion-slip currents. Their critical findings include that increasing Hall and ion-slip parameter improves primary velocity, skin friction, heat and mass transfer rates while decreasing secondary velocity, temperature and concentration. Hall and ion-slip effects play a significant role in many geophysical and astrophysical applications in addition to thermal engineering problems.

Amongst the classes of non-Newtonian nanofluids, Casson fluid is one of the most acceptable non-Newtonian fluid to simulate shear thinning liquids containing rod-like solids and is well known in analysing inks, emulsions, food stuffs, certain gels and paints. Casson fluid model is able to accommodate complex rheological properties of a fluid when compared to other fluid models such as the power law, second, third or fourth-grade models (Andersson et al. 1996; Sajid et al. 2009). According to Casson (1959) and Dash, Mehta, and Jayaraman (1996), Casson fluid is a shear thinning liquid which is assumed to have an infinite viscosity at zero rate of shear, a yield stress below which no flow occurs, and a zero viscosity at an infinite rate of shear. It is based on the structure of liquid phase and interactive behaviour of solid of a two-phase suspension. Examples of Casson fluids include Jelly, honey, tomato sauce and concentrated fruit juices. Possible applications of Casson fluids involve fibrinogen, cancer homeo-therapy, protein and red blood cells form a chain type structure. Casson fluid theory has also been used in advanced polymeric flow processing (Pham and Mitsoulis 1994). Casson fluid flow problems on various geometries have been extensively considered because of the significant effect of Casson fluid on heat transfer rate and its possible applications in food processing and bioengineering operations. Amanulla, Nagendra, and Reddy (2018) analysed the boundary layer flow of Casson nanofluid over a semi-infinite vertical plate surface and concluded that the velocity, temperature and nanoparticle concentration fields decrease with increment in Casson fluid parameter.

Ghadikolaei et al. (2018) studied magneto Casson nanofluid flow past a stretching sheet by considering the effects of nonlinear thermal radiation, Joule heating, chemical reaction, heat generation/absorption, viscous dissipation, Brownian motion and thermophoresis. The influence of Casson fluid parameter on temperature and concentration profiles is noted to be opposite to that reported by Amanulla, Nagendra, and Reddy (2018). Other relevant results include that increment in temperature profile increase with radiation parameter and nanoparticle concentration diminish with chemical reaction parameter. Gbadeyan, Titiloye, and Adeosun (2020) pondered the combined influence of variable thermal conductivity, variable fluid viscosity and non-linear radiation on MHD Casson nanofluid flow over a vertical flat plate and concluded that velocity increases, whereas both temperature and nanoparticle volume fraction decrease with increment in variable thermal conductivity and viscosity. Das et al. (2019) considered unsteady MHD chemically reactive double-diffusive Casson fluid past a flat surface with heat and mass transfer. The introduction of motile microorganisms into the sytem can be beneficial for the suspension of nanofluids since it helps to stabilise the suspended nanoparticles. It is noted that the above-mentioned studies were considered in the absence of motile microorganisms.

The first pioneers of the notion of bioconvection are Wager (1911) and Platt (1961). Bioconvection is a phenomenon that emerge as a result of upswimming microorganisms, which are less dense than water in suspensions. When the upper surface of the suspensions becomes more dense because of the assembling of microorganisms, it becomes unstable and microorganisms fall to produce bioconvection. It is very important to comprehend the behaviour of the microorganisms in suspensions of nanofluids due to its applications in fields of biotechnology and medicine. Behaviour of nanoparticles accompanied with microorganisms are significant in bioinspired systems including artificial swimmers of drug particles, which can be used in the process of drug delivery. Self-propelled microorganisms are denser than the cell fluid and this cause bioconvection and take place because of overturning instability resulted from microorganisms swimming to the upper surface of a fluid, which has a lower density than that of the microorganisms. Gyrotactic microorganism is based on the balance of gravitational and viscous torques causing bottom-heavy microorganisms to deviate from the vertical (Plesset 1974). Most of the time, gryrotactic microorganisms swim opposite to the gravity where the base fluid is water. Nevertheless, once bioconvection emerge, their swimming direction is determined by the balance of two torques which are the viscous torque acting on the body placed in a shear flow and the torque produced by gravity (Nayak et al. 2019; Shahid et al. 2018). The inclusion of gyrotactic microorganisms in non-Newtonian nanofluid is necessary since it helps in improving thermal performances and extrusion systems in different transport processes. Possible applications of nanofluid bioconvection include nanomaterial processing and automotive coolants.

The onset of nanofluid bioconvection was first considered by Kuznestov (2011). Several researchers then considered bioconvective nanofluid flow with various geometrical configurations. Bhatti and Michelide (Bhatti and Michaelides 2020) considered thermo-bioconvection flow of a nanofluid containing gyrotactic

towards a Riga plate and established that the motile microorganism profile decreases significantly with increment in both bioconvection Schmidt number and Peclet number. The three-dimensional nanofluid flow over rotating circular plates filled with nanoparticles and gyrotactic microorganisms was examined by Zhang et al. (2020). Beg, Uddin, and Khan (2015) studied bioconvetion flow of non-Newtonian nanofluid over a horizontal surface in a porous media filled with gyrotactic microorgansims. They found that the boundary layer flow accelerates with higher bioconvection Rayleigh number and nanofluid buoyancy ratio. Also, the motile microorganism density function was noted to elevate due to increment in bioconvection Lewis number while suppressed with the Peclet number. Al-Khaled, Khan, and Khan (2020) investigated the bioconvection flow of tangent hyperbolic nanoliquid over an accelerated moving surface with gyrotactic microorganisms, chemical reaction and nonlinear radiation. Heat transfer rate was established to improve with escalating radiation parameter, thermophoresis and Brownian motion. Magagula, Shaw, and Kairi (2020) examined double-dispersed bioconvective Casson nanofluid flow past a nonlinear stretching sheet with nonlinear radiation and chemical reaction. The density of motile microorganisms was disclosed to decrease with increase in the Casson number, while enhance with increase in the density ratio of the motile microorganism. Experiments have shown that the influence of radiation on microorganisms have destruction effects on organisms such as bacteria and fungi. As a result, radiation in microorgansisms has been extensively utilised in waste water sludge management. Sabir et al. (2019) analysed two-phase Casson nanofluid flow past a stretching sheet with chemical reaction and gyrotactic microoganisms. Chemical reaction plays a vital role in processes such as food processing, manufacturing of ceramics and drying.

The effectiveness of heat transfer in fluids is mostly dependent on their thermo-physical features. Among these features, we have fluid viscosity and thermal conductivity, which are significant factors in the heat transfer processes. In the majority of earlier published works, viscosity and thermal conductivity have been considered as constants. However, experiments have shown that the importance of these physical properties in isotropic fluid is quite limited. In case of variable thermo-physical properties, the effects of such physical quantities cannot be declined. To accurately analyse the flow and heat transfer processes it is necessary to consider fluid viscosity and thermal conductivity of variable nature. Several researchers have studied the effects of variable fluid properties on non-Newtonian nanofluids containing gyrotactic microorganisms. Oyelakin, Mondal, and Sibanda (2019) investigated bioconvective Casson nanofluid flow over a moving wedge nonlinear radiation and concentration dependent fluid properties. It was reported that the flow fields, skin friction coefficient, heat and motile microorganism transfer rates increase by varying the transport properties. Khan, Hehzad, and Ali (2020) studied bioconvection flow of Williamson nanofluid over an oscillatory stretching surface with motile microorganisms and variable thermal conductivity. Their results indicated that the presence of variable thermal conductivity, thermophoresis and Brownian motion effects are more frequent for enhancement of heat transfer. Abdelmalek et al. (2020) explored bioconvection flow of Williamson

nanofluid over a stretching cylinder with variable thermal conductivity. Sohail et al. (2019) studied the effects of variable thermal conductivity and mass diffusion on three-dimensional flow of Casson nanofluid over a nonlinear stretched surface with gyrotactic microorganisms. The above studies ignored the influence of exponentially varying fluid viscosity.

The purpose of the present work is to analyse MHD three-dimensional bioconvection flow of Casson nanofluid filled with gyrotactic microorganisms by considering the combined effects of nonlinear thermal radiation, exponentially varying viscosity and thermal conductivity. Nonlinear thermal radiation features are found in applications such as thermal extrusion phenomenon, solar system, missile technology, heavy mechanical apparatus, fission and fusion reactions. The inertial contribution in the porous medium model is accounted for through the inclusion of a velocity squared term in the momentum equation, which is referred to as Forchheimer's extension. Muhammad et al. (2019) considered a fully developed Darcy-Forchheimer mixed convection flow over a curved surface and noted that the fluid velocity decays for the Forchheimer number. Hayat et al. (2018) investigated water-based carbon nanotubes nonlinear stretched flow through a Darcy-Forchheimer porous medium in the presence of heat source/sink and nonlinear thermal radiation. Their results showed that the magnitude of skin friction coefficients increase for larger inertia coefficient, whereas higher radiation and temperature difference parameters boost the magnitude of heat transfer rate. The Buongiorno model Buongiorno (2006) is employed in the present analysis by incorporating the aspects of Brownian motion and thermophoretic diffusion. The literature review clearly indicates that bioconvective flow of non-Newtonian Casson nanofluid over a vertical plate surface in a non-Darcy porous medium with nonlinear radiation features, temperature dependent thermal conductivity and exponential variable fluid viscosity in the presence of heat source/sink, viscous dissipation, Joule heating, chemical reaction, Hall and ionslip currents has not been reported yet. Thus, in view of significance of nanofluid bioconvection, the authors are motivated to tackle this problem. The current flow analysis can contribute towards enhancing the efficiency of thermal energy transportation systems. To achieve such maximum efficiency and improve the production process, we consider one of the important non-Newtonian fluid with useful factors and valuable applications. The dimensional model equations are first reduced into dimensionless form and then solved numerically using the recently developed overlapping multi-domain bivariate spectral quasilinearisation method (OMD-BSQLM)(Mkhatshwa, Motsa, and Sibanda 2019; Mkhatshwa et al. 2020, 2020?). The method applies the multi-domain technique in both space and time and further uses the overlapping grid approach in the spatial domain. The method was found to require few grid points to achieve highly accurate results. The improved accuracy is attributed to the use of overlapping grid which makes the coefficient matrices in matrix equation that results from collocation process to be less dense, thus easy to invert. The present study assesses the convergence and accuracy of the method by performing convergence and residual error analysis which is limited in the previous studies.

2. Mathematical analysis

We consider MHD bioconvective flow of a viscous, incompressible and partially-ionised electrically conducting Casson nanofluid containing gyrotactic microorganisms adjacent to a non-isothermal vertical surface embedded in a non-Darcy saturated porous medium with variable fluid properties. For controlling the temperature field, features of nonlinear thermal radiation and heat generation/absorption are adopted in the energy equation. First-order homogeneous chemical reaction is also considered in the concentration equation to improve the mass transport. The features of Brownian motion and thermophoresis effects are included in the system for the nanofluid flow through deploying the Buongiorno's nanofluid model (Buongiorno 2006). The motile microorganisms are basically used to stabilised the suspended nanoparticles due to bioconvection generated by combined effect of buoyancy forces and magnetic field. The physical model of the problem and Cartesian coordinates is shown in Figure 1. The plate surface is in the x-z plane, where x and y-axes are parallel and normal,respectively, and the z-axis coincides with the leading edge of the plate. The magnetic field with component B_0 acts only in the y-direction. The magnetic Reynolds number is small enough for the partially ionised fluid so that inducted magnetic field can be neglected. However, relative motion of the particles in the fluid can occur and the electron-atom collision frequency is assumed to be high enough for Hall and ionslip currents to be significant. The influence of Hall current gives rise to a force in the z-direction, which induces a cross flow in that direction, and hence the flow becomes three-dimensional. Initially, the vertical surface and Casson fluid are maintained at the same temperature T_w, nanoparticle concentration C_w, and density of motile microorganism N_w. The ambient fluid temperature, concentration and density number of motile microorganisms are given by T_∞, C_∞ and N_∞, respectively. The fluid viscosity is assumed to vary as an exponential function of temperature, whereas thermal conductivity vary linearly as a function of temperature. The rheological equation of an isotropic and incompressible flow of Casson fluid is given by Sharada and Shankar (2015), Mukhopadhyay and Bhattacharyya (2013), and Kala (2016)

$$\tau_{ij} = \begin{cases} 2\left(\mu_B + \dfrac{P_y}{\sqrt{2\pi}}\right) e_{ij}, & \text{if}\pi > \pi_c, \\ 2\left(\mu_B + \dfrac{P_y}{\sqrt{2\pi_c}}\right) e_{ij}, & \text{if}\pi < \pi_c, \end{cases} \tag{1}$$

Here, P_y is the yield stress of the Casson fluid, which can be expressed in the form

$$P_y = \frac{\mu_B \sqrt{2\pi}}{\beta}, \tag{2}$$

$\pi = e_{ij}e_{ij}$ is the product of the component of deformation rate, with e_{ij} as (i,j)-th component of the deformation rate, π_c is critical value of π based on the non-Newtonian model, μ_B is the plastic dynamic viscosity of the non-Newtonian fluid. For the case of Casson fluid flow, where $\pi > \pi_c$, we can write that

$$\mu_f = \mu_B + \frac{P_y}{\sqrt{2\pi}}. \tag{3}$$

Making use of Equation (2) in Equation (3), the kinematic viscosity becomes

$$\nu_f = \frac{\mu_f}{\rho_f} = \frac{\mu_B}{\rho_f}\left(1 + \frac{1}{\beta}\right), \tag{4}$$

Under the above assumptions along with boundary layer and Boussinesq's approximations, and using the Darcy-Forchheimer model, the governing equations of bioconvection flow of Casson nanofluid in the presence of viscous dissipation and Joule heating effects are given by Abo-Eldahab and Aziz (2005), Gaffar, Prasad, and Reddy (2016), Gaffar, Prasad, and Reddy (2016), and Amanulla, Nagendra, and Reddy (2018):

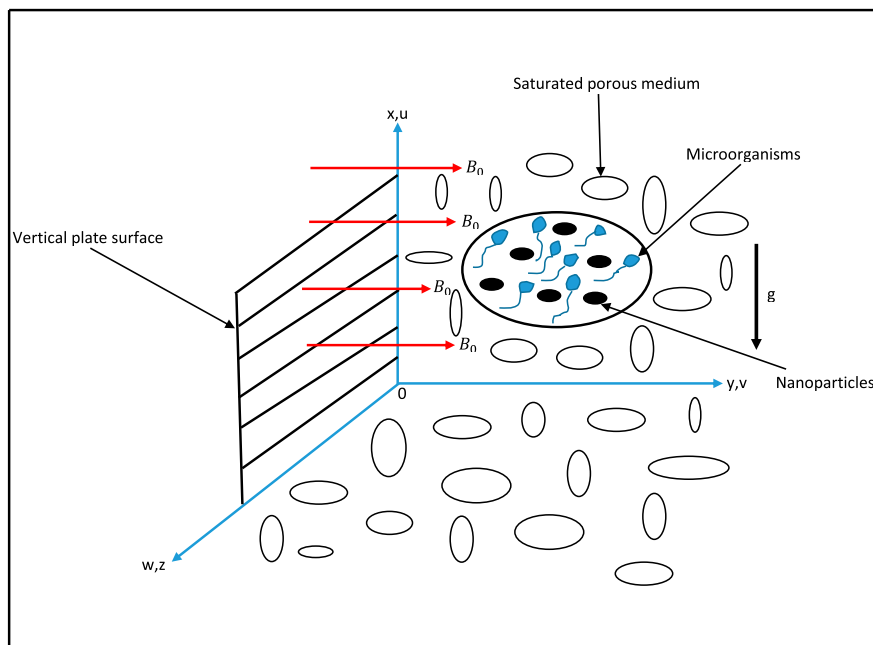$$\frac{\partial u}{\partial x} + \frac{\partial v}{\partial y} = 0, \tag{5}$$

Figure 1. Physical model and coordinate system

$$u\frac{\partial u}{\partial x} + v\frac{\partial u}{\partial y} = \frac{1}{\rho_f}\left(1 + \frac{1}{\beta}\right)\frac{\partial}{\partial y}\left(u_B(T)\frac{\partial u}{\partial y}\right)$$

$$- \frac{\sigma B_0^2}{\rho_f(\alpha_e^2 + \beta_e^2)}(\alpha_e u + \beta_e w) - b_1\frac{u^2}{k_p}$$

$$- \frac{\mu_B(T)}{\rho_f k_p}\left(1 + \frac{1}{\beta}\right)u + g^*[\beta_T(T - T_\infty)$$

$$+ \beta_C(C - C_\infty) + \beta_N(N - N_\infty)], \tag{6}$$

$$u\frac{\partial w}{\partial x} + v\frac{\partial w}{\partial y} = \frac{1}{\rho_f}\left(1 + \frac{1}{\beta}\right)\frac{\partial}{\partial y}\left(u_B(T)\frac{\partial w}{\partial y}\right)$$

$$- \frac{\mu_B(T)}{\rho_f k_p}\left(1 + \frac{1}{\beta}\right)w - b_1\frac{w^2}{k_p} + \frac{\sigma B_0^2}{\rho_f(\alpha_e^2 + \beta_e^2)}(\beta_e u - \alpha_e w)$$

$$\tag{7}$$

$$u\frac{\partial T}{\partial x} + v\frac{\partial T}{\partial y} = \frac{1}{(\rho c)_p}\frac{\partial}{\partial y}\left(k(T)\frac{\partial T}{\partial y}\right)$$

$$+ \tau\left[D_B\frac{\partial T}{\partial y}\frac{\partial C}{\partial y} + \frac{D_T}{T_\infty}\left(\frac{\partial T}{\partial y}\right)^2\right] + \frac{\sigma B_0^2}{(\rho c)_p(\alpha_e^2 + \beta_e^2)}(u^2 + w^2)$$

$$+ \frac{\mu_B(T)}{(\rho c)_p}\left(1 + \frac{1}{\beta}\right)\left[\left(\frac{\partial u}{\partial y}\right)^2 + \left(\frac{\partial w}{\partial y}\right)^2\right]$$

$$+ \frac{Q_0}{(\rho c)_p}(T - T_\infty) + \frac{16\sigma^*}{3k^*(\rho c)_p}\frac{\partial}{\partial y}\left(T^3\frac{\partial T}{\partial y}\right), \tag{8}$$

$$u\frac{\partial C}{\partial x} + v\frac{\partial C}{\partial y} = D_B\frac{\partial^2 C}{\partial y^2} + \frac{D_T}{T_\infty}\frac{\partial^2 T}{\partial y^2} - k_c(C - C_\infty), \tag{9}$$

$$u\frac{\partial N}{\partial x} + v\frac{\partial N}{\partial y} + \frac{bW_c}{C_w - C_\infty}\frac{\partial}{\partial y}\left(N\frac{\partial C}{\partial y}\right) = D_N\frac{\partial^2 N}{\partial y^2}, \tag{10}$$

where u, v and w are velocity components in the x, y, z directions, T is the temperature, C is the nanoparticle concentration, N is the density of motile microorganisms, ρ_f is the density of the base fluid, c_p is the specific heat, g^* is the acceleration due to gravity, $\sigma = \frac{e^2 n_e t_e}{m_e}$ is electrical conductivity of the fluid, e is the electron charge, t_e is the electron collision time, n_e is the electron number density, m_e is the mass of the electron, k_p is the permeability of the porous medium, $\beta = \frac{2\sqrt{2\pi}}{P_y}$ is the Casson fluid parameter, β_T, β_C and β_N represents volumetric coefficient of thermal, solutal and motile microorganism expansions, B_0 is the magnetic field intensity, Q_0 is the heat generation/absorption coefficient, k^* is the mean absorption coefficient, σ^* is the Stefan-Boltzman constant, D_B is the Brownian motion coefficient, D_T is the thermophoresis diffusion coefficient, D_N is the diffusivity of the motile microorganisms, $\tau = \frac{(\rho c)_p}{(\rho c)_f}$ is the ratio of heat capacity of nanoparticles material and heat capacity of base fluid, b is the chemotaxis constant, W_c is the maximum cell swimming speed, k_c is the chemical reaction coefficient, b_1 is the Forchheimer form-drag parameter, $\alpha_e = 1 + \beta_i\beta_e$, where $\beta_i = \frac{en_e B_0}{(1+n_e/n_a)k_{ai}}$ is the ion-slip parameter with n_a being the neutral particle number density and k_{ai} is the friction coefficient between ions and neutral particles, and $\beta_e = \omega_e t_e$ is the hall current with ω_e being the electron frequency. The transport properties of the fluid are assumed to be constants, except for the temperature dependent fluid viscosity $\mu_B(T)$ and thermal conductivity $k(T)$ expressed in the form Gbadeyan, Titiloye, and

Adeosun (2020), Jawali, Chamkha, and Mohiuddin (2016), Mahmoud and Megahed (2009), Megahed (2019), and Oyelakin and Sibanda (2020)

$$\mu_B(T) = \mu_\infty e^{-\alpha\frac{T-T_\infty}{T_w - T_\infty}}, \quad k(T) = k_\infty\left[1 + \varepsilon\frac{T - T_\infty}{T_w - T_\infty}\right], \tag{11}$$

where u_∞ and k_∞ are the respective ambient fluid viscosity and thermal conductivity, α and ε are the variable viscosity parameter and thermal conductivity parameter, respectively.

The boundary conditions are given by

$$u = v = w = 0, \quad T = T_w,$$

$$D_B\frac{\partial C}{\partial y} + \frac{D_T}{T_\infty}\frac{\partial T}{\partial y} = 0, N = N_w, \text{at } y = 0,$$

$$u \to 0, \quad w \to 0, T \to T_\infty, C \to C_\infty, N \to N_\infty, \text{as } y \to \infty, \tag{12}$$

To transform the nonlinear PDEs (5)–(10) into a dimensionless form, we introduce the following similarity transformations:

$$\xi = \frac{x^{1/2}}{L^{1/2}}, \quad \eta = \frac{C_1 y}{x^{1/4}}, \Psi = 4\nu_f C_1 x^{3/4} f(\xi, \eta),$$

$$\theta(\xi, \eta) = \frac{T - T_\infty}{T_w - T_\infty}, \phi(\xi, \eta) = \frac{C - C_\infty}{C_w - C_\infty},$$

$$\chi(\xi, \eta) = \frac{N - N_\infty}{N_w - N_\infty}, C_1 = \left\{\frac{g^*\beta_T(T_w - T_\infty)}{4\nu_f^2}\right\}^{1/4},$$

$$w = 4\nu_f C_1^2 x^{1/2} G(\xi, \eta), \tag{13}$$

where L denotes characteristic length of the plate, ξ, η are the dimensionless tangential and normal coordinates, respectively, Ψ is the stream function defined by $u = \frac{\partial\Psi}{\partial y}$ and $v = -\frac{\partial\Psi}{\partial x}$, f, G, θ, ϕ and χ are the respective dimensionless stream function, lateral velocity, temperature, nanoparticle concentration and denity of motile microorganisms.

In view of equations (13), the equation for conservation of mass (5) is identically satisfied and the remaining equations (6)–(10) reduce to

$$\left(1 + \frac{1}{\beta}\right)e^{-\alpha\theta}[f''' - \alpha\theta'f''] + 3ff'' - 2f'^2$$

$$- \frac{2}{DaGr_x^{1/2}}\xi^4\left(1 + \frac{1}{\beta}\right)e^{-\alpha\theta}f' - \frac{4Fs}{Da}\xi^2 f'^2$$

$$- \frac{2M}{\alpha_e^2 + \beta_e^2}\xi[\alpha_e f' + \beta_e G] + 2(\delta_T\theta + \delta_C\phi + \delta_N\chi)$$

$$= 2\xi\left(f'\frac{\partial f'}{\partial\xi} - f''\frac{\partial f}{\partial\xi}\right), \tag{14}$$

$$\left(1 + \frac{1}{\beta}\right)e^{-\alpha\theta}[G'' - \alpha\theta'G'] + 3fG' - 2Gf'$$

$$- \frac{2}{DaGr_x^{1/2}}\xi^4\left(1 + \frac{1}{\beta}\right)e^{-\alpha\theta}G$$

$$- \frac{4Fs}{Da}\xi^2 G^2 - \frac{2M}{\alpha_e^2 + \beta_e^2}\xi[\alpha_e G - \beta_e f']$$

$$= 2\xi\left(f'\frac{\partial G}{\partial\xi} - G'\frac{\partial f}{\partial\xi}\right), \tag{15}$$

$$\left[1 + \varepsilon\theta + \frac{4}{3}Rd\left(1 + (\theta_w - 1)\theta\right)^3\right]\theta'' + \varepsilon\theta'^2$$

$$+ 4Rd\left(1 + (\theta_w - 1)\theta\right)^2(\theta_w - 1)\theta'^2$$

$$+ PrNb\theta'\phi' + PrNt\theta'^2 + 2Pr\xi\lambda\theta + 3Prf\theta'$$

$$+ \frac{4PrMEc}{\alpha_e^2 + \beta_e^2}\xi^3[f'^2 + G^2]$$

$$+ 4PrEc\xi^2\left(1 + \frac{1}{\beta}\right)e^{-\alpha\theta}[f''^2 + G'^2]$$

$$= 2Pr\xi\left(f'\frac{\partial\theta}{\partial\xi} - \theta'\frac{\partial f}{\partial\xi}\right), \tag{16}$$

$$\phi'' + Le\left[3f\phi' - \xi K\phi\right] + \frac{Nt}{Nb}\theta'' = 2Le\xi\left(f'\frac{\partial\phi}{\partial\xi} - \phi'\frac{\partial f}{\partial\xi}\right), \tag{17}$$

$$\chi'' + 3Lbf\chi' - Pe\left[(\Omega + \chi)\phi'' + \phi'\chi'\right]$$

$$= 2Lb\xi\left(f'\frac{\partial\chi}{\partial\xi} - \chi'\frac{\partial f}{\partial\xi}\right), \tag{18}$$

subject to the boundary conditions

$$f(\xi, 0) = 0, \quad f'(\xi, 0) = 0, \ G(\xi, 0) = 0,$$

$$\theta(\xi, 0) = 1, \ Nb\phi'(\xi, 0) + Nt\theta'(\xi, 0) = 0, \ \chi(\xi, 0) = 1,$$

$$f'(\xi, \infty) = 0, \ G(\xi, \infty) = 0, \ \theta(\xi, \infty) = 0,$$

$$\phi(\xi, \infty) = 0, \ \chi(\xi, \infty) = 0, \tag{19}$$

where $\delta_T = \frac{g^*\beta_T(T_w - T_\infty)}{2v_f^2 C_1^4}$ is the thermal buoyancy parameter, $\delta_C = \frac{g^*\beta_C(C_w - C_\infty)}{2v_f^2 C_1^4}$ is the solutal buoyancy parameter, $\delta_N = \frac{g^*\beta_N(N_w - N_\infty)}{2v_f^2 C_1^4}$ is the gyrotactic microorganism buoyancy parameter, $\lambda = \frac{Q_0 L^{1/2}}{2\rho_f c_p v_f C_1^2}$ is the heat source/sink parameter, $Pr = \frac{v_f \rho_f c_p}{k_f}$ is the Prandtl number, $M = \frac{\sigma B_0^2 L^{1/2}}{2\rho_f v_f C_1^2}$ is the magnetic field parameter, $Ec = \frac{4C_1^4 v_f^2 L}{c_p(T_w - T_\infty)}$ is the Eckert number, $Le = \frac{v_f}{D_B}$ is the Lewis number, $Rd = \frac{4\sigma^* T_\infty^3}{v_f k^* \rho_f c_p}$ is the radiation parameter, $K = \frac{k_c L^{1/2}}{v_f C_1^2}$ is the chemical reaction parameter, $Da = \frac{k_p}{L^2}$ is the Darcy number, $Fs = \frac{b_1}{L}$ is the Forchheimer parameter, $Nt = \frac{\tau D_T(T_w - T_\infty)}{v_f T_\infty}$ is the thermophoresis parameter, $Nb = \frac{\tau D_B(C_w - C_\infty)}{v_f}$ is the Brownian motion parameter, $\theta_w = \frac{T_w}{T_\infty}$ is the temperature ratio parameter, $Gr_x = \frac{g^*\beta_T(T_w - T_\infty)x^3}{v_f^2}$ is the local Grashof number, $Pe = \frac{bW_c}{D_N}$ is the bioconvection Peclet number, $Lb = \frac{v_f}{D_N}$ is the bioconvection Lewis number and $\Omega = \frac{N_\infty}{N_w - N_\infty}$ is the density ratio of motile microorganism.

The engineering quantities of physical interest are the skin friction coefficients C_{fx} and C_{gz} along $x-$ and $z-$ directions, local Nusselt number Nu_x, Sherwood number Sh_x and density number of the motile microorganisms Nn_x expressed in dimensionless form as

$$C_{fx} = \left(1 + \frac{1}{\beta}\right)e^{-\alpha\theta(\xi, 0)}f''(\xi, 0),$$

$$C_{gz} = \left(1 + \frac{1}{\beta}\right)e^{-\alpha\theta(\xi, 0)}G'(\xi, 0),$$

$$Nu_x = -\frac{1}{\sqrt{2}}Gr^{1/4}\left[1 + \varepsilon\theta(\xi, 0)\right.$$

$$\left. + \frac{4}{3}Rd\left(1 + (\theta_w - 1)\theta(\xi, 0)\right)^3\right]\theta'(\xi, 0)$$

$$Sh_x = -\frac{1}{\sqrt{2}}Gr^{1/4}\phi'(\xi, 0), \ Nn_x = -\frac{1}{\sqrt{2}}Gr^{1/4}\chi'(\xi, 0), \tag{20}$$

3. Numerical procedure

This section presents the implementation of the OMD-BSQLM in simplifying the system of PDEs (14)–(18). The proposed method involves splitting the time computational domain into non-overlapping subintervals and the spatial domain into overlapping subintervals. The solution algorithm uses the the the quasilinearisation method (QLM)(Bellman and Kalaba 1965) to linearise the nonlinear PDEs. Then the multidomain spectral collocation method is implemented on the linearised iterative scheme, where the resulting PDEs are solved independently over each time interval. It is worth noting that the solution in the space direction is computed simultaneously across all subintervals. To apply the OMD-BSQLM, we let the time variable $\xi \in J$, where $J = [0, \xi_f]$. The time interval J is decomposed into q equal non-overlapping subintervals, defined as

$$J_\varrho = [\xi_{\varrho-1}, \xi_\varrho], \quad \xi_{\varrho-1} < \xi_\varrho \quad \varrho = 1, 2, 3, \ldots, q, \tag{21}$$

where each subinterval J_ϱ is further discretised into $(N_\xi + 1)$ Chebyshev Gauss-Lobatto collocation points. The rest of the grid in the time variable can be shown as follows:

$$\left\{0 = \xi_{N_\xi}^{(1)}, \ldots, \xi_0^{(1)} = \xi_{N_\xi}^{(2)}, \ldots, \xi_0^{(\varrho-1)} = \xi_{N_\xi}^{(\varrho)}, \ldots,\right.$$

$$\left.\xi_0^{(q)} = \xi_f, \ldots, 2 \leq \varrho \leq q\right\}$$

On the other hand, the semi-finite space interval $[0, \infty)$ is replaced with a truncated domain $[0, \eta_\infty]$, where η_∞ is the finite value chosen to allow the application of the method at infinity. The interval $I = [0, \eta_\infty]$ is then decomposed into p overlapping subintervals, denoted by

$$I_\varpi = [\eta_0^\varpi, \eta_{N_\eta}^\varpi], \quad \varpi = 1, 2, 3, \ldots, p, \tag{22}$$

where each subinterval I_ϖ is further discretised into $N_\eta + 1$ collocation points. The spatial domain decomposition is illustrated in Figure 2, where the last two points in the I_ϖ subinterval is noted to coincide with the first two points of the $I_{\varpi+1}$ subinterval, respectively, and remain common. For the overlap to be possible, each subinterval I_ϖ must be of the same length given by

$$L_\eta = \frac{\eta_\infty}{p + \frac{1}{2}(1 - p)(1 - \cos\frac{\pi}{N_\eta})}, \tag{23}$$

Moreover, the same number of collocation points $(N_\eta + 1)$ must be used in each subinterval. For the derivation of equation (24) the reader is refereed to Mkhatshwa et al. (2020). Applying QLM at each subinterval, the nonlinear PDEs (14)- (18) reduces to the
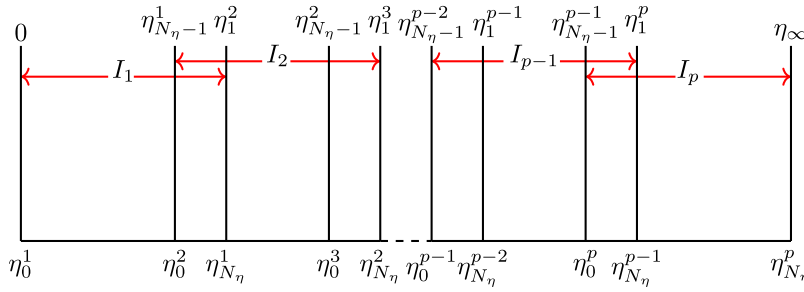
Figure 2. Overlapping grid ($\eta-$ domain)

following linear PDEs:

$$\delta_{0,r}\frac{\partial^3 f_{r+1}^{(\varpi,\varrho)}}{\partial\eta^3} + \delta_{1,r}\frac{\partial^2 f_{r+1}^{(\varpi,\varrho)}}{\partial\eta^2} + \delta_{2,r}\frac{\partial f_{r+1}^{(\varpi,\varrho)}}{\partial\eta} + \delta_{3,r}f_{r+1}^{(\varpi,\varrho)}$$

$$+ \delta_{4,r}G_{r+1}^{(\varpi,\varrho)} + \delta_{5,r}\frac{\partial\theta_{r+1}^{(\varpi,\varrho)}}{\partial\eta} + \delta_{6,r}\theta_{r+1}^{(\varpi,\varrho)}$$

$$+ \delta_{7,r}\phi_{r+1}^{(\varpi,\varrho)} + \delta_{8,r}\chi_{r+1}^{(\varpi,\varrho)} + \delta_{9,r}\frac{\partial}{\partial\eta}\left(\frac{\partial f_{r+1}^{(\varpi,\varrho)}}{\partial\xi}\right)$$

$$+ \delta_{10,r}\frac{\partial f_{r+1}^{(\varpi,\varrho)}}{\partial\xi} = \delta_{11,r}, \tag{24}$$

$$\iota_{0,r}\frac{\partial^2 G_{r+1}^{(\varpi,\varrho)}}{\partial y^2} + \iota_{1,r}\frac{\partial G_{r+1}^{(\varpi,\varrho)}}{\partial y} + \iota_{2,r}G_{r+1}^{(\varpi,\varrho)} + \iota_{3,r}\frac{\partial f_{r+1}^{(\varpi,\varrho)}}{\partial y}$$

$$+ \iota_{4,r}f_{r+1}^{(\varpi,\varrho)} + \iota_{5,r}\frac{\partial\theta_{r+1}^{(\varpi,\varrho)}}{\partial\eta} + \iota_{6,r}\theta_{r+1}^{(\varpi,\varrho)}$$

$$+ \iota_{7,r}\frac{\partial G_{r+1}^{(\varpi,\varrho)}}{\partial\xi} + \iota_{8,r}\frac{\partial f_{r+1}^{(\varpi,\varrho)}}{\partial\xi} = \iota_{9,r} \tag{25}$$

$$\kappa_{0,r}\frac{\partial^2\theta_{r+1}^{(\varpi,\varrho)}}{\partial\eta^2} + \kappa_{1,r}\frac{\partial\theta_{r+1}^{(\varpi,\varrho)}}{\partial\eta} + \kappa_{2,r}\theta_{r+1}^{(\varpi,\varrho)} + \kappa_{3,r}\frac{\partial^2 f_{r+1}^{(\varpi,\varrho)}}{\partial\eta^2}$$

$$+ \kappa_{4,r}\frac{\partial f_{r+1}^{(\varpi,\varrho)}}{\partial\eta} + \kappa_{5,r}f_{r+1}^{(\varpi,\varrho)} + \kappa_{6,r}\frac{\partial G_{r+1}^{(\varpi,\varrho)}}{\partial\eta}$$

$$+ \kappa_{7,r}G_{r+1}^{(\varpi,\varrho)} + \kappa_{8,r}\frac{\partial\phi_{r+1}^{(\varpi,\varrho)}}{\partial\eta} + \kappa_{9,r}\frac{\partial\theta_{r+1}^{(\varpi,\varrho)}}{\partial\xi}$$

$$+ \kappa_{10,r}\frac{\partial f_{r+1}^{(\varpi,\varrho)}}{\partial\xi} = \kappa_{11,r} \tag{26}$$

$$\frac{\partial^2\phi_{r+1}^{(\varpi,\varrho)}}{\partial\eta^2} + \varsigma_{1,r}\frac{\partial\phi_{r+1}^{(\varpi,\varrho)}}{\partial\eta} + \varsigma_{2,r}\phi_{r+1}^{(\varpi,\varrho)} + \varsigma_{3,r}\frac{\partial f_{r+1}^{(\varpi,\varrho)}}{\partial\eta}$$

$$+ \varsigma_{4,r}f_{r+1}^{(\varpi,\varrho)} + \varsigma_{5,r}\frac{\partial^2\theta_{r+1}^{(\varpi,\varrho)}}{\partial\eta^2}$$

$$+ \varsigma_{6,r}\frac{\partial\phi_{r+1}^{(\varpi,\varrho)}}{\partial\xi} + \varsigma_{7,r}\frac{\partial f_{r+1}^{(\varpi,\varrho)}}{\partial\xi} = \varsigma_{8,r}, \tag{27}$$

$$\frac{\partial^2\chi_{r+1}^{(\varpi,\varrho)}}{\partial\eta^2} + \gamma_{1,r}\frac{\partial\chi_{r+1}^{(\varpi,\varrho)}}{\partial\eta} + \gamma_{2,r}\chi_{r+1}^{(\varpi,\varrho)} + \gamma_{3,r}\frac{\partial f_{r+1}^{(\varpi,\varrho)}}{\partial\eta}$$

$$+ \gamma_{4,r}f_{r+1}^{(\varpi,\varrho)} + \gamma_{5,r}\frac{\partial^2\phi_{r+1}^{(\varpi,\varrho)}}{\partial\eta^2} + \gamma_{6,r}\frac{\partial\phi_{r+1}^{(\varpi,\varrho)}}{\partial\eta}$$

$$+ \gamma_{7,r}\frac{\partial\chi_{r+1}^{(\varpi,\varrho)}}{\partial\xi} + \gamma_{8,r}\frac{\partial f_{r+1}^{(\varpi,\varrho)}}{\partial\xi} = \gamma_{9,r}, \tag{28}$$

where r and $r+1$ signify previous and current iteration and the variable coefficients are defined as

$$\delta_{0,r} = \left(1 + \frac{1}{\beta}\right)e^{-\alpha\theta_r^{(\varpi,\varrho)}},$$

$$\delta_{1,r}^{(\varpi,\varrho)} = 3f_r^{(\varpi,\varrho)} + 2\xi\frac{\partial f_r^{(\varpi,\varrho)}}{\partial\xi} - \left(1 + \frac{1}{\beta}\right)\alpha\frac{\partial\theta_r^{(\varpi,\varrho)}}{\partial\eta}e^{-\alpha\theta_r^{(\varpi,\varrho)}},$$

$$\delta_{2,r}^{(\varpi,\varrho)} = -4\frac{\partial f_r^{(\varpi,\varrho)}}{\partial\eta} - \left(1 + \frac{1}{\beta}\right)\frac{2\xi^4}{DaGr_x^{1/2}}e^{-\alpha\theta_r^{(\varpi,\varrho)}}$$

$$- \frac{8Fs\xi^2}{Da}\frac{\partial f_r^{(\varpi,\varrho)}}{\partial\eta} - \frac{2M\xi\alpha_e}{\alpha_e^2 + \beta_e^2} - 2\xi\frac{\partial}{\partial\eta}\left(\frac{\partial f_r^{(\varpi,\varrho)}}{\partial\xi}\right),$$

$$\delta_{3,r}^{(\varpi,\varrho)} = 3\frac{\partial^2 f_r^{(\varpi,\varrho)}}{\partial\eta^2}, \ \delta_{4,r}^{(\varpi,\varrho)} = -\frac{2M\xi\beta_e}{\alpha_e^2 + \beta_e^2},$$

$$\delta_{5,r}^{(\varpi,\varrho)} = -\left(1 + \frac{1}{\beta}\right)\alpha\frac{\partial^2 f_r^{(\varpi,\varrho)}}{\partial\eta^2}e^{-\alpha\theta_r^{(\varpi,\varrho)}}, \ \delta_{6,r}^{(\varpi,\varrho)} = 2\delta_T$$

$$+ \left(1 + \frac{1}{\beta}\right)\alpha e^{-\alpha\theta_r^{(\varpi,\varrho)}}\left[\alpha\frac{\partial\theta_r^{(\varpi,\varrho)}}{\partial\eta}\frac{\partial^2 f_r^{(\varpi,\varrho)}}{\partial\eta^2}\right.$$

$$\left. + \frac{2\xi^4}{DaGr_x^{1/2}}\frac{\partial f_r^{(\varpi,\varrho)}}{\partial\eta} - \frac{\partial^3 f_r^{(\varpi,\varrho)}}{\partial\eta^3}\right], \delta_{7,r}^{(\varpi,\varrho)} = 2\delta_C,$$

$$\delta_{8,r}^{(\varpi,\varrho)} = 2\delta_N,$$

$$\delta_{9,r}^{(\varpi,\varrho)} = -2\xi\frac{\partial f_r^{(\varpi,\varrho)}}{\partial\eta}, \ \delta_{10,r}^{(\varpi,\varrho)} = 2\xi\frac{\partial^2 f_r^{(\varpi,\varrho)}}{\partial\eta^2},$$

$$\delta_{11,r}^{(\varpi,\varrho)} = \left(1 + \frac{1}{\beta}\right)\alpha^2\frac{\partial\theta_r^{(\varpi,\varrho)}}{\partial\eta}\frac{\partial^2 f_r^{(\varpi,\varrho)}}{\partial\eta^2}\theta_r^{(\varpi,\varrho)}e^{-\alpha\theta_r^{(\varpi,\varrho)}}$$

$$- \left(1 + \frac{1}{\beta}\right)e^{-\alpha\theta_r^{(\varpi,\varrho)}}\left[\alpha\frac{\partial^2 f_r^{(\varpi,\varrho)}}{\partial\eta^2}\frac{\partial\theta_r^{(\varpi,\varrho)}}{\partial\eta}\right.$$

$$+ \alpha\frac{\partial^3 f_r^{(\varpi,\varrho)}}{\partial\eta^3}\theta_r^{(\varpi,\varrho)} - \frac{2\alpha\xi^4}{DaGr_x^{1/2}}\frac{\partial f_r^{(\varpi,\varrho)}}{\partial\eta}\theta_r^{(\varpi,\varrho)}\right]$$

$$- \left(\frac{\partial f_r^{(\varpi,\varrho)}}{\partial\eta}\right)^2 + 3f_r^{(\varpi,\varrho)}\frac{\partial^3 f_r^{(\varpi,\varrho)}}{\partial\eta^3} - \frac{4Fs\xi^2}{Da}\left(\frac{\partial f_r^{(\varpi,\varrho)}}{\partial\eta}\right)^2$$

$$- 2\xi\frac{\partial f_r^{(\varpi,\varrho)}}{\partial\eta}\frac{\partial}{\partial\eta}\left(\frac{\partial f_r^{(\varpi,\varrho)}}{\partial\xi}\right) + 2\xi\frac{\partial^2 f_r^{(\varpi,\varrho)}}{\partial\eta^2}\frac{\partial f_r^{(\varpi,\varrho)}}{\partial\xi}, \ \iota_{0,r}$$

$$= \left(1 + \frac{1}{\beta}\right)e^{-\alpha\theta_r^{(\varpi,\varrho)}}, \ \iota_{1,r}^{(\varpi,\varrho)} = 3f_r^{(\varpi,\varrho)}$$

$$+ 2\xi \frac{\partial f_r^{(\varpi,\varrho)}}{\partial \xi} - \left(1 + \frac{1}{\beta}\right)\alpha \frac{\partial \theta_r^{(\varpi,\varrho)}}{\partial \eta} e^{-\alpha \theta_r^{(\varpi,\varrho)}},$$

$$\iota_{2,r}^{(\varpi,\varrho)} = -2\frac{\partial f_r^{(\varpi,\varrho)}}{\partial \eta} - \left(1 + \frac{1}{\beta}\right)\frac{2\xi^4}{DaGr_x^{1/2}} e^{-\alpha \theta_r^{(\varpi,\varrho)}}$$
$$- \frac{8Fs\xi^2}{Da} G_r^{(\varpi,\varrho)} - \frac{2M\xi\alpha_e}{\alpha_e^2 + \beta_e^2},$$

$$\iota_{3,r}^{(\varpi,\varrho)} = -2G_r^{(\varpi,\varrho)} + \frac{2M\xi\beta_e}{\alpha_e^2 + \beta_e^2} - 2\xi \frac{\partial G_r^{(\varpi,\varrho)}}{\partial \xi},$$

$$\iota_{4,r}^{(\varpi,\varrho)} = 3\frac{\partial G_r^{(\varpi,\varrho)}}{\partial \eta}, \quad \iota_{5,r}^{(\varpi,\varrho)} = -\left(1 + \frac{1}{\beta}\right)\alpha \frac{\partial G_r^{(\varpi,\varrho)}}{\partial \eta} e^{-\alpha \theta_r^{(\varpi,\varrho)}},$$

$$\iota_{6,r}^{(\varpi,\varrho)} = -\left(1 + \frac{1}{\beta}\right)\alpha \frac{\partial^2 G_r^{(\varpi,\varrho)}}{\partial \eta^2} e^{-\alpha \theta_r^{(\varpi,\varrho)}}$$
$$+ \left(1 + \frac{1}{\beta}\right)\alpha e^{-\alpha \theta_r^{(\varpi,\varrho)}}\left[\alpha \frac{\partial \theta_r^{(\varpi,\varrho)}}{\partial \eta} \frac{\partial G_r^{(\varpi,\varrho)}}{\partial \eta}\right.$$
$$\left. + \frac{2\xi^4}{DaGr_x^{1/2}} G_r^{(\varpi,\varrho)}\right], \iota_{7,r}^{(\varpi,\varrho)} = -2\xi \frac{\partial f_r^{(\varpi,\varrho)}}{\partial \eta},$$

$$\iota_{8,r}^{(\varpi,\varrho)} = -2\xi \frac{\partial G_r^{(\varpi,\varrho)}}{\partial \eta},$$

$$\iota_{9,r}^{(\varpi,\varrho)} = 3f_r^{(\varpi,\varrho)} \frac{\partial G_r^{(\varpi,\varrho)}}{\partial \eta} + \left(1 + \frac{1}{\beta}\right)\theta_r^{(\varpi,\varrho)} e^{-\alpha \theta_r^{(\varpi,\varrho)}}$$
$$\times \left[\alpha^2 \frac{\partial \theta_r^{(\varpi,\varrho)}}{\partial \eta} \frac{\partial G_r^{(\varpi,\varrho)}}{\partial \eta} + \frac{2\alpha\xi^4}{DaGr_x^{1/2}} G_r^{(\varpi,\varrho)}\right]$$
$$- \left(1 + \frac{1}{\beta}\right)\alpha e^{-\alpha \theta_r^{(\varpi,\varrho)}}\left[\frac{\partial G_r^{(\varpi,\varrho)}}{\partial \eta} \frac{\partial \theta_r^{(\varpi,\varrho)}}{\partial \eta} + \frac{\partial^2 G_r^{(\varpi,\varrho)}}{\partial \eta^2}\theta_r^{(\varpi,\varrho)}\right]$$
$$- \frac{4Fs\xi^2}{Da}\left(G_r^{(\varpi,\varrho)}\right)^2 - 2G_r^{(\varpi,\varrho)} \frac{\partial f_r^{(\varpi,\varrho)}}{\partial \eta}$$
$$- 2\xi \frac{\partial f_r^{(\varpi,\varrho)}}{\partial \eta} \frac{\partial G_r^{(\varpi,\varrho)}}{\partial \xi} + 2\xi \frac{\partial G_r^{(\varpi,\varrho)}}{\partial \eta} \frac{\partial f_r^{(\varpi,\varrho)}}{\partial \xi},$$

$$\kappa_{0,r}^{(\varpi,\varrho)} = 1 + 4Rd(\theta_w - 1)\theta_r^{(\varpi,\varrho)} + 4Rd(\theta_w - 1)^2 \left(\theta_r^{(\varpi,\varrho)}\right)^2$$
$$+ \frac{4}{3}Rd + \frac{4}{3}Rd(\theta_w - 1)^3 \left(\theta_r^{(\varpi,\varrho)}\right)^3 + \varepsilon\theta_r^{(\varpi,\varrho)}, \kappa_{1,r}^{(\varpi,\varrho)} = 3Prf_r^{(\varpi,\varrho)}$$
$$+ 8Rd(\theta_w - 1)\frac{\partial \theta_r^{(\varpi,\varrho)}}{\partial \eta} + 2NtPr\frac{\partial \theta_r^{(\varpi,\varrho)}}{\partial \eta}$$
$$+ \left[2\varepsilon + 16Rd(\theta_w - 1)^2\theta_r^{(\varpi,\varrho)}\right]\frac{\partial \theta_r^{(\varpi,\varrho)}}{\partial \eta}$$
$$+ 8Rd(\theta_w - 1)^3 \left(\theta_r^{(\varpi,\varrho)}\right)^2 \frac{\partial \theta_r^{(\varpi,\varrho)}}{\partial \eta} + NbPr\frac{\partial \phi_r^{(\varpi,\varrho)}}{\partial \eta} + 2Pr\xi$$
$$+ \frac{\partial f_r^{(\varpi,\varrho)}}{\partial \xi}, \kappa_{2,r}^{(\varpi,\varrho)} = \varepsilon \frac{\partial^2 \theta_r^{(\varpi,\varrho)}}{\partial \eta^2} + 4Rd(\theta_w - 1)\frac{\partial^2 \theta_r^{(\varpi,\varrho)}}{\partial \eta^2}$$
$$+ 8Rd(\theta_w - 1)^2\theta_r^{(\varpi,\varrho)} \frac{\partial^2 \theta_r^{(\varpi,\varrho)}}{\partial \eta^2} + 2\xi Pr\lambda$$
$$- 4PrEc\alpha\xi^2\left(1 + \frac{1}{\beta}\right)e^{-\alpha \theta_r^{(\varpi,\varrho)}}$$

$$\times \left[\left(\frac{\partial^2 f_r^{(\varpi,\varrho)}}{\partial \eta^2}\right)^2 + \left(\frac{\partial G_r^{(\varpi,\varrho)}}{\partial \eta}\right)^2\right]$$
$$+ 4Rd(\theta_w - 1)^3 \left(\theta_r^{(\varpi,\varrho)}\right)^2 \frac{\partial^2 \theta_r^{(\varpi,\varrho)}}{\partial \eta^2}$$
$$+ 8Rd\left[(\theta_w - 1)^2 + (\theta_w - 1)^3\theta_r^{(\varpi,\varrho)}\right]\left(\frac{\partial \theta_r^{(\varpi,\varrho)}}{\partial \eta}\right)^2,$$

$$\kappa_{3,r}^{(\varpi,\varrho)} = 8PrEc\xi^2\left(1 + \frac{1}{\beta}\right)\frac{\partial^2 f_r^{(\varpi,\varrho)}}{\partial \eta^2} e^{-\alpha \theta_r^{(\varpi,\varrho)}},$$

$$\kappa_{4,r}^{(\varpi,\varrho)} = \frac{8PrEc\xi^3}{\alpha_e^2 + \beta_e^2}\frac{\partial f_r^{(\varpi,\varrho)}}{\partial \eta} - 2Pr\xi \frac{\partial \theta_r^{(\varpi,\varrho)}}{\partial \xi},$$

$$\kappa_{6,r}^{(\varpi,\varrho)} = 8PrEc\xi^2\left(1 + \frac{1}{\beta}\right)\frac{\partial G_r^{(\varpi,\varrho)}}{\partial \eta} e^{-\alpha \theta_r^{(\varpi,\varrho)}},$$

$$\kappa_{5,r}^{(\varpi,\varrho)} = 3Pr\frac{\partial \theta_r^{(\varpi,\varrho)}}{\partial \eta}, \kappa_{7,r}^{(\varpi,\varrho)} = \frac{8PrEc\xi^3}{\alpha_e^2 + \beta_e^2}G_r^{(\varpi,\varrho)},$$

$$\kappa_{8,r}^{(\varpi,\varrho)} = NbPr\frac{\partial \theta_r^{(\varpi,\varrho)}}{\partial \eta}, \kappa_{9,r}^{(\varpi,\varrho)} = -2Pr\xi \frac{\partial f_r^{(\varpi,\varrho)}}{\partial \eta},$$

$$\kappa_{10,r}^{(\varpi,\varrho)} = 2Pr\xi \frac{\partial \theta_r^{(\varpi,\varrho)}}{\partial \eta}, \kappa_{11,r}^{(\varpi,\varrho)} = \varepsilon\theta_r^{(\varpi,\varrho)} \frac{\partial^2 \theta_r^{(\varpi,\varrho)}}{\partial \eta^2}$$
$$+ 3Prf_r^{(\varpi,\varrho)} \frac{\partial \theta_r^{(\varpi,\varrho)}}{\partial \eta} + \left(\frac{\partial \theta_r^{(\varpi,\varrho)}}{\partial \eta}\right)^2 [\varepsilon + NtPr]$$
$$+ NbPr\frac{\partial \theta_r^{(\varpi,\varrho)}}{\partial \eta} \frac{\partial \phi_r^{(\varpi,\varrho)}}{\partial \eta} + 4Rd(\theta_w - 1)\theta_r^{(\varpi,\varrho)} \frac{\partial^2 \theta_r^{(\varpi,\varrho)}}{\partial \eta^2}$$
$$+ \frac{4MPrEc\xi^3}{\alpha_e^2 + \beta_e^2}\left[\left(\frac{\partial f_r^{(\varpi,\varrho)}}{\partial \eta}\right)^2 + \left(G_r^{(\varpi,\varrho)}\right)^2\right]$$
$$- 2Pr\xi \frac{\partial f_r^{(\varpi,\varrho)}}{\partial \eta} \frac{\partial \theta_r^{(\varpi,\varrho)}}{\partial \xi} + 2Pr\xi \frac{\partial \theta_r^{(\varpi,\varrho)}}{\partial \eta} \frac{\partial f_r^{(\varpi,\varrho)}}{\partial \xi}$$
$$+ 4PrEc\xi^2\left(1 + \frac{1}{\beta}\right)e^{-\alpha \theta_r^{(\varpi,\varrho)}}$$
$$\times \left[\frac{\partial^2 f_r^{(\varpi,\varrho)}}{\partial \eta^2} + \frac{\partial G_r^{(\varpi,\varrho)}}{\partial \eta}\right]$$
$$- 4PrEc\xi^2\alpha\left(1 + \frac{1}{\beta}\right)e^{-\alpha \theta_r^{(\varpi,\varrho)}}\theta_r^{(\varpi,\varrho)}\left[\frac{\partial^2 f_r^{(\varpi,\varrho)}}{\partial \eta^2} + \frac{\partial G_r^{(\varpi,\varrho)}}{\partial \eta}\right]$$
$$+ 12Rd(\theta_w - 1)^3 \left(\theta_r^{(\varpi,\varrho)}\right)^2 \left(\frac{\partial \theta_r^{(\varpi,\varrho)}}{\partial \eta}\right)^2$$
$$+ 4Rd(\theta_w - 1)\left[(\theta_w - 1)\left(\theta_r^{(\varpi,\varrho)}\right)^2\right.$$
$$\times \left[2 + (\theta_w - 1)\left(\theta_r^{(\varpi,\varrho)}\right)\right]\frac{\partial^2 \theta_r^{(\varpi,\varrho)}}{\partial \eta^2}$$
$$\left. + \left[1 + 4(\theta_w - 1)\theta_r^{(\varepsilon,\varrho)}\right]\left(\frac{\partial \theta_r^{(\varpi,\varrho)}}{\partial \eta}\right)^2\right],$$

$$\varsigma_{1,r}^{(\varpi,\varrho)} = 3Lef_r^{(\varpi,\varrho)} + 2Le\xi\frac{\partial f_r^{(\varpi,\varrho)}}{\partial \xi}, \quad \varsigma_{2,r}^{(\varpi,\varrho)} = -\xi LeK,$$

$$\varsigma_{3,r}^{(\varpi,\varrho)} = -2Le\xi\frac{\partial \phi_r^{(\varpi,\varrho)}}{\partial \xi}, \quad \varsigma_{4,r}^{(\varpi,\varrho)} = 3Le\frac{\partial \phi_r^{(\varpi,\varrho)}}{\partial \eta},$$

$$\varsigma_{5,r}^{(\varpi,\varrho)} = \frac{Nt}{Nb}, \quad \varsigma_{6,r}^{(\varpi,\varrho)} = -2Le\xi\frac{\partial f_r^{(\varpi,\varrho)}}{\partial \eta},$$

$$\varsigma_{7,r}^{(\varpi,\varrho)} = 2Le\xi\frac{\partial \phi_r^{(\varpi,\varrho)}}{\partial \eta}, \quad \varsigma_{8,r}^{(\varpi,\varrho)} = 3Lef_r^{(\varpi,\varrho)}\frac{\partial \phi_r^{(\varpi,\varrho)}}{\partial \eta}$$

$$- 2Le\xi\frac{\partial f_r^{(\varpi,\varrho)}}{\partial \eta}\frac{\partial \phi_r^{(\varpi,\varrho)}}{\partial \xi} + 2Le\xi\frac{\partial \phi_r^{(\varpi,\varrho)}}{\partial \eta}\frac{\partial f_r^{(\varpi,\varrho)}}{\partial \xi},$$

$$\gamma_{1,r}^{(\varpi,\varrho)} = 3Lbf_r^{(\varpi,\varrho)} - Pe\frac{\partial \phi_r^{(\varpi,\varrho)}}{\partial \eta} + 2Lb\xi\frac{\partial f_r^{(\varpi,\varrho)}}{\partial \xi},$$

$$\gamma_{2,r}^{(\varpi,\varrho)} = -Pe\frac{\partial^2 \phi_r^{(\varpi,\varrho)}}{\partial \eta^2}, \gamma_{3,r}^{(\varpi,\varrho)} = -2Lb\xi\frac{\partial \chi_r^{(\varpi,\varrho)}}{\partial \xi},$$

$$\gamma_{4,r}^{(\varpi,\varrho)} = 3Lb\frac{\partial \chi_r^{(\varpi,\varrho)}}{\partial \eta}, \gamma_{5,r}^{(\varpi,\varrho)} = -Pe\chi_r^{(\varpi,\varrho)} - Pe\Omega,$$

$$\gamma_{6,r}^{(\varpi,\varrho)} = -Pe\frac{\partial \chi_r^{(\varpi,\varrho)}}{\partial \eta}, \quad \gamma_{7,r}^{(\varpi,\varrho)} = -2Lb\xi\frac{\partial f_r^{(\varpi,\varrho)}}{\partial \eta},$$

$$\gamma_{8,r}^{(\varpi,\varrho)} = 2Lb\xi\frac{\partial \chi_r^{(\varpi,\varrho)}}{\partial \eta}, \gamma_{9,r}^{(\varpi,\varrho)} = 3Lbf_r^{(\varpi,\varrho)}\frac{\partial \chi_r^{(\varpi,\varrho)}}{\partial \eta}$$

$$- Pe\chi_r^{(\varpi,\varrho)}\frac{\partial^2 \phi_r^{(\varpi,\varrho)}}{\partial \eta^2} - Pe\frac{\partial \phi_r^{(\varpi,\varrho)}}{\partial \eta}\frac{\partial \chi_r^{(\varpi,\varrho)}}{\partial \eta}$$

$$- 2Lb\xi\frac{\partial f_r^{(\varpi,\varrho)}}{\partial \eta}\frac{\partial \chi_r^{(\varpi,\varrho)}}{\partial \xi} + 2Lb\xi\frac{\partial \chi_r^{(\varpi,\varrho)}}{\partial \eta}\frac{\partial f_r^{(\varpi,\varrho)}}{\partial \xi},$$

Since the spectral collocation method is valid in the domain $[-1, 1]$, the time interval J_ϱ and space interval I_ϖ are respectively transformed into $\hat{\xi} \in [-1, 1]$ and $\hat{\eta} \in [-1, 1]$, using the linear transformations

$$\xi_j^\varrho = \frac{1}{2}(\xi_\varrho - \xi_{\varrho-1})\hat{\xi}_j + \frac{1}{2}(\xi_\varrho + \xi_{\varrho-1}), \ \left\{\hat{\xi}_j\right\}_{j=0}^{N_\xi} = \cos\left(\frac{\pi j}{N_\xi}\right),$$

$$\eta_i^\varpi = \frac{L_\eta}{2}(\hat{\eta}_i + 1), \quad \left\{\hat{\eta}_i\right\}_{i=0}^{N_\eta} = \cos\left(\frac{\pi i}{N_\eta}\right). \tag{29}$$

We suppose that at each subdomain, the needed solution, for instance $f(\eta, \xi)$ can be approximated by a bivariate Lagrange interpolation polynomial of the form

$$f^{(\varpi,\varrho)}(\eta, \xi) \approx \sum_{k=0}^{N_\eta}\sum_{s=0}^{N_\xi} f^{(\varpi,\varrho)}(\hat{\eta}_k, \hat{\xi}_s)\mathcal{L}_k(\hat{\eta})\mathcal{L}_s(\hat{\xi}), \tag{30}$$

where the functions $\mathcal{L}_k(\eta)$ and $\mathcal{L}_s(\xi)$ are the well known characteristic Lagrange cardinal polynomial based on the chebyshev-Gauss-Lobatto points (Canuto et al. 2006). The first derivative of $f^{(\varpi,\varrho)}(\eta, \xi)$ with respect to η and ξ at the Chebyshev-Gauss-Lobatto points $(\hat{\eta}_i, \hat{\xi}_j)$ are computed as

$$\frac{\partial f_{r+1}^{(\varpi,\varrho)}}{\partial \eta}\bigg|_{(\eta=\eta_i,\xi=\xi_j)} = \sum_{k=0}^{N_\eta} \hat{D}_{i,k}^{(\varpi)}F_{r+1}^{(\varpi,\varrho)}(\hat{\eta}_k, \hat{\xi}_j) = \mathbf{DF}_{j,r+1}^{(\varpi,\varrho)},$$

$$\frac{\partial f_{r+1}^{(\varpi,\varrho)}}{\partial \xi}\bigg|_{(\eta=\eta_i,\xi=\xi_j)} = \left(\frac{2}{\xi_\varrho - \xi_{\varrho-1}}\right)\sum_{s=0}^{N_\xi} \hat{d}_{j,s}F_{r+1}^{(\varpi,\varrho)}(\hat{\eta}_i, \hat{\xi}_s)$$

$$= \sum_{s=0}^{N_\xi} \mathbf{d}_{j,s}\mathbf{F}_{s,r+1}^{(\varpi,\varrho)}, \tag{31}$$

where $\hat{d}_{j,s}(j, s = 0, 1, \ldots, N_\xi)$ are entries of the standard first order Chebyshev differentiation matrix $\mathbf{d} = \left(\frac{2}{\xi_\varrho - \xi_{\varrho-1}}\right)[d_{i,j}]$ of size $(N_\xi + 1) \times (N_\xi + 1)$ (Canuto et al. 2006), $\hat{D}_{i,k}^{(\varpi)} = \frac{2}{\eta_{N_\eta}^\varpi - \eta_0^\varpi} D_{i,k}(i, k = 0, 1, \ldots, N_\eta)$ with $D_{i,k}$ being the standard first order Chebyshev-Gauss-Lobatto differentiation matrix of size $(N_\eta + 1) \times (N_\eta + 1)$. The vector $\mathbf{F}_j^{(\varpi,\varrho)}$ is defined as

$$\mathbf{F}_j^{(\varpi,\varrho)} = \left[f^{(\varpi,\varrho)}(\eta_0^\varpi, \xi_j), f^{(\varpi,\varrho)}(\eta_1^\varpi, \xi_j), \ldots, f^{(\varpi,\varrho)}(\eta_{N_\eta}^\varpi, \xi_j)\right]^T, \tag{32}$$

where T is the transpose. Since the last two points in the ϖth subinterval and the first two points in the $(\varpi + 1)^{th}$ subinterval overlap and remains common, the differentiation matrix $\mathbf{D}$ for overlapping grid in η is assembled by carefully discarding the rows corresponding to the recurrent points as shown below:

$$\begin{bmatrix} \hat{D}_{0,0}^{(p)} & \hat{D}_{0,1}^{(p)} & \cdots & \hat{D}_{0,N_\eta-1}^{(p)} & \hat{D}_{0,N_\eta}^{(p)} \\ \hat{D}_{1,0}^{(p)} & \hat{D}_{1,1}^{(p)} & \cdots & \hat{D}_{1,N_\eta-1}^{(p)} & \hat{D}_{1,N_\eta}^{(p)} \\ \ddots & \ddots & \ddots & \ddots & \ddots \\ \hat{D}_{N_\eta-1,0}^{(p)} & \hat{D}_{N_\eta-1,1}^{(p)} & \cdots & \hat{D}_{N_\eta-1,N_\eta-1}^{(p)} & \hat{D}_{N_\eta-1,N_\eta}^{(p)} \\ & & & \hat{D}_{1,0}^{(p-1)} & \hat{D}_{1,1}^{(p-1)} & \cdots \\ & & & \hat{D}_{2,0}^{(p-1)} & \hat{D}_{2,1}^{(p-1)} & \cdots \\ & & & \ddots & \ddots & \ddots \\ & & & \hat{D}_{N_\eta-1,0}^{(p-1)} & \hat{D}_{N_\eta-1,1}^{(p-1)} & \cdots \end{bmatrix}$$

$$\begin{bmatrix} \hat{D}_{1,N_\eta-1}^{(p-1)} & \hat{D}_{1,N_\eta}^{(p-1)} \\ \hat{D}_{2,N_\eta-1}^{(p-1)} & \hat{D}_{2,N_\eta}^{(p-1)} \\ \ddots & \ddots \\ \hat{D}_{N_\eta-1,N_\eta-1}^{(p-1)} & \hat{D}_{N_\eta-1,N_\eta}^{(p-1)} \\ \ddots & \ddots \\ \hat{D}_{1,0}^{(1)} & \hat{D}_{1,1}^{(1)} & \cdots & \hat{D}_{1,N_\eta-1}^{(1)} & \hat{D}_{1,N_\eta}^{(1)} \\ \hat{D}_{2,0}^{(1)} & \hat{D}_{2,1}^{(1)} & \cdots & \hat{D}_{2,N_\eta-1}^{(1)} & \hat{D}_{2,N_\eta}^{(1)} \\ \ddots & \ddots & \ddots & \ddots & \ddots \\ \hat{D}_{N_\eta,0}^{(1)} & \hat{D}_{N_\eta,1}^{(1)} & \cdots & \hat{D}_{N_\eta,N_\eta-1}^{(1)} & \hat{D}_{N_\eta,N_\eta}^{(1)} \end{bmatrix}, \tag{33}$$

where the empty entries of coefficient matrix $\mathbf{D}$ are zeros (leading to sparse matrix) and $\hat{D}^{(\varpi)}$ represents the Chebyshev differentiation matrix in the ϖth subinterval in space. It is worth noting

that the spatial derivative operator becomes a full matrix if only a single domain is used in the calculation. The size of matrix $\mathbf{D}$ is $(\Lambda + 1) \times (\Lambda + 1)$, where $\Lambda = N_\eta + (N_\eta - 1) \times (p - 1)$ is the total number of collocation points in the entire spatial domain. The higher order (n^{th}) differentiation matrix with respect to η can be obtained using matrix multiplication as follows:

$$\left. \frac{\partial^n f_{r+1}^{(\varpi,\varrho)}}{\partial \eta^n} \right|_{(\eta=\eta_i, \xi=\xi_j)} = \sum_{k=0}^{N_\eta} \left[\hat{D}_{i,k}^{(\varpi)} \right]^n F_{r+1}^{(\varpi,\varrho)}(\hat{\eta}_k, \hat{\xi}_j) = \mathbf{D}^n \mathbf{F}_{j,r+1}^{(\varpi,\varrho)},$$
(34)

Applying the spectral method by evaluating equations (24)–(28) at the collocation points and making use of assembled differentiation matrices and the initial condition gives the following matrix equations:

$$A_{11}^{(i)} \mathbf{F}_{i,r+1}^{(\varpi,\varrho)} + A_{12}^{(i)} \mathbf{G}_{i,r+1}^{(\varpi,\varrho)} + A_{13}^{(i)} \Theta_{i,r+1}^{(\varpi,\varrho)} + A_{14}^{(i)} \Phi_{i,r+1}^{(\varpi,\varrho)} + A_{15}^{(i)} \chi_{i,r+1}^{(\varpi,\varrho)}$$
$$+ \delta_{9,r}^{(i)} \sum_{j=0}^{N_\xi-1} \mathbf{d}_{i,j} \mathbf{DF}_{j,r+1}^{(\varpi,\varrho)} + \delta_{10,r}^{(i)} \sum_{j=0}^{N_\xi-1} \mathbf{d}_{i,j} \mathbf{F}_{j,r+1}^{(\varpi,\varrho)} = \mathbf{R}_{1,r}^{(i)},$$
(35)

$$A_{21}^{(i)} \mathbf{F}_{i,r+1}^{(\varpi,\varrho)} + A_{22}^{(i)} \mathbf{G}_{i,r+1}^{(\varpi,\varrho)} + A_{23}^{(i)} \Theta_{i,r+1}^{(\varpi,\varrho)} + \iota_{7,r}^{(i)} \sum_{j=0}^{N_\xi-1} \mathbf{d}_{i,j} \mathbf{G}_{j,r+1}^{(\varpi,\varrho)}$$
$$+ \iota_{8,r}^{(i)} \sum_{j=0}^{N_\xi-1} \mathbf{d}_{i,j} \mathbf{F}_{j,r+1}^{(\varpi,\varrho)} = \mathbf{R}_{2,r}^{(i)},$$
(36)

$$A_{31}^{(i)} \mathbf{F}_{i,r+1}^{(\varpi,\varrho)} + A_{32}^{(i)} \mathbf{G}_{i,r+1}^{(\varpi,\varrho)} + A_{33}^{(i)} \Theta_{i,r+1}^{(\varpi,\varrho)} + A_{34}^{(i)} \Phi_{i,r+1}^{(\varpi,\varrho)}$$
$$+ \kappa_{9,r}^{(i)} \sum_{j=0}^{N_\xi-1} \mathbf{d}_{i,j} \Theta_{j,r+1}^{(\varpi,\varrho)} + \kappa_{10,r}^{(i)} \sum_{j=0}^{N_\xi-1} \mathbf{d}_{i,j} \mathbf{F}_{j,r+1}^{(\varpi,\varrho)} = \mathbf{R}_{3,r}^{(i)},$$
(37)

$$A_{41}^{(i)} \mathbf{F}_{i,r+1}^{(\varpi,\varrho)} + A_{43}^{(i)} \Theta_{i,r+1}^{(\varpi,\varrho)} + A_{44}^{(i)} \Phi_{i,r+1}^{(\varpi,\varrho)} + \varsigma_{6,r}^{(i)} \sum_{j=0}^{N_\xi-1} \mathbf{d}_{i,j} \Phi_{j,r+1}^{(\varpi,\varrho)}$$
$$+ \varsigma_{7,r}^{(i)} \sum_{j=0}^{N_\xi-1} \mathbf{d}_{i,j} \mathbf{F}_{j,r+1}^{(\varpi,\varrho)} = \mathbf{R}_{4,r}^{(i)},$$
(38)

$$A_{51}^{(i)} \mathbf{F}_{i,r+1}^{(\varpi,\varrho)} + A_{54}^{(i)} \Phi_{i,r+1}^{(\varpi,\varrho)} + A_{55}^{(i)} \chi_{i,r+1}^{(\varpi,\varrho)} + \gamma_{7,r}^{(i)} \sum_{j=0}^{N_\xi-1} \mathbf{d}_{i,j} \chi_{j,r+1}^{(\varpi,\varrho)}$$
$$+ \gamma_{8,r}^{(i)} \sum_{j=0}^{N_\xi-1} \mathbf{d}_{i,j} \mathbf{F}_{j,r+1}^{(\varpi,\varrho)} = \mathbf{R}_{5,r}^{(i)},$$
(39)

where

$$A_{11}^{(i)} = \delta_{0,r}^{(i)} \mathbf{D}^{(3)} + \delta_{1,r}^{(i)} \mathbf{D}^{(2)} + \delta_{2,r}^{(i)} \mathbf{D} + \delta_{3,r}^{(i)} \mathbf{I}, \; A_{12}^{(i)} = \delta_{4,r}^{(i)} \mathbf{I},$$

$$A_{13}^{(i)} = \delta_{5,r}^{(i)} \mathbf{D} + \delta_{6,r}^{(i)} \mathbf{I}, \; A_{14}^{(i)} = \delta_{7,r}^{(i)} \mathbf{I},$$

$$A_{15}^{(i)} = \delta_{8,r}^{(i)} \mathbf{I}, \; A_{21}^{(i)} = \iota_{3,r}^{(i)} \mathbf{D} + \iota_{4,r}^{(i)} \mathbf{I}, \; A_{22}^{(i)} = \iota_{0,r}^{(i)} \mathbf{D}^{(2)} + \iota_{1,r}^{(i)} \mathbf{D} + \iota_{2,r}^{(i)} \mathbf{I},$$

$$A_{23}^{(i)} = \iota_{5,r}^{(i)} \mathbf{D} + \iota_{6,r}^{(i)} \mathbf{I},$$

$$A_{31}^{(i)} = \kappa_{3,r}^{(i)} \mathbf{D}^{(2)} + \kappa_{4,r}^{(i)} \mathbf{D} + \kappa_{5,r}^{(i)} \mathbf{I}, \; A_{32}^{(i)} = \kappa_{6,r}^{(i)} \mathbf{D} + \kappa_{7,r}^{(i)} \mathbf{I},$$

$$A_{33}^{(i)} = \kappa_{0,r}^{(i)} \mathbf{D}^{(2)} + \kappa_{1,r}^{(i)} \mathbf{D} + \kappa_{2,r}^{(i)} \mathbf{I},$$

$$A_{34}^{(i)} = \kappa_{8,r}^{(i)} \mathbf{D}, \; A_{41}^{(i)} = \varsigma_{3,r}^{(i)} \mathbf{D} + \varsigma_{4,r}^{(i)} \mathbf{I}, \; A_{43}^{(i)} = \varsigma_{5,r}^{(i)} \mathbf{D}^{(2)},$$

$$A_{44}^{(i)} = \mathbf{D}^{(2)} + \varsigma_{1,r}^{(i)} \mathbf{D} + \varsigma_{2,r}^{(i)} \mathbf{I},$$

$$A_{51}^{(i)} = \gamma_{3,r}^{(i)} \mathbf{D} + \gamma_{4,r}^{(i)} \mathbf{I}, \; A_{54}^{(i)} = \gamma_{5,r}^{(i)} \mathbf{D}^{(2)} + \gamma_{6,r}^{(i)} \mathbf{D},$$

$$A_{55}^{(i)} = \mathbf{D}^{(2)} + \gamma_{1,r}^{(i)} \mathbf{D} + \gamma_{2,r}^{(i)} \mathbf{I},$$

$$\mathbf{R}_{1,r}^{(i)} = \delta_{11,r}^{(i)} - \delta_{10,r}^{(i)} \mathbf{d}_{i,N_\xi} \mathbf{F}_{N_\xi,r}^{(\varpi,\varrho)} - \delta_{9,r}^{(i)} \mathbf{d}_{i,N_\xi} \mathbf{DF}_{N_\xi,r}^{(\varpi,\varrho)},$$

$$\mathbf{R}_{2,r}^{(i)} = \iota_{9,r}^{(i)} - \iota_{7,r}^{(i)} \mathbf{d}_{i,N_\xi} \mathbf{G}_{N_\xi,r}^{(\varpi,\varrho)} - \iota_{8,r}^{(i)} \mathbf{d}_{i,N_\xi} \mathbf{F}_{N_\xi,r}^{(\varpi,\varrho)},$$

$$\mathbf{R}_{3,r}^{(i)} = \kappa_{11,r}^{(i)} - \kappa_{9,r}^{(i)} \mathbf{d}_{i,N_\xi} \Theta_{N_\xi,r}^{(\varpi,\varrho)} - \kappa_{10,r}^{(i)} \mathbf{d}_{i,N_\xi} \mathbf{F}_{N_\xi,r}^{(\varpi,\varrho)},$$

$$\mathbf{R}_{4,r}^{(i)} = \varsigma_{8,r}^{(i)} - \varsigma_{6,r}^{(i)} \mathbf{d}_{i,N_\xi} \Phi_{N_\xi,r}^{(\varpi,\varrho)} - \varsigma_{7,r}^{(i)} \mathbf{d}_{i,N_\xi} \mathbf{F}_{N_\xi,r}^{(\varpi,\varrho)},$$

$$\mathbf{R}_{5,r}^{(i)} \gamma_{9,r}^{(i)} - \gamma_{7,r}^{(i)} \mathbf{d}_{i,N_\xi} \chi_{N_\xi,r}^{(\varpi,\varrho)} - \gamma_{8,r}^{(i)} \mathbf{d}_{i,N_\xi} \mathbf{F}_{N_\xi,r}^{(\varpi,\varrho)},$$

Here, $\mathbf{I}$ is an $(\Lambda + 1)(\Lambda + 1)$ identity matrix, $\mathbf{F}_{i,r+1}, \mathbf{G}_{i,r+1}, \Theta_{i,r+1}, \Phi_{i,r+1}$ and $\chi_{i,r+1}$ denote values of f, G, θ, ϕ and χ at the collocation points. The boundary conditions are imposed on equation (35)–(39) for each $i = 0, 1, 2, \ldots, N_\xi$. After imposing the boundary conditions the resulting equations can be written as a matrix system that can be solved iteratively to give the approximate solutions for $f(\eta, \xi), G(\eta, \xi), \theta(\eta, \xi), \phi(\eta, \xi)$ and $\chi(\eta, \xi)$.

4. Results and discussion

This section presents the numerical results computed using the method discussed in the previous section. In the entire computational process, $N_\eta = 20$ and $N_\xi = 5$ collocation points in space and time, respectively, were found to be sufficient to give accurate and consistent results. The time and spatial domains were each decomposed into $p = q = 5$ subintervals, while the edge of the boundary was taken as $\eta_\infty = 15$. The values of physical parameters where chosen as $\beta = 1, \alpha = 0.5, \varepsilon = 0.2, \delta_T = 0.5, \delta_C = 0.5, \delta_N = 1, Gr_x = 1, Pr = 0.71, Le = 0.6, K = 0.5, Da = 1, Fs = 0.1, Ec = 0.1, M = 0.5, \beta_i = 0.4, \beta_e = 0.5, \Omega = 0.2, Rd = 0.2, \theta_w = 1.2, Nt = 0.5, Nb = 0.5, \lambda = 0.01, Lb = 0.5$ and $Pe = 0.3$. These values were fixed throughout the numerical study unless otherwise stated. In order to validate the accuracy of the OMD-BSQLM, the obtained numerical results were compared with previously published results for the limiting cases. The results are presented in Table 1 and Table 2, and are in satisfactory accordance. It is worth mentioning that Abo-Eldahab and El-Aziz (Abo-Eldahab and Aziz 2005) employed fifth-order Runge–Kutta–Fehlberg scheme with Newton Raphson shooting method, whereas (Gaffar, Prasad, and Reddy 2016) used Keller-Box implicit difference method in solving the boundary value problems governing the flow. However, spectral collocation based methods are known to be highly accurate, more efficient and low computational cost than traditional methods such as the Keller-Box implicit difference method (Canuto et al. 2006).

Table 1. Comparison of $-\theta'(0,0)$ for various values Pr when $M = \beta_e = K = \beta_i = Le = Lb = Pe = \Omega = \delta_T = \delta_C = \delta_N = Ec = Fs = Rd = Nt = Nb = \lambda = Le = \xi = 0, Gr_x \to \infty, Da \to \infty$ and $\beta \to \infty$.

Pr	Takhar, Gorla, and Soundal-gekar (1996)	Abo-Eldahab and Aziz (2005)	Gaffar, Prasad, and Reddy (2016)	Present results
0.5	0.4412	0.441191	0.4410	0.4411670
0.733	–	0.504599	0.5043	0.5046342
0.72	0.5079	0.507872	0.5077	0.5079077
0.9	0.5465	0.546501	0.5463	0.5465363

When applied to problems with smooth solutions, they use few grid points and require minimal computational time to generate accurate solutions, thus they are better than traditional methods. The excellent agreement demonstrated by the set of results justify the reliability, applicability and accuracy of the present method.

To assess the convergence of the method, we have taken the norm of difference in the values of two successive iterations. The error norm between two successive iterations is defined as

$$E_\Omega = \max_{0 \leq i \leq N_\xi} ||\boldsymbol{\Omega}_{i,r+1} - \boldsymbol{\Omega}_{i,r}||_\infty, \qquad (40)$$

where $\boldsymbol{\Omega} = \{\mathbf{F}^{(\varpi,\varrho)}, \mathbf{G}^{(\varpi,\varrho)}, \boldsymbol{\Theta}^{(\varpi,\varrho)}, \boldsymbol{\Phi}^{(\varpi,\varrho)}, \boldsymbol{\chi}^{(\varpi,\varrho)}\}$. Figure 3(a) shows the variation in the error norms against the number of iterations. It can be seen that the error norms decrease monotonically with increasing number of iterations. This is an indication that the method converges as the number of iterations increases. Full convergence is achieved after about seven iterations for all solutions with error norms close to 10^{-14}. The accuracy of the OMD-BSQLM can be assessed by considering the residual errors defined as

$$||Res(\xi)||_\infty = \left|\left| \Delta_\xi \left[\mathbf{F}^{(\varpi,\varrho)}, \mathbf{G}^{(\varpi,\varrho)}, \boldsymbol{\Theta}^{(\varpi,\varrho)}, \boldsymbol{\Phi}^{(\varpi,\varrho)}, \boldsymbol{\chi}^{(\varpi,\varrho)}\right] \right|\right|_\infty \qquad (41)$$

where Δ_ξ signifies the nonlinear PDEs (14)–(18), $\mathbf{F}^{(\varpi,\varrho)}, \mathbf{G}^{(\varpi,\varrho)}, \boldsymbol{\Theta}^{(\varpi,\varrho)}, \boldsymbol{\Phi}^{(\varpi,\varrho)}, \boldsymbol{\chi}^{(\varpi,\varrho)}$ are the OMD-BSQLM solutions. Figure 3b depicts the variation of residual errors of the five governing equations (14) -(18) against the number of iterations. The residual errors are observed to decrease significantly with the increase in the number of iterations and converge with residual errors of close to 10^{-14} after about five iterations. The smaller values of the residual errors suggest the accuracy of the method. The above results sufficiently confirm the accuracy and convergence of the OMD-BSQLM, thus the method can be trusted.

Figure 4 illustrates the impact of Hall parameter on the flow and transverse velocity profiles. Figure 4(a) shows that increment in Hall parameter decelerates the tangential velocity profile and reinforce the boundary layer thickness near the wall, while it shrinks distant from the surface. This is because the magnetic damping on the tangential velocity diminishes as the Hall parameter escalates, and the magnetic field has a propelling effect on the primary velocity. Figure 4(b) elucidates that the lateral velocity profile and momentum boundary layer thickness also intensify with diminutive effects, as the Hall parameter increases from zero to unity ($\beta_e \leq 1$). This is because the inclusion of the Hall parameter suppresses the resistive effect of the magnetic field. As a result, increment in Hall parameter enhances the fluid velocity. It is worth noting that the maximum velocity is reached for $\beta_e = 1$ and diminishes for values of the Hall parameter greater than unity ($\beta_e > 1$), being equal zero when the Hall parameter becomes very large. This findings concur with results obtained by Abo-Eldahab and Aziz (2005) in the absence of nanoparticles and motile gyrotactic microorganisms. Figure 5 portrays the influence of ion-slip parameter on the primary and secondary velocity profiles. The magnitude of primary velocity is enhanced when the ion-slip parameter increases, whereas the secondary velocity drops with an elevation in the ion-slip parameter. The ion slip is observed to have a significant impact on the

induced flow in the z-direction than in the x-direction. Ion slip arises in the parameter $\alpha_e = 1 + \beta_i \beta_e$, which causes a heating effect as the ions slip in the magnetic field and a reduction in the secondary flow.

Figure 6 exhibits the repercussions of Casson fluid parameter on the primary and secondary velocity. The profiles of velocity are found to increase with escalating values of the Casson fluid parameter close to the surface. Further away from the surface, the velocity components and thickness of the momentum boundary layer decrease with increasing values of the Casson fluid parameter. This is because increasing values of Casson fluid number makes the fluid to be more viscous, thus producing more resistance to the fluid flow, which in turn diminishes the momentum boundary layer thickness. It is worth mentioning that increasing the Casson number reduces the yield stress, which means that the fluid behaves as Newtonian fluid when Casson fluid parameter become large, thus suppresses the fluid velocity. The influence of variable fluid viscosity parameter on the primary and secondary velocity is presented in Figure 7. An increase in the variable viscosity produces enhancement in the flow velocity close to the surface. Further away from the surface, the flow velocity decelerates when the variable viscosity parameter grows. During fluid flow both velocity and friction have opposite effects. Thus, increment in the viscosity of the fluid corresponds to increasing the friction between the molecules and internal force of attraction. This causes resistance to the fluid flow which in turn suppresses the velocity of the fluid. Figure 8 depicts the effects of variable thermal conductivity parameter on the primary and secondary velocity distributions. We observe that the velocity fields and associated boundary layer thickness enhances slightly with increasing variable thermal conductivity parameter. This occurs because an increase in variable thermal conductivity parameter improves the temperature difference $(T_w - T_\infty)$, thus weakening Casson fluid bond and reducing the strength of Casson plastic dynamic viscosity. Similar results were reported by Gbadeyan, Titiloye, and Adeosun (2020) in the absence of motile microorganisms.

Figure 9 shows the impact of radiation parameter and Casson fluid parameter on the temperature profiles. The temperature field and thermal boundary layer thickness enhances for larger values of radiation parameter as seen in Figure 9(a). Physically, increment in radiation parameter releases thermal radiation energy into the flow, since increasing radiation parameter implies a reduction in the Rosseland radiation absorption. Accordingly, this maximises the rate of radiative heat transferred to the fluid, thus increases the temperature of the fluid. Figure 9 indicates that the temperature profile and thermal boundary layer thickness retard for higher values of the non-Newtonian Casson fluid number since increment in Casson fluid number implies reduction in yield stress, consequently the thickness of the thermal boundary layer reduces. Figure 10 presents the influence of variable fluid viscosity and thermal conductivity parameters on the temperature distributions. Figure 10a shows that the fluid temperature and thermal boundary layer thickness decrease with increasing variable fluid viscosity parameter. As the variable viscosity parameter escalates, the viscosity of the fluid improves leading to an increase in viscous forces which opposes the fluid motion. This increase in the viscous force leads to a fall in the temperature of the flow and the reduction rate of

Table 2. Comparison of $f''(\xi, 0)$ and $G'(\xi, 0)$ for various values of $M, \beta_e, \beta_i, \lambda$ and Ec when $Pr = 0.72, \delta_T = 0.5, \xi = 0.4, K = Le = Lb = Pe = \Omega = \delta_C = \delta_N = Fs = Rd = Nt = Nb = Le = 0, Gr_x \to \infty, Da \to \infty$ and $\beta \to \infty$.

					Abo-Eldahab and Aziz (2005)		Present Results	
M	Ec	β_e	β_i	λ	$f''(\xi, 0)$	$G'(\xi, 0)$	$f''(\xi, 0)$	$G'(\xi, 0)$
1.0	0.3	1.0	0.5	0.01	0.63693082901	0.0383893132	0.6369315	0.0383871
2.0	0.3	1.0	0.5	0.01	0.59706823575	0.0643022634	0.5970646	0.0643001
3.0	0.3	1.0	0.5	0.01	0.56068338930	0.0811004043	0.5606865	0.0811088
1.0	0.0	1.0	0.5	0.01	0.63473777182	0.0382936717	0.6347306	0.0382909
1.0	1.0	1.0	0.5	0.01	0.64720993236	0.0387984582	0.6472009	0.0387920
1.0	2.0	1.0	0.5	0.01	0.66049461582	0.0393185271	0.6604913	0.0393138
1.0	0.3	0.0	0.5	0.01	0.59835234145	0.0	0.5983540	0.0000000
1.0	0.3	0.1	0.5	0.01	0.60217361460	0.0094174445	0.6021726	0.0094131
1.0	0.3	0.5	0.5	0.01	0.61954847255	0.0316335848	0.6195405	0.0316324
1.0	0.3	1.0	0.5	0.01	0.63693082901	0.0383893132	0.6369315	0.0383871
1.0	0.3	2.0	0.5	0.01	0.65519306619	0.0338307267	0.6551983	0.0338394
1.0	0.3	3.0	0.5	0.01	0.66324252266	0.0275347841	0.6632498	0.0275397
1.0	0.3	4.0	0.5	0.01	0.66746644037	0.0227866200	0.6674647	0.0227879
1.0	0.3	1.0	0.0	0.01	0.63058178496	0.0612420061	0.6305829	0.0612497
1.0	0.3	1.0	1.0	0.01	0.64312951983	0.0255745858	0.6431205	0.0255794
1.0	0.3	1.0	3.0	0.01	0.65788414992	0.0080167629	0.6578878	0.0080168
1.0	0.3	1.0	0.5	−0.9	0.57357816680	0.0353441224	0.5735739	0.0353485
1.0	0.3	1.0	0.5	−0.6	0.59261453147	0.0362969610	0.5926108	0.0362979
1.0	0.3	1.0	0.5	−0.3	0.61339672553	0.0372992234	0.6133942	0.0372987
1.0	0.3	1.0	0.5	0.0	0.64558564656	0.0383531893	0.6455849	0.0383523
1.0	0.3	1.0	0.5	0.3	0.66395613639	0.0394596683	0.6639597	0.0394594
1.0	0.3	1.0	0.5	0.6	0.68840238136	0.0406190713	0.6884080	0.0406105
1.0	0.3	1.0	0.5	0.9	0.71839291545	0.0418303872	0.7183972	0.0418352
1.0	0.3	1.0	0.5	1.2	0.75124292543	0.0430892029	0.7512494	0.0430866
1.0	0.3	1.0	0.5	1.5	0.78713651857	0.0443920884	0.7871310	0.0443901

(a) Solution error norms against iterations

(b) Residual errors against iterations
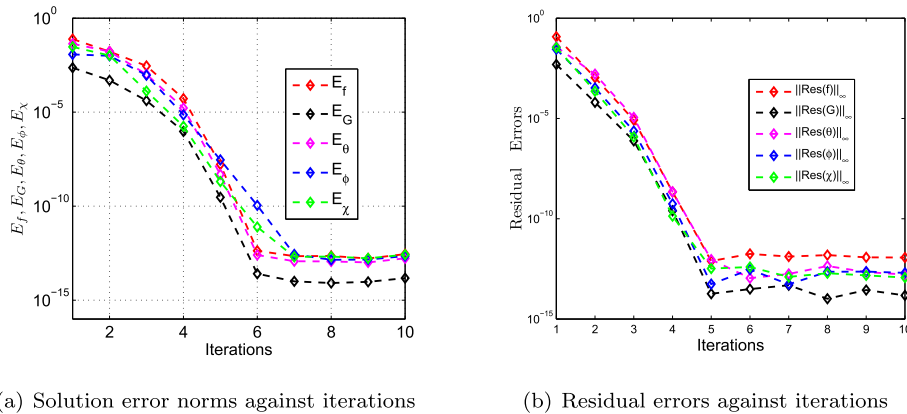
Figure 3. Error norms and residual error graphs. (a) Solution error norms against iterations. (b) Residual errors against iterations.

(a) Primary velocity profiles

(b) Secondary velocity profiles
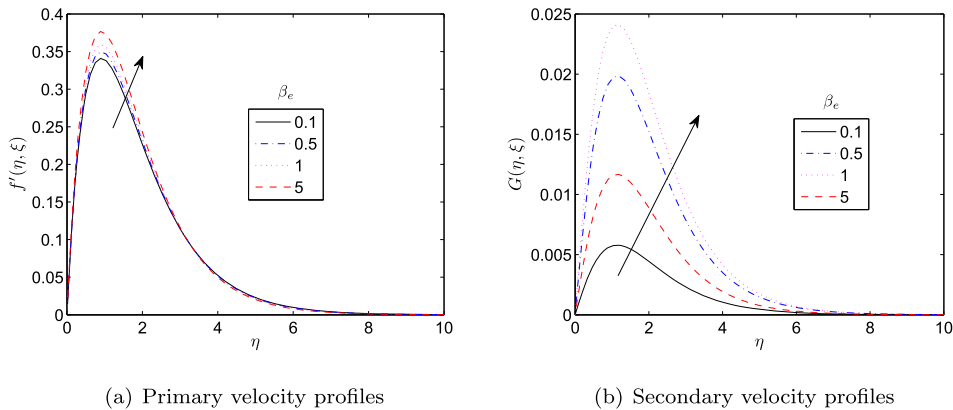
Figure 4. Effect of Hall current parameter. (a) Primary velocity profiles. (b) Secondary velocity profiles

the temperature fields. Figure 10(b) shows that an increment in the variable thermal conductivity enhances the fluid temperature since more heat is exchanged from the surface to the fluid

particles, consequently increasing the temperature of nanoparticles. It is also worth noting that the thermal boundary layer becomes thicker as thermal diffusivity improves. This observation implies that the inclusion of variable thermal conductivity can be useful to improve the heat transportation characteristics in different thermal extrusion processes.

Figure 11 discloses the effects of thermophoresis and Brownnan motion parameters on the concentration fields. It is observed that the concentration profiles increases as the thermophoresis parameter increases close to the surface. Away from the surface the concentration distribution along with corresponding boundary layer thickness enhance with increasing values of thermophoresis parameter. This implies that escalating thermophoresis parameter induces resistance to the diffusion of

the solute which helps in the reduction of the concentration gradient at the surface. The enhancement in nanoparticle concentration boundary layer thickness is basically due to the fact that thermophoresis force transport the nanoparticles from the hotter region to the colder region, thus improving the concentration of the fluid. These results are consistent with findings reported by Abbas et al. (2019). The opposite trend is true for the Brownian motion parameter, where the concentration retards by increasing the Brownian motion. This is due to the fact that an increment in the Brownian motion parameter augments the interaction between fluid particles, which leads to significant fall in the fluid concentration and associated boundary layer thickness. Figure 12 demonstrates the repercussions of chemical reaction and Casson fluid parameters on the concentration profiles. As
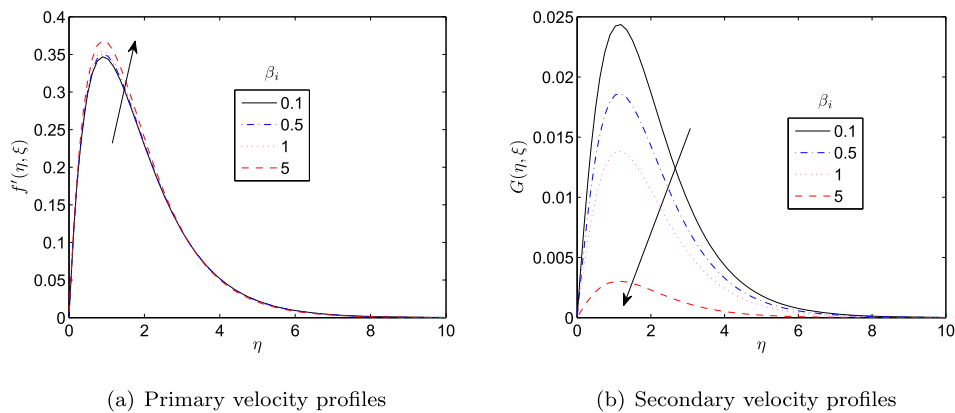

(a) Primary velocity profiles

(b) Secondary velocity profiles

Figure 5. Effect of ionslip parameter. (a) Primary velocity profiles. (b) Secondary velocity profiles

Table 3. Values of skin friction coefficients, Nusselt number, Sherwood number and density number of the motile microorganisms for different values of $\alpha, \varepsilon, \beta, Rd, Nt, Nb, Pe$ and Lb when $\xi = 1, \delta_T = 0.5, \delta_C = 0.5, \delta_N = 1, K = 0.5, Gr_x = 1, Pr = 0.71, Le = 0.6, Da = 1, Fs = 0.1, Ec = 0.1, M = 0.5, \beta_i = 0.4, \beta_e = 0.5, \Omega = 0.2, \theta_w = 1.2,$ and $\lambda = 0.01$.

α	ε	Rd	β	Nt	Nb	Pe	Lb	C_{fx}	C_{gz}	Nu_x	Sh_x	Nn_x
0.0	0.2	0.2	1.0	0.5	0.5	0.3	0.5	1.4814310	0.0411883	0.5875137	−0.1261842	0.2687709
0.3	0.2	0.2	1.0	0.5	0.5	0.3	0.5	1.3978105	0.0443793	0.6298827	−0.1352841	0.2907701
0.6	0.2	0.2	1.0	0.5	0.5	0.3	0.5	1.3069146	0.0460863	0.6702606	−0.1439563	0.3120635
1.0	0.2	0.2	1.0	0.5	0.5	0.3	0.5	1.1776300	0.0461080	0.7203813	−0.1547211	0.3387466
0.5	0.0	0.2	1.0	0.5	0.5	0.3	0.5	1.3354358	0.0455384	0.6458856	−0.1449474	0.3034519
0.5	0.5	0.2	1.0	0.5	0.5	0.3	0.5	1.3414744	0.0458971	0.6733758	−0.1358708	0.3073115
0.5	1.0	0.2	1.0	0.5	0.5	0.3	0.5	1.3469485	0.0462283	0.6995660	−0.1282196	0.3106446
0.5	1.5	0.2	1.0	0.5	0.5	0.3	0.5	1.3519332	0.0465353	0.7246160	−0.1216615	0.3135655
0.5	0.2	0.0	1.0	0.5	0.5	0.3	0.5	1.2508160	0.0405579	0.3301161	−0.2750968	0.2491368
0.5	0.2	0.5	1.0	0.5	0.5	0.3	0.5	1.2936145	0.0429046	0.4693279	−0.1995442	0.2791422
0.5	0.2	1.0	1.0	0.5	0.5	0.3	0.5	1.3198526	0.0444965	0.5726093	−0.1634159	0.2948473
0.5	0.2	1.5	1.0	0.5	0.5	0.3	0.5	1.3379244	0.0456855	0.6570493	−0.1411188	0.3050681
0.5	0.2	0.2	0.5	0.5	0.5	0.3	0.5	1.4456794	0.0399372	0.5741325	−0.1233102	0.2689322
0.5	0.2	0.2	1.0	0.5	0.5	0.3	0.5	1.3379244	0.0456855	0.6570493	−0.1411188	0.3050681
0.5	0.2	0.2	2.0	0.5	0.5	0.3	0.5	1.2498740	0.0472094	0.7088974	−0.1522546	0.3286404
0.5	0.2	0.2	∞	0.5	0.5	0.3	0.5	1.1149879	0.0462695	0.7715823	−0.1657178	0.3580509
0.5	0.2	0.2	1.0	0.1	0.5	0.3	0.5	1.3902571	0.0457488	0.6548074	−0.0281275	0.3317472
0.5	0.2	0.2	1.0	0.3	0.5	0.3	0.5	1.3644206	0.0457324	0.6560967	−0.0845485	0.3183701
0.5	0.2	0.2	1.0	0.5	0.5	0.3	0.5	1.3379244	0.0456855	0.6570493	−0.1411188	0.3050681
0.5	0.2	0.2	1.0	0.7	0.5	0.3	0.5	1.3108096	0.0456099	0.6576559	−0.1977488	0.2918627
0.5	0.2	0.2	1.0	0.5	0.5	0.3	0.5	1.3379244	0.0456855	0.6570493	−0.1411188	0.3050681
0.5	0.2	0.2	1.0	0.5	1.0	0.3	0.5	1.3718015	0.0458050	0.6490566	−0.0697011	0.3221870
0.5	0.2	0.2	1.0	0.5	1.5	0.3	0.5	1.3827929	0.0458353	0.6462987	−0.0462700	0.3278476
0.5	0.2	0.2	1.0	0.5	2.0	0.3	0.5	1.3882309	0.0458486	0.6449034	−0.0346275	0.3306683
0.5	0.2	0.2	1.0	0.5	0.5	0.2	0.5	1.3322222	0.0454532	0.6548695	−0.1406507	0.3153478
0.5	0.2	0.2	1.0	0.5	0.5	0.5	0.5	1.3494689	0.0461539	0.6614300	−0.1420597	0.2846636
0.5	0.2	0.2	1.0	0.5	0.5	0.8	0.5	1.3671329	0.0468661	0.6680466	−0.1434808	0.2544896
0.5	0.2	0.2	1.0	0.5	0.5	1.2	0.5	1.3913195	0.0478325	0.6769345	−0.1453897	0.2151991
0.5	0.2	0.2	1.0	0.5	0.5	0.3	0.3	1.3904389	0.0484281	0.6966927	−0.1496333	0.2325015
0.5	0.2	0.2	1.0	0.5	0.5	0.3	0.6	1.3181305	0.0447168	0.6440161	−0.1383196	0.3335449
0.5	0.2	0.2	1.0	0.5	0.5	0.3	1.0	1.2603464	0.0420146	0.6116382	−0.1313656	0.4210455
0.5	0.2	0.2	1.0	0.5	0.5	0.3	1.5	1.2127177	0.0398948	0.5902911	−0.1267807	0.4994455

(a) Primary velocity profiles
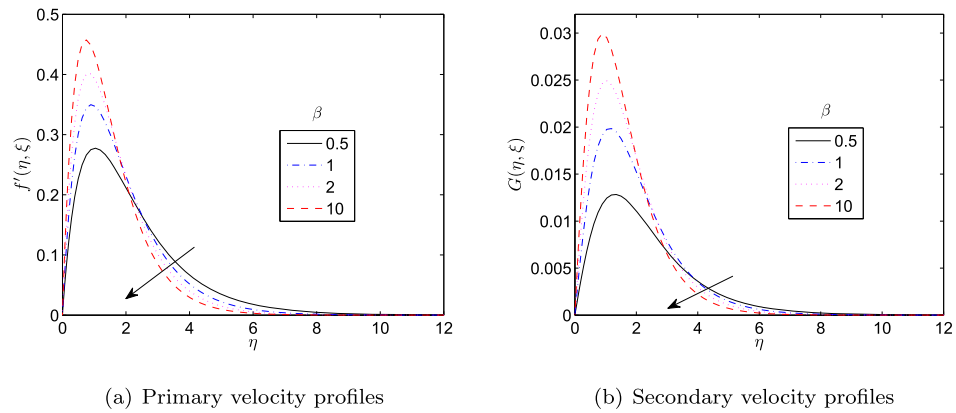
(b) Secondary velocity profiles

Figure 6. Effect of Casson fluid parameter. (a) Primary velocity profiles. (b) Secondary velocity profiles

the chemical reaction parameter enhances, the concentration fields as well as the solutal boundary layer thickness reduce as seen in Figure 12(a). This is because the chemical reaction reinforces the rate of interfacial mass transfer and shrinks the local concentration. Figure 12(b) depicts that the concentration of the fluid slightly decay by increasing the Casson fluid parameter due to the increasing viscosity that resists the fluid flow. In Figure 13 there is a slight reduction in the fluid concentration with increment in the variable fluid viscosity parameter, whereas slight augmentation is noted with the variable thermal conductivity. This observation suggests that the concentration of the fluid is weakly affected by the temperature dependent fluid properties.

This weakly influence is due to the fact that these variable fluid properties do not occur in the nanoparticle concentration equation.

The influence of bioconvection parameters on the density of motile microorganisms is shown in Figure 14. It is seen that the dimensionless density of motile microorganisms decreases strongly with escalating bioconvection Lewis number. In actual fact, the increment in the bioconvection Lewis number implies reduction in the diffusion of microorganisms, thus both density and associated boundary layer thickness of motile microorganisms diminish with amplifying bioconvection Lewis number. On the other hand, the density and boundary layer thickness

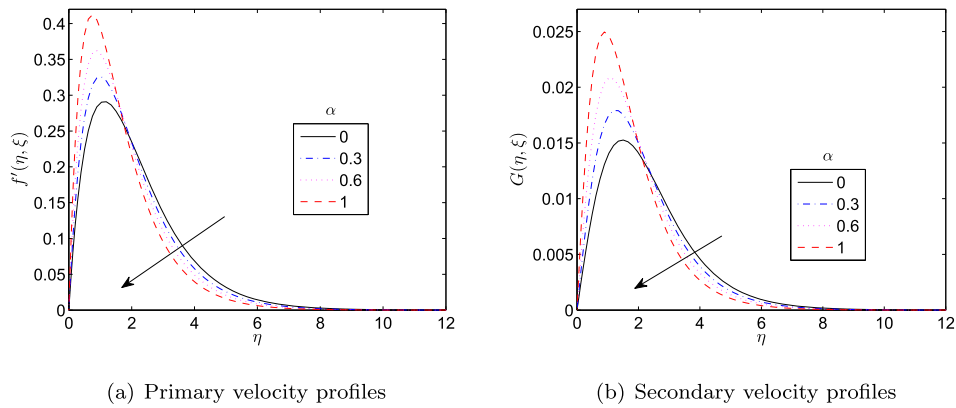(a) Primary velocity profiles

(b) Secondary velocity profiles

Figure 7. Effect of variable viscosity parameter. (a) Primary velocity profiles. (b) Secondary velocity profiles

(a) Primary velocity profiles

(b) Secondary velocity profiles

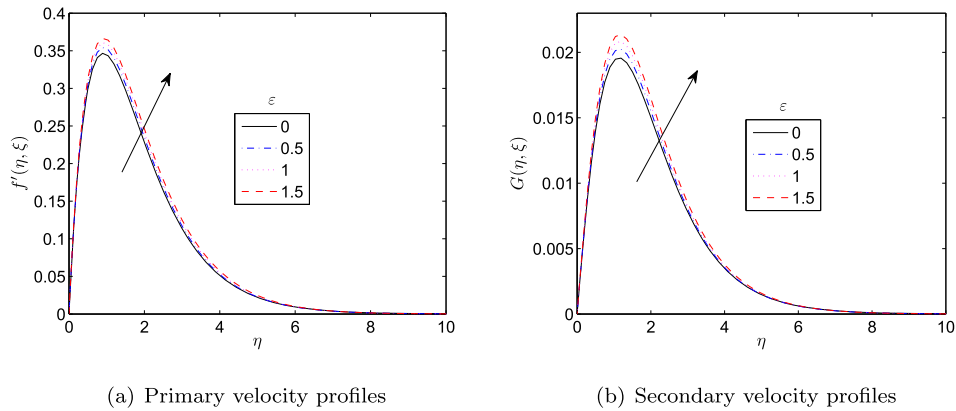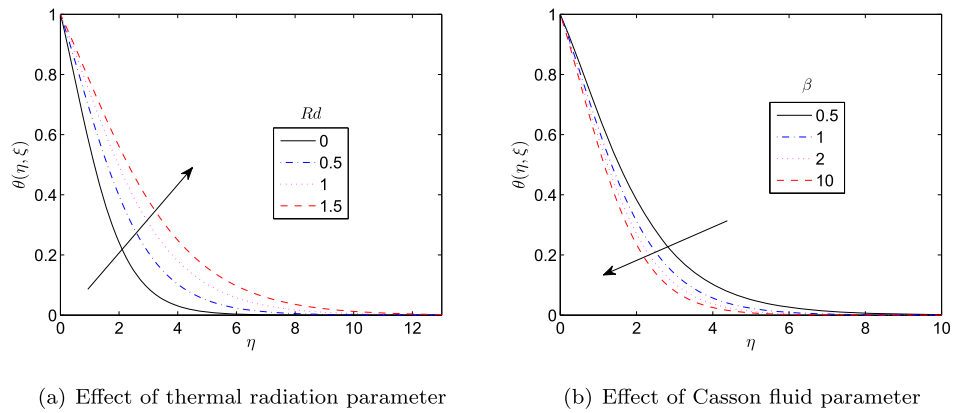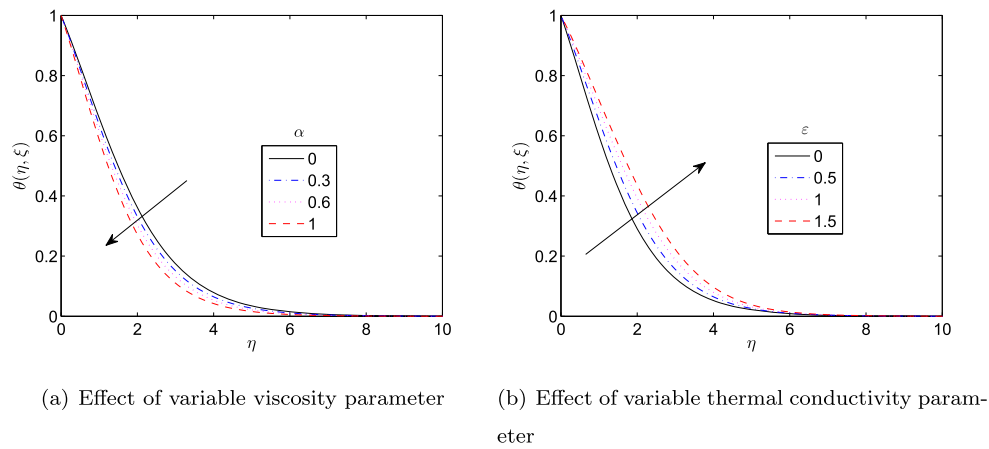**Figure 8.** Effect of variable thermal conductivity parameter. (a) Primary velocity profiles. (b) Secondary velocity profiles.

(a) Effect of thermal radiation parameter

(b) Effect of Casson fluid parameter

Figure 9. Temperature profiles. (a) Effect of thermal radiation parameter. (b) Effect of Casson fluid parameter.

(a) Effect of variable viscosity parameter

(b) Effect of variable thermal conductivity parameter

Figure 10. Temperature profiles. (a) Effect of variable viscosity parameter. (b) Effect of variable thermal conductivity parameter

of motile microorganisms strongly augments with increasing values of the bioconvection Peclet number close to the surface. However, the motile microorganisms weakly diminish by increasing the bioconvection Peclet number away from the surface. This might be because the Peclet number achieves reverse relation with microorganism diffusivity away from the surface. Figure 15 presents the influence of the Casson fluid number and variable viscosity parameter on the dimensionless density of motile microorganisms. Higher values of the Casson fluid number and variable fluid viscosity parameter are noted to retard

the density and boundary layer thickness of motile microorganisms. This means that the intermolecular forces are strengthened with increment in variable viscosity and Casson fluid parameter. Physically, larger intermolecular forces implies higher fluid viscosity.

The numerical values of local skin friction coefficients, Nusselt number, Sherwood number and wall motile microorganisms for selected values of important physical parameters are presented in Table 3. The dimensional wall stress in both $x-$ and $z-$ directions increases with escalating bioconvection Peclet number,

(a) Effect of thermophoresis parameter

(b) Effect of Brownian motion parameter

Figure 11. Concentration profiles. (a) Effect of thermophoresis parameter. (b) Effect of Brownian motion parameter.

(a) Effect of chemical reaction parameter

(b) Effect of Casson fluid parameter

Figure 12. Concentration profiles.(a) Effect of chemical reaction parameter. (b) Effect of Casson fluid parameter.

(a) Effect of variable viscosity parameter
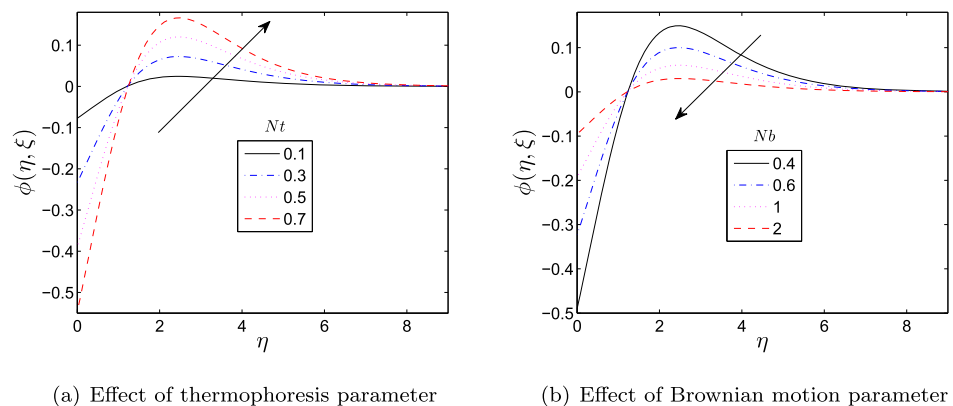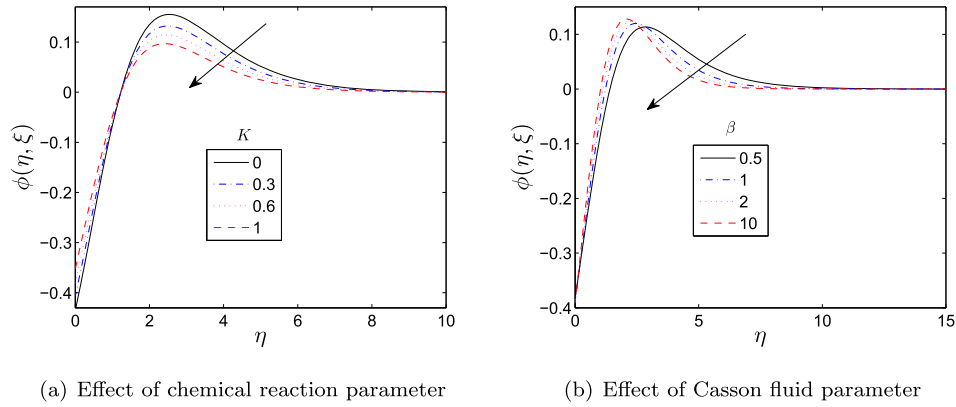
(b) Effect of variable thermal conductivity parameter
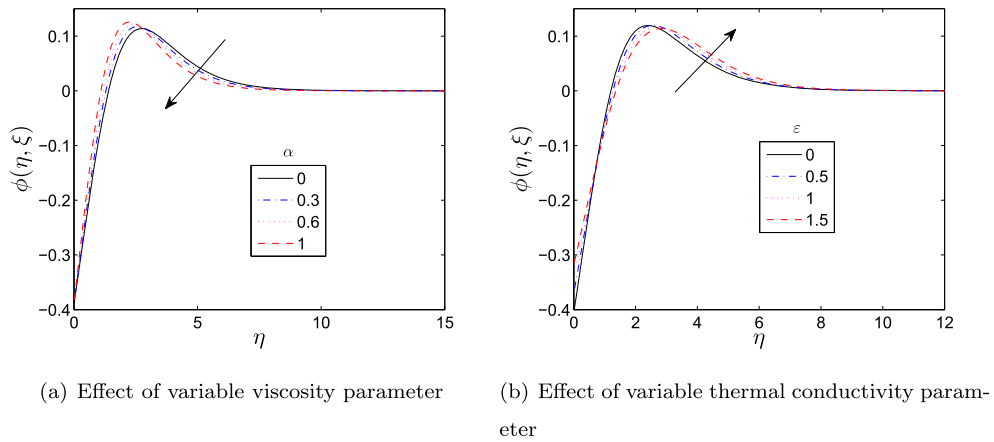
Figure 13. Concentration profiles. (a) Effect of variable viscosity parameter. (b) Effect of variable thermal conductivity parameter

variable thermal conductivity, thermal radiation and Brownian motion, whereas diminishes by increasing bioconvection Lewis number and thermophoresis parameter. The reverse trend is observed in the case of Casson fluid and variable fluid viscosity parameters. The reduction in skin friction coefficients due to increment in bioconvection Lewis number is caused by the increase in mass diffusion at the surface which restricts the flow near the surface. The heat transfer rate enhances with increment in variable fluid viscosity, thermal conductivity, thermal radiation, Casson fluid, thermophoresis force and bioconvection Peclet number (due to advective convection increment) while

retards with augmentation in Brownian motion and bioconvection Lewis number. The mass transfer rates improves when variable thermal conductivity, thermal radiation, Brownian motion and bioconvection Lewis number increases, but declines when variable fluid viscosity, Casson fluid, thermophoresis force and bioconvection Peclet number escalate. Lastly, the local density of the motile microorganisms amplifies for larger values of the variable viscosity, thermal conductivity, thermal radiation, Casson fluid, Brownian motion and bioconvection Lewis number, whereas suppresses for higher values of thermophoresis parameter and bioconvection Peclet number. The increment in density

(a) Effect of bioconvection Lewis number

(b) Effect of bioconvection Peclet number

Figure 14. Density of motile microorganisms profiles. (a) Effect of bioconvection Lewis number. (b) Effect of bioconvection Peclet number.

(a) Casson fluid parameter

(b) Effect of variable viscosity parameter

Figure 15. Density of motile microorganisms profiles. (a) Casson fluid parameter. (b) Effect of variable viscosity parameter.

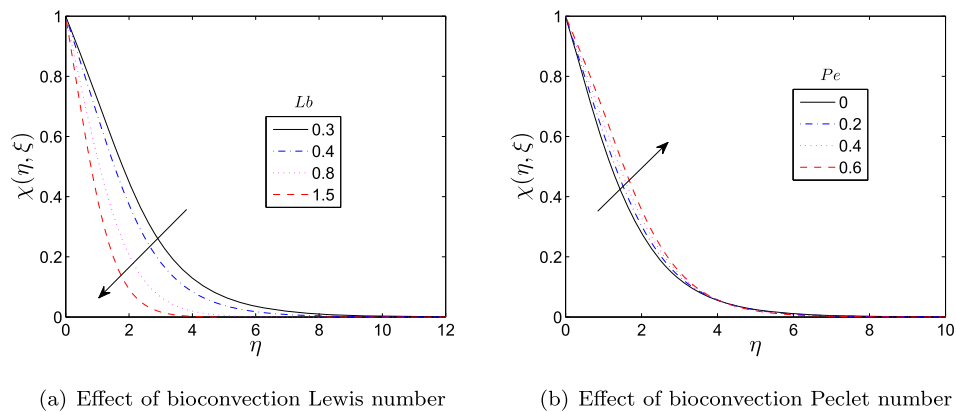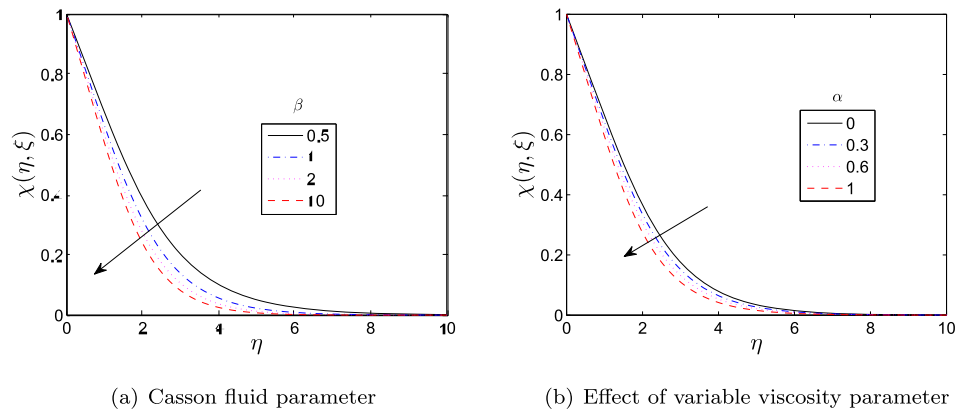number of motile microorganisms because of escalating bioconvection Lewis number is due to the fact that this it assists in suppressing the microorganism concentration layer thickness as already highlighted above.

5. Conclusion

The present work analysed the influence of variable fluid properties on MHD bioconvective radiative flow of Casson nanofluid containing gyrotactic microorganisms from a vertical surface. The transformed conservation equations were solved using the OMD-BSQLM. The convergence and accuracy of the method were assessed. The OMD-BSQLM was found to give accurate results after few iterations and using less grid points in each subinterval. The theoretical results have demonstrated that fluid viscosity and thermal conductivity cannot be assumed constants since physical properties of the fluid may change significantly with temperature. The flow fields diminish by considering fluid viscosity of variable nature while improve for the non-Newtonian fluid behaviour in the porous medium. It is worth noting that the influence of physical parameters on tangential and lateral velocities is more pronounced near the wall and maximum velocity is also reached close to the wall. The rest of the findings can be summarised as follows:

- Increasing Hall parameter accelerates both primary and secondary flows. However, rising the ion-slip parameter weakly accelerates the primary flow and strongly decelerates the secondary flow.
- The temperature of the fluid along with heat and mass transfer rates augment with the inclusion of variable thermal conductivity and nonlinear radiative heat flux into the system.
- The concentration and associated boundary layer thickness intensify as thermophoresis force becomes stronger while dropping with growing Brownian motion and chemical reaction.
- The density and boundary layer thickness of the motile microorganisms are suppressed by the bioconvection parameters.
- The skin friction coefficients amplify with escalating bioconvection Peclet number, variable thermal conductivity, thermal radiation and Brownian motion, whereas decreases with

increasing bioconvection Lewis number and thermophoresis parameter.
- An increment in variable fluid viscosity and Casson fluid parameters enhances the rates of heat transfer and density number of motile microorganisms, but retards the mass transfer rate.
- Increasing Brownian motion elevates mass and motile microorgansism transfer rates while causing decrement in heat transfer rate. The opposite trend is true for the thermophoresis parameter.

Disclosure statement

No potential conflict of interest was reported by the author(s).

ORCID

Musawenkhosi Patson Mkhatshwa http://orcid.org/0000-0001-7284-8498

References

Abbas, S. Z., W. A. Khan, H. Sun, M. Irfan, M. I. Khan, and M. Waqas. 2019. "Von Kármán Swirling Analysis for Modeling Oldroyd-B Nanofluid Considering Cubic Autocatalysis." *Physica Scripta* 95 (1): 015206. doi:10.1088/1402-4896/ab450f

Abdelmalek, Z., S. U. Khan, H. Waqas, A. Riaz, I. A. Khan, and I. Tlili. 2020. "A Mathematical Model for Bioconvection Flow of Williamson Nanofluid Over a Stretching Cylinder Featuring Variable Thermal Conductivity, Activation Energy and Second-order Slip." *Journal of Thermal Analysis and Calorimetry*. doi:10.1007/s10973-020-09450-z.

Abo-Eldahab, E. M., and M. A. Aziz. 2005. "Viscous Dissipation and Joule Heating Effects on MHD-free Convection From a Vertical Plate with Power-law Variation in Surface Temperature in the Presence of Hall and Ion-slip Currents." *Applied Mathematical Modelling* 29: 579–595. doi:10.1016/j.apm.2004.10.005

Al-Khaled, K., S. U. Khan, and I. Khan. 2020. "Chemically Reactive Bioconvection Flow of Tangent Hyperbolic Nanoliquid with Gyrotactic Microorganisms and Nonlinear Thermal Radiation." *Heliyon* 6: e03117. doi:10.1016/j.heliyon.2019.e03117

Amanulla, C. H., N. Nagendra, and M. S. Reddy. 2018. "Computational Analysis of Non-Newtonian Boundary Layer Flow of Nanofluid Past a Semi-infinite Vertical Plate with Partial Slip." *Nonlinear Engineering* 7 (1): 29–43. doi:10.1515/nleng-2017-0055

Andersson, H. I., J. B. Aarseth, N. Braud, and B. S. Dandapat. 1996. "Flow of a Power-law Fluid Film on An Unsteady Stretching Surface." *Journal of Non-Newtonian Fluid Mechanics* 62 (1): 1–8. doi:10.1016/0377-0257(95)01392-X

Beg, O. A., J. Uddin, and W. A. Khan. 2015. "Bioconvective Non-Newtonian Nanofluid Transport in Porous Media Containing Microorganisms in a

Moving Free Stream." *Journal of Mechanics in Medicine and Biology* 15 (5): 1550071. doi:10.1142/S0219519415500712

Bellman, R. E., and R. E. Kalaba. 1965. *Quasilinearization and Nonlinear Boundary-Value Problems*. New York: Elsevier.

Bhatti, M. M., and E. E. Michaelides. 2020. "Study of Arrhenius Activation Energy on the Thermo- Bioconvection Nanofluid Flow Over a Riga Plate." *Journal of Thermal Analysis and Calorimetry* doi:10.1007/s10973-020-09492-3.

Buongiorno, J.. 2006. "Convective Transport in Nanofluids." *ASME Journal of Heat Transfer* 128: 240–250. doi:10.1115/1.2150834

Canuto, C., M. Y. Husseini, A. Quarteroni, and T. A. Zang. 2006. *Spectral Methods: Fundamentals in Single Domains*. New York: Springer-Verlag.

Casson, N. 1959. A flow equation for pigment-oil suspensions of the printing ink type. Rheology of disperse systems.

Choi, S. U. S. 1995. "Enhancing Thermal Conductivity of Fluids with Nanoparticles." *ASME Fluids Engineering Division,* 231: 99–105.

Das, M., G. Mahanta, S. Shaw, and S. B. Parida. 2019. "Unsteady MHD Chemically Reactive Double-diffusive Casson Fluid Past a Flat Plate in Porous Medium with Heat and Mass Transfer." *Heat Transfer-Asian Research* 48 (5): 1761–1777. doi:10.1002/htj.2019.48.issue-5

Dash, R. K., K. N. Mehta, and G. Jayaraman. 1996. "Casson Fluid Flow in a Pipe Filled with a Homogeneous Porous Medium." *International Journal of Engineering Science* 34 (10): 1145–1156. doi:10.1016/0020-7225(96)00012-2

Eastman, J. A., S. U. S. Choi, S. Li, W. Yu, and L. J. Thompson. 2001. "Anomalously Increased Effective Thermal Conductivities of Ethylene Glycol-based Nanofluids Containing Copper Nanoparticles." *Applied Physics Letters* 78 (6): 718–720. doi:10.1063/1.1341218

Gaffar, S. A., V. R. Prasad, and E. K. Reddy. 2016. "MHD Free Convection Flow of Eyring–Powell Fluid From Vertical Surface in Porous Media with Hall/ionslip Currents and Ohmic Dissipation." *Alexandria Engineering Journal* 55: 875–905. doi:10.1016/j.aej.2016.02.011

Gaffar, S. A., V. R. Prasad, and E. K. Reddy. 2016. "Computational Study of MHD Free Convection Flow of Non-Newtonian Tangent Hyperbolic Fluid From a Vertical Surface in Porous Media with Hall/Ionslip Currents and Ohmic Dissipation." *International Journal of Applied and Computational Mathematics* 3 (2): 859–890. doi:10.1007/s40819-016-0135-1

Gbadeyan, J. A., E. O. Titiloye, and A. T. Adeosun. 2020. "Effect of Variable Thermal Conductivity and Viscosity on Casson Nanofluid Flow with Convective Heating and Velocity Slip." *Heliyon* 6: e03076. doi:10.1016/j.heliyon.2019.e03076

Ghadikolaei, S. S., K. Hosseinzadeh, D. Ganji, and B. Jafari. 2018. "Nonlinear Thermal Radiation Effect on Magneto Casson Nanofluid Flow with Joule Heating Effect Over An Inclined Porous Stretching Sheet." *Case Studies in Thermal Engineering* 12: 176–187. doi:10.1016/j.csite.2018.04.009

Gireesha, B. J., G. Sowmya, M. I. Khan, and H. F. Öztop. 2020. "Flow of Hybrid Nanofluid Across a Permeable Longitudinal Moving Fin Along with Thermal Radiation and Natural Convection." *Computer Methods and Programs in Biomedicine* 185: 105166. doi:10.1016/j.cmpb.2019.105166

Hayat, T., S. Ahmad, M. I. Khan, and A. Alsaedi. 2018. "Modeling and Analyzing Flow of Third Grade Nanofluid Due to Rotating Stretchable Disk with Chemical Reaction and Heat Source." *Physica B: Condensed Matter* 537: 116–126. doi:10.1016/j.physb.2018.01.052

Hayat, T., M. I. Khan, T. A. Khan, M. I. Khan, S. Ahmad, and A. Alsaedi. 2018. "Entropy Generation in Darcy-Forchheimer Bidirectional Flow of Water-based Carbon Nanotubes with Convective Boundary Conditions." *Journal of Molecular Liquids* 265: 629–638. doi:10.1016/j.molliq.2018.06.017

Hayat, T., M. Waleed Ahmed Khan, A. Alsaedi, and M. Ijaz Khan. 2017. "Squeezing Flow of Second Grade Liquid Subject to Non-Fourier Heat Flux and Heat Generation/absorption." *Colloid and Polymer Science* 295 (6): 967–975. doi:10.1007/s00396-017-4089-6

Ibrahim, M., and M. I. Khan. 2020. "Mathematical Modeling and Analysis of SWCNT-Water and MWCNT-Water Flow Over a Stretchable Sheet." *Computer Methods and Programs in Biomedicine* 187: 105222. doi:10.1016/j.cmpb.2019.105222

Javed, M. F., M. Waqas, M. I. Khan, N. B. Khan, R. Muhammad, M. U. Rehman, S. W. Khan, and M. T. Hassan. 2019. "Transport of Jefrey Nanomaterial in Cubic Autocatalytic Chemically Nonlinear Radiated Flow with Entropy Generation." *Applied Nanoscience* 10: 3011–3019. doi:10.1007/s13204-019-01071-9

Javed, M. F., M. Waqas, N. B. Khan, R. Muhammad, M. U. Rehman, M. I. Khan, S. W. Khan, and M. T. Hassan. 2019. "On Entropy Generation Effectiveness in Flow of Power Law Fluid with Cubic Autocatalytic Chemical Reaction." *Applied Nanoscience* 9: 1205–1214. doi:10.1007/s13204-019-01064-8

Jawali, C. U., A. J. Chamkha, and S. Mohiuddin. 2016. "Combined Effect of Variable Viscosity and Thermal Conductivity on Free Convection Flow of a Viscous Fluid in a Vertical Channel." *International Journal of Numerical Methods for Heat and Fluid Flow* 26: 18–39. doi:10.1108/HFF-12-2014-0385

Kala, B. S.. 2016. "The Numerical Investigation of Effects of Darcy and Forchheimer Parameters on Magnetohydrodynamic Casson Fluid Flow Through Non-Darcy Porous Media." *International Journal of Mathematica Trends and Technology* 40 (4): 266–275. doi:10.14445/22315373/IJMTT-V40P534

Khan, M. I., A. Alsaedi, T. Hayat, and N. B. Khan. 2019. "Modeling and Computational Analysis of Hybrid Class Nanomaterials Subject to Entropy Generation." *Computer Methods and Programs in Biomedicine* 179: 104973. doi:10.1016/j.cmpb.2019.07.001

Khan, S. U., S. A. Hehzad, and N. Ali. 2020. "Bioconvection Flow of Magnetized Williamson Nanoliquid with Motile Organisms and Variable Thermal Conductivity." *Applied Nanoscience* 10: 3325–3336. doi:10.1007/s13204-020-01282-5

Kuznestov, A. V.. 2011. "Bio-thermal Convection Induced by Two Different Species of Microorganisms." *International Communication in Heat Mass Transfer* 38 (5): 548–553. doi:10.1016/j.icheatmasstransfer.2011.02.006

Magagula, V. M., S. Shaw, and R. R. Kairi. 2020. "Double Dispersed Bioconvective Casson Nanofluid Fluid Flow Over Nonlinear Convective Stretching Sheet in Suspension of Gyrotactic Microorgansisms." *Heat Transfer* 49: 2449–2471. doi:10.1002/htj.v49.5

Mahmoud, M. A., and A. M. Megahed. 2009. "MHD Flow and Heat Transfer in a Non-Newtonian Liquid Film Over An Unsteady Stretching Sheet with Variable Fluid Properties." *Canadian Journal of Physics* 87 (10): 1065–1071. doi:10.1139/P09-066

Megahed, A. M.. 2019. "Williamson Fluid Flow Due to a Nonlinearly Stretching Sheet with Viscous Dissipation and Thermal Radiation." *Journal of Egyptian Mathematical Society* 27 (1): 12. doi:10.1186/s42787-019-0016-y

Mkhatshwa, M. P., S. S. Motsa, M. S. Ayano, and P. Sibanda. 2020. "MHD Mixed Convective Nanofluid Flow About a Vertical Slender Cylinder Using Overlapping Multi-domain Spectral Collocation Approach." *Case Studies in Thermal Engineering* 18: 100598. doi:10.1016/j.csite.2020.100598

Mkhatshwa, M. P., S. S. Motsa, and P. Sibanda. 2019. "Overlapping Multi-domain Spectral Method For Conjugate Problems of Conduction and MHD Free Convection Flow on Nanofluids Over Flat Plates." *Mathematical and Computational Applications* 24 (3): 75. doi:10.3390/mca24030075

Mkhatshwa, M., S. Motsa, and P. Sibanda. 2020. "Overlapping Multi-domain Bivariate Spectral Method for Systems of Nonlinear PDEs with Fluid Mechanics Applications." In *Advances in Fluid Dynamics. Lecture Notes in Mechanical Engineering*, Rushi Kumar B., Sivaraj R., Prakash J., eds. Singapore: Springer. doi:10.1007/978-981-15-4308-1_54.

Muhammad, R., M. I. Khan, M. Jameel, and N. B. Khan. 2019. "Fully Developed Darcy-Forchheimer Mixed Convective Flow Over a Curved Surface with Activation Energy and Entropy Generation." *Computer Methods and Programs in Biomedicine* 188: 105298. doi:10.1016/j.cmpb.2019.105298

Mukhopadhyay, S., and K. Bhattacharyya. 2013. "Exact Solutions for the Flow of Casson Fluid Over a Stretching Surface with Transpiration and Heat Transfer Effects." *Chinese Physics B* 22: 114701. doi:10.1088/1674-1056/22/11/114701

Nayak, M. K., J. Prakash, D. Tripathi, V. S. Pandey, S. Shaw, and O. D. Makinde. 2019. "3D Bioconvective Multiple Slip Flow of Chemically Reactive Casson Nanofluid with Gyrotactic Microorganisms." *Heat Transfer-Asian Research* 49: 135–153. doi:10.1002/htj.21603

Oyelakin, I. S., S. Mondal, and P. Sibanda. 2019. "Nonlinear Radiation in Bioconvective Casson Nanofluid Flow." *International Journal of Applied and Computational Mathematics* 5: 124. doi:10.1007/s40819-019-0705-0

Oyelakin, I. S., and P. Sibanda. 2020. "Analysis of Exponentially Varying Viscosity and Thermal Conductivity on a Tangent Hyperbolic Fluid." *SeMa Journal* 77: 257–273. doi:10.1007/s40324-020-00215-0

Pham, T. V., and E. Mitsoulis. 1994. "Entry and Exit Flows of Casson Fluids." *Canandian Journal of Chemical Engineering* 72: 1080–1084. doi:10.1002/cjce.v72:6

Platt, J. R.. 1961. "Bioconvection Pattern in Cultures of Free-Swimming Organism." *Science (New York, N.Y.)* 133: 1766–1767.

Plesset, M. S.. 1974. "Bioconvection Patterns in Swimming Micro-organism Cultures As An Example of Rayleigh-Taylor Instability." *Nature* 248: 441–443. doi:10.1038/248441a0

Qayyum, S., M. Ijaz Khan, T. Hayat, A. Alsaedi, and M. Tamoor. 2018. "Entropy Generation in Dissipative Flow of Williamson Fluid Between Two Rotating Disks." *International Journal of Heat and Mass Transfer* 127: 933–942. doi:10.1016/j.ijheatmasstransfer.2018.08.034

Rashid, M., M. I. Khan, T. Hayat, M. I. Khan, and A. Alsaedi. 2018. "Entropy Generation in Flow of Ferromagnetic Liquid with Nonlinear Radiation and Slip Condition." *Journal of Molecular Liquids* 276: 441–452. doi:10.1016/j.molliq.2018.11.148

Sabir, Z., R. Akhtar, Z. Zhiyu, M. Umar, A. Imran, H. A. Wahab, M. Shoaib, and M. A. Z. Raja. 2019. "A Computational Analysis of Two-Phase Casson Nanofluid Passing a Stretching Sheet Using Chemical Reactions and Gyrotactic Microorganisms." *Mathematical Problems in Engineering* 2019: 1490571. doi:10.1155/2019/1490571

Sajid, M., I. Ahmad, T. Hayat, and M. Ayub. 2009. "Unsteady Flow and Heat Transfer of a Second Grade Fluid Over a Stretching Sheet. Communications in Nonlinear Science and Numerical Simulation." *Communications in Nonlinear Science and Numerical Simulation* 14 (1): 96–108. doi:10.1016/j.cnsns.2007.07.014

Shahid, A., Z. Zhou, M. M. Bhatti, and D. Tripathi. 2018. "Magnetohydrodynamics Nanofluid Flow Containing Gyrotactic Microorganisms Propagating Over a Stretching Surface by Successive Taylor Series Linearization Method." *Microgravity Science and Technology* 30: 445–455. doi:10.1007/s12217-018-9600-2

Sharada, K., and B. Shankar. 2015. "MHD Mixed Convection Flow of a Casson Fluid Over An Exponentially Stretching Surface with the Effects of Soret, Dufour, Thermal Radiation and Chemical Reaction." *World Journal of Mechanics* 5: 165–177. doi:10.4236/wjm.2015.59017

Sohail, M., R. Naz, Z. Shah, P. Kumam, and P. Thounthong. 2019. "Exploration of Temperature Dependent Thermophysical Characteristics of Yield Exhibiting Non-Newtonian Fluid Flow Under Gyrotactic Microorganisms." *AIP Advances* 9: 125016. doi:10.1063/1.5118929

Takhar, H. S., R. S. Gorla, and V. M. Soundalgekar. 1996. "Short Communication Radiation Effects on MHD Free Convection Flow of a Gas Past a Semi-infinite Vertical Plate." *International Journal of Numerical Methods for Heat and Fluid Flow* 6 (2): 77–83. doi:10.1108/09615539610113118

Wager, H.. 1911. "On the Effect of Gravity Upon the Movements and Aggregation of Euglena Viridis, Ehrb., and Other Micro-organisms." *Philosophy Transactions of the Royal Society B* 201: 333–390.

Zhang, L., M. B. Arain, M. M. Bhatti, A. Zeeshan, and H. Hal-Sulami. 2020. "Effects of Magnetic Reynolds Number on Swimming of Gyrotactic Microorganisms Between Rotating Circular Plates Filled with Nanofluids." *Applied Mathematics and Mechanics* 41 (4): 637–654. doi:10.1007/s10483-020-2599-7

Part B:
Application of the overlapping grid spectral method in space and time variables

Chapter 8

Numerical solution of time-dependent Emden-Fowler equations using bivariate spectral collocation method on overlapping grids

In Part A, the overlapping grid approach was used only in the space variable when applying the spectral quasilinearisation method and bivariate spectral quasilinearisation method to solve ordinary and partial differential equations. In Part B, the overlapping grid approach is implemented in both space and time variables when using the bivariate spectral quasilinearisation method to solve partial differential equations. In this chapter, the method is tested by solving Emden-Fowler partial differential equations. To determine the accuracy and convergence of the numerical scheme, approximate solutions are compared to exact solutions. We present useful error bound theorems along with their proofs to highlight the merits of the method.

Musawenkhosi P. Mkhatshwa*, Sandile S. Motsa, and Precious Sibanda

Numerical solution of time-dependent Emden-Fowler equations using bivariate spectral collocation method on overlapping grids

Abstract: In this work, we present a new modification to the bivariate spectral collocation method in solving Emden-Fowler equations. The novelty of the modified approach is the use of overlapping grids when applying the Chebyshev spectral collocation method. In the case of nonlinear partial differential equations, the quasilinearisation method is used to linearize the equation. The multi-domain technique is applied in both space and time intervals, which are both decomposed into overlapping subintervals. The spectral collocation method is then employed in the discretization of the iterative scheme to give a matrix system to be solved simultaneously across the overlapping subintervals. Several test examples are considered to demonstrate the general performance of the numerical technique in terms of efficiency and accuracy. The numerical solutions are matched against exact solutions to confirm the accuracy and convergence of the method. The error bound theorems and proofs have been considered to emphasize on the benefits of the method. The use of an overlapping grid gives a matrix system with less dense matrices that can be inverted in a computationally efficient manner. Thus, implementing the spectral collocation method on overlapping grids improves the computational time and accuracy. Furthermore, few grid points in each subinterval are required to achieve stable and accurate results. The approximate solutions are established to be in excellent agreement with the exact analytical solutions.

Keywords: bivariate spectral quasilinearisation method; multi-domain; overlapping grid; Emden-Fowler equations; Neumann and Dirichlet boundary conditions

1 Introduction

The challenge of finding more accurate and computationally efficient numerical methods for solving linear and strongly nonlinear problems still persists. The development of numerical methods that are easily to handle and highly accurate has been a subject of interest to a growing number of researchers in the recent past years. Spectral collocation based methods are known to be one of the powerful numerical tools for the solution of time-dependent partial differential equations (PDEs) when compared with traditional methods such as finite difference methods and finite volume schemes [1]. The finite volume and finite difference methods can be applied in solving complex problems, but require a high number of grid points to give accurate results. Spectral collocation methods have been widely used for solving problems with smooth solutions because of their efficiency, exponential rates convergence, low computational cost and high order of accuracy [2–5] achieved using a minimal number of grid points. It is known that the accuracy of spectral methods increases with an increase in grid points but beyond a certain number of grid points, the accuracy rapidly deteriorates. The limitation of spectral methods is that their accuracy deteriorates for complicated domains, for instance, when the computational time domain becomes large. Also, spectral methods produce a matrix system with dense matrices that cannot be inverted in a computationally efficient manner.

Motsa et al. [6] introduced the bivariate spectral quasilinearisation method (BSQLM) and applied the method in solving nonlinear evolution PDEs. This numerical approach gave accurate results for smaller time domains.

*Corresponding Author: Musawenkhosi P. Mkhatshwa, School of Mathematics, Statistics & Computer Science, University of Kwazulu Natal, Private Bag X01, Scottsville, 3209, Pietermaritzburg, South Africa, E-mail: patsonmkhatshwa@gmail.com
Sandile S. Motsa, School of Mathematics, Statistics & Computer Science, University of Kwazulu Natal, Private Bag X01, Scottsville, 3209, Pietermaritzburg, South Africa

Department of Mathematics, University of Eswatini, Private Bag 4, M201, Kwaluseni, Kingdom of Eswatini,
E-mail: sandilemotsa@gmail.com
Precious Sibanda, School of Mathematics, Statistics & Computer Science, University of Kwazulu Natal, Private Bag X01, Scottsville, 3209, Pietermaritzburg, South Africa, E-mail: sibandap@ukzn.ac.za

However, the level of accuracy deteriorated when the time domain increases. Magagula et al. [7] proposed the non-overlapping multi-domain bivariate spectral quasi-linearisation method as an alternative to increase the accuracy of the BSQLM over large time intervals. In the non-overlapping multi-domain BSQLM, the multi-domain technique was only applied in time. Recently, Mkhatshwa et al. [8, 9] found that the accuracy of the BSQLM can be improved by applying the overlapping multi-domain technique in the space interval and the non-overlapping multi-domain technique in the time interval. Teleei and Dehghan [10] introduced a numerical scheme for the solution of sine-Gordon equation when only space discretization is performed by an overlapping multi-domain pseudo-spectral technique. The present work seeks to improve the performance of the standard BSQLM by applying the overlapping multi-domain technique in both space and time intervals. The BSQLM is based on Chebyshev-Gauss-Lobatto points and uses the spectral method for the discretization of both space and time variables. According to Olmos and Shizgal [11], using the overlapping domain decomposition method reduces the round off error for the Chebyshev collocation method and bring about the stability of the method with large step size for time. The proposed method is applied in solving singular time-dependent Emden-Fowler equations since developing a robust and computationally efficient method for Emden-Fowler equations with a large computational time domain remains a challenging task. In this paper, we consider the following singular time-dependent Emden-Fowler heat equation:

$$\frac{\partial^2 u(x, t)}{\partial x^2} + \frac{k}{x} \frac{\partial u(x, t)}{\partial x} + \sigma f(x, t)G(u) + h(x, t) = \frac{\partial u(x, t)}{\partial t},$$
$$0 < x < \epsilon, \ t > 0, \ k > 0, \tag{1.1}$$

where $f(x, t)G(u) + h(x, t)$ is the nonlinear heat source, $u(x, t)$ is the temperature and t is the dimensionless time variable. On the other hand, we consider the singular wave-type equation:

$$\frac{\partial^2 u(x, t)}{\partial x^2} + \frac{k}{x} \frac{\partial u(x, t)}{\partial x} + \sigma f(x, t)G(u) + h(x, t) = \frac{\partial^2 u(x, t)}{\partial t^2},$$
$$0 < x < \epsilon, \ t > 0, \ k > 0, \tag{1.2}$$

where $f(x, t)G(u) + h(x, t)$ is the nonlinear source and $u(x, t)$ is the displacement of the wave at the position x and at time t. The heat and wave-type equations are solved subject to the following Neumann and Dirichlet boundary conditions:

$$\frac{\partial u(0, t)}{\partial x} = 0, \quad u(1, t) = g(t), \tag{1.3}$$

and initial condition $u(x, 0) = v(x)$. Equations (1.1)-(1.2) can be used in modelling various phenomena in areas of mathematical physics and astrophysics such as the diffusion of heat perpendicular to the surface of parallel planes, the theory of stellar structure, the thermal behaviour of a spherical cloud of gas, isothermal gas sphere and theory of thermionic currents [12–14]. Finding the numerical solution of the time-dependent Emden-Fowler equation as well as different linear and nonlinear singular initial value problems (IVPs) in quantum mechanics and astrophysics has been a difficult task because of the singularity behaviour at $x = 0$.

Numerous research work has been carried out to study singular boundary value problems of the form (1.1)-(1.2) using various methods. El-Gamel et al. [15] used B-spline collocation method to find the numerical solution of time-dependent Emden-Fowler equations. Wazwaz [16] applied the Domain decomposition method, while Singh and Wazwaz [17] employed the modified decomposition method in the analysis of the time dependent Emden-Fowler equations. Batiha [18], and Wazwaz [19] studied the time-dependent Emden-Fowler equations using the variation iteration method. Bataineh et al. [20] applied the homotopy analysis method in finding approximate analytical solutions of time-dependent Emden-Fowler type equations. Babolian et al. [21] gave some notes on the implementation of the homotopy perturbation method in solving time-dependent differential equations. Singh et al. [22] proposed a modified homotopy perturbation method and used it to solve nonlinear time-dependent Emden-Fowler equations with boundary conditions. Ullah and Shah [23] considered numerical analysis of Lane Emden-Folwer PDEs with initial condition via the Laplace Adomian decomposition method. Recently, Singh et al. [24] applied the Haar wavelet collocation method in solving Lane-Emden equations with Dirichlet, Newman and Newman-Robin boundary conditions. Mohammadi et al. [25] extended the application of Haar wavelet collocation method to solve nonlinear fractional time-dependent Emden-Fowler equations with initial and boundary conditions. The case where the fractional equations reduces to equations of the form (1.1) was also considered in the study.

Sharma et al. [26] introduced the Chebyshev Operational Matrix Method that uses first kind Chebyshev operation matrix of differentiation to solve linear and non-linear Lane-Emden singular initial value problems. Öztürk [27] used an efficient method that uses Chebyshev spectral operational matrix method to solve a system Lane-Emden ordinary differential equations occurring in engineering. The benefit of the approaches used in these stud-

ies is that only small-size operational matrix is required to achieve highly accurate results. This is because the differentiation matrix contains a lot of zero elements, thus minimizes the run time and lower operation count, resulting in less cumulative truncated errors and improved accuracy. To the best of the author's knowledge, the Chebyshev spectral collocation method on multidomain overlapping grids has not been used to solve time-dependent Emden-Fowler PDEs. The use of overlapping grids has the potential to produce a matrix system with less dense (sparse) matrices with a lot of zero elements. The sparsity of matrices minimizes the storage of large matrices and makes it easy to perform matrix-vector multiplications. Thus, the proposed method requires less computer memory and computational time to produce highly accurate results.

2 Numerical procedure

In this section, we present the implementation of the bivariate spectral collocation method on overlapping grids in solving the time-dependent Emden-Fowler PDEs with singular behaviour. To apply the bivariate spectral method over overlapping grid on the $x - t$ plane, we let $x \in I$, where the space interval $I = [a, b]$ is split into s overlapping subintervals given as

$$I_y = [x_0^y, x_{N_x}^y], \quad y = 1, 2, 3, \ldots, s. \tag{2.1}$$

Similarly, we let $t \in K$, where the time interval $K = [t_0, t_f]$ is decomposed into m overlapping subintervals defines as

$$K_\iota = [t_0^\iota, t_{N_t}^\iota], \quad \iota = 1, 2, 3, \ldots, m. \tag{2.2}$$

Each I_y and K_ι are further discretized into (N_x+1) and (N_t+1) Chebyshev Gauss-Lobatto points (collocation points), respectively. The intervals are split by overlapping one grid point as shown in Figure 1. It can be seen from the figure that the last two points in the I_y and K_ι subintervals overlap with the first two points of the I_{y+1} and $K_{\iota+1}$ subintervals, respectively, and remain common. For the overlap to be possible, the subintervals must be of equal length given by

$$L_x = \frac{b - a}{s + \frac{1}{2}(1 - s)(1 - \cos\frac{\pi}{N_x})}, \tag{2.3}$$

$$L_t = \frac{t_f - t_0}{m + \frac{1}{2}(1 - m)(1 - \cos\frac{\pi}{N_t})}, \tag{2.4}$$

and the same number of collocation points $(N_x + 1)$ and (N_t+1) are used in each subinterval, respectively. To derive the formula in Eq. (2.3), we remark that the total length of

the spatial domain is

$$b - a = 2L_x - \alpha + (2L_x - 2\alpha)\left(\frac{s}{2} - 1\right) \tag{2.5}$$

$$= 2L_x - \alpha + (L_x - \alpha)(s - 2) = \alpha(1 - s) + sL_x, \tag{2.6}$$

where α is the overlapping distance between two intervals. We note that $\alpha = x_0 - x_1$. Considering the first interval I_1 in which $x \in [a, x_{N_x}^1]$, we can define the length $L_x = x_{N_x}^1 - a$. The linear transformation $x = \frac{L_x}{2}\hat{x} + \frac{a+x_{N_x}^1}{2}$ can be used to transform the interval $[a, x_{N_x}^1]$ into $[-1, 1]$. Thus, using the Gauss-Lobatto collocation points $\hat{x}_i = \cos\left(\frac{\pi i}{N_x}\right)$, where $i = 0, 1, 2, 3, \ldots, N_x$, we obtain

$$x_0 - x_1 = \frac{L_x}{2}(\hat{x}_0 - \hat{x}_1) = \frac{L_x}{2}\left(1 - \cos\frac{\pi}{N_x}\right). \tag{2.7}$$

Therefore, Eq. (2.7) becomes

$$b - a = \alpha(1 - s) + sL_x = \frac{L_x}{2}\left(1 - \cos\frac{\pi}{N_x}\right)(1 - s) + sL_x, \tag{2.8}$$

which upon rearranging and making L_x the subject of the formula gives Eq. (2.3). The formula for the length of time domain is derived in a similar manner. In each subinterval, we must solve the heat equation

$$\frac{\partial^2 u^{(y,\iota)}}{\partial x^2} + \frac{k}{x^y}\frac{\partial u^{(y,\iota)}}{\partial x} + \sigma f(x^y, t^\iota)G(u^{(y,\iota)}) + h(x^y, t^\iota) = \frac{\partial u^{(y,\iota)}}{\partial t}, \tag{2.9}$$

where G is the nonlinear function. To solve Eq. (2.9), we first linearise the nonlinear problem using the quasilinearisation method (QLM) [28]. The QLM assumes that the difference between approximate solutions at two successive iterations represented by u_r and u_{r+1} is very small. Consequently, applying the QLM on Eq. (2.9) gives

$$\frac{\partial^2 u_{r+1}^{(y,\iota)}}{\partial x^2} + \frac{k}{x^y}\frac{\partial u_{r+1}^{(y,\iota)}}{\partial x}$$
$$+ \sigma f(x^y, t^\iota)\left[G\left(u_r^{(y,\iota)}\right) + \left(u_{r+1}^{(y,\iota)} - u_r^{(y,\iota)}\right)\frac{\partial G}{\partial u}\left(u_r^{(y,\iota)}\right)\right]$$
$$+ h(x^y, t^\iota) = \frac{\partial u_{r+1}^{(y,\iota)}}{\partial t}, \quad r = 0, 1, 2, 3, \ldots \tag{2.10}$$

which can be written in the form

$$\frac{\partial^2 u_{r+1}^{(y,\iota)}}{\partial x^2} + \frac{k}{x^y}\frac{\partial u_{r+1}^{(y,\iota)}}{\partial x} + \sigma f(x^y, t^\iota)\Lambda_r u_{r+1}^{(y,\iota)} - \frac{\partial u_{r+1}^{(y,\iota)}}{\partial t} =$$
$$\sigma f(x^y, t^\iota)\Lambda_r u_r^{(y,\iota)} - h(x^y, t^\iota) - G\left(u_r^{(y,\iota)}\right), \tag{2.11}$$

where $\Lambda = \frac{\partial G}{\partial u}$. Before the spectral collocation method is applied at each subinterval, the intervals I_y and K_ι are respectively transformed into $\hat{x} \in [-1, 1]$ and $\hat{t} \in [-1, 1]$ using the linear transformations

$$x_i^y = \frac{x_{N_x}^y - x_0^y}{2}\hat{x} + \frac{x_{N_x}^y + x_0^y}{2}, \quad \{\hat{x}_i\}_{i=0}^{N_x} = \cos\left(\frac{\pi i}{N_x}\right), \tag{2.12}$$
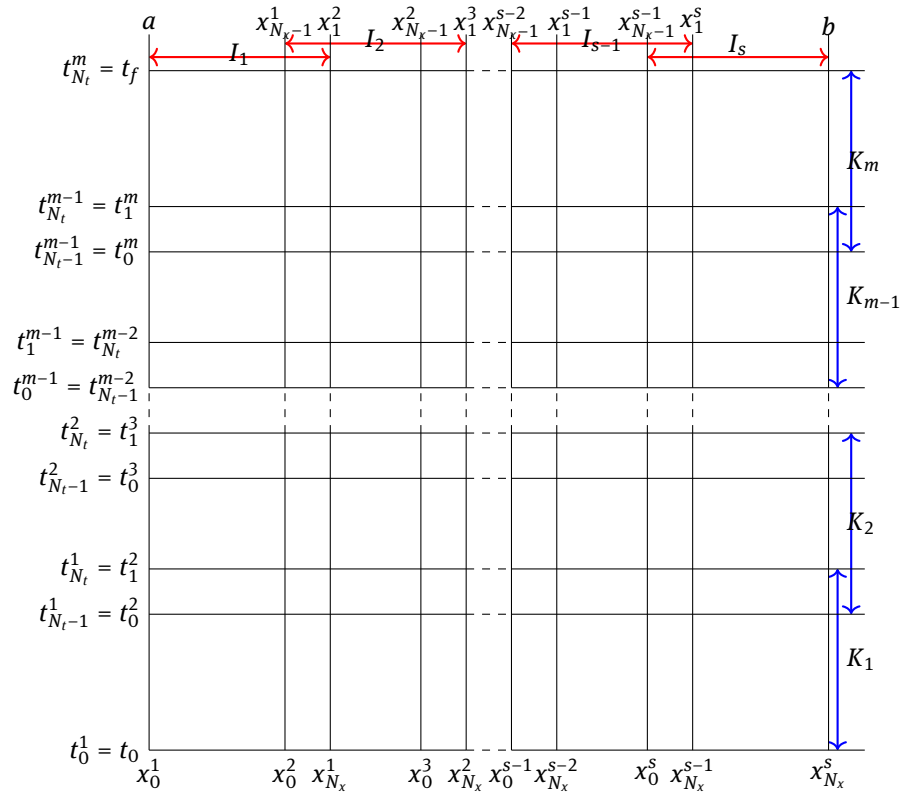
Figure 1: Overlapping grid

$$t_j^t = \frac{t_{N_t}^t - t_0^t}{2}\hat{t} + \frac{t_{N_t}^t + t_0^t}{2}, \quad \left\{\hat{t}_j\right\}_{j=0}^{N_t} = \cos\left(\frac{\pi j}{N_t}\right), \quad (2.13)$$

We assume that at each subinterval, the solution can be approximated by the bivariate Lagrange interpolation polynomial of the form

$$u^{(y,\iota)}(x,t) \approx U^{(y,\iota)}(x,t) = \sum_{z=0}^{N_x}\sum_{\tau=0}^{N_t} U^{(y,\iota)}(x_z, t_\tau)\mathcal{L}_z(x)\mathcal{L}_\tau(t), \quad (2.14)$$

where $\mathcal{L}_z(x)$ and $\mathcal{L}_\tau(t)$ are the well known characteristic Lagrange cardinal polynomial based on the Chebyshev-Gauss-Lobatto points [2, 5]. The first order derivatives of $u^{(y,\iota)}(x,t)$ with respect to x and t at the Gauss-Lobatto points $(\hat{x}, \hat{t})$ are computed as

$$\left.\frac{\partial U^{(y,\iota)}}{\partial x}\right|_{(x=x_i, t=t_j)} = \frac{2}{L_x}\sum_{z=0}^{N_x}\sum_{\tau=0}^{N_t} U^{(y,\iota)}(x_z, t_\tau)\mathcal{L}_\tau(t_j)\left.\frac{d\mathcal{L}_z(x)}{dx}\right|_{x=x_i}$$

$$= \sum_{z=0}^{N_x}\left[\bar{D}_{i,z}^{(y)}\right]^{(1,0)} U^{(y,\iota)}(x_z, t_j) = \left[\mathbf{D}^{(y)}\right]^{(1,0)}\mathbf{U}_j^{(y,\iota)},$$

$$i = 0, 1, 2, ..., M, \quad (2.15)$$

$$\left.\frac{\partial U^{(y,\iota)}}{\partial t}\right|_{(x=x_i, t=t_j)} = \frac{2}{L_t}\sum_{z=0}^{N_x}\sum_{\tau=0}^{N_t} U^{(y,\iota)}(x_z, t_\tau)\mathcal{L}_z(x_i)\left.\frac{d\mathcal{L}_\tau(t)}{dt}\right|_{t=t_j}$$

$$= \sum_{\tau=0}^{N_t}\left[\hat{D}_{j,\tau}^{(\iota)}\right]^{(0,1)} U^{(y,\iota)}(x_i, t_\tau) = \sum_{\tau=0}^{N_t}\left[\hat{D}_{j,\tau}^{(\iota)}\right]^{(0,1)}\mathbf{U}_\tau^{(y,\iota)},$$

$$j = 0, 1, 2, ..., P, \quad (2.16)$$

where $\left[\bar{D}_{i,z}^{(y)}\right]^{(1,0)} = \frac{2}{x_{N_x}^y - x_0^y}D_{i,z}$, with $D_{i,z} = \frac{d\mathcal{L}_z(\hat{x}_i)}{d\hat{x}}$ being the ith and zth entry of the standard first derivative Chebyshev differentiation matrix of size $(N_x + 1) \times (N_x + 1)$ and $\left[\hat{D}_{j,\tau}^{(\iota)}\right]^{(0,1)} = \frac{2}{t_{N_t}^\iota - t_0^\iota}d_{j,\tau}$, with $d_{j,\tau} = \frac{d\mathcal{L}_\tau(\hat{t}_j)}{d\hat{t}}$ being the jth and τth entry of the standard first derivative Chebyshev differentiation matrix of size $(N_t + 1) \times (N_t + 1)$ [5], $M = N_x + (N_x - 1)(s - 1)$ and $P = N_t + (N_t - 1)(m - 1)$ are the total number of collocation point in the entire spatial and time domain, respectively. The second order space and time derivatives are obtained as

$$\left.\frac{\partial^2 U^{(y,\iota)}}{\partial x^2}\right|_{(x=x_i, t=t_j)} = \sum_{z=0}^{N_x}\left[\bar{D}_{i,z}^{(y)}\right]^{(2,0)} U^{(y,\iota)}(x_z, t_j)$$

$$= \left[\mathbf{D}^{(y)}\right]^{(2,0)}\mathbf{U}_j^{(y,\iota)}, \quad (2.17)$$

$$\left.\frac{\partial^2 U^{(y,\iota)}}{\partial t^2}\right|_{(x=x_i, t=t_j)} = \sum_{\tau=0}^{N_t}\left[\hat{D}_{j,\tau}^{(\iota)}\right]^{(0,2)} U^{(y,\iota)}(x_i, t_\tau)$$

$$= \sum_{\tau=0}^{N_t}\left[\hat{D}_{j,\tau}^{(\iota)}\right]^{(0,2)}\mathbf{U}_\tau^{(y,\iota)}, \quad (2.18)$$

The approximate solution to the linearized QLM scheme (2.11) is obtained using the spectral collocation method on the overlapping grids over the entire interval. We apply the overlapping grid multi-domain spectral collocation method by first assembling the differentiation matrices in the space and time variables. Since the last two points in the yth sub-interval and the first two points in the $(y + 1)$th sub-interval overlap and remain common, we remove the rows corresponding to the recurrent grid points and assemble the Chebyshev differentiation matrix $\mathbf{D}$ using $\mathbf{D}^{(y)}$ for the multi-domain technique in x as follows

$$
\mathbf{D} = \begin{bmatrix}
D_{0,0}^{(s)} & D_{0,1}^{(s)} & \cdots & D_{0,N-1}^{(s)} & D_{0,N_x}^{(s)} \\
D_{1,0}^{(s)} & D_{1,1}^{(s)} & \cdots & D_{1,N_x-1}^{(s)} & D_{1,N_x}^{(s)} \\
\ddots & \ddots & \ddots & \ddots & \ddots \\
D_{N_x-1,0}^{(s)} & D_{N_x-1,1}^{(s)} & \cdots & D_{N_x-1,N_x-1}^{(s)} & D_{N_x-1,N_x}^{(s)} \\
 & & & D_{1,0}^{(s-1)} & D_{1,1}^{(s-1)} & \cdots & D_{1,N_x-1}^{(s-1)} & D_{1,N_x}^{(s-1)} \\
 & & & D_{2,0}^{(s-1)} & D_{2,1}^{(s-1)} & \cdots & D_{2,N_x-1}^{(s-1)} & D_{2,N_x}^{(s-1)} \\
 & & & \ddots & \ddots & \ddots & \ddots & \ddots \\
 & & & D_{N_x-1,0}^{(s-1)} & D_{N_x-1,1}^{(s-1)} & \cdots & D_{N_x-1,N_x-1}^{(s-1)} & D_{N_x-1,N_x}^{(s-1)} \\
 & & & & & \ddots & & \ddots \\
 & & & & & & D_{1,0}^{(1)} & D_{1,1}^{(1)} & \cdots & D_{1,N_x-1}^{(1)} & D_{1,N_x}^{(1)} \\
 & & & & & & D_{2,0}^{(1)} & D_{2,1}^{(1)} & \cdots & D_{2,N_x-1}^{(1)} & D_{2,N_x}^{(1)} \\
 & & & & & & \ddots & \ddots \,_D \ddots & \ddots & \ddots \\
 & & & & & & D_{N_x,0}^{(1)} & D_{N_x,1}^{(1)} & \cdots & D_{N_x,N_x-1}^{(1)} & D_{N_x,N_x}^{(1)}
\end{bmatrix} \tag{2.19}
$$

where the empty entries are zeros, which makes the matrix to be sparse, and $D^{(y)}$ denotes Chebyshev differentiation matrix in the yth subinterval. The size of matrix $\mathbf{D}$ is $(M+1)\times(M+1)$, which reduces to a full matrix if only a single domain is used in the calculation. The differentiation matrix in t is assembled using $\hat{\mathbf{D}}^{(l)}$ in a similar manner to obtain a matrix system $\hat{\mathbf{D}}$ of size $(P + 1) \times (P + 1)$. The second order differentiation matrices are computed using matrix multiplications. Using the assembled differentiation matrices in x and t directions in Eq. (2.11) yields the following system of linear equations:

$$
\left[\mathbf{D}^{(2,0)} + \frac{k}{x_i^y}\mathbf{D}^{(1,0)} + \sigma f(x_i^y, t_j^\mu)\Lambda_r\mathbf{I}\right] \mathbf{U}_{j,r+1}^{(y,\iota)} - \sum_{j=0}^{P} \hat{D}_{i,j}^{(0,1)}\mathbf{U}_{j,r+1}^{(y,\iota)} = \sigma f(x_i^y, t_j^t)\Lambda_r u_r^{(y,\iota)} - h(x_i^y, t_j^t) - G(u_r^{(y,\iota)}), \tag{2.20}
$$

Making use of the relevant initial condition, Eq. (2.20) yields

$$
\left[\mathbf{D}^{(2,0)} + \frac{k}{x_i^y}\mathbf{D}^{(1,0)} + \sigma f(x_i^y, t_j^t)\Lambda_r\mathbf{I}\right] \mathbf{U}_{j,r+1}^{(y,\iota)} - \sum_{j=0}^{P-1} \hat{D}_{i,j}^{(0,1)}\mathbf{U}_{j,r+1}^{(y,\iota)} = \mathbf{R}_{i,r}^{(y,\iota)}, \tag{2.21}
$$

where $\mathbf{R}^{(y,\iota)} = \sigma f(x_i^y, t_j^t)\Lambda_r\mathbf{U}_r^{(y,\iota)} - h(x_i^y, t_j^t) - G(\mathbf{U}_r^{(y,\iota)}) + \hat{D}_{j,P}^{(0,1)}\mathbf{U}_P^{(y,\iota)}$. Equation (2.21) can be expressed as an $P(M+1)\times P(M+1)$ matrix system of the form

$$
\begin{bmatrix}
\mathbf{A}_{0,0} & \mathbf{A}_{0,1} & \cdots & \mathbf{A}_{0,P-1} \\
\mathbf{A}_{1,0} & \mathbf{A}_{1,1} & \cdots & \mathbf{A}_{1,P-1} \\
\vdots & \vdots & \ddots & \vdots \\
\mathbf{A}_{P-1,0} & \mathbf{A}_{P-1,1} & \cdots & \mathbf{A}_{P-1,P-1}
\end{bmatrix}
\begin{bmatrix}
\hat{\mathbf{U}}_0 \\
\hat{\mathbf{U}}_1 \\
\vdots \\
\hat{\mathbf{U}}_{P-1}
\end{bmatrix}
=
\begin{bmatrix}
\hat{\mathbf{R}}_0 \\
\hat{\mathbf{R}}_1 \\
\vdots \\
\hat{\mathbf{R}}_{P-1}
\end{bmatrix}, \tag{2.22}
$$

where

$$
\mathbf{A}_{i,i} = \mathbf{D}^{(2,0)} + \frac{k}{x_i^y}\mathbf{D}^{(1,0)} + \sigma f(x_i^y, t_j^t)\Lambda_r\mathbf{I} - \hat{D}_{i,i}^{(0,1)}\mathbf{I}, \;\; i = j, \tag{2.23}
$$

$$
\mathbf{A}_{i,j} = -\hat{D}_{i,j}^{(0,1)}\mathbf{I}, \quad i \neq j, \tag{2.24}
$$

and $\mathbf{I}$ is an identity matrix of size $(M + 1) \times (M + 1)$. For brevity, the application of the BSQLM on overlapping grids in solving the time dependent Emden-Fowler wave equation has been omitted.

3 Numerical examples

This section demonstrates the implementation of the BSQLM on overlapping grids to popular time dependent Emden-Fowler heat-wave equations with known analytical solutions. In all our numerical calculations, we consider Neumann and Dirichlet boundary conditions. The space interval is taken as $[a, b] = [0, 1]$ and the time interval $[t_0, t_f] = [0, T]$ is varied.

3.1 Singular heat-type equations

Example 1. We consider the linear homogeneous time-dependent Emden-Fowler heat equation [17]:

$$\frac{\partial^2 u(x, t)}{\partial x^2} + \frac{5}{x} \frac{\partial u(x, t)}{\partial x} - \left(12t^2 - 2tx^2 + 4t^4 x^2\right) u(x, t)$$
$$= \frac{\partial u(x, t)}{\partial t}, \tag{3.1}$$

subject to the Neumann and Dirichlet boundary conditions

$$\frac{\partial u(0, t)}{\partial x} = 0, \quad u(1, t) = e^{t^2}, \tag{3.2}$$

and initial condition $u(x, 0) = 1$. The exact solution is $u(x, t) = e^{x^2 t^2}$.

Example 2. In the next example, we consider the linear nonhomogeneous time-dependent Emden-Fowler heat equation [15, 16, 19, 23]:

$$\frac{\partial^2 u(x, t)}{\partial x^2} + \frac{2}{x} \frac{\partial u(x, t)}{\partial x} - \left(5 + 4x^2\right) u(x, t)$$
$$= \frac{\partial u(x, t)}{\partial t} + (6 - 5x^2 - 4x^4), \tag{3.3}$$

with the boundary conditions

$$\frac{\partial u(0, t)}{\partial x} = 0, \quad u(1, t) = 1 + e^{1+t}, \tag{3.4}$$

and the initial condition $u(x, 0) = x^2 + e^{x^2}$. The exact solution is given by $u(x, t) = x^2 + e^{x^2 + t}$.

Example 3. Next, we consider the nonlinear time-dependent Emden-Fowler equation [15–17]:

$$\frac{\partial^2 u(x, t)}{\partial x^2} + \frac{5}{x} \frac{\partial u(x, t)}{\partial x} = \frac{\partial u(x, t)}{\partial t} + \left(24t + 16t^2 x^2\right) e^{u(x, t)}$$
$$+ 2x^2 e^{\frac{1}{2} u(x, t)}, \tag{3.5}$$

subject to the boundary conditions

$$\frac{\partial u(0, t)}{\partial x} = 0, \quad u(1, t) = -2 \ln(1 + t), \tag{3.6}$$

and initial condition $u(x, 0) = 0$. The exact solution is known as $u(x, t) = -2 \ln(1 + tx^2)$.

Example 4. In this example, we consider the nonlinear time-dependent Emden-Fowler heat equation [15, 17]:

$$\frac{\partial^2 u(x, t)}{\partial x^2} + \frac{k}{x} \frac{\partial u(x, t)}{\partial x} = \frac{\partial u(x, t)}{\partial t}$$
$$+ \left[t \, (tx)^{(-2+p)} p \left(x^2 - t(-1 + k + p)\right)\right] e^{u(x, t)}$$
$$+ \left[t^2 \, (tx)^{(-2+2p)} p^2\right] e^{2u(x, t)}, \tag{3.7}$$

where k and p are physical parameters. The problem is solved subject to the boundary conditions

$$\frac{\partial u(0, t)}{\partial x} = 0, \quad u(1, t) = \ln\left(\frac{1}{3 + t^p}\right), \tag{3.8}$$

and initial condition $u(x, 0) = \ln(\frac{1}{3})$. The analytical solution is given by $u(x, t) = \ln(\frac{1}{3 + (xt)^p})$. In the present work, the numerical results are obtained for the cases when ($k = 1, p = 2$) and ($k = p = 2$).

3.2 Singular wave-type equations

Example 5. We consider the linear time-dependent Emden-Fowler wave equation [21]:

$$\frac{\partial^2 u(x, t)}{\partial x^2} + \frac{4}{x} \frac{\partial u(x, t)}{\partial x} - (18x + 9x^4) u(x, t) =$$
$$\frac{\partial^2 u(x, t)}{\partial t^2} - 2 - (18x + 9x^4) t^2, \tag{3.9}$$

subject to the boundary conditions

$$\frac{\partial u(0, t)}{\partial x} = 0, \quad u(1, t) = t^2 + e^1, \tag{3.10}$$

and initial condition $u(x, 0) = e^{x^3}$. The analytical solution is given by $u(x, t) = t^2 + e^{x^3}$.

Example 6. Lastly, we consider the nonlinear time-dependent Emden-Fowler wave equation [17]:

$$\frac{\partial^2 u(x, t)}{\partial x^2} + \frac{3}{x} \frac{\partial u(x, t)}{\partial x} = \frac{\partial^2 u(x, t)}{\partial t^2} - 8t e^{u(x, t)}$$
$$+ \left(4t^2 x^2 - x^4\right) e^{2u(x, t)}, \tag{3.11}$$

with the boundary conditions

$$\frac{\partial u(0, t)}{\partial x} = 0, \quad u(1, t) = \ln\left(\frac{1}{5 + t}\right), \tag{3.12}$$

and initial condition $u(x, 0) = \ln(\frac{1}{5})$. The analytical solution is known as $u(x, t) = \ln\left(\frac{1}{5 + tx^2}\right)$.

4 Convergence and stability of the spectral collocation method on overlapping grids

4.1 Convergence

For a numerical scheme to be adopted it needs to resemble the PDEs that is approximated. A numerical method is said to be convergent if the solution of the discrete equations tends to exact solution of the differential equation as the distance between the computational grids is defined. The benefit of spectral methods is that they achieve a high degree of numerical accuracy with little more resolution than the one required to achieve moderate accuracy [29]. The main challenge of numerical analysis in the boundary value problems is to obtain the approximate solution $u(x, t)$ which converges to exact solution as the collocation points increases for some time interval $[t_0, t_f]$. To estimate the error, the approximate solution is subtracted from the exact solution. The basic results is the Lax-Richtmyer equivalence theorem which states that stability is equivalent to converge for consistent approximations to well-posed linear problems. It is worth noting that the theorem is applicable to any discretization. Let the infinity error norm be computed as

$$E_i = ||u_i - \hat{u}_i||_\infty, \quad 0 \le i \le M, \tag{4.1}$$

where u_i is the approximated solution, $\hat{u}_i$ is the exact solution at time level t, M denote the number of collocation points in space direction. The scheme is consistent if as M tends to infinity, infinity norm error goes to zero and then the scheme is convergent [30]. To assess the convergence of the iterative scheme, we record the infinity error norms of the solutions between successive iterations. This values are called solution error, and can be written as

$$||E||_\infty = ||\mathbf{U}_{r+1} - \mathbf{U}_r||_\infty. \tag{4.2}$$

4.2 Stability

The stability analysis of the iterative scheme is accessed by obtaining the condition numbers of the coefficient matrix (in matrix equation that results from collocation process). To compute the condition number of coefficient matrix $\mathbf{A}$, we invoke the Matlab cond($\mathbf{A}$). The condition number of the matrix measures the ratio of the maximum relative stretching to the maximum relative shrinking that matrix does to any non-zero vectors. The 2-norm condition

number of a matrix $A \in \mathbb{C}^{q \times q}$ is given by

$$\varepsilon(A) = ||A||_2 ||A^{-1}||_2. \tag{4.3}$$

Without any preconditioning $\varepsilon(A_q)$ grows proportionally with m, which is better than the typical growth of $O(q^{2Q})$ in the condition number for the standard tau and collocation methods. It is worth noting that the condition number of the linear system is independent of the number of collocation points, and the boundary conditions are imposed exactly.

4.3 Error bounds theorem in spectral collocation method on overlapping grids

This section examines an upper bound theorem for the absolute error and gives a procedure to estimate the absolute error. The error bound theorems that govern polynomial interpolation error in a Bivariate Lagrange interpolating polynomial constructed using Chebyshev Gauss-Lobatto nodes which are basically the relative extremes of the N_x-th degree Chebyshev polynomial of the first kind $T_{N_x}(\hat{x}) = \cos\left[N_x \cos^{-1}(\hat{x})\right]$, $\hat{x} \in [-1, 1]$. A complete set of the Chebyshev Gauss-Lobatto nodes are the roots of the N_x-th degree Chebyshev polynomial defined as

$$L_{N_x+1}(\hat{x}) = \left(1 - \hat{x}^2\right) T'_{N_x}(\hat{x}), \tag{4.4}$$

Next we present the theorem that benchmarks formulation of the error bounds theorems on bivariate polynomial interpolation [31, 32]:

Theorem 1: Let $u(x, t) \in C^{N_x+N_t+2}\left([a, b] \times [t_0, t_f]\right)$ be sufficiently smooth such that at least (N_x+1)-th partial derivative with respect to x, $(N_t + 1)$-th partial derivative with respect to t, and (N_x+N_t+2)-th mixed partial derivative with respect to x and t exists and are all continuous, then there exists values $\delta_x, \delta'_x \in (a, b)$ and $\delta_t, \delta'_t \in (t_0, t_f)$, such that

$$u(x, t) - U(x, t) = \frac{\partial^{N_x+1} u(\delta_x, t)}{\partial^{N_x+1}(N_x + 1)!} \prod_{i=0}^{N_x} (x - x_i)$$

$$+ \frac{\partial^{N_t+1} u(x, \delta_t)}{\partial^{N_t+1}(N_t + 1)!} \prod_{j=0}^{N_t} (t - t_j)$$

$$+ \frac{\partial^{N_x+N_t+2} u(\delta'_x, \delta'_t)}{\partial^{N_x+1}\partial^{N_t+1}(N_x + 1)!(N_t + 1)!} \prod_{i=0}^{N_x} (x - x_i) \prod_{j=0}^{N_t} (t - t_j),$$

$$\tag{4.5}$$

where $U(x, t)$ is a bivariate interpolating polynomial of $u(x, t)$ at $\{x_i\}_{i=0}^{N_x}$ grid points in $x-$ variable and $\{t_j\}_{j=0}^{N_t}$ grid points in $t-$ variable. Similar results to Eq. (4.5) were also

obtained by Brawy [33]. Taking absolute values of Eq. (4.5), we have

$$
u(x, t) - U(x, t) \le \max_{(x,t)\in\Lambda} \left| \frac{\partial^{N_x+1}u(\delta_x, t)}{\partial^{N_x+1}} \right| \frac{\left| \prod_{i=0}^{N_x}(x - x_i) \right|}{(N_x + 1)!}
$$

$$
+ \max_{(x,t)\in\Lambda} \left| \frac{\partial^{N_t+1}u(x, \delta_t)}{\partial^{N_t+1}} \right| \frac{\left| \prod_{j=0}^{N_t}(t - t_j) \right|}{(N_t + 1)!}
$$

$$
+ \max_{(x,t)\in\Lambda} \left| \frac{\partial^{N_x+N_t+2}u(\delta_x', \delta_t')}{\partial^{N_x+1}\partial^{N_t+1}} \right| \frac{\left| \prod_{i=0}^{N_x}(x - x_i) \right| \left| \prod_{j=0}^{N_t}(t - t_j) \right|}{(N_x + 1)!(N_t + 1)!},
$$

$$
\tag{4.6}
$$

where $\Lambda = [a, b] \times [t_0, t_f]$. Since the function $u(x, t)$ is assumed to be smooth on the interval of approximation, it follows that its derivatives are bounded and there exists constants C_1, C_2 and C_3 such that

$$
\max_{(x,t)\in\Lambda} \left| \frac{\partial^{N_x+1}u(\delta_x, t)}{\partial^{N_x+1}} \right| \le C_1, \quad \max_{(x,t)\in\Lambda} \left| \frac{\partial^{N_t+1}u(x, \delta_t)}{\partial^{N_t+1}} \right| \le C_2,
$$

$$
\max_{(x,t)\in\Lambda} \left| \frac{\partial^{N_x+N_t+2}u(\delta_x', \delta_t')}{\partial^{N_x+1}\partial^{N_t+1}} \right| \le C_3,
$$

$$
\tag{4.7}
$$

4.3.1 Error bound on a single domain

The error bound theorem for the bivariate polynomial interpolation using Chebyshev Gauss-Lobatto nodes on a single domain is governed by the theorem below:

Theorem 2: (The error bound on single domain). The forthcoming error bound when the Chebyshev Gauss-Lobatto grid points $\{x_i\}_{i=0}^{N_x}$ in $x-$ variable and $\{t_j\}_{j=0}^{N_t}$ in $t-$ variable are used in bivariate polynomial interpolation is as follows :

$$
E(x, t) \le C_1 \frac{8\left(\frac{b-a}{4}\right)^{N_x+1}}{(N_x + 1)!} + C_2 \frac{8\left(\frac{t_f-t_0}{4}\right)^{N_t+1}}{(N_t + 1)!}
$$

$$
+ C_3 \frac{8^2\left(\frac{b-a}{4}\right)^{N_x+1}\left(\frac{t_f-t_0}{4}\right)^{N_t+1}}{(N_x + 1)!(N_t + 1)!},
$$

$$
\tag{4.8}
$$

Proof: First, using the relation in [34], we express Eq. (4.4) in the form

$$
L_{N_x+1}(\hat{x}) = (1 - \hat{x}^2)T'_{N_x}(\hat{x}) = -N_x\hat{x}T_{N_x}(\hat{x}) + N_x T_{N_x-1}(\hat{x}).
$$

$$
\tag{4.9}
$$

Using the triangular inequality and noticing that $|T_{N_x}(\hat{x})| \le 1$, $\forall \hat{x} \in [-1, 1]$, we have

$$
L_{N_x+1}(\hat{x}) = |-N_x\hat{x}T_{N_x}(\hat{x}) + N_x T_{N_x-1}(\hat{x})|
$$

$$
\le |-N_x\hat{x}T_{N_x}(\hat{x})| + |N_x T_{N_x-1}(\hat{x})| \le 2N_x. \tag{4.10}
$$

The leading coefficients of $L_{N_x+1}(\hat{x})$ is $2^{N_x-1}N_x$, where the components 2^{N_x-1} and N_x, respectively, emerge from the leading coefficient of $T_{N_x}(\hat{x})$ and the application of the N_x-th rule of differentiation on T_{N_x}. The product factor in the first term of the error bound expression given at Eq. (4.6) can be considered as the factorised form of monic polynomial $\frac{L_{N_x+1}(\hat{x})}{2^{N_x-1}N_x}$. We have,

$$
\prod_{i=0}^{N_x}(\hat{x} - \hat{x}_i) = \frac{L_{N_x+1}(\hat{x})}{2^{N_x-1}N_x}, \hat{x} \in [-1, 1]. \tag{4.11}
$$

Using Eq. (4.10), it is easy to show that the monic polynomial (4.11) is bounded by

$$
\left| \prod_{i=0}^{N_x}(\hat{x} - \hat{x}_i) \right| = \left| \frac{L_{N_x+1}(\hat{x})}{2^{N_x-1}N_x} \right| \le \frac{2N_x}{2^{N_x-1}N_x} = \frac{4}{2^{N_x}}, \tag{4.12}
$$

In view of the general interval $x \in [a, b]$, we can exhibit that the first product factor in Eq. (4.6) is bounded by

$$
\max_{a\le x\le b} \left| \prod_{i=0}^{N_x}(x - x_i) \right| = \max_{-1\le\hat{x}\le1} \left| \prod_{i=0}^{N_x} \frac{(b - a)}{2}(\hat{x} - \hat{x}_i) \right|
$$

$$
= \left(\frac{b - a}{2}\right)^{N_x+1} \max_{-1\le\hat{x}\le1} \left| \prod_{i=0}^{N_x}(\hat{x} - \hat{x}_i) \right|
$$

$$
= \left(\frac{b - a}{2}\right)^{N_x+1} \max_{-1\le\hat{x}\le1} \left| \frac{L_{N_x+1}(\hat{x})}{2^{N_x-1}N_x} \right|
$$

$$
\le \frac{4\left(\frac{b-a}{2}\right)^{N_x+1}}{2^{N_x}} = 8\left(\frac{b - a}{4}\right)^{N_x+1} \tag{4.13}
$$

Similarly, the second product factor is bounded above by

$$
\max_{t_0\le t\le t_f} \left| \prod_{j=0}^{N_t}(t - t_j) \right| = \left(\frac{t_f - t_0}{2}\right)^{N_t+1} \max_{-1\le\hat{t}\le1} \left| \frac{L_{N_t+1}(\hat{t})}{2^{N_t-1}N_t} \right|
$$

$$
\le \frac{4\left(\frac{t_f-t_0}{2}\right)^{N_t+1}}{2^{N_t}} = 8\left(\frac{t_f - t_0}{4}\right)^{N_t+1}, \tag{4.14}
$$

Using Eq. (4.13), (4.14) and Eq. (4.6) and (4.7) complete the proof.

4.3.2 Error bound theorem in overlapping multiple intervals

In this section, the bivariate polynomial interpolation error bound theorem for single domain is extended to accommodate decomposed domains. It is worth mentioning that the number of grid points is assumed to be the same for all subintervals in either space or time direction.

Error bound in the decomposed domain: The error bound when the Chebyshev Gauss-Lobatto grid points $\{x_i\}_{i=0}^{N_x} \in [x_0^y, x_{N_x}^y]$, $y = 1, 2, 3, ..., s$, in space variable and $\{t_j\}_{j=0}^{N_t} \in [t_0^\iota, t_{N_t}^\iota]$, $\iota = 1, 2, 3, ..., m$, in time variable are used in bivariate polynomial interpolation is as follows:

$$E(x, t) \leq C_1 \frac{8\left(\frac{L_x}{4}\right)^{N_x+1}}{(N_x + 1)!} + C_2 \frac{8\left(\frac{L_t}{4}\right)^{N_t+1}}{(N_t + 1)!}$$
$$+ C_3 \frac{8^2\left(\frac{L_x}{4}\right)^{N_x+1}\left(\frac{L_t}{4}\right)^{N_t+1}}{(N_x + 1)!(N_t + 1)!}, \tag{4.15}$$

where L_x and L_t represent the length of each subinterval in x and t, as given in Eq. (2.3) and (2.4).

Proof: First, we consider the x variable. In the entire spatial domain $[a, b]$, we have that

$$\left|\prod_{i=0}^{N_x}(x - x_i)\right| \leq 8\left(\frac{b - a}{4}\right)^{N_x+1}, x \in [a, b]. \tag{4.16}$$

Since the interpolation is done piece-wise and taking into account that the error bound depends on the length of the interval as from the previous theorem, there is a straight-forward inference that in the decomposed domain and at each subinterval is x, we must have

$$\left|\prod_{i=0}^{N_x}(x - x_i)\right| \leq 8\left(\frac{L_x}{4}\right)^{N_x+1}, \{x_i\}_{i=0}^{N_x} \in [x_0^y, x_{N_x}^y],$$
$$y = 1, 2, 3, ..., s. \tag{4.17}$$

Using the assumption that the unknown function $u(x, t)$ is smooth, it is necessary to state that $\exists \, \delta_\kappa \in (x_0^\kappa, x_{N_x}^\kappa)$, $\kappa = 1, 2, 3, ..., s$, for which the values of the $(N_x + 1)$th partial derivatives of $u(x, t)$ with respect to x in each subdomain, is the absolute extrema. This allows us to split the first term $C_1 \frac{8\left(\frac{b-a}{4}\right)^{N_x+1}}{(N_x+1)!}$, which appears in the error bound expression at Eq. (4.8), into separate components that are certainly not equal in the divided x domain, as

$$\left\{C_1^{(y)} \frac{8\left(\frac{L_x}{4}\right)^{N_x+1}}{(N_x + 1)!}\right\}_{y=1}^s, \tag{4.18}$$

where

$$\max_{(x,t)\in\Lambda} \left|\frac{\partial^{N_x+1} u(x, t)}{\partial^{N_x+1}}\right| = \left|\frac{\partial^{N_x+1} u(\delta_x, t)}{\partial^{N_x+1}}\right| \leq C_1^y, x \in [x_0^y, x_{N_x}^y]. \tag{4.19}$$

We define

$$\|\bar{C}_1\|_\infty \equiv \max\left\{C_1^{(1)}, C_1^{(2)}, C_1^{(3)}, ..., C^{(s)}\right\}, \tag{4.20}$$

to represent the maximum absolute value of the $(N_x + 1)$-th partial derivatives of $u(x, t)$ with respect to $x \in [a, b]$. Distinctly, $\|\bar{C}_1\|_\infty = C_1$, where C_1 is identical to the given Eq. (4.8). To expand the error bound over the x domain, we shall consider the largest possible error across all overlapping subintervals in x, which is

$$C_1 \frac{8\left(\frac{L_x}{4}\right)^{N_x+1}}{(N_x + 1)!}. \tag{4.21}$$

The same procedure can be used to show that the second component in the error bound Eq. (4.8) in the decomposed t domain gives

$$C_2 \frac{8\left(\frac{L_t}{4}\right)^{N_t+1}}{(N_t + 1)!}, \tag{4.22}$$

Accordingly, the third component in Eq. (4.8) becomes

$$C_3 \frac{8^2\left(\frac{L_x}{4}\right)^{N_x+1}\left(\frac{L_t}{4}\right)^{N_t+1}}{(N_x + 1)!(N_t + 1)!}, \tag{4.23}$$

in the decomposed domain and $\left(\frac{L_x}{4}\right)^{N_x+1} \ll \left(\frac{b-a}{4}\right)^{N_x+1}$ and $\left(\frac{L_t}{4}\right)^{N_t+1} \ll \left(\frac{t_f-t_0}{4}\right)^{N_t+1}$ for large number of subintervals y and ι in x and t, respectively. Using Eq. (4.21)-(4.23) completes the proof.

5 Results and discussion

In this section, we present the numerical results of the time dependent Emden-Fowler equations obtained using spectral collocation method on overlapping grids. In order to assess the performance and reliability of the method, the numerical results are compared with results from the literature and exact solutions. The level of accuracy of the approximate solution in comparison with the exact solution is measured by calculating the maximum error E_N defined as

$$E_N = \max_i \left\{\left|u(x_i, t) - \hat{u}(x_i, t)\right|, : 0 \leq i \leq N\right\}, \tag{5.1}$$

where $u(x_i, t)$ is the approximate solution and $\hat{u}(x_i, t)$ is the exact solution.

5.1 Maximum error estimates for varying time and space grid points

The maximum errors for the numerical examples are presented in Tables 1 - 8 at different collocation points in space

for varying time t. The central processing unit (CPU) computational time is presented at the bottom of each table. Table 1 displays the maximum error estimates for example 1 when $N_t = 10$, and $m = s = 3$. When $N_x = 4$, the BSQLM on overlapping grids produces maximum errors of about 10^{-11} for small time ($t = 0.1$) and 10^{-5} for increasing time ($t = 0.8, 1$). On the other hand, when $N_x = 10, 12$ the method gives maximum errors of about 10^{-12} for both small and increasing time. This observation suggests that increasing the number of grid points from $N_x = 4$ to $N_x = 10$ gives more accurate solutions with accuracy not deteriorating with increasing time variable. Increasing space grid points beyond $N_x = 10$ does not significantly improve the accuracy of the BSQLM on overlapping grids. We can remark that these accurate results are achieved using a minimal number of grid points and convergence of the method is reached within few seconds. From table 1, it is also noted that the modified decomposition method gives a maximum error of up to 10^{-3}, while the BSQLM on overlapping grids gives a maximum error of up to 10^{-13}. This implies that the BSQLM on overlapping grids is more accurate than other methods including the modified decomposition method employed by Singh and Wazwaz [17].

Table 2 summarizes the maximum error estimates for example 2 obtained by the proposed method using $N_t = 10$, and $m = s = 3$. For $N_x = 4$, the BSQLM on overlapping grids gives a maximum error of about 10^{-4} and for $N_x = 10, 12$, the maximum error is 10^{-11} on average. It is clear from the table that the computed maximum errors decline monotonically as the number of grid points increases. A maximum of $N_x = 10$ grid points is enough to ensure that the numerical method converged to the desired accuracy in a fraction of seconds. Hence, the numerical method uses few grid points and less computational time to achieve accurate results. For comparison, we have shown that the maximum errors obtained in the present study are relatively lower than those obtained by El-Gamel et al. [15] using the B-spline collocation method. This observation suggests that the BSQLM on overlapping grids performs better than the B-spline collocation method.

In Table 3, the maximum error estimates for example 3 are presented when $N_t = 10$, and $m = s = 3$. When $N_x = 4$, the BSQLM on overlapping grids produces maximum errors of about 10^{-8} for small time ($t = 0.1$) and 10^{-5} for increasing time ($t = 0.6, 0.7, 0.8, 1$). On the other hand, when $N_x = 10, 12$ the method gives maximum errors close to 10^{-13} for both small and increasing time. We observe that using $N_x = 10$ for the BSQLM on overlapping grids gives more accurate results. Once again, increasing space grid points beyond $N_x = 10$ does not significantly

improve the accuracy of the method. We also compare the maximum error estimates with those obtained using B-Spline collocation method of El-Gamel [15] and Modified Decomposition method of Singh and Wazwaz [17]. The absolute errors from the proposed method were also compared with errors computed using modified homotopy perturbation method by Singh et al. [22], Adomian decomposition method by Wazwaz [16] and Haar wavelet collocation method by Mohammadi et al. [25]. The results are shown in Table 4 for varying x.. From these comparisons, it is clear that the errors obtained using the BSQLM on overlapping grids are less than those obtained using the B-Spline collocation, Decomposition method, homotopy perturbation method and Haar wavelet collocation method. Thus, it can be deduced that the BSQLM on overlapping grids gives highly accurate results and computationally efficient when compared to other methods.

Tables 5 and 6 display the maximum error estimates for example 4, which were obtained using the BSQLM on overlapping grids when $N_t = 10, p = 2$, and $m = s = 3$. When $N_x = 4$, the BSQLM on overlapping grids gives maximum errors of about 10^{-12} for small time ($t = 0.1$) and 10^{-5} for increasing time ($t = 1.7, 2$). On the other hand, when $N_x = 10, 12$ the method produces maximum errors of about 10^{-12} for both small and large time. It can be seen that varying the constants k and p does not affect the accuracy of the method since the maximum error estimates do not change significantly when the same number of grid points are used. It is also noted that increasing the number of grid points decreases the maximum error and a maximum of $N_x = 10$ space grid points is sufficient to ensure convergence of the method to the desired accuracy within a fraction of seconds. The accuracy of the method does not improve when increasing space grid points above $N_x = 10$. The maximum errors computed using the BSQLM on overlapping grids are seen to be smaller than those obtained by Singh and Wazwaz [17] using the Modified Decomposition method. These numerical outcome indicates high accuracy and efficiency of the proposed method.

Table 7 presents the maximum error estimates for example 5 generated using the BSQLM on overlapping grids when $N_t = 5, m = s = 3$. The decrease in the maximum errors as the time t becomes large implies that the accuracy of the BSQLM on overlapping grids does not deteriorate as t increases. Thus, it can be concluded that decomposing the main intervals into overlapping subintervals improves the accuracy of the BSQLM method. For $N_x = 6$, the BSQLM on overlapping grids gives a maximum error of about 10^{-6} and for $N_x = 10, 12$, the maximum error is about 10^{-10}. We observe that increasing the number of grid points decreases the maximum error and $N_x = 10$ space grid points

Table 1: Maximum errors E_N for example 1 using $N_t = 10$ and $m = s = 3$

$t \backslash N_x$	4	6	8	10	12	Singh and Wazwaz [17]
0.1	2.7032e-011	6.2594e-013	9.9853e-013	2.8331e-012	2.2855e-012	-
0.2	1.9447e-009	2.6690e-013	3.4772e-012	1.0118e-011	1.0050e-011	-
0.3	2.4218e-008	4.9165e-012	1.3165e-012	3.8836e-012	1.4514e-011	-
0.4	1.4964e-007	5.3980e-011	6.3749e-013	5.4465e-012	1.1304e-011	-
0.5	6.3576e-007	3.7258e-010	9.2948e-013	2.7414e-012	4.9281e-012	1.68682e-003
0.6	2.1447e-006	1.8983e-009	1.7959e-012	3.6626e-012	9.9449e-012	-
0.7	6.2927e-006	7.8670e-009	1.0117e-011	4.0949e-012	1.8006e-011	-
0.8	1.6564e-005	2.8185e-008	3.7555e-011	6.2184e-012	1.5489e-011	-
1	9.1402e-005	2.6887e-007	6.0193e-010	4.2895e-012	8.5687e-012	2.49443e-002
CPU Time	0.030678	0.068325	0.135047	0.164138	0.241184	-

Table 2: Maximum errors E_N for example 2 using $N_t = 10$ and $m = s = 3$

$t \backslash N_x$	4	6	8	10	12	El-Gamel et al. [15]
0.1	1.3627e-004	3.6444e-007	7.7253e-010	1.1648e-011	1.9944e-011	1.541e-05
0.2	1.5067e-004	4.0335e-007	8.5353e-010	7.8915e-012	1.2781e-011	-
0.4	1.8404e-004	4.9282e-007	1.0442e-009	1.5382e-011	2.4286e-011	-
0.5	2.0340e-004	5.4465e-007	1.1539e-009	6.6538e-012	2.2956e-011	2.431e-05
0.8	2.7456e-004	7.3521e-007	1.5547e-009	1.6607e-011	6.6873e-011	-
1	3.3534e-004	8.9798e-007	1.9099e-009	1.0463e-011	1.8777e-011	4.008e-05
1.2	4.0959e-004	1.0968e-006	2.3222e-009	2.4110e-011	8.3839e-011	-
1.4	5.0027e-004	1.3396e-006	2.8322e-009	3.3756e-011	8.2454e-011	-
1.6	6.1104e-004	1.6362e-006	3.4713e-009	4.2048e-011	4.2372e-011	-
2	9.1156e-004	2.4410e-006	5.1725e-009	7.0948e-011	7.3666e-011	-
CPU Time	0.027655	0.059255	0.105297	0.161377	0.247752	-

Table 3: Maximum errors E_N for example 3 using $N_t = 10$ and $m = s = 3$

$t \backslash N_x$	4	6	8	10	12	Sing and Wazwaz [17]	El-Gamel et al. [15]
0.1	7.9494e-008	3.6645e-011	1.1463e-013	5.9744e-013	1.0649e-012	-	5.202e-05
0.2	5.1143e-007	4.1489e-010	4.7408e-013	7.0116e-013	7.9162e-013	-	1.148e-04
0.3	1.7218e-006	2.0603e-009	3.3333e-012	1.0248e-012	6.8643e-012	-	-
0.4	3.9985e-006	6.1430e-009	1.2917e-011	6.0660e-013	3.3857e-012	-	-
0.5	7.5313e-006	1.3838e-008	3.4698e-011	1.4209e-012	6.2185e-012	8.1151e-003	-
0.6	1.2374e-005	2.6808e-008	7.9783e-011	4.0957e-012	8.1165e-012	-	-
0.7	1.8436e-005	4.8558e-008	1.5799e-010	3.6885e-012	8.6302e-012	-	-
0.8	2.5473e-005	8.0908e-008	2.8350e-010	7.0806e-012	9.1263e-012	-	-
1	4.1074e-005	1.8904e-007	7.5399e-010	3.7352e-012	4.1977e-012	2.49443e-002	-
CPU Time	0.145928	0.279091	0.503767	0.849340	1.378707	-	-

is enough to ensure that the numerical method converged to the exact solution over the large computational time domain. Using $N_t = 5$ and $N_x = 10$ as well as employing the overlapping grid strategy reduces the size of the coefficient matrix which in turn reduces the computational time. Thus, the BSQLM on overlapping grids uses fewer grid points and minimal computational time to achieve more accurate results for large time domains.

Table 8 displays the maximum error estimates for example 6 using $N_t = 5$, and $m = s = 3$. Just like in the previous example, the accuracy of the BSQLM on overlapping grids in solving example 6 does not worsen as t becomes large. When $N_x = 4$, the BSQLM on overlapping grids gives maximum errors of about 10^{-7} for small time ($t = 0.1$) and 10^{-4} for large time ($t = 10, 12, 14, 16, 18, 19$). On the other hand, when $N_x = 8, 10, 12$ the method gener-

Table 4: Maximum errors E_N for example 3 using $N_t = N_x = 10$, $m = s = 3$, and $t = 0.5$

x	Singh et al. [22]	Wazwaz [16]	Mohammadi et al. [25]	Present results
0.1	2.2300e-04	5.3985e-15	3.8818e-07	1.5556e-014
0.2	2.1300e-04	2.0974e-11	4.6257e-07	8.7764e-013
0.3	3.1900e-04	2.6652e-09	6.8850e-07	1.1586e-013
0.4	2.3500e-04	8.1781e-08	4.6909e-06	2.3337e-012
0.5	2.3600e-04	1.1487e-06	2.5043e-05	3.1268e-012
0.6	3.3100e-04	9.8258e-06	7.0896e-05	5.6095e-012
0.7	2.2700e-04	5.9617e-05	1.5046e-04	3.8346e-012
0.8	1.3300e-04	2.8116e-04	2.6759e-04	6.7432e-012
0.9	2.6000e-05	1.0935e-03	4.2135e-04	3.4377e-012
1	0.000000	3.6531e-03	6.0658e-04	3.7352e-012

Table 5: Maximum errors E_N for example 4 using $N_t = 10$, $m = s = 3$ and $k = 1$, $p = 2$

$t \backslash N_x$	4	6	8	10	12	Singh and Wazwaz [17]
0.1	2.0992e-012	8.4777e-013	2.3177e-012	2.7267e-012	4.3436e-012	-
0.2	1.5251e-010	3.1997e-013	2.1863e-012	2.6663e-012	1.5183e-012	-
0.3	1.7306e-009	3.9879e-013	1.2415e-012	3.1604e-012	2.9396e-012	-
0.5	3.1536e-008	1.1303e-011	1.3922e-012	3.7710e-012	2.1513e-011	7.6164e-004
0.7	1.7269e-007	8.6033e-011	6.6991e-013	3.6995e-012	7.2982e-012	-
1	1.0054e-006	1.5192e-009	3.2312e-012	4.2584e-012	9.2206e-012	9.4733e-004
1.2	2.8188e-006	5.9746e-009	1.5796e-011	3.3356e-012	7.6605e-012	-
1.5	8.9536e-006	2.9790e-008	8.7292e-011	3.8634e-012	9.0561e-012	-
1.7	1.9056e-005	6.8365e-008	2.2445e-010	4.6017e-012	6.6456e-012	-
2	4.8793e-005	1.8736e-007	7.6246e-010	7.9028e-012	4.8510e-012	-
CPU Time	0.135166	0.269503	0.478339	0.841058	1.329802	-

Table 6: Maximum errors E_N for example 4 using $N_t = 10$, $m = s = 3$ and $k = p = 2$

$t \backslash N_x$	4	6	8	10	12	Singh and Wazwaz [17]
0.1	2.0728e-012	4.3587e-013	1.3951e-012	5.6384e-012	5.2225e-012	-
0.2	1.4708e-010	2.4425e-013	3.5532e-012	2.9743e-012	1.0799e-011	-
0.3	1.6640e-009	6.0574e-013	1.4022e-012	3.3729e-012	1.3267e-011	-
0.5	3.0413e-008	1.1060e-011	4.3743e-013	2.7836e-012	1.1411e-011	8.022e-005
0.7	1.6844e-007	8.9288e-011	2.0448e-012	6.0698e-012	3.8620e-012	-
1	1.1188e-006	1.5465e-009	3.8647e-012	3.7705e-012	3.3966e-012	9.929e-005
1.2	3.1528e-006	5.9507e-009	1.3870e-011	3.2589e-012	9.7775e-012	-
1.5	1.0284e-005	2.9659e-008	9.1938e-011	4.3012e-012	4.4464e-012	-
1.7	1.8836e-005	6.9950e-008	2.4621e-010	5.4248e-012	1.0157e-011	-
2	4.3144e-005	2.0118e-007	8.9129e-010	6.3878e-012	6.1879e-012	-
CPU Time	0.129197	0.259293	0.484481	0.836222	1.320742	-

ates maximum errors of close to 10^{-8} for both small and large time. An increase in the number of grid points results in a decrease in the maximum error from $N_x = 4$ to $N_x = 8$. However, the decrease in the maximum error estimates from $N_x = 8$ to $N_x = 12$ is not significant particularly for small values of time t. This suggest that $N_x = 8$ space grid points is sufficient to ensure that the method converged to the exact solution over the large time domain.

Numerical solutions for example 6 were obtained using few grid points and less computational time.

Table 7: Maximum errors E_N for example 5 using $N_t = 5$, $m = s = 3$

$t\backslash N_x$	6	8	10	12
1	1.4597e-005	7.5077e-007	6.0796e-008	3.6887e-008
2	6.1951e-006	4.5171e-008	1.1547e-009	2.6870e-009
4	6.0941e-006	4.4383e-008	3.7191e-010	2.3821e-010
6	5.8925e-006	4.3594e-008	2.9772e-010	1.4603e-010
8	5.9088e-006	4.3606e-008	5.3856e-010	6.9367e-010
10	5.9090e-006	4.3792e-008	2.8747e-010	4.3056e-010
12	5.9090e-006	4.3710e-008	4.2081e-010	1.6001e-009
14	5.9090e-006	4.3384e-008	5.0292e-010	6.6805e-010
16	5.9090e-006	4.3686e-008	3.2327e-010	1.1920e-010
18	5.9090e-006	4.3778e-008	4.5924e-010	5.9612e-010
CPU Time	0.011878	0.016307	0.022972	0.036610

Table 8: Maximum errors E_N for example 6 using $N_t = 5$, $m = s = 3$

$t\backslash N_x$	4	6	8	10	12
1	7.0535e-007	7.7687e-007	7.6292e-007	8.1070e-007	6.8236e-007
2	1.8492e-006	3.0200e-007	2.9740e-007	2.9900e-007	3.0049e-007
4	1.2359e-005	7.4108e-007	7.4364e-007	7.4269e-007	7.4347e-007
8	7.4115e-005	5.6244e-007	2.1912e-007	2.1937e-007	2.1932e-007
10	1.3696e-004	8.3875e-007	6.4378e-008	6.4580e-008	6.5044e-008
12	2.2265e-004	1.3686e-006	2.7446e-008	2.6343e-008	2.6126e-008
14	3.3358e-004	2.0690e-006	3.7544e-008	3.2172e-008	3.2208e-008
16	4.7201e-004	2.9250e-006	6.4639e-008	4.3655e-008	4.3647e-008
18	6.3984e-004	3.9047e-006	1.0723e-007	7.4644e-008	7.4522e-008
19	7.5118e-004	4.6086e-006	1.2866e-007	8.9153e-008	8.9262e-008
CPU Time	0.126031	0.228421	0.324762	0.518048	0.916834

5.2 Maximum error estimates for varying subintervals

Tables 9 -12 present maximum errors for the different number of overlapping subintervals for the heat equations (examples 1, 2 and 5) when $N_t = N_x = 10$ and $t = 1$ and wave equation (example 5), when $N_t = 5$, $N_x = 10$ and $t = 16$. It is worth noting that $m = s = 1$ represent the single domain BSQLM and $m, s = 2, 3, 4, 5$ represent the BSQLM on overlapping grids. It is observed from all tables that the maximum errors are smaller when both space and time intervals are split into overlapping subintervals. This implies that the accuracy of the method improves by employing the overlapping grid strategy in both space and time. It is worth mentioning that the maximum error also decreases when the overlapping grid strategy is applied only in space but not in time. This suggests that the overlapping grid strategy has a significant impact on the space interval than in the time interval.

6 Stability

To assess the stability of the numerical scheme, we computed condition numbers of the associated coefficient matrices of the system of linearized equations being solved.

Table 9: Maximum errors E_N for example 1 using $N_t = N_x = 10$ and $t = 1$.

$m\backslash s$	1	2	3	4	5
1	2.0147e-008	9.0459e-010	9.3860e-010	9.2397e-010	9.3621e-010
2	1.9919e-008	3.6569e-011	6.8341e-012	1.5237e-011	6.4912e-011
3	1.9920e-008	3.6278e-011	4.2895e-012	4.2371e-011	2.0932e-011
4	1.9920e-008	3.4636e-011	6.6422e-012	1.3078e-011	1.1076e-011
5	1.9920e-008	3.4639e-011	9.1882e-012	7.8106e-012	1.5590e-011

Table 10: Maximum errors E_N for example 2 using $N_t = N_x = 10$ and $t = 1$.

$m\backslash s$	1	2	3	4	5
1	3.5346e-008	1.1623e-010	8.0965e-011	6.2935e-011	1.2047e-010
2	3.5338e-008	1.2065e-010	1.8076e-011	2.3173e-011	5.9133e-011
3	3.5338e-008	1.1539e-010	1.0463e-011	9.9980e-011	3.6071e-011
4	3.5338e-008	1.1726e-010	1.2884e-011	3.5653e-011	9.5985e-011
5	3.5338e-008	1.1433e-010	1.4735e-011	8.3071e-011	7.5446e-011

Table 11: Maximum errors E_N for example 3 using $N_t = N_x = 10$ and $t = 1$.

$m\backslash s$	1	2	3	4	5
1	1.0558e-007	1.2804e-010	8.1803e-011	8.8232e-011	7.4566e-011
2	1.0562e-007	6.3431e-011	4.4183e-012	4.5055e-012	9.8677e-012
3	1.0562e-007	6.1951e-011	3.7352e-012	2.5439e-012	1.6987e-011
4	1.0562e-007	6.2194e-011	1.6095e-011	9.8566e-012	2.0757e-011
5	1.0562e-007	6.6759e-011	3.6396e-012	2.3268e-011	1.4699e-011

Table 12: Maximum errors E_N for example 5 using $N_t = 5$, $N_x = 10$ and $t = 16$.

$m\backslash s$	1	2	3	4	5
1	1.5564e-006	6.1810e-009	2.7467e-010	3.0298e-011	1.2164e-011
2	1.5584e-006	6.1370e-009	4.6242e-010	1.2660e-009	1.1395e-009
3	1.5586e-006	6.1313e-009	3.2327e-010	1.1237e-009	1.1646e-009
4	1.5585e-006	6.2987e-009	1.9559e-009	1.0264e-009	4.5667e-009
5	1.5585e-006	6.0227e-009	8.6720e-010	1.2012e-009	4.6034e-009

We have shown results for both single domain BSQLM and BSQLM on overlapping grids in Tables 13 and 14. Looking at the sizes of the coefficient matrices, the condition numbers for the spectral collocation method on overlapping grids are smaller than those from the spectral collocation method on single domains. This indicate that the system linear algebraic equations is well posed, hence the proposed numerical scheme is stable and accurate. It is also noted that the errors are always smaller in the spectral collocation method on decomposed domains than on single domains. Also, when the computational time domain becomes large on the single domain approach, the error become very large. This means that the accuracy deteriorates as the computational domain becomes large on single domain approach, which is not the case with spectral collocation method on overlapping grids. The CPU time is

also observed to be less for the spectral collocation method on overlapping grids. This is attributed to the sparse coefficient matrices, which are easy to invert. Sparse matrices are well conditioned, and results to a well-posed problem, thus leading to stable results. Based on the above observations, we can conclude that spectral collocation method on overlapping grids is computationally efficient, gives stable and accurate solutions using few grid points in each subinterval. The use of few grid points in each subinterval minimizes the effects of round-off errors that are related to approximating functions with interpolating polynomials of higher degree.

Table 13: Maximum errors E_N and condition numbers of coefficient matrices on single domain ($p = q = 1$) when $N_x = 80$ and $N_t = 10$.

Examples	t	Matrix size	Maximum Error	Condition number	CPU Time
1	1	810 × 810	5.2184e-009	1.5831e+008	5.134862
2	1	810 × 810	5.0243e-009	5.7068e+007	5.133314
3	1	810 × 810	2.9086e-009	6.2421e+008	6.662206
4 ($k = 1$)	1	810 × 810	1.4420e-009	9.1551e+007	5.498131
5	16	810 × 810	8.4671e-001	2.3711e+009	6.144010
6	16	810 × 810	5.8116e-002	7.7582e+009	6.517864

Table 14: Maximum errors E_N and condition numbers of coefficient matrices on overlapping grids ($p = q = 3$) when $N_x = 10$ and $N_t = 10$.

Examples	t	Matrix size	Maximum Error	Condition number	CPU Time
1	1	812 × 812	4.2895e-012	2.4893e+004	0.193104
2	1	812 × 812	1.0463e-011	7.3162e+003	0.159363
3	1	812 × 812	4.3758e-012	7.2365e+004	0.168091
4 ($k = 1$)	1	812 × 812	4.2584e-012	1.1610e+004	0.160681
5	16	812 × 812	1.0738e-009	7.2525e+005	0.159894
6	16	812 × 812	1.7448e-009	6.2315e+006	0.162404

6.1 Comparison of exact and approximate solutions

Figures 2 - 7 show analytic and approximate solutions for the Emden-Fowler equations at different time level. The graphs for the heat-type equations were plotted using $N_t = N_x = 10$, $m = s = 3$, while the graphs for the wave-type equations were generated using $N_t = 5, N_x = 10$, $m = s = 3$. The approximate solution being superimposed on the exact solutions suggests that the BSQLM on overlapping grids converged to the exact solution over the domain $x \in [0, 1]$. Figures 8 -13 show the space-time graph of the exact and numerical solutions for the heat and wave-type equations when $m = s = 3$ and $t = 1$. The number of
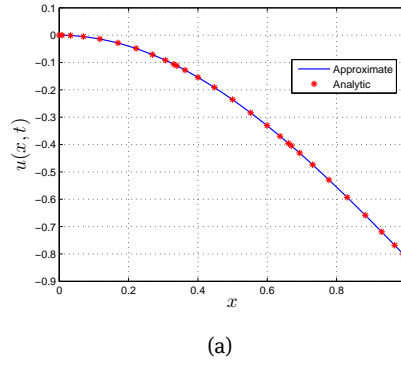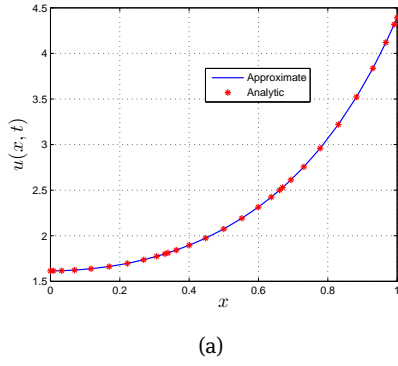
grid points used are $N_t = N_x = 10$ in the heat-type equations and $N_t = 5, N_x = 10$ in the wave-type equations. The figure shows that the exact and computed numerical solutions have similar behaviour, thus they are in satisfactory accordance with each other, assuring that the numerical method converged to the exact solutions over the domain $x \in [0, 1]$. The match between the exact and approximate solutions validates the accuracy and computational efficiency of the BSQLM on overlapping grids.

(a)

(b)
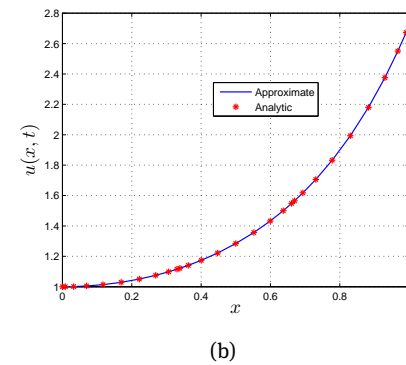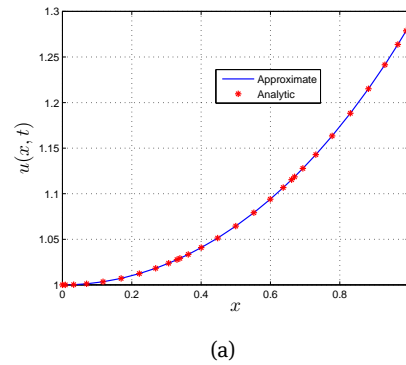
Figure 2: Analytical and approximate solution for example 1 at (a) $t = 0.5$ and (b) $t = 1$

(a)

(b)

Figure 3: Analytical and approximate solution for example 2 at (a) $t = 0.5$ and (b) $t = 2$

(a)

(b)

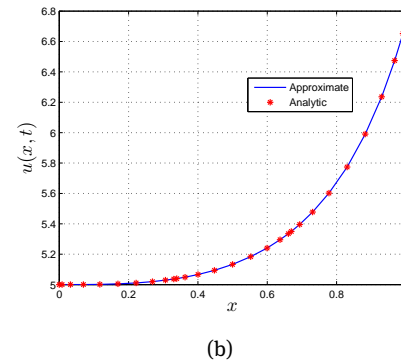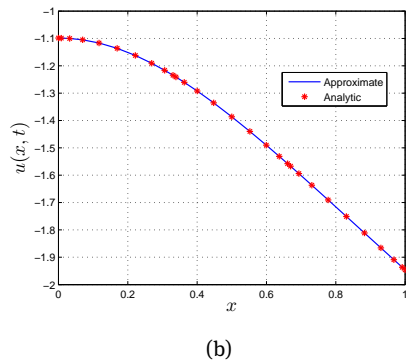**Figure 4:** Analytical and approximate solution for example 3 at (a) $t = 0.5$ and (b) $t = 1$
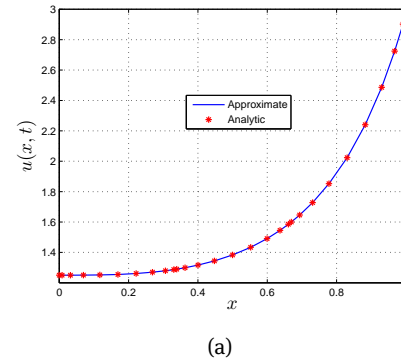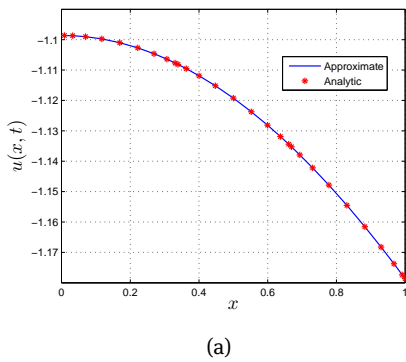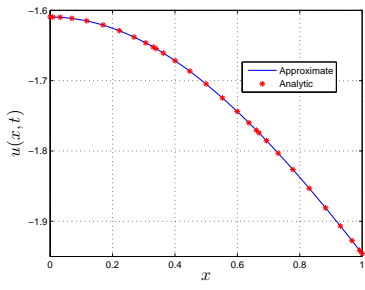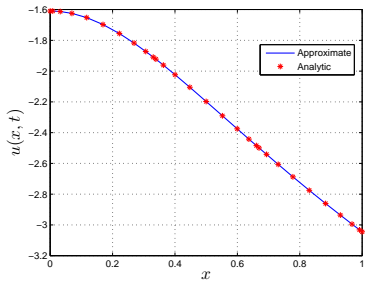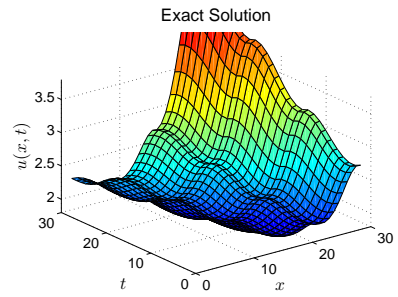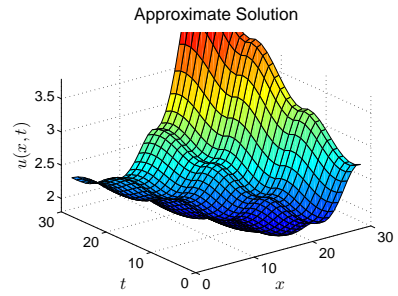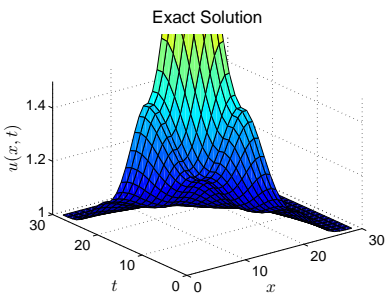

(a)

(b)

Figure 5: Analytical and approximate solution for example 4 when $k = 1$, $p = 2$ at (a) $t = 0.5$ and (b) $t = 2$

(a)

(b)

Figure 6: Analytical and approximate solution for example 5 at (a) $t = 0.5$ and (b) $t = 2$

(a)

(b)

Figure 7: Analytical and approximate solution for example 6 at (a) $t = 2$ and (b) $t = 16$

(a)

(b)

Figure 8: Space-time graph of the exact solution and approximate solution for example 1

(a)

(b)

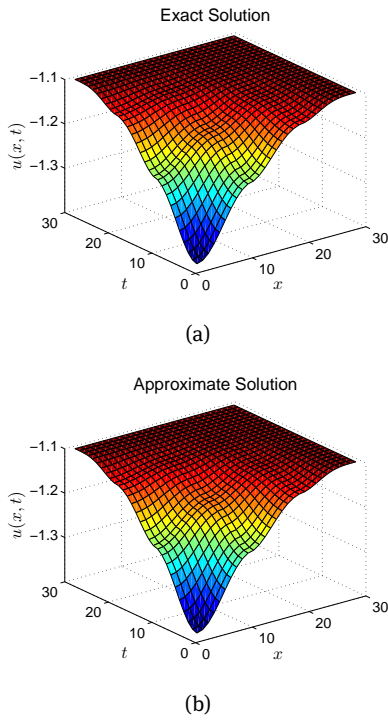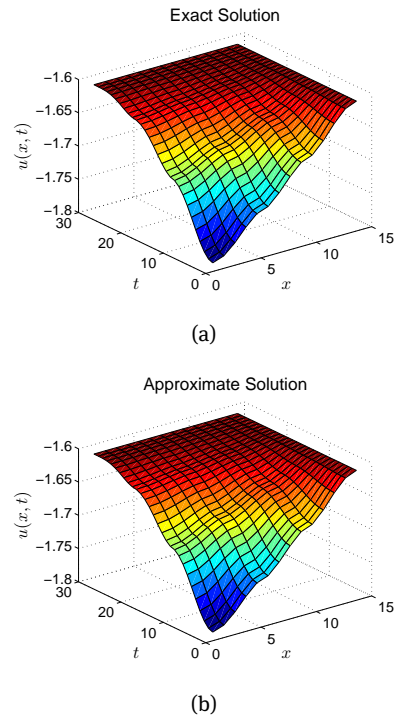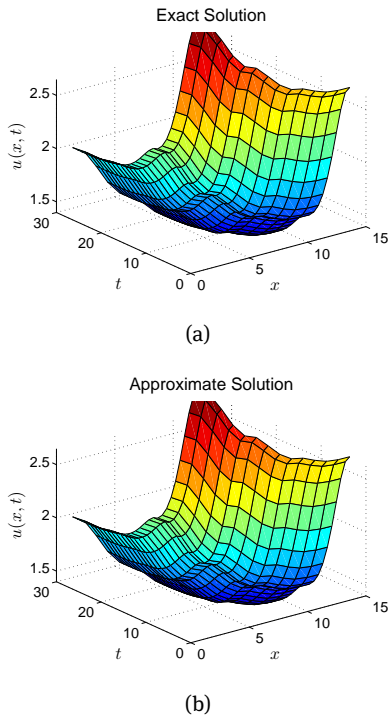**Figure 9:** Space-time graph of the exact solution and approximate solution for example 2
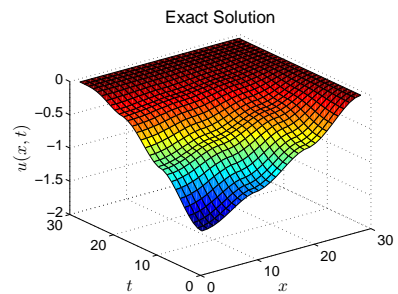

(a)
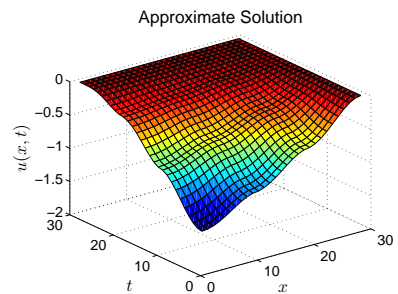
(b)

Figure 10: Space-time graph of the exact solution and approximate solution for example 3

(a)

(b)

Figure 11: Space-time graph of the exact solution and approximate solution for example 4 when $k = 1, p = 2$

(a)

(b)

Figure 13: Space-time graph of the exact solution and approximate solution for example 6


(a)

(b)

Figure 12: Space-time graph of the exact solution and approximate solution for example 5

6.2 Convergence graphs

Figures 14-16 compare the convergence and accuracy of the single domain BSQLM ($m = s = 1$) and BSQLM on overlapping grids ($m = s = 3$) for nonlinear examples 3, 4 and 6 when $t = 1$. The number of collocation points used are $N_t = N_x = 10$ in the heat-type equations and $N_t = 5, N_x = 10$ in the wave-type equations. It can be seen from the figures that the single domain BSQLM method converges to a less accurate solution compared to the BSQLM on overlapping grids. Figure 14 shows that the single domain BSQLM converges after about six iterations to an error of 10^{-7}, while the BSQLM on overlapping grids converges to an error of about 10^{-12} after six iterations.

In Figure 15, the single domain BSQLM converges after about three iterations to an error of 10^{-7}, while the BSQLM on overlapping grids converges to an error of close to 10^{-12} after four iterations. Figure 16 depicts that the single domain BSQLM converges after approximately six iterations to an error of 10^{-4}, while the BSQLM on overlapping grids converges to an error of approximately 10^{-8} after six iterations. These findings suggest that the BSQLM on overlapping grids is more accurate than the single domain
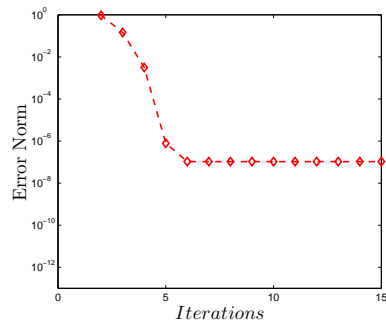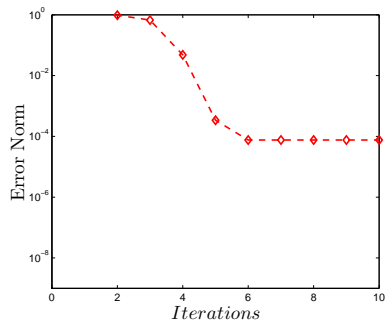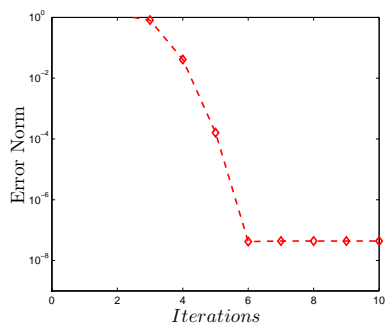
(a) No overlapping ($m = s = 1$)
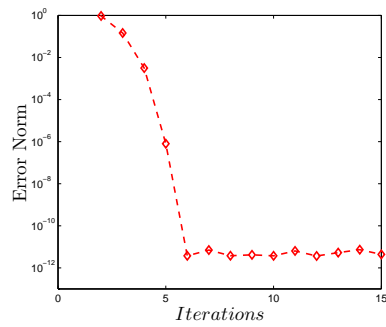
(b) Overlapping ($m = s = 3$)

Figure 14: Convergence graphs for example 3 when $t = 1$ and $N_t = N_x = 10$.
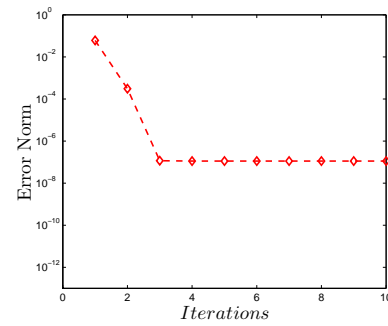
(a) No overlapping ($m = s = 1$)
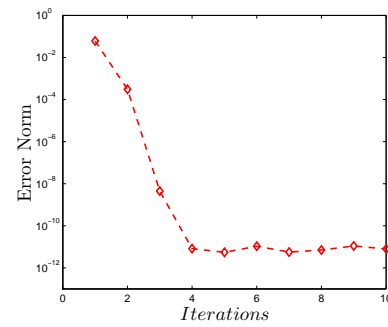
(b) Overlapping ($m = s = 3$)

Figure 15: Convergence graphs for example 4 when $t = 2$, $k = 1$, $p = 2$, and $N_t = N_x = 10$.

BSQLM, hence suitable for approximating the solution of nonlinear Emden-Fowler heat and wave type-equations.

7 Conclusion

In this paper, we introduced the bivariate spectral collocation method on overlapping grids and determined its accuracy, robustness and effectiveness in solving time-dependent Emden-Fowler PDEs. The method uses the quasilinearisation technique and bivariate Lagrange interpolation polynomials based on Chebyshev–Gauss–Lobatto grid points in both space and time. Space and time intervals were each decomposed into overlapping subintervals and the linearized equations were solved across the overlapping subintervals. The use of an overlapping grid approach was found to give a matrix system with less dense matrices that can be inverted in a computationally efficient manner. Consequently, implementing the spectral collocation method on overlapping grids significantly improves the computational time and accuracy using fewer grid points at each subinterval. This is because splitting the domains into smaller subintervals

and accordingly minimizing the number of grid points per subinterval reduces the size of the coefficient matrix at each subinterval, thus requiring less time to invert. The use of fewer grid points also minimizes the effects of round-off errors, thus producing stable results which are evident from the small condition numbers. The BSQLM on overlapping grids performed fast and converged to highly accurate results than the single domain BSQLM using few iterations. The obtained numerical results show that the approximate solutions obtained using the BSQLM on overlapping grids are in close agreement with exact solutions. The error bounds theorem showed that the error in bivariate polynomial interpolation is smaller when interpolation is conducted on multidomain overlapping grids than on a single domain. The Chebyshev Gauss-Lobatto nodes are beneficial for interpolation when using spectral collocation methods to solve boundary value problems since they are appropriate for assembling differentiation matrices as they contain the boundary nodes, which is useful when imposing boundary conditions. The present analysis adds to literature a new technique that can be extended to coupled systems of time-dependent Emden-Fowler equations and other complex nonlinear PDEs arising in other fields.

(a) No overlapping ($m = s = 1$)

(b) Overlapping ($m = s = 3$)

Figure 16: Convergence graphs for example 6 when $t = 16$, $N_t = 5$ and $N_x = 10$.

References

[1] Buck A., Klaunick G., Kumar J., Peglow M., Tsotsas E., Numerical simulation of particulate processes for control and estimation by spectral methods, AICHE J., 2012, 58, 2309–2319.

[2] Canuto C., Hussaini M. Y., Quarteroni A., Zang T. A., Spectral Methods in Fluid Dynamics; Springer: Berlin, Germany, 1988.

[3] Boyd J. P., Chebyshev and Fourier Spectral Methods; Springer: Berlin, Germany; New York, NY, USA, 1989.

[4] Fornberg B., A Practical Guide to Pseudo-spectral Methods, Cambridge Monographs on Applied and Computational Mathematics, Cambridge University Press, Cambridge, 1996.

[5] Trefethen L. N., Spectral Methods in Matlab; SIAM: Philadelphia, PA, USA, 2000.

[6] Motsa S. S., Magagula V. M., Sibanda P., A Bivariate Chebyshev Spectral Collocation Quasilinearization Method for Nonlinear Evolution Parabolic Equations, The Sci. World J., 2014, 2014, 1–13.

[7] Magagula V. M., Motsa S. S., Sibanda P., A Multi-Domain Bivariate Pseudospectral Method for Evolution Equations, Int. J. Comput, Meth., 2017, 14, 1750041 (27 pages).

[8] Mkhatshwa M. P., Motsa S. S., Sibanda P., Overlapping Multi-Domain Spectral Method for Conjugate Problems of Conduction and MHD Free Convection Flow of Nanofluids over Flat Plates, Math. Comput. Appl., 2019, 24, 75.

[9] Mkhatshwa M. P., Motsa S. S., Ayano M. S., Sibanda P., MHD mixed convective nanofluid flow about a vertical slender cylin-der using overlapping multi-domain spectral collocation approach, Case Stud. Therm. Eng., 2020, 18, 100598.

[10] Teleei A., Dehghan M., A pseudo-spectral method that uses an overlapping multi-domain technique for the numerical solution of sine-Gordon equation in one and two spatial dimensions, Math. Meth. Appl. Sci., 2013, 37, 1909–1923.

[11] Olmos D., Shizgal B. D., A pseudo-spectral method of solution of Fisher's equation, J. Comput. Appl. Math., 2006, 193, 219–242.

[12] Chandrasekhar S., Introduction to the Study of Stellar Structure; Dover, New York, 1967.

[13] Davis H. T., Introduction to Nonlinear Differential and Integral Equations; Dover, New York, 1962.

[14] Richardson O. U., The Emission of Electricity from Hot Bodies; Logmans Green, London, 1921.

[15] M. El-Gamel M., El-bashbashy W., El-Shenawy A., Numerical Solutions for the Time-Dependent Emden-Fowler-Type Equations by B-Spline Method, Appl. Math., 2014, 5, 593–600.

[16] Wazwaz A. M., Analytical solution for the time-dependent Emden−Fowler type of equations by Adomian decomposition method, Appl. Math. Comput., 2005, 166, 638–651.

[17] Singh R., Wazwaz A. M., Numerical Solution of the Time Dependent Emden-Fowler Equations with Boundary Conditions using Modified Decomposition Method, Appl. Math. Inf. Sci., 2016, 10, 403–408.

[18] Batiha K., Approximate Analytical Solutions For Time-Dependent Emden-Fowler-Type Equations By Variational Iteration Method, Am. J. Appl. Sci. 2007, 4, 439–443.

[19] Wazwaz A. M., A reliable iterative method for solving the time-dependent singular Emden-Fowler equations, Cent. Eur. J. Eng., 2013, 3, 99–105.

[20] Bataineh A. S., Noorani M. S. M, Hashim I., Solutions of time-dependent Emden−Fowler type equations by homotopy analysis method, Phys. Lett. A, 2007, 371, 72–82

[21] Babolian E., Azizi A., Saeidian, J., Some notes on using the homotopy perturbation method for solving time-dependent differential equations, Math. Comput. Model., 2009, 50, 213–224.

[22] Singh R., Singh S., Wazwaz A. M., A modified homotopy perturbation method for singular time dependent Emden−Fowler equations with boundary conditions, J. Math. Chem., 2016, 54, 918–931.

[23] Ullah A., Shah K., Numerical analysis of Lane Emden−Fowler equations, J. Taibah Univ. Sci., 2018, 12, 180–185.

[24] Singh R., Garg H., Guleria V., Haar wavelet collocation method for Lane−Emden equations with Dirichlet, Neumann and Neumann−Robin boundary conditions, J. Comput. Appl. Math., 2019, 346, 150–161.

[25] Mohammadi A., Aghazadeh N., Rezapour S., Haar wavelet collocation method for solving singular and nonlinear fractional time-dependent Emden-Fowler equations with initial and boundary conditions, Math. Sci., 2019, 13, 255–265.

[26] Sharma B., Kumar S., Paswan M. K., Mahato D., Chebyshev Operational Matrix Method for Lane-Emden Problem, Nonlinear Eng., 2018; aop. doi.org/10.1515/nleng-2017-0157.

[27] Öztürk* Y., An efficient numerical algorithm for solving system of Lane-Emden type equations arising in engineering, Nonlinear Eng., 2019, 8, 429–437

[28] Bellman R. E., Kalaba R. E., Quasilinearization and Nonlinear Boundary Value Problems; RAND Corporation: Santa Monica,

CA, USA, 1965.

[29] Gottlieb, D., Orszag, S. A. Numerical analysis of spectral methods: theory and applications, 1977, 26. SIAM.

[30] Ben-Yu, G. Spectral methods and their applications, World Scientific, 1998.

[31] Herbert E. S., Converting interpolation series into chebyshev series by recurrence formulas, Math. Comput., 1976, 30, 295-302.

[32] Mutua F. S., Motsa S. S., A highly accurate trivariate spectral collocation method of solution for two-dimensional nonlinear initial-boundary value problems, Appl. Math. Comput., 2019, 360, 221–235

[33] Bhrawy A. H., A Highly Accurate Collocation Algorithm for 1 + 1 and 2 + 1 Fractional Percolation Equations, Journal of Vibration and Control, 2015, 5, 1-23.

[34] Martínez C. A. T., Fuentes, C., Applications of Radial Basis Function Schemes to Fractional Partial Differential Equations. In Fractal Analysis-Applications in Physics, Engineering and Technology. IntechOpen, 2017.

Chapter 9

MHD mixed convective radiative flow of Eyring-Powell fluid over an oscillatory stretching sheet using bivariate spectral method on overlapping grids

The well-known linear and nonlinear partial differential equations solved in Chapter 8 have exact solutions. In this chapter, the method is extended to solve non-similar boundary layer flow equations without exact solutions. The bivariate spectral quasilinearisation method on overlapping grids is utilized in solving nonlinear partial differential equations that describe an unsteady MHD mixed convection flow of a non-Newtonian Eyring-Powell fluid over an oscillatory stretching sheet. Error norms and residual errors are used in assessing the convergence and accuracy of the numerical scheme. The effects of certain significant variables on the fluid properties and transport phenomena are discussed in detail.

RESEARCH ARTICLE

MHD mixed convective radiative flow of Eyring-Powell fluid over an oscillatory stretching sheet using bivariate spectral method on overlapping grids

Musawenkhosi P. Mkhatshwa[1] | **Sandile S. Motsa**[1,2] | **Precious Sibanda**[1]

[1]Department of Mathematics, School of Mathematics, Statistics and Computer Science, University of Kwazulu Natal, Pietermaritzburg, South Africa

[2]Department of Mathematics, University of Eswatini, Eswatini

Correspondence
Musawenkhosi P. Mkhatshwa, School of Mathematics, Statistics and Computer Science, University of Kwazulu Natal, Private Bag X01, Scottsville 3209, Pietermaritzburg, South Africa.
Email: patsonmkhatshwa@gmail.com

Abstract

The bivariate spectral quasilinearization method (BSQLM) on overlapping grids is presented and applied in the analysis of unsteady magnetohydrodynamic mixed convection flow of Eyring-Powell fluid over an oscillatory stretching sheet embedded in a non-Darcy porous medium with nonlinear radiative heat flux and variable thermophysical properties. The fluid properties, namely the fluid viscosity, thermal conductivity, and mass diffusivity, are assumed to vary with temperature. It is assumed that the first-order chemical reaction with heat generation/absorption takes place in the flow. The flow domain is subject to uniform transverse magnetic field perpendicular to the stretching surface. The transformed flow equations are solved numerically using BSQLM on overlapping grids. The convergence properties and accuracy of the method are assessed. The proposed method is computationally efficient, and it gives stable and highly accurate results after few iterations and using few grid points in each subinterval. The improved accuracy rests upon the use of the overlapping grid, which produces sparse coefficient matrices that are easy to invert and have small condition numbers. The effects of physical parameters on the flow fields, local skin friction, the

Nusselt number, and the Sherwood number are exhibited through graphs and tables. Amongst other findings, we found that the amplitude of the fluid flow along with flow characteristics may efficiently improve through the utilization of variable fluid viscosity. Heat and mass transportation processes enhance with the inclusion of nonlinear radiative heat flux, temperature-dependent thermal conductivity, and mass diffusion coefficient, whereas they diminish with the increase in the local inertia coefficient. The current flow analysis can be useful in various engineering applications including paper production, polymer solution, glass blowing, extrusion of thermal system manufacturing process, and heat transportation enhancement.

KEYWORDS

bivariate spectral quasilinearization method, chemical reaction, Eyring-Powell fluid, multidomain overlapping grid, nonlinear radiation, oscillatory stretching sheet, variable fluid properties

1 | INTRODUCTION

In the past few years, the boundary layer flow, together with heat and mass transfer, along a stretching sheet has captured attention of several researchers due to its significant relevance in countless engineering and industrial applications including paper production, packed sphere bed, hot rolling, and continuous casting of metal. The first encounter of boundary layer theory for a linearly stretching surface was reported by Crane.[1] The flow over a stretching surface has been successfully considered in non-Newtonian fluid flow models. Non-Newtonian fluids have become significant and suitable in modern engineering, because heat and mass transfer characteristics for the flow are difficult to understand using Newtonian fluid models. Non-Newtonian fluids have various applications in engineering and industries such as heat exchanger design, glass blowing melt spinning, production of glass fibers, fiber and wire coating, and industrialization of rubber, and plastic sheets. Unfortunately, there is no specific constitutive equation available that describes the entire non-Newtonian materials. Thus, several researchers[2-8] have used various constitutive equations according to their rheological properties about non-Newtonian behavior. Shafiq and Sindhu[2] considered the hydromagnetic flow of Williamson fluid over a stretched surface with thermal radiation. Shafiq et al[4] investigated the influence of radiation on a stagnation point flow of Walter's B fluid induced by a Riga plate. Mabood et al[5] investigated the magnetohydrodynamic (MHD) mixed convection flow of a second-grade fluid over a vertical cylinder with suction. Rasool et al[7] analyzed the MHD Darcy-Forchheimer Williamson nanofluid flow over a nonlinear stretching surface embedded in a porous medium. Rasool et al[8] investigated the heat and mass transfer analysis in Jeffrey nanofluid in a porous medium under Darcy-Forchheimer relation. The Darcy-Forchheimer model is the most well-known modification to the Darcian flow used in similarity inertia effects. Amongst the different

non-Newtonian fluids, we also have an Eyring-Powell fluid,[9] which forms an integral part of the non-Newtonian fluids theory. The Eyring-Powell fluid model is mathematically complex but very important in the sense that it reduces to Newtonian behavior for low and high shear rates. The applications of Eyring-Powell fluids include formulating flows of modern industrial materials, for instance, powdered graphite and ethylene glycol. Numerous studies[10-15] have been conducted on flows of Eyring-Powell fluids over a stretching sheet. Ahmed[11] analyzed the effects of variable fluid thermal conductivity on the flow and heat transfer of an Eyring-Powell fluid over a stretching porous sheet. Parmar and Jain[14] considered the unsteady convective flow for MHD Powell-Eyring fluid over a stretching sheet embedded in a porous medium with variable thermal conductivity. Ogunseye et al[15] studied the flow and heat transfer in a Powell-Eyring nanofluid flow past a stretching surface using the nanofluid viscosity and thermal conductivity models.

The above studies focus on the fluid flow over a stretched sheet. However, there are situations where the sheet is stretched and oscillates periodically in its own plane. This phenomenon is the time-dependent flow for which the various features of fluid motion can be scrutinized at different times. Wang[16] became the first author to study the viscous flow due to the oscillatory stretching surface. Several authors[17-24] extended the work of Wang[16] and studied heat and mass transfer in the non-Newtonian fluid flow over an oscillatory stretching surface. Khan et al[25] introduced flow and heat transfer of Eyring-Powell fluid over an oscillatory stretching surface with thermal radiation effects. Khan et al[26] considered the influence of convective heat and mass conditions on the unsteady flow of Eyring-Powell nanofluid over an oscillatory stretching surface in the presence of heat generation/absorption. Khan et al[27] also analyzed the effects of cross-diffusion, heat generation/absorption, and chemical reaction on the MHD flow of Eyring-Powell fluid over an oscillatory stretching surface. Dawar et al[28] studied the effects of thermal radiation and heat source/sink on Eyring-Powell fluid flow over an unsteady porous stretching surface. Alharbi et al[29] scrutinized the entropy generation in MHD Eyring-Powell fluid over an unsteady oscillating porous stretching sheet with thermal radiation and heat source/sink effects.

In the aforementioned studies, the fluid viscosity, thermal conductivity, and mass diffusivity were taken as constants in the analysis of the non-Newtonian Eyring-Powell fluid flow over an oscillatory stretching surface. Furthermore, these studies incorporated linear radiation effects instead of nonlinear thermal radiation for the heat transfer analysis. The linear radiative heat transfer repercussions are only valid for small temperature differences. However, the nonlinearized Rosseland diffusion approximation for studying nonlinear radiative heat transfer accommodates both smaller and larger temperature differences of the surface and ambient fluid. Nonlinear thermal radiation has various applications, namely thermal extrusion phenomenon, solar system, missile technology, environmental applications, heavy mechanical apparatus, and fission and fusion reactions. Experiments have shown that the magnitude of viscosity is inversely proportional to the temperature of liquids, whereas thermal conductivity and mass diffusivity properties are directly proportional to the temperature. To accurately predict the flow, together with heat and mass transfer characteristics, it is important to consider the variation of viscosity, thermal conductivity, and mass diffusivity. Ramzan et al[30] studied the impact of variable thermal conductivity and nonlinear thermal radiation on Eyring-Powell nanofluid flow past a constantly moving surface with chemical reaction. Parmar and Jain[31] investigated the MHD flow of Eyring-Powell fluid over a cylinder with nonlinear radiation and variable thermal conductivity. Reddy et al[32] considered the unsteady flow of the nonlinear radiative Powell-Eyring fluid over an inclined stretching sheet with chemical reaction. Khan et al[33] examined the MHD mixed convection Eyring-Powell nanofluid flow over an inclined surface with exponentially varying viscosity. Wahab et al[34] studied the influence of variable viscosity and thermal conductivity on the MHD flow of Eyring-Powell fluid over a nonlinear stretching sheet.

The aim of the present work is to study the effects of temperature-dependent fluid properties and nonlinear thermal radiation on the unsteady MHD mixed convection flow, heat and mass transfer of Eyring-Powell fluid over an oscillatory stretching surface with viscous dissipation, heat source/sink, and chemical reaction. The inertia effect in the porous media is considered through the inclusion of a velocity-squared term in the momentum equation, which is known as Forchheimer's extension. To the authors' best knowledge, no study has been reported in literature on the heat and mass transfer in the Eyring-Powell fluid flow over an oscillatory stretching surface in a non-Darcy porous medium with variable fluid properties and nonlinear radiation features. The role of physical properties in isotropic liquids is quite limited; thus, in case of variable thermophysical properties, the effects of such physical quantities cannot be ignored. It is also important to determine the extent to which these variable fluid properties can affect the boundary layer in the oscillatory stretched surface. Khan et al[35] studied the double-diffusive flow of Jeffrey nanofluid over an oscillatory stretched surface under the influence of temperature-dependent thermal conductivity. Ahmad et al[36] scrutinized the unsteady flow of Oldroyd-B fluid along an oscillatory stretched surface with variable thermal conductivity and heat generation/absorption. Recently, Khan et al[37] investigated the mixed convection flow of the Carreau nanofluid past an oscillatory stretching sheet by considering variable thermal conductivity and thermal radiation features. These studies reported that fluid temperature and the associated thermal boundary layer thickness enhance with escalating variable thermal conductivity. The current analysis intends to contribute toward enhancing the efficiency of thermal energy transportation systems. To achieve such maximum efficiency as well as improve the production process, we have considered one of the important non-Newtonian fluid with some more useful factors and valuable applications. The novelty of the present study also lies in the use of efficient bivariate spectral quasilinearization method (BSQLM) on overlapping grids[38] in solving the dimensionless flow equations. The single-domain BSQLM was introduced by Motsa et al[39] and used in solving nonlinear evolution partial differential equations (PDEs). Subsequently, the method has been employed by several researchers[40-44] in solving boundary layer flow problems. The single-domain BSQLM method uses quasilinearization technique,[45] the Chebyshev spectral collocation method, as well as the bivariate Lagrange interpolation polynomial with Chebyshev-Gauss-Lobatto grid points. The overlapping multidomain technique with pseudospectral methods has been considered by several researchers.[46-49] In all these studies, the overlapping multidomain approach was applied only in the spatial domain, and it was found that the accuracy of pseudospectral methods improved through the use of overlapping grid procedure. Mkhatshwa et al[48] and Mkhatshwa et al[49] considered nonlinear PDEs modeling problems that arise in fluid mechanics. The BSQLM on overlapping grids was introduced by Mkhatshwa et al[38] and implemented to solve time-dependent Emden-Fowler equations. This method remains to be generalized and its robustness remains to be tested in the case of highly nonlinear PDEs with strong coupling. The BSQLM on overlapping grids involves using multidomain strategy in both space and time variables, which are each split into overlapping subintervals of equal length. The current study presents the first opportunity in which this numerical method is used to solve nonlinear PDEs modeling boundary layer fluid flow problem.

2 | FLOW ANALYSIS

We consider the unsteady, two-dimensional MHD boundary layer flow of an incompressible Eyring-Powell fluid over an oscillatory stretching sheet embedded in a non-Darcy porous medium. The sheet is assumed to coincide with $\bar{y}$ in a rectangular coordinate system $(\bar{x}, \bar{y})$. The flow takes place in the semi-finite porous space $(\bar{y} > 0)$ of constant permeability. To stabilize

the boundary layer flow, the uniform magnetic field B_0 is applied perpendicular to the stretching sheet along the $\bar{y}$ direction. The induced magnetic field is neglected, which is supposed to be small as compared with the applied magnetic field. The first-order chemical reaction is adopted in the concentration equation to control the mass transport, whereas the heat transfer mechanism is analyzed by utilizing the phenomena of heat source/sink and nonlinear thermal radiation, which permit both small and large temperature differences into the flow. It is assumed that the elastic sheet is stretched back and forth periodically with velocity $u_w = b\bar{x} \sin \omega t$, where b is the stretching rate and ω denotes the oscillatory frequency of the sheet. Concentration C_w and temperature T_w at the wall are kept uniform where these values are supposed to be greater than ambient concentration C_∞ and temperature T_∞ far away from the sheet. The fluid properties are assumed to be constant, except for the viscosity of the fluid that is assumed to change exponentially with temperature, whereas the fluid thermal conductivity and mass diffusivity are considered to vary linearly with temperature. The theory of rate processes is utilized in deriving the Eyring-Powell model for describing the shear stress of non-Newtonian flow. The shear stress tensor for the Eyring-Powell fluid model is expressed as[9]

$$\tau_{ij} = \mu \frac{\partial u_i}{\partial x_i} + \frac{1}{\beta} \sinh^{-1}\left(\frac{1}{C_1} \frac{\partial u_i}{\partial x_i}\right), \tag{1}$$

where μ is the dynamic viscosity, β and C_1 are the rheological fluid parameters of the Eyring-Powell fluid model, and

$$\sinh^{-1}\left(\frac{1}{C_1} \frac{\partial u_i}{\partial x_i}\right) \approx \frac{1}{C_1} \frac{\partial u_i}{\partial x_i} - \frac{1}{6}\left(\frac{1}{C_1} \frac{\partial u_i}{\partial x_i}\right)^3, \quad \left|\frac{1}{C_1} \frac{\partial u_i}{\partial x_i}\right| \ll 1. \tag{2}$$

Under these assumptions along with the boundary layer approximations, and considering viscous dissipation, the unsteady boundary layer equations governing flow of Eyring-Powell fluid are given by[25,27-29]

$$\frac{\partial u}{\partial \bar{x}} + \frac{\partial v}{\partial \bar{y}} = 0, \tag{3}$$

$$\frac{\partial u}{\partial t} + u\frac{\partial u}{\partial \bar{x}} + v\frac{\partial u}{\partial \bar{y}} = \frac{1}{\rho_\infty} \frac{\partial}{\partial \bar{y}}\left(\mu(T)\frac{\partial u}{\partial \bar{y}}\right) + \frac{1}{\rho_\infty \beta C_1} \frac{\partial^2 u}{\partial \bar{y}^2} - \frac{1}{2\rho_\infty \beta C_1^3}\left(\frac{\partial u}{\partial \bar{y}}\right)^2 \frac{\partial^2 u}{\partial \bar{y}^2},$$

$$-\frac{\sigma B_0^2}{\rho_\infty}u - \frac{c_b}{\sqrt{k_p}}u^2 + g\beta_t(T - T_\infty) + g\beta_c(C - C_\infty), \tag{4}$$

$$\frac{\partial T}{\partial t} + u\frac{\partial T}{\partial \bar{x}} + v\frac{\partial T}{\partial \bar{y}} = \frac{1}{\rho_\infty c_p} \frac{\partial}{\partial \bar{y}}\left(K(T)\frac{\partial T}{\partial \bar{y}}\right) + \frac{\sigma B_0^2}{\rho_\infty c_p}u^2 + \frac{Q_0}{\rho_\infty c_p}(T - T_\infty) + \frac{16\sigma^*}{3k^*\rho_\infty c_p} \frac{\partial}{\partial \bar{y}}\left(T^3\frac{\partial T}{\partial \bar{y}}\right)$$

$$+ \frac{\mu(T)}{\rho_\infty c_p}\left(\frac{\partial u}{\partial \bar{y}}\right)^2, \tag{5}$$

$$\frac{\partial C}{\partial t} + u\frac{\partial C}{\partial \bar{x}} + v\frac{\partial C}{\partial \bar{y}} = \frac{\partial}{\partial \bar{y}}\left(D(T)\frac{\partial C}{\partial \bar{y}}\right) - k_0(C - C_\infty), \tag{6}$$

where u and v are velocity components in the $\bar{x}$-and $\bar{y}$-directions, T is the fluid temperature, C is the concentration, g is the acceleration due to gravity, ρ_∞ is the fluid density, $\mu(T)$, $K(T)$, and $D(T)$ are

the respective temperature-dependent viscosity, thermal conductivity, and mass diffusivity of the fluid, σ is the electrical conductivity of the fluid, β and C_1 are fluid parameters of the Eyring-Powell fluid, Q_0 is the heat source/sink coefficient, β_t is the coefficient of thermal expansion, β_c is the coefficient of concentration expansion, B_0 is the applied uniform magnetic field, σ^* is the Stefan-Boltzmann coefficient, k^* is the mean absorption coefficient, c_p is the specific heat capacity, k_p is the the permeability of the porous medium, c_b is the form of drag coefficient, and k_0 is the chemical reaction coefficient.

The appropriate boundary conditions are given by

$$u = u_\omega = b\bar{x}\sin\omega t, \quad v = \pm v_w, \quad T = T_w, \quad C = C_w, \quad \text{at} \quad \bar{y} = 0, t > 0, \tag{7}$$

$$u = 0, \quad T = T_\infty, \quad C = C_\infty, \quad \text{as} \quad y \to \infty, \tag{8}$$

where v_w represents suction/injection. To reduce Equations (3) to (6) into a dimensionless form, we make use of the subsequent similarity transformations[19,27,37]:

$$\Psi(\bar{x}, \bar{y}, t) = \sqrt{\nu_\infty b}\,\bar{x}f(y, \tau), y = \sqrt{\frac{b}{\nu_\infty}}\,\bar{y}, \tau = t\omega, \theta(y, \tau) = \frac{T - T_\infty}{T_w - T_\infty}, \phi(y, \tau) = \frac{C - C_\infty}{C_w - C_\infty}. \tag{9}$$

The velocity components are derived from the stream function (Ψ) as follows:

$$u = \frac{\partial\Psi}{\partial\bar{y}} = b\bar{x}f'(y, \tau), v = -\frac{\partial\Psi}{\partial\bar{x}} = -\sqrt{\nu_\infty b}f(y, \tau). \tag{10}$$

In the present work, the exponentially varying viscosity, thermal conductivity, and mass diffusivity take the form[36,50-53]

$$\mu(T) = \mu_\infty e^{-\varsigma\theta(y,\tau)}, \quad K(T) = K_\infty(1 + \delta_1\theta(y, \tau)), \quad D(T) = D_\infty(1 + \delta_2\theta(y, \tau)), \tag{11}$$

where μ_∞, K_∞, and D_∞ represent the viscosity, thermal conductivity, and mass diffusivity of the fluid far away from the sheet, respectively, ς is the variable viscosity parameter that measures the rate of dynamic viscosity with temperature, δ_1 is the variable thermal conductivity parameter that measures the rate of change of thermal conductivity with temperature, and δ_2 is the variable mass diffusion coefficient that measures the rate of change of chemical diffusivity with temperature.

Employing Equations (9) to (11) in Equations (3) to (6), Equation (3) is satisfied identically and the remaining set of equations reduces to the following dimensionless nonlinear PDEs:

$$[\Gamma + e^{-\varsigma\theta} - \varpi\Gamma f''^2]f''' + [f - \varsigma e^{-\varsigma\theta}\theta']f'' - M^2f' - (1 + Fs)f'^2 + \gamma(\theta + N\phi) = S\frac{\partial f'}{\partial\tau}, \tag{12}$$

$$(1 + \delta_1\theta)\theta'' + \delta_1\theta'^2 + \frac{4}{3}Rd(1 + (\theta_w - 1)\theta)^3\theta'' + 4Rd(1 + (\theta_w - 1)\theta)^2(\theta_w - 1)\theta'^2$$
$$+ Pr[f\theta' + \lambda\theta + Ec(M^2f'^2 + e^{-\varsigma\theta}f''^2)] = PrS\frac{\partial\theta}{\partial\tau}, \tag{13}$$

$$(1 + \delta_2\theta)\phi'' + \delta_2\theta'\phi' + Sc[f\phi' - k_c\phi] = ScS\frac{\partial\phi}{\partial\tau}, \tag{14}$$

subject to the boundary conditions:

$$f'(0, \tau) = \sin \tau, \quad f(0, \tau) = f_w, \quad \theta(0, \tau) = 1, \quad \phi(0, \tau) = 1, \tag{15}$$

$$f'(\infty, \tau) = 0, \quad \theta(\infty, \tau) = 0, \quad \phi(\infty, \tau) = 0, \tag{16}$$

where $Sc = \frac{\nu_\infty}{D_\infty}$ signifies the Schmidt number, $S = \frac{\omega}{b}$ represents the ratio of the oscillation frequency of the sheet to its stretching rate (unsteady parameter), $k_c = \frac{k_0}{b}$ is the chemical reaction parameter, $Fs = \frac{c_b \bar{x}}{\sqrt{k_p}}$ is the local inertia (Forchheimer) coefficient, $Gr_x = \frac{g\beta_t(T_w - T_\infty)\bar{x}^3}{\nu_\infty^2}$ is the Grashof number, $Rd = \frac{4\sigma^* T_\infty^3}{k^* k_\infty}$ is the nonlinear thermal radiation parameter, $\theta_w = \frac{T_w}{T_\infty}$ is the temperature ratio parameter, $\gamma = \frac{Gr_x}{Re_x^2}$ is the mixed convection parameter, $N = \frac{\beta_c(C_w - C_\infty)}{\beta_t(T_w - T_\infty)}$ is the concentration buoyancy parameter, $M^2 = \frac{\sigma B_0^2}{b\rho_\infty}$ is the Hartmann number, $Pr = \frac{\mu_\infty c_p}{k_\infty}$ is the Prandtl number, $Ec = \frac{(b\bar{x})^2}{c_p(T_w - T_\infty)}$ is the Eckert number, $\lambda = \frac{Q_0}{b\rho_\infty c_p}$ is the heat source ($\lambda > 0$) or sink ($\lambda < 0$) parameter, $f_w = \frac{-v_w}{\sqrt{\nu_\infty b}}$ is the suction ($f_w > 0$) or injection ($f_w < 0$) parameter, and $\Gamma = \frac{1}{\mu_\infty \beta C_1}$ and $\varpi = \frac{b^3 \bar{x}^2}{2\nu_\infty C_1^2}$ are the material fluid parameters. It is worth noting that the product $\varpi\Gamma$ is preferred to be sufficiently smaller than unity (ie, $\varpi\Gamma \ll 1$).[10]

The local skin friction coefficient (C_{fx}), Nusselt number (Nu_x), and Sherwood number, (Sh_x), are given by

$$C_{fx} = \frac{\tau_w}{\rho_\infty u_w^2}, \quad Nu_x = \frac{\bar{x} q_w}{k_\infty(T_w - T_\infty)}, \quad Sh_x = \frac{\bar{x} q_m}{D_\infty(C_w - C_\infty)}, \tag{17}$$

where τ_w, q_w, and q_m are the wall shear stress, surface heat, and mass fluxes, respectively, defined as

$$\tau_w = \left[\mu(T)\left(\frac{\partial u}{\partial \bar{y}}\right) + \frac{1}{\beta C_1}\frac{\partial u}{\partial \bar{y}} - \frac{1}{6\beta C_1^3}\left(\frac{\partial u}{\partial \bar{y}}\right)^3 \right]_{y=0}, q_w$$

$$= -\left[\left(K(T) + \frac{16\sigma^*}{3k^*}T^3 \right)\frac{\partial T}{\partial \bar{y}} \right]_{y=0}, \quad q_m = -D(T)\frac{\partial C}{\partial \bar{y}}\Big|_{y=0}. \tag{18}$$

Using similarity transformations (9) to (11), the dimensionless form of the skin friction coefficient, Nusselt number, and Sherwood number are obtained as

$$Re_x^{1/2} C_{fx} = [\Gamma + e^{-\varsigma\theta(0,\tau)}]f''(0, \tau) - \frac{\varpi\Gamma}{3}[f''(0, \tau)]^3,$$

$$Re_x^{-1/2} Nu_x = -\left[1 + \delta_1\theta(0, \tau) + \frac{4}{3}Rd[1 + (\theta_w - 1)\theta(0, \tau)]^3 \right]\theta'(0, \tau), Re_x^{-1/2}Sh_x$$

$$= -[1 + \delta_2\theta(0, \tau)]\varphi'(0, \tau), \tag{19}$$

where $Re_x = u_w\bar{x}/\nu_\infty$ is the local Reynolds number.

3 | NUMERICAL METHOD

This section presents the implementation of the BSQLM on overlapping grids to simplify the nonlinear PDEs (12) to (14). The proposed method involves splitting the computational

domains into overlapping subintervals. The spectral collocation method is employed in the discretization of the iterative scheme to give a matrix system to be solved simultaneously across the overlapping subintervals. We let the time variable $\tau \in J$, where $J = [\tau_0, \tau_f]$. The time interval J is split into q overlapping subintervals, defined as

$$J_\varrho = [\tau_0^\varrho, \tau_{N_\tau}^\varrho], \quad \varrho = 1, 2, 3, ..., q, \tag{20}$$

where each subinterval J_ϱ is further discretized into $(N_\tau + 1)$ Chebyshev-Gauss-Lobatto collocation points. However, the semi-finite space interval $[0, \infty)$ is replaced with a truncated domain $[0, y_\infty]$, where y_∞ is the finite value chosen to allow the application of the method at infinity. The truncated interval of integration $I = [0, y_\infty]$ is decomposed into p overlapping subintervals, denoted by

$$I_\varepsilon = [y_0^\varepsilon, y_{N_y}^\varepsilon], \quad \varepsilon = 1, 2, 3, ..., p, \tag{21}$$

where each subinterval I_ε is further discretized into $N_y + 1$ collocation points. The domain decomposition is illustrated in Figure 1, where the last two points in the I_ε and J_ϱ subintervals are noted to coincide with the first two points of the $I_{\varepsilon+1}$ and $J_{\varrho+1}$ subintervals, respectively, and remain common.

For the overlap to be possible, the length of subintervals I_ε and J_ϱ must be the same and, respectively, given as
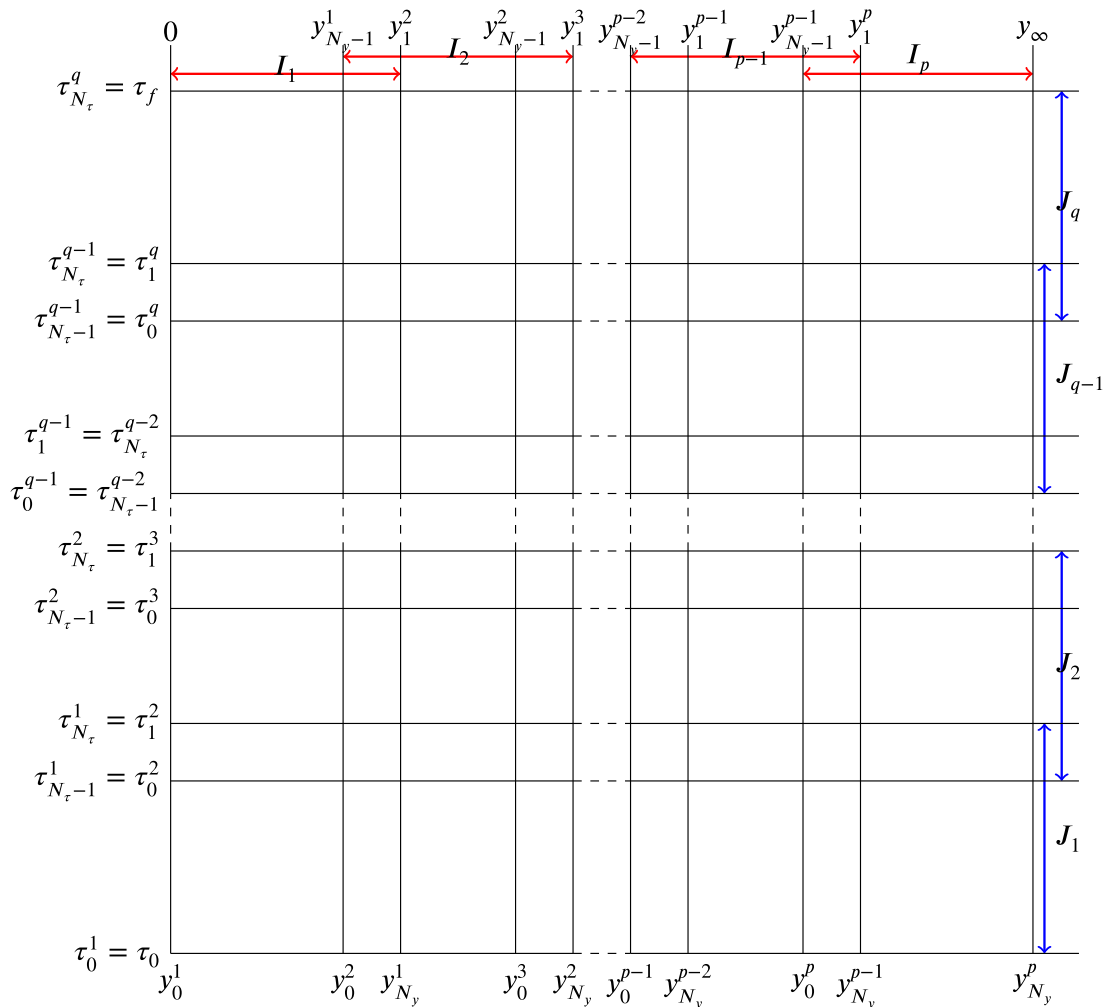

FIGURE 1 The overlapping grid [Color figure can be viewed at wileyonlinelibrary.com]

$$L_x = \frac{y_\infty}{p + \frac{1}{2}(1-p)\left(1 - \cos\frac{\pi}{N_y}\right)}, \tag{22}$$

$$L_\tau = \frac{\tau_f - \tau_0}{q + \frac{1}{2}(1-q)\left(1 - \cos\frac{\pi}{N_\tau}\right)}. \tag{23}$$

Moreover, the same number of collocation points $(N_y + 1)$ and $(N_\tau + 1)$ are used in each sub-interval. To derive Equation (22), we remark that the total length of the spatial domain is given by

$$y_\infty = 2L_x - \omega + (2L_x - 2\omega)\left(\frac{p}{2} - 1\right) = 2L_x - \omega + (L_x - \omega)(p - 2) = \omega(1 - p) + pL_x, \tag{24}$$

where ω is the overlapping distance between two subintervals. It is worth noting that $\omega = y_0 - y_1$. Considering the first interval I_1 in which $y \in \left[0, y_{N_y}^1\right]$, we can define the length $L_x = y_{N_y}^1$. The linear transformation $y = \frac{L_x}{2}\hat{y} + \frac{y_{N_y}^1}{2}$ can be used to transform the interval $\left[0, y_{N_y}^1\right]$ to $[-1, 1]$. Thus, using the Gauss-Lobatto collocation points $\hat{y}_i = \cos\left(\frac{\pi i}{N_y}\right)$, where $i = 0, 1, 2, ..., N_y$, we obtain

$$y_0 - y_1 = \frac{L_x}{2}(\hat{y}_0 - \hat{y}_1) = \frac{L_x}{2}\left(1 - \cos\frac{\pi}{N_y}\right). \tag{25}$$

Therefore, Equation (24) becomes

$$y_\infty = \frac{L_x}{2}\left(1 - \cos\frac{\pi}{N_y}\right)(1 - p) + pL_x, \tag{26}$$

and making L_x the subject of the formula in Equation (26) gives Equation (22). The formula for the length of time domain can be derived in a similar manner. Applying the quasilinearization method[45] at subintervals J_ϱ and I_ε,, the nonlinear PDEs (12) to (14) reduce to the following linear PDEs:

$$\varphi_{0,r}^{(\varepsilon,\varrho)}\frac{\partial^3 f_{r+1}^{\varepsilon,\varrho}}{\partial y^3} + \varphi_{1,r}^{(\varepsilon,\varrho)}\frac{\partial^2 f_{r+1}^{(\varepsilon,\varrho)}}{\partial y^2} + \varphi_{2,r}^{(\varepsilon,\varrho)}\frac{\partial f_{r+1}^{(\varepsilon,\varrho)}}{\partial y} + \varphi_{3,r}^{(\varepsilon,\varrho)}f_{r+1}^{(\varepsilon,\varrho)} + \varphi_{4,r}^{(\varepsilon,\varrho)}\frac{\partial\theta_{r+1}^{(\varepsilon,\varrho)}}{\partial y} + \varphi_{5,r}^{(\varepsilon,\varrho)}\theta_{r+1}^{(\varepsilon,\varrho)}$$

$$+ \varphi_{6,r}^{(\varepsilon,\varrho)}\phi_{r+1}^{(\varepsilon,\varrho)} - S\frac{\partial}{\partial y}\left(\frac{\partial f_{r+1}^{(\varepsilon,\varrho)}}{\partial\tau}\right) = \varphi_{7,r}^{(\varepsilon,\varrho)}, \tag{27}$$

$$\vartheta_{0,r}^{(\varepsilon,\varrho)}\frac{\partial^2\theta_{r+1}^{(\varepsilon,\varrho)}}{\partial y^2} + \vartheta_{1,r}^{(\varepsilon,\varrho)}\frac{\partial\theta_{r+1}^{(\varepsilon,\varrho)}}{\partial y} + \vartheta_{2,r}^{(\varepsilon,\varrho)}\theta_{r+1}^{(\varepsilon,\varrho)} + \vartheta_{3,r}^{(\varepsilon,\varrho)}\frac{\partial^2 f_{r+1}^{(\varepsilon,\varrho)}}{\partial y^2} + \vartheta_{4,r}^{(\varepsilon,\varrho)}\frac{\partial f_{r+1}^{(\varepsilon,\varrho)}}{\partial y} + \vartheta_{5,r}^{(\varepsilon,\varrho)}f_{r+1}^{(\varepsilon,\varrho)}$$

$$- PrS\frac{\partial\theta_{r+1}^{(\varepsilon,\varrho)}}{\partial\tau} = \vartheta_{6,r}^{(\varepsilon,\varrho)}, \tag{28}$$

$$\psi_{0,r}^{(\varepsilon,\varrho)}\frac{\partial^2\phi_{r+1}^{(\varepsilon,\varrho)}}{\partial y^2} + \psi_{1,r}^{(\varepsilon,\varrho)}\frac{\partial\phi_{r+1}^{(\varepsilon,\varrho)}}{\partial y} + \psi_{2,r}^{(\varepsilon,\varrho)}\phi_{r+1}^{(\varepsilon,\varrho)} + \psi_{3,r}^{(\varepsilon,\varrho)}\frac{\partial\theta_{r+1}^{(\varepsilon,\varrho)}}{\partial y} + \psi_{4,r}^{(\varepsilon,\varrho)}\theta_{r+1}^{(\varepsilon,\varrho)} + \psi_{5,r}^{(\varepsilon,\varrho)}f_{r+1}^{(\varepsilon,\varrho)}$$

$$- ScS\frac{\partial\phi_{r+1}^{(\varepsilon,\varrho)}}{\partial\tau} = \psi_{6,r}^{(\varepsilon,\varrho)}, \tag{29}$$

where the variable coefficients are defined as

$$\varphi_{0,r}^{(\varepsilon,\varrho)} = \Gamma + e^{-\varsigma\theta_r^{(\varepsilon,\varrho)}} - \varpi\Gamma\left(\frac{\partial^2 f_r^{(\varepsilon,\varrho)}}{\partial y^2}\right)^2, \quad \varphi_{1,r}^{(\varepsilon,\varrho)} = f_r^{(\varepsilon,\varrho)} - 2\varpi\Gamma\frac{\partial^2 f_r^{(\varepsilon,\varrho)}}{\partial y^2}\frac{\partial^3 f_r^{(\varepsilon,\varrho)}}{\partial y^3} - \varsigma\frac{\partial\theta_r^{(\varepsilon,\varrho)}}{\partial y}e^{-\varsigma\theta_r^{(\varepsilon,\varrho)}},$$

$$\varphi_{2,r}^{(\varepsilon,\varrho)} = -2(1 - Fs)\frac{\partial f_r^{(\varepsilon,\varrho)}}{\partial y}$$

$$- M^2, \varphi_{3,r}^{(\varepsilon,\varrho)} = \frac{\partial^2 f_r^{(\varepsilon,\varrho)}}{\partial y^2}, \quad \varphi_{4,r}^{(\varepsilon,\varrho)} = -\varsigma\frac{\partial^2 f_r^{(\varepsilon,\varrho)}}{\partial y^2}e^{-\varsigma\theta_r^{(\varepsilon,\varrho)}}, \quad \varphi_{6,r}^{(\varepsilon,\varrho)} = \gamma N,$$

$$\varphi_{5,r}^{(\varepsilon,\varrho)} = \varsigma^2\frac{\partial\theta_r^{(\varepsilon,\varrho)}}{\partial y}\frac{\partial^2 f_r^{(\varepsilon,\varrho)}}{\partial y^2}e^{-\varsigma\theta_r^{(\varepsilon,\varrho)}} + \gamma - \varsigma\frac{\partial^3 f_r^{(\varepsilon,\varrho)}}{\partial y^3}e^{-\varsigma\theta_r^{(\varepsilon,\varrho)}},$$

$$\varphi_{7,r}^{(\varepsilon,\varrho)} = f_r^{(\varepsilon,\varrho)}\frac{\partial^2 f_r^{(\varepsilon,\varrho)}}{\partial y^2} - \varsigma\frac{\partial^2 f_r^{(\varepsilon,\varrho)}}{\partial y^2}\frac{\partial\theta_r^{(\varepsilon,\varrho)}}{\partial y}e^{-\varsigma\theta_r^{(\varepsilon,\varrho)}} + \left[\varsigma^2\frac{\partial\theta_r^{(\varepsilon,\varrho)}}{\partial y}\frac{\partial^2 f_r^{(\varepsilon,\varrho)}}{\partial y^2} - \varsigma\frac{\partial^3 f_r^{(\varepsilon,\varrho)}}{\partial y^3}\right]\theta_r^{(\varepsilon,\varrho)}e^{-\varsigma\theta_r^{(\varepsilon,\varrho)}}$$

$$- (1 + Fs)\left(\frac{\partial f_r^{(\varepsilon,\varrho)}}{\partial y}\right)^2$$

$$- 2\varpi\Gamma\frac{\partial^3 f_r^{(\varepsilon,\varrho)}}{\partial y^3}\left(\frac{\partial^2 f_r^{(\varepsilon,\varrho)}}{\partial y^2}\right)^2, \quad \vartheta_{0,r}^{(\varepsilon,\varrho)} = 1 + \frac{4}{3}Rd + 4Rd(\theta_w - 1)\theta_r^{(\varepsilon,\varrho)} + 4Rd(\theta_w - 1)^2(\theta_r^{(\varepsilon,\varrho)})^2$$

$$+ \frac{4}{3}Rd(\theta_w - 1)^3(\theta_r^{(\varepsilon,\varrho)})^3$$

$$+ \delta_1\theta_r^{(\varepsilon,\varrho)}, \quad \vartheta_{1,r}^{(\varepsilon,\varrho)} = 8Rd(\theta_w - 1)\frac{\partial\theta_r^{(\varepsilon,\varrho)}}{\partial y} + [2\delta_1 + 16Rd(\theta_w - 1)^2\theta_r^{(\varepsilon,\varrho)}]\frac{\partial\theta_r^{(\varepsilon,\varrho)}}{\partial y} + Prf_r^{(\varepsilon,\varrho)}$$

$$+ 8Rd(\theta_w - 1)^3(\theta_r^{(\varepsilon,\varrho)})^2\frac{\partial\theta_r^{(\varepsilon,\varrho)}}{\partial y},$$

$$\vartheta_{2,r}^{(\varepsilon,\varrho)} = \delta_1\frac{\partial^2\theta_r^{(\varepsilon,\varrho)}}{\partial y^2} + Pr\lambda + 4Rd(\theta_w - 1)\frac{\partial^2\theta_r^{(\varepsilon,\varrho)}}{\partial y^2} + 8Rd(\theta_w - 1)^2\theta_r^{(\varepsilon,\varrho)}\frac{\partial^2\theta_r^{(\varepsilon,\varrho)}}{\partial y^2}$$

$$+ 4Rd(\theta_w - 1)^3(\theta_r^{(\varepsilon,\varrho)})^2\frac{\partial^2\theta_r^{(\varepsilon,\varrho)}}{\partial y^2}$$

$$+ 8Rd[(\theta_w - 1)^2 + (\theta_w - 1)^3\theta_r^{(\varepsilon,\varrho)}]\left(\frac{\partial\theta_r^{(\varepsilon,\varrho)}}{\partial y}\right)^2 - PrEc\varsigma\left(\frac{\partial^2 f_r^{(\varepsilon,\varrho)}}{\partial y^2}\right)^2 e^{-\varsigma\theta_r^{(\varepsilon,\varrho)}}, \quad \vartheta_{3,r}^{(\varepsilon,\varrho)} = 2PrEc\frac{\partial^2 f_r^{(\varepsilon,\varrho)}}{\partial y^2}e^{-\varsigma\theta_r^{(\varepsilon,\varrho)}},$$

$$\vartheta_{4,r}^{(\varepsilon,\varrho)} = 2M^2PrEc\frac{\partial f_r^{(\varepsilon,\varrho)}}{\partial y}, \quad \vartheta_{6,r}^{(\varepsilon,\varrho)} = \delta_1\theta_r^{(\varepsilon,\varrho)}\frac{\partial^2\theta_r^{(\varepsilon,\varrho)}}{\partial y^2} + \delta_1\left(\frac{\partial\theta_r^{(\varepsilon,\varrho)}}{\partial y}\right)^2 + Prf_r^{(\varepsilon,\varrho)}\frac{\partial\theta_r^{(\varepsilon,\varrho)}}{\partial y}$$

$$+ 4Rd(\theta_w - 1)\theta_r^{(\varepsilon,\varrho)}\frac{\partial^2\theta_r^{(\varepsilon,\varrho)}}{\partial y^2}$$

$$+ PrEc\left(\frac{\partial^2 f_r^{(\varepsilon,\varrho)}}{\partial y^2}\right)^2 e^{-\varsigma\theta_r^{(\varepsilon,\varrho)}} + PrEcM^2\left(\frac{\partial f_r^{(\varepsilon,\varrho)}}{\partial y}\right)^2 + 4Rd[2(\theta_w - 1)^2(\theta_r^{(\varepsilon,\varrho)})^2 + (\theta_w - 1)^3(\theta_r^{(\varepsilon,\varrho)})^3]\frac{\partial^2\theta_r^{(\varepsilon,\varrho)}}{\partial y^2}$$

$$+ 4Rd(\theta_w - 1)\left(\frac{\partial\theta_r^{(\varepsilon,\varrho)}}{\partial y}\right)^2 + 12Rd(\theta_w - 1)^3(\theta_r^{(\varepsilon,\varrho)})^2\left(\frac{\partial\theta_r^{(\varepsilon,\varrho)}}{\partial y}\right)^2 + 16Rd(\theta_w - 1)^2\theta_r^{(\varepsilon,\varrho)}\left(\frac{\partial\theta_r^{(\varepsilon,\varrho)}}{\partial y}\right)^2$$

$$- \varsigma PrEc\theta_r^{(\varepsilon,\varrho)}\left(\frac{\partial^2 f_r^{(\varepsilon,\varrho)}}{\partial y^2}\right)^2 e^{-\varsigma\theta_r^{(\varepsilon,\varrho)}}, \quad \vartheta_{5,r}^{(\varepsilon,\varrho)} = Pr\frac{\partial\theta_r^{(\varepsilon,\varrho)}}{\partial y}, \quad \psi_{0,r}^{(\varepsilon,\varrho)} = 1 + \delta_2\theta_r^{(\varepsilon,\varrho)}, \quad \psi_{1,r}^{(\varepsilon,\varrho)} = Scf_r^{(\varepsilon,\varrho)} + \delta_2\frac{\partial\theta_r^{(\varepsilon,\varrho)}}{\partial y},$$

$$\psi_{2,r}^{(\varepsilon,\varrho)} = -Sck_c,$$

$$\psi_{3,r}^{(\varepsilon,\varrho)} = \delta_2\frac{\partial\phi_r^{(\varepsilon,\varrho)}}{\partial y}, \quad \psi_{4,r}^{(\varepsilon,\varrho)} = \delta_2\frac{\partial^2\phi_r^{(\varepsilon,\varrho)}}{\partial y^2}, \quad \psi_{5,r}^{(\varepsilon,\varrho)} = Sc\frac{\partial\phi_r^{(\varepsilon,\varrho)}}{\partial y}, \quad \psi_{6,r}^{(\varepsilon,\varrho)} = Scf_r^{(\varepsilon,\varrho)}\frac{\partial\phi_r^{(\varepsilon,\varrho)}}{\partial y} + \delta_2\theta_r^{(\varepsilon,\varrho)}\frac{\partial^2\phi_r^{(\varepsilon,\varrho)}}{\partial y^2}$$

$$+ \delta_2\frac{\partial\phi_r^{(\varepsilon,\varrho)}}{\partial y}\frac{\partial\theta_r^{(\varepsilon,\varrho)}}{\partial y}.$$

As the spectral collocation method is valid in the domain $[-1, 1]$, the time interval J_ϱ and space interval I_ε are, respectively, transformed into $\hat{\tau} \in [-1, 1]$ and $\hat{y} \in [-1, 1]$, using the linear transformations

$$\tau_j^\varrho = \frac{L_\tau}{2}(\hat{\tau}_j + 1), \quad \{\hat{\tau}_j\}_{j=0}^{N_\tau} = \cos\left(\frac{\pi j}{N_\tau}\right), \tag{30}$$

$$y_i^\varepsilon = \frac{L_x}{2}(\hat{y}_i + 1), \quad \{\hat{y}_i\}_{i=0}^{N_y} = \cos\left(\frac{\pi i}{N_y}\right). \tag{31}$$

We suppose that at each subdomain, the needed solution, for instance, $f(y, \tau)$ can be approximated by a bivariate Lagrange interpolation polynomial of the form

$$f^{(\varepsilon, \varrho)}(y, \tau) \approx \sum_{k=0}^{N_y} \sum_{s=0}^{N_\tau} f^{(\varepsilon, \varrho)}(\hat{y}_k, \hat{\tau}_s) \mathscr{L}_k(\hat{y}) \mathscr{L}_s(\hat{\tau}), \tag{32}$$

where functions $\mathscr{L}_k(y)$ and $\mathscr{L}_s(\tau)$ are the well-known characteristic Lagrange cardinal polynomial based on the Chebyshev-Gauss-Lobatto points.[54] The first derivative of $f^{(\varepsilon, \varrho)}(y, \tau)$ with respect to y and τ at the Chebyshev-Gauss-Lobatto points $(\hat{y}_i, \hat{\tau}_j)$ are computed as

$$\left(\frac{\partial f_{r+1}^{(\varepsilon, \varrho)}}{\partial y}\right)\bigg|_{(y=y_i, \tau=\tau_j)} = \sum_{k=0}^{N_y} \hat{D}_{i,k}^{(\varepsilon)} F_{r+1}^{(\varepsilon, \varrho)}(\hat{y}_k, \hat{\tau}_j) = \mathbf{DF}_{j, r+1}, \tag{33}$$

$$\left(\frac{\partial f_{r+1}^{(\varepsilon, \varrho)}}{\partial \tau}\right)\bigg|_{(y=y_i, \tau=\tau_j)} = \left(\frac{2}{\tau_{N_\tau}^\varrho - \tau_0^\varrho}\right) \sum_{s=0}^{N_\tau} \hat{d}_{j,s}^{(\varrho)} F_{r+1}^{(\varepsilon, \varrho)}(\hat{y}_i, \hat{\tau}_s) = \sum_{s=0}^{N_\tau} d_{j,s} \mathbf{F}_{s, r+1}, \tag{34}$$

where $\hat{D}_{i,k}^{(\varepsilon)} = \frac{2}{y_{N_y}^\varepsilon - y_0^\varepsilon} D_{i,k} (i, k = 0, 1, 2, ..., N_y)$, with $D_{i,k}$ being the standard first-order Chebyshev-Gauss-Lobatto differentiation matrix of size $(N_y + 1) \times (N_y + 1)$, as defined in Reference [54], and $\hat{d}_{j,s}^{(\varrho)} = \frac{\tau_{N_\tau}^\varrho - \tau_0^\varrho}{2} d_{j,s} (j, s = 0, 1, 2, ..., N_\tau)$ being entries of the standard first-order Chebyshev differentiation matrices of size $(N_\tau + 1) \times (N_\tau + 1)$. The vector $\mathbf{F}_j$ is defined as

$$\mathbf{F}_j = [f^{(\varepsilon, \varrho)}(y_0, \tau_j), f^{(\varepsilon, \varrho)}(y_1, \tau_j), ..., f^{(\varepsilon, \varrho)}(y_{N_y}, \tau_j)]^T, \tag{35}$$

where T is the transpose. As the last two points in the εth subinterval and the first two points in the $(\varepsilon + 1)$th subinterval overlap and remain common, the differentiation matrix $\mathbf{D}$ for the overlapping grid in y is assembled by carefully discarding the rows corresponding to the recurrent points as shown below:

$$
\mathbf{D} = \begin{bmatrix}
\hat{D}_{0,0}^{(p)} & \hat{D}_{0,1}^{(p)} & \cdots & \hat{D}_{0,N_y-1}^{(p)} & \hat{D}_{0,N_y}^{(p)} \\
\hat{D}_{1,0}^{(p)} & \hat{D}_{1,1}^{(p)} & \cdots & \hat{D}_{1,N_y-1}^{(p)} & \hat{D}_{1,N_y}^{(p)} \\
\ddots & \ddots & \ddots & \ddots & \ddots \\
\hat{D}_{N_y-1,0}^{(p)} & \hat{D}_{N_y-1,1}^{(p)} & \cdots & \hat{D}_{N_y-1,N_y-1}^{(p)} & \hat{D}_{N_y-1,N_y}^{(p)} \\
 & & & \hat{D}_{1,0}^{(p-1)} & \hat{D}_{1,1}^{(p-1)} & \cdots & \hat{D}_{1,N_y-1}^{(p-1)} & \hat{D}_{1,N_y}^{(p-1)} \\
 & & & \hat{D}_{2,0}^{(p-1)} & \hat{D}_{2,1}^{(p-1)} & \cdots & \hat{D}_{2,N_y-1}^{(p-1)} & \hat{D}_{2,N_y}^{(p-1)} \\
 & & & \ddots & \ddots & \ddots & \ddots & \ddots \\
 & & & \hat{D}_{N_y-1,0}^{(p-1)} & \hat{D}_{N_y-1,1}^{(p-1)} & \cdots & \hat{D}_{N_y-1,N_y-1}^{(p-1)} & \hat{D}_{N_y-1,N_y}^{(p-1)} \\
 & & & & & \ddots & \ddots \\
 & & & & & & \hat{D}_{1,0}^{(1)} & \hat{D}_{1,1}^{(1)} & \cdots & \hat{D}_{1,N_y-1}^{(1)} & \hat{D}_{1,N_y}^{(1)} \\
 & & & & & & \hat{D}_{2,0}^{(1)} & \hat{D}_{2,1}^{(1)} & \cdots & \hat{D}_{2,N_y-1}^{(1)} & \hat{D}_{2,N_y}^{(1)} \\
 & & & & & & \ddots & \ddots & \ddots & \ddots & \ddots \\
 & & & & & & \hat{D}_{N_y,0}^{(1)} & \hat{D}_{N_y,1}^{(1)} & \cdots & \hat{D}_{N_y,N_y-1}^{(1)} & \hat{D}_{N_y,N_y}^{(1)}
\end{bmatrix}
\tag{36}
$$

where the empty entries of coefficient matrix $\mathbf{D}$ are zeros (leading to sparse matrix) and $\hat{D}^{(\varepsilon)}$ represents the Chebyshev differentiation matrix in the εth subinterval in space. It is worth noting that the spatial derivative operator becomes a full matrix if only a single domain is used in the calculation. The size of matrix $\mathbf{D}$ is $(V+1) \times (V+1)$, where $V = N_y + (N_y - 1) \times (p - 1)$ is the total number of collocation points in the entire spatial domain. The higher order (nth) differentiation matrix with respect to y can be obtained using matrix multiplication as follows:

$$
\frac{\partial^n f_{r+1}^{\varepsilon,\varrho}}{\partial y^n}\bigg|_{(y=y_i,\tau=\tau_j)} = \sum_{k=0}^{N_y} [\hat{D}_{i,k}^{(\varepsilon)}]^n F_{r+1}^{(\varepsilon,\varrho)}(\hat{y}_k, \hat{\tau}_j) = \mathbf{D}^n \mathbf{F}_{j,r+1}.
\tag{37}
$$

The global structure of the time derivative operator $\left(\frac{\partial}{\partial \tau}\right)$ has a similar structure as in Equation (36), with size of $(W+1) \times (W+1)$, where $W = N_\tau + (N_\tau - 1) \times (q - 1)$ is the total number of collocation points in the entire time domain. Applying the spectral method by evaluating Equations (27) to (29) at the collocation points and making use of assembled differentiation matrices give

$$
\mathbf{A}_{11}^{(i)}\mathbf{F}_{i,r+1} + \mathbf{A}_{12}^{(i)}\mathbf{\Theta}_{i,r+1} + \mathbf{A}_{13}^{(i)}\mathbf{\Phi}_{i,r+1} - S\sum_{j=0}^{W} d_{i,j}\mathbf{D}\mathbf{F}_{j,r+1} = \mathbf{R}_{1,r}^{(i)},
\tag{38}
$$

$$
\mathbf{A}_{21}^{(i)}\mathbf{F}_{i,r+1} + \mathbf{A}_{22}^{(i)}\mathbf{\Theta}_{i,r+1} + \mathbf{A}_{23}^{(i)}\mathbf{\Phi}_{i,r+1} - PrS\sum_{j=0}^{W} d_{i,j}\mathbf{\Theta}_{j,r+1} = \mathbf{R}_{2,r}^{(i)},
\tag{39}
$$

$$
\mathbf{A}_{31}^{(i)}\mathbf{F}_{i,r+1} + \mathbf{A}_{32}^{(i)}\mathbf{\Theta}_{i,r+1} + \mathbf{A}_{33}^{(i)}\mathbf{\Phi}_{i,r+1} - ScS\sum_{j=0}^{W} d_{i,j}\mathbf{\Phi}_{s,r+1} = \mathbf{R}_{3,r}^{(i)},
\tag{40}
$$

where

$$\mathbf{A}_{11}^{(i)} = \boldsymbol{\varphi}_{0,r}^{(\varepsilon,\varrho)}\mathbf{D}^{(3)} + \boldsymbol{\varphi}_{1,r}^{(\varepsilon,\varrho)}\mathbf{D}^{(2)} + \boldsymbol{\varphi}_{2,r}^{(\varepsilon,\varrho)}\mathbf{D} + \boldsymbol{\varphi}_{3,r}^{(\varepsilon,\varrho)}\mathbf{I}, \quad \mathbf{A}_{12}^{(i)} = \boldsymbol{\varphi}_{4,r}^{(\varepsilon,\varrho)}\mathbf{D} + \boldsymbol{\varphi}_{5,r}^{(\varepsilon,\varrho)}\mathbf{I}, \quad \mathbf{A}_{13}^{(i)} = \boldsymbol{\varphi}_{6,r}^{(\varepsilon,\varrho)}\mathbf{I},$$

$$\mathbf{R}_{1,r}^{(i)} = \boldsymbol{\varphi}_{7,r}^{(\varepsilon,\varrho)},$$

$$\mathbf{A}_{21}^{(i)} = \boldsymbol{\vartheta}_{3,r}^{(\varepsilon,\varrho)}\mathbf{D}^{(2)} + \boldsymbol{\vartheta}_{4,r}^{(\varepsilon,\varrho)}\mathbf{D} + \boldsymbol{\vartheta}_{5,r}^{(\varepsilon,\varrho)}\mathbf{I}, \quad \mathbf{A}_{23}^{(i)} = \mathbf{0}, \quad \mathbf{A}_{22}^{(i)} = \boldsymbol{\vartheta}_{0,r}^{(\varepsilon,\varrho)}\mathbf{D}^{(2)} + \boldsymbol{\vartheta}_{1,r}^{(\varepsilon,\varrho)}\mathbf{D} + \boldsymbol{\vartheta}_{2,r}^{(\varepsilon,\varrho)}\mathbf{I},$$

$$\mathbf{R}_{2,r}^{(i)} = \boldsymbol{\vartheta}_{6,r}^{(\varepsilon,\varrho)},$$

$$\mathbf{A}_{32}^{(i)} = \boldsymbol{\psi}_{3,r}^{(\varepsilon,\varrho)}\mathbf{D} + \boldsymbol{\psi}_{4,r}^{(\varepsilon,\varrho)}, \quad \mathbf{A}_{31}^{(i)} = \boldsymbol{\psi}_{5,r}^{(\varepsilon,\varrho)}, \quad \mathbf{A}_{33}^{(i)} = \boldsymbol{\psi}_{0,r}^{(\varepsilon,\varrho)}\mathbf{D}^{(2)} + \boldsymbol{\psi}_{1,r}^{(\varepsilon,\varrho)}\mathbf{D} + \boldsymbol{\psi}_{2,r}^{(\varepsilon,\varrho)}, \quad \mathbf{R}_{3,r}^{(i)} = \boldsymbol{\psi}_{6,r}^{(\varepsilon,\varrho)},$$

$$(41)$$

where $\mathbf{I}$ is an $(V + 1)(V + 1)$ identity matrix, $\mathbf{0}$ is an $(V + 1)(V + 1)$ matrix of zeros, $\mathbf{F}_{i,r+1}, \boldsymbol{\Theta}_{i,r+1}$ and $\boldsymbol{\Phi}_{i,r+1}$ denote values of f, θ, and ϕ at the collocation points. The boundary conditions are imposed on Equations (38) to (40) for each $i = 0, 1, 2, ..., W$. Equations (38) to (40) can be written as a matrix system of the form

$$\mathbf{B}_r\boldsymbol{\Lambda}_{r+1} = \mathbf{K}_r, \tag{42}$$

which can be solved iteratively to give the approximate solutions of $f(y, \tau), \theta(y, \tau)$, and $\phi(y, \tau)$. For the structure of coefficient matrix $\mathbf{B}_r$ and vectors $\boldsymbol{\Lambda}_{r+1}$ and $\mathbf{K}_r$, the reader is refereed to Goqo et al.[42]

4 | RESULTS AND DISCUSSION

The system of nonlinear PDEs (12) to (14) was solved numerically using BSQLM on overlapping grids. In the entire numerical computational process, the parameter values were chosen as $\tau = 10\pi, \Gamma = 0.1, \gamma = 0.5, Fs = 0.1, Pr = 0.4, S = 0.5, M = 0.5, \lambda = 0.3, N = 0.4, Rd = 0.2, Ec = 0.2, \theta_w = 1.2, \varpi = 0.1, \varsigma = 0.2, \delta_1 = 0.2, \delta_2 = 0.6, k_c = 0.5, f_w = 1$, and $Sc = 0.22$. The spatial domain y was truncated to $y_\infty = 15$. We used $N_\tau = 5$ and $N_y = 20$ collocation points in space and time, respectively. These values were sufficient to give accurate and consistent results, as a further increase in the number of collocation points did not change the numerical results. The space and time intervals were split into $p = q = 3$ subintervals. The above values were treated the same in the entire study, except the varied values in the respective figures and tables. To asses the convergence of the method, we have considered the error norms between two successive iterations. The error norms are defined as

$$E_w = \max_{0 \le j \le N_\tau} \parallel \Omega_{r+1,j} - \Omega_{r,j} \parallel_\infty, \quad w = \{f, \theta, \phi\}, \quad \Omega = \{\mathbf{F}, \boldsymbol{\Theta}, \boldsymbol{\Phi}\}. \tag{43}$$

The errors given by Equation (43) can be considered to be solution-based errors, and they measure the number of correct digits in the approximate solutions at the rth iteration level. Figure 2 shows the variation in the error norms E_f, E_θ, and E_ϕ against the number of iterations for both BSQLM on overlapping grids and single-domain BSQLM. It can be seen that the error norms decrease monotonically with increasing number of iterations, which indicates convergence of the methods. Full convergence is achieved after about six iterations for all solutions with a solution error of up to 10^{-11} for single-domain BSQLM and 10^{-14} for BSQLM on overlapping grids. It is worth noting that the smaller values of solution errors for the BSQLM on overlapping grids are attributed to the use of few number of grid points in each subinterval.
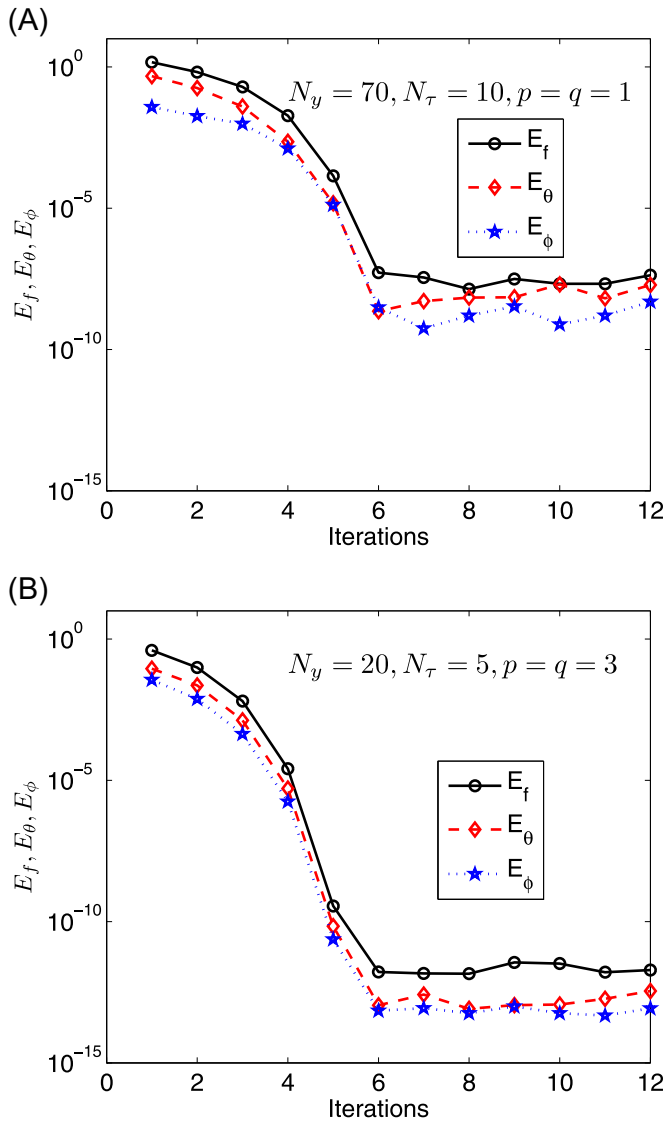
(A)

(B)

The accuracy of the method can be estimated by considering the residual errors, which measure the extent to which the numerical solutions approximate the true solution of the conservation Equations (12) to (14). The residual errors are defined as follows:

$$Res(w) = \| \Delta_w[\mathbf{F}_{r+1,j}, \mathbf{\Theta}_{r+1,j}, \mathbf{\Phi}_{r+1,j}] \|_\infty, \quad w = \{f, \theta, \phi\}, \tag{44}$$

where Δ_w represents the nonlinear PDEs (12) to (14), $\mathbf{F}_j$, $\mathbf{\Theta}_j$, and $\mathbf{\Phi}_j$ are the approximate solutions. Figures 3 to 5 depict the variation of residual errors against the time scale τ for different number of iterations in both BSQLM on overlapping grids and single-domain BSQLM. The reduction in the residual errors with an increase in the number of iterations demonstrates the convergence of the methods. The smaller values of the residual errors in the BSQLM on overlapping grids imply high accuracy of the proposed method. It can be seen that the residual errors are nearly uniform across time τ, particularly after six iterations. This observation suggests that the accuracy of the method does not deteriorate with an increase in the time variable. Also, the residual errors do not change significantly after six iterations, which means six iterations are enough to give accurate results. The accuracy of our numerical results was

FIGURE 3 Residual error graphs [Color figure can be viewed at wileyonlinelibrary.com]

(A)

$N_y = 70, N_\tau = 10, p = q = 1$

Iterations
2 — 3 — 6 — 8

(B)

Iterations
2 — 3 — 6 — 8

$N_y = 20, N_\tau = 5, p = q = 3$
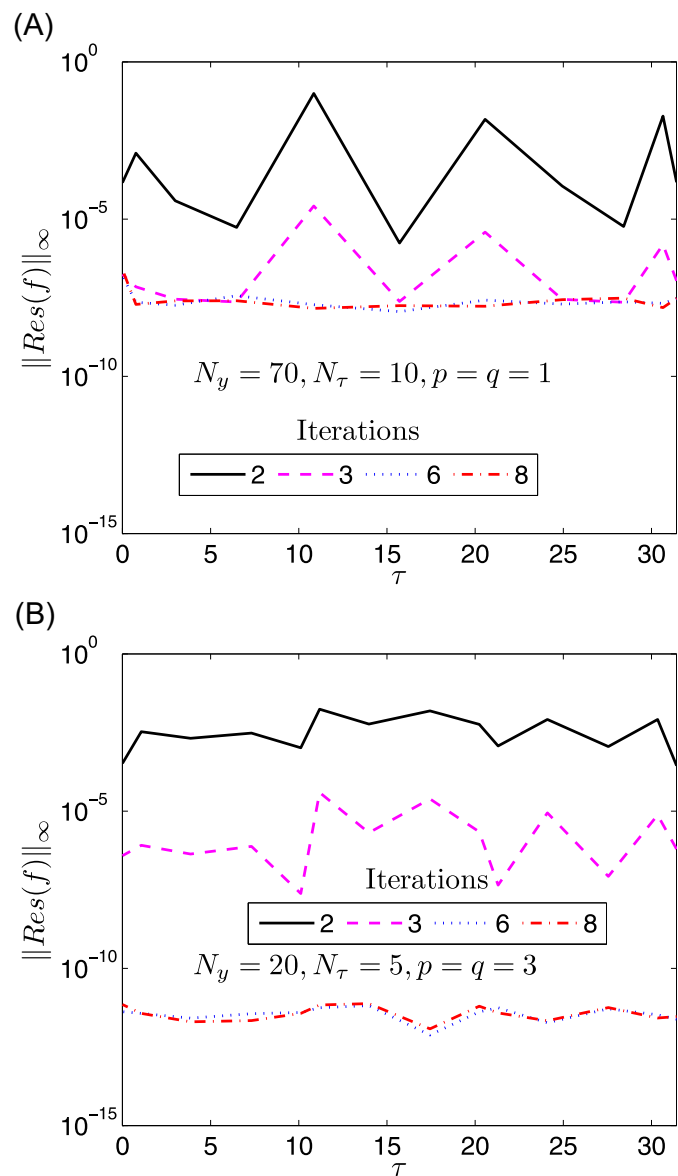
determined by comparing the values of the skin friction coefficient with previously published works of Zheng et al[19] and Khan et al.[25] The comparison is shown in Table 1, where results are noted to be in good agreement. Hence, the accuracy and efficiency of the proposed method can be justified.

In this study, we have also studied the effects of varying the number of subdomains and the number of collocation points. Table 2 depicts that the residual errors for the BSQLM on overlapping grids are smaller than errors for the single-domain BSQLM. The condition numbers of the coefficient matrices as well as the computational time in the BSQLM on overlapping grid are also observed to be smaller when compared with those from the single-domain BSQLM. These observations suggest that the proposed method gives stable and highly accurate results that are computed in a short CPU time. The high accuracy and computationally efficiency are attributed to the use of overlapping multidomain grid, which makes the coefficient matrices to be sparse, thus easy to invert. The sparsity of matrices minimizes the storage of huge matrices and allows easier matrix-vector multiplications on account of the many zero entries. Also, the sparse coefficient matrices are beneficial in the sense that they are well conditioned, rendering a

(A)

(B)
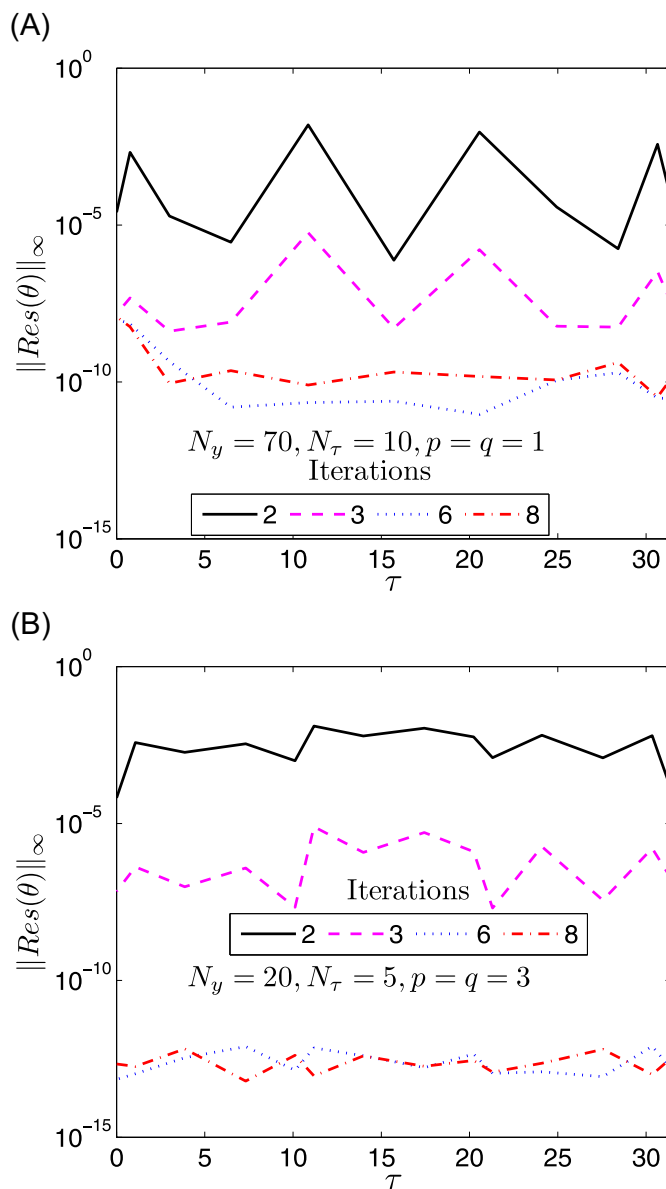
FIGURE 4 Residual error graphs [Color figure can be viewed at wileyonlinelibrary.com]

well-posed problem and leading to stable results. Table 2 also indicates that the residual errors, condition numbers, and CPU time decrease as the number of subintervals increases, whereas there is a decrease in the number of collocation points. This means that the accuracy, stability, and performance of the method improve when the number of subintervals increases, and few grid points in each subinterval and the entire domain are required to achieve stable and accurate results. The use of fewer grid points is advantageous in a way that it minimizes the effects of round-off errors that are linked to approximating functions with interpolating polynomials of a higher degree.

Figures 6 to 11 elucidate the repercussions of flow parameters on the profiles of velocity, thermal, and concentration. Figure 6 depicts the impact of variable viscosity and thermal conductivity on the velocity profiles. Figure 6A shows that the magnitude of velocity diminishes with the variable viscosity. Moreover, the plots show that for a particular value of variable viscosity, the velocity increases rapidly to a peak value near the wall and then decays to the relevant freestream velocity. Physically, larger values of variable viscosity parameter imply a higher temperature difference between the surface and the ambient fluid. The opposite trend is

**FIGURE 5** Residual error graphs [Color figure can be viewed at wileyonlinelibrary.com]
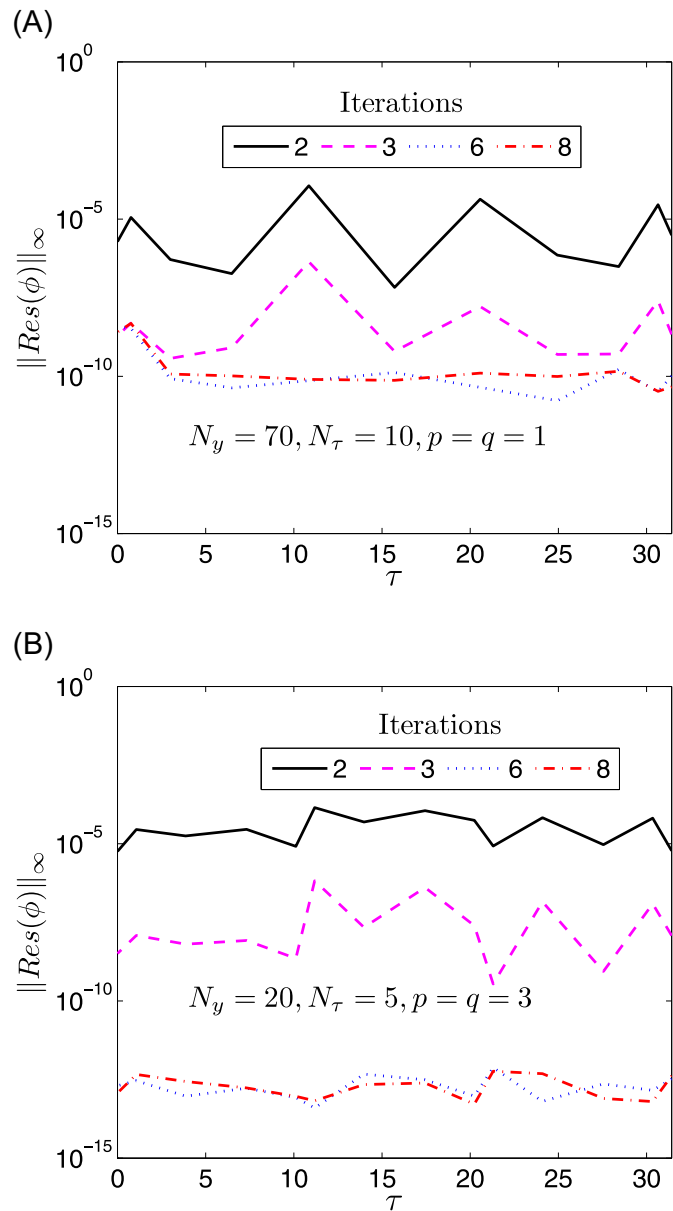
true for the variable thermal conductivity, as an increment in temperature-dependent thermal conductivity elevates the magnitude of velocity, as shown in Figure 6B. Figure 7 exhibits the impact of local inertia coefficient and Eyring-Powell fluid parameter on the velocity distribution. Near the wall, the velocity profiles decline with rising values of the inertia parameter, as seen in Figure 7A, because an increase in the inertia parameter decelerates the fluid flow for

TABLE 1 Comparison of $f''(0, \tau)$ when $\Gamma = \varpi = Fs = \gamma = N = \varsigma = f_w = 0$

S	M^2	τ	Zheng et al[19]	Khan et al[25]	Present results
1.0	12	1.5π	11.678565	11.678656	11.6785617
		5.5π	11.678706	11.678707	11.6787049
		9.5π	11.678656	11.678656	11.6786536

TABLE 2 Residual errors for different number of subdomains and collocation points after six iterations

p	N_y	V	q	N_τ	W	$\| Res(f) \|_\infty$	$\| Res(\theta) \|_\infty$	$\| Res(\phi) \|_\infty$	cond(B)	CPU time, s
1	100	100	1	13	13	1.03387e−006	4.82840e−011	4.85392e−011	1.7122e+009	44.201376
1	100	100	3	5	13	1.11325e−008	4.82840e−011	4.85392e−011	2.8499e+008	33.892935
2	50	99	3	5	13	1.32873e−009	8.97381e−012	5.13287e−012	3.4627e+007	33.787799
4	25	97	3	5	13	3.06673e−010	2.90403e−012	9.63030e−013	4.2733e+006	31.901032
5	20	96	3	5	13	1.67599e−010	8.53648e−013	6.19184e−013	2.1765e+006	30.371750
10	10	91	3	5	13	1.22488e−010	7.03150e−013	1.88389e−013	2.6350e+005	26.475420
20	5	81	3	5	13	2.81906e−011	9.22077e−014	4.52945e−014	2.9892e+004	19.834545
25	4	76	3	5	13	1.38659e−011	4.03204e−014	2.40710e−014	1.4262e+004	17.535074
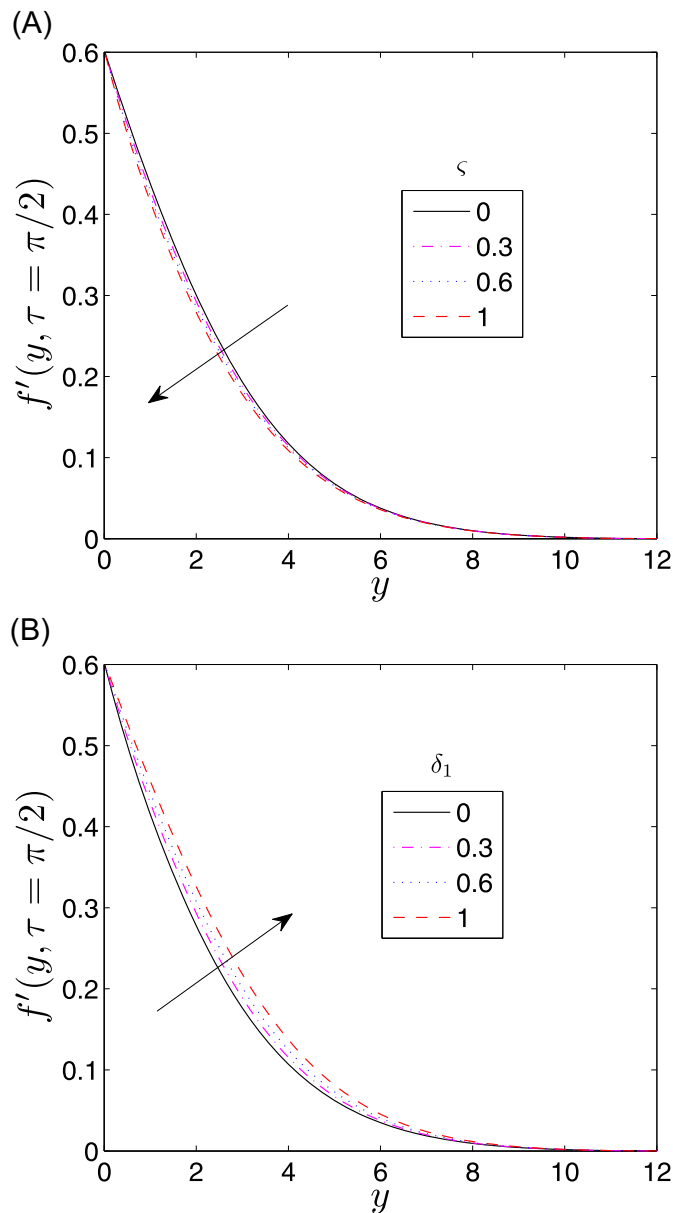
FIGURE 6 Velocity profiles at $\tau = \pi/2$ [Color figure can be viewed at wileyonlinelibrary.com]
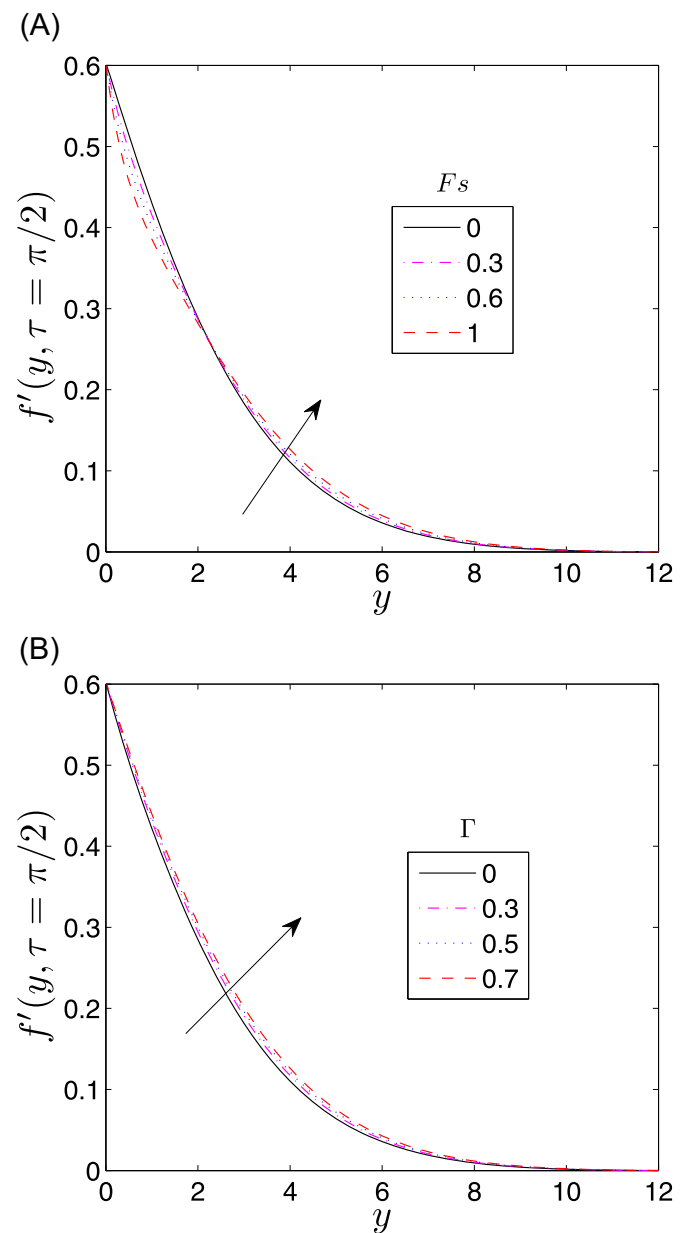
some distance near the wall. The inertial quadratic drag is also noticed to have a stronger effect closer to the wall. The increase in Forchheimer drag significantly swamps the momentum development, thereby decelerating the flow, in particular near the wall. Away from the wall, the velocity increases slightly to the relevant freestream velocity. This observation indicates that the momentum boundary layer thickness is weakly influenced by the Forchheimer effect far from the oscillatory surface. Figure 7B shows that velocity distribution increases by amplifying the Eyring-Powell fluid parameter throughout the boundary layer regime. It is worth noting that when $\Gamma = 0$, the flow equations reduce to those of a Newtonian viscous flow model. It is clear that the magnitude of velocity is greater in the case of non-Newtonian fluid when compared with the Newtonian fluid. This is due to the fact that the Eyring-Powell fluid is a shear-thinning fluid, where the viscosity diminishes with the shear rate, thus leading to enhancement in the fluid velocity.

Figure 8 reveals the influence of variable thermal conductivity parameter and local inertia coefficient on the thermal distribution. It is observed in Figure 8A that an increment in variable

(A)

(B)
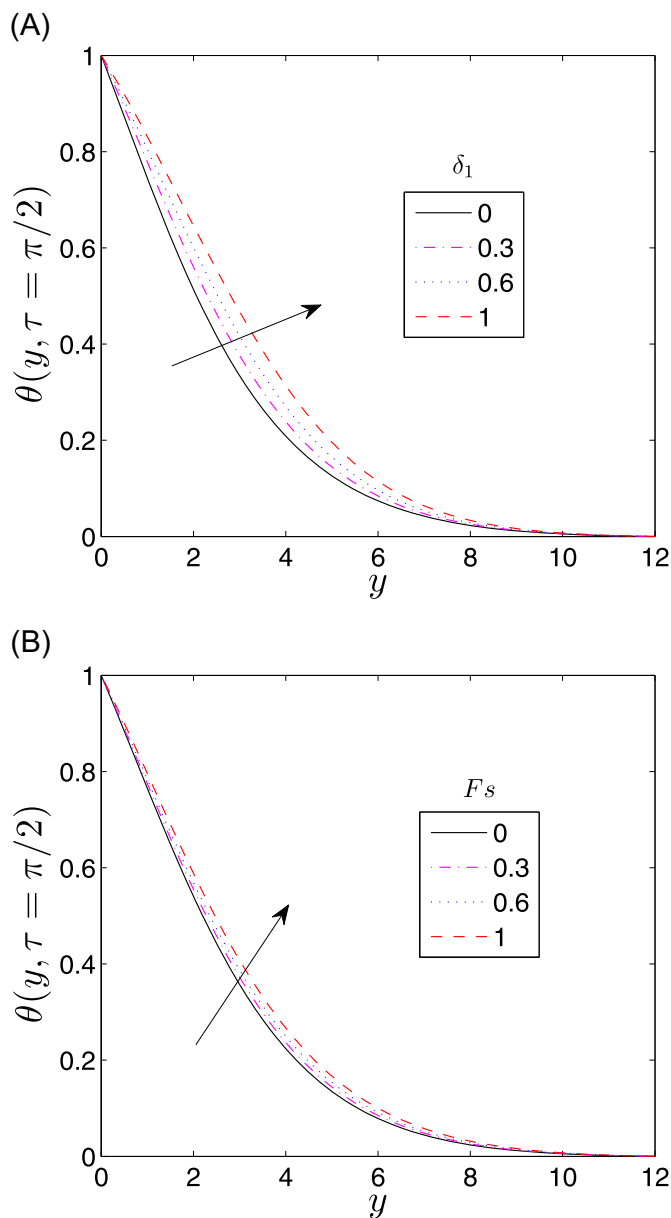
FIGURE 8   Temperature profiles at $\tau = \pi/2$ [Color figure can be viewed at wileyonlinelibrary.com]

thermal conductivity enhances the fluid temperature. This is because the thermal boundary layer becomes thicker as thermal diffusivity improves. This observation implies that the inclusion of variable thermal conductivity can be significant in improving heat transfer characteristics in different thermal extrusion processes. Similar results were reported by Ahmad et al[36] in the absence of variable fluid viscosity and mass diffusivity. Figure 8B shows that the thermal distribution augments by increasing the Forchheimer parameter. This is due to the fact that as the fluid flow is decelerated, energy is dissipated as heat, thus increasing the fluid temperature. Figure 9 elucidates the repercussions of thermal radiation parameter and temperature ratio parameter on the thermal distribution. The temperature field and thermal boundary layer thickness enhance for larger values of both radiation parameter and temperature ratio parameter. Physically, an increment in the radiation parameter releases thermal radiation energy into the flow, as the increase in the radiation parameter suggests a reduction in the Rosseland radiation absorption. Consequently, this maximizes the rate of radiative heat transferred to the fluid, thus increasing the temperature of the fluid. However, the increment in

FIGURE 9 Temperature profiles at $\tau = \pi/2$ [Color figure can be viewed at wileyonlinelibrary.com]

(A)

(B)
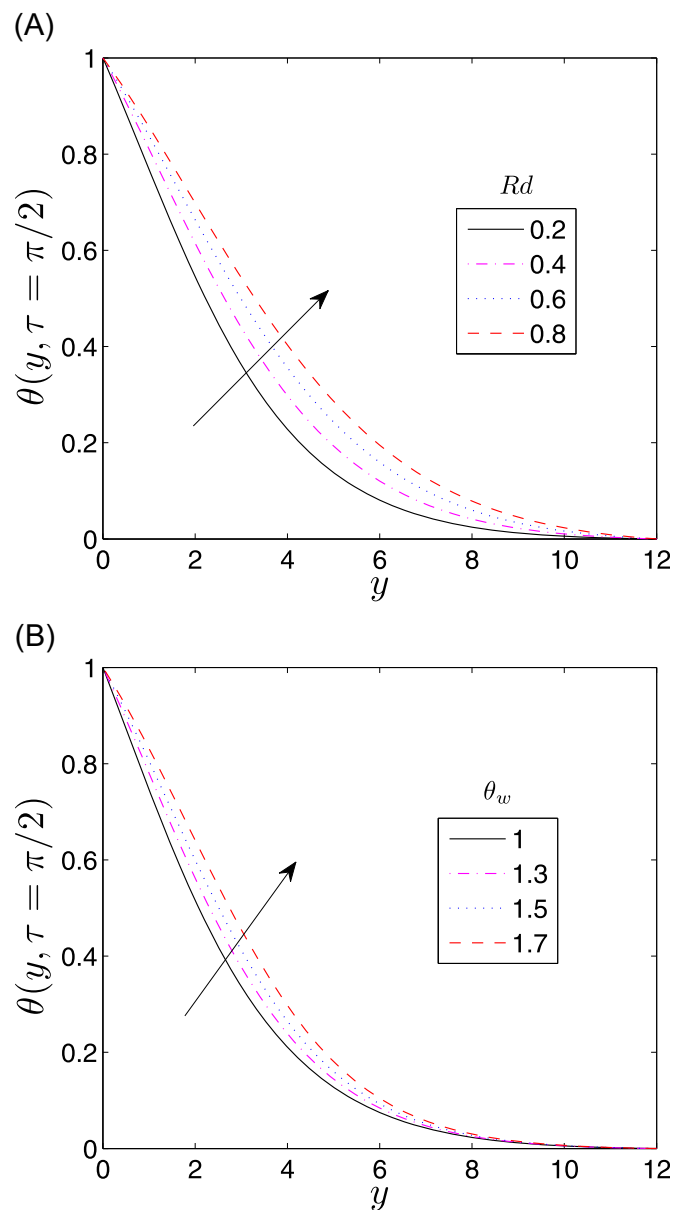
the temperature ratio parameter implies high temperature close to the walls of the oscillatory stretching sheet and lower temperature far from the wall.

Figure 10 presents the influence of the temperature-dependent mass diffusion coefficient and chemical reaction parameter on the mass fields. It evident from Figure 10A that an upsurge in the variable mass diffusion coefficient enhances the solutal boundary layer thickness, which, in turn, results in elevation of the concentration profiles. Also, the concentration of solute in the fluid of variable mass diffusivity is noted to be higher than the concentration of solute in the fluid of constant mass diffusivity. This is because the solute of temperature-dependent mass diffusion coefficient diffuses faster than the solute of constant mass diffusivity. These results suggest that the presence of variable mass diffusivity is more useful to improve the mass transportation characteristics. Figure 10B indicates that the concentration profiles decrease with growing values of the chemical reaction parameter. This is because the solute molecules undergoing chemical reaction improve as chemical reaction parameter increases, which leads to a decrease in the concentration field and solutal boundary layer thickness. Figure 11
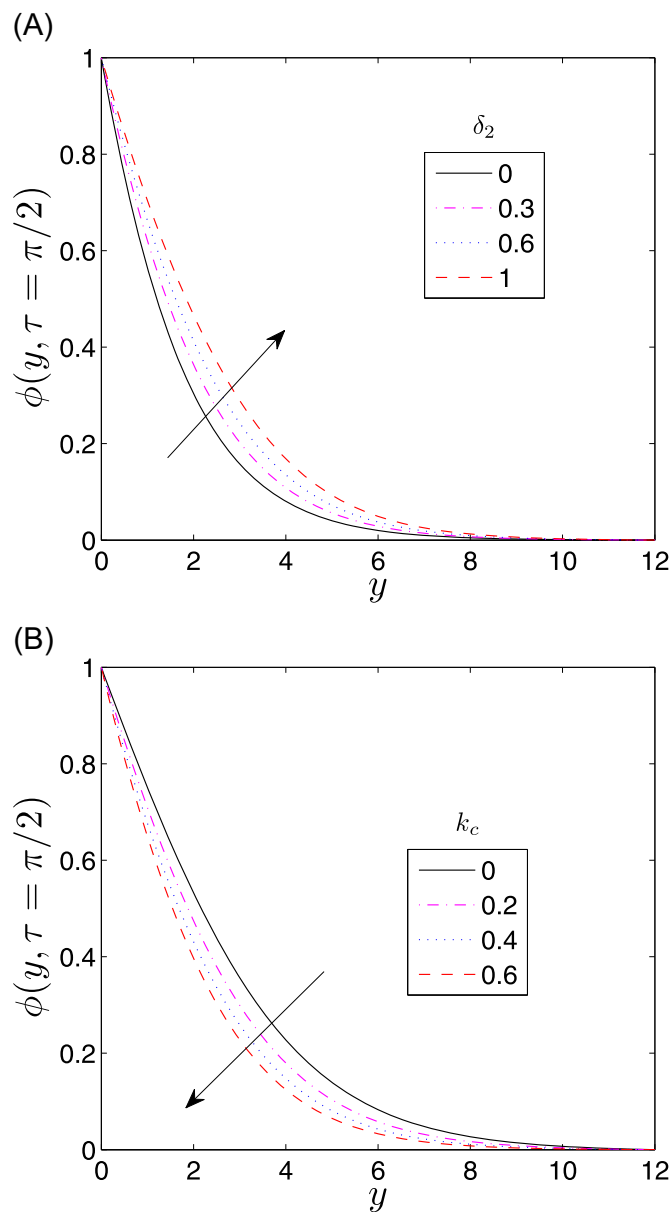
(A)

(B)

FIGURE 10 Concentration profiles at $\tau = \pi/2$ [Color figure can be viewed at wileyonlinelibrary.com]

illustrates the impact of the mixed convection parameter and suction parameter on the concentration profile. Figure 11A reveals that the concentration distribution decreases with larger values of mixed convection parameter. This is because the rapid fluid motion removes the species, which stabilizes and causes shrinkage in the thickness of diffusion boundary layers along the walls. The species concentration and solutal boundary layer thickness also decline with increasing values of the suction parameter.

Figures 12 and 13 present the influence of selected pertinent parameters on the time series of the velocity profiles. The impact of the Eyring-Powell fluid parameter and variable viscosity parameter on the velocity as a function of time is depicted in Figure 12. It is noted from Figure 12A that a phase shift takes place and the amplitude of the flow motion increases by escalating the Eyring-Powell fluid parameter. This is because the Eyring-Powell fluid parameter has an inverse relation with the viscosity of the fluid. As the Eyring-Powell fluid parameter

FIGURE 11 Concentration profiles at $\tau = \pi/2$ [Color figure can be viewed at wileyonlinelibrary.com]

(A)

(B)
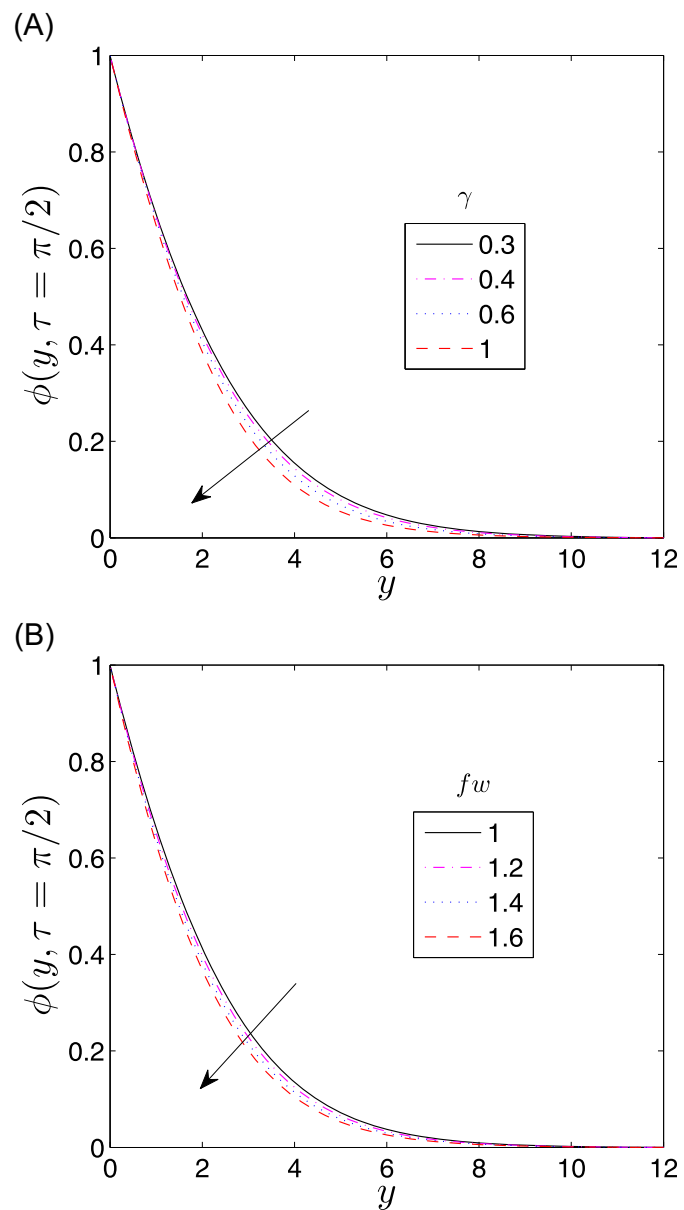
intensifies, the fluid becomes less viscous, leading to an increase in the rate of deformation; thus, the fluid velocity is enhanced. A similar observation was reported by Khan et al[27] in the case of constant fluid properties. Figure 12B exhibits that the amplitude of the fluid velocity diminishes when the temperature-dependent fluid viscosity parameter rises. This is because an increment in the viscosity parameter improves the viscosity of the fluid, thus causing the fluid velocity to decrease. Again, one can easily see that a phase shift occurs, which increases for large values of the temperature-dependent fluid viscosity. Figure 13A indicates that the buoyancy force makes the mixed convection parameter to augment the amplitude of velocity. The higher values of the mixed convection parameter result in a stronger buoyancy effect in the mixed convection flow, thus accelerating the flow, which intensifies the velocity of the fluid particles. These results concur with findings of Khan et al.[33] Figure 13B shows that a phase shift arises and the amplitude of velocity decreases with the increase in the suction parameter. This is because an increment in the suction parameter implies reduction in the permeability of the

(A)

(B)
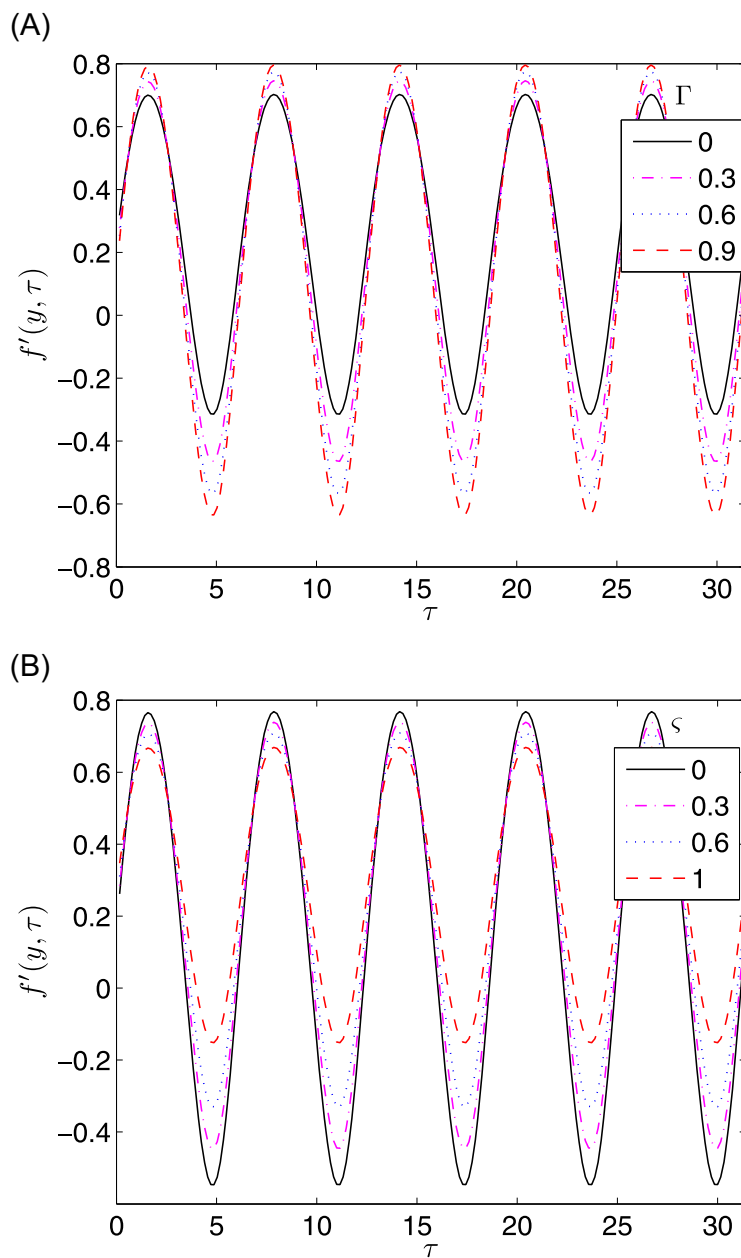
FIGURE 12 Time series of the velocity and profiles in the first five periods $[0, 10\pi]$ [Color figure can be viewed at wileyonlinelibrary.com]

porous medium. The presence of suction stabilizes the growth of the boundary layer, which, in turn, diminishes the thickness of the momentum boundary layer.

Figures 14 and 15 are plotted to show the impact of some important flow parameters on the time series of skin friction coefficient. Figure 14A discloses that amplitude of skin friction coefficient increases by elevating the Eyring-Powell fluid parameter. It can be seen that a phase shift occurs, which increases for large values of the Eyring-Powell fluid parameter. This observation suggests that skin friction for a Newtonian fluid flowing over an oscillatory stretching sheet is less in comparison with its value for Eyring-Powell fluid accomplishing the same motion. However, a phase shift occurs and the amplitude of skin friction coefficient decreases by increasing the variable fluid viscosity, as seen in Figure 14B. Figure 15A reveals that the time series of skin friction coefficient decreases by increasing the Forchheimer parameter. This is expected as the inertial quadratic drag swamps the momentum development and more resistance is produced by the porous medium to the fluid flow. Figure 15B shows that a phase

FIGURE 13 Time series of the velocity and profiles in the first five periods $[0, 10\pi]$ [Color figure can be viewed at wileyonlinelibrary.com]
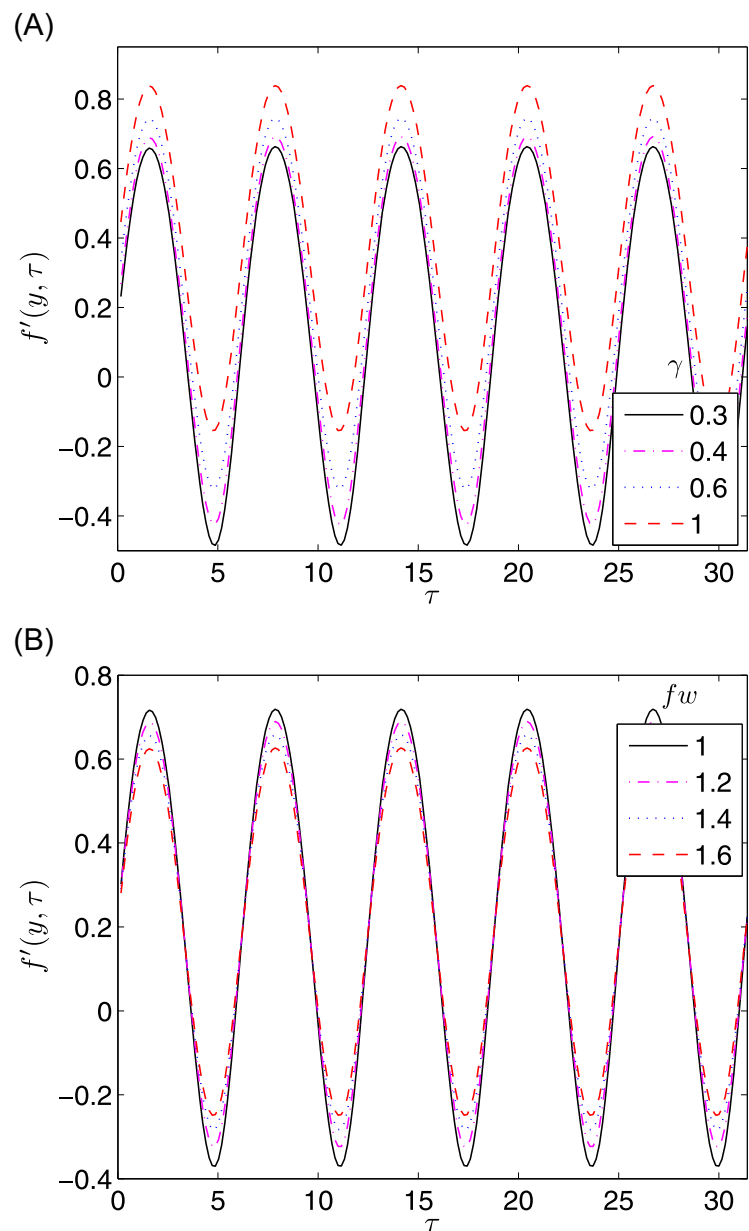
shift takes place and the amplitude of skin friction coefficient is enhanced by increasing the suction parameter.

The numerical values of Nusselt number and Sherwood number are presented in Table 3 for some important physical parameters. It is noted that the Nusselt number augments with the thermal radiation parameter, Eyring-Powell fluid parameter, variable thermal conductivity, mixed convection parameter, variable mass diffusion coefficient, and suction parameter, whereas it retards with the variable fluid viscosity, Forchheimer parameter, and chemical reaction parameter. However, the Sherwood number augments with the thermal radiation parameter, Eyring-Powell fluid, chemical reaction parameter, variable thermal conductivity, variable mass diffusion coefficient, mixed convection parameter, and suction parameter, whereas it diminishes with the variable fluid viscosity and Forchheimer parameter.

(A)

(B)
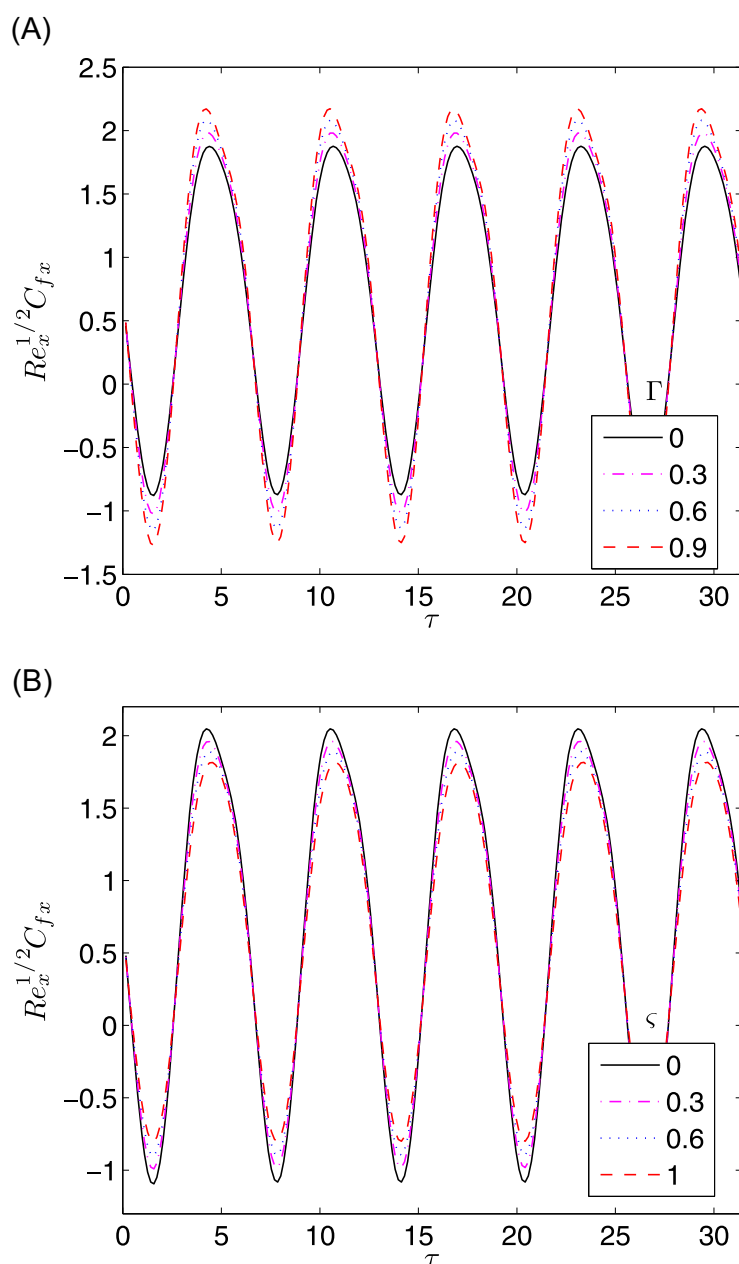
FIGURE 14 Time series of the skin friction in the first five periods $[0, 10\pi]$ [Color figure can be viewed at wileyonlinelibrary.com]

5 | CONCLUSION

In this study, numerical treatment of the unsteady MHD mixed convection flow of Eyring-Powell fluid over an oscillatory stretched surface adjacent to a non-Darcian porous medium with nonlinear thermal radiation, chemical reaction, and variable fluid properties was carried out. The transformed conservation equations have been solved numerically using efficient BSQLM on overlapping grids. Numerical simulations were conducted to highlight the convergence behavior and accuracy of the proposed iterative scheme. Simulations showed that the method converges to highly accurate and stable results that are computed in a short CPU time, after few iterations and using minimal number of grid points in each subinterval. The improved accuracy comes from the use of the overlapping grid, which makes the coefficient matrices in the matrix system that results from collocation process to be less dense, thus leading to small condition numbers and stable results. The computationally efficiency of the proposed method is

FIGURE 15 Time series of the skin friction coefficient in the first five periods $[0, 10\pi]$ [Color figure can be viewed at wileyonlinelibrary.com]

(A)

(B)
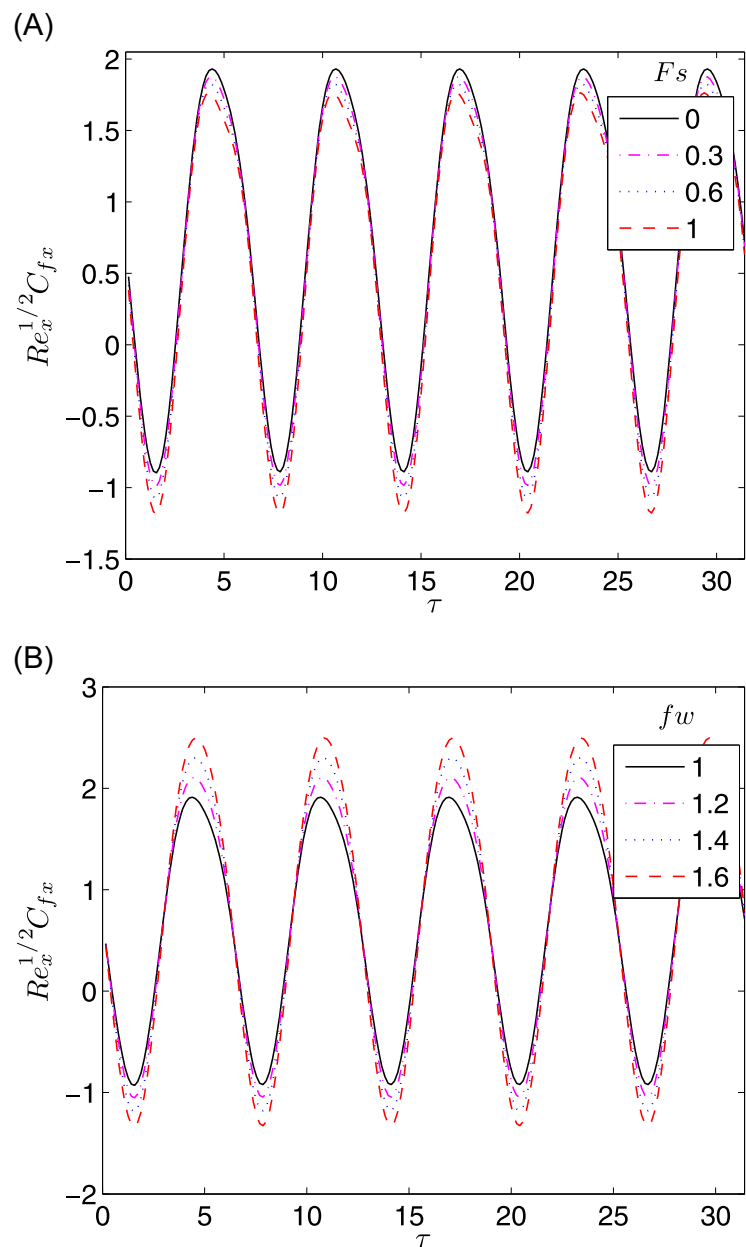
attributed to the ease of inverting the less dense coefficient matrices in the matrix system. The remaining conclusion remarks are summarized below:

- Introducing the temperature-dependent fluid viscosity decelerates the amplitude of fluid flow as well as the flow characteristics. However, the variable thermal conductivity and mass diffusion coefficient increase the flow fields and heat and mass transfer rates.
- An increase in the thermal radiation parameter significantly enhances the fluid temperature and heat and mass transfer coefficients.
- Higher values of the Forchheimer parameter augment the fluid velocity and concentration, whereas they retard the heat and mass transfer rates.

TABLE 3 Numerical values of the Nusselt number and Sherwood number for different values of ς, Γ, Rd, Fs, k_c, δ_1, δ_2, γ, and f_w when $\tau = \pi/2$, $N = 0.4$, $Pr = 0.4$, $S = 0.5$, $M = 0.5$, $\lambda = 0.3$, $\theta_w = 1.2$, $\varpi = 0.1$, $Ec = 0.2$, and $Sc = 0.22$

Rd	Γ	ς	Fs	k_c	δ_1	δ_2	γ	f_w	$Re_x^{-1/2} Nu_x$	$Re_x^{-1/2} Sh_x$
0.2	0.1	0.2	0.1	0.5	0.2	0.6	0.5	1.0	0.3950233	0.6205288
0.6	0.1	0.2	0.1	0.5	0.2	0.6	0.5	1.0	0.4007908	0.6372256
1.0	0.1	0.2	0.1	0.5	0.2	0.6	0.5	1.0	0.4122425	0.6473552
1.5	0.1	0.2	0.1	0.5	0.2	0.6	0.5	1.0	0.4334121	0.6552868
0.2	0.0	0.2	0.1	0.5	0.2	0.6	0.5	1.0	0.3908409	0.6190016
0.2	0.2	0.2	0.1	0.5	0.2	0.6	0.5	1.0	0.3987293	0.6219446
0.2	0.4	0.2	0.1	0.5	0.2	0.6	0.5	1.0	0.4050897	0.6244970
0.2	0.5	0.2	0.1	0.5	0.2	0.6	0.5	1.0	0.4078674	0.6256558
0.2	0.1	0.1	0.1	0.5	0.2	0.6	0.5	1.0	0.3964990	0.6246651
0.2	0.1	0.3	0.1	0.5	0.2	0.6	0.5	1.0	0.3957452	0.6225122
0.2	0.1	0.6	0.1	0.5	0.2	0.6	0.5	1.0	0.3946778	0.6196007
0.2	0.1	1.0	0.1	0.5	0.2	0.6	0.5	1.0	0.3934251	0.6163052
0.2	0.1	0.2	0.1	0.5	0.2	0.6	0.5	1.0	0.3950233	0.6205288
0.2	0.1	0.2	0.3	0.5	0.2	0.6	0.5	1.0	0.3864498	0.6190650
0.2	0.1	0.2	0.6	0.5	0.2	0.6	0.5	1.0	0.3741135	0.6170428
0.2	0.1	0.2	1.0	0.5	0.2	0.6	0.5	1.0	0.3585552	0.6146252
0.2	0.1	0.2	0.1	0.2	0.2	0.6	0.5	1.0	0.4031733	0.5116399
0.2	0.1	0.2	0.1	0.4	0.2	0.6	0.5	1.0	0.3973449	0.5868259
0.2	0.1	0.2	0.1	0.6	0.2	0.6	0.5	1.0	0.3929870	0.6522514
0.2	0.1	0.2	0.1	0.8	0.2	0.6	0.5	1.0	0.3895648	0.7109270
0.2	0.1	0.2	0.1	0.5	0.1	0.6	0.5	1.0	0.3936677	0.6188513
0.2	0.1	0.2	0.1	0.5	0.3	0.6	0.5	1.0	0.3963380	0.6221431
0.2	0.1	0.2	0.1	0.5	0.6	0.6	0.5	1.0	0.4000757	0.6266369
0.2	0.1	0.2	0.1	0.5	1.0	0.6	0.5	1.0	0.4046774	0.6319138
0.2	0.1	0.2	0.1	0.5	0.2	0.1	0.5	1.0	0.3864174	0.5650341
0.2	0.1	0.2	0.1	0.5	0.2	0.3	0.5	1.0	0.3901337	0.5891735
0.2	0.1	0.2	0.1	0.5	0.2	0.6	0.5	1.0	0.3950233	0.6205288
0.2	0.1	0.2	0.1	0.5	0.2	1.0	0.5	1.0	0.4005749	0.6558012
0.2	0.1	0.2	0.1	0.5	0.2	0.6	0.3	1.0	0.2945285	0.6113618
0.2	0.1	0.2	0.1	0.5	0.2	0.6	0.5	1.0	0.3950233	0.6205288
0.2	0.1	0.2	0.1	0.5	0.2	0.6	0.8	1.0	0.4769445	0.6330776
0.2	0.1	0.2	0.1	0.5	0.2	0.6	1	1.0	0.5133172	0.6405679

TABLE 3 (Continued)

Rd	Γ	ς	Fs	k_c	δ_1	δ_2	γ	fw	$Re_x^{-1/2}Nu_x$	$Re_x^{-1/2}Sh_x$
0.2	0.1	0.2	0.1	0.5	0.2	0.6	0.5	1.0	0.3950233	0.6205288
0.2	0.1	0.2	0.1	0.5	0.2	0.6	0.5	1.5	0.5625264	0.6770711
0.2	0.1	0.2	0.1	0.5	0.2	0.6	0.5	1.8	0.6662814	0.7141180
0.2	0.1	0.2	0.1	0.5	0.2	0.6	0.5	2.0	0.7363413	0.7402338

- An escalation in the Eyring-Powell fluid parameter intensifies the amplitude of flow motion, skin friction, and heat and mass transfer coefficients.
- Higher values of the suction parameter diminish the flow fields, whereas they amplify the flow characteristics.
- The chemical reaction and mixed convection parameter decay the concentration distribution and solutal boundary layer thickness, whereas they cause elevation in the rate of mass transfer.

The results of the current work can be beneficial in industrial and engineering applications such as metal extrusion, polymeric sheets, energy production, food processing, and other manufacturing processes. The study facilitates a better comprehension of the absorption of incident solar radiation and controlling heat transfer in polymer processing industry through the involvement of a nonlinear radiation term. Considering the advantages of the proposed method, it can be utilized in solving complex differential equations with large parameter values and those defined over large computational domains. The overlapping grid approach can be used in problems where solution profiles change rapidly within a narrow region on the problem domain.

NOMENCLATURE

u, v	velocity components, m/s
$\bar{x}, \bar{y}$	Cartesian coordinates, m
t	time, s
f	dimensionless stream function
B_0	magnetic field strength, kg/A·s^2
b	stretching rate
g	gravitational acceleration, m/s^2
T	fluid temperature, K
C	concentration, mol/m^3
T_w	temperature of the fluid at the wall, K
C_w	concentration at the wall, mol/m^3
T_∞	ambient temperature, K
C_∞	ambient concentration, mol/m^3
u_w	stretching velocity, m/s
v_w	suction/injection velocity, m/s
Q_0	volumetric heat transfer
D	mass diffusivity, m^2/s
D_∞	mass diffusivity away from the sheet, m^2/s

c_p	specific heat capacity, J/kg·K
k_p	permeability of the porous medium
K	thermal conductivity of the fluid, W/m·K
K_∞	thermal conductivity at the ambient temperature, W/m·K
c_b	form of drag coefficient
Pr	Prandtl number
k_0	reaction rate constant, s^{-1}
C_1	fluid parameter of Eyring-Powell model
k^*	mean absorption coefficient, m^{-1}
M	Hartmann parameter
S	ratio of frequency to stretching rate
Sc	Schmidt number
Sr	Soret number
k_c	chemical reaction parameter
Fs	local inertia coefficient
Ec	Eckert number
N	concentration buoyancy parameter
Rd	nonlinear radiation parameter
f_w	suction/injection parameter
y	similarity variable
Gr_x	Grashof number
C_{fx}, Nu_x, Sh_x	skin friction coefficient, Nusselt number, and Sherwood number
q_w	surface heat flux, W/m^2
q_m	surface mass flux, mol/m^2·s

GREEK SYMBOLS

ω	oscillation frequency
ρ_∞	fluid density, kg/m^3
ν_∞	kinematic viscosity far away from the sheet, m^2/s
μ	dynamic viscosity, kg/m·s
μ_∞	dynamic viscosity far away from the sheet, kg/m·s
σ^*	Stefan-Boltzmann coefficient, W/m^2·K^4
λ	heat absorption/generation parameter
ς	variable fluid viscosity parameter
δ_1	variable thermal conductivity parameter
δ_2	variable mass diffusion coefficient
σ	electrical conductivity, S/m
β	fluid parameter of the Eyring-Powell model
β_t	thermal expansion coefficient, K^{-1}
β_c	concentration expansion coefficient, K^{-1}
γ	mixed convection parameter
θ_w	temperature ratio parameter
Γ, ϖ	material fluid parameters
θ	dimensionless temperature
ϕ	dimensionless concentration
τ_w	wall shear stress, N/m^2
Ψ	stream function, m^2/s

ORCID

Musawenkhosi P. Mkhatshwa ![ORCID] https://orcid.org/0000-0001-7284-8498
Precious Sibanda ![ORCID] http://orcid.org/0000-0003-2115-4642

REFERENCES

1. Crane LJ. Flow past a stretching plate. *J Appl Math Phys.* 1970;21:645-647.
2. Shafiq A, Sindhu TN. Statistical study of hydromagnetic boundary layer flow of Williamson fluid regarding a radiative surface. *Results Phys.* 2017;7:3059-3067. https://doi.org/10.1016/j.rinp.2017.07.077
3. Shafiq A, Rasool G, Khalique CM, Aslam S. Second grade bioconvective nanofluid flow with buoyancy effect and chemical reaction. *Symmetry.* 2020;4:621. https://doi.org/10.3390/sym12040621
4. Shafiq A, Hammouch Z, Turab A. Impact of radiation in a stagnation point flow of Walters' B fluid towards a Riga plate. *Therm Sci Eng Prog.* 2018;6:27-33. https://doi.org/10.1016/j.tsep.2017.11.005
5. Mabood F, Tlili I, Shafiq A. Features of inclined magnetohydrodynamics on a second-grade fluid impinging on vertical stretching cylinder with suction and Newtonian heating. *Math Method Appl Sci.* 2020(special issue):1–13. https://doi.org/10.1002/mma.6489
6. Shafiq A, Khalique CM. Lie group analysis of upper convected Maxwell fluid flow along stretching surface. *Alex Eng J.* 2020. https://doi.org/10.1016/j.aej.2020.04.017. In press.
7. Rasool G, Zhang T, Chamkha AJ, Shafiq A, Tlili I, Shahzadi G. Entropy generation and consequences of binary chemical reaction on MHD Darcy-Forchheimer Williamson nanofluid flow over a non-linearly stretching surface. *Entropy.* 2020;22(1):18. https://doi.org/10.3390/e22010018
8. Rasool G, Shafiq A, Durur H. Darcy-Forchheimer relation in magnetohydrodynamic Jeffrey nanofluid flow over stretching surface. *Discrete Cont Dyn Syst.* 2020. https://doi.org/10.3934/dcdss.2020399. In press.
9. Powell RE, Eyring H. Mechanism for relaxation theory of viscosity. *Nature.* 1944;154:427-428.
10. Javad T, Ali N, Abbas Z, Sajid M. Flow of an Eyring-Powell non-Newtonian fluid over a stretching sheet. *Chem Eng Comm.* 2013;200(3):327-336. https://doi.org/10.1080/00986445.2012.703151
11. Megahed AM. Flow and heat transfer of Powell-Eyring fluid due to an exponential stretching sheet with heat flux and variable thermal conductivity. *Z Naturforsch.* 2015;70(3):163-169. https://doi.org/10.1515/zna-2014-0310
12. Malik MY, Khan I, Hussain A, Salahuddin T. Mixed convection flow of MHD Eyring-Powell nanofluid over a stretching sheet: a numerical study. *AIP Adv.* 2015;5(11):117118. https://doi.org/10.1063/1.4935639
13. Narayana PVS, Tarakaramu N, Akshit SM, Ghori JP. MHD flow and heat transfer of an Eyring-Powell fluid over a linear stretching sheet with viscous dissipation—a numerical study. *Front Heat Mass Transf.* 2017;9:9. https://doi.org/10.5098/hmt.9.9
14. Parmar AA, Jain BS. Unsteady convective flow for MHD Powell-Eyring fluid over inclined permeable surface. *J Comput Appl Res Mech Eng.* 2019;9(18):297-312. https://doi.org/10.22061/JCARME.2019.3423.1388
15. Ogunseye HA, Mondal H, Sibanda P, Mambili-Mamboundou H. Lie group analysis of a Powell-Eyring nanofluid flow over a stretching surface with variable properties. *SN Appl Sci.* 2020;2:115. https://doi.org/10.1007/s42452-019-1852-y
16. Wang C. Nonlinear streaming due to the oscillatory stretching of a sheet in a viscous fluid. *Acta Mech.* 1988;72(3-4):261-268. https://doi.org/10.1007/BF01178312
17. Siddappa D, Abel S, Hongunti V. Oscillatory motion of a viscoelastic fluid past a stretching sheet. *ll Nuovo Cimento D.* 1988;17(1):53-60. https://doi.org/10.1007/BF02451602
18. Abbas Z, Wang Y, Hayat T, Oberlack M. Hydromagnetic flow in a viscoelastic fluid due to the oscillatory stretching surface. *Int J Nonlinear Mech.* 2008;43(8):783-797. https://doi.org/10.1016/j.ijnonlinemec.2008.04.009
19. Zheng LC, Jin X, Zhang XX, Zhang JH. Unsteady heat and mass transfer in MHD flow over an oscillatory stretching surface with Soret and Dufour effects. *Acta Mech Sin.* 2013;29(5):667-675. https://doi.org/10.1007/s10409-013-0066-6
20. Ali N, Khan SU, Abbas Z. Hydromagnetic flow and heat transfer of a Jeffrey fluid over an oscillatory stretching surface. *Z Naturforsch A.* 2015;70(7):567-576. https://doi.org/10.1515/zna-2014-0273

21. Khan SU, Ali N, Abbas Z. Hydromagnetic flow and heat transfer over a porous oscillating stretching surface in a viscoelastic fluid with porous medium. *PLoS One*. 2015;10(12):e0144299. https://doi.org/10.1371/journal.pone.0144299

22. Ali N, Khan SU, Sajid M, Abbas Z. MHD flow and heat transfer of couple stress fluid over an oscillatory stretching sheet with heat source/sink in porous medium. *Alex Eng J*. 2016;55(2):915-924. https://doi.org/10.1016/j.aej.2016.02.018

23. Khan SU, Shehzad SA, Rauf A, Ali N. Mixed convection flow of couple stress nanofluid over oscillatory stretching sheet with heat source/sink effects. *Results Phys*. 2018;8:1223-1231. https://doi.org/10.1016/j.rinp.2018.01.054

24. Khan SU, Shehzad SA, Ali N. Darcy-Forchheimer MHD couple stress liquid flow by oscillatory stretched sheet with thermophoresis and heat generation/absorption. *J Porous Media*. 2018;21(12):1197-1213. https://doi.org/10.1615/JPorMedia.20180290100

25. Khan SU, Ali N, Abbas Z. Hydromagnetic flow and heat transfer of Eyring-Powell fluid over an oscillatory stretching sheet with thermal radiation. *Appl Appl Math*. 2015;10:893-908.

26. Khan SU, Ali N, Abbas Z. Influence of heat generation/absorption with convective heat and mass conditions in unsteady flow of Eyring-Powell nanofluid over porous oscillatory stretching surface. *J Nanofluids*. 2016; 5(3):351-362. https://doi.org/10.1166/jon.2016.1224

27. Khan SU, Ali N, Abbas Z. Soret and Diffour effect on hydromagnetic flow of Eyring-Powel fluid over an oscillatory stretching surface with heat generation/absorption and chemical reaction. *Therm Sci*. 2018; 22(1B):533-543. https://doi.org/10.2298/TSCI150831018U

28. Dawar A, Shah Z, Idrees M, Khan W, Islam S, Gul T. Impact of thermal radiation and heat source/sink on Eyring-Powell fluid flow over an unsteady oscillatory porous stretching surface. *Math Comput Appl*. 2018; 23(2):20. https://doi.org/10.3390/mca23020020

29. Alharbi SO, Dawar AD, Shah Z, et al. Entropy generation in MHD Eyring-Powell fluid flow over an unsteady oscillatory porous stretching surface under the impact of thermal radiation and heat source/sink. *Appl Sci*. 2018;8(12):2588. https://doi.org/10.3390/app8122588

30. Ramzan M, Bilal M, Kanwal S, Chung D. Effects of variable thermal conductivity and non-linear thermal radiation past an Eyring-Powell nanofluid flow with chemical reaction. *Commun Theor Phys*. 2017;67(6):723. https://doi.org/10.1088/0253-6102/67/6/723

31. Parmar A, Jain S. MHD Powell-Eyring fluid flow with non-linear radiation and variable thermal conductivity over a permeable cylinder. *Int J Heat Technol*. 2018;36(1):56-64. https://doi.org/10.18280/ijht.360108

32. Reddy AMR, Reddy JVR, Sandeep N, Sugunamma V. Unsteady flow of nonlinear radiative Powell-Eyring fluid past an inclined stretching sheet with first order chemical reaction. *Middle-East J Sci Res*. 2016;24(7): 2366-2374. https://doi.org/10.5829/idosi.mejsr.2016.24.07.23795

33. Khan I, Fatima S, Malik MY, Sakahuddin T. Exponentially varying viscosity of magnetohydrodynamic mixed convection Eyring-Powell nanofluid flow over an inclined surface. *Results Phys*. 2018;8:1194-1203. https://doi.org/10.1016/j.rinp.2017.12.074

34. Wahab HA, Zeb S, Gulistan M, Kadry S, Nam Y. Numerical study for the effects of temperature dependent viscosity flow of non-Newtonian fluid with double stratification. *Appl Sci*. 2020;10(2):708. https://doi.org/10.3390/app10020708

35. Khan SU, Shehzad SA, Abbasi FM, Hussain S. Thermo diffusion aspects in Jeffrey nanofluid over periodically moving surface with time dependent thermal conductivity. *Therm Sci*. 2019. https://doi.org/10.2298/TSI190428312U

36. Ahmad I, Aziz S, Khan SU, Ali N. Periodically moving surface in an Oldroyd-B fluid with variable thermal conductivity and Cattaneo-Christov heat flux features. *Heat Transfer*. 2020. https://doi.org/10.1002/htj.21772

37. Khan SU, Shehzad SA. Electrical MHD Carreau nanofluid over porous oscillatory stretching surface with variable thermal conductivity: applications of thermal extrusion system. *Physica A*. 2020;550:124132. https://doi.org/10.1016/j.physa.2020.124132

38. Mkhatshwa MP, Motsa SS, Sibanda P. Numerical solution of time-dependent Emden-Fowler equations using bivariate spectral collocation method on overlapping grids. *J Nonlinear Eng*. 2020;9:299-318. https://doi.org/10.1515/nleng-2020-0017

39. Motsa SS, Mgagula VM, Sibanda P. A bivariate Chebyshev spectral collocation quasilinearization method for nonlinear evolution parabolic equations. *Sci World J*. 2014;2014:581987. https://doi.org/10.1155/2014/581987

40. Motsa SS, Ansari MS. Unsteady boundary layer flow and heat transfer of Oldroyd-B nanofluid towards a stretching sheet with variable thermal conductivity. *Therm Sci*. 2015;19:S239-S248. https://doi.org/10.2298/TSCI15S1S39M

41. Goqo SP, Oloniiju SD, Mondal H, Sibanda P, Motsa SS. Entropy generation in MHD radiative viscous nanofluid flow over a porous wedge using the bivariate spectral quasi-linearization method. *Case Stud Therm Eng*. 2018;12:774-788. https://doi.org/10.1016/j.csite.2018.10.005

42. Goqo SP, Mondal H, Sibanda P, Motsa SS. Efficient multi-domain bivariate spectral collocation solution for MHD laminar natural convection flow from a vertical permeable flat plate with uniform surface temperature and thermal radiation. *Int J Comput Methods*. 2019;16(6):1840029. https://doi.org/10.1142/S021987618400297

43. Oloniiju SD, Goqo SP, Sibanda P. Heat and mass transfer in an unsteady second grade nanolfuid with viscous dissipation and heating dissipation. *Int J Comput Methods*. 2019;17(5):1940005. https://doi.org/10.1142/S021987621940005X

44. Dhlamini M, Mondal H, Sibanda P, Motsa SS. Rotational nanofluids for oxytactic microorganisms with convective boundary conditions using bivariate spectral quasi-linearization method. *J Cent South Univ*. 2020;27(3):824-841. https://doi.org/10.1007/s11771-020-4334-x

45. Bellman RE, Kalaba RE. *Quasilinearization and Nonlinear Boundary Value Problems*. Santa Monica, CA: RAND Corporation; 1965.

46. Olmos D, Shizgal BD. A pseudospectral method of solution of Fisher's equation. *J Comput Appl Math*. 2006;193(1):219-242. https://doi.org/10.1016/j.cam.2005.06.028

47. Teleei A, Dehghan M. A pseudo-spectral method that uses an overlapping multidomain technique for the numerical solution of sine-Gordon equation in one and two spatial dimensions. *Math Methods Appl Sci*. 2013;37:1909-1923. https://doi.org/10.1002/mmm.2943

48. Mkhatshwa MP, Motsa SS, Sibanda P. Overlapping multi-domain spectral method for conjugate problems of conduction and MHD free convection flow of nanofluids over flat plates. *Math Comput Appl*. 2019;24(3):75. https://doi.org/10.3390/mca24030075

49. Mkhatshwa MP, Motsa SS, Ayano MS, Sibanda P. MHD mixed convective nanofluid flow about a vertical slender cylinder using overlapping multi-domain spectral collocation approach. *Case Stud Therm Eng*. 2020;18:100598. https://doi.org/10.1016/j.csite.2020.100598

50. Mahmoud MA, Megahed AM. MHD flow and heat transfer in a non-Newtonian liquid film over an unsteady stretching sheet with variable fluid properties. *Can J Phys*. 2009;87(10):1065-1071. https://doi.org/10.1139/P09-066

51. Megahed AM. Williamson fluid flow due to a nonlinearly stretching sheet with viscous dissipation and thermal radiation. *J Egypt Math Soc*. 2019;27:12. https://doi.org/10.1186/s42787-019-0016-y

52. Mjankwi MA, Masanja VG, Mureithi EW, James MN. Unsteady MHD flow of nanofluid with variable properties over a stretching sheet in the presence of thermal radiation and chemical reaction. *Int J Math Math Sci*. 2019;2019:7392459. https://doi.org/10.1155/2019/7392459

53. Oyelakin IS, Sibanda P. Analysis of exponentially varying viscosity and thermal conductivity on a tangent hyperbolic fluid. *SeMA J*. 2020. https://doi.org/10.1007/s40324-020-00215-0

54. Trefethen LN. *Spectral methods in MATLAB*. Philadelphia, PA: SIAM; 2000.

Chapter 10

Conclusion

It this thesis, spectral collocation methods have been modified through computational grid-manipulation to improve accuracy, convergence and computational efficiency. The grid-manipulation involved using the multi-domain technique along with the overlapping grid approach. In Part A, the overlapping grid approach was used in the space domain to improve the accuracy of the spectral quasilinearisation method (SQLM) and bivariate spectral quasilineariation method (BSQLM). In Part B, the overlapping grid technique was used in space and time domains to improve the accuracy of the BSQLM. The improved numerical techniques were then used to solve fluid flow problems. The convergence and accuracy of the methods was demonstrated through error analysis. The accuracy of the methods was further determined by comparing the results with previously published results produced using other methods. The results were found to be satisfactory and in line with those in previous studies. Among the major findings, we found that the methods performed better and converged to more accurate solutions than other comparative methods. Sufficiently accuracy and stable results were achieved using only a few iterations, small computational time and the least possible number of grid points in each subinterval. The low number of grid points in every subinterval reduced the propagation of round-off errors that could otherwise caused instabilities. By increasing the number of overlapping subintervals, the accuracy further improved which is to be expected because increasing the number of overlapping subintervals reduces the number of grid points in the entire domain. The overlapping grid approach produces matrix systems with low density coefficient matrices that may be inverted in a computationally efficient manner. The findings from each chapter are summarized below.

In Chapter 2, the overlapping grid spectral quasilinearisation method was proposed and used to solve highly nonlinear and coupled ordinary differential equations. The flow equations modelled the flow of the MHD Casson nanofluid over a stretching surface with temperature dependent fluid properties. The fluid velocity was shown to decline with variable fluid properties, whereas the temperature and concentration distributions decreased. In Chapter 3, we developed and applied the overlapping multi-domain bivariate spectral quasilinearisation method (OMD-BSQLM) to find solutions for nonlinear partial differential equations arising in boundary layer fluid flows. The method was tested on fluid flow problems in two and three variables, respectively. Series solutions were used to authenticate the computed results and results showed a good correlation.

In Chapter 4, the focus was on the use of the OMD-BSQLM to solve nonlinear coupled partial differential equations describing conjugate heat transfer in MHD free convective flow of nanofluids. The silver-water nanofluid had higher velocity and temperature fields, shear stress and surface temperature than the copper-water nanofluid. This is because viscosity and thermal conductivity of silver are higher than that of copper. Different results were obtained for surface temperature, skin friction and heat transfer coefficients for parameters having the same values but in different geometries (either vertical or horizontal flat plate). This findings confirm that the geometry may affect the fluid properties. In Chapter 5, we studied the impact of Hall current, chemical reaction, diffusion-thermo and thermal-diffusion on the MHD flow of nanofluid over a vertical cylinder. The problem comprised of three coupled partial differential equations which were solved using the OMD-BSQLM. The fluid properties were shown to be higher when considering a curved surface than when considering a flat surface. This findings further highlight the significance of geometry in flow behaviour. With regard to mass transport, the mass transfer rate increased on the inclusion of a chemical reaction, Hall current and Soret effects.

In Chapter 6, we analyzed the problem of MHD mixed convective flow over an exponentially decreasing mainstream with a chemical reaction, heat convection boundary conditions and the influence of non-uniform heat source/sink. The OMD-BSQLM was used to solve the partial differential equations. The numerical results were compared with results obtained using the SQLM, BSQLM

and multi-domain bivariate spectral quasilinearisation method (MD-BSQLM). The OMD-BSQLM was shown to use least number of grid points to yield accurate solutions. Increasing thermal Biot number and non-uniform heat source/sink parameters was established to augment the fluid properties while diminishing the changes in shear stress and the heat transfer rate. In Chapter 7, we investigated heat and mass transport, and the movement of motile microorganisms on MHD bio-convective flow in a Casson nanofluid over a vertical surface. The fluid viscosity and thermal conductivity were assumed to vary with temperature. We assumed zero mass flux at the boundary and solved the flow equations using the OMD-BSQLM. The heat and motile microorgansms transfer rates were enhanced by increasing the variable viscosity and Cassson fluid parameter. The fluid temperature, heat and mass transfer characteristics were enhanced by incorporating variable thermal conductivity and radiative heat flux in the problem.

In Chapter 8, the overlapping grid approach was used in both space and time domains when applying the BSQLM in solving the Emden-Fowler partial differential equations. To highlight the merits of the method, we presented error bound theorems and their proofs. Approximate solutions were compared with exact solutions to verify the accuracy and convergence of the method. The numerical solutions were in good agreement with exact solutions. In Chapter 9, we analyzed the flow of an Eyring-Powell fluid over an oscillatory stretching surface taking into account temperature dependent fluid properties. The equations were solved using the overlapping grid BSQLM. We determined the impact of pertinent parameters on the fluid properties and flow characteristics. The heat and mass transport were enhanced with variable thermal conductivity and mass diffusion coefficient while decreased with Forchheimer parameter. Increasing the Eyring-Powell fluid parameter accelerated the amplitude of flow motion, changes in shear stress, heat and mass transport. The presence of suction enhanced the flow characteristics while reducing the fluid properties.

Contributions

The numerical techniques presented here add to a growing body of literature on accurate numerical methods for solving complex nonlinear differential equations that model fluid flow problems. The

methods can be used to validate results obtained using other numerical methods. The theoretical studies have indicated that fluid properties may not be presumed to be always constants because the physical properties of a fluid may vary considerably with temperature. Considering the variation of the fluid properties with temperature and using similar analysis as in the presented study, many previous results could be improved significantly. The use of nanofluids possess the effect of maximizing the effective heat transfer properties of fluids by improving the thermal conductivity and convective properties of fluids. This understanding was confirmed in this study and can assist in filling the gap between theory and practice. The study provided further insights into fluid flow with convective transport over various geometries. These findings may have applications in areas such as solar energy generation systems, polymer extrusion, nuclear reactor cooling systems, magnetic field control of materials processing systems, paper production, glass blowing, energy production and food processing.

Future Work

The methods presented here give accurate results and will find applications in other areas of science and engineering. The overlapping grid spectral collocation methods are best suited for problems with large computational domain and where the solution profiles vary rapidly within a narrow region along the problem domain. The use of the overlapping grid approach discussed in this work has been limited to one-dimensional ordinary differential equations and two-dimensional time-dependent partial differential equations. In future, the method may be extended to three-dimensional partial differential equations including those with two-space dependent variables and two-time dependent variables. The current study had a narrow focus of establishing if the methods are applicable to limited types of differential equations, and for these the efficacy of the method was established. The novelty of the study centred around the use of the new methods. Some numerical methods are more suitable for particular types of equations, whereas others may produce superior accuracy. Owing to these limitations, the methods remain to be checked for other properties, including stability and consistency. Since the current study was theoretical, experiments could validate the results obtained through the mathematical modelling techniques.

References

[1] F. John, *Partial Differential Equations*. 4th edition, Springer-Verlag, New York, 1982.

[2] P. Aviles and J. Sandefur, "Nonlinear second order equations with applications to partial differential equations," *Journal of Differential Equations*, vol. 58, no. 3, pp. 404–427, 1985.

[3] N. Hale and D. R. Moore, "A sixth-order extension to the MATLAB package bvp4c of J. Kierzenka and L. Shampine," tech. rep., Oxford University Computing Laboratory, UK, 2008.

[4] T. Sochi, "Flow of non-Newtonian fluids in porous media," *Journal of Polymer Science Part B: Polymer Physics*, vol. 48, no. 23, pp. 2437–2767, 2010.

[5] R. P. Chhabra and J. F. Richardson, *Non-Newtonian flow and applied rheology: engineering applications*. Butterworth-Heinemann, 2011.

[6] S. U. S. Choi and J. A. Eastman, "Enhancing thermal conductivity of fluids with nanoparticles," *ASME-Publications-Fed*, vol. 231, pp. 99–106, 1995.

[7] S. K. Das, S. U. S. Choi, and H. E. Patel, "Heat transfer in nanofluids - a review," *Heat Transfer Engineering*, vol. 27, no. 10, pp. 3–19, 2006.

[8] B. A. Bhanvase, D. P. Barai, S. H. Sonawane, N. Kumar, and S. S. Sonawane, "Intensified heat transfer rate with the use of nanofluids," in *Handbook of Nanomaterials for Industrial Applications*, pp. 739–750, Elsevier, 2018.

[9] M. Goyal and R. Bhargava, "Boundary layer flow and heat transfer of viscoelastic nanofluids past a stretching sheet with partial slip conditions," *Applied Nanoscience*, vol. 4, no. 6, pp. 761–767, 2014.

[10] C. B. Sobhan and G. P. Peterson, *Microscale and nanoscale heat transfer: fundamentals and engineering applications*. CRC Press, 2008.

[11] J. P. Holman, *Heat transfer*. McGraw-Hill, Singapore, 1986.

[12] L. C. Burmeister, *Convective heat transfer*. John Willey and Sons, Canada, 1993.

[13] M. Thirumaleshwar, *Fundamentals of heat and mass transfer*. Dorling Kindersley, Delhi, India, 2006.

[14] Y. A. Cengel and A. Ghajar, *Heat and mass transfer (A practical approach, SI version)*. McGraw-Hill Education, New York, 2011.

[15] W. M. Kays and M. E. Crawford, *Convective heat and mass transfer*. McGraw-Hill, 1993.

[16] M. Modest, *Radiative heat transfer*. Academic Press, 2003.

[17] J. R. Welty, C. E. Wicks, and R. E. Wilson, *Fundamentals of momentum, heat and mass transfer*. Willey and Sons, New York, 1984.

[18] Y. Jaluria and K. Himasekhar, "Buoyancy-induced two-dimensional vertical flows in a thermally stratified environment," *Computers and Fluids*, vol. 11, no. 1, pp. 39–49, 1983.

[19] A. D. Kraus, A. Aziz, and J. R. Welty, *Extended surface heat transfer*. Willey, New York, 2001.

[20] C. A. Yunus and J. G. Afshin, *Heat and mass transfer: fundamentals and applications*. Tata McGraw-Hill, New Delhi, 2011.

[21] F. Irgens, *Rheology and non-Newtonian fluids*. Springer, Berlin, 2014.

[22] R. S. R. Gorla and D. M. Pratt, "Second law analysis of a non-Newtonian laminar falling liquid film along an inclined heated plate," *Entropy*, vol. 9, no. 1, pp. 30–41, 2007.

[23] S. S. Ghadikolaei, K. Hosseinzadeh, M. Yassari, H. Sadeghi, and D. D. Ganji, "Analytical and numerical solution of non-Newtonian second-grade fluid flow on a stretching sheet," *Thermal Science and Engineering Progress*, vol. 5, pp. 309–316, 2018.

[24] N. Casson, "A flow equation for pigment-oil suspensions of the printing ink type," in *Rheology of Disperse Systems*, pp. 84–104, Pergamon Press, Oxford, 1959.

[25] A. S. Rao, V. R. Prasad, N. B. Reddy, and O. A. Bég, "Heat transfer in a Casson rheological fluid from a semi-infinite vertical plate with partial slip," *Heat Transfer-Asian Research*, vol. 44, no. 3, pp. 272–291, 2015.

[26] I. S. Oyelakin, S. Mondal, and P. Sibanda, "Unsteady MHD three-dimensional Casson nanofluid flow over a porous linear stretching sheet with slip condition," *Frontiers in Heat and Mass Transfer*, vol. 8, 37, pp. 1–9, 2017.

[27] Prashu and R. Nandkeolyar, "A numerical treatment of unsteady three-dimensional hydromagnetic flow of a Casson fluid with Hall and radiation effects," *Results in Physics*, vol. 11, pp. 966–974, 2018.

[28] R. E. Powell and H. Eyring, "Mechanisms for the relaxation theory of viscosity," *Nature*, vol. 154, pp. 427–428, 1944.

[29] T. M. Agbaje, S. S. M. S. Mondal, and P. Sibanda, "A numerical study of unsteady non-newtonian powell-eyring nanofluid flow over a shrinking sheet with heat generation and thermal radiation," *Alexandria Engineering Journal*, vol. 56, no. 1, pp. 81–91, 2017.

[30] H. A. Ogunseye, P. Sibanda, and H. Mondal, "Mhd mixed convective stagnation-point flow of Eyring-Powell nanofluid over stretching cylinder with thermal slip conditions," *Journal of Central South University*, vol. 26, no. 5, pp. 1172–1183, 2019.

[31] H. A. Ogunseye, Y. O. Tijani, and P. Sibanda, "Entropy generation in an unsteady Eyring-Powell hybrid nanofluid flow over a permeable surface: A lie group analysis," *Heat Transfer*, vol. 49, no. 6, pp. 3374–3390, 2020.

[32] H. E. Schaefer, *Nanoscience: The science of the small in physics, engineering, chemistry, biology and medicine*. Springer-Verlag Berlin Heidelberg, 2010.

[33] C. Kleinstrauer, *Microfluidics and nanofluidics, theory and selected applications*. New Jersey: Wiley, 2013.

[34] J. Buongiorno, "Convective transport in nanofluids," *ASME Journal of Heat Transfer*, vol. 128, no. 3, pp. 240–250, 2006.

[35] M. Sheikholeslami and H. B. Rokni, "CVFEM for effect of lorentz forces on nanofluid flow in a porous complex shaped enclosure by means of non-equilibrium model," *Journal of Molecular Liquids*, vol. 254, pp. 446–462, 2018.

[36] K. M. Shirvan, R. Ellahi, M. Mamourian, and M. Moghiman, "Effect of wavy surface characteristics on natural convection heat transfer in a cosine corrugated square cavity filled with nanofluid," *International Journal of Heat and Mass Transfer*, vol. 107, pp. 1110–1118, 2017.

[37] S. Rashidi, S. Akar, M. Bovand, and R. Ellahi, "Volume of fluid model to simulate the nanofluid flow and entropy generation in a single slope solar still," *Renewable Energy*, vol. 115(C), pp. 400–410, 2018.

[38] I. A. Hassanien, "Flow and heat transfer on continuous stretching flat surface moving in a parallel free steam with variable properties," *Zeitschrift fur Angewandte Mathematik and Mechanik*, vol. 79, no. 11, pp. 786–792, 1999.

[39] E. M. E. Elbarbary and N. S. Elgazery, "Chebyshev finite difference method for the effect of variable viscosity on magneto-micropolar fluid flow with radiation," *International Communications in Heat and Mass Transfer*, vol. 31, no. 3, pp. 409–419, 2004.

[40] M. A. Seddeek and A. M. Salem, "The effect of an axial magnetic field on the flow and heat transfer about a fluid underlying the axisymmetric spreading surface with temperature dependent viscosity and thermal diffusivity," *Computational Mechanics*, vol. 39, no. 4, pp. 401–408, 2007.

[41] N. S. Elzagery and N. Y. A. Elazem, "The effect of variable thermal conductivity on micropolar fluid flow by Chebyshev collocation method," *Chemical Engineering Communications*, vol. 197, no. 3, pp. 400–422, 2010.

[42] I. S. Oyelakin and P. Sibanda, "Analysis of exponentially varying viscosity and thermal conductivity on a tangent hyperbolic fluid," *SeMA Journal*, vol. 77, pp. 257–273, 2020.

[43] A. S. Idowu, M. T. Akolade, J. U. Abubakar, and B. O. Falodun, "MHD free convective heat and mass transfer flow of dissipative Casson fluid with variable viscosity and thermal conductivity effects," *Journal of Taibah University for Science*, vol. 14, no. 1, pp. 851–862, 2020.

[44] H. A. Ogunseye, H. Mondal, and P. Sibanda, "Lie group analysis of a Powell–Eyring nanofluid flow over a stretching surface with variable properties," *SN Applied Science*, vol. 2, 115, 2020.

[45] A. S. Idowu and B. O. Falodun, "Variable thermal conductivity and viscosity effects on non-Newtonian fluids flow through a vertical porous plate under Soret-Dufour influence," *Mathematics and Computers in Simulation*, vol. 177, pp. 358–384, 2020.

[46] P. Sanghera, *Quantum physics for scientists and technologists : fundamental principles and applications for biologists, chemists, computer scientists, and nanotechnologists*. John Wiley and Sons, New Jersey, 2011.

[47] D. Pal, "Hall current and MHD effects on heat transfer over an unsteady stretching permeable surface with thermal radiation," *Computers and Mathematics with Applications*, vol. 66, no. 7, pp. 1161–1180, 2013.

[48] D. Pal, "Heat and mass transfer in stagnation-point flow towards a stretching surface in the presence of buoyancy force and thermal radiation," *Meccanica*, vol. 44, pp. 145–158, 2009.

[49] I. S. Oyelakin, S. Mondal, and P. Sibanda, "Nonlinear radiation in bioconvective Casson nanofluid flow," *International Journal of Applied and Computational Mathematics*, vol. 5, 124, 2019.

[50] K. Gangadhar, D. Vijayakumar, A. J. Chamkha, T. Kannan, and G. Sakthivel, "Effects of Newtonian heating and thermal radiation on micropolar ferrofluid flow past a stretching surface: spectral quasilinearization method," *Heat Transfer*, vol. 49, no. 2, pp. 838–857, 2020.

[51] A. A. Afify, "Similarity solution in MHD: Effects of thermal diffusion and diffusion thermo on free convective heat and mass transfer over a stretching surface considering suction or injection," *Communications in Nonlinear Science and Numerical Simulation*, vol. 14, no. 5, pp. 2202–2214, 2009.

[52] R. Sharma, R. Bhargava, and P. Bhargava, "A numerical solution of unsteady MHD convection heat and mass transfer past a semi-infinite vertical porous moving plate using element free Galerkin method," *Computational Materials Science*, vol. 48, no. 3, pp. 537–543, 2010.

[53] J. Argyris and M. Haase, "An engineer's guide to soliton phenomena: Application of the finite element method," *Computer Methods in Applied Mechanics and Engineering*, vol. 61, no. 1, pp. 71–122, 1987.

[54] T. Cebeci and P. Bradshaw, "Finite-difference solution of boundary-layer equations," in *Physical and Computational Aspects of Convective Heat Transfer*, pp. 385–428, Springer, Berlin, Heidelberg, 1984.

[55] A. Asaithambi, "A second-order finite-difference method for the Falkner–Skan equation," *Applied Mathematics and Computation*, vol. 156, no. 3, pp. 779–786, 2004.

[56] S. S. Motsa, "A new spectral local linearization method for nonlinear boundary layer flow problems," *Journal of Applied Mathematics*, vol. 2013, pp. 1–15, 2013.

[57] D. Olmos and B. D. Shizgal, "A pseudo-spectral method of solution of Fisher's equation," *Journal of Computational and Applied Mathematics*, vol. 193, no. 1, pp. 219–242, 2006.

[58] A. Taleei and M. Dehghan, "A pseudo-spectral method that uses an overlapping multi-domain technique for the numerical solution of sine- Gordon equation in one and two spatial dimensions," *Mathematical Methods in the Applied Sciences*, vol. 37, no. 13, pp. 1909–1923, 2013.

[59] R. E. Bellman and R. E. Kalaba, *Quasilinearization and nonlinear boundary-value problems*. Santa Monica, CA: RAND Corporation, 1965.

[60] H. Mondal and S. Bharti, "Spectral quasilinearization for MHD nanofluid stagnation boundary layer flow due to a stretching/shrinking surface," *Journal of Applied Computational Mechanics*, vol. 6, no. 4, pp. 1058–1068, 2020.

[61] S. Das, H. Mondal, P. K. Kundu, and P. Sibanda, "Spectral quasi-linearization method for Casson fluid with homogeneous heterogeneous reaction in presence of nonlinear thermal radiation over an exponential stretching sheet," *Multidiscipline Modelling in Materials and Structures*, vol. 15, no. 2, pp. 398–417, 2019.

[62] I. Wubshet, "Spectral quasilinearisation method for solution of convective heating condition," *Engineering Transactions*, vol. 68, no. 1, pp. 69–87, 2020.

[63] S. S. Motsa, P. G. Dlamini, and M. Khumalo, "Spectral relaxation method and spectral quasilinearization method for solving unsteady boundary layer flow problems," *Advances in Mathematical Physics*, vol. 2014, pp. 1–12, 2014.

[64] S. S. Motsa, V. M. Magagula, and P. Sibanda, "A bivariate Chebyshev spectral collocation quasilinearisation method for nonlinear evolution parabolic equations," *The Scientific World Journal*, vol. 2014, pp. 1–13, 2014.

[65] V. M. Magaula, S. S. Motsa, and P. Sibanda, "A multi-domain bivariate pseudo-spectral method for evolution equations," *International Journal of Computational Methods*, vol. 14, no. 4,1750041, 2017.

[66] V. M. Magaula, S. S. Motsa, and P. Sibanda, "Multi-domain bivariate pseudo-spectral quasilinearisation method for systems of nonlinear partial differential equations," *Computational and Mathematical Methods*, vol. 2, no. 4, e1096, 2020.